JAERI-M
92-027

INDC(JPN)-157/L

PROCEEDINGS OF THE 1991 SYMPOSIUM ON NUCLEAR DATA

November 28-29, 1991, JAERI, Tokai, Ibaraki-ken, Japan

March 1992

(Eds.) Mamoru BABA* and Tsuneo NAKAGAWA

日本原子力研究所
Japan Atomic Energy Research Institute

JAERI-Mレポートは，日本原子力研究所が不定期に公刊している研究報告書です。
入手の問合わせは，日本原子力研究所技術情報部情報資料課（〒319-11茨城県那珂郡東海村）あて，お申しこしください。なお，このほかに財団法人原子力弘済会資料センター（〒319-11 茨城県那珂郡東海村日本原子力研究所内）で複写による実費頒布をおこなっております。

JAERI-M reports are issued irregularly.
Inquiries about availability of the reports should be addressed to Information Division Department of Technical Information, Japan Atomic Energy Research Institute, Tokai-mura, Naka-gun, Ibaraki-ken 319-11, Japan.

編集兼発行　日本原子力研究所
印　　刷　いばらき印刷㈱

JAERI-M 92-027

Proceedings of the 1991 Symposium on Nuclear Data November 28-29, 1991, JAERI, Tokai, Ibaraki-ken, Japan

(Eds.) Mamoru BABA* and Tsuneo NAKAGAWA

Japanese Nuclear Data Committee
Tokai Research Establishment
Japan Atomic Energy Research Institute
Tokai-mura, Naka-gun, Ibaraki-ken

(Received January 31, 1992)

The 1991 Symposium on Nuclear Data was held at Tokai Research Establishment, Japan Atomic Energy Research Institute (JAERI), on 28th and 29th of November, 1991. This symposium was organized by Japanese Nuclear Data Committee and Nuclear Data Center, JAERI. In the oral session, presented were 15 papers on nuclear data activities in Thailand, status reviews of JENDL-3 and its special purpose files, OMEGA program and ESNIT promoted by JAERI and related nuclear data, reviews of nuclear theories, nuclear data in the intermediate energy region, topics on knowledge technology and reactor physics. In the poster session, twenty-three papers were presented, which were related to nuclear data measurements, benchmark tests of evaluated data and evaluation. All of the 38 papers are compiled in the proceedings.

Keywords: Nuclear Data, Symposium, Proceedings, JENDL, Special Purpose Files, Nuclear Theory, OMEGA Program, ESNIT, Knowledge Technology, Measurements, Benchmark Tests, Evaluation

---

* Tohoku University

JAERI－M 92－027

１９９１年核データ研究会報文集

1991年11月28～29日，日本原子力研究所東海研究所

日本原子力研究所東海研究所
シグマ研究委員会
（編）馬場　護* ・中川　庸雄

（1992年１月31日受理）

1991年11月28日と29日の両日，日本原子力研究所東海研究所において「１９９１年核データ研究会」が開かれた。この研究会は，シグマ研究委員会と原研核データセンターにより開催されたものである。口頭発表では，タイにおける核データ活動，JENDL-3 とその特殊目的核データファイルの現状，原研が行っているオメガ計画やESNIT とそれに必要な核データ，原子核理論の解説，中高エネルギーにおける核データ，知識工学や炉物理の話題など15件の報告があった。ポスター発表では，23件の報告があり，それらは，核データの測定やベンチマークテスト，核データ評価に関するものであった。本報文集にはこれら全ての発表がまとめられている。

東海研究所：〒319-11　茨城県那珂郡東海村白方字白根2-4
＊東北大学

Program Committee

Mamoru Baba (Chairman)	(Tohoku University)
Satoshi Chiba	(Japan Atomic Energy Research Institute)
Tetsuo Iguchi	(University of Tokyo)
Jun-ichi Katakura	(Japan Atomic Energy Research Institute)
Norio Kishida	(CRC Research Institute, Inc.)
Hideo Kitazawa	(Tokyo Institute of Technology)
Kouichi Maki	(Energy Research Laboratory, Hitachi Ltd.)
Tsuneo Nakagawa	(Japan Atomic Energy Research Institute)
Ken Nakajima	(Japan Atomic Energy Research Institute)
Yutaka Nakajima	(Japan Atomic Energy Research Institute)
Naoki Yamano	(Sumitomo Atomic Energy Industries, Ltd.)

プログラム委員会

馬場　護（委員長）	（東北大学）
千葉　敏	（日本原子力研究所）
井口　哲夫	（東京大学）
片倉　純一	（日本原子力研究所）
岸田　則生	（㈱ＣＲＣ総合研究所）
北沢日出男	（東京工業大学）
真木　紘一	（日立製作所エネルギー研究所）
中川　庸雄	（日本原子力研究所）
中島　健	（日本原子力研究所）
中島　豊	（日本原子力研究所）
山野　直樹	（住友原子力工業㈱）

Contents

目　　次

1. PROGRAM OF 1991 SYMPOSIUM ON NUCLEAR DATA

The 1991 symposium on nuclear data was held at the JRR-1 building in Tokai Research Establishment of Japan Atomic Energy Reasearch Institute on 28th and 29th November 1991. A program of the symposium is listed below. Among the papers in the oral sessions, that of Kajino in Session 8 was not presented because he could not attend the symposium incidentally. Therefore, fourteen papers were presented at the oral sessions, and Session 8 was changed to the second poster session. However, his paper is included in this proceedings, since Kajino provided a manuscript of his talk. In the poster session which was held from 9:00 to 10:30 and from 13:00 to 13:45 on the second day, twenty-three papers were presented, which were related to nuclear data measurements, benchmark tests, and nuclear data evaluation. Those 15 papers in the oral sessions and 23 papers in the poster session are compiled in Chapters 2 and 3, respectively.

Program of the 1991 Symposium on Nuclear Data

Numbers in ( ) show time for presentation and discussion.

November 28 (Thursday)

11:00 ～ 11:05

1. Opening Address — M. Ishii(JAERI)

11:05 ～ 11:55

2. Topic 1 — Chairman: Y. Kikuchi(JAERI)

Nuclear Data Activities in Thailand (40+10 m)

T. Vilaithong(Chiang Mai Univ.)

11:55 ～ 13:00 Lunch

13:00 ～ 14:20

3. Present Status of JENDL-3 and Special Purpose Files — Chairman: Y. Nakajima(JAERI)

3.1 Present Status and Future Plan of JENDL-3 (15+5 m)

T. Nakagawa(JAERI)

3.2 Status of JENDL KERMA/PKA File (25+5 m)
○M. Kawai(Toshiba), T. Fukahori, S. Chiba(JAERI)
3.3 Evaluation of JENDL Fusion File (25+5 m)
○S. Chiba(JAERI), B. Yu(IAE), T. Fukahori(JAERI)

14:20 ～ 15:45
4. Topic 2 Chairman: M. Kawai(Toshiba)
4.1 OMEGA Program and Required Nuclear Data (35+10 m) H. Yoshida(JAERI)
4.2 Overview of ESNIT and Nuclear Data (30+10 m) M. Sugimoto(JAERI)

15:45 ～ 16:00 Coffee break

16:00 ～ 17:30
5. Progress of Nuclear Theory Chairman: H. Kitazawa(Tokyo Inst. Technol.)
5.1 Statistical Multi-step Process in Nuclear Reactions (40+10 m)
Y. Watanabe(Kyushu Univ.)
5.2 Theoretical Models for Calculation of Fission Neutron Spectra (30+10 m) T. Ohsawa(Kinki Univ.)

18:00 ～ 20:00 Reception

November 29 (Friday)
9:00 ～ 10:30
6. Poster Session (23 papers)

10:30 ～ 11:50
7. Nuclear Data in Intermediate and High Energy Regions
Chairman: N. Kishida(CRC)
7.1 Trend of Activity on Medium Energy Nuclear Data (30+10 m)
T. Nakamura(Tohoku Univ.)
7.2 Partial-Wave Analysis of High-Energy Neutron-Proton Scattering (30+10 m) ○N. Hoshizaki(Kyoto Univ.),
T. Watanabe(Tokyo Electric Power)

11:50 ～ 13:00 Lunch

13:00 ～ 13:45

8. Topic 3 Chairman: M. Igashira(Tokyo Inst. Technol.)

8.1 Growing Process of Primodial Universe and Nuclear Data (35+10 m)
T. Kajino(Tokyo Metropolitan Univ.)

----> This session was changed to poster session

13:45 ～ 15:00

9. Advanced Methods for Nuclear Data Evaluation
Chairman: T. Iguchi(Univ. Tokyo)

9.1 Advanced Techniques of Information Processing (35+10 m)
M. Kitamura(Tohoku Univ.)

9.2 A Guidance System for Nuclear Data Evaluation in Object Oriented Environment (25+5 m) S. Iwasaki(Tohoku Univ.)

15:00 ～ 15:15 Coffee break

15:15 ～ 16:20

10. Topics in Reactor Physics Chairman: A. Zukeran(Hitachi)

10.1 Thermal Reactor Benchmark Test of JENDL-3 (30+5 m)
○H. Takano(JAERI), LWR Integral Data Testing WG

10.2 Reactivity Scale for Reactor Physics Analysis
－ Present Status －(25+5 m) M. Nakano(JAERI)

16:20 ～ 16:30

11. Closing Address Y. Kanda(Kyushu Univ.)

2. PAPERS PRESENTED AT ORAL SESSION

2.1 TOPIC 1

2.1.1 NUCLEAR DATA ACTIVITIES IN THAILAND

Thiraphat Vilaithong

Fast Neutron Research Facility
Department of Physics, Faculty of Science

and

Institute for Science and Technology Research and Development
Chiang Mai University, Chiang Mai 50002, THAILAND

ABSTRACT

The Thai Research Reactor-1 (TRR-1) in Bangkok went critical for the first time in October 1962. This event initiated subsequent development of nuclear technology in Thailand. In 1972 a small 14 MeV neutron generator of modest flux was installed at Chiang Mai University. The (n,2n) cross sections from the reactions of 14.3 MeV neutrons with K-39, Fe-54, and Zr-90 were first measured with this neutron generator. The Fast Neutron Research Facility (FNRF) was subsequently established in 1984 with the aim to promote fast neutron studies. The main equipment consist of new medium-size neutron generator with a nanosecond pulsing system, contemporary spectrometers, based on or coupled to desktop computer. Various excitation functions of fast neutron induced reactions were studied. A program to measure and analyse 14 MeV neutron induced neutron emission cross sections was initiated and is at present being actively pursued.

The spectrum of nuclear data activities in Thailand shall be presented in this presentation.

1. Introduction

The Thai Research Reactor (TRR-1) in Bangkok went critical for the first time in October 1962. This event initiated subsequent development of nuclear science and technology in Thailand. In 1972, a small sealed tube neutron generator of modest flux was installed at Chiang Mai University/1/. While the reactor has been used primarily for isotope

production,neutron activation analysis and neutron radiography, the neutron generator was mainly utilised for teaching nuclear physics and fast neutron activation analysis. The (n,2n) cross sections from the reaction of 14.3 MeV neutrons with K-39, Fe-54, Zr-90 were measured for the first time in the country with this neutron generator/2/.

In 1982, the International Atomic Energy Agency (IAEA) supported the establishment of the Fast Neutron Research Facility (FNRF) at Chiang Mai University, with the aim to promote fast neutron studies, and to enable University staff and their students to conduct research on an advanced level. A program to measure and analyse fast neutron induced reaction cross sections was initiated at about the same time, with additional supports from Nuclear Data section of the IAEA and the International Program in Physical Science (IPPS), Uppsala University.

Activation cross sections were first measured in the range 13.84-14.70 MeV by the new drifted tube J25 neutron generator employing a non-analysed deuteron beam of 150 keV. An associated alpha-particle TOF spectrometer with moderate energy resolution was subsequently developed. A pulsed neutron machine was constructed by modifying an existing continuous beam generator to incorporate beam chopping and bunching devices. The project is now fully operational and provides a good quality pulsed neutron beam for double differential cross section measurement. At present FNRF is the only facility engaged in nuclear data activities in Thailand.

2. Nuclear data measurement

Nuclear data measurement program has been performed since the establishment of FNRF in 1984. In the beginning, the facility utilized a continuous beam 150 keV, 2.5 mA J25 electrostatic accelerator to produce 14 MeV neutrons for activation cross section measurement. A time-of-flight (TOF) method based on an associated particle and a pulsed beam were developed and implemented for nuclear data measurements.

2.1 Cross section measurement by activation method

In addition to check the reaction model the accurate knowledge of (n,p) reaction cross section curves of ^{27}Al and ^{28}Si is needed to unfold fast neutron spectra and to determine the neutron fluence in fusion experiments. Cross sections for the reactions $^{27}Al(n,p)^{27}Mg$ and $^{28}Si(n,p)^{28}Al$ were measured by activation method between 13.40 and 14.83 MeV neutron energy/3/. An accuracy of about 4% was achieved using the $^{27}Al(n,\alpha)^{24}Na$ where the relative excitation function was also measured. In the energy range from 13.84 to 14.70 MeV

Table 1 Measured values of (n,p) and (n,α) reaction cross sections on ^{27}Al and ^{28}Si around 14 MeV neutron energy

E_n(MeV)	$^{27}Al(n,\alpha)^{24}Na$ σ(mb)[b]	$^{27}Al(n,p)^{27}Mg$ σ(mb)[c]	$^{28}Si(n,p)^{28}Al$ σ(mb)[c]
14.83	111.9±1.2%	72.5	228.0
14.74	112.2	76.0	239.0
14.71[a]	113.9	75.1	245.2
14.62[a]	114.7	78.6	254.0
14.46	115.6	80.2	255.0
14.38[a]	118.1	75.2	260.1
14.01	122.0	84.0	270.0
14.07[a]	122.0	80.3	279.1
13.84[a]	122.9	85.2	292.0
13.74	124.4	89.0	302.0
13.48	127.1	93.0	315.0
13.40	126.4	91.0	320.0

[a] *Measured in Chiang Mai*
[b] *Accepting* $\sigma = 122.0$ *mb at* $E_n = 14.1$ *MeV*
[c] *Total error is* $\sim \pm 4\%$

irradiations were performed by the J25 neutron generator. Table 1 shows the results obtained for different neutron energies around 14 MeV. Fig.1 displays the relative cross section curve for the reaction $^{27}Al(n,\alpha)^{24}Na$. It has a flat region around 14.1 MeV. Therefore, this reaction can be considered as an excellent reference to determine the neutron fluxes around 14 MeV.

2.2 Associated particle time-of-flight measurement.

An associated alpha-particle time-of-flight (APTOF) neutron spectrometer was based on a 12.7 cm diam. x 5.1 cm thick liquid scintillator/4/. Neutrons were produced from an electrostatic accelerator by the $T(d,n)^4He$ reaction. The neutron generator was housed in a temperature and humidity controlled cage. The beam line is 2.50 meters above floor level. The low scattering experimental hall is 12 m by 12 m and 9.5 m high.

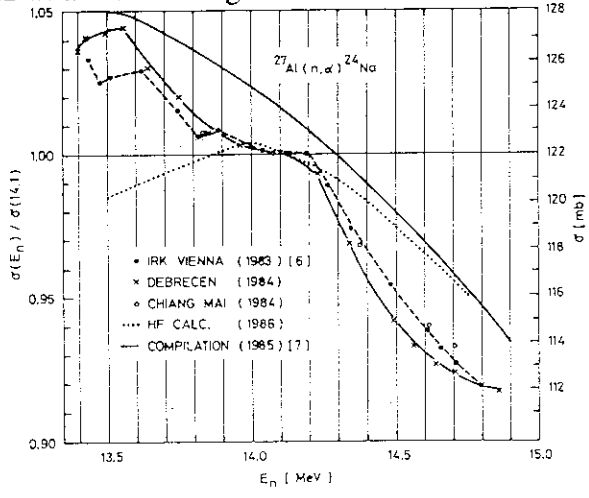

Fig. 1 Measured, evaluated and calculated excitation functions for the reaction $^{27}Al(n,\alpha)^{24}Na$ around 14 MeV.

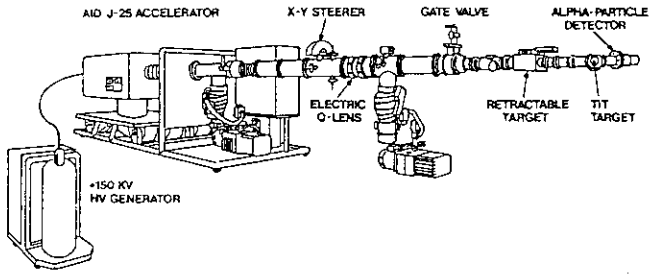

Fig. 2 Sketch of the modified J-25 accelerator, used in APTOF experiment.

A 140 keV continuous D^+ beam from the accelerator first passed through a 3 cm diam aperture of the first water-cooled copper slit, where the unfavorable diverse component of D^+ beam was taken out. The beam could be moved horizontally and vertically by X-Y deflectors. After leaving the Y-deflector, the beam entered an electrostatic quadrupole doublet which focuses it through another 3 cm diam aperture of the second water-cooled copper slit. A retractable target and a rotating probe were parts of the beam line up stream from the 45 degree target holder. Fig.2. shows a schematic diagram of the modified J-25 accelerator.

The neutron detector was placed inside a heavy movable shield as shown in Fig.3. A shadow bar made of iron, paraffin, and lead shielded the main neutron detector from direct

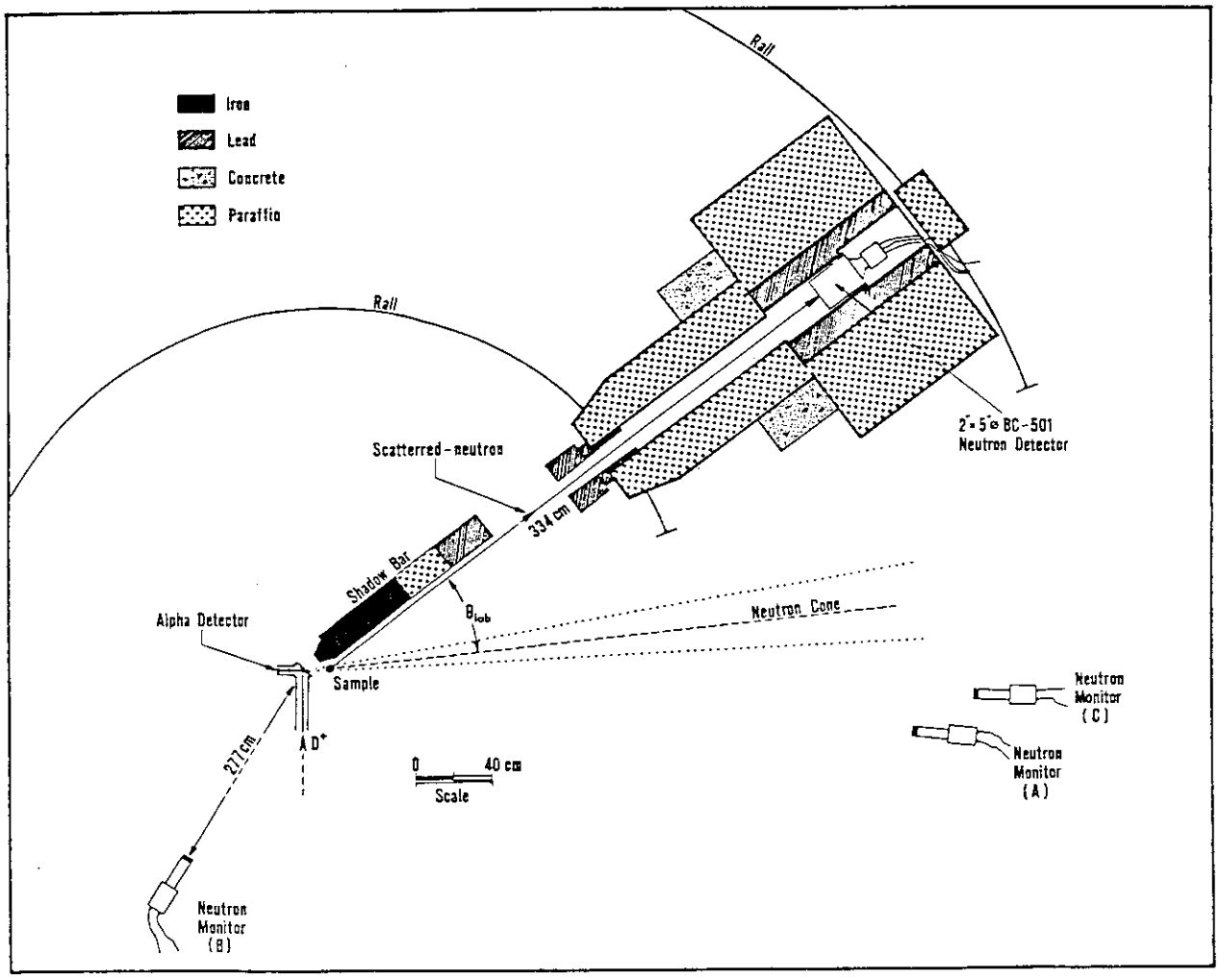

Fig. 3 Experimental arrangement of TOF measurement by associated particle method.

neutrons. This set up allowed the measurement of scattered neutrons from 15 degrees-155 degrees with a 3.34 m flight path.

A typical spectrum for carbon is shown is Fig.4. Data accumulation time was about 12 hours. Four peaks are observed clearly. The spectrum shows a time-independent (flat) background both before and after the region of interest. A sample out run also confirmed this time-independent nature. Time-of-flight spectra were measured in the angular range from 15 degrees to 155 degrees. Differential scattering cross sections to the ground state and the first excited state of carbon are shown in Fig.5 and Fig.6 respectively. Results of the measurements from carbon are also compared with data of Takahashi et al./5/ and the values recommended by Hansen/6/. The recommended set has been extracted from experiments carried out at various time-of-flight facilities since 1976. These measurements cover a range of incident neutron energies from 13.94 to 14.20 MeV.

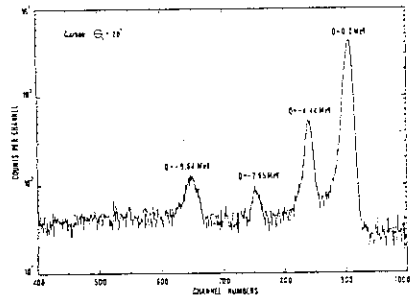

Fig. 4 TOF spectrum for scattering of 14.1 MeV neutrons from carbon.

2.3 Double differential neutron emission cross sections measurement

Since 1984 we have initiated a program to construct a pulsed neutron facility at the FNRF by modifying an existing continuous beam generator to incorporate beam chopping and bunching devices/7/. The design of the nanosecond pulsed beam line and related electronics system was adopted from the OKTAVIAN facility at the Osaka University in Japan. The schematic diagram shown in Fig.7 is a layout of the beam line components from the ion source to the target. A burst of

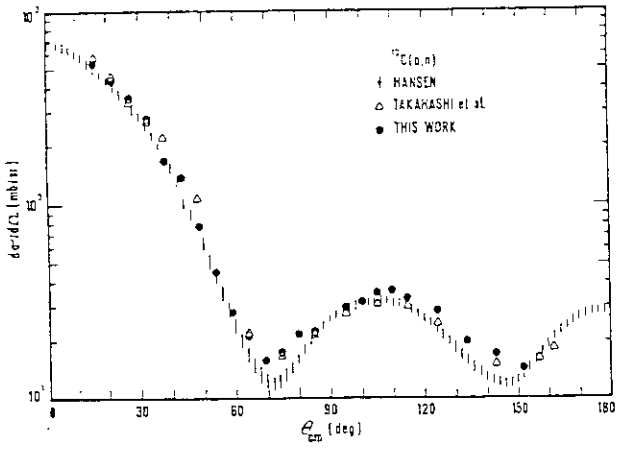

Fig. 5 Angular distributions for neutron elastic scattering by carbon at 14.1 MeV. The data of Takahashi et al.[5] and Hansen[6] are shown for comparison.

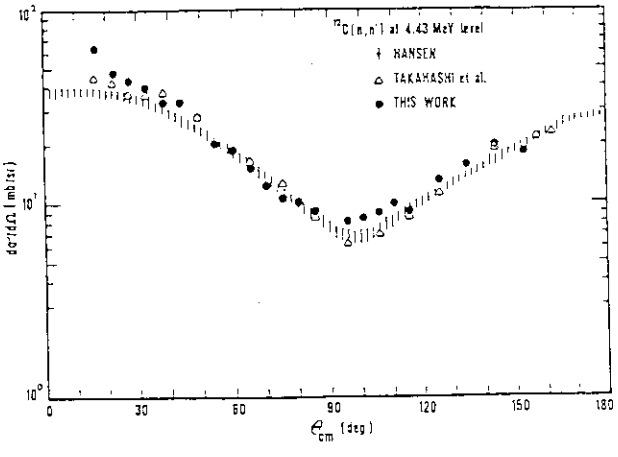

Fig. 6 Angular distributions for neutron inelastic scattering by carbon at 14.1 MeV. The data of Takahashi et al.[5] and Hansen[6] are shown for comparison.

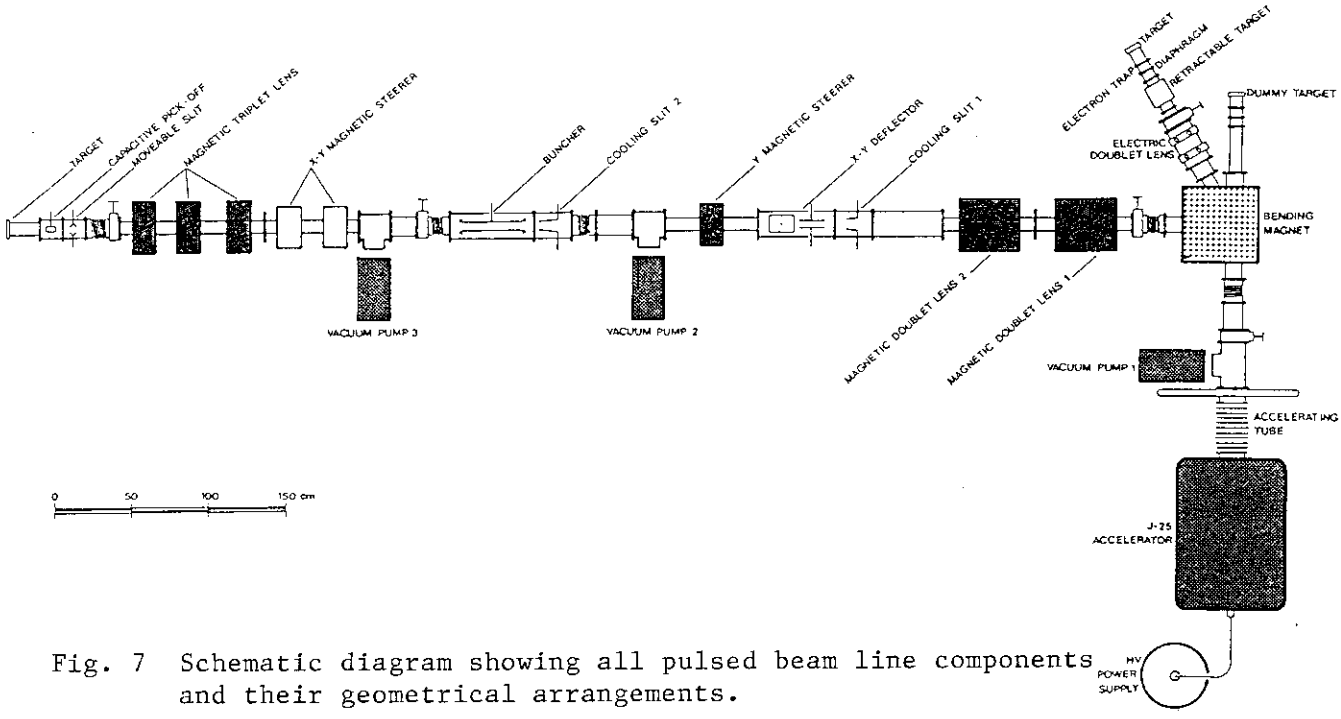

Fig. 7 Schematic diagram showing all pulsed beam line components and their geometrical arrangements.

deuterium ions incident on a tritium target produces a short pulse of neutrons from the D-T reaction. At a beam current of about 20 μA on target a neutron pulse of about 1.5 ns width at 2-MHz repetition rate is realised. For the present high-resolution neutron time-of-flight measurement, a BC-501 liquid scintillator of diameter 25.0 cm and thickness 10.0 cm is used. This main scintillator is coupled directly to a RCA 8854 photo-multiplier tube. The neutron detector is located at an extended flight path of 10 m inside a well-shielded underground tunnel. Collimating and shielding systems were constructed from various absorbing materials to minimize unwanted in-scattered backgrounds. The schematic diagram for the shielding and collimating systems are shown in Fig.8. A sample rotation technique provides the capability of measuring scattered neutrons over an angular range of 20 to 160 degrees.

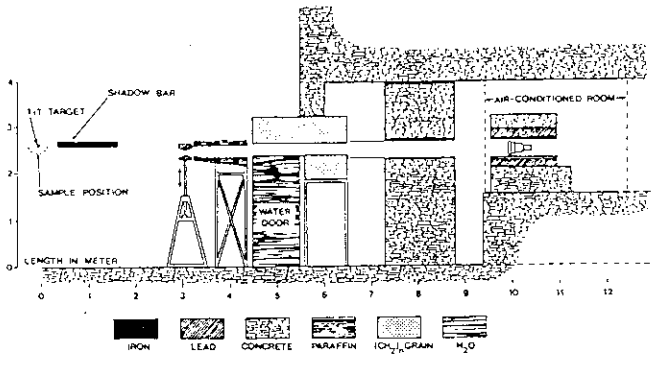

Fig. 8 Geometrical arrangement of the time-of-flight spectrometer.

The source neutron spectrum was measured and the result is shown in Fig.9. Typical double differential cross sections (DDX) data are shown in Fig.10(a) and Fig.10(b) for natural iron. The data of Takahashi et al./8/ from Osaka University, Baba et al./9/ from Tohoku University and JENDL-3/10/ are shown for comparison.

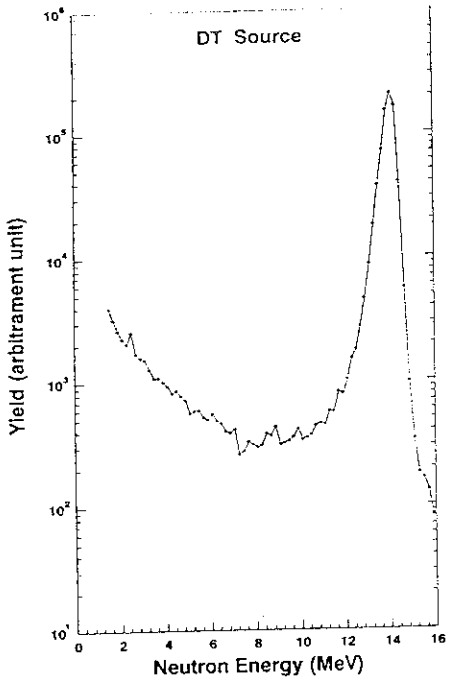

Fig. 9 Measured source neutron spectrum.

3. Nuclear data calculation

Work on nuclear reaction model calculation started at about the same time as an experimental program. The main emphasis at that time was on determining neutron optical model parameters for various nuclei which are candidates for structural materials of fusion reactor/11/. In this work mentioned, the neutron optical parameters for Ti, Va, Cr, Mn, Fe, Co and Ni were determined by fitting the experimental data of the cross sections and elastic scattering angular distributions for energies 1 keV to 30 MeV. Both SOM code GENOA and CCOM code JUPITOR-1 were

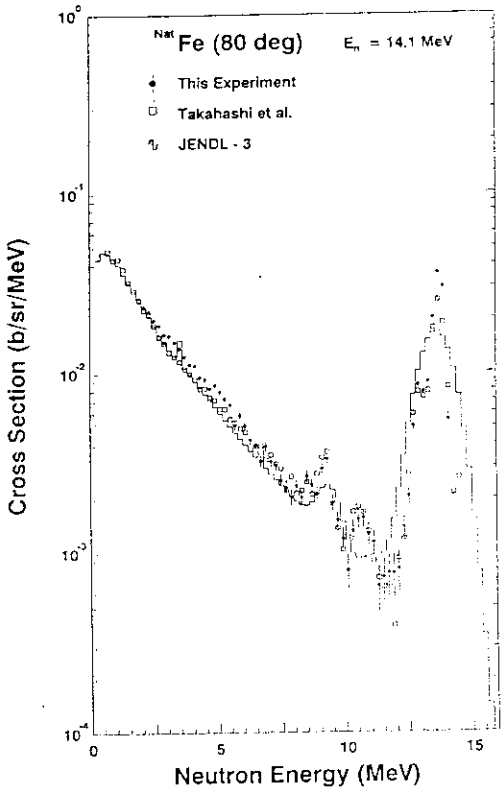

Fig. 10(a) Comparison of DDX spectrum of iron at 80° with other works.

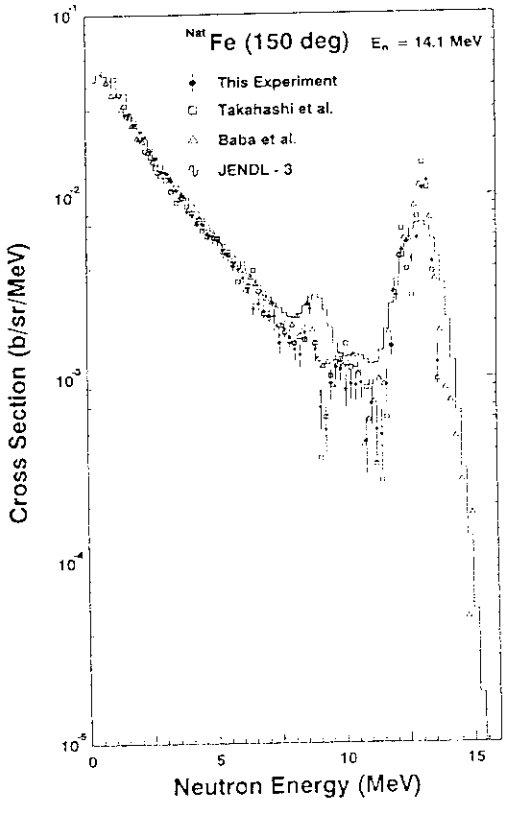

Fig. 10(b) Comparison of DDX spectrum of iron at 150° with other works.

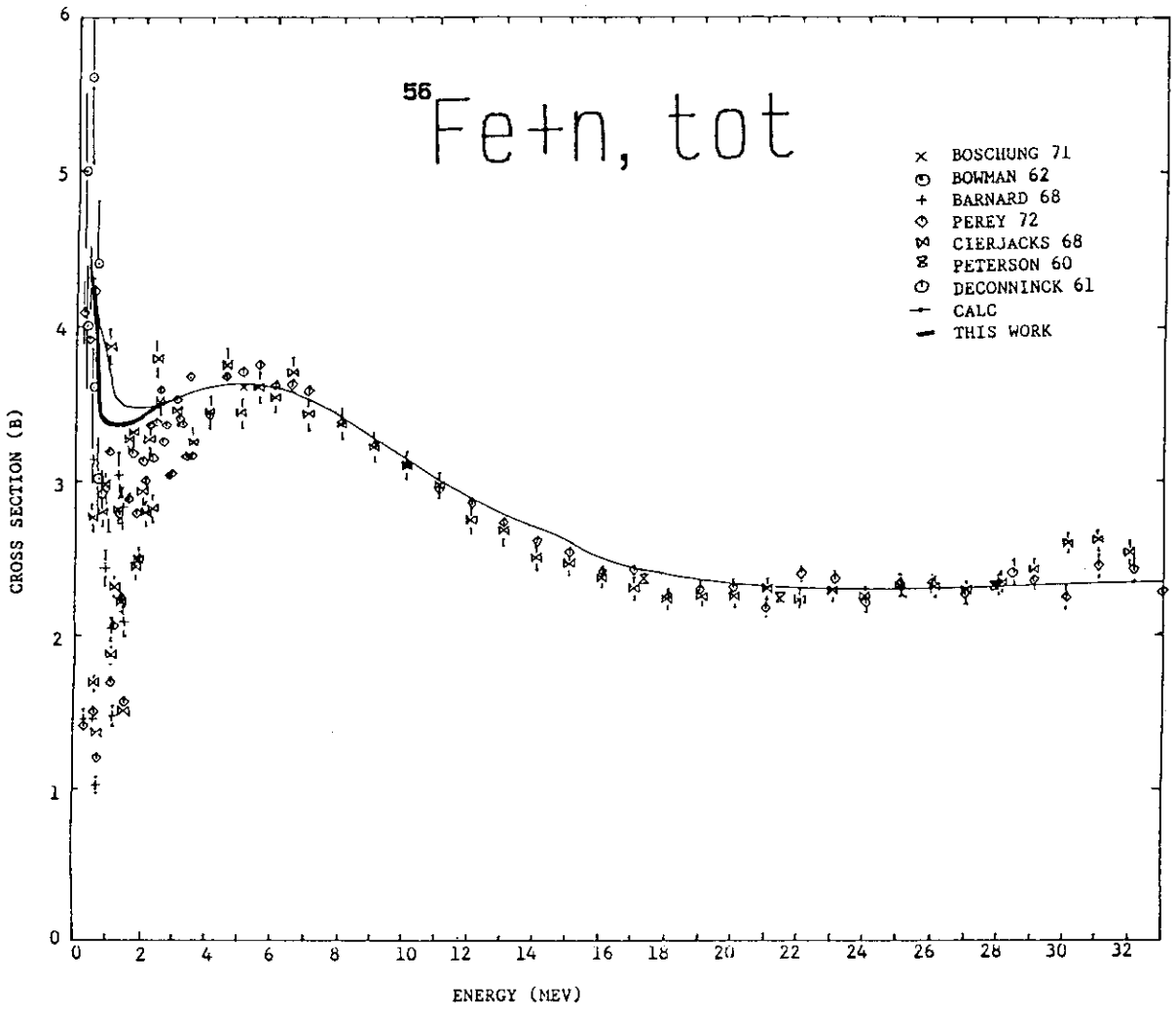

Fig. 11 Comparison of experimental and calculated total neutron cross sections for iron for various incident energies.

employed for various parameter searches. The total cross sections and the elastic angular distribution were then calculated with obtained optical model parameters. The comparison between the theoretical and the recommended experimental values for the total cross section of Fe is shown in Fig.11. A typical elastic angular distribution is displayed in Fig.12.

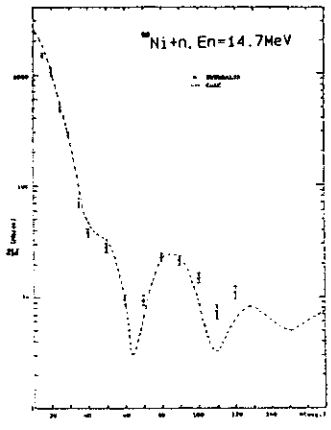

Fig. 12 Comparison of differential elastic scattering angular distribution for certain nuclei. Incident energies are already specified in the figures.

4. Future work plan

For our experimental work we shall continue with the DDX measurement for materials relevant to nuclear fusion reactor program. A high resolution TOF spectrometer with multi array detectors is being developed and should be ready for experiment in the second half of 1992. We hope to start analysing the neutron emission spectra based current-nuclear reaction models in the near future.

The author on behalf of the staff of FNRF wishes to thank professor A. Takahashi and Dr. H. Maekawa for their continuous supports. The assistance given by the Japan Atomic Energy Research Establishment through the STA program is gratefully acknowledged.

References

1. T. Vilaithong, D. Boonyawan, P. Chareonkwan, N. Chirapatpimol, G.G. Hoyes, S. Na-Chiang Mai, W. Pairsuwan, S. Singkarat, D. Suwannakachorn and V. Teeyasoontranon, *Two Decades of Fast Neutron Study at Chiang Mai, Report CPHY/FNRF*, July, 1991.
2. V. Teeyasoontranon, *M.S. Thesis*, Chiang Mai University, 1978.
3. J. Csikai, Zs. Lantos, S. Sudar, T. Chimoye, T. Vilaithong and N. Chirapatpimol, *Z. Phys*, A325, 69 (1986).
4. S. Singkarat, N. Chirapatpimol, D. Suwannakachorn, W. Pairsuwan, G.G Hoyes and T. Vilaithong, *Proceeding of the International Conference on Nuclear Data for Science and Technology (S. Igarasi, Ed.)* Mito, Japan, May 30 - June 3, 1988.
5. A. Takahashi, H. Sugimoto and E. Ichimura, *Proceedings of the International Conference on Fast Neutron Physics (D. Miljanic, Ed.)* Dubrovnik, Yugoslavia, May, 1986.
6. L.F. Hansen, *UCRL-95890*, 1986.
7. T. Vilaithong, S. Singkarat, W. Pairsuwan, J.F. Kral, D. Boonyawan, D. Suwannakachorn, S. Konklong, P. Kanjanarat and G. G. Hoyes, *Proceedings of the International Conference on Nuclear Data for Science and Technology (S.M. Qaims, Ed.)* Julich, Germany, May 1990.
8. A. Takahashi et al., *private communication*, 1991.
9. M. Baba et al., *private communication*, 1991.
10. S. Chiba, *as communicated by H. Maekawa*, 1991.
11. S. Wiboolsake, *Proceeding of the International Symposium on Fast Neutrons in Science and Technology (S. Wiboolsake and T. Vilaithong, Ed.)* Chiang Mai, Thailand, February, 1985.

2.2 PRESENT STATUS OF JENDL-3 AND SPECIAL PURPOSE FILES

2.2.1 PRESENT STATUS AND FUTURE PLAN OF JENDL-3

Tsuneo NAKAGAWA

Nuclear Data Center, Department of Physics
Japan Atomic Energy Research Institute
Tokai-mura, Naka-gun, Ibaraki-ken 319-11

The JENDL-3 revision 2 (JENDL-3.2) is being planned, because some drawbacks have been found in the current version of JENDL-3 (JENDL-3.1). In this presentation, the drawbacks of JENDL-3.1 are summarized. They will be modified, and JENDL-3.2 will be released at the end of March 1993. The present status of JENDL special purpose files is also described briefly.

1. Introduction

JENDL-3 was released in December 1989. This version[1] contains neutron data for 171 nuclides evaluated in the energy range from 10^{-5} eV to 20 MeV. In December 1990, the JENDL-3 revision 1 (JENDL-3.1) was released after adding the evaluated data for 172 fission product nuclides[2] and making corrections of some trivial compilation errors and incorrect neutron spectra near threshold energies revealed by Tian et al.[3]

In JENDL-3.1, the evaluated data are given for 324 nuclides in the ENDF-5 format with about 980,000 records. However, JENDL-3.1 has still drawbacks to be modified. Further modification will be made in a coming year and JENDL-3 revision 2 (JENDL-3.2) will be released presumably at the end of FY 1992 (the end of March 1993).

In the following sections, the drawbacks of JENDL-3.1 are summarized. In the final section, the present status of JENDL special purpose files is briefly described.

2. Double Differential Neutron Emission Cross Sections

Many efforts have been made for precise evaluation of the data around a neutron energy of 14 MeV, because one of main application areas of JENDL-3 is fusion neutronics. For this reason, the evaluation

was made to reproduce well the double differential cross sections (DDX) of emitted neutrons measured at Osaka University and Tohoku University. However, discrepancies between the measured DDX data and those calculated from JENDL-3 have been found for nuclides such as ^{9}Be, ^{14}N, ^{19}F, ^{27}Al, Ti, ^{59}Co, Zr, Mo, Ta, W, ^{209}Bi, etc. The direct inelastic scattering process has not been taken into account in the evaluation for some of them. Figure 1 gives an example of the DDX of Mo. The experimental data in the figure were measured by Takahashi et al.[4] at Osaka university. JENDL-3 cannot reproduce the experimental data in the secondary neutron energy range from 4 to 13 MeV, because the direct inelastic scattering was not considered in the evaluation.

The data for nuclides from ^{27}Al to ^{209}Bi are being modified for a JENDL Fusion File which will be reported by Chiba[5] at this symposium. The data of ^{14}N have been reevaluated by Kanda et al.[6] The JENDL-3.2 will adopt all or a part of these new evaluated data.

3. Total Cross Sections

Benchmark tests for fusion neutronics and shielding calculations indicated drawbacks of the total cross sections of C, O, Na and Fe.[7,8] The total cross section of Fe is shown in Fig. 2. The iron total cross section for JENDL-3 was evaluated[9] by mainly taking fine resolution experiments done by Carlson et al.[10] in this energy range. However, the shape of the total cross section for ENDF/B-IV[11] is much sharper than JENDL-3, and the ENDF/B-IV gives better results in the shielding benchmark tests[8] than JENDL-3. In the ENDF/B-VI evaluation, the experimental data measured at ORNL were adopted and the shape of cross section was refined. It seems to be better to adopt more narrow shape than the current JENDL-3 because even the high resolution measurements were broadened by its experimental resolution and the Doppler broadening effect.

For some light and medium weight nuclides, smooth total cross sections calculated with the optical model were adopted. They should be replaced with more reliable values based on experimental data showing fine structure.

4. Dosimetry Reactions

The JNDC Dosimetry Integral Test Working Group compiled the JENDL

Dosimetry File by mainly taking the cross section data from JENDL-3, and made benchmark calculations.[12] The benchmark test shows discrepancies between the JENDL-3 data and measured average cross sections. Figure 3 is an example of the comparison, in which average cross sections calculated from the JENDL Dosimetry File in the ^{252}Cf spontaneous fission neutron spectrum are compared with the measured values recommended by Mannhart[13]. From this figure, it is seen that the cross sections of $^{19}F(n,2n)^{18}F$, $^{24}Mg(n,p)^{24}Na$, $^{59}Co(n,\gamma)^{60}Co$, $^{60}Ni(n,p)^{60}Co$, $^{63}Cu(n,2n)^{62}Cu$ and $^{63}Cu(n,\gamma)^{64}Cu$ reactions are discrepant from the experimental data. Similar comparisons were made by using several standard neutron fields, and discrepancies were found for $^{45}Sc(n,\gamma)^{46}Sc$, $^{46}Ti(n,p)^{46}Sc$, $^{47}Ti(n,p)^{47}Sc$, $^{55}Mn(n,2n)^{54}Mn$, $^{54}Fe(n,p)^{54}Mn$, $^{58}Fe(n,\gamma)^{59}Fe$, $^{59}Co(n,2n)^{58}Co$, $^{58}Ni(n,\gamma)^{59}Ni$ and $^{63}Cu(n,\alpha)^{60}Co$ reactions.

5. γ-ray production cross sections

The γ-ray production cross sections are given for 59 nuclides in JENDL-3. Figure 4 shows the DDX of γ-rays emitted from Fe. JENDL-3 is obviously larger than the experimental data of Hasegawa et al.[14] and Chapman et al.[15] in the γ-ray energy range from 4 to 7 MeV. The data for Fe will be modified by considering these experimental data. These drawbacks might exist in the data for other nuclides. Further investigation is needed to identify the data to be modified.

6. Data of important actinides

The prompt fission neutron spectrum of ^{233}U should be revised, because incorrect level density parameters were used in the calculation with Madland-Nix formula[16]. The ^{238}U fission neutron spectrum is not in good agreement with that measured by Baba et al.[17]

The resolved resonance parameters adopted for important actinides in JENDL-3 are based on rather old evaluations. Table 1 compares resonance formula, range of resolved resonance region, number of resonance levels and upper boundary of the unresolved resonance region of JENDL-3, ENDF/B-VI and JEF-2 for ^{235}U, ^{238}U, ^{239}Pu and ^{241}Pu. In the case of ^{235}U, for example, the resolved resonance region and number of resonances of JENDL-3 is quite different from those of ENDF/B-VI and JEF-2. Background cross sections are given in JENDL-3, but not in ENDF/B-VI and JEF-2. The background cross sections are not

desirable for calculation of shielding factors. It is obvious that the evaluations for ENDF/B-VI and JEF-2 are superior to that for JENDL-3. In the case of ^{238}U and ^{241}Pu, the present status of JENDL-3 is almost the same as ^{235}U. The resonance parameters for these nuclides should be replaced with new evaluations. However, disadvantage of these precise evaluation is a long computing time for reconstruction of cross sections. For example, it takes about 1000 times longer CPU time to calculate the resonance cross sections of ^{235}U from ENDF/B-VI than the calculation from JENDL-3.

For ^{239}Pu, JENDL-3 adopted the parameters evaluated by Derrien et al.[18] After this evaluation, Derrien has continued further evaluation of resonance parameters of ^{239}Pu up to 2.5 keV[19]. He used transmission data measured by Harvey et al.[20] and fission cross section by Weston and Todd[21] at ORNL. The SAMMY code[22] based on the R-Matrix formula and Bayes' method was employed to fit the experimental data. Figure 5 shows the results in the energy range from 2.3 to 2.4 keV. The data of ^{239}Pu in JENDL-3 will be replaced with this new set of resonance parameters.

The upper boundary of the unresolved resonance region of ^{238}U is too low in JENDL-3. It should be extended up to 100 keV at least.

7. Working Groups for JENDL-3.2

The drawbacks of JENDL-3 mentioned above will be modified and JENDL-3.2 will be released in March 1993. In order to perform this modification, two working groups have been organized in JNDC: the Working Group for correction of heavy nuclide data and the Working Group for correction of γ-ray production data. The former will make reevaluation of data for important actinide nuclides, and will discuss reliability of reevaluated data with help of reactor physicists. The latter will investigate the current status of the γ-ray production data stored in JENDL-3, and make reevaluation and/or new evaluation of the data. Other working groups of JNDC are also expected to contribute to JENDL-3.2.

8. JENDL Special Purpose Files

The following two files were released in July 1991.

JENDL Dosimetry File[12]: Cross-section data were mainly taken from JENDL-3 and covariance matrices from IRDF-85. The data are

given for 61 reactions. The cross-section data are given separately in a group-wise file with 640 group structure and in a pointwise file.

JENDL Gas Production Cross-Section File: Data of p, d, t and α production cross sections were taken from JENDL-3 for 23 nuclides from Li to Mo.

Other special purpose files are under preparation.

JENDL Activation Cross Section File: This file will contain about 1000 activation cross sections.[23]

JENDL (α,n) Cross Section File: Data for 12 elements will be stored in this file. Compilation work is behind the schedule.

JENDL Decay Data File: Decay data are taken from JNDC FP Decay Data Library 2 and ENSDF for about 2000 nuclides.

JENDL Fusion File: DDX data for 21 elements from Al to Bi important for fusion neutronics are represented with MF6 of the ENDF-6 format. The present status is explained by Chiba[5] in this symposium.

JENDL KERMA/PKA File: This file is being made by the JNDC PKA Spectrum Working Group, and will consist of data up to 50 MeV for 48 materials. The pesent status is described by Kawai[24] in this symposium.

JENDL Photo Reaction File: Evaluation of data for 30 element in the energy range up to 140 MeV is under way in the JNDC Photonuclear Data Working Group.[25]

JENDL Actinide File: This is a file for evaluation of isotope production and depletion of actinide nuclides.

According to the present schedule, these files will be available in FY 1992 or FY 1993 except the JENDL Actinide File which will be compiled after JENDL-3.2.

References

1) Shibata K., Nakagawa T., Asami T., Fukahori T., Narita T., Chiba S., Mizumoto M., Hasegawa A., Kikuchi Y., Nakajima Y., and Igarasi S.: "Japanese Evaluated Nuclear Data Library, Version-3", JAERI 1319 (1990).

2) Kawai M., Iijima S., Nakagawa T., Nakajima Y., Sugi T., Watanabe T., Matsunobu H., Sasaki M., and Zukeran A.: submitted to J. Nucl.

Sci. Technol.

3) Tian D., Hasegawa A., Nakagawa T., and Kikuchi Y.: Proc. 1991 Symposium on Nuclear Data, JAERI-M 91-032, p.148 (1991).

4) Takahashi A., Sugimoto H., Gotoh M., Yamanaka K., Kanazawa H., and Maekawa F.: "Measurement of Double Differential Neutron Emission Cross Sections at 14.1 MeV for Ti, Mo and Sn", JAERI-M 90-220 (1990).

5) Chiba S., Yu B., and Fukahori T.: "Evaluation of JENDL Fusion File", presented at this symposium.

6) Kanda Y., Murata T., Nakajima Y., and Asami T.: Proc. 1991 Symposium on Nuclear Data, JAERI-M 91-032, p.376 (1991).

7) Oyama Y., and Maekawa H.: Proc. 2nd Specialists' Meeting on Nuclear Data for Fusion Reactors, JAERI-M 91-062, p.228 (1991).

8) Kawai M., Hasegawa A., Ueki K., Yamano N., Sasaki K., Matsumoto Y., Takemura M., Ohtani N., and Sakurai K.: "Shielding Benchmark Test of JENDL-3", to be published as JAERI report.

9) Iijima S., Asami T., Shibata K., and Yamakoshi H.: Proc. Conf. on Nuclear Data for Science and Technology, Mito, May 30 - June 3, 1988, p.627 (1988).

10) Carlson A.D., and Cerbone R.J.: Nucl. Sci. Eng., 42, 28 (1970).

11) Fu C.Y., and Perey F.G.: "ENDF/B Summary Documentation", BNL 17541, (1975).

12) Nakazawa M., Kobayashi K., Iwasaki S., Iguchi T., Sakurai K., Ikeda Y., and Nakagawa T.: "JENDL Dosimetry File", to be published as JAERI report.

13) Mannhart W.: "Handbook on Nuclear Data", IAEA Technical Reports Series No.273, p.413 (1987).

14) Hasegawa K., Mizumoto M., Chiba S., Sugimoto M., Yamanouti Y., Igashira M., and Kitazawa H.: Proc. Conf. on Nuclear Data for Science and Technology, Juelich, May 13 - 17, 1991 (to be published).

15) Chapman G.T., Morgan G.L., Perey F.G.: "Re-measurement of the Neutron-induced Gamma-ray Production Cross Sections for Iron in the Energy Range 850 $\leqq E_n \leqq$ 20 MeV", ORNL/TM-5416 (1976).

16) Madland D.G., and Nix J.R.; Nucl. Sci. Eng., 81, 213 (1982).

17) Baba M., Wakabayashi H., Ito N., Maeda K., and Hirakawa N.: J. Nucl. Sci. Technol., 27, 601 (1990).

18) Derrien H., de Saussure G., and Perez R.B.: Nucl. Sci. Eng., 106, 434 (1990).

19) Derrien H.: to be published.

20) Harvey J.A., Hill N.W., and Perey F.G.: Proc. Conf. on Nuclear Data for Science and Technology, Mito, May 30 - June 3, 1988, p.115 (1988).
21) Weston L.W., and Todd J.H.: private communication.
22) Larson N.M.: "Updated Users' Guide for SAMMY: Multilevel R-Matrix Fit to Neutron Data Using Bayes' Equations", ORNL/TM-9179/R1 (1985).
23) Nakajima Y.: Proc. 1991 Symposium on Nuclear Data, JAERI-M 91-032, p.43 (1991).
24) Kawai M., Fukahori T., and Chiba S.: "Status of JENDL KERMA/PKA File", presented at this symposium.
25) Kishida N.: Proc. 1991 Symposium on Nuclear Data, JAERI-M 91-032, p.58 (1991).

Table 1 Comparison of resonance parameters

Nuclide	JENDL-3	ENDF/B-VI	JEF-2
U-235	SLBW 1 - 100 eV 148 res 30 keV	R-M 0 - 2.25 keV 3355 res 25 keV	R-M 0.15eV - 2.25keV 3355 res 25 keV
U-238	MLBW 0 - 9.5 keV 841 res 50 keV	R-M 0 - 10 keV 1913 res 149.5 keV	R-M 0 - 10 keV 1653 res 300 keV
Pu-239	R-M 0 - 1 keV 393 res 30 keV	R-M 0 - 2 keV 787 res 30 keV	R-M 0 - 1 keV 393 res 30 keV
Pu-241	SLBW 0 - 100 eV 92 res 30 keV	R-M 0 - 300 eV 243 res 40.2 keV	R-M 0 - 300 eV 243 res 162.2 keV

In each box, the following are given from the top:

Resonance formula

SLBW: Single-Level Breit-Wigner formula

MLBW: Multilevel Breit-Wigner formula

R-M: Reich-Moore multilevel formula

Energy range of the resolved resonance region

Number of resolved resonances

Upper boundary of the unresolved resonance region

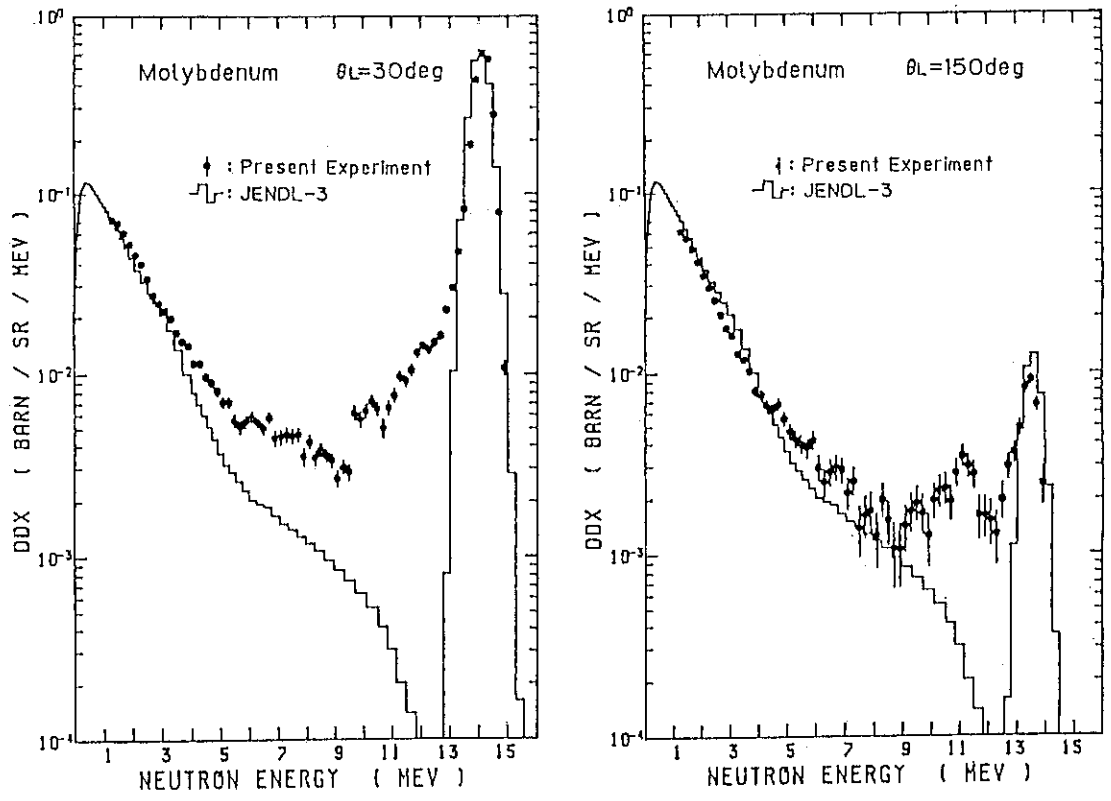

Fig. 1 DDX of neutrons emitted from Mo. These figures were taken from Ref. 4.

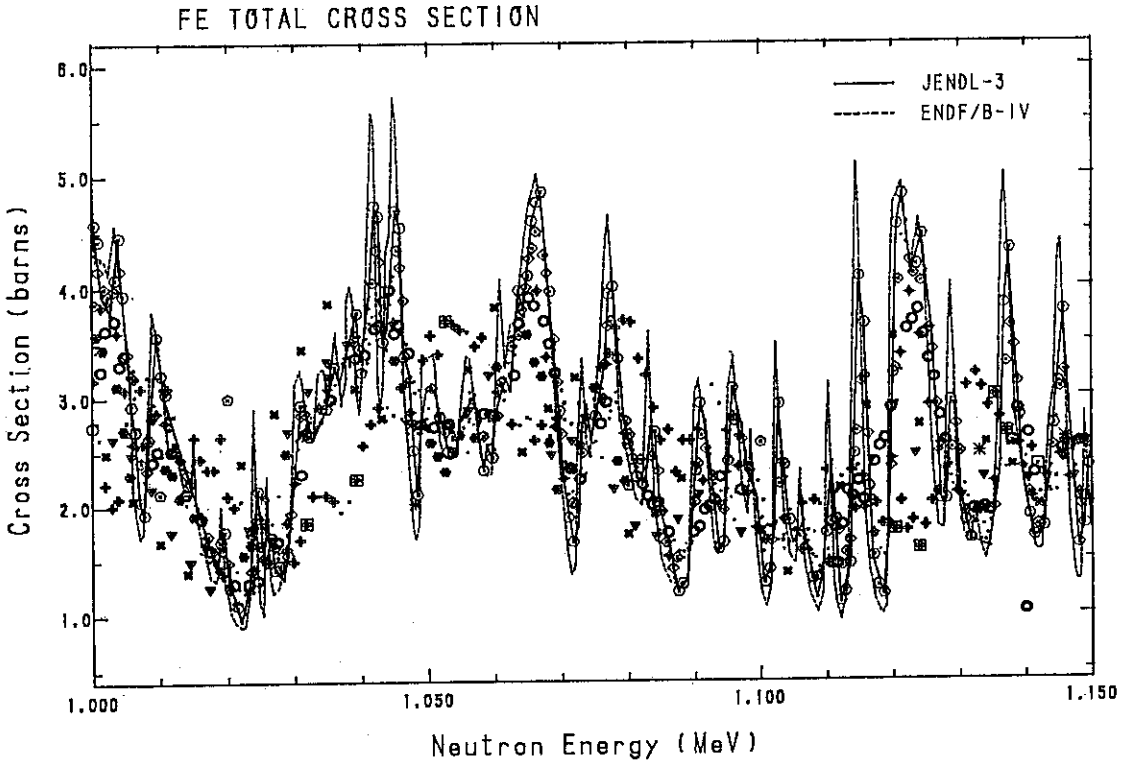

Fig. 2 Total cross section of Fe.

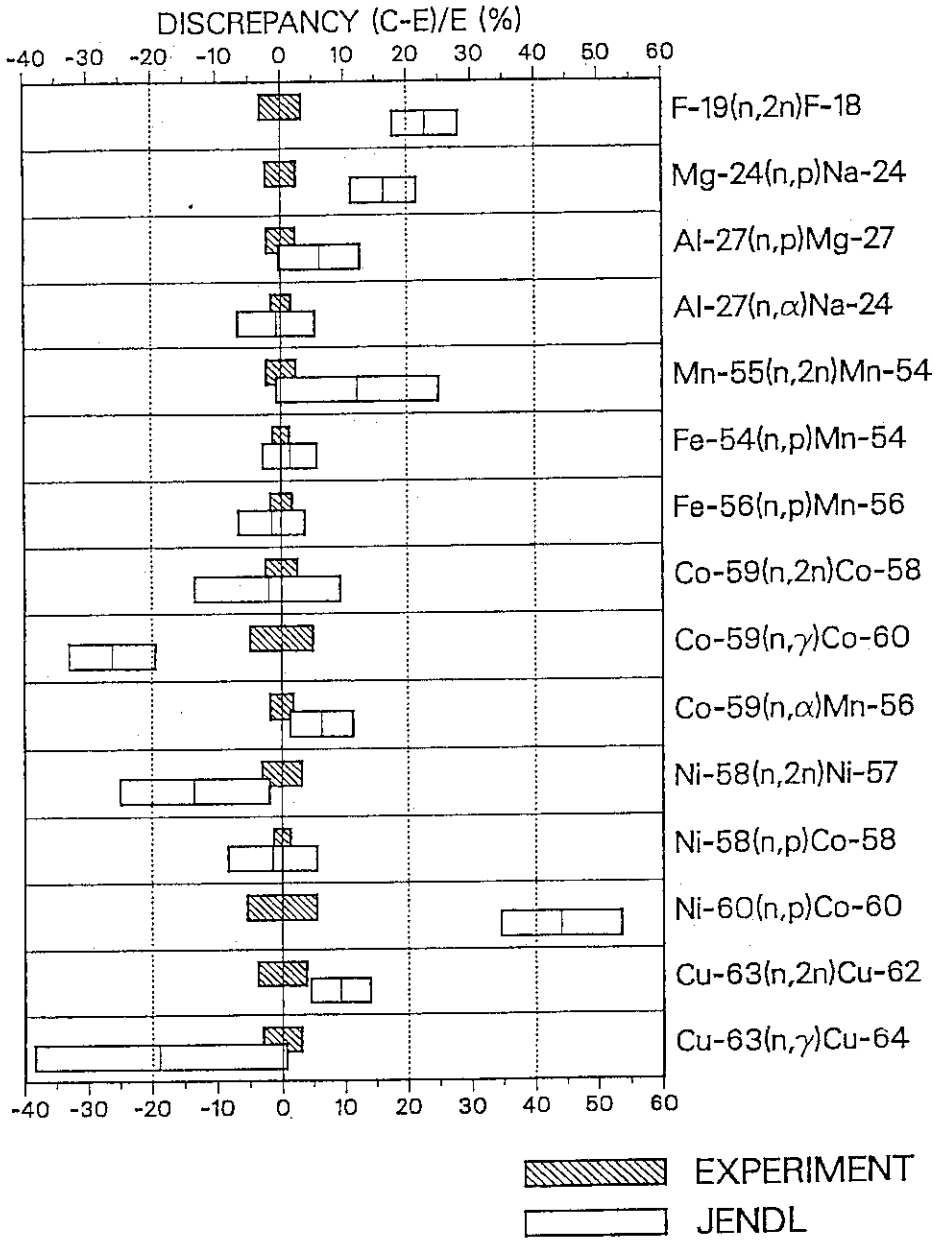

Fig. 3 Comparison of average cross sections in the ^{252}Cf spontaneous fission neutron fields. Discrepancies are calculated as $(\sigma_{cal} - \sigma_{exp})/\sigma_{exp} \times 100$, where σ_{cal} is calculated from JENDL-3 and σ_{exp} experimental data recommended by Mannhart[13]. The center of each open box corresponds to the discrepancy from the experimental data. Errors (1σ) of the calculated data, expressed by width of the open boxes, were estimated from the covariance matrices of the JENDL Dosimetry File and the ^{252}Cf spontaneous fission neutron spectrum. Width of the shaded boxes shows errors of the experimental data.

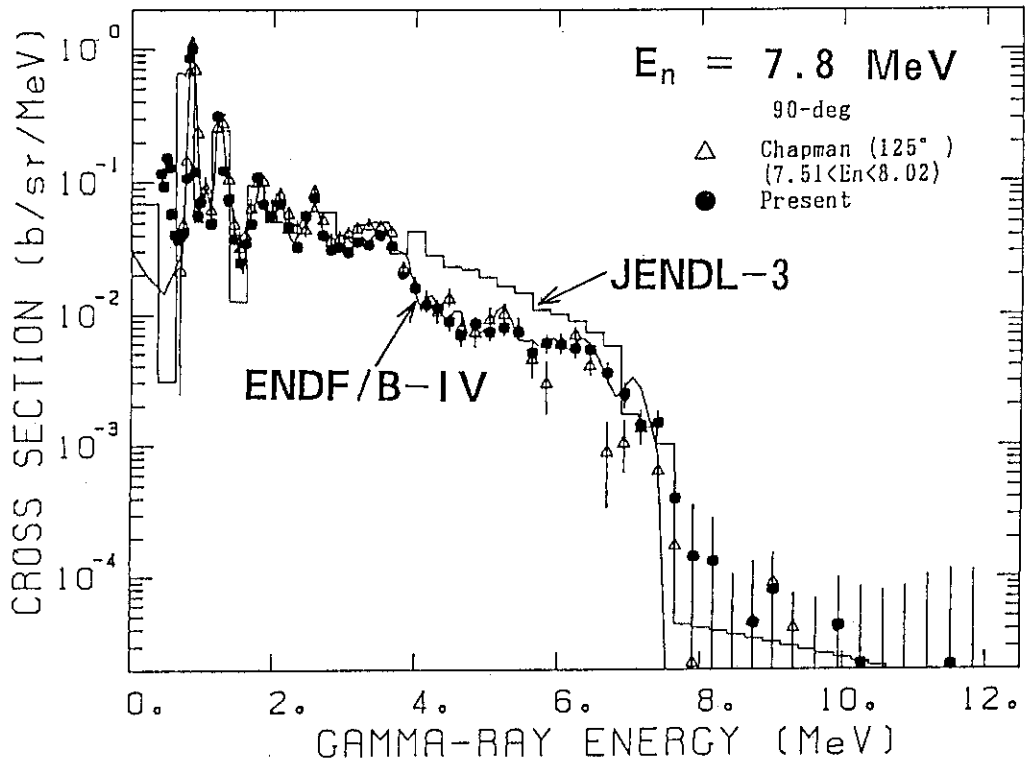

Fig. 4 DDX of γ-rays from Fe. Solid circles are the data measured by Hasegawa et al.[14] and triangles are those measured by Chapman et al.[15]

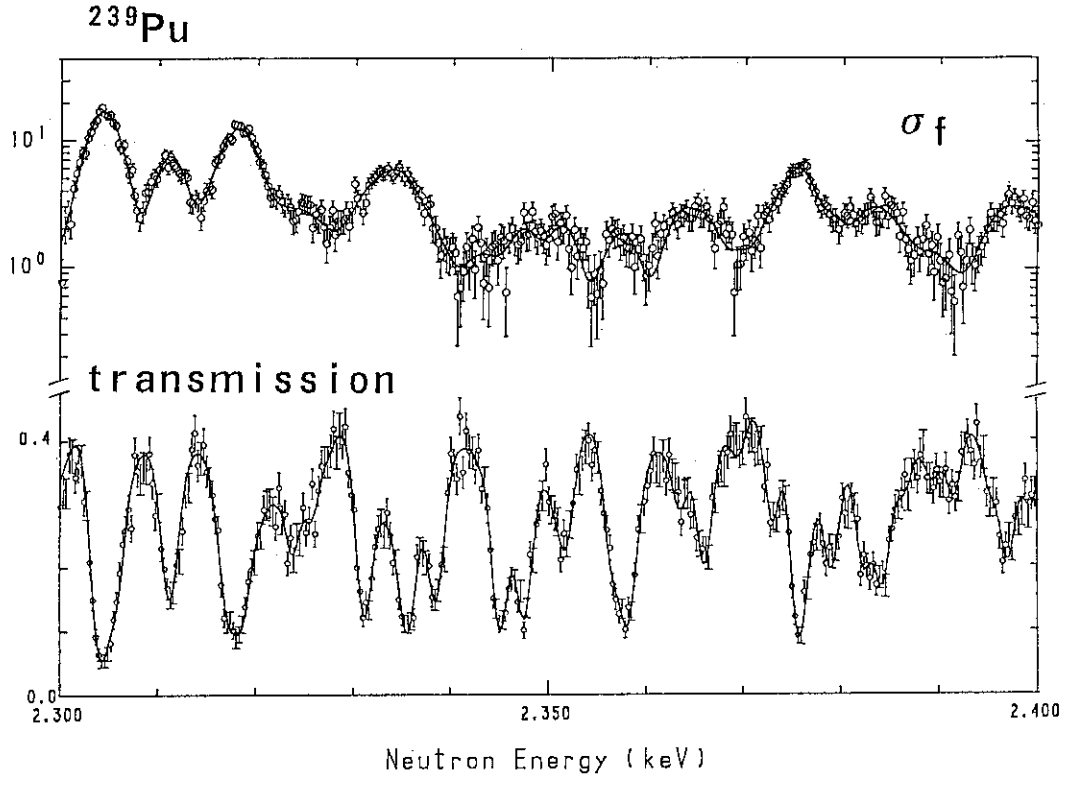

Fig. 5 An example of R-matrix fit by Derrien[19]. The fission cross section was measured by Weston and Todd[21], and the transmission by Harvey et al.[20]

2.2.2 STATUS OF JENDL KERMA/PKA FILE*

M. Kawai
Nuclear Enginnering Laboratory, Toshiba Corporation
4-1 Ukishima-cho, Kawasaki-ku, Kawasaki 210

T. Fukahori and S. Chiba
Nuclear Data Center, Japan Atomic Energy Research Institute
Tokai-mura, Naka-gun, Ibaraki 319-11

The JENDL KERMA/PKA file is one of the special purpose files of JENDL, giving the cross section data for neutron radiation damage studies. Two codes, PKAR and KERMA, have been developed to generate the file by processing the composite spectra of emitted neutron and charged particles with the effective single particle emission model. The calculated results for iron generally agree with those of the Monte Carlo method which is based on the exciton and evaporation models for PKA spectra and with those calculated by Howerton et al. for KERMA factors. Future scope of the file generation is also described.

1. Introduction

The present work is made to generate the JENDL-based libray containing PKA (primary knock-on atom) spectra, KERMA (kinetic energy rereased in material) factors and DPA (displacement per atom) cross sections in the neutron energy region between 10^{-5} eV and 50 MeV. Recently, urgent data needs are raised from the various kinds of fields as follows: PKA spectra for radiation damage studies, represented by ESNIT project[1], KERMA factors and DPA cross sections for nuclear plant designs concerning nuclear heating estimation and radiation damage estimation, KERMA factors

---

N.B. *) The work is made as one of the activities of PKA Spectrum Working Group of JNDC. The working group members are T. Aruga, T. Fukahori, T. Sugi, Y. Yamanouti (JAERI), K. Maki (Hitachi), N. Yamano (SAEI), K. Kitao (NIRS), A. Takahashi (Osaka Univ.) and M. Kawai (Toshiba). Collabaration is also made by S. Chiba (JAERI) and N. Kishida (CRC).

for radiation dosimetry, PKA spectra and KERMA factors for health physics and medical applications such as neutron therapy, and PKA spectra for space applications. The energy integrated quantities such as KERMA factors and DPA cross sections can be calculated with simplified formula[2], but the PKA spectra can be obtained by processing the energy-and-angle dependent doubly differential cross sections (DDX).
Therefore, new processing codes have been developed and tested for calculation of PKA spectra as well as KERMA factors. The codes will be applied to generate the data library.

2. Scope of the File

The JENDL KERMA/PKA file will be generated with the following scopes:
(1) Covered neutron energy range is from 10^{-5} eV to 50 MeV. The maximum energy of 50 MeV is required from the ESNIT project.
(2) The file is composed of primary and secondary files. The former contains resonance parameters, reaction cross sections, particle production cross sections, PKA spectra (DDX), and damage energy spectra (EDX). The latter has KERMA factors and DPA cross sections.
(3) The ENDF-6 format is adopted to treat DDX data and EDX of charged particles and PKA.
(4) PKA spectra are calculated by processing the evaluated or calculated nuclear data such as JENDL-3. The high energy neutron cross sections and charged particle spectra are calculated with the GNASH code[8].
(5) High energy reactions have many open channel. It is diffiucult to treat the kinematics of these reaction channels unless the PKA calculation is made simultaneously with the cross section calculations.
Accordingly, the following approximations are adopted:

(a) To process the composite continuum spectra for n, p, d, t, ^{3}He, α and photon. Binary rections such as elastic and discrete inelastic scattering are separately treated.

(b) Energy-and-angular correlation of particles in continuum was assumed to obey the systematics of Kumabe[4] or Kalbach[5].

(c) Effective single particle emission model to disregard low energy particle likely emitted through multiple step processes.

Then, the PKA spectrum for the composite particle x is expressed by

$$\sigma_x(E_n, E_p, \theta_p) = \frac{(M/m_1)^{3/2} E_p \varepsilon_x \sigma_{x\text{-prod}}(E_n, \varepsilon_x, \theta_x)}{\sum_x \int_{\varepsilon_{x(min)}} d\varepsilon_x \int d\theta_x \sigma_{x\text{-prod}}(E_n, \varepsilon_x, \theta_x)/\sigma_{cont}(E_n)}$$

where,

$\sigma_{x\text{-prod}}(E_n, \varepsilon_x, \theta_x)$: x-particle production cross section for incident neutron energy E_n,

σ_{cont}: summation of continuum particle emission cross section,

M, m_1: masses of emitted particle and compound nucleus, respectively,

$\varepsilon_{x(min)}$: lower energy limit of integration to satisfy the energy conservation in effective single particle emission model (typical example is illustrated in Fig. 1),

θ_x, θ_p: scattering angles for emitted particle and recoiled atom (PKA), respectively,

E_p: energy of recoiled atom.

(6) KERMA factors and DPA cross sections are calculated by integrating thus obtained PKA spectra.

3. Present Status

Processing codes, PKAR and KERMA have been developed and its testing is in progress by comparing the calculated results with the reference calculations. Figure 2 shows the flow chart generating the KERMA/PKA file in the present system. JENDL-3 provides the base neutron reaction cross sections up to 20 MeV and GNASH does composite spectra up to 50 MeV. Test calculations were made for iron.

The comparison of PKA spectrum was made between PKAR and MCEXCITON[6]. The latter is the Monte Carlo code based on the exciton model considering composite particle emission by Iwamoto-Harada[7] and evaporation model; in the calculation, particle emission was assumed to be isotropic in the center of mass system. Figure 3 shows the calculated results for total PKA spectra for 10 MeV neutron incidence. Good agreement is observed in lower energy spectrum which is contributed by neutron emission reactions. Large discrepancy above 8 MeV is attributed to the difference of angular distributions of alpha particle emitted from (n, α) reaction, as shown in Fig. 4.

For KERMA factors, general agreement is also obtained with the direct calculation by Howerton et al.[8] and Caswell[9], as shown in Fig. 5.

4. Conclusion

A code system generating KERMA/PKA library has been developed. Test calculations for iron shows that a general agreement is obtained with those by Monte Carlo calculation for PKA spectra and by Howerton and Caswell for KERMA factors. Large discrepancy of PKA spectrum for alpha particle may come from the difference of anisotropy and spectrum of alpha particle due to the different models and nuclear model parameters. Thus, the code is expected to give practical data even in the energy region above 20 MeV as well as lower energy region. The file will be generated in these 3 fiscal years. It will contain the following materials as much as posible: ^{1}H, ^{2}D, ^{6}Li, ^{7}Li, ^{9}Be, ^{10}B, ^{11}B, ^{12}C, ^{14}N, ^{16}O, ^{19}F, ^{23}Na, Mg, ^{27}Al, Si, P, S, Cl, K, Ca, Ti, V, Cr, ^{55}Mn, Fe, ^{59}Co, Ni, Cu, Ge, Ga, ^{75}As, ^{89}Y, Zr, ^{93}Nb, Mo, Ag, Cd, Sn, Sb, Ba, Eu, Gd, Hf, ^{181}Ta, W, ^{197}Au, Pb and Bi.

Acknowledgements:

The authors would like to thank Dr. N. Kishida for his kind offering his data calculated with the MCEXCITON code.

References:

(1) Kondo, T. et al.: J. Fusion Energy, 8, 229 (1989)

(2) Iijima, S. and Kawai, M.: J. Nucl. Sci. Technol., 27, 375 (1990).

(3) Young, P.G. and Arthur, E.D.: "GNASH: A Preequilibrium, Statistical Nuclear Model Code for Calculation of Cross Sections and Emission Spectra", LA-6947 (1977).

(4) Kumabe, I. et al.: Nucl. Sci. Eng., 104, 280 (1990).

(5) Kalbach, C.: Phys. Rev., C37, 2350 (1988).

(6) Kishida, N. and Kadotani, H.: "Onthe Validity of the Intranuclear Cascade and Evaporation Model for High-Energy Proton Induced Reactions", Proc. of Nuclear Data for Science and Technology, 1988 Mito, p. 1209 (1988) JAERI; see also Kishida, N. et al.: "Evaluation for IC Single Event Upset Rate Using Charged Particle Nuclear Data [in Japanese]", 1990 AESJ Fall Meet. B8 (1990)

(7) Iwamoto, A. and Harada, K.: Phys. Rev., C28, 1821 (1982).

(8) Howerton, R.J.: "Calculated Neutron KERMA Factors Based on the LLNL ENDL Data File", UCRL-50400, Vol. 27 (1986).

(9) Caswell, R.S., et al.: Radiation Research, 83, 217 (1980).

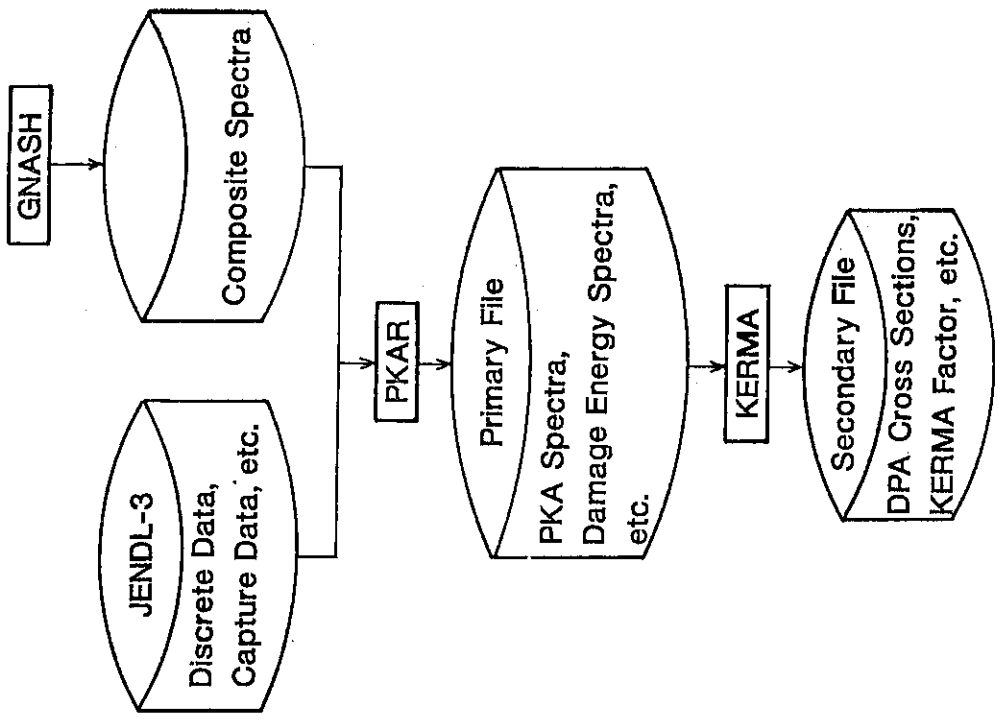

Fig. 2 System of file generation.

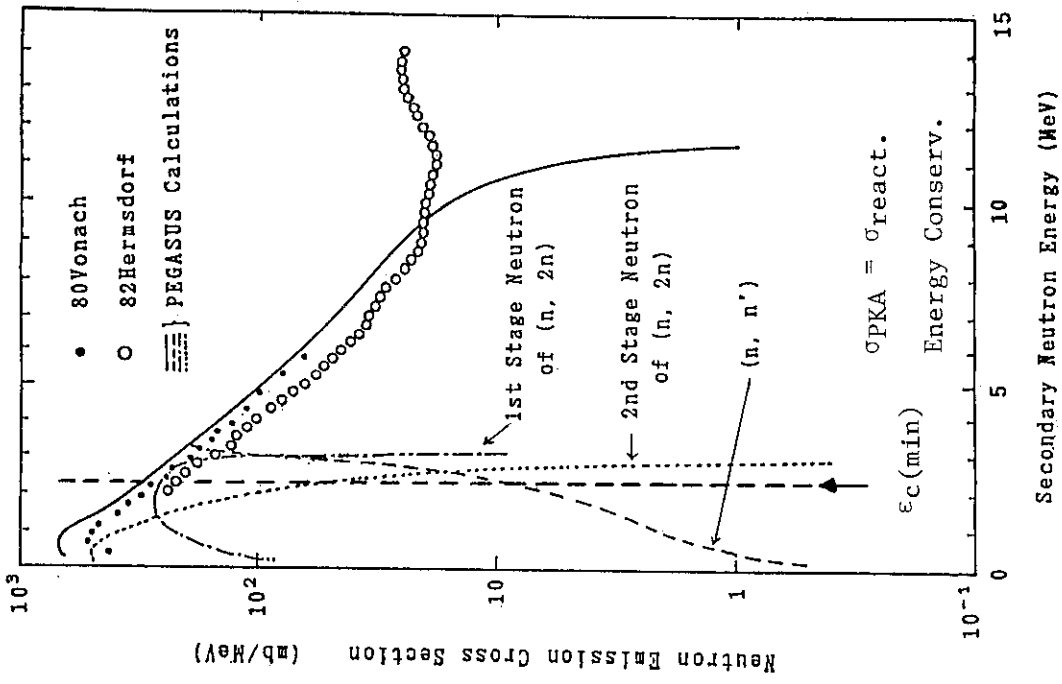

Fig. 1 Illustration of lower energy limit of integration of neutron spectra in case of 14 MeV neutron incidence reaction for iron.

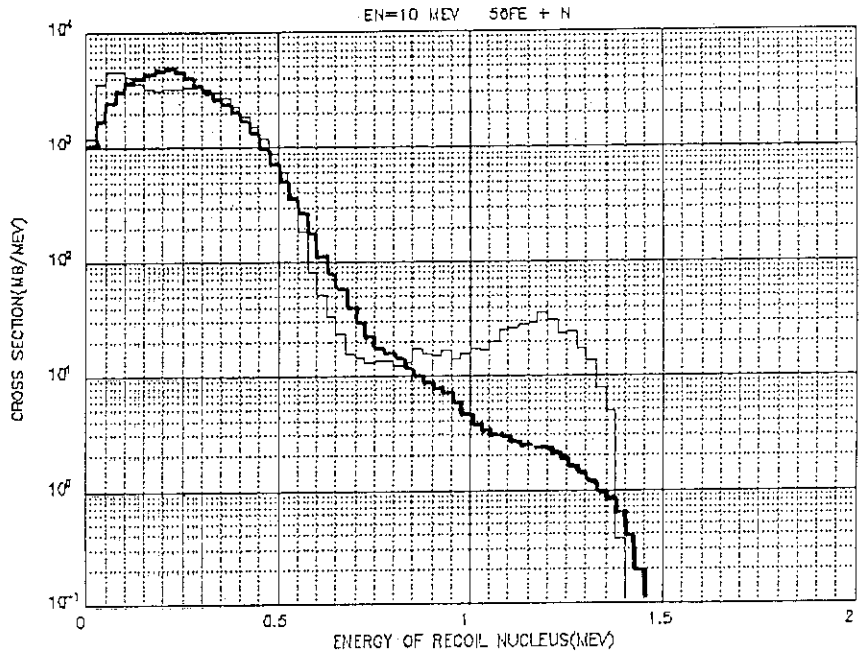

Fig. 3 Comparison of total PKA spectra for iron at En=10 MeV between PKAR (thick line) and MCEXCITON (thin line).

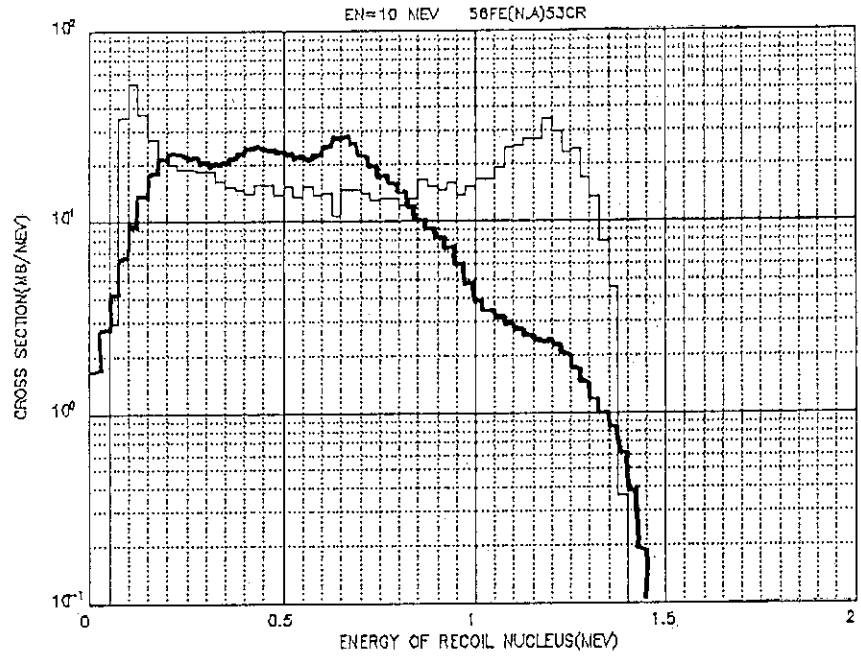

Fig. 4 Comparison of PKA spectra due to alpha emission reaction for iron at En = 10 MeV between PKAR (thick line) and MCEXCITON (thin line).

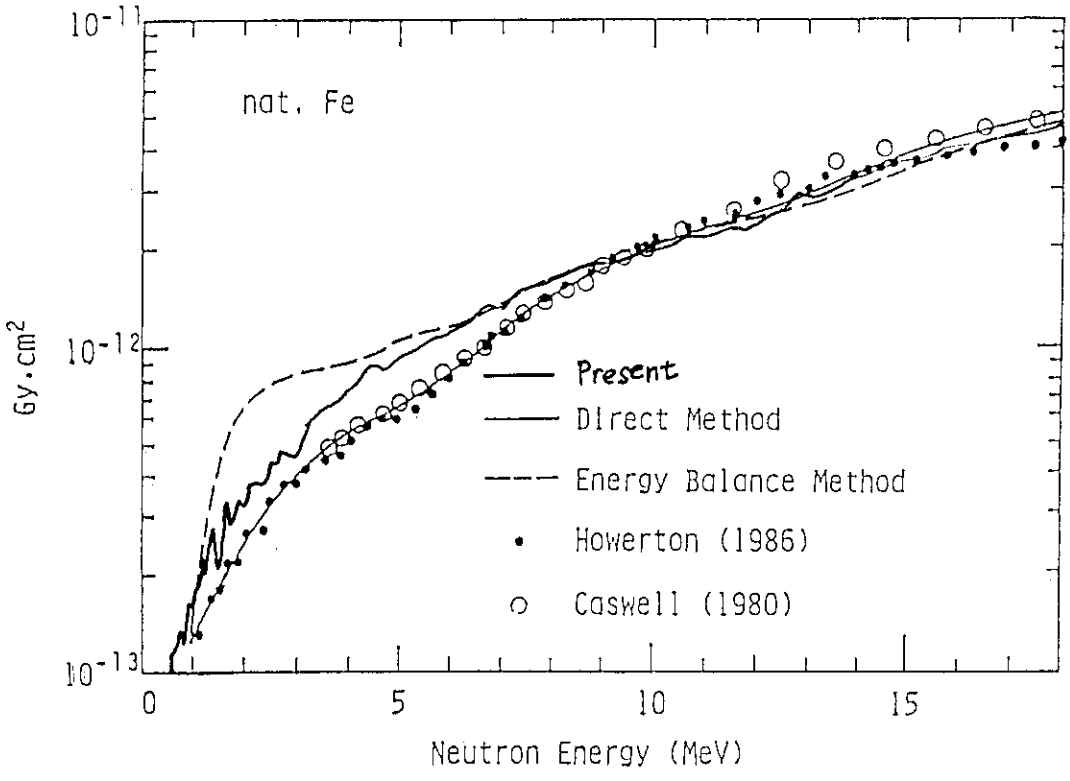

Fig. 5 Comparison of KERMA factors as a function of incident neutron energy between PKAR and the direct calculations by Howerton et al. and Caswell et al.

2.2.3 EVALUATION OF JENDL FUSION FILE

Satoshi Chiba, Baosheng YU* and Tokio Fukahori

Japan Atomic Energy Research Institute
Tokai-mura, Naka-gun, Ibaraki-ken 319-11, Japan

* China Institute of Atomic Energy
Beijing, People's Republic of China

In order to improve accuracy of neutron DDX (double differential cross section) related data stored in JENDL-3, preparation of a special purpose file, "JENDL Fusion File", is in progress. ENDF-6 format is adopted for this file, and the energy-angle correlation in measured data is taken into consideration. This file contains not only the neutron DDX but also those of charged particles. The latter is needed for material damage estimation. The DDXs are expressed by a compact form calculated from systematics. The multistep statistical model calculation is carried out to provide basic data needed in the systematics calculations.

I. Introduction

The DDX data are required as basic input data to the neutron transport calculations essentially in any applications where neutrons are used. They are especially important in fusion neutronics applications in order to predict many important aspects which determine the characteristics of a D-T fusion reactor as a nuclear system; neutron energy loss, multiplication, tritium production rate, nuclear heating, nuclear transmutation, etc. Recent studies show that there is a strong energy-angle correlation in neutron spectra produced by 10-20 MeV neutrons[1].

In JENDL-3, the DDXs are not given explicitly, so they must be constructed as a product of cross section, angular distribution and energy distribution given in MF=3, 4 and 5, respectively[2]. This representation, however, cannot reproduce the energy-angle correlation correctly, and was claimed to be inadequate from both the differential and integral experimenters[3]. Furthermore, it was pointed out that the DDXs of secondary

charged particles are also strongly required because these data are essential in material damage investigation such as primary knock-on atom (PKA) spectra and kinetic energy release in materials (KERMA) calculations[4]. Therefore, it was decided by the JENDL compilation group to prepare a special purpose file, JENDL Fusion File, to improve accuracy of the DDX data of secondary neutrons and to provide those of secondary charged particles.

The energy-angle correlation seen in measured data can be predicted by several quantum mechanical theories (e.g., **Ref. 5, 6** and **7**). These theories, however, usually require a lot of input data and long computation time, or are able to predict only a restricted aspect of the continuum spectra of secondary particles. Thus, it must be concluded at present that these sophisticated methods are impractical in nuclear data evaluation where a huge amount of computation is needed to provide the data for many nuclei (about 100 in JENDL Fusion File) in an energy range up to 20 MeV. In the present work, therefore, the DDXs were calculated by systematics[8,9]. Validity of these systematics in fusion neutronics was examined in our previous paper[10]. In the light mass region, the problem of DDXs seems less serious because the DDX is expressed in JENDL-3 by a pseudo-level representation for ^{6}Li, ^{7}Li, ^{10}B and ^{14}N which can take the energy-angle correlation into account automatically.

II. Basic Strategy

The present file is being prepared under the following basic strategy.

1. Data (cross sections, angular distributions of discrete levels, secondary neutron spectra, γ-ray production data, etc.) should be basically taken from JENDL-3. These data should be modified only if problems are found (especially in the DDX point of view).
2. DDX of neutron and charged particles should be added as compactly as possible in order to keep the file in manageable size.
3. DDXs should be calculated from the systematics.
4. ENDF-6 format should be used.
5. Basic quantities required in applying the systematics should be provided by the SINCROS-II code system[11] based on the multistep statistical model corrected for the precompound effects.
6. Data of Al, Si, Ca, Ti, Cr, Mn, Fe, Co, Ni, Cu, As, Ge, Zr, Sb, Sn, Nb, Mo, W, Pb and Bi should be given in JENDL Fusion File, including

their stable isotopes.

7. Data of ^{6}Li, ^{7}Li, ^{9}Be, ^{10}B, ^{11}B, ^{12}C, ^{14}N and ^{16}O should be taken from JENDL−3 and converted to ENDF−6 format, and small modifications should be done if necessary.

III. General Outline of the Evaluation Method

A schematic diagram of the method of evaluation and compilation of JENDL Fusion File is shown in **Fig. 1**. The SINCROS−II code system[11] was used to calculate the partial reaction cross sections, particle spectra and their multistep direct fractions (f_{MSD}). The f_{MSD} is required in calculation of the DDX by systematics[8,9,10]. This quantity depends on the incident and outgoing particle energy, and outgoing particle species, but was assumed to be independent of reaction channels (i.e., $f_{MSD} = f_{MSD}(E_a, E_b, b)$, where E_a denotes incident neutron energy, E_b outgoing particle energy, b the outgoing particle). In the present evaluation, the f_{MSD} was taken to be equal to the fraction of the precompound plus direct reaction component in a total secondary particle spectrum. This choice might slightly overestimate f_{MSD} because it includes a small contribution from the MSC (multistep compound) processes. However, we hope that it is compensated somewhat by the fact that the precompound effect is considered in SINCROS−II only in the first step of the multistep reactions. Parameters needed in the SINCROS−II calculation were adjusted through comparisons with experiments. Then, the DDX data of neutrons and charged particles were created by program F15TOB[12] by combining the f_{MSD} and composite particle spectra stored in an output file on the logical unit 15 (referred to as file 15 in **Fig. 1**) of EGNASH2[11] (ELIESE−3[13] + GNASH[14]) with the other data given in JENDL−3. In the present work, DDXs of charged particles were given only as composite forms expressed by Kalbach's systematics[9] for its compactness. The energy differential cross section (EDX) and the DDX were then compared with the experimental data. If it could not reproduce the experimental data, a few modifications were made by CRECTJ5[15]. For example, some cross sections were replaced by those calculated by EGNASH2[11], CASTHY2Y[11,16] and DWUCKY[11,17] programs, or by directly adjusting the cross sections stored in JENDL−3. Finally, several checks on the format and physical consistency were made by programs provided from NNDC/BNL[18].

In making the DDXs by the F15TOB program, Kumabe's systematics[8] was mainly used for neutron DDX. This systematics can reproduce the

measured neutron DDX in the angular range from 30 to 150−deg. very well. However, we found later that this systematics sometimes overestimates the cross sections in the very forward angles (θ < 30−deg.). Therefore, a new formula was sought, by changing the A_l parameter as $A_l = 0.0561 + 0.0377 \cdot l(l+1)$, instead of Eq. (5a) of Ref. 8. The new formula gives slightly less cross section in the angular region less than 30 degrees, and bigger values at backward angles (θ > 150−deg.). This made agreement with the experimental data sometimes better, although not always. We refer this formula as "modified Kumabe's systematics'. In the angular region between 40 and 150−degrees, cross sections calculated by the Kumabe's and this modified version are almost indistinguishable. We used Kumabe's and this modified systematics case−by−case.

IV. Results and Discussion

In Figs. 2 and 3, the DDXs of ^{59}Co and natural Cu at 14.1 MeV are displayed. The DDXs evaluated in the present work, reproduced from JENDL−3 and ENDF/B−VI[19] are compared with the experimental data[20,21].

The data reproduced from JENDL−3 obviously overestimate the discrete inelastic scattering cross section of ^{59}Co as shown in Fig. 2. In the present result, the overestimation disappeared because all of the inelastic scattering cross sections were replaced with a new calculation. Furthermore, the JENDL−3 overestimates the higher energy part of (n,n') continuum spectra at middle and backward angles. The DDXs reproduced from ENDF/B−VI underestimate the same part of DDX at forward angles. The present result can reproduce the measured variation of the DDX with respect to emission angle and secondary neutron energy fairly well.

In the DDX of Cu shown in Fig. 3, difference among the present result, JENDL−3 and ENDF/B−VI is less than the previous example. This trend was found true in other important structural materials (Cr, Fe, Ni, etc.). The DDX obtained from JENDL−3 slightly understimates the measured data at forward angles. However, it is consistent with the data of Baba et al. at backward angles. The present result, which is based on the modified Kumabe's systematics, can reproduce the measured data reasonably well.

The energy spectra of proton and α−particle emitted from ^{93}Nb at 15.0 MeV are shown in Fig. 4 and 5, respectively. It is seen that agreement between the measured data[22,23,24] and the present result is remarkable.

V. Summary Remarks

JENDL-3 Fusion File is being prepared placing an emphasis on the neutron and charged particle DDX. These DDXs were calculated by Kumabe's (or modified Kumabe's) systematics for neutrons and Kalbach's systematics for charged particles. The multistep direct fractions in continuum secondary particle spectra were calculated by a multistep statistical model with the pre-equilibrium contributions in the first step. It was shown that JENDL Fusion File can reproduce the overall variation of measured data with respect to the angle and energy reasonably well.

So far, evaluation for Al, Si, Cr, Mn, Co, Ni, Cu and Nb was finished. Evaluation of the whole nuclides will be finished by March 1993.

Acknowledgements

The authors would like to thank Dr. N. Yamamuro for a lot of useful and helpful advice on the SINCROS-II code system. They also wish to acknowledge valuable discussions with the members of JAERI Nuclear Data Center: Drs. Y. Kikuchi, T. Nakagawa and Y. Nakajima. Special thanks must be addressed to Drs. A. Takahashi and M. Baba for providing their data in timely manner and helpful discussions on the data.

References

1) e.g., Hodgson, P.E.: "NUCLEAR REACTIONS", Proceedings of a workshop on Applied Nuclear Theory and Nuclear Model Calculations for Nuclear Technology Applications, Trieste, Italy, 15 Feb. - 19 Mar. ,1988, edited by Mehta, M.K. and Schmidt, J.J., World Scientific.
2) Shibata, K., Nakagawa, T., Asami, T., Fukahori, T., Narita, T., Chiba, S., Mizumoto, M., Hasegawa, A., Kikuchi, Y., Nakajima, Y. and Igarasi, S.: "Japanese Evaluated Nuclear Data Library, Version-3, -JENDL-3 -", JAERI 1319 (1990).
3) Nakajima, Y. and Maekawa, H. (ed.): Proceedings of the Second Specialists' Meeting on Nuclear Data for Fusion Reactors, JAERI-M 91-062 (1991).
4) Kawai, M. and Fukahori, T.: private communication.
5) Tamura, T., Udagawa, T. and Lenske, H.: Phys. Rev. C26, 379(1982).
6) Feshbach, H., Kerman, A. and Koonin, S.: Annals of Physics 125,

429(1980).

7) Luo, Y.L. and Kawai, M.: Phys. Lett. B235, 211(1990).

8) Kumabe, I., Watanabe, Y., Nohtomi, Y. and Hanada, M.: Nucl. Sci. Eng. 104, 280(1990).

9) Kalbach, C.: Phys. Rev. C37, 2350(1988).

10) Yu, B., Chiba, S. and Fukahori, T.: submitted to J. Nucl. Sci. Technol.

11) Yamamuro, N.: "A NUCLEAR CROSS SECTION CALCULATION SYSTEM WITH SIMPLIFIED INPUT-FORMAT VERSION II (SINCROS-II)", JAERI-M 90-006 (1990).

12) Chiba, S.: Program "F15TOB", unpublished.

13) Igarasi, S.: "Program ELIESE-3; Program for Calculation of the Nuclear Cross Sections by Using Local and Non-Local Optical Models and Statistical Model", JAERI 1224 (1972).

14) Young, P. and Arthur, E.: "GNASH: A Preequilibrium, Statistical Nuclear-Model Code for Calculation of Cross Sections and Emission Spectra", LA-6947 (1977).

15) Nakagawa, T.: Program "CRECTJ5", to be published.

16) Igarasi, S. and Fukahori, T.: "Program CASTHY − Statistical Model Calculation for Neutron Cross Sections and Gamma Ray Spectrum −", JAERI 1321 (1991).

17) Kunz, P.D.: program DWUCK4, University of Colorado, unpublished.

18) Dunford, C. L.: "Release of ENDF Utility Codes, Version 6.6", unpublished memorandom, NNDC/BNL, June 13, 1990.

19) NNDC/BNC: "ENDF/B-VI", to be published.

20) e.g., Takahashi, A., Ichimura, E., Sasaki, Y. and Sugimoto, H.: J. Nucl. Sci. Technol. , 25, 215(1988); Takahashi, A., Ichimura, E., Sasaki, Y. and Sugimoto, H.: "DOUBLE AND SINGLE DIFFERENTIAL NEUTRON EMISSION CROSS SECTIONS AT 14.1 MEV", OKTAVIAN Report A-87-03 (1987).

21) e.g., Baba, M., Ishikawa, M., Yabuta, N., Kikuchi, T., Wakabayshi, H. and Hirakawa, N.: "DOUBLE-DIFFERENTIAL NEUTRON EMISSION SPECTRA FOR Al, Ti, V, Cr, Mn, Fe, Ni, Cu and Zr", Proc. of Int. Conf. on Nucl. Data for Sci. and Technol., Mito, Japan, May 30-June 3, 1988, Ed. Igarasi, S., Saikon Pub. (1988).

22) Fischer, R., Uhl, M. and Vonach, H.: Phys. Rev. C37, 578(1988).

23) Traxler, G., Chalupka, A., Fischer, R., Strohmaier, B., Uhl, M. and Vonach, H.: Nucl. Sci. Eng. 90, 174(1985).

24) Grimes, S., Haight, R., and Anderson, J.: Phys. Rev. C17, 508(1978).

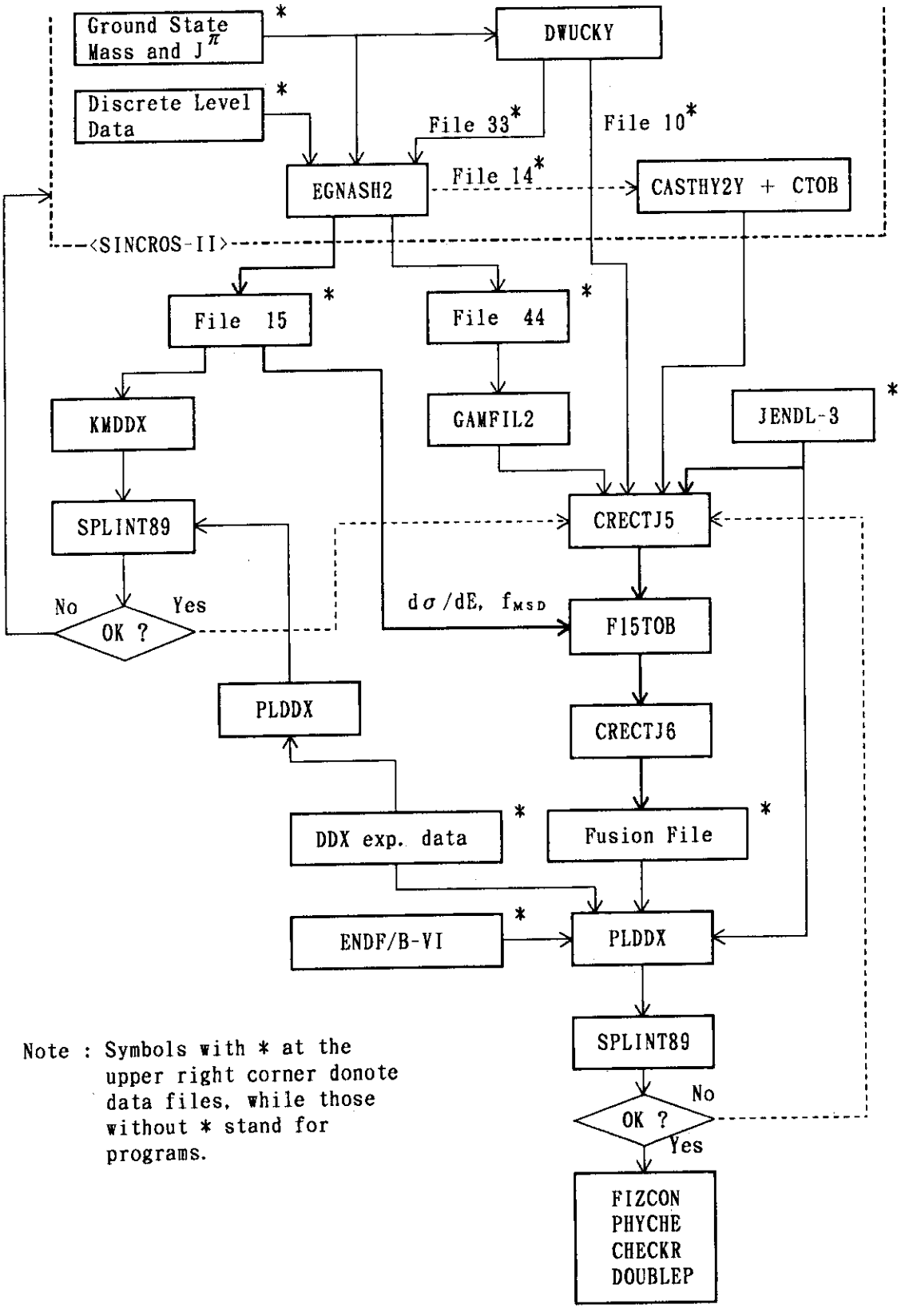

Fig. 1 Schematic flow of evaluation and compilation of JENDL Fusion File.

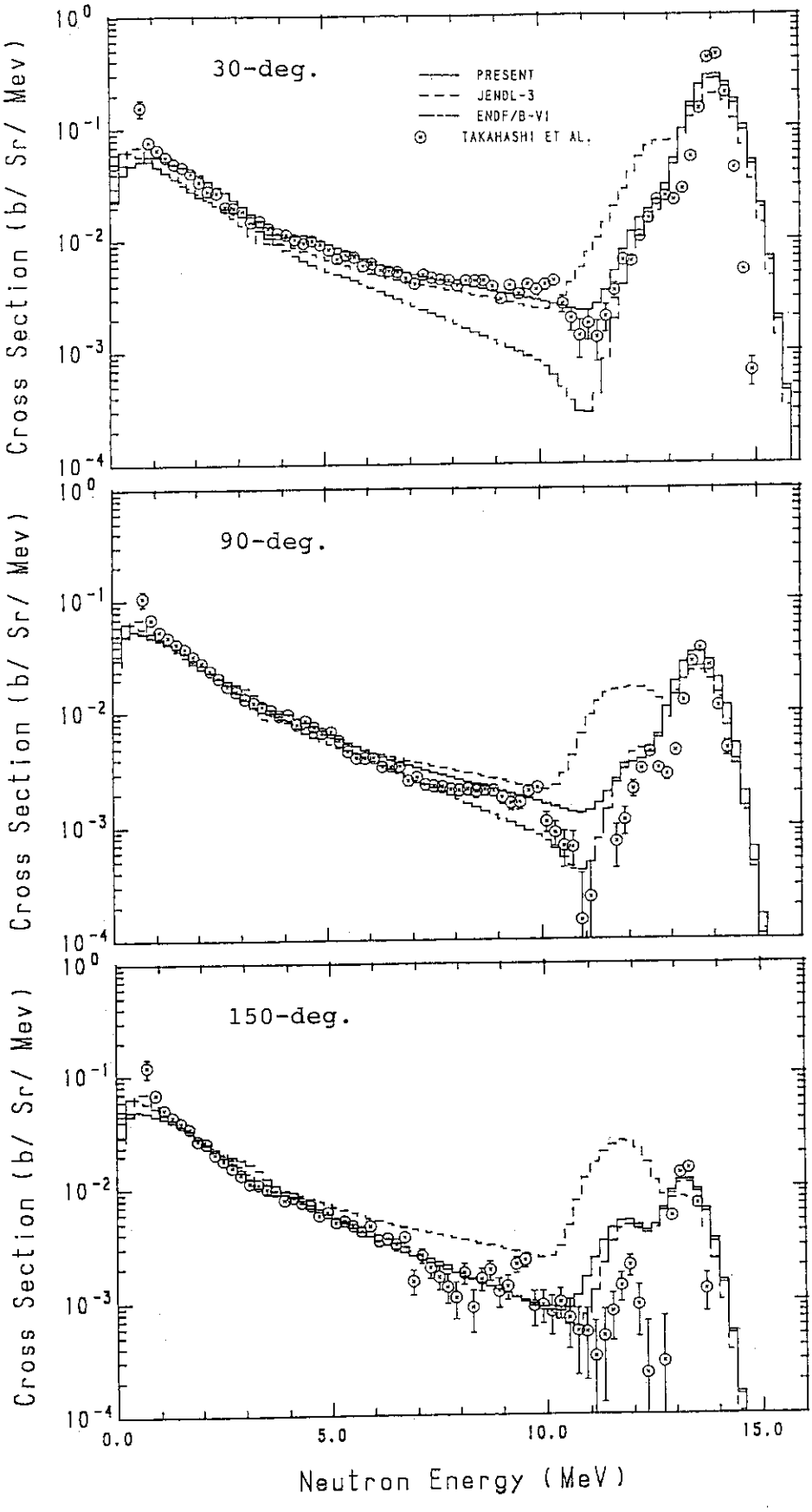

Fig. 2 DDX of ^{59}Co at 14.1 MeV.

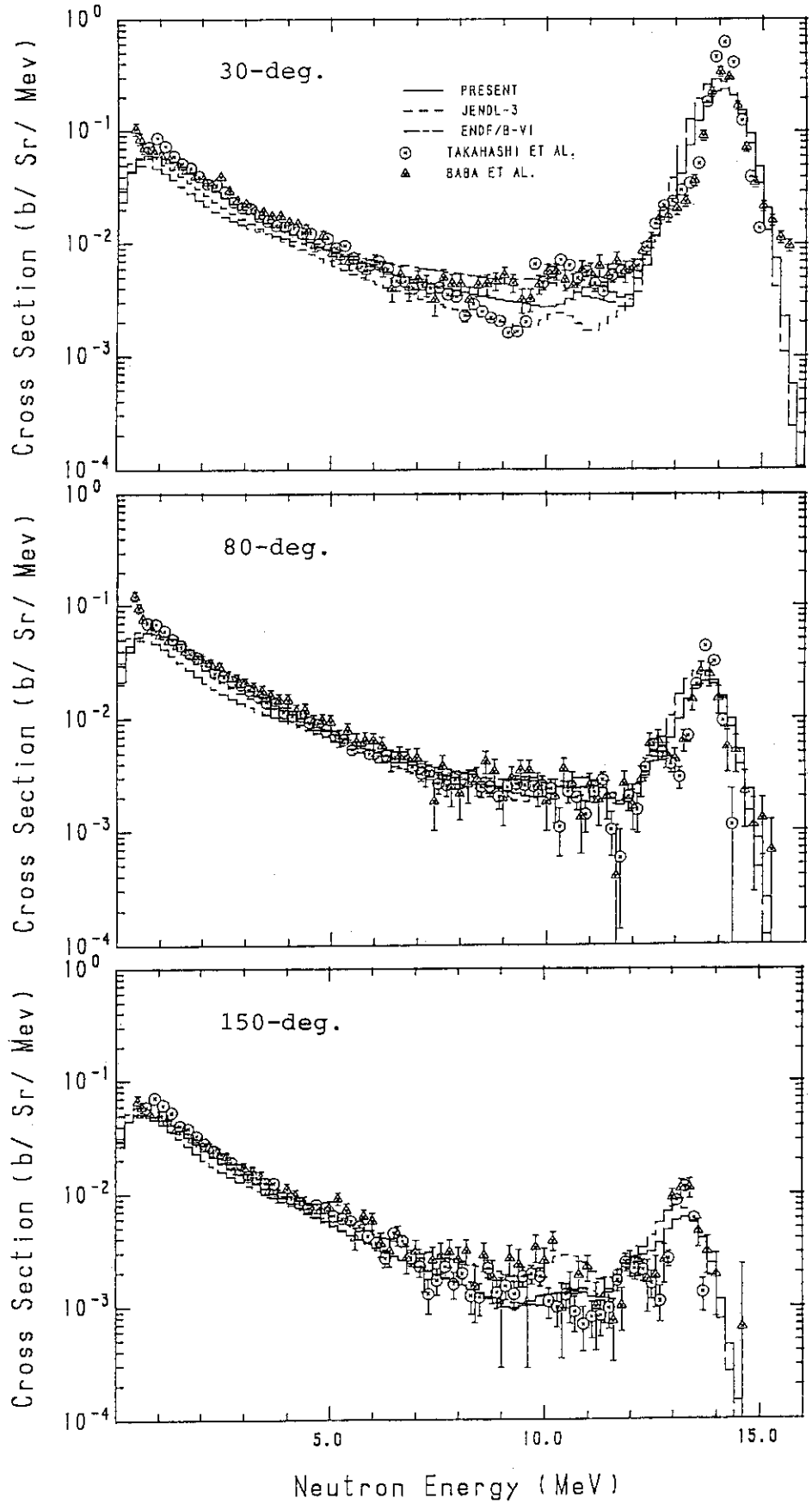

Fig. 3 DDX of natural Cu at 14.1 MeV.

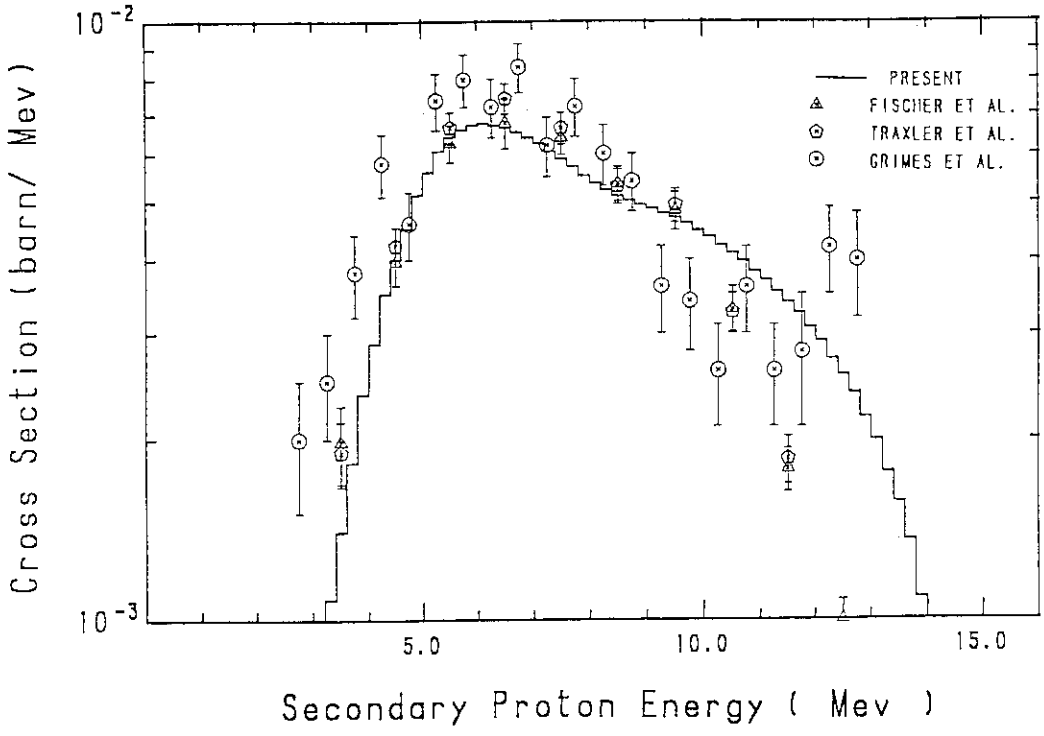

Fig. 4 EDX of ^{93}Nb(n,xp) reaction at 15.0 MeV.

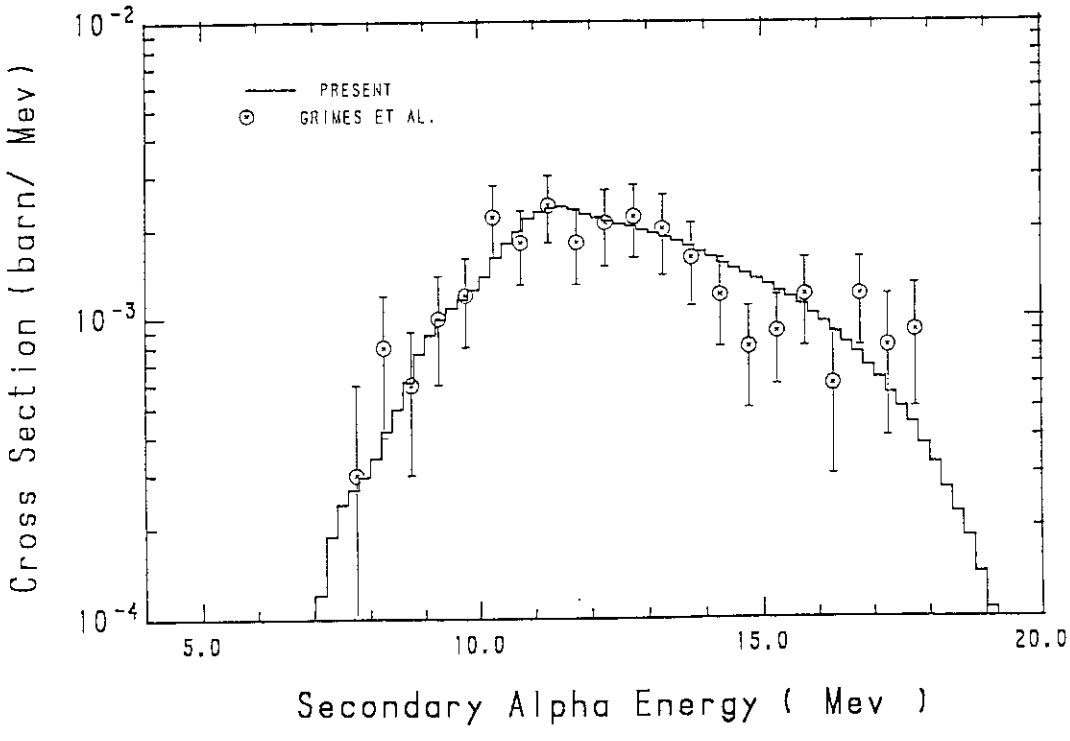

Fig. 5 EDX of ^{93}Nb(n,xα) reaction at 15.0 MeV.

2.3 TOPIC 2

2.3.1 THE OMEGA PROGRAM AND REQUIRED NUCLEAR DATA

Hiroyuki YOSHIDA
Japan Atomic Energy Research Institute

The OMEGA program has proceeded in Japan since 1989 for research and development of partitioning and transmutation of minor actinides and FPs in high level radioactive waste (HLW) generated from reprocessing. The present paper describes an outline of the OMEGA program and the JAERI's R&D activities on partitioning and transmutation. And a discussion is made on nuclear data needed to study transmutation systems proposed in JAERI.

1. INTRODUCTION

National policy of managing high level radioactive waste (HLW) is to solidify in a stable form and to dispose of ultimately into deep geological formation after 30-50 years for cooling. The other hand, it has been recognized that long-term basic research into utilization of HLW by separation into individual minor actinides and fission products could produce many benefits and The Japan's Atomic Energy Commission submitted in 1988 a report entitled "Long-Term Program for Research and Development on Nuclide Partitioning and Transmutation", which plots a course of technical development up to the year 2000.

The program was jointly stimulated by the collaborative effort of JAERI and PNC, and CRIEPI has been also carrying out R&Ds on this subjects. Under the program, JAERI has conducted R&Ds on the advanced partitioning technology, minor actinide burner reactor and intense proton accelerator-driven transmutation system.

In the design study of transmutation systems, reliable basic data including nuclear data are indispensable, but these are insufficient at present. The Japan's Nuclear Data Center has already compiled the nuclear data needed for nuclear design of transmutation system based on nuclear reactor as the JENDL, and now has started to evaluate the nuclear dater needed for proton

accelerator-driven transmutation system.

2. THE OMEGA PROGRAM

The program is to proceed in two phases. The phase-1 covers a period up to about 1996, and the basic studies and testing are to be conducted to evaluate various concepts and to develop required technologies. The phase-2 covers a period from about 1997 to about 2000, and engineering tests of technologies and/or demonstration of concepts are planned. After the year 2000, pilot facilities will be built to demonstrate the partitioning and transmutation.

2.1 Partitioning

The principal technologies to be developed are as follows;

- technology for nuclide partitioning of HLW,
- technology for recovering useful metals in insoluble residue,
- technology for utilizing the separated elements.

The nuclide partitioning is especially important in the program and is to separate HLW into four groups; minor actinide elements, Sr/Cs elements, Tc/platinum group elements and others. In addition to the wet process, feasibility and applicability of dry process are also investigated.

2.2 Transmutation

The principal technologies to be developed are as follows;

- application of nuclear reactors for transmutation,
- application of accelerators for transmutation.

Nuclear reactor provides an extremely rational means for the possible earlier realization of transmutation technology for minor actinide nuclides. Sodium-cooled fast reactor with MOX or metallic fuel can be applied to transmute many kinds of minor actinide nuclides due to its relatively large high-energy fissioning. Minor actinide burner reactor is another candidate to be developed due to its potentially more efficient transmutation capability than conventional fast reactor. Thermal reactor is an

alternative, when plutonium is used as its nuclear fuel.

Owing to the recent remarkable advance of accelerator technology, application of accelerators is becoming attractive as a means of transmutation. Proton accelerator is to be developed to transmute minor actinides and long-lived FPs by spallation and associated large number of emitted neutrons. Electron accelerator might be investigated. Hybrid system combining an accelerator with a subcritical target should be studied to improve overall energy balance of the transmutation system.

2.3 Related Basic Research

Reliable data base of minor actinide nuclides and long-lived FPs is indispensable. Underlying studies on physical and chemical properties of these nuclides will improve understandings of the science and technology for separation and recovery of these nuclides from HLW, for fabrication of minor actinide fuel for recycling to reactors or accelerator-driven systems to transmute, and for their utilization. Nuclear data and thermodynamic data of these nuclides should be measured, compiled and evaluated for nuclear design and material development.

The areas covered by the OMEGA program and R&D activities are illustrated in Fig.1.

3. RESEARCH AND DEVELOPMENT ACTIVITIES IN JAERI

A concept of double strata nuclear fuel cycle has been developed in JAERI and is illustrated in Fig.2. The first cycle is the conventional fuel cycle and the second is the partitioning and transmutation cycle (P-T cycle). The partitioning process and transmutation systems being developed in JAERI are the major technologies in the P-T cycle.

The nuclides to be partitioned and transmuted were determined based on analyses of long-term radiotoxicity of HLW as shown in Fig.3. A goal of transmutation capability was also determined to incinerate the accumulated minor actinides as early as possible, basing on an assumed nuclear power growth.

3.1 Partitioning of HLW

The selected elements and their separation rates are as follows; Pu:99.9%, Np:99.5%, Am:99.99%, Cm:99.9%, Sr and Cs:99.9% Tc and I:99%.

The partitioning process[1] has been developed to separate elements including the above-mentioned elements in HLW into four groups as described in the OMEGA program. It was found by the tests using actual or simulated HLW that more than 99.95% of Np, more than 99.99% of Am and Cm, and more than 99% of Tc were extracted by the proposed partitioning process. This process will be tested as a whole with actual HLW at NUCEF in near future.

3.2 Minor Actinide Burner Reactor

Miner actinide burner reactor (ABR) design study has been carried out and two types of reactor design were obtained[2] until now. The reactors are fast reactors designed to burn minor actinides effectively. Their major component of fuel is minor actinides and neutron energy spectrum is very hard to fission these nuclides which have fission thresholds at neutron energy of about 700KeV.

The first is a sodium-cooled metallic fuel reactor (M-ABR). The advantages of metallic fuel are the hard neutron spectrum and the compact fuel cycle facilities when pyrochemical reprocessing is used. The second is a helium-cooled nitride particle fuel reactor (P-ABR). This has very high power density since heat removal in a core is very efficient because of a large heat transfer surface per volume of particle fuel. The reactor performance parameters of M-ABR and P-ABR at the equilibrium cycle are given in Table 1.

A series of the integral experiments were carried out at FCA of JAERI[3] to evaluate and modify neutron cross-sections of minor actinides used in the ABR design study. To verify accuracy of these cross-sections, chemical analysis of minor actinide samples irradiated at PFR in the united kingdom is under preparation, and further irradiation experiments are also planned at FFTF in the USA. Measurements relating to delayed neutron and

fission yields of minor actinides are planned at Missouri University in the USA.

3.3 Proton Accelerator-driven Transmutation System

Conceptual design study of accelerator-driven transmutation system has been performed. The proposed system[4] is a hybrid one consisting of an intense proton accelerator, a tungsten target and a subcritical assembly with minor actinide based alloy fuels.

The main design parameters of the system are given in Table 2 and its energy balance is briefly shown in Fig.4. Another design study of a system with chloride molten salt assembly is in progress to transmute not only minor actinides but long-lived FPs such as Tc-99 and I-129.

Construction of the Engineering Test Accelerator (ETA)[5] with a proton energy of 1.5GeV and a current of 10mA is planned. Various engineering tests will be performed by using ETA for an accelerator-driven transmutation system. As the first step to develop ETA, the Basic Technology Accelerator (BTA) with a proton energy of 10MeV and a current of 10mA is to be built to study a low energy portion of ETA.

To evaluate the reliability of the nuclear data and computer codes developed in JAERI, the integral experiments relating to spallation reaction have been performed since 1990, by using a lead bulky target and 500MeV protons from the booster facility at the KEK[6]. The Institute of Theoretical and Experimental Physics (ITEP) in Moscow recently sent an eager proposal to JAERI for the collaborative physics measurements relating to spallation reactions by using an intense accelerator at ITEP. The proposal is being investigated for further accumulation of the integral data.

4. REQUIRED NUCLEAR DATA

Much of the nuclear data of minor actinides and long-lived FPs are compiled in JENDL to use nuclear design studies of thermal and fast reactors. H.Takano, and S.Iijima et al. have already discussed in detail the nuclear data used to transmutation analy-

ses in fission reactors and fusion reactors[7]. And the recent nuclear data sheet requested to WRENDA from T.Mukaiyama gives the required nuclides, reaction types and accuracies. The sheet also shows the present status of their accuracies in JENDL estimated by T.Nakagawa.

T.Nishida et al. recommended in detail the nuclear data needed for design study of intense proton accelerator-driven transmutation systems[8]. They pointed out that their design study needs reliable nuclear data for various nuclear reactions with charged particle, meson and high energy neutron. According to this recommendation, JAERI's NDC started to accumulate and to evaluate these nuclear data in the collaboration with Japan's NDC.

5. CONCLUSION

Various R&Ds on partitioning and transmutation have been performed in Japan under the framework of the OMEGA program. The R&D activities will be reviewed by Japan's Atomic Energy Commission, and the partitioning and transmutation technologies will become more and more worthy to reduce the long-term burdens of nuclear waste disposal and to enhance the effective utilization of resources. However, it should be recognized that The OMEGA program is not to seek a short-term alternative for established or planned fuel cycle back-end policies, but is conceived as a research effort to pursue benefits for future generations through long-term basic R&Ds.

REFERENCES

(1) M.Kubota et al.: Development of Partitioning Process in JAERI ,Proc.of the First OECD/NEA Information Exchange Meeting on Actinide and Fission Products Separation and Transmutation, p158-173, Mito-city (1990).

(2) T.Mukaiyama et al.: Minor Actinide Transmutation using Minor Actinide Burner Reactors, Proc.Int Conf.on Fast Reactors and Related Fuel Cycles, Kyoto (1991).

(3) S.Okajima et al.: Evaluation and Adjustment of Actinide Cross Sections using Integral Data measured at FCA, Proc.Int Conf. on Nuclear Data for Science and Technology, Mito (1988).

(4) T.Takizuka et al.: Conceptual Design of Transmutation Plant, Proc.Specialist Meeting on Accelerator Driven Transmutation Technology for Radwastes and Other Application, Stockholm (1991).
(5) M.Mizumoto et al.: Intense Proton Accelerator Development Program, ibid., Stockholm (1991).
(6) H.Takada et al.: Integral Experiment on Lead Bulk System Bombarded with High Energy Protons, ibid.,Stockholm (1991).
(7) T.Takano : Nuclear Data News, No.31 (1988), in Japanese. S.Iijima and Y.Fukai : ibid.
(8) T.Nishida et al.: Nuclear Data News, No.37 (1990),in Japanese.

Table 1 Design parameters of minor actinide burner reactor

	M-ABR[1]		P-ABR[2]	
Fuel concept	pin-bundle		coated particle	
material	IC[3]:Np-22Pu-20Zr OC:AmCm-35Pu-5Y		$(66NpAmCm\text{-}34Pu)_{1.0}N_{1.0}$	
MA initial loading,[4] kg	666		2065	
Np/Am,Cm/Pu	255/199/212		765/598/702	
Reactor power, MWth	170		1200	
Coolant material	Sodium		Helium	
velocity, m/s	8	total flow, kg/s	1088	
		inlet pressure, MPa	10	
		pressure drop, kPa	13	
inlet temperature,℃	300		127	
outlet temperature(core max),℃	IC:484 OC:440		340	
Fuel temperature,℃ max[5]	IC:834 OC:809		722	
Clad temperature,℃ max[6]	IC:517 OC:484	Frit temperature, max	560	
Neutron flux, $10^{15}n/cm^2 \cdot sec$	IC:4.1 OC:3.4		8.4	
Neutron fluence (E>0.1MeV), $10^{23}n/cm^2$	IC:2.2 OC:1.7		2.2	
Core averaged mean neutron energy, keV	IC:766 OC:785		743	
Reactivity (% $\Delta k/k$)				
Na-void reactivity/core	2.52		——	
Doppler reactivity/core(Δt=300℃)	-0.01		-0.01	
Kinetic parameters				
β_{eff}	1.55×10^{-3}		1.72×10^{-3}	
$_p$, sec	6.84×10^{-8}		1.08×10^{-8}	
Cycle length, full-power days[7]	730		300	
MA transmutation, %/cycle	26.0		25.3	
MA burnup, %/cycle	17.8		17.3	

1) M-ABR:MA metallic fuel actinide burner reactor
2) P-ABR :MA particle fuel actinide burner reactor
3) IC:Inner Core, OC:Outer Core
4) After 1st cycle,only Np,Am,Cm are added.
5) Predicted melting point of fuel 900℃ for M-ABR
   Max. allowable temp. of fuel 727℃ (1/3 of M.P. 3000K) for P-ABR
6) Max. allowable temp. of cladding/frit (HT-9) 650℃
7) Fuel irradiation time

Table 2 Design parameters of minor actinide transmutation system assisted by an intense proton LINAC

Proton beam current		39 mA
Actinide inventory		3160 kg
Effective neutron multiplication factor		0.89
No. of neutrons per incident photon		40 n/p
No. of fissions	(>15MeV)	0.45 f/p
	(<15MeV)	100 f/p
Neutron flux		4×10^{15}n/cm^2 · s
Mean neutron Energy		690 keV
Burnup		250 kg/y
MA thermal output	fuel	800 MW
	tungsten	20 MW
	total	820 MW
Power density	maximum	930 MW/m^3
	average	400 MW/m^3
Linear power ratio	maximum	61 kW/m
	average	27 kW/m
Coolant temperature		
outlet	maximum	473 ℃
	average	430 ℃
Maximum temperature		
fuel	center	890 ℃
	surface	548 ℃
clad	inside	528 ℃
	outside	484 ℃

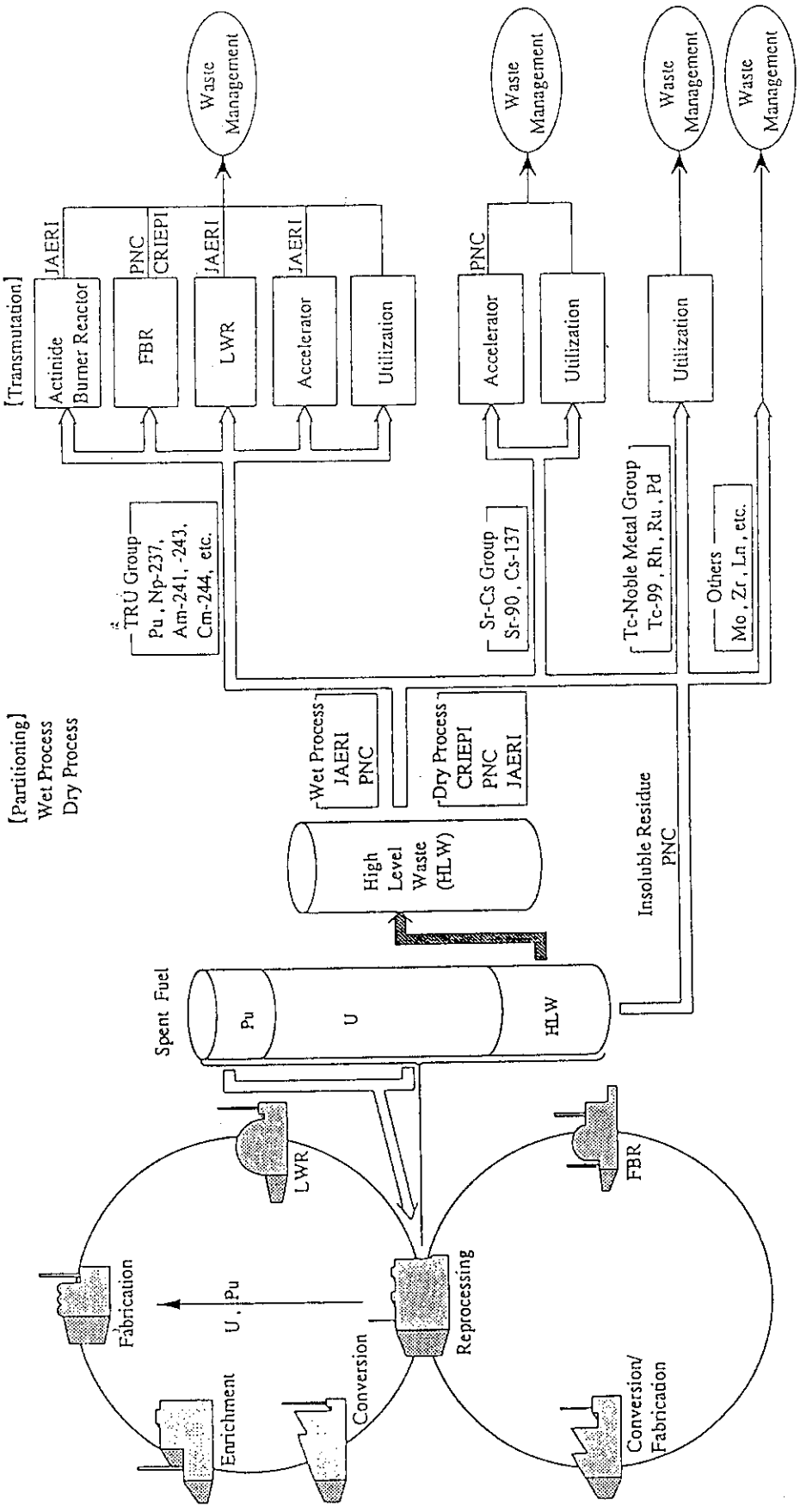

Fig. 1 P-T R&D activities under the OMEGA program

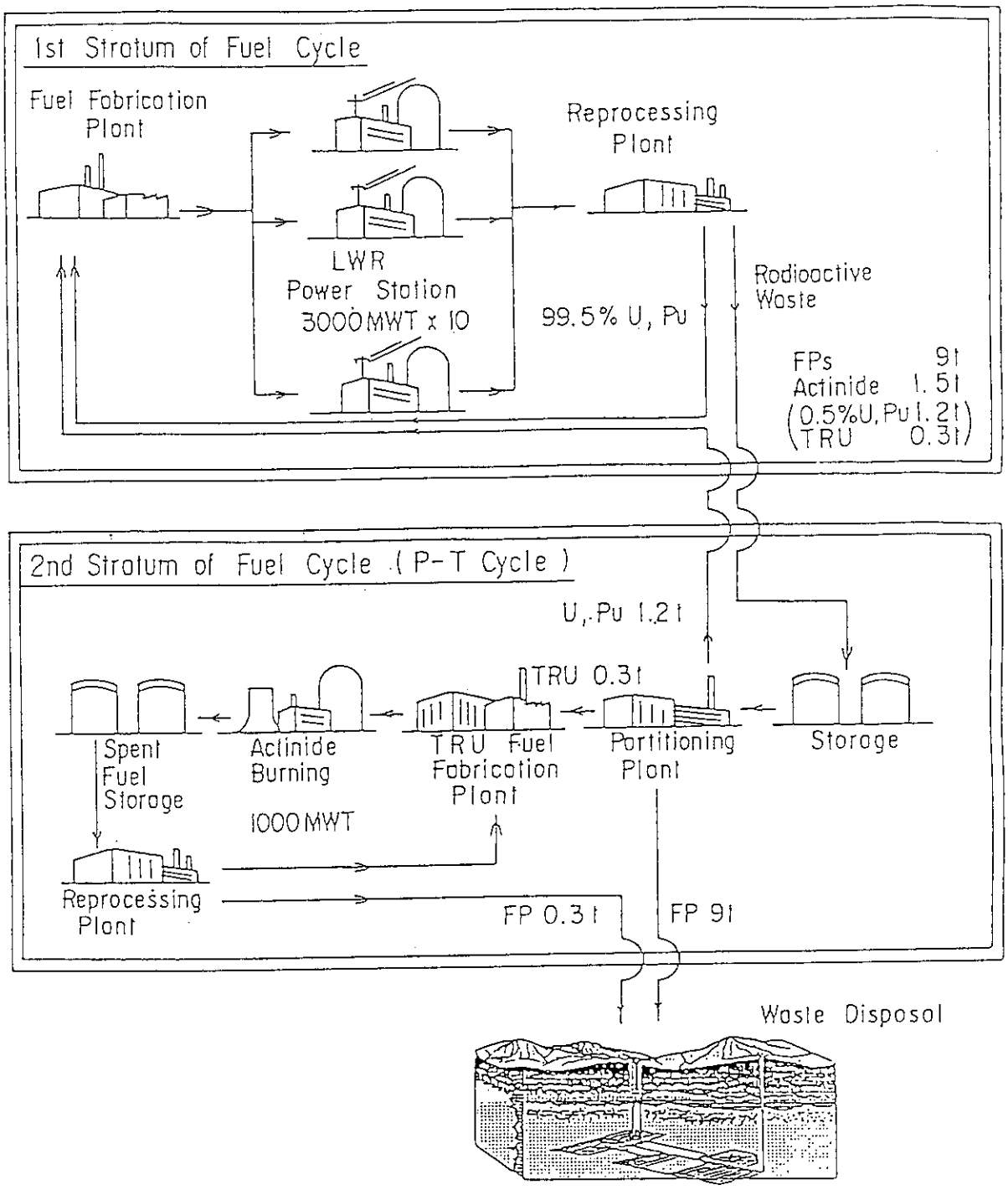

Fig. 2 Flow of radioactive waste per year through double strata fuel cycle combined with partitioning and transmutation.

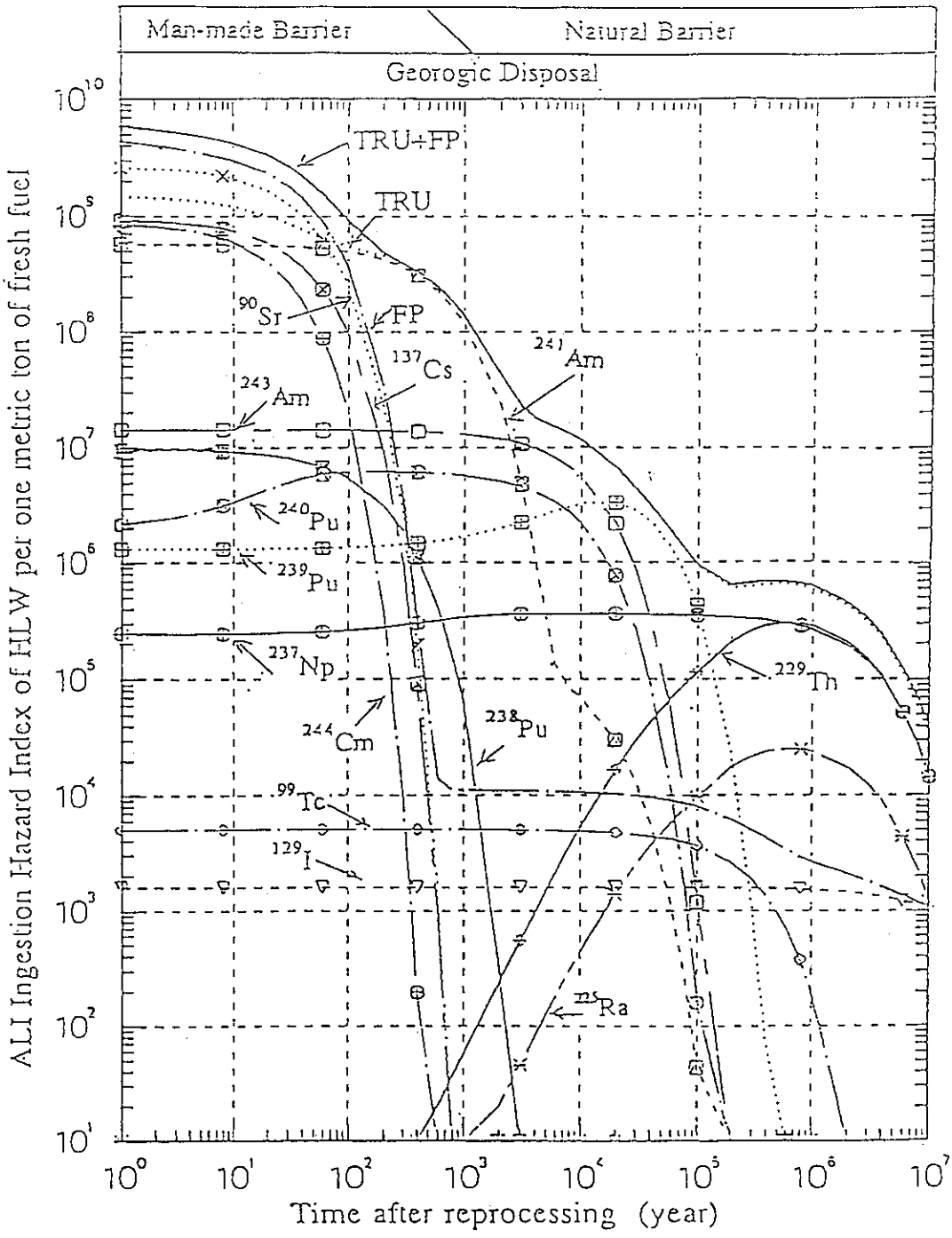

Fig. 3 Potential hazard index vs time for HLW from PWR spent fuel.

ALI ingestion hazard index is defined as the ratio of the amount (in Bq unit) of a nuclide to ALI value of the nuclide. HLW is recovered from the reprocessing of PWR spent fuel (burnup of 33GWD/MT, 3 years cooling). U, Pu recovery is 99.5%. (TRU: total transuranium elements, FP: total fission products)

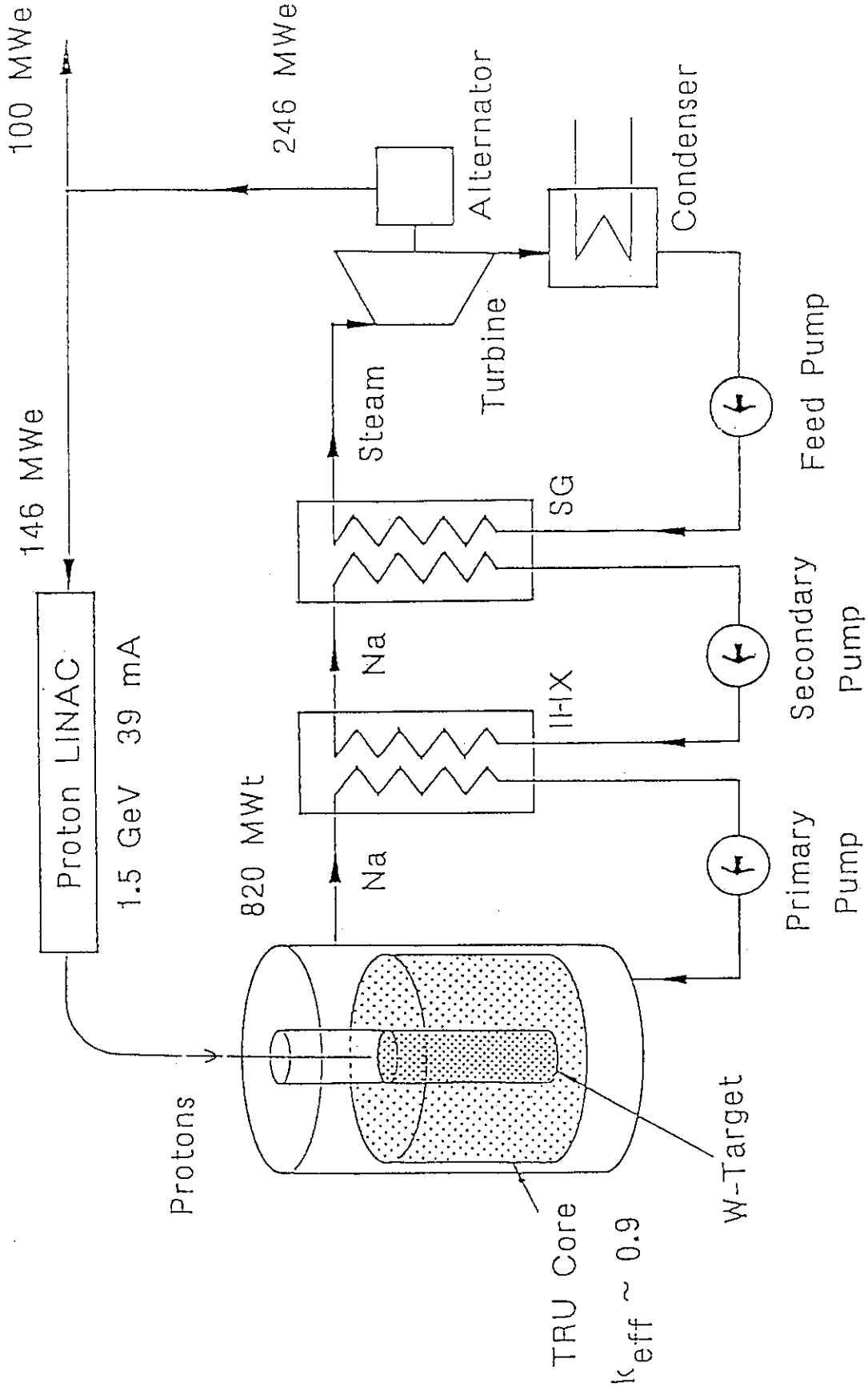

Fig. 4 Transmutation plant concept driven by intense proton LINAC.

2.3.2 OVERVIEW OF ESNIT AND NUCLEAR DATA

M. Sugimoto, K. Noda, Y. Kato, H. Ohno and T. Kondo

Japan Atomic Energy Research Institute,
Tokai-mura, Naka-gun, Ibaraki-ken, 319-11 Japan

Energy Selective Neutron Irradiation Test Facility (ESNIT) provides the high energy and high intensity neutron irradiation field for the materials researches. It can vary the neutron energy spectrum by changing the incident deuteron energy from 10 to 40 MeV using the d-Li source reaction. The objectives of ESNIT, the status and the perspectives of the program, and the technical issues on the accelerator and target systems are reviewed. The requirements for the nuclear data are also discussed.

1. Introduction

The Energy Selective Neutron Irradiation Test Facility (ESNIT) has been conceived as a key component in the base technology program on materials since 1988. It is an accelerator-based neutron source using a high current deuteron linear accelerator, and it can provide the high-energy intense neutron irradiation field for materials researches[1]. The Fig. 1 shows a conceptual view of such a facility, which consists of the three major components: (1) accelerator, (2) target, and (3) experimental systems.

The objectives of the ESNIT and the relationship to the other programs are shown in Fig.2. Fundamentally, ESNIT is a research tool for the base technology and basic researches. From the viewpoint of the fusion energy development, the fundamental medium fluence study will be performed in the ESNIT, whereas a more intensive neutron source -IFMIF(International Fusion Material Irradiation Facility)[2] is planned for engineering demonstration test and the critical high fluence study as the international program. The fluence level of the ESNIT is about half of the FMIT project[3] cancelled in mid 80's.

The advisory committee (Nuclear Materials Research Committee) was organized to raise such idea. In addition to the neutron source itself,

the complementary facility, MODULAB (MODUlar LABoratory), is also conceived to carry out the post irradiation experiments using the modular hot cells in the subcommittee. The conventional neutron source based on the fission reactors is also useful to some types of experiments and it should be linked to the ESNIT-MODULAB facility. The characteristics of the irradiation field and the test matrices of the ESNIT have been discussed in the Fusion Materials Research Committee, too.

The Fig.3 shows the main characteristics of the ESNIT[4]. The intensity of the neutron flux is equivalent to the wall load of the DEMO reactor, 1.5 − 3.0 x10^{14} n/cm^2/s in a 5x5x5 cm^3 irradiation volume, at maximum. The energy selectivity is attained by using the d−Li stripping reaction, which gives the neutron spectra with 5, 10 and 14−15 MeV peaks (at least these three different spectra are required). There are many technological issues in the development of the deuteron cw linear accelerator and the liquid lithium metal target systems, which would be carefully considered in design stage and should be resolved in the R&D stage. The ESNIT provides three types of irradiation tests, (1) in−situ tests, (2) the capsule irradiation, and (3) tests using PIE cells (MODULAB).

The various energy spectra obtained by ESNIT and the other neutron sources are shown in Fig.4. The ESNIT spectra are not monoenergetic and a large amount of component above its peak energy, called high−energy tail, however, the neutron flux is restricted in a narrow energy region compared with the other conventional sources, such as FBR, HFIR, or spallation source. The comparison at the higher energy region is given in Fig.5. The proposed beam plasma source spectrum is closest to the DEMO spectrum, but it needs a lot of development time to realize. The spallation sources (EURAC and SPALL) have no peak and it is difficult to estimate the effects of high energy neutrons. The H(t,n) source is proposed recently at KfK[2] to suppress the high energy tail component, but high current triton acceleration is very difficult task. The ESNIT employs Li(d,n) source as a main source reaction, and it also accelerates hydrogen molecular ions and produces another neutron spectrum using Li(p,n) reaction.

2. Status and perspectives of ESNIT program

From the technical aspects, the Accelerator−based neutron facility

Subcommittee in the Nuclear Materials Research Committee has three working groups: (a) the accelerator, (b) the target, and (c) the remote experimentation. For checking the suitability of the characteristics of ESNIT to the many research items, the technical surveys were carried out for the following subjects:

(a) accelerator
- conceptional study with design parameter evaluation
- capacity optimization, trade off study

(b) target
- conceptional study with design parameter evaluation (based on FMIT model)
- energy selectivity design (e.g. flow rate vs. film thickness)
- thermal−hydraulic characteristics
- heat removal technique

(c) experimental system
- modular hot cell laboratory (MODULAB)
- small specimen test technique (e.g. small punch test)

(d) neutron field characterization
- d−Li stripping experiment
- spectra vs. flux−volume calculation
- nuclear data evaluation
- transmutation and damage parameter calculation

The workshop of technical reviewing was held on Aug 26−30 and on Oct. 7, 1991, and the above items are reviewed in details and the critical issues and the long−term/short−term R&D plans are discussed[5].

The perspectives of ESNIT program in the future are expected as:

Final evaluation	FY 1992
——end of Base technology phase——	
Second phase	FY 1993−95
conceptional design	
supplementary R&D program	
Construction phase	FY 1995/96−
Operation phase	FY 1999/2000−

There is a worldwide consensus to build a d−Li neutron source facility

as most potential near term source and the national fusion development strategies favor the earlier construction of such facility, too.

3. Technical review on accelerator and target systems

3.1 Neutron field characterization

The neutron field characteristics obtained at the ESNIT facility is summarized in Fig. 6. The deuteron (exactly saying, charge−to−mass ratio = 1/2) linac, which can accelerate D^+(or H_2^+) and D^- simultaneously, produces 50 mA beam at maximum in a cw mode operation. The required conditions to the beams are: (i) pause between the consecutive beam pulses is less than 1 μs, and (ii) stability of the peak current is better than 5%. Using the d−Li reaction, the neutron spectrum can be varied by selecting the proper beam energy, and the highest neutron flux is obtained at the highest beam energy. As an alternative neutron source, the p−Li reaction produces neutrons with smaller intensity than that of the d−Li source by a order of magnitude, but there is no severe high energy tail component in the spectrum. Fig. 7 shows the d−Li source neutron spectra measured at Ed=32 MeV using the JAERI tandem accelerator. The measurements at Ed=8, 16, and 24 MeV are also carried out to support the irradiation field evaluation for ESNIT. Fig 8. compares the results of the flux−volume calculations at various beam energies. The 40 MeV, 50 mA beam is necessary to retain 125 cm^3 volume with $>1.5\times10^4$ $n/cm^2/s$ flux. The irradiation volume and the maximum flux can be altered by changing the beam spot size, and such beam control is featured in the conceptual study.

3.2 Accelerator system

To satisfy the energy selectivity requirement, the output beam energy should be varied from 10 to 40 MeV, which corresponds to the neutron peak energy from 5 to 15 MeV, respectively, in a 5 MeV step size. These energies can be obtained by switching on and off the RF power to the accelerator tank modules. As shown in Fig. 9, the accelerator system consists of three major parts: (1) the injector section, (2) the main accelerator section, and (3) the beam control section. The preliminary study on the conceptual design for the accelerator system has been carried out in FY 1990. Presently, we employ 120 MHz RF frequency for the accelerators.

The injector section has several types of ion sources, low energy beam transport (LEBT) line and radio-frequency quadrupole linear accelerator (RFQ). They supply the positive or negative deuterons, and the hydrogen molecular ions. They can also provide a low-duty (< 1 %) pulsed beam concurrently with the steady cw beam having the opposite sign of charge.

The main accelerator section has several drift tube linear accelerator (DTL) tank modules, which are individually fed by the mega watt class RF sources.

The beam control section has high energy beam transport (HEBT) line, the target interface, and control/safety system including beam diagnosis. The target interface consists of the instruments to control the beam spot size, its distribution, the energy dispersion, and the bunch structure. They are very important to produce well controlled neutron field at the irradiation volume for a long period of the irradiation tests.

3.3 Target system

The target system needs to handle the liquid lithium metal to remove the heat deposited by the high power beam, and the basic idea using the bent back wall to confine the filmed flow with its centrifugal force was invented in the FMIT project. Fig. 10 is a sketch of the target assembly for the ESNIT. The situation is dissimilar to the FMIT project when the incident beam has the various energies. From the result of the preliminary study of heat removal in the target system, the boiling condition on the surface area becomes severe for the lower beam energy. Some mechanism to adjust the flow thickness according to the beam energy is necessary if the flux is maintained to be as high as possible at every time. The purification system to remove O, N, C, and the radioactive products is also an essential issue to operate the Li loop safely.

4. Nuclear data required for ESNIT

The almost issues of the nuclear data required for ESNIT arise from the high-energy tail component of the neutron spectrum in the energy range of 14 − 55 MeV. The required nuclear data and the related activities in the US[5] and Japan are:

(1) *neutron spectrum from the source reactions*

There are reliable data at Ed=35 MeV point, which were measured

for the FMIT project. The new experiments are carried out at JAERI tandem in the energy range, Ed=8−32 MeV.

(2) *neutron data for the transport calculations and for flux monitoring*
The experimental data are available from ORNL(ORELA) and LANL(LAMPF). The evaluation and calculation are performed at ORNL(using TNG), LANL(using GNASH), and JAERI(using EGNASH and SINCROS).

(3) *PKA data for damage calculations*
The damage parameter calculations are performed at LANL(damage energy for isotopes using NJOY(91)) and PNL(pka spectra using SPECTR for isotopes / SPECOM for compounds).
The transmutation calculations are carried out by using REAC*2,3 at WHC, and undergone at JAERI.

(4) *deuteron induced activities and radiations for the shielding calculations*

The critical issues are discussed in the international workshop on the technical review of ESNIT[5] and summarized as:

1. The evaluated nuclear data file should be verified by measured data, including proton induced reactions.
2. The calculated source neutron spectrum should be compared with the experiments, especially in the high−energy tai region.
3. Benchmark tests using the neutron fields are requested for shielding and transmutation calculations.
4. Experiments of PKA at 14 MeV are necessary for the selected targets.
5. Theoretical benchmark calculations and their intercomparison are needed.

5. Summary

The key concept of the ESNIT is "starting at smaller scale and upgrade according to the research stage". Initially, it was conceived as one−fifth scale of the FMIT, however, it is already increased to the half scale now, due to the requests from the fusion energy development research. To avoid the excessive R&D items and to construct the facility in a short lead term, we must decide the realistic start point and the upgrade path urgently.

References

1) T. Kondo, H. Ohno, M. Mizumoto and M. Odera, J. Fusion Energy, 8 (1989), 229.
2) International Fusion Materials Irradiation Facility(IFMIF) Workshop, San Diego, Feb. 14–17, 1989.
3) E. K. Opperman, HEDL–TME 81–45, 1981.
4) K. Noda, H. Matsuo, K. Watanabe, M. Sugimoto, Y. Kato, H. Sakai, T. Kikuchi, Y. Oyama, H. Ohno and T. Kondo, J. Nucl. Mater. 179 (1991), 1147.
5) Workshop on Reviewing ESNIT – Accelerator, Target, and Experimental Systems, Aug. 26–30, 1991, (and Supplementary Workshop on Reviewing ESNIT – Evaluation of Neutron Irradiation Field Characteristics, Damage Parameters and Nuclear Data, Oct. 7, 1991) held at JAERI, Tokai. (proceedings will be published)

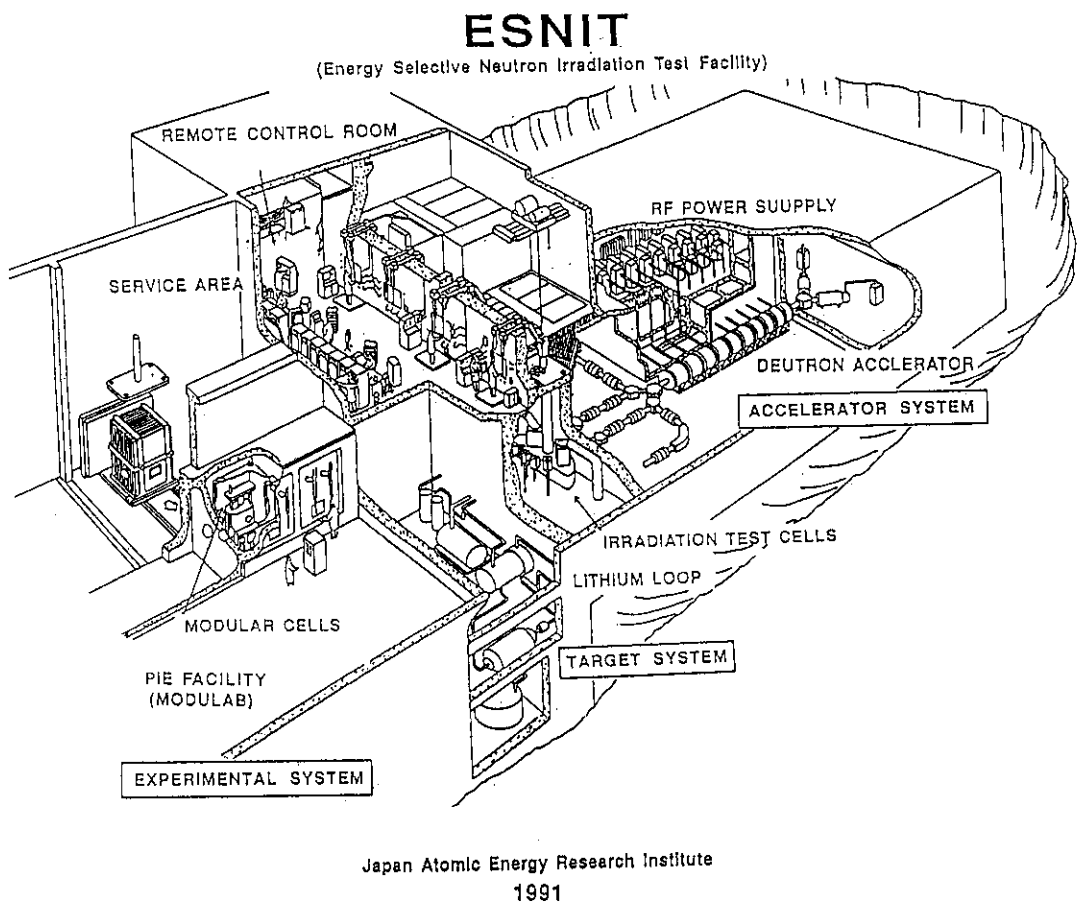

Fig. 1 A conceptual view of the ESNIT facility.

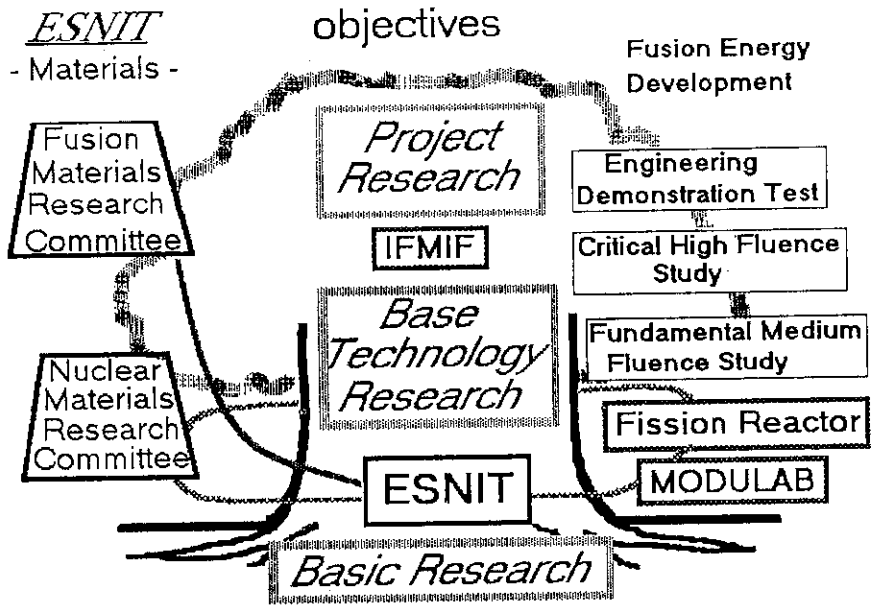

Fig. 2 The objectives of the ESNIT program and the relationship to the IFMIF program.

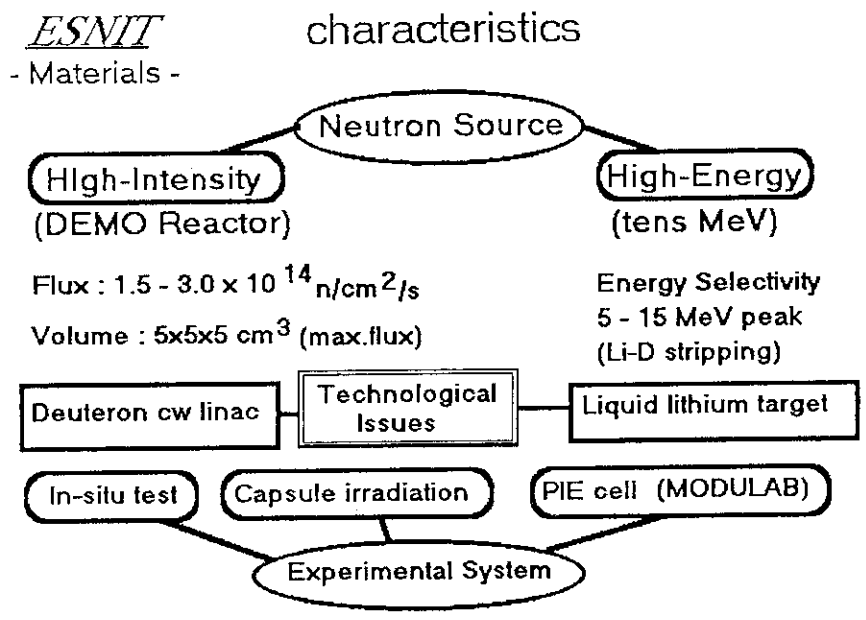

Fig. 3 The characteristics of the ESNIT and the major issues for development.

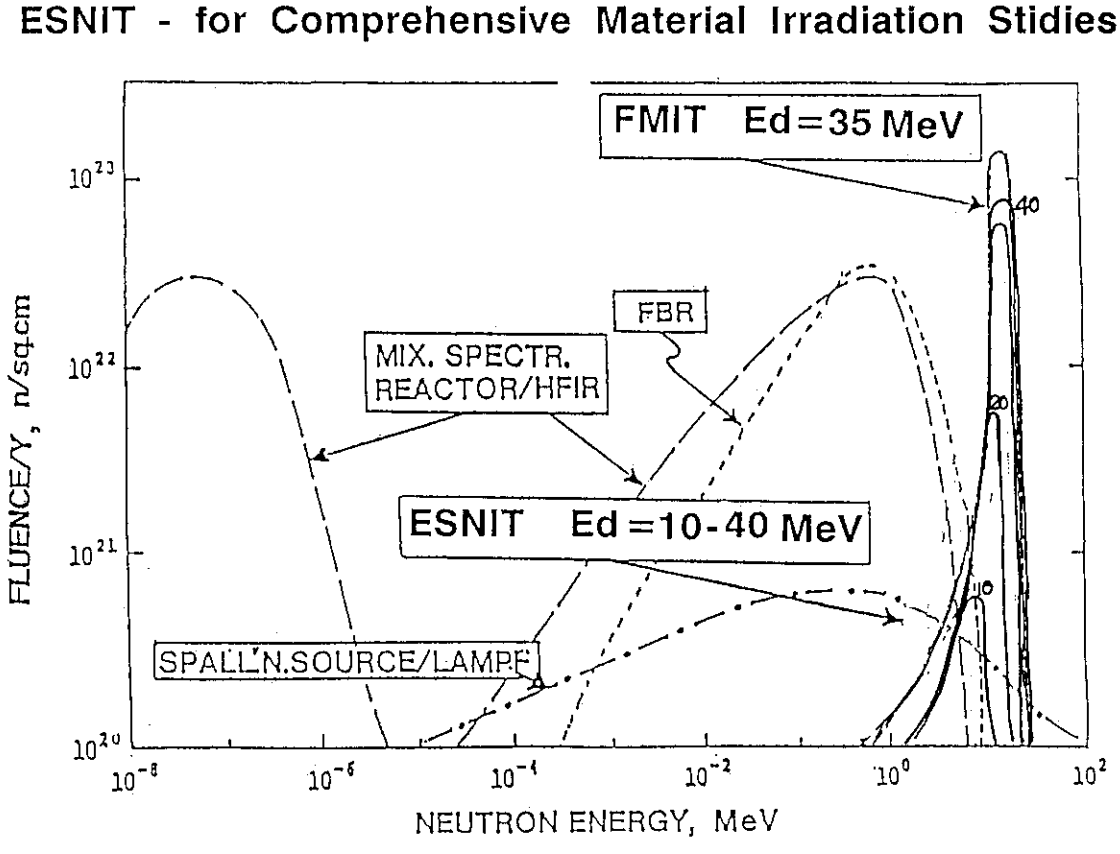

Fig. 4 The comparison of neutron fluence among the intense neutron sources for material irradiation studies.

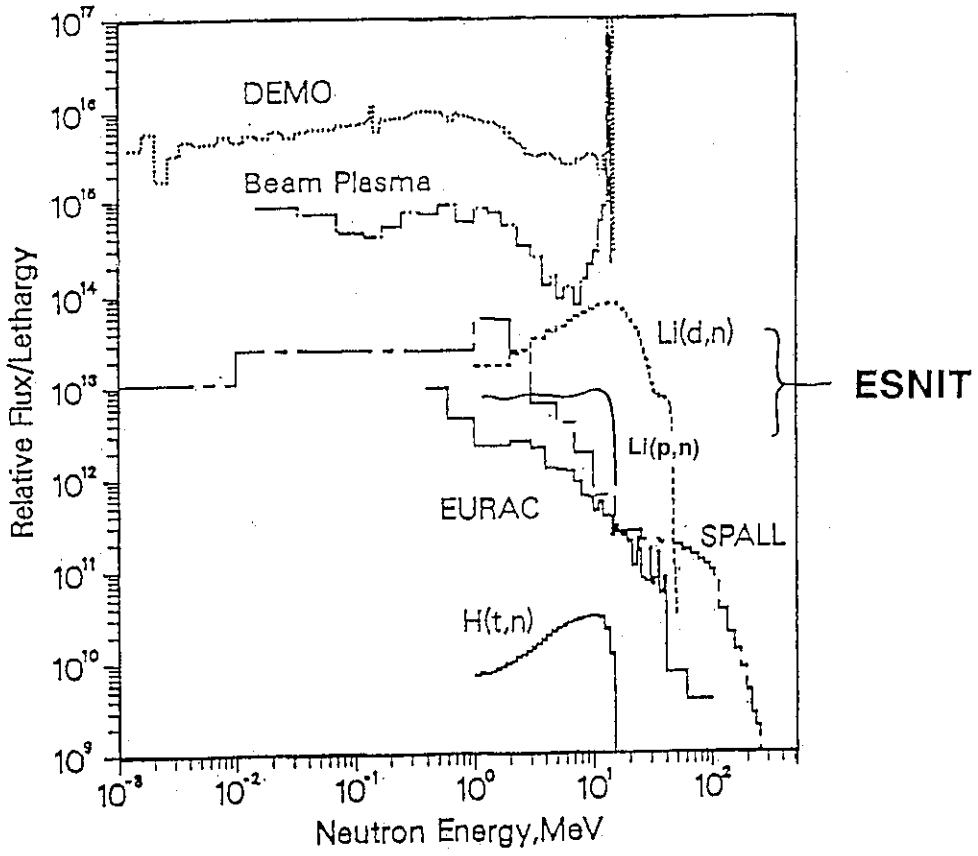

Fig. 5 The energy spectra obtained from the various neutron sources proposed for fusion materials research.

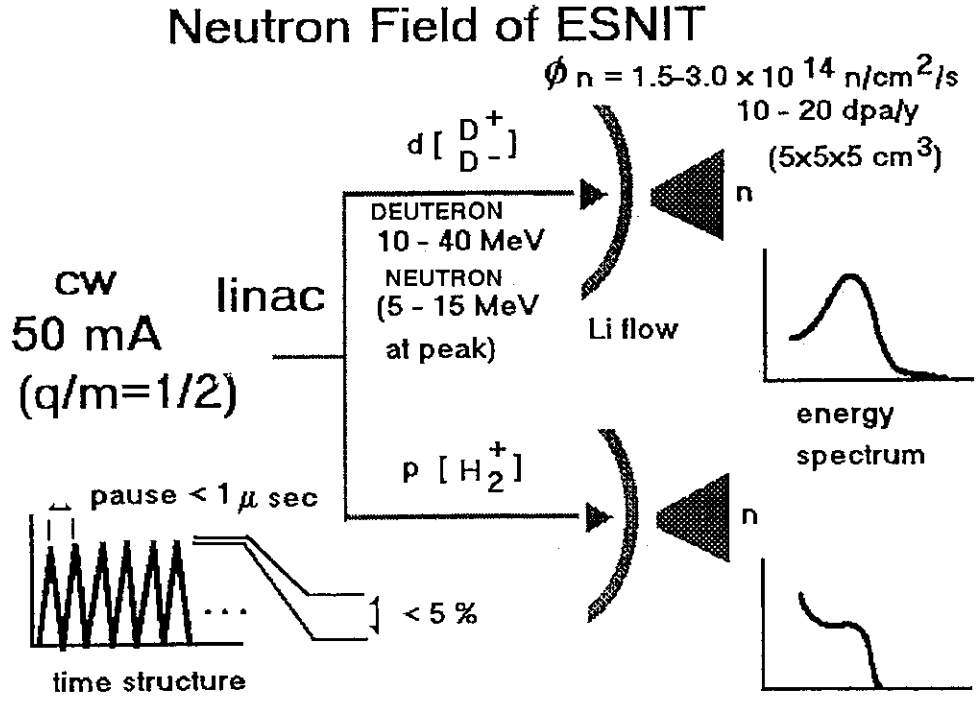

Fig. 6 The requirements to the beam conditions and the resulting neutron energy spectra.

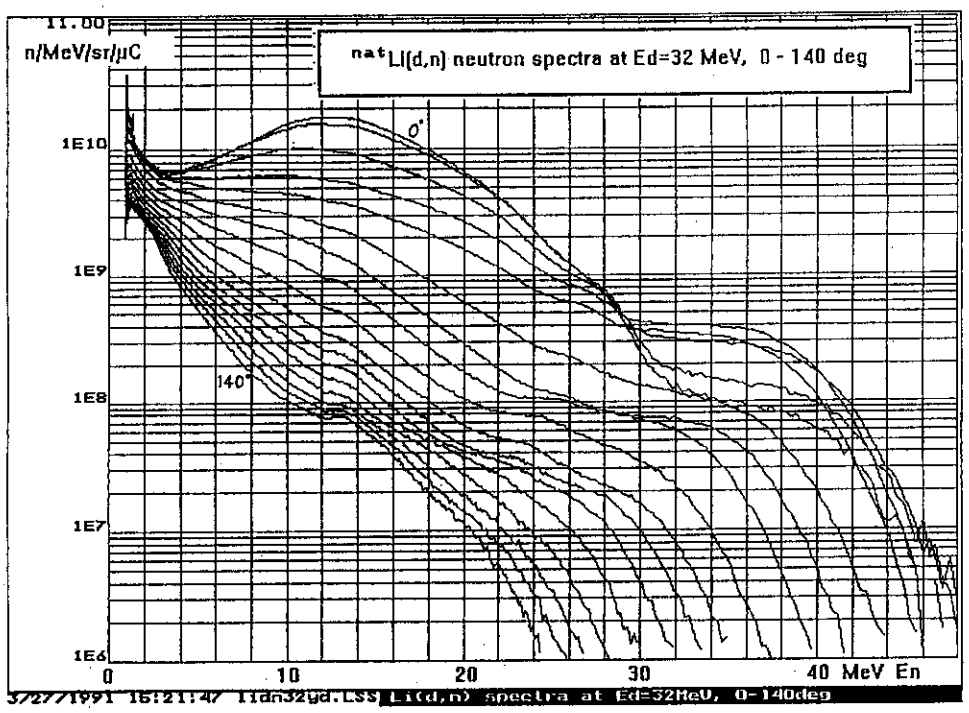

Fig. 7 The measured neutron spectra of the d-Li reaction, at Ed=32 MeV, and θn=0-140°.

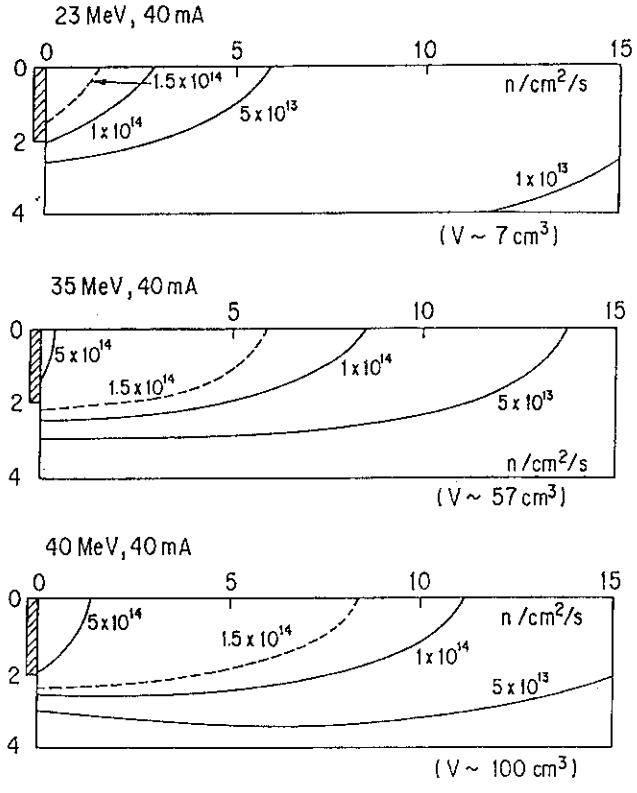

Fig. 8 The calculated neutron flux map and the irradiation volumes where $\phi_n \geq 1.5\times10^{14}$n/cm^2/s.

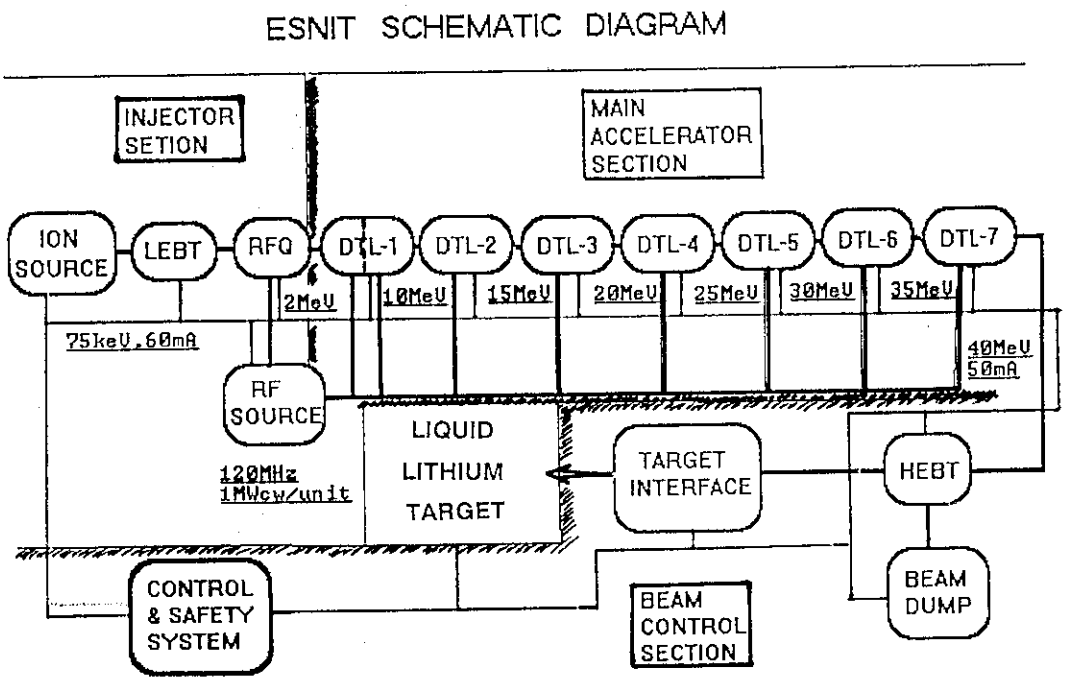

Fig. 9 The schematic diagram of the accelerator system for ESNIT.

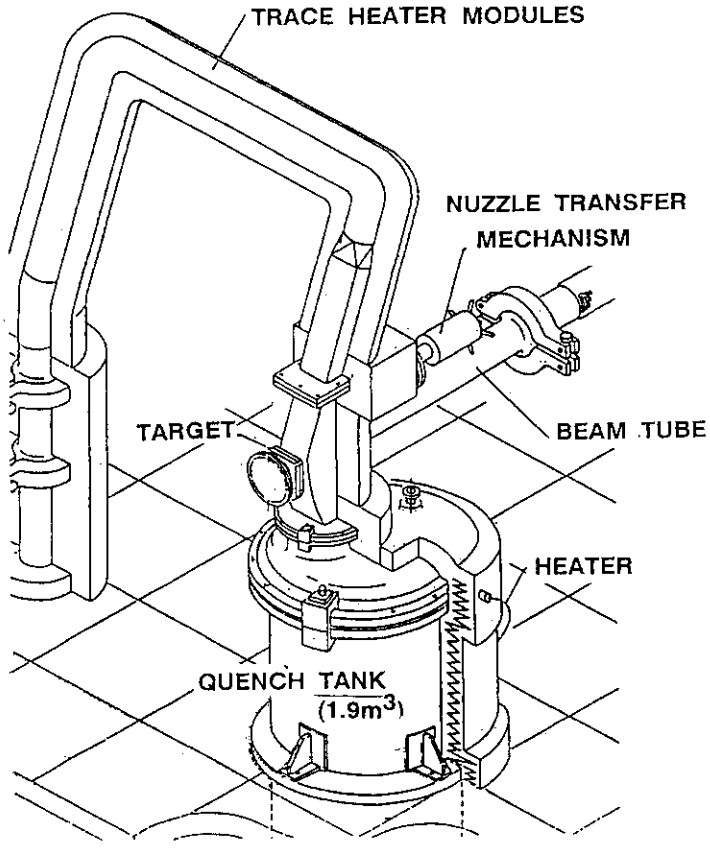

Fig. 10 The liquid lithium target assembly for ESNIT.

2.4 PROGRESS OF NUCLEAR THEORY

2.4.1 STATISTICAL MULTISTEP PROCESSES IN NUCLEAR REACTIONS

Yukinobu Watanabe

Department of Energy Conversion Engineering, Kyushu University,
Kasuga, Fukuoka 816, Japan

Quantum-mechanical theories and models of statistical multistep processes in nuclear reactions are reviewed. Effect of the multistep compound process on continuum angular distributions is investigated within the framework of the quantum-mechanical model in relation to applications of the Kalbach-Mann systematics.

1. Introduction

Preequilibrium processes make substantial contributions to the cross sections of nuclear reactions at bombarding energies above 10 MeV per nucleon. The spectrum of emitted particles in such reactions is schematically illustrated in Fig.1 together with brief explanations of the reaction processes dominant in each classified energy region: evaporation, preequilibrium and direct region. The preequilibrium region of interest exhibits a continuous spectrum with a high energy tail where the angular distribution is peaked forward.

The preequilibrium process has been extensively studied since the exciton model was proposed by J.J. Griffin[1] in 1966. The exciton model has been extended and refined through analyses of many experimental data, and several models have been developed within the framework of semiclassical or phenomenological approaches[2]: the hybrid model[3], the geometry-dependent hybrid model[4], and the generalized exciton model[5] and so on. These models can provide reasonable fit to the observed energy and angular distributions of the emitted particles using some adjustable parameters and have led to quite successful results in neutron nuclear data evaluation.

On the other hand, in 1980's, fully quantum-mechanical (QM) theories of preequilibrium processes have been developed by several groups: Feshbach, Kerman, and Koonin[6] (FKK theory), Tamura et al.[7] (TUL theory), Nishioka et al.[8] (NWY theory), Kalka et al.[9] (SMD-SMC model) and so on. In more recent years, the application of the QM theories to nuclear data evaluation has been proposed through analyses of many experimental data.[10,11] In the QM theories, multistep reaction processes are divided into two different processes: multistep direct (MSD) and multistep compound (MSC) reaction processes. Some statistical treatments are made in the above QM theories because one deals with the continuum region with a high level density.

Several excellent reviews of the statistical multistep process have so far been

published[10-12]. In them, one can know the present status of the theories and models related to the statistical multistep processes or preequilibrium process. In this review, only the essentials of the FKK theory[6], the TUL theory[7] and the SMD-SMC model[9] as the QM theories are briefly summarized together with their application to neutron-induced reactions at 14 MeV and recent analyses of (p,p') and (p,n) reactions in 80-200 MeV. In addition, of a particular interest is the effect of the MSC process on continuum angular distributions for nucleon-induced reactions in 10-20 MeV region in relation to the application of the Kalbach-Mann systematics. Finally the preliminary result is also discussed in this paper.

2. The quantum mechanical theories of statistical multistep processes

2.1 Multistep description of a nuclear reaction

The basic physical picture underlying the quantum-mechanical multistep theory can be given in a series of nucleon-nucleon interaction between the projectile and the target nucleons in terms of the single particle model. It is the same as for the exciton model. The first interaction creates a 2 particle 1-hole (2p1h) state, and subsequent interactions create additional p-h pairs and lead to 3p2h states. Such process continues until the energy deposited in the nucleus is spread to produce a fully-equilibrated nucleus which then decays statistically.

As shown in Fig.2, one can consider separately the states with at least one particle in the continuum (the states $P\Phi$) and the states with all particles bound ($Q\Phi$) at each stage, where P and Q are the projection operators acting on the total wavefunction Φ and $P+Q=1$. The set of states $P\Phi$ contributes to the multistep direct (MSD) process leading to a forward-peaked angular distribution and the other set of states $Q\Phi$ to the multistep compound (MSC) process leading to a 90° symmetric angular distribution.

The preequilibrium emission can occur directly at each stage from the P-chain or indirectly from the Q-chain as shown in Fig.2. In the latter case the emission process has to go through states in the P-chain. The MSD reactions take place down the P-chain rapidly, while the MSC reactions take place down the Q-chain much more slowly. In the the MSC process via the Q-chain, a large number of interactions taking place without changing the exciton number lead to quasi-equilibrium at each stage of the Q-chain and result in particle emissions with a 90° symmetric angular distribution.

As typical theories and models of the statistical multistep process, the FKK theory, the TUL theory, and the SMD-SMC model are summarized with recent progress in the following subsections.

2.2 The FKK theory

Under the above-mentioned physical picture, the FKK theory[6] gives a unified description of the statistical multistep process, which is expressed as an incoherent sum of the contribution from statistical multistep direct (SMDE) and compound (SMCE) emission.

The double differential cross section for the SMCE process is given by the product of three factors: (i) the probability of formation of the compound system, (ii) the probability of the system arriving to the N-th stage without particle emission, (iii) the probability that a particle will be emitted into the continuum from N-th stage. That is,

$$\frac{d^2\sigma}{d\Omega d\varepsilon} = \pi\lambda^2 \sum_J (2J+1) \sum_{N=1}^{r} \sum_{ls\lambda\nu} \left\{ C^{\lambda}_{lsJ} P_{\lambda}(cos\theta) \sum_{\nu=N-1}^{N+1} \frac{\langle \Gamma^{\uparrow lsv}_{NJ}(U) \rho^N_J(U) \rangle}{\langle \Gamma_{NJ} \rangle} \times \right.$$

$$\left. \times \left(\prod_{m=1}^{N-1} \frac{\langle \Gamma^{\uparrow}_{mJ} \rangle}{\langle \Gamma_{mJ} \rangle} \right) \right\} \frac{2\pi \langle \Gamma^{in}_{lJ} \rangle}{\langle D_{lJ} \rangle} \quad . \tag{2.1}$$

Each symbol used here is the same as in Ref.11. All the factors in the above expressions are calculated quantum-mechanically or obtained from the systematics of nuclear properties. Several improvements of the SMCE model have recently been made with the realistic wavefunctions of the interacting nucleons and inclusion of the distinction between neutrons and protons.[13)]

On the other hand, the double differential cross section for the SMDE is given by

$$\frac{d^2\sigma}{d\Omega d\varepsilon} = \left(\frac{d^2\sigma}{d\Omega d\varepsilon} \right)_{one\text{-}step} + \left(\frac{d^2\sigma}{d\Omega d\varepsilon} \right)_{multi\text{-}step} \quad . \tag{2.2}$$

$$\left(\frac{d^2\sigma}{dUd\Omega} \right)_{Multistep} = \sum_N \sum_{M=N-1}^{N+1} \int \frac{dk_1}{(2\pi)^3} \cdots \frac{dk_N}{(2\pi)^3} \left[\frac{d^2W_{M,N}(k_f,k_n)}{dU_f d\Omega_f} \right] \cdots$$

$$\cdots \left[\frac{d^2W_{2,1}(k_2,k_1)}{dU_2 d\Omega_2} \right] \left[\frac{d^2\sigma_{1,i}(k_1,k_i)}{dU_1 d\Omega_1} \right]_{one\text{-}step} \quad . \tag{2.3}$$

$$\frac{d^2W_{N,N-1}}{dU_N d\Omega_N} = 2\pi^2 \rho_c(k_N) \rho_N(U_N) \left| \langle \chi^{(-)}_N | V_{N,N-1} | \chi^{(+)}_{N-1} \rangle \right|^2 \tag{2.4}$$

The terminology used here is identical with that in Ref.11. An effective nucleon-nucleon interaction $V(r)$ is applied for the calculation of the matrix element $V_{N,N-1}$ between the nuclear states N-1 and N and is assumed to be a Yukawa potential with range 1 fm. The transition probability given in Eq.(2.4) is averaged over many final states under the leading particle statistics[14)], so that the interference terms cancel and the orbital angular momenta contribute incoherently.

Applications of this theory have been reported to (N,N) data[15)] and (p,α) data[16)] for projectile energies upto 200 MeV and a broad mass range of target nuclei. Some results of recent analyses[17,18)] of experimental data on (p,p') and (p,n) reactions at 120 MeV are shown in Fig.3, In these analysis[12,17,18)], dependence of the strength V_0 of the effective nucleon-nucleon interaction on the projectile energy E_p has been investigated. The result has indicated that the strength V_0 shows a dependence on E_p that follows that of optical model potentials and the central part of the scalar-isoscalar NN interaction.

There is a controversy related to the formalism of the SMDE process[19-21)]: it is a problem whether the transition matrix element for the multistep process is expressed as the

DWBA form (Eq.(2.4)) or the non-DWBA form $\langle\chi_N^{(+)}|V_{N,N-1}|\chi_{N-1}^{(+)}\rangle$. The question has been answered by Feshbach[22] and the DWBA form has been implemented in the calculation of the SMDE[15-18]. However there is still an opinion that the use of the DWBA form may lead to oversimplification[14].

As the incident energy decreases, the contribution of the SMCE becomes important even at relatively high outgoing energies and a combination of the SMCE and SMDE models is necessary to analyze such reactions. A typical example[23] is shown for the ^{209}Bi(n,xn) reaction at 20 MeV in Fig.4. The calculated result gives satisfactory agreement with experimental data over the whole outgoing energy range.

2.3 The Tamura-Udagawa-Lenske (TUL) theory

This theory is referred to as the Multistep Direct Reaction (MSDR) theory[7] and closely tied to the early direct-reaction methods such as DWBA and CC methods. A statistical assumption is introduced to obtain relatively simple expression of the energy-averaged cross section: it is related to randomness called residual-system statistics[14] that the configuration mixing due to the interaction within the residual nucleus has a random character. According to the TUL theory, the double differential cross sections for one-step and two-step transitions are given by

$$\frac{d^2\sigma^{(1)}(E_b;\theta_b)}{dE_b d\Omega_b} = \sum_J \rho_J(E_x)\frac{d\sigma_J^{(1)}(E_b,\theta_b)}{d\Omega_b} \quad , \tag{2.5}$$

$$\frac{d^2\sigma^{(2)}(E_b;\theta_b)}{dE_b d\Omega_b} = \sum_{J_1J_2}\int dE_c \rho_{J_1}(E_x)\rho_{J_2}(E_x')\sum_J \frac{d\sigma^{(2)}_{J_1J_2;J}(E_b,E_c;\theta_b)}{d\Omega_b} \quad , \tag{2.6}$$

where $\rho_J(E_x) = \sum_B C_B(E_x)(d_J^{BA})^2$ is the spectroscopic density, and the coefficient $C_B(E_x)$ can be interpreted as the relative contribution of the model state B to the real level with energy E_x and d_J^{BA} is the spectroscopic amplitude. The cross sections $d\sigma^{(1)}/d\Omega_b$ and $d\sigma^{(2)}/d\Omega_b$ are the first and second order DWBA cross sections.

Tamura et al.[7] have applied this theory to analyses of cross sections and analyzing powers for several (p,p') and (p,α) reactions at 62 or 65 MeV and (p,n) data at lower energy, and generally satisfactory results have been obtained. The TUL theory has also been used to calculate 14 MeV (n,xn) cross section.[24-26] The results are shown in Figs 5 and 6. As shown in Fig.6, the high energy part with structures due to collective excitations is well reproduced by the one- and two-step MSDR components. In Fig.5, the solid line is a incoherent sum of the one-step MSDR contribution (RPA-DWBA) and multistep contributions calculated using the generalized exciton model. The MSDR approach has also been applied to heavy-ion induced reactions[27]. A code ORION-TRISTAR[28] is now available as a computer program based on this theory. Note that this code can calculate only the one-step cross section.

2.4 The SMD-SMC model (Kalka model)

This model[9] gives a unique description of emission spectra, angular distributions and activation cross sections with a pure statistical multistep approach based on both Green's function formula and random matrix physics. According to this model, analytical expressions for the cross section are obtained as an incoherent sum of each process,

(a,xb) = (SMD) + (SMC) + (MPE),

where (SMD) and (SMC) are statistical multistep direct and compound cross sections, respectively. (MPE) denotes multiparticle emissions which are treated as a pure SMC concept.

Mean squared matrix elements between bound and/or unbound configurations are expressed analytically by using a simple surface-delta residual interaction of the strength F_0=27.5 MeV. Collective amplitudes for phonon excitations (e.g. 2^+ and 3^- for even-even nuclei) and γ-emissions are considered in the matrix elements. As a result, collective excitations [vib] are also treated as well as particle-hole excitations [ex] in the SMD process as follows: [ex], [vib], [2ex], [vib,ex], [2vib], [3ex], [4ex], and [5ex].

The basic formula of SMC processes is defined by the SMC-formation cross section, the escape width and the mean-life time given as the solution of the time-integrated master equation. The similar expression is given in the random matrix model (AWM theory[29]). The SMC-formation cross section can be calculated from flux conservation that the SMD and SMC cross sections become equal to the optical model reaction cross section. For proton-induced reactions isospin conservation is taken into account.[30]

A code EXIFON[31] has been developed on the basis of this model. The code can calculate reactions with emission of neutrons, protons, α-particles and photons, with one parameter set (F_0,r_0,E_F), where r_0 and E_F is the nuclear radius parameter and Fermi energy. Some calculated results[30] for (n,xn), (p,xp), and (p,xn) reactions are shown with experimental data in Fig.7. The agreement with the experimental data is very good. The code can also calculate continuum angular distributions from simple parametrizations based on the Kalbach-Mann systematics. In nuclear data evaluation for more than 20 MeV, the code EXIFON can be used as a very useful tool because time-consuming calculations are not required and the adjustable parameter is only the pairing shift.

3. Effect of the MSC process on continuum angular distributions

A phenomenological approach based on systematics is also used widely for calculations of angular distributions of preequilibrium particle emission. As well-known systematics, there are (i) Kalbach-Mann (KM) systematics[32], (ii) Kalbach systematics[33] and (iii) Kumabe-Watanabe systematics[34] (the modified version of KM systematics). The concept of statistical multistep process is adopted in these systematics. According to (i) and (iii), the double differential cross section for the reaction (a,b) is described in terms of the Legendre polynomials:

$$\frac{d^2\sigma}{d\Omega d\varepsilon} = a_0(MSD)\sum_{l=0}^{l_{max}} b_l P_l(cos\theta) + a_0(MSC) \sum_{l=0,\Delta l=2}^{l_{max}} b_l P_l(cos\theta) \ , \tag{3.1}$$

where the following relation holds for the a_0 values:

$$a_0(MSD) + a_0(MSC) = a_0(tot) = 1/4\pi(d\sigma/d\varepsilon), \tag{3.2}$$

and the Legendre coefficient b_l is parametrized as a function of the outgoing energy.

As seen from Eqs.(3.1) and (3.2), it is necessary to know the relative ratio of the MSD and MSC components at a given outgoing energy. For simplicity, division of the cross section into the MSD part and the MSC part is often replaced by conventional division[34] into the preequilibrium part and the equilibrium part in terms of the exciton model and the evaporation model. Hereafter the former is referred to as the MSD/MSC method and the latter as the PRE/EV method. The energy spectrum of MSC component is harder than that of the pure evaporation component because the MSC component includes emission from states with lower exciton numbers (n=3 or 5). Therefore, it is significant to investigate the effect of the MSD/MSC distinction on the shape of angular distributions in the region where both MSD and MSC components are comparable.

The coefficients b_1 is very sensitive to the MSD/MSC distinction for forward-peaked angular distributions. Thus we compare the coefficients b_1 derived from the experimental data for the 14.1 and 18MeV(n,xn) reactions[35] with those calculated for the above two methods. The code EXIFON[31] based on the SMD-SMC model is used for the MSD/MSC method, while the exciton model and the evaporation model are applied for the PRE/EV method. The results are shown in Fig.8. Note that calculations for the PRE/EV method have been performed by the other group[35]. The coefficients b_1 calculated with the MSD/MSC method are in better agreement with the experimental b_1 than those with the PRE/EV method. In particular, the difference becomes pronounced for target nuclide with low mass number. These results seem indicate the validity of the MSD/MSC method in calculations of angular distributions based on the systematics.

Figure 9 shows the angular distributions calculated with the Kumabe-Watanabe systematics[34] using both the two methods of MSD/MSC distinction. The difference appears clearly in backward angular region and the cross sections calculated from the MSD/MSC method are about 20% larger than those from the PRE/EV method. This is because the MSC component has a 90° symmetry angular distribution and the fraction of the MSC component obtained from the MSD/MSC method is larger than that from the PRE/EV method. However, there is no distinct difference between both the two methods at forward angles. As shown in Fig.9, the two methods do not give rise to much large difference on the shape of the angular distributions. Therefore, more detailed discussion will be necessary through similar analyses of proton-induced reactions, because one can generally obtain more precise data on statistical errors in proton experiments.

4. Conclusions

Various theoretical models have been proposed and developed to aim at a unified description of nuclear reactions including the preequilibrium process. In this paper, typical three models of them were briefly reviewed along the QM approaches which treat the preequilibrium process as the statistical multistep process. There are the other QM theories and models that were not mentioned here: for example, the NWY theory[8], the Luo-Kawai model[36] and so on.

In general, the QM models except the SMD-SMC model require much more time-consuming calculations than the semiclassical models such as the exciton model. However these two kinds of models should be used in a complementary way as mentioned in Ref.11.: the semiclassical models are adequate for fast global computations and are supplemented by the QM models for requirements of more detail and accuracy.

From the practical viewpoint, the SMD-SMC model is considered to have a higher applicability to nuclear data evaluation at present. As discussed in Sec.3, the systematics with the MSD/MSC distinction based on this model results in better agreement with experimental angular distributions. With respect to angular distributions, a reasonable link between the phenomenological and QM approaches is made in the SMD-SMC model.

In future, the QM theories will be applied to a wider range of reactions and will be extensively used in nuclear data evaluation with further improvement.

Acknowledgements

I would like to thank Dr. H. Kalka for kindly offering a code EXIFON and his useful advise. I am also grateful to Dr. M. Baba and his colleague for giving me their experimental data of 14.1 and 18 MeV (n,xn) reactions. Finally I acknowledge valuable discussions with Prof. M. Kawai through co-operative work on the Luo-Kawai model.

References

1) J.J. Griffin, Phys. Rev. Lett. **17**, 478 (1966)
2) M. Blann, Annu. Rev. Nucl. Sci. **25**, 123 (1975) and the papers cited therein
3) M. Blann, Phys. Rev. Lett. **27**, 337 (1971)
4) M. Blann, Nucl. Phys. **A213**, 570 (1973)
5) G. Mantzouranis et al., Z. Phys. A **276**, 145 (1976)
6) H. Feshbach, A. Kerman, and S. Koonin, Ann. Phys. (N.Y.) **125**, 429 (1980).
7) T. Tamura, T. Udagawa, and H. Lenske, Phys. Rev. C **26**, 379 (1982)
8) N. Nishioka, H.A. Weidenmüller, and S. Yoshida, Ann. Phys. (N.Y.), **183**, 166 (1988); **193**, 195 (1989)
9) H. Kalka, D. Seeliger and F.A. Zhivopistsev, Z. Phys. A **329**, 331 (1988); H. Kalka, M. Torjman, and D. Seeliger, Phys. Rev. C **40**, 1619 (1989).

10) M. Uhl, *Proceedings of the Int. Conf. on Nuclear Data for Science and Technology*, Mito, Japan, Ed. S. Igarashi (SAIKON PUBLISHING Co. Ltd., 1988) p.435.
11) P.E. Hodgson, *ibid.*, p.655
12) P.E. Hodgson, *Proceedings of the XXth Int. Symp. on Nuclear Physics, Nuclear Reaction Mechanism,* Germany, Ed. D. Seeliger and H. Kalka (World Scientific, 1991) p.103
13) R. Bonetti and L. Colombo, Phys. Rev. C **28**, 980 (1983); M.B. Chadwick et al., J. Phys. **G15**, 237 (1989)
14) A.J. Koning and J.M. Akkermans, Ann. Phys. (N.Y.) **208**, 216 (1991)
15) R. Bonetti, M. Camnasio and L. Colli Milazzo, Phys. Rev. C **24**, 71 (1981); R. Bonetti, L. Colli-Milazzo, I. Dona and P.E. Hodgson, Phys. Rev. C **26**, 2417 (1982); Y. Holler et al., Nucl. Phys. **A442**, 79 (1985); E, Mordhost et al., Phys. Rev. C **34**, 103 (1986)
16) R. Bonetti, F. Crespi and K.I. Kubo, Nucl. Phys. **A499**, 381 (1989)
17) W. Scobel et al., Phys. Rev. C **41**, 2010 (1990)
18) A.A. Cowley et al., Phys. Rev. C **43**, 678 (1991)
19) T. Udagawa, K.S. Low, and T. Tamura, Phys. Rev. C **28**, 1033 (1983)
20) M.S. Hussein and R. Bonetti, Phys. Lett. **112B**, 189 (1984)
21) I. Kumabe, H. Haruta, M. Hyakutake and M. Matoba, Phys. Lett. **140B**, 272 (1984)
22) H. Feshbach, Ann. Phys. (NY), **159**, 150 (1985)
23) A. Marcinkowski et al., Nucl. Phys. **A530**, 75 (1991)
24) I. Kumabe, K. Fukuda, and M. Matoba, Phys. Lett. **92B**, 15 (1980)
25) Y. Watanabe, M. Hyakutake and I. Kumabe, Tech. Rep. Kyushu Univ. **59**, 469 (1986)
26) H. Lenske and H.H. Wolter, *Proceedings of the XXth Int. Symp. on Nuclear Physics, Nuclear Reaction Mechanism*, Germany, Ed. D. Seeliger and H. Kalka (World Scientific, 1991) p.87
27) H. Lenske et al., Phys. Lett. **122B**, 333 (1983)
28) T. Tamura, T. Udagawa, and M. Benhamou, Comp. Phys. Comm. **29**, 391 (1983)
29) D. Agassi, H.A. Weidenmüller and G. Mantzouranis, Phys. Rep. **22**, 145 (1975)
30) H. Kalka, To be published in *Proc. of Int. Conf. on Nuclear Data for Science and Technology*, 1991, Jülich, Germany
31) H. Kalka, code EXIFON (version 2), (1991).
32) C. Kalbach and F.M. Mann, Phys. Rev. C **23**, 112 (1981)
33) C. Kalbach, Phys. Rev. C **37**, 2350 (1988)
34) I. Kumabe and Y. Watanabe et al., Nucl. Scie and Eng. **104**, 280 (1990)
35) M. Baba and S. Matsuyama et al., private communication (1991)
36) Y.L. Luo and M. Kawai, Phys. Lett. B **235**, 211 (1990); Y.L. Luo and M. Kawai, Phys. Rev. C **43**, 2367 (1991).

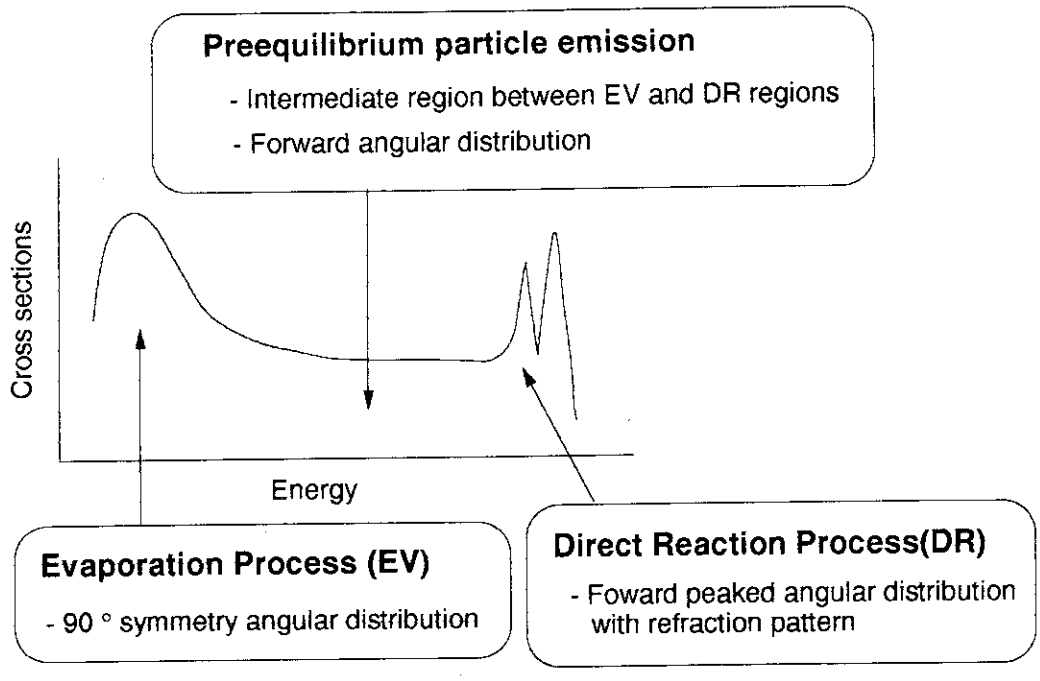

Fig. 1 Schematic spectrum of particles emitted from a nuclear reaction at the projectile energy above 10 MeV per nucleon.

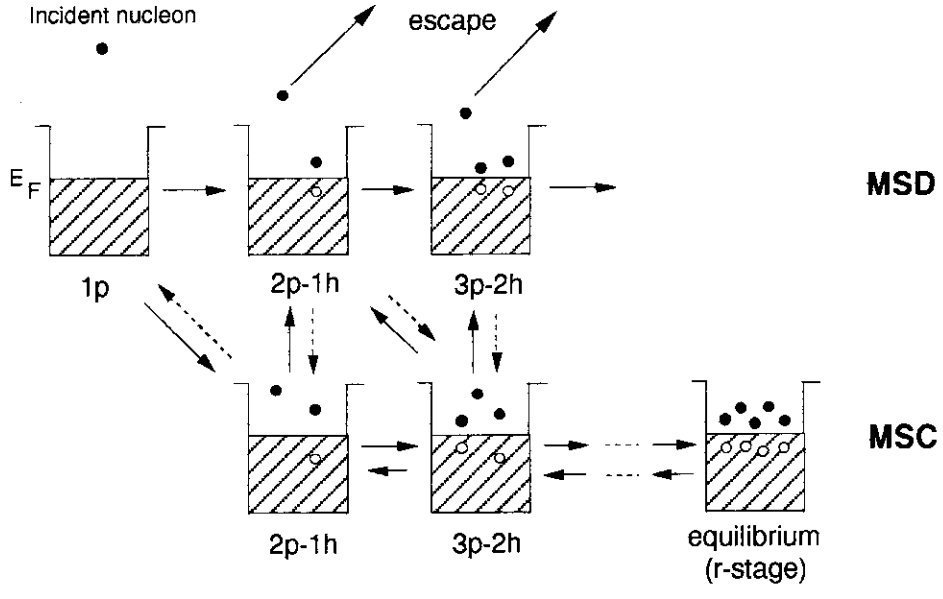

Fig. 2 Schematic representation of multistep reaction process.

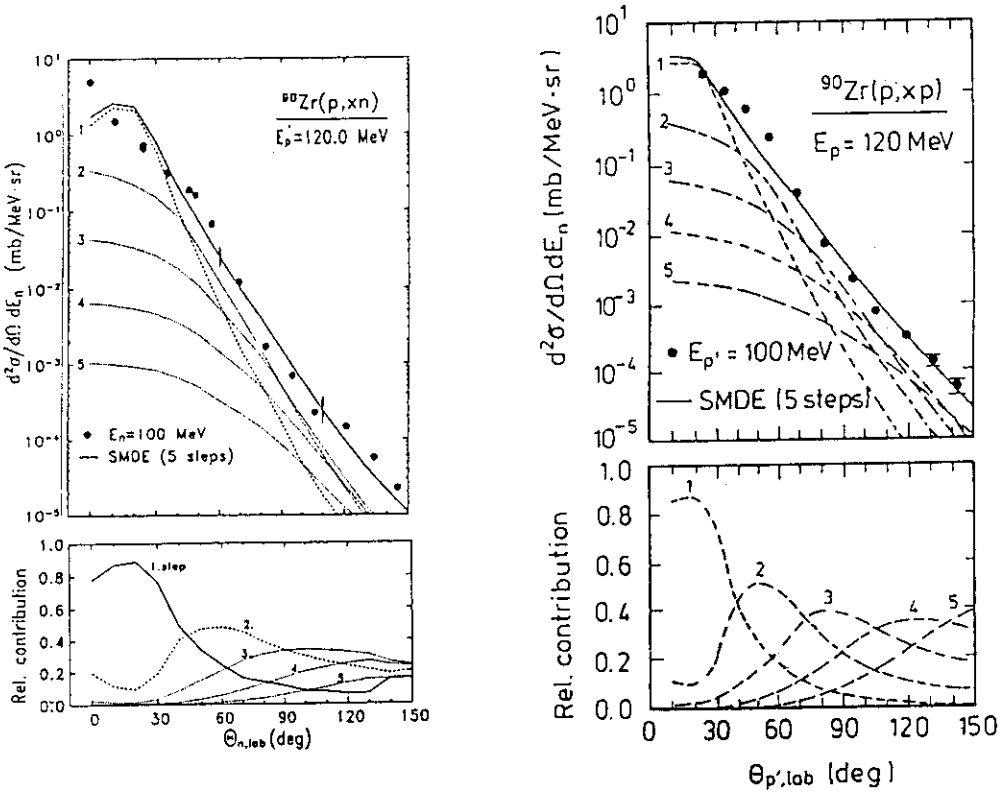

Fig. 3 Absolute and relative contributions of the leading five SMDE steps in comparison to experimental angular distributions from ^{90}Zr(p,n) and (p,p') for E_p=120 MeV (Cowley et al.[17]) and Scobel et al.[18]).

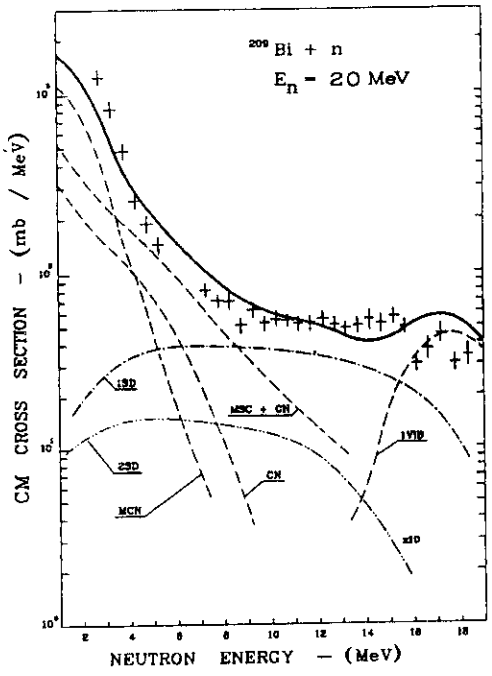

Fig. 4 Comparison of the neutron emission spectrum from the ^{209}Bi + n reaction measured at 20 MeV incident energy with that calculated on the basis of the FKK theory. (Marcinkowski et al.[23])

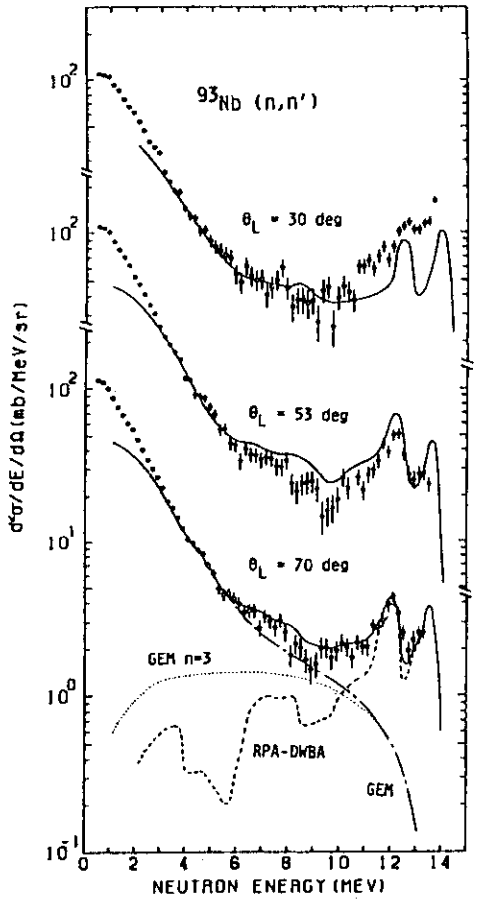

Fig. 5 Comparison of experimental double-differential neutron emission cross sections for ^{93}Nb at En=14 MeV with those calculated by combination of the TUL model and the generalized exciton model. (Watanabe et al.[25])

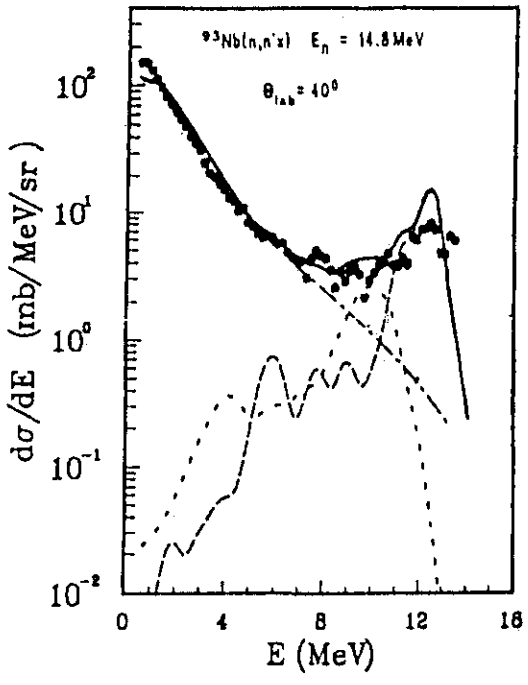

Fig. 6 Spectrum for ^{93}Nb(n,n'x) at En=14.8 MeV and θ=40°. One-step (long-dashed) and two-step (short-dashed) MSDR-contributions and MSC components (dashed-dotted) and their sum (full line) are compared to data (full circle). (Lenske and Wolter[26])

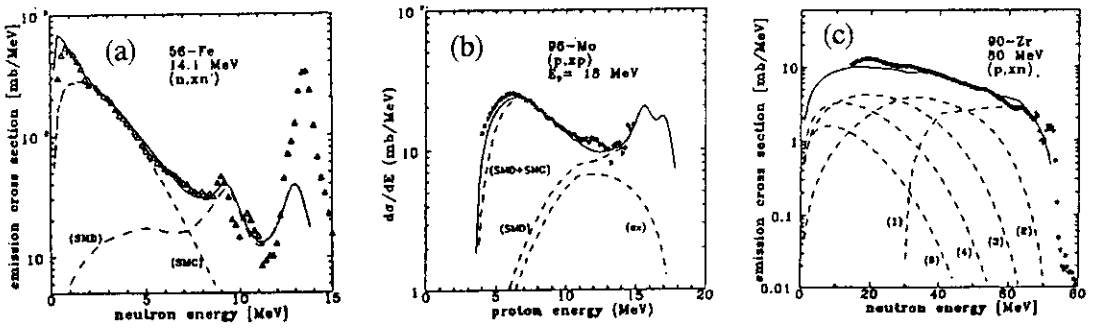

Fig. 7 Comparison of experimental spectra of emitted particles with those calculated using the code EXIFON. (a) (n,xn) emission spectrum at 14.1 MeV incident energy (b) (p,xp)-emission spectrum at 18 MeV incident energy (c) (p,xn) spectrum at 80 MeV incident energy. (Kalka et al.[30])

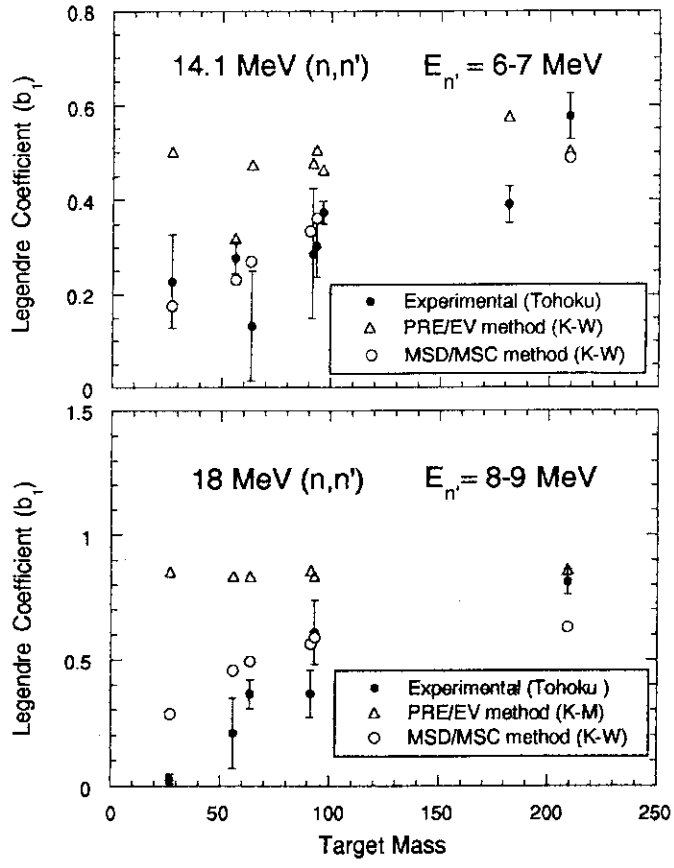

Fig. 8 Comparison of experimental Legendre coefficients b_1 of the first order and those calculated with the systematics for (a) En'=6-7 MeV in 14.1 MeV (n,xn) reactions and (b) En'=8-9 MeV for 18 MeV (n,xn) reactions. Experimental data are from Ref. 35.

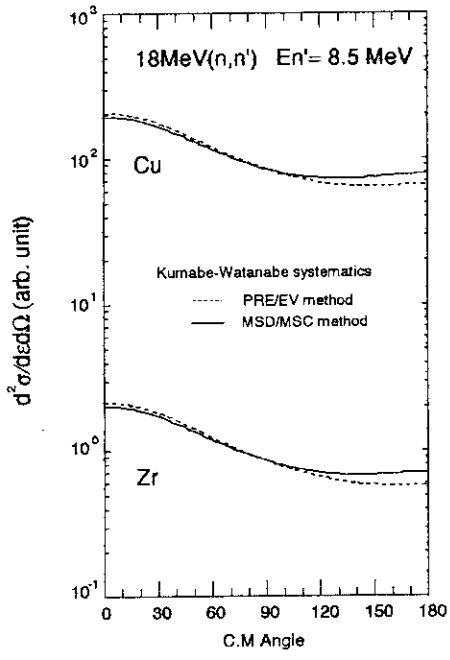

Fig. 9 Calculated angular distributions of neutrons emitted at En'=8-9 MeV from 18 MeV (n,xn) reactions for Cu and Zr. The calculation is based on the Kumabe-Watanabe systematics. The MSD/MSC distinction is made using the MSD/MSC method (solid lines) or the PRE/EV method (dashed lines) as described in the text.

2.4.2 THEORETICAL MODELS FOR CALCULATION OF FISSION NEUTRON SPECTRA

Takaaki Ohsawa

Atomic Energy Research Institute, Kinki University
3-4-1 Kowakae, Higashi-osaka 577 Japan

Abstract

Progress in the theoretical calculation of the fission neutron spectra is reviewed with emphasis on recent developments.

New developments in the study of theoretical models to describe the neutron emission from fission fragments have been made during the last ten years. The models are grouped into three categories: *(1)* Approximate statistical models, such as Madland-Nix model; *(2)* Cascade evaporation models, as proposed by Märten and Seeliger, and also by Hu and Wang; *(3)* Hauser-Feshbach-type models, as proposed by Browne and Dietrich and refined by Gerasimenko *et al.*

In this review, the essential features of these models are outlined, and relevant problems of each model are discussed. Some recent attempts of improvement of the Madland-Nix model, including that proposed by the present author, are also mentioned.

1. Introduction

Most evaluations contained in presently available nuclear data files have still been based on either a Maxwellian or Watt spectrum. This is because these phenomenological formulas, represented by elementary mathematical functions with one or two parameters, are easy to handle both for evaluation and application purposes. However, it has been recognized that these models are not free from defects, *i.e.*,

(a) These models neglect some important features (such as distribution of fragment excitation energy and distinction between light and heavy fragments) in the physics of neutron emission in fission.

(b) As a result of lack of sound physical basis for involved parameter(s), there is only poor predictive power in evaluation of the fission spectra for higher actinides and/or for higher incident energies for which no or scarce data are available.

(c) Close examination of the calculated and experimental spectra reveals that there is a systematic difference between them.

These considerations have led to investigation of more sophisticated models that are able to describe exactly the existing data and, at the same time, able to predict the fission spectra required for applications. New models have been developed during the last ten years that describe the neutron emission from fission fragments. The models are grouped into three categories:

1- Approximate evaporation model : Madland-Nix[1]
2- Cascade evaporation model : Märten-Seeliger[2], Hu-Wang[3]
3- Hauser-Feshbach-type model : Browne-Dietrich[4], Gerasimenko-Rubchenya[5]

Among the three groups, the Madland-Nix (MN) model is easy to calculate while

requiring minimal input, and has been applied to produce evaluated data for some important actinides in JENDL-3 and ENDF/B-VI. A problem of this model is that the low- and high-energy wings of the calculated spectra tend to be underestimated. The cascade evaporation model aims at a complete description of neutron cascade emission, and as a result, requires longer computational time and a substantial input. The Hauser-Feshbach-type model accounts explicitly for the competition of neutron and gamma-ray emission in a given fragment as well as the effects of angular momentum. It also provides a possibility of calculation of the gamma-ray spectrum from fission fragments. However, at present, the model has not attained good accuracy, presumably because of insufficient knowledge of the level density of fission fragments.

Efforts to improve the original MN model have been made in recent years in the following approaches, *i.e.* by taking into account

a) the mass and charge distributions of fission fragments emitting neutrons, instead of two representative fragments in the original MN model;

b) anisotropy of neutron emission in the fragment center-of-mass system;

c) non-equality of the nuclear temperatures of the typical light and heavy fragments.

It is known that the approaches *a)* and *b)* lead to a slight improvement of the calculated spectrum but there still remains discrepancy from experimental data. The present author has been trying to improve the calculation by approach *c)*. This approach is based on the consideration that the deformation energies of the two fragments at the scission point, which are different for the nascent fragments, eventually converts into the internal excitation energies that are different for light and heavy fragments. In addition, the level density parameters for the pair of fragments are generally not equal, so that the nuclear temperatures of the fragment pair are different, in contradiction to the equitemperature assumption used in the MN model. Some results of calculations made along this approach together with discussion on relevant problems are also described.

2. Recent Theoretical Models

2.1 Madland-Nix Model

Madland and Nix[1] proposed a model for fission neutron spectrum calculation which took into account the following points:

a) Nuclear temperature distribution characterizing the emission of neutrons from fission fragments

b) Movement of the fission fragments

c) Energy-dependence of the cross sections for inverse processes

d) Multiple-chance fission in the MeV region

(1) Center-of-Mass Spectrum

According to the Weisskopf evaporation theory, the energy spectrum of neutrons in the center-of-mass (CM) system is written as

$$\phi(\varepsilon) = \frac{1}{T^2}\varepsilon \exp\left(-\frac{\varepsilon}{T}\right)$$

where T stands for the nuclear temperature of fragments after neutron emission. It should be Note that the neutron energy ε is assumed to be small compared with the excitation energy

of the residual nucleus in the derivation of the above formula.

In the case of cascade emission of neutrons, the energy spectrum is gives by the formula of Le Couteur[6]:

$$\Phi(\varepsilon) = k\varepsilon^{\lambda}\exp\left(-\frac{\varepsilon}{T_{eff}}\right)$$

where $\lambda = 5/11$, $T_{eff} = (11/12)T_m$, and

$$k = [\Gamma(16/11)\, T_{eff}^{16/11}]^{-1}$$

where $\Gamma(x)$ is the gamma function.

Every time a neutron is emitted, the nuclear temperature of the residual nucleus decreases. Thus the CM neutron spectrum is a superposition of spectra each with different nuclear temperature. Terrell[7] has found out that the temperature distribution in such a cascade emission could be well represented by the triangular distribution of the form

$$\begin{aligned} P(T) &= 2T/T_m^2, \quad && T<T_m \\ &= 0, && T>T_m \end{aligned}$$

The maximum nuclear temperature T_m is defined as follows,

$$\begin{aligned} <E^*> &= <E_r>+<B_n>+<E_n>+<E_f^{tot}> \\ &= aT_m^2 \end{aligned}$$

where a is the level density parameter. Kapoor[8] showed that, if the inverse reaction cross section was constant, the average spectrum was written as

$$\Phi(\varepsilon) = \frac{2\varepsilon}{T_m^2}E_1(\varepsilon/T_m)$$

(2) Conversion from CM- to L-system

Madland and Nix obtained the neutron spectrum in the laboratory (L) system for the case of constant inverse cross section as follows:

$$\begin{aligned} N(E,E_f) &= \frac{1}{4E_f^{1/4}}\int_{(\sqrt{E}-\sqrt{E_f})^2}^{(\sqrt{E}+\sqrt{E_f})^2}\frac{\Phi(\varepsilon)}{\varepsilon^{1/2}}d\varepsilon \\ &= \frac{1}{3(E_fT_m)^{1/2}}\left[u_2^{3/2}E_1(u_2) - u_1^{3/2}E_1(u_1) + \gamma(3/2,u_2) - \gamma(3/2,u_1)\right] \end{aligned}$$

where

$$u_1=(E-E_f)^2/T_m$$

$$u_2=(E+E_f)^2/T_m$$

$$\gamma(a,x) = \int_0^x u^{a-1}\exp(-u)du$$

(imcomplete gamma function)

The kinetic energies per nucleon for the light and heavy fragments are given by

$$E_{fL}=(A_H/A_L)(<E_f^{tot}>/A) \sim 1 \text{ MeV}$$

$$E_{fH}=(A_L/A_H)(<E_f^{tot}>/A) \sim 0.5 \text{ MeV}$$

respectively. The total neutron spectrum in the L-system is written as

$$N(E)=(1/2)[N(E,E_{fL}) + N(E,E_{fH})]$$

The average energy for this spectrum is given by

$$<E>=(1/2)[E_{fL} + E_{fH}]+(4/3)T_m$$

In the above argument, it was assumed that the inverse cross section for neutron emission was constant. When the energy-dependence of the cross section is taken into account, the CM-spectrum for a fixed nuclear temperature T is given by the well-known Weisskopf formula

$$\phi(\varepsilon,\sigma_c) = k(T)\sigma_c(\varepsilon)\varepsilon\exp(-\varepsilon/T)$$

where the normalization constant $k(T)$ is

$$k(T) = \left[\int_0^\infty \sigma_c(\varepsilon)\varepsilon\exp(-\varepsilon/T)d\varepsilon\right]^{-1}$$

which is temperature-dependent. Integrating the CM-spectrum over the triangular temperature distribution, we have for the CM-spectrum of neutrons

$$\Phi(\varepsilon,\sigma_c) = \frac{2\sigma_c(\varepsilon)\varepsilon}{T_m^2}\int_0^{T_m} k(T)T\exp(-\varepsilon/T)dT$$

A result of calculation with this model for ^{252}Cf(sf) is shown in **Fig.1.** It can be observed that the overall shape of the spectrum is well reproduced but the calculation tends to underestimate in the region below several hundred keV and above several MeV.

2.2 Cascade Evaporation Model

Marten *et al.*[2] proposed a model which took into account the following effects:

a) Excitation energy distribution of fragments at each stage of cascade evaporation on neutrons;

b) Movement of the center of mass;
c) Anisotropy of neutron emission in the CM system;
d) Energy dependence of the inverse cross sections;
e) Mass and kinetic Energy distributions of fission fragments;
f) Semi-empirical level density formula for fission fragments.

The CM spectrum of neutrons emitted from a fragment of mass A and excitation energy E^* is given by the Weisskopf formula

$$\phi_i(\varepsilon,E^*,A) = C\sigma_c(\varepsilon,A-1)\,\varepsilon\,\rho(E^*-B_n-\varepsilon,A-1)$$

The CM spectrum of neutrons emitted from a fragment of mass A and total kinetic energy TKE is represented as a sum of integrations of the above spectrum (weighted with the distribution function $P_i(E^*,A,TKE)$) over the excitation energy E^*;

$$\phi(\varepsilon,A,TKE) = \sum_i \int_{B_i}^{\infty} \phi_i(\varepsilon,E^*,A-i)\,P_i(E^*,A,TKE)\,dE^*$$

The L-system spectrum of neutrons emitted from fragments with mass A and total kinetic energy TKE is calculated by the following equation:

$$N(E,A,TKE) = \frac{1}{4E_f^{1/2}} \int_{(\sqrt{E}+\sqrt{E_f})^2}^{(\sqrt{E}-\sqrt{E_f})^2} \frac{\phi(\varepsilon,A,TKE)}{\varepsilon^{1/2}} \left[\frac{1+b[(E-E_f-\varepsilon)^2/4\varepsilon E_f]}{1+b/3}\right] d\varepsilon$$

where E_f is the kinetic energy per nucleon and the coefficient b is the strength of anisotropy in the CM system. The total neutron spectrum is given by

$$N(E) = \sum_A \int P(A,TKE)\,N(E,A,TKE)\,d(TKE)$$

The basic idea of this model is to simulate the neutron emission process as exactly as possible without adopting simplifying assumptions (such as triangular nuclear temperature distribution). On the other hand, this model requires considerable amount of input data and computating time, which limit the application of this model to nuclides for which those data are available somehow.

Figure 2 shows a result of calculation. The experimental data are best represented by the curve with anisotropy coefficient b=0.1 (β=0.1 in the figure). However, it should be noted, as will be stated later, that recent measurements do not confirm such a strong anisotropy in the CM system.

2.3 Hauser-Feshbach Type Models

Fission neutron emission is nothing other than neutron emission from excited nuclus. It is possible, in principle, to calculate the spectrum with the Hauser-Feshbach formalism. Browne and Dietrich[4] were the first ones to apply the idea to obtain the fission neutron spectrum. Assuming that the initial excitation energies and spins are distributed according to the Gaussian distribution:

$$P(E,J) = (2J+1)\exp[-\{E - E^*(Z,A)\}^2/2\sigma_{E(A,Z)} - J(J+1)/B^2_{Z,A,E}]$$

the CM spectrum can be represented as

$$\phi(\varepsilon) = \sum_J \int \frac{P(E,J)\ \Sigma G_n(E\to E',J\to J')}{D(E,J)} dE$$

$$D(E,J) = \sum_{J'} \int G_n(E\to E',J\to J')dE + \sum_{J''} \int G_g(E\to E'',J\to J'')dE''$$

$$G_n(E\to E',J\to J'') = \sum_{l,s} T_l(E\to E',J\to J'')\ \rho(E',J',Z,A-1)$$

$$G_g(E\to E'',J\to J'') = T_g(E\to E'',J\to J'')\ \rho(E'',J'',Z,A)$$

Figure 3 shows a result of calculation for ^{252}Cf(sf). Compared with the measured data of Green[9], the calculation is higher by 25% at 2 MeV and lower by 70% at 10 MeV. The calculation is sensitive to the level density, but not so sensitive to the neutron transmission coefficients nor to spin cut-off parameter. The Gilbert-Cameron level density formula[10] was used in this calculation but it is questionable if this formula represents adequately the actual level density of neutron-rich nuclides located far from the beta-stability line.

Geresimenko *et al.*[5] made some improvements to this approach, *i.e.*,

a) Ignatyuk's level density formula[11], which took into account the energy-dependence of the level density parameter, was used;

b) Exact formula was used to calculate the partial neutron spectra during the cascade process;

c) The excitation energy was calculated with the following equation in which the pairing effects are explicitly considered.

$$E^*(A,Z) = \nu(A)[\varepsilon(A)+B_n(A,Z)+\delta(A-1,Z)]+B_n(A,Z)/2$$

The weighted sum of spectra calculated for 14 nuclides chosen from A=96 to 156 for ^{252}Cf(sf) is depicted in **Fig.4**. An improvement can be seen in the agreement with experimental data over the results by Browne and Dietrich. It is reported that the calculation is sensitive to the items *a)* and *c)* among the above improvements.

3. Improvements of Madland-Nix Model

Attempts have been made to remove the deficiencies of the Madland-Nix model. Four approaches have been proposed during the last several years.

3.1 Improvements by Märten et al.

Märten *et al.*[12] proposed to generalize the MN model by taking into consideration the following factors:

a) the mass distribution of fragments;

b) competition of neutron and gamma emission;

c) the CM anisotropy of neutron emission.

Märten *et al.* showed that, accoding to this improvement, the spectrum components in the regions below 1 MeV and above 4 MeV are somewhat increased, in better agreement with experimental data (**Fig.5**). A drawback of this approach is that considerable amount of input data, such as kinetic energy and neutron multiplicity as a function of fragment mass, is required to perform the calculations.

3.2 Improvement by Madland *et al.*

In an effort to improve their model, Madland *et al.*[13] made calculations accunting for the effects of

a) fragment mass distribution, representing the distribution by 28 nuclides;
b) fragment charge distribution, approximating the distribution by two Gaussian function;
c) using experimental values for the fragment kinetic energies instead of the values inferred from systematics;
d) using measured data for the neutron multiplicity as a function of fragment mass.

A comparison of the original and refined models is shown in **Fig.6** for ^{252}Cf(sf). The refined model calculation agrees better than the original model, but there is still room for further improvement.

3.3 Improvement by Walsh *et al.*

It is considered that the fission fragments receive a large orbital angular momentum of about 7±2 $\hbar$ at the moment of scission. As a result, it has been inferred that fission neutrons are emitted anisotropically in the fragment CM system, the degree of anisotropy being about 10%. Walsh *et al.*[14] took this effect into account in the framework of the Madland-Nix model and showed that an assumtion of anisotropy of strength b=0.1 slightly enhanced the low-energy (E_n<0.5MeV) and high-energy (E_n>6MeV) components of the spectrum (**Fig.7**). However, recent multiparameter measurements for ^{252}Cf(sf) have shown that the coefficient of anisotropy b is smaller than 0.1 by one order of magnitude. These data, if correct, suggest that the anisotropy of neutron emission is not a decisive factor in improving the model.

3.4 Improvement by the Author: Non-equitemperature Model

The original Madland-Nix model assumed that the same temperature distribution applied to both of the fragments. This would be the case, if the nuclear system were in statistical equilibrium at the scission point. However, it is questionable if this assumption should be valid.[15] Even if equilibrium were established at the scission point, since the total excitation energy availble for neutron emission is a sum of internal excitation energy $a_i T_{oi}^2$ and the total deformation energy D_i at the scission point, *i.e.*,

$$\langle E_i^* \rangle = a_i T_{0i}^2 + D_i = a_i T_{mi}^2$$

i=L (light fragment) or H (heavy fragment)

and since the deformation energy is strongly affected by the nuclear structure of the fragments, the temperatures for the two fragments are generally not equal. Defining the ratio

of the maximum temperatures for the light and heavy fragments as $R_T=T_{mL}/T_{mH}$, and considering the energy conservation, we have

$$T_{mL} = [AR_T^2/(A_L R_T^2+A_H)]^{1/2} T_m$$

$$T_{mH} = [A/(A_L R_T^2+A_H)]^{1/2} T_m$$

Figure 8 compares the spectra of ^{235}U(n,f) for E_n=0.53 MeV for different values of R_T. It can be seen that accounting for the non-equitemperature nature improves the agreement between calculation and measurement. It should be noted here that the above results are based on the constant inverse-cross section model.

Calculations based on the energy-dependent inverse cross-section model have been made using two different global optical potentials, *i.e.*, Becchetti-Greenlees[16] and Wilmore-Hodgson[17]. The calculated inverse cross setions for two typical fission fragments ^{96}Sr and ^{140}Xe in ^{235}U(n,f) are shown in **Fig.9** and the fission neutron spectra calculated with them are compared in **Figs.10**. It can be observed that taking into consideration the energy dependence of the inverse cross section somewhat distorts the spectrum shapes, *i.e.* softens the high-energy part and hardens the low-energy part of the spectrum. We can also observe that accounting for the non-equitemperature nature improves the agreement with the experimental data in these cases too. It should be noted that the same level density parameter (a=A/9.6) as was determined from the constant-cross-section model were applied in these caculations. Calculations for various values of the level density parameter, while keeping the temperature ratio constant R_T=1.13, are shown in **Figs.11**. It was found that a level density parameter a little smaller than A/9.6 gave better fitting to the experimental data for either of the inverse cross section set.

4. Concluding Remarks

Recent theoretical models for calculation of the fission neutron spectra were reviwed. Aside from exact simulation of the physics of fission neutron emission for the time being, in view of the practical application for the purpose of nuclear data evaluation, a suitable model should satisfy the following two conditions: *(1)* it reproduces the measured data for important nuclides, such as ^{235}U and ^{252}Cf, for which much experimental information is available, to the degree of accuracy that is required from nuclear design and dosimetry calculations; *(2)* it can be used for prediction of the spectra for *nuclides* as well as for higher *incident energies* for which less efforts have been made thus far to measure the data but still will be important for extended burnup analysis and nuclear incinerator design. In this respect, the Madland-Nix model, with its rather simple structure and small amount of input data required, seems to provide a good basis from which to start toward a more exact prescription of calculation of the fission neutron spectra. The non-equitemperature model proposed by the present author is an attempt in that direction. A problem to be solved for this model lies in finding a method to estimate the nuclear temperature ratio on the basis of some model or semi-empirical systematics.

References

1. D.G.Madland and J.R.Nix, Nucl. Sci. Eng. **81**, 213 (1982)

2. H.Märten, D.Neumann and D.Seeliger, IAEA-TECDOC-335, p.255 (1985)

3. Hu Ji-min and Wang Zheng-shing, Physica Energiae Fortis et Physica Nuclearis, **3**, 772 (1979) (in Chinese)

4. J.C.Browne and F.S.Dietrich, Phys. Rev. **C10**, 2545 (1974)

5. B.F.Gerasimenko and V.A.Rubchenya, Proc. All-Union Conf. on Neutron Physics, Kiev (1980) p.114; *ibid.*, Kiev (1983) p.349

6. K.J.Le Couteur, Proc. Phys. Soc. **A65**, 718 (1952)

7. J.Terrell, Phys. Rev. **113**, 527 (1959)

8. S.S.Kapoor, R.Ramanna and P.N.Rama Rao, Phys. Rev. **131**, 283 (1963)

9. L.Green, J.A.Mitchell and N.M.Steen, Nucl. Sci. Eng. **50**, 257 (1973)

10. A.Gilbert and A.G.W.Cameron, Can. J. Phys. **43**, 1446 (1965)

11. A.V.Ignatyuk, INDC(CCP)-233/L (1985)

12. H.Märten and D.Seeliger, Nucl. Sci. Eng. **93**, 370 (1986)

13. D.G.Madland *et al.*, Proc. IAEA/AGM on Physics of Neutron Emission in Fission, Mito, (1989), p.259

14. R.L.Walsh, Nucl. Sci. Eng. **102**, 119 (1989)

15. T.Ohsawa and T.Shibata, Proc. Int. Conf. on Nuclear Data for Science and Technology, Jülich, 1991, to be published.

16. F.D.Becchetti, Jr., and G.W.Greenlees, Phys. Rev. **182**, 11190 (1969)

17. D.Wilmore and P.E.Hodgson, Nucl. Phys. **55**, 673 (1964)

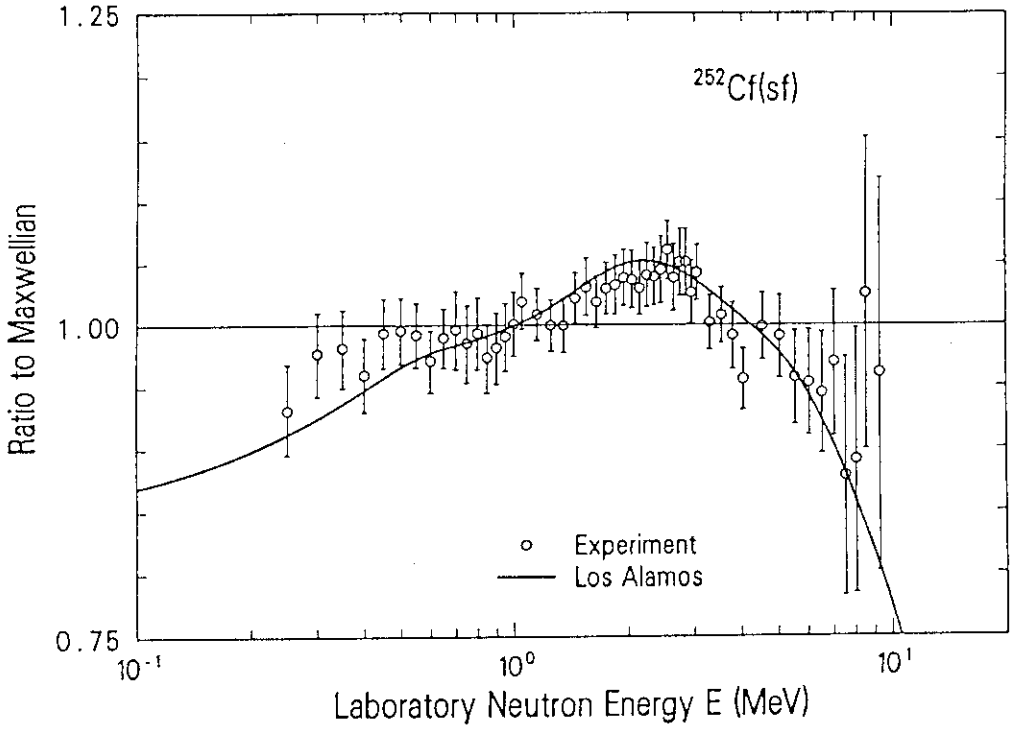

Fig. 1 Fission neutron spectrum for $^{252}Cf(sf)$ calculated with the original Madland-Nix model.

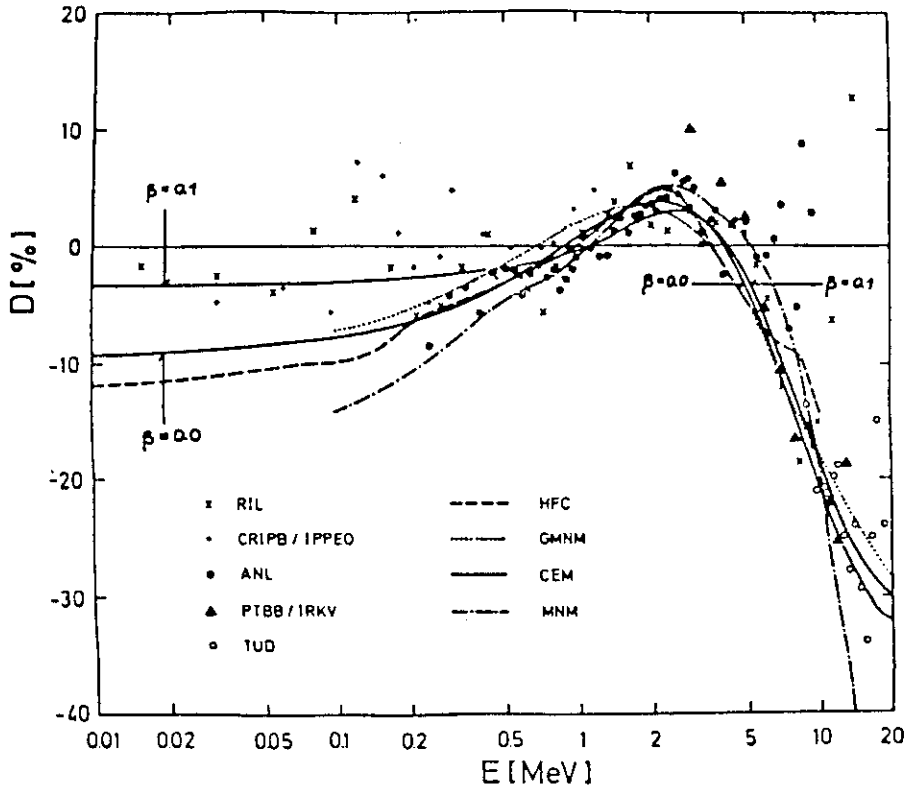

Fig. 2 Fission neutron spectra for $^{252}Cf(sf)$ calculated with the complex cascade evaporation model[2].

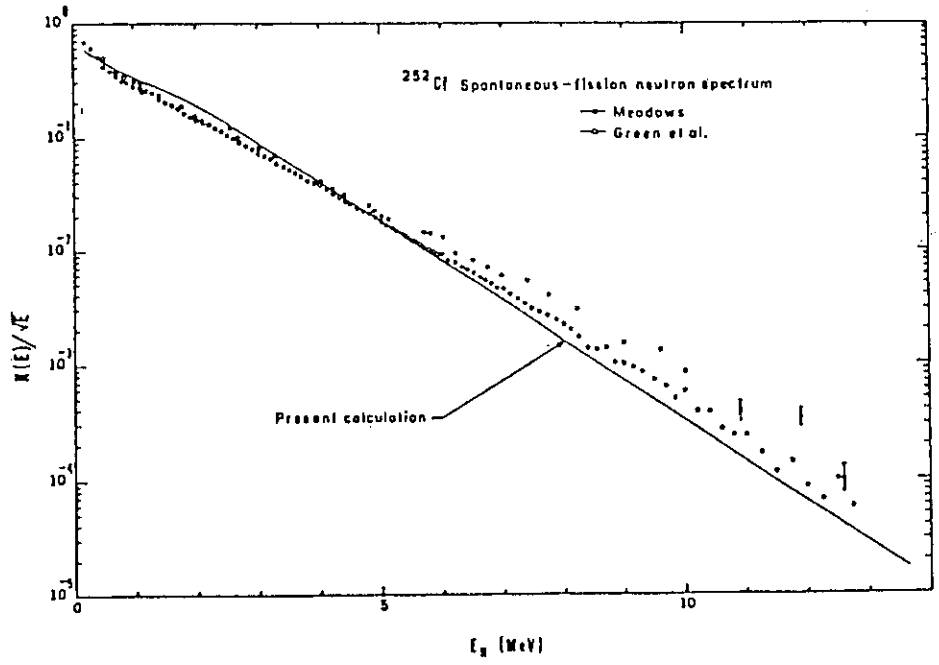

Fig. 3 Fission neutron spectrum for $^{252}Cf(sf)$ calculated with the Hauser-Feshbach-type model of Browne-Dietrich[4].

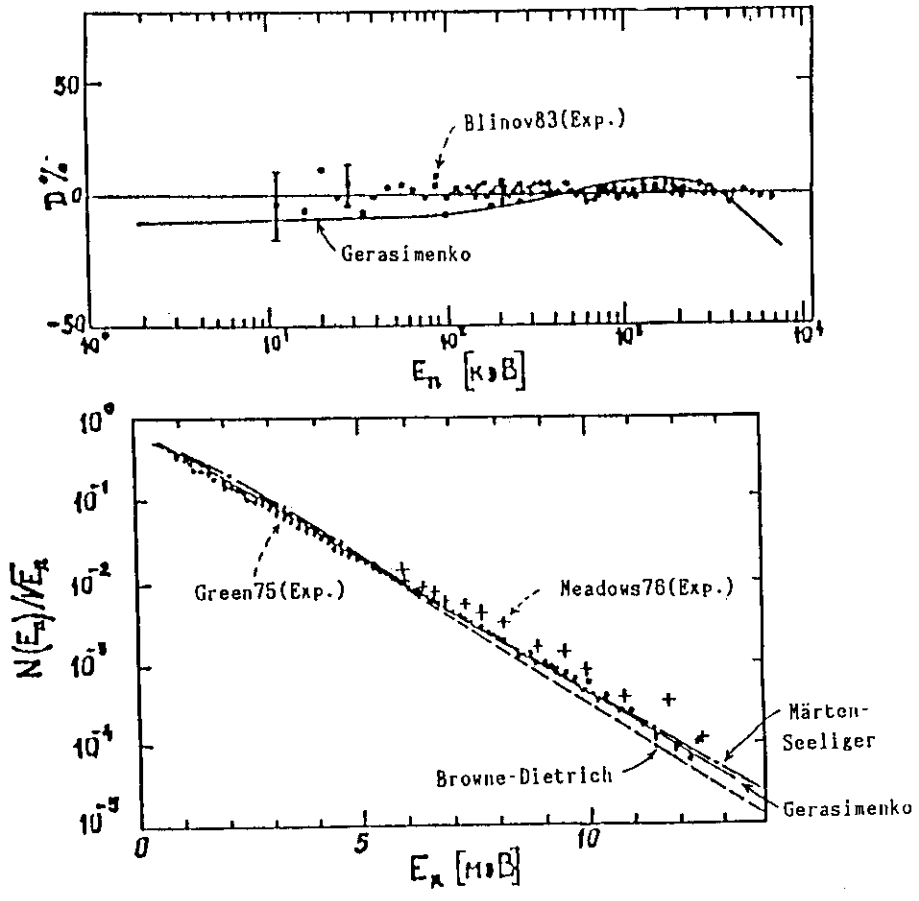

Fig. 4 Fission neutron spectra for $^{252}Cf(sf)$ calculated by Gerasimenko et al.[5]

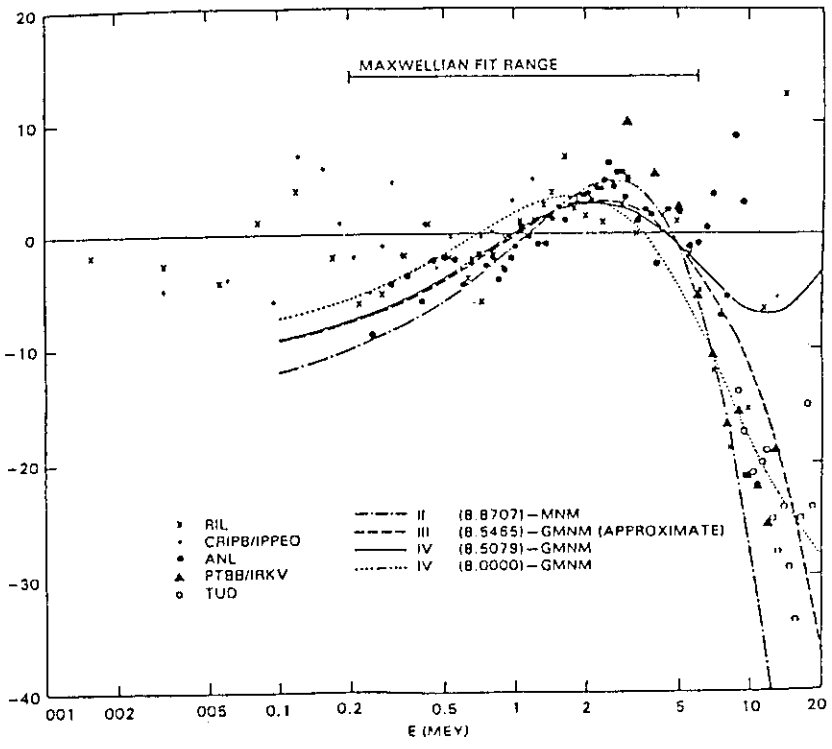

Fig. 5 Fission neutron spectra for $^{252}Cf(sf)$ calculated by Märten et al.[12] The ordinate represents the ratio to Maxwellian distribution with T=1.42 MeV. The numbers in the parentheses are the values of C when the level density parameter is represented as a=A/C.

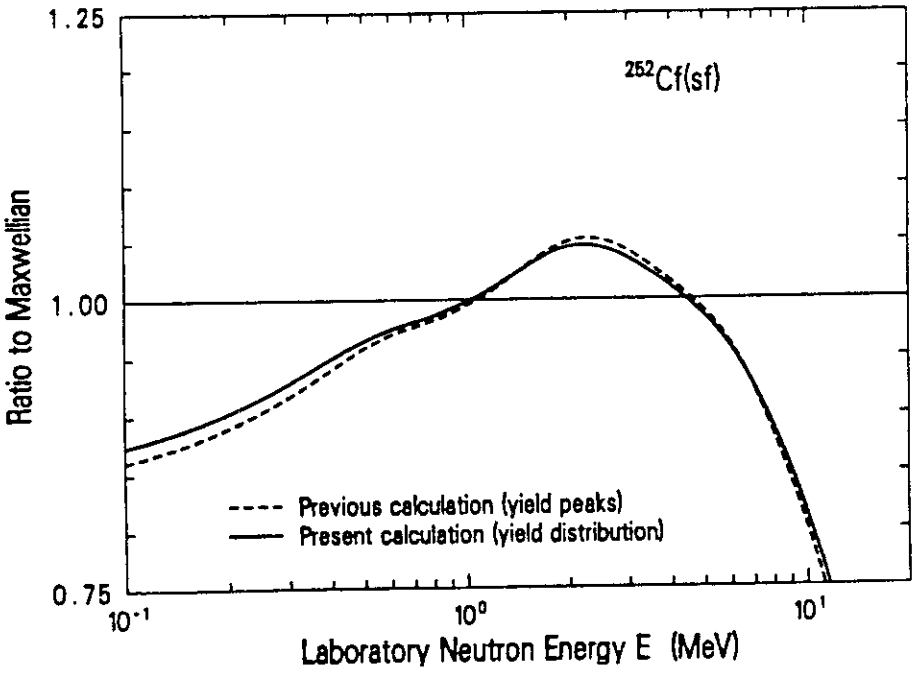

Fig. 6 Effect of accounting for the mass yield distribution of fission fragments (after Madland[13]).

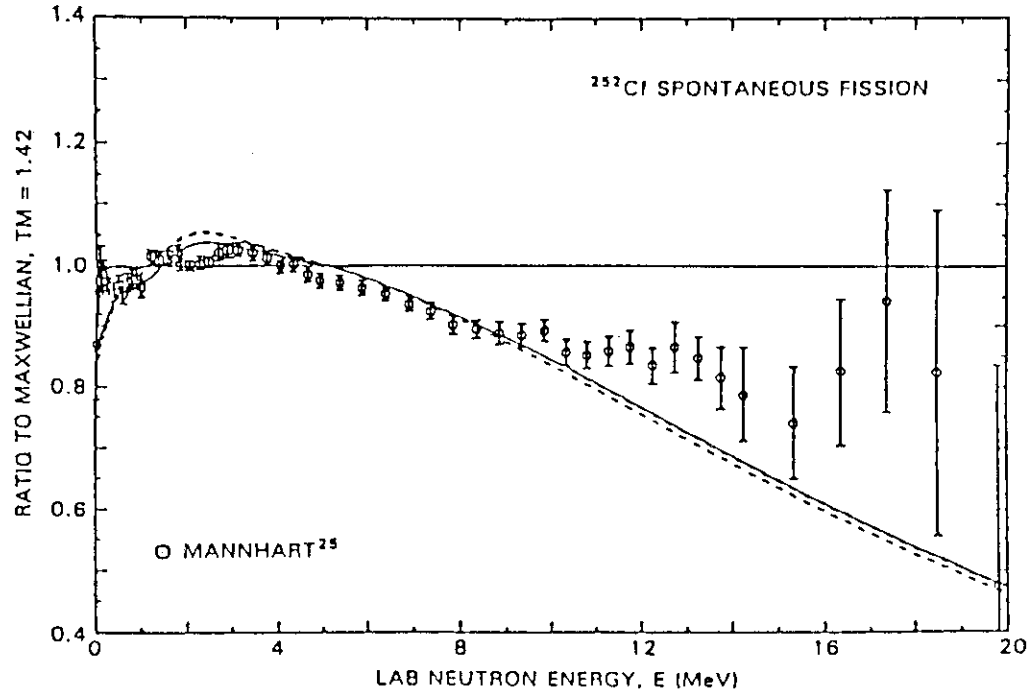

Fig. 7 Effect of center-of-mass anisotropy of neutron emission on fission neutron spectra (after Walsh[14]).

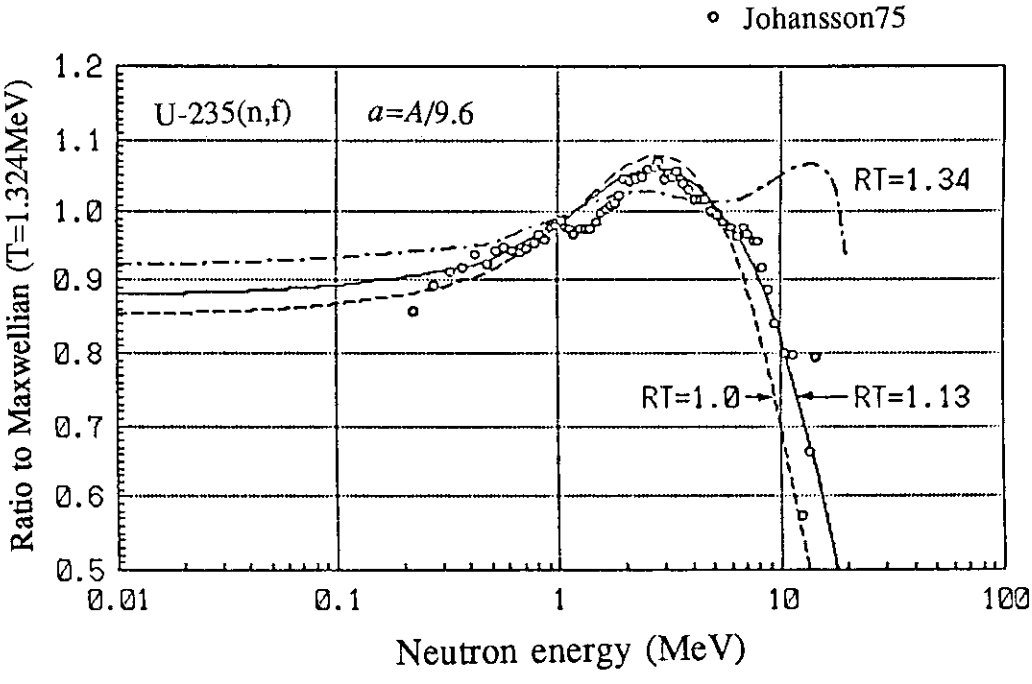

Fig. 8 Fission neutron spectra for ^{235}U(n,f) calculated with non-equitemperature Madland-Nix model using constant inverse cross section.

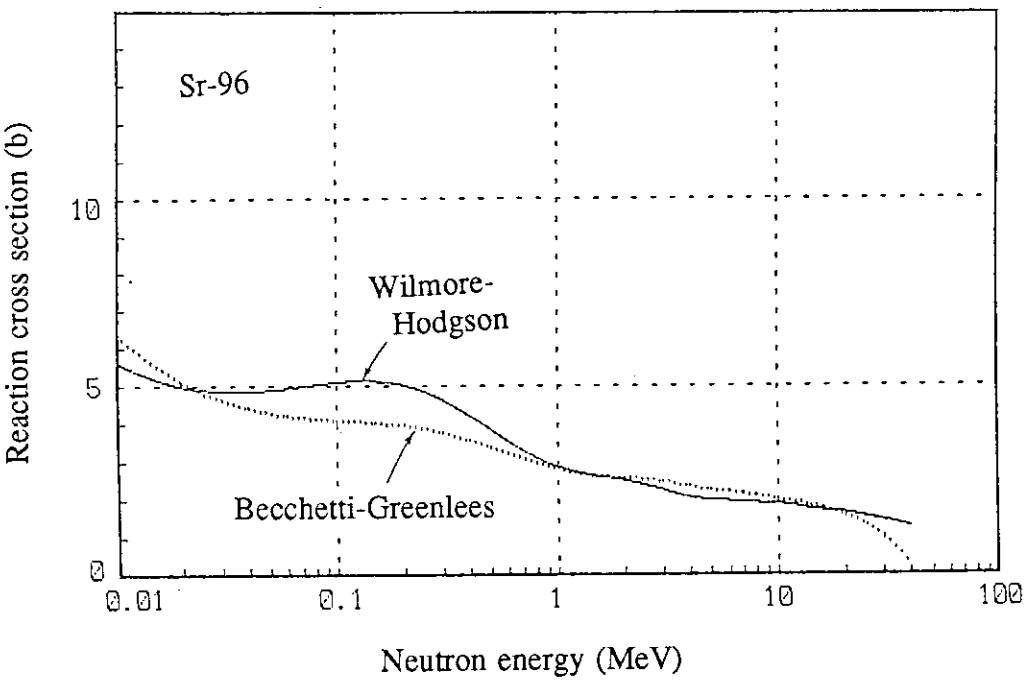

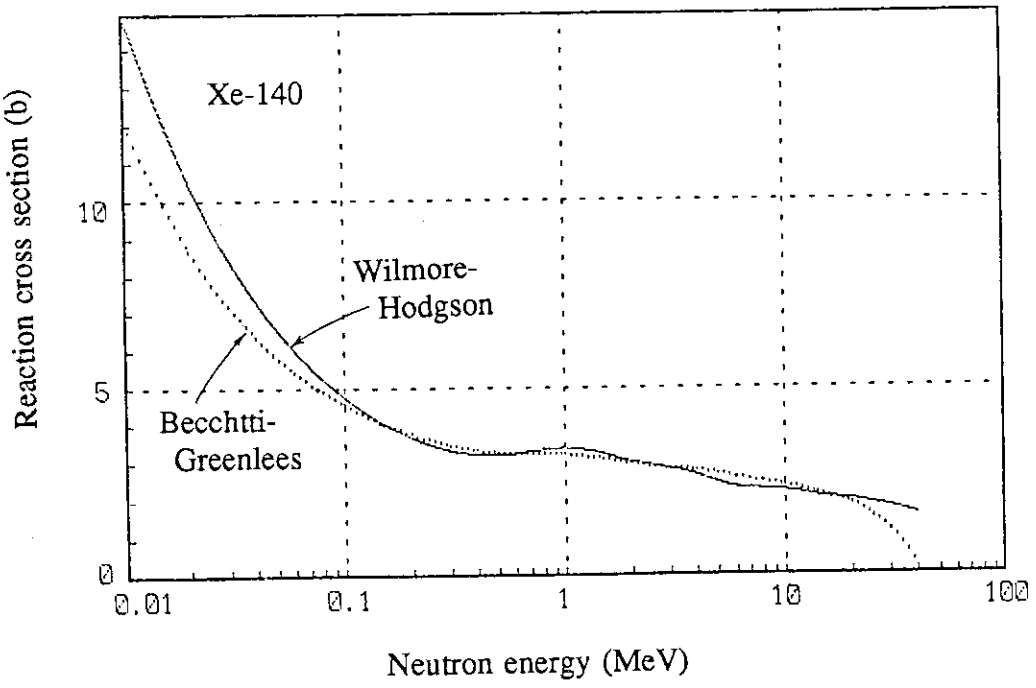

Fig. 9 Inverse cross sections calculated with Becchetti-Greenlees and Wilmore-Hodgson optical potentials.

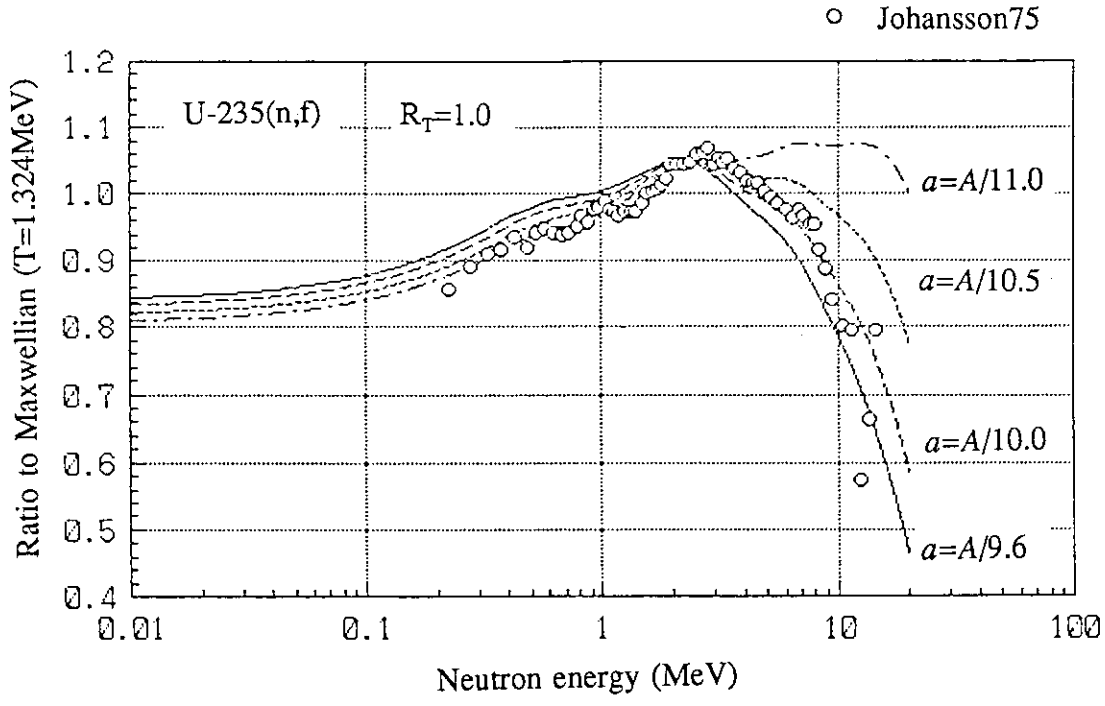

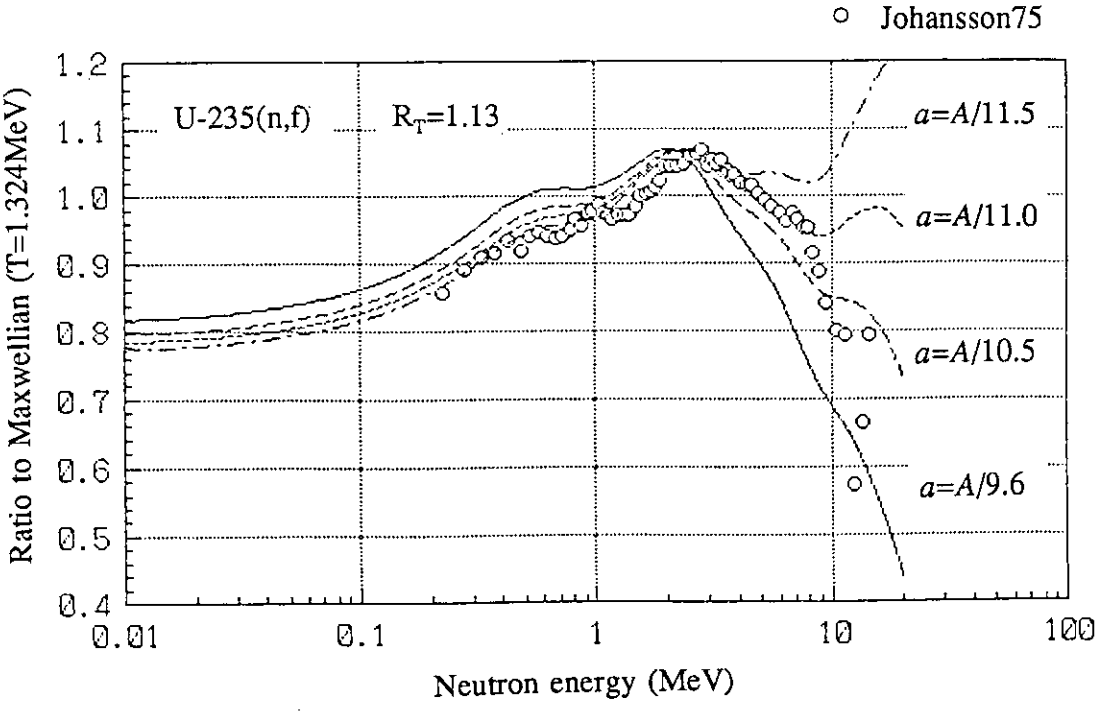

Fig. 10 Fission neutron spectra for $^{235}U(n,f)$ calculated with non-equitemperature Madland-Nix model using energy-dependent inverse cross sections. The top figure shows the case for R_T=1.0 and the bottom for R_T=1.13.

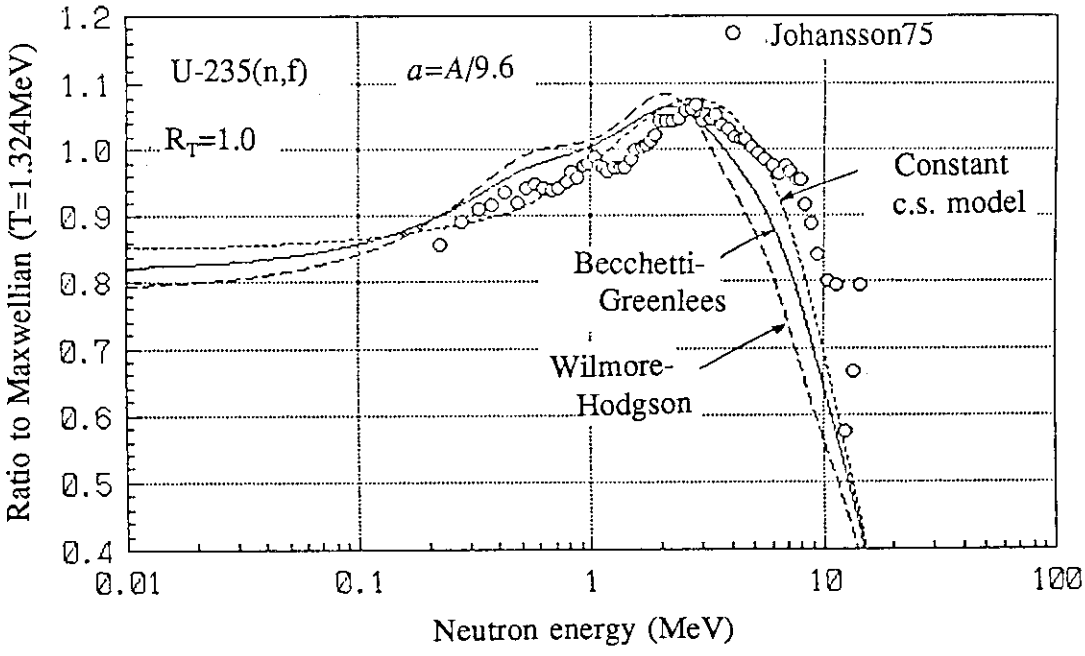

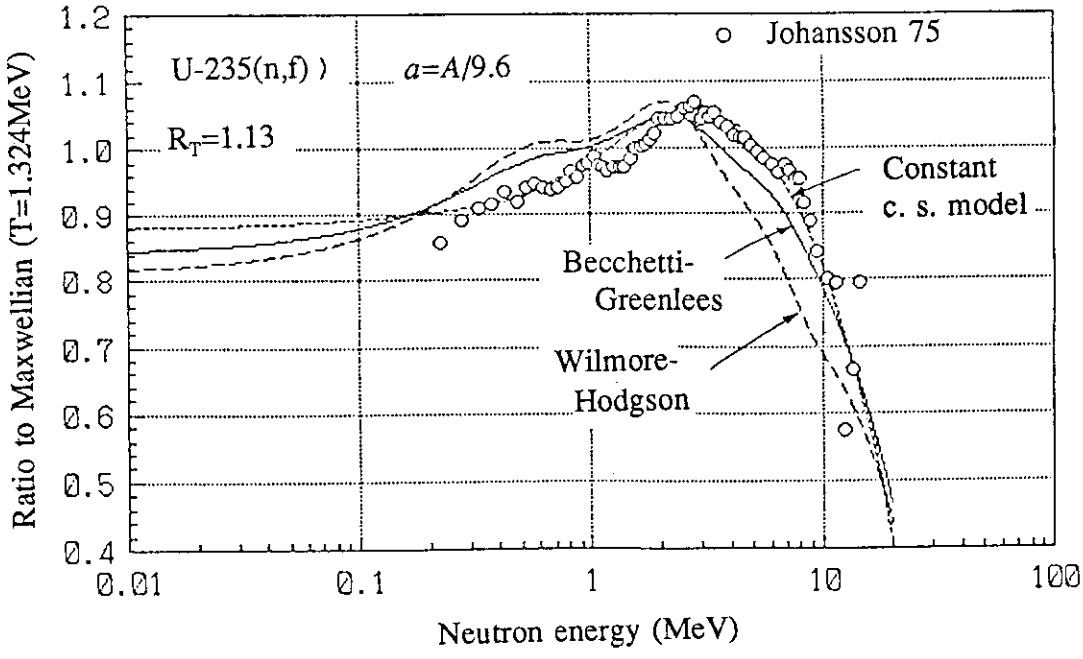

Fig. 11 Fission neutron spectra for $^{235}U(n,f)$ calculated with non-equitemperature Madland-Nix model using energy-dependent inverse cross sections for various values of the level density parameter, keeping the temperature ratio constant.

2.5 NUCLEAR DATA IN INTERMEDIATE AND HIGH ENERGY REGIONS

2.5.1 TREND OF ACTIVITY ON MEDIUM ENERGY NUCLEAR DATA

Takashi Nakamura

Cyclotron and Radioisotope Center, Tohoku University

Aoba, Aramaki, Sendai 980, Japan

Abstract

A trend of activity on medium energy nuclear data is briefly summarized from the proceedings of the NEA-NDC specialists' meeting and the candidates for neutron cross section standards above 20 MeV are listed.

At present, the interest to medium energy (energy higher than 20 MeV) nuclear data is rapidly increasing from the viewpoint of intense neutron source production for material damage study, particulate radiation therapy, accelerator breeding and transmutation, accelerator shielding, space applications and so on. Under this circumstance, the NEANDC specialists' meeting on neutron cross section standards for the energy region above 20 MeV was held in Uppsala this May, 1991, where the following topics had been discussed; status of the data base for n-p scattering, status of nucleon-nucleon phase shift calculations, recent and planned experimental works on n-p cross section measurements and facilities, instruments for utilizing the H(n,n) standard for neutron fluence measurements, proposal for other neutron cross section standards, monitor reactions for radiation dosimetry.[1]

The states-of-the-art of the nuclear data activitities in the facilities where neutron-related cross section studies have been performed are as follows,

1) WNR at LAMPF

White neutron source from thick tungsten target is used in the energy range from 100 keV to 800 MeV.

(p,Xn) cross section and double differential neutron spectra from 80 to 800 MeV

n-p scattering cross section around 800 MeV

(n,f) cross sections for Th, U, Pu and Np from 3 to 400 MeV

neutron total cross sections up to 800 MeV

2) Univ. of Calif. Davis

^{7}Li(p,n) neutron source is used.

(n,p) and (n,n'x) cross sections around 60 MeV

3) Uppsala Univ.

^{7}Li(p,n) neutron source is used.

(n,p) and (n, charged particle) cross sections for 50 to 200 MeV

4) TRIUMF

^{7}Li(p,n) neutron source is used.

(n,p) and (p,n) cross sections from 200 to 500 MeV

5) Indiana Univ.

(p,n) and (n,p) cross sections from 100 to 200 MeV

6) CEN-Saclay

(n,p) cross section around 1100 MeV

7) Karlsruhe

(n,p) cross section from 20 to 70 MeV

8) RIKEN

^{7}Li(p,n) source is used.

(n,p) cross section and detector response around 200 MeV

9) Takasaki-JAERI

^{7}Li(p,n) source is used.

shielding, neutron activation and neutron total cross section etc. from 20 to 90 MeV

10) INS, Univ. of Tokyo

^{7}Li(p,n) and ^{9}Be(p,n) sources are used.

neutron activation cross section from 10 to 40 MeV

The n-p differential scattering cross section, especially H(n,n)p elastic scattering, is generally recognized as the primary standard cross section for determining neutron fluence in the region above 20 MeV. Standard n-p cross section data exist up to tens of MeV. For example, the data in the ENDF/B-VI standards file extend from 10^{-5} eV to 30 MeV. Above 30 MeV there is no standard data file although there are phase shift analyses of the experimental data, for example, "VL-35" by Arndt. New measurements have been made in recent years on the total n-p cross section (Los Alamos), the differential cross section and polarization (Karlsruhe), and spin observables (Los Alamos and Saclay). Further n-p measurements are planned at Uppsala, at Ohio University (with NIST and Triangle Universities Nuclear Laboratory), at TUNL, at Los Alamos (with NIST and Ohio University), and at the National Accelerator Center in South Africa.

The secondary neutron cross section standard is considered to be the neutron fission cross sections of ^{235}U and ^{238}U as a result of easy use. Figure 1 shows the

fission cross section data of ^{235}U and ^{238}U as a function of neutron energy.(1)

The following list (Table 1) of the types of standards (excluding the hydrogen scattering cross section) and suggested candidates was proposed. This list is necessarily not complete since very little data are available for many of the candidates for standards in this energy range. The explanation of the priority rating is given in Table 1.

In order to determine radiation damage in high energy neutron fields, and to design high energy neutron sources and accelerator shielding, the main problem is the neutron reaction (activation) cross sections above 20 MeV up to a few hundreds of MeV. All such cross sections available up to now are calculated. The calculations have to be verified by differential measurements. Integral measurements may give some confidence in calculated cross sections but not an absolute knowledge. Several neutron reaction cross section measurements above 20 MeV are now being performed. Table 2 gives the list of the activation reactions commonly used in high energy neutron dosimetry. Among of these reactions, the $^{27}Al(n,X)^{22}Na$ and ^{24}Na reactions should be considered as reference reactions, and therefore need special priority for evaluation.

Reference

(1) NEA Nuclear Data Committee, Proceedings of A Specialists' Meeting on "Neutron Cross Section Standards for the Energy Region above 20 MeV", Uppsala, Sweden, May 21-23, 1991.

Table 1 Types of neutron cross section standards and suggested candidates above 20 MeV[1].

I The cross section is fairly well defined and can be used as a standard now. Further work would be helpful.

II More work needs to be done however there may be regions where the cross section can be used as a standard. May be conceptually a good standard.

III The data base is fairly poor or there may be fundamental problems with this cross section as a standard. More work may be necessary to determine the usefulness of this as a standard.

STANDARDS FOR SCATTERING:

REACTION	PRIORITY	COMMENT
C(n,n)	II	more data and modeling needed, 4.4 MeV first excited state is advantageous
^{4}He(n,n)	III	highly forward peaked angular distribution

STANDARDS FOR CAPTURE AND INELASTIC SCATTERING:

REACTION	PRIORITY	COMMENT
C(n,n'γ)	II	—
Fe(n,n'γ)	II(possibly I)	good since 100 mb at 100 MeV
^{208}Pb(n,n'γ)	II	—
^{7}Li(n,n'γ)	III	—
Al(n,γ)	III	—
Fe(n,2nγ)	III	good, there are thresholds

STANDARDS FOR CHARGED PARTICLE PRODUCTION:

REACTION	PRIORITY	COMMENT
C(n,p)	II	—
^{3}He(n,p)	III	—
^{3}He(n,d)	III	—
Ti(n,p)	III	needs exploratory work
V(n,xα)	III	—

STANDARDS FOR FISSION:

REACTION	PRIORITY	COMMENT
^{232}Th(n,f)	I	not sensitive to low energy neutrons, not special nuclear material
^{235}U(n,f)	I	best data base but sensitive to low energy neutrons
^{238}U(n,f)	I	not sensitive to low energy neutrons
^{209}Bi(n,f)	II	good where high threshold required, better than ^{208}Pb(n,f),very poor data base though
^{208}Pb(n,f)	III	—

Table 2 Activation reactions used in high energy neutron dosimetry[1].

^{27}Al(n,x)	^{22}Na, ^{24}Na, ^{7}Be
Sc(n,x)	^{44}Sc, ^{42}K
Ti(n,x)	^{46}Sc, ^{47}Sc, ^{48}Sc, ^{48}V, ^{44}Sc, ^{44}Ti, ^{42}Ar
Fe(n,x)	^{51}Cr, ^{54}Fe, ^{56}Fe, ^{52}Mn, ^{54}Mn,
^{59}Co(n,x)	^{57}Co, ^{58}Co, ^{59}Fe, ^{52}Mn, ^{54}Mn, ^{56}Mn
Ni(n,x)	^{58}Co, ^{60}Co, ^{57}Ni, ^{57}Co, ^{52}Mn, ^{54}Mn, ^{56}Co
Cu(n,x)	^{44}Sc, ^{46}Sc, ^{47}Sc, ^{48}Sc, ^{60}Co
	^{51}Cr, ^{52}Mn, ^{54}Mn, ^{56}Co, ^{57}Co, ^{58}Co
Zr(n,x)	^{89}Zr
Nb(n,x)	^{92}Nb
Tm(n,x)	^{167}Tm, ^{168}Tm
Au(n,x)	^{195}Au, ^{196}Au
Fe(n,x)	He
Cu(p,x)	^{65}Zn
Fe(p,x)	^{56}Co
Ti(p,x)	^{48}V
Co(p,x)	^{56}Ni, ^{57}Ni

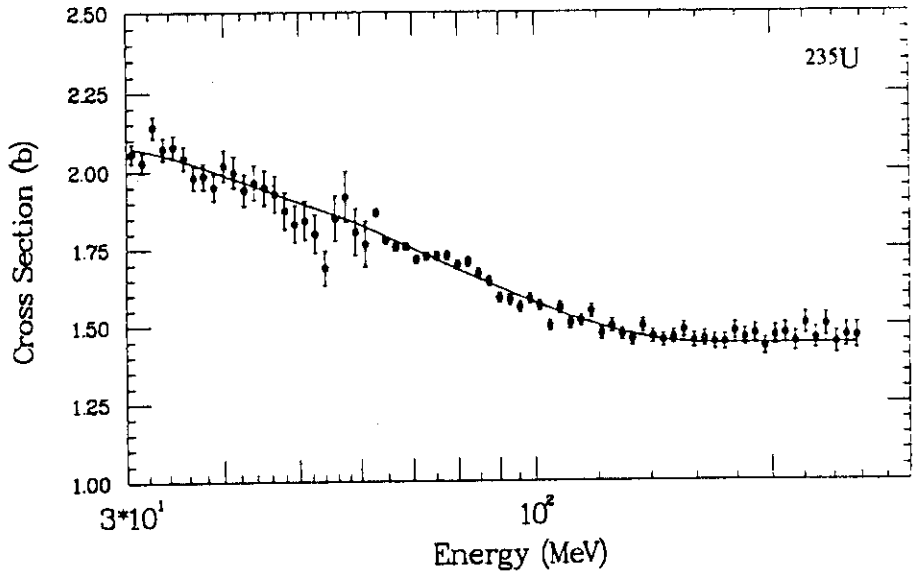

(a)

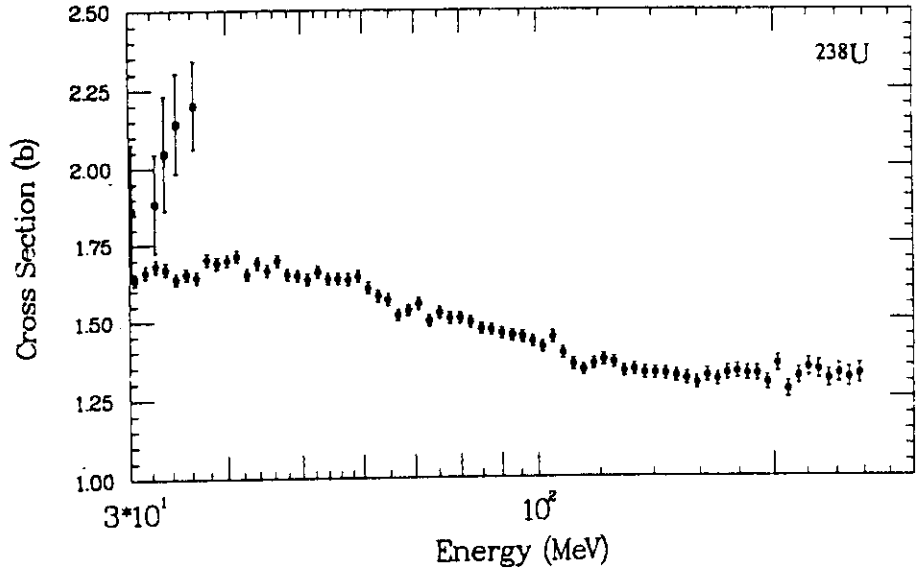

(b)

Fig. 1 Fission cross sections of (a) ^{235}U and (b) ^{238}U as a function of neutron energy[1]. The smooth curve in (a) is a polynominal parameterization of the data.

2.5.2 PARTIAL-WAVE ANALYSIS OF HIGH-ENERGY NEUTRON-PROTON SCATTERING

Norio Hoshizaki and Takatoshi Watanabe*)

Department of Nuclear Engineering

Faculty of Engineering, Kyoto University

Kyoto 606

We report results of our recent neutron-proton phase-shift analyses with and without I=0 absorption performed in the range from 430-800MeV. The I=1 phase parameters have been fixed to those values given in a separate report. Solutions with I=0 absorption are better, in particular at 625 and 645 MeV, and reveal a narrow resonance in the $^1P_1$ wave. It is an inelastic resonance with I=0, J^P=1$^-$ and having the mass and width of M=2168MeV/c^2 and Γ=25MeV, respectively. The np reaction cross section for I=0 state is predicted to have a sharp peak at 625 MeV in agreement with experiments by Dunaitsev and Prokoshkin. Predictions for other several observables are given together with the experimental data.

The contents of this talk have been published in Prog. Theor. Phys. 86, No.2 (1991) with the following titles and abstracts. Tables of the summary of data kinds and data points used and of the obtained phase shift values and resonance parameters are given there. The I-spin 1 part of the neutron-proton phase parameters used in the present analysis has been

---

*) Present address: Tokyo Electric Power Co. Ltd., Fukushima Nuclear Power Station No.1, Ohkuma-cho, Futaba-gun, Fukushima, Japan.

published in Prog. Theor. Phys. 86, No.1 (1991), whose title, authors and abstract are also given below for reference. The I=1 phase shift values are given there together with the summary of data kinds and data points used.

Prog.Theor.Phys. 86(1991), 17

Intermediate Energy *NN* Phase Shifts - I

Yoshio HIGUCHI, Norio HOSHIZAKI, Hiroaki MASUDA*) and Hiroomi NAKAO+)

Department of Nuclear Engineering

Faculty of Engineering, Kyoto University

Kyoto 606

A *pp* phase shift analysis is reported incorporating the *pp* world data from 430-800MeV. The solutions show half-looping and anticlockwise motion for the $^1D_2$ and $^3F_3$ amplitudes. Similar structure is observed in the $^3P_2$ wave.

Prog.Theor.Phys. 86(1991), 321

Intermediate Energy *NN* Phase Shifts - II

Norio HOSHIZAKI and Takatoshi WATANABE

Department of Nuclear Engineering

Faculty of Engineering, Kyoto University

Kyoto 606

Neutron-proton phase-shift analyses with and without I=0 absorption

---

*) Present address: SLAC, Bin96, Stanford University, P.O.Box 4349, Stanford, CA94309, U.S.A.

+) Present address: Integrated Circuit CAD Department, Mitsubishi Electric Corporation, ASIC Design Engineering Center 401, Mizuhara, Itami City, Hyogo 664, Japan.

are performed in the range from 430-800MeV with the I=1 phases being fixed to those values given previously. Solutions with I=0 absorption are better, in particular at 625 and 645 MeV, and reveal a narrow resonance in the $^1P_1$ wave.

Prog.Theor.Phys. 86(1991), 327

Narrow I-spin zero NN Resonance

Norio HOSHIZAKI and Takatoshi WATANABE

Department of Nuclear Engineering

Faculty of Engineering, Kyoto University

Kyoto 606

A narrow np inelastic resonance with I=0, J^P=1$^-$ and M=2168MeV/c^2 is reported on the basis of phase shift solutions given in the preceding paper. The np reaction cross section for I=0 state is predicted to have a sharp peak at 625 MeV in agreement with experiments by Dunaitsev and Prokoshkin.

2.6 TOPIC 3

2.6.1 SIGNATURES OF INHOMOGENEOUS COSMOLOGIES INTERMEDIATE-MASS NUCLEOSYNTHESIS AND RADIOACTIVE NUCLEAR BEAMS

T. KAJINO
Department of Physics, Tokyo Metropolitan University
Hachiohji, Tokyo 192, Japan

ABSTRACT

Several new astronomical observations of the primordial abundances of light atomic nucleides and the nuclear measurements of radioactive beams are shedding light on the cosmological models of inhomogeneous primordial nucleosynthesis. A mechanism of forming the inhomogeneous baryon-number density distribution at the epoch of cosmological phase transition in quantum chromodynamics (QCD) is discussed. The primordial nucleosynthesis of intermedaite-mass nuclei as a test of the inhomogeneous models is discussed.

1. INTRODUCTION

Although the standard big-bang model[1] was believed to explain the primordial nucleosynthesis of light element abundances, several advances in astronomical observations provide some evidence against the standard homogeneous model.

For one, recent careful analysis[2] of the correlation between the ^{4}He abundance and those of CNO in old halo stars indicates a smaller ^{4}He abundance by at least 8% than the previous one, leading to a serious problem that any single value of $\Omega_B = \rho_B/\rho_C$ can not explain the observed abundances of ^{2}H, ^{3}He and ^{7}Li as well as ^{4}He in the standard big-bang model.

Another observational evidence which is unfavorable of the standard model is a large primordial abundance of ^{9}Be. Two independent astronomer groups[3,4] have recently succeeded in an actual detection of Be line in old halo metal-deficient dwarf HD 140283, which shows probably a primordial abundance; $\log[N(^9Be)/N(H)] = -12.8 \pm 0.3$ and

-13.25 ± 0.40. Their observed values are larger than the prediction from the standard big-bang model by at least two orders of magnitude but are in reasonable agreement with those predicted in the inhomogeneous models.[5-7]

There is another disadvantage of the standard model. The observed total mass density parameter, $\Omega^{(obs)} = \rho^{(obs)}/\rho_C$, turns out to be 0.1 - 0.4 [ref. 8], which is at least ten times that of the observed luminous baryonic mass density parameter, $\Omega_B{}^{(lum)} = \rho_B{}^{(lum)}/\rho_C \approx 0.01$. One must assume an existence of non-baryonic dark matter in the standard model although the inhomogeneous models are likely to explain this large value of $\Omega^{(obs)}$ by baryonic mass alone.[9,10] There are many non-baryonic dark matter candidates like weakly interacting massive particles (WIMPs), axions or SUSY particles. However, recent experiment done at CERN[11] of measuring the decay of neutral weak boson has excluded all WIMPs having a mass less than 45 GeV.

Although the inhomogeneous models[12,13] thus seem to be better than the standard model in some respects, it has been pointed out[14,15] as a major failure that the ^{7}Li abundance is overestimated by at least one order of magnitude from that observed in Population II dwarfs, $\log[N(^7Li)/N(H)] \approx -10$. The effect of neutron back diffusion during and after the nucleosynthesis epoch was proposed to reduce ^{7}Li through the ^{7}Be(n, p)^{7}Li(p, γ)2^{4}He reaction in high-density proton-rich zones.[15,16] It was discussed,[9] however, that an efficient neutron diffusion back to the high-density region is hindered strongly due to a high pressure of baryons and that the destruction of ^{7}Li is not enough for explaining the observed Pop. II abundance of ^{7}Li.

One possible solution[17] has recently been proposed theoretically: The photon pressure tends to decrease below the baryon pressure at later times when the temperature of the expanding universe was cooled to an order of T ≈ 20 keV. Now the adiabatic fluctuation of baryons ignites spontaneous dissolution of high density zones, which is called homogenization. Due to a violent mixing of matter including even protons as well as neutrons ^{7}Li is destroyed in all spaces. Namely, ^{7}Li(p, α)^{4}He in the neutron-rich zones and ^{7}Be(n, α)^{4}He or ^{7}Be(n, p)^{7}Li(p, α)^{4}He in the proton-rich zones destroy A = 7 nucleides. Having this solution, we are in the next stage to look for another observational evidence for or against the inhomogeneous big-bang model. I would like to show in this paper that the primordial nucleosynthesis of intermediate-mass nuclei may provide a clear signature of inhomogeneous nucleosynthesis.[18]

There is still a theoretical criticism to the inhomogeneous models as that they have too many parameters which need fine tuning for describing the spatial configuration of inhomogeneous baryon density distribution. These models are based upon a first order

cosmological QCD phase transition prior to nucleosynthesis which leads to largely inhomogeneous matter distribution as its remnants.[19] The spatial configuration of inhomogeneous baryon density distribution is described by the macroscopic quantities which have been treated as free adjustable parameters in the previous nucleosynthesis calculations. It is theoretically a very challenging problem to deduce these cosmological quantities from the physics of QCD.[20,21]

The first purpose of this paper is to show our theoretical approach to describe the baryon inhomogeneity. Constructing an effective phenomenological model[22] of QCD and applying it to the study of cosmological phase transition,[21] we will conclude that the baryon inhomogeneity can be extremely large as we wish from the studies of the primordial nucleosynthesis. Having confirmed this, we next explore the observational evidence for the inhomogeneous models in primordial nucleosynthesis.[5,6,23] The second purpose is to show that the elemental abundances of intermediate-mass nuclei $12 \leq A$ in old stars will provide a critical test for discriminating the inhomogeneous models from the standard one.[18] In the next section the dark matter problem (called sometimes the Ω problem) is briefly reviewed in connection with the primordial nucleosynthesis. The cosmological QCD phase transition as a source of baryon inhomogeneity is discussed in sect. 3, and the inhomogeneous nucleosynthesis is discussed in sect. 4. Finally, in sect. 5, the present study is summarized.

2. DARK MATTER PROBLEM

Baryonic dark matter is classified in two ranks according to its origin: The first is the primordial one like strange quark matter or mini black hole, and the second rank includes stellar black hole, neutron star and brown dwarf which are to be formed after the nucleosynthesis.

Let me briefly discuss the theoretical possibility[24] of marginally closed universe by baryonic mass alone, $\Omega_B^{(lum)} + \Omega_{BDM}^{(pre)} + \Omega_{BDM}^{(post)} = 1$, which satisfies the requirement from inflationary cosmology. Theoretical constraints from the nucleosynthesis are applied to $\Omega_B^{(lum)}$ and $\Omega_{BDM}^{(post)}$. Only the post-nucleosynthesis dark matter candidates are far from closing the universe because both standard and inhomogeneous models infer $\Omega_B^{(lum)} + \Omega_{BDM}^{(post)} \approx 0.03$ (standard) and ≤ 0.2 (inhomogeneous) which are smaller than unity. On the other hand, a marginally closed universe could be possible if the pre-nucleosynthesis dark matter candidates exist. It is explored in the next section if the strange quark matter, which is thought of as one of pre-

nucleosynthesis baryonic dark matter, could be formed at the epoch of QCD phase transition.

Theoretical models of inhomogeneous cosmologies are thus attractive for providing an astrophysical site of generating the primordial strange quark matter[19,21,24] as well as the inhomogeneous baryon-gas distribution which leads to the inhomogeneous nucleosynthesis.[5,6,9,12-18]

3. BARYON INHOMOGENEITY AT THE COSMOLOGICAL QCD PHASE TRANSITION

3.1 Baryon Penetrability

When the expanding universe was first cooled below the critical temperature T_C of the QCD phase transition, hadron bubbles were nucleated in the sea of quark-gluon plasma. Then the latent heat is liberated from phase boundary and reheats the universe. During the coexistence epoch at $T = T_C$, the baryon number is transferred between two phases. If the baryon number transfer takes place very slowly, a striking inhomogeneity may be formed with gradual concentration of excess quarks in the shrinking quark-gluon plasma region. If, on the other hand, it works efficiently, the universe may be almost homogeneous in baryons. The penetrability of baryons is thus a very important parameter for the generation of inhomogeneity. However, it was difficult to estimate it theoretically because the mechanism of quark confinement is not known clearly.

A simple estimate which has been used in the previous calculations is to assume that the absorption probability of baryons by the quark-gluon plasma is almost 100%, which is similar to an absorption of an H_2O molecule in gas phase by a water droplet.[25,26] The principle of the detailed balance gives us a large evaporation probability of baryons. However, this is not a good approximation because several essential properties of QCD, i.e. the quark confinement and the asymptotic freedom, etc., are not at all taken into consideration in the classical arguments.

To remedy these shortcomings we adopted the chromoelectric flux tube model[27,28] which is an effective model for quark confinement in QCD. In this model the flux of evaporating baryons from the quark-gluon plasma is calculated[22] by

$$J_B = \sum_q \frac{n_q}{Z_q} \int d^3k_0 \exp\left(-\frac{E_0}{T}\right)\frac{k_{z0}}{E_0}$$

$$\int dk_z^B \int dE^B \frac{1}{k_C^2} \exp\left[-\frac{E_0}{k_C^2}\left\{(k_{z0}-k_z^B)+\frac{1}{2E_{z0}}\left((k_z^B E_z - k_{z0}E_{z0})+m_q^2 \ln\frac{k_z^B+E_z}{k_{z0}+E_{z0}}\right)\right\}\right], \quad (1)$$

where Z_q is the partition function and E_0 is the averaged thermal energy of an initial quark. $k_C = \{3\sigma_0^3/2\pi\alpha_C p\}^{1/2}$ is a typical linear momentum which is lost before the baryon evaporation and include unknown quantity p of diquark-antidiquark pair creation and fission in the tube. We adopted the p-values determined from the jet phenomenology.[29] $\sigma_0 = 0.177$ GeV^2 is an energy density per unit length of the tube deduced from Regge trajectories of hadrons, which denotes the strength of a linear confinement potential for quarks. $\alpha_C = 2$ is QCD coupling constant. The integrand of the right hand side is the evaporation probability of baryon with an energy E^B and momentum k_z^B for an given initial quark momentum k_0 and k_{z0} when it passes through the boundary. Integral is over the threshold energy and momentum satisfying the kinematical conditions.

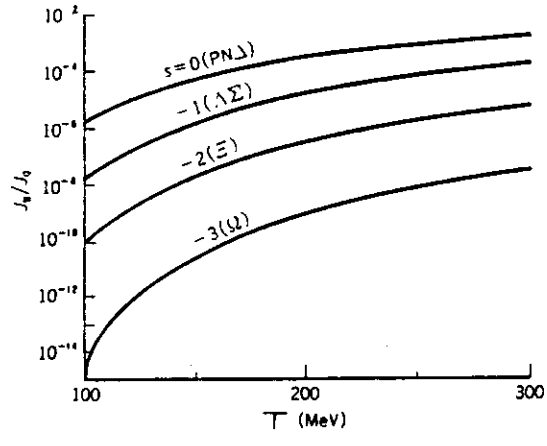

Fig. 1 Calculated baryon number flux[22] penetrating through the phase boundary between the quark-gluon plasma and the hadron gas, divided by the quark flux. S is the strangeness of baryons.

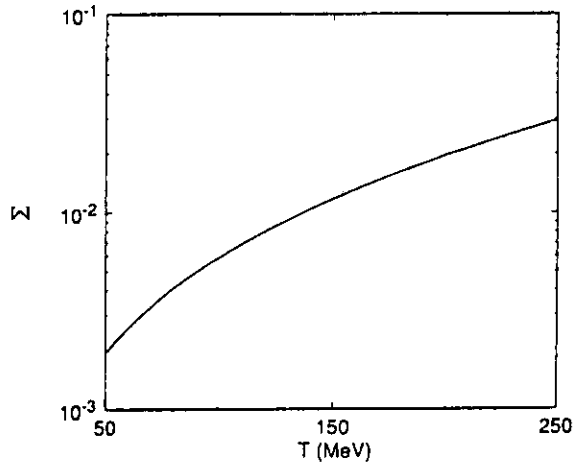

Fig. 2 Calculated baryon number flux[22] divided by the maximum flux permitted by detailed balance, which has been used in the previous studies[25,26], as a function of temperature.

Figure 1 displays the calculated flux of baryons evaporating from the quark-gluon plasma normalized to the quark flux.[22] Non-strange baryons have the largest flux

among the baryon octet and decuplet. Difference among different baryons does not affect very much the dynamics of the evolution of baryon number density in the weak equilibrium condition. We hereafter take account of only the nucleon.

Figure 2 displays the ratio of the present result[22] to the flux of thermally averaged nucleons which was used in the previous calculations:[25,26]

$$\Sigma = \frac{J_B}{n_B^h \{T/2\pi M_B\}^{1/2}} . \tag{2}$$

Our calculation gives two orders of magnitude smaller baryon penetrability than the previous estimate which was based upon the classical arguments.

3.2 Time Evolution of Baryon-Number Densities

Having known the baryon penetrability in a quantum theory, we are in the stage of calculating time evolution of baryon-number densities in the two phases by solving the coupled differential equations:[20,21]

$$\frac{dn_B^q}{dt} = -\lambda n_B^q + \lambda' n_B^h - \left\{\frac{dV/dt}{V} + \frac{df_V/dt}{f_V}\right\} n_B^q, \tag{3}$$

$$\frac{dn_B^h}{dt} = \frac{f_V}{1 - f_V}\left\{-\lambda' n_B^h + \lambda n_B^q + \frac{df_V/dt}{f_V} n_B^h\right\} - \frac{dV/dt}{V} n_B^h, \tag{4}$$

where n_B^q and n_B^h are the net baryon number densities in the quark-gluon plasma phase and hadron phase, respectively. V is the horizon volume and f_V is the volume fraction of quark-gluon plasma. These quantities are obtained as analytic functions of time by solving the Einstein equation in weak supercooling.[30] In these equations, λ is the baryon number transfer rate from the quark-gluon plasma to the hadron gas, defined[21] by

$$\lambda = \frac{4\pi r^2 N_n V_i}{f_V V} J_B / n_B^q, \tag{5}$$

and λ' is determined from the detailed balance condition. In this equation r(t) is the

average bubble radius and N_n is the density of nucleation sites which is calculated in isothermal fluctuation theory as a function of QCD parameters.[21]

Figure 1 indicates that only one baryon out of 10^4 quarks can evaporate per unit time. The duration of the phase transition is of order 10 - 100 μsec. Although this time scale is long enough for the strong and electroweak interactions to be in equilibrium, it is too short for the evaporating baryons to reach the equilibrium condition statistically.

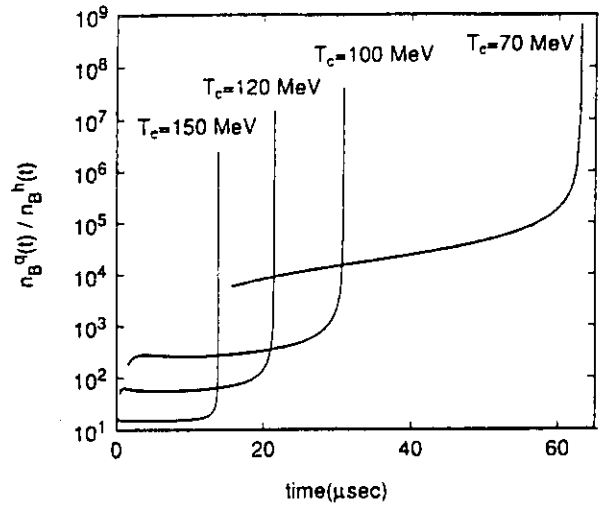

Fig. 3 Time evolution of baryon-number density ratio n_B^q/n_B^h during the cosmological quark-hadron phase transition for various QCD parameters[21]. Time = 0 refers to the epoch when T_C is first reached.

Figure 3 displays the solution of eqs. (3) and (4).[21] In this example we set T_C =100 MeV and $\sigma = 10^6$ MeV^3. Time = 0 refers to the epoch when T_C is first reached and the calculated baryon number densities are shown from the end of the weak supercooling epoch. If the whole system is in equilibrium until the end of the phase transition, the ratio of n_B's in the two phases should be constant,

$$n_B^q/n_B^h = \frac{2}{9}\left\{\frac{\pi^3}{8}\right\}^{1/2}\left\{\frac{T_C}{M_B}\right\}^{3/2}\exp\left\{\frac{-M_B}{T_C}\right\}. \qquad (6)$$

But, the numerical result is quite different. Figure 3 shows clearly the fact that the baryon number transfer between the quark-gluon plasma phase and the hadron gas phase takes place under the strongly non-equilibrium condition near the end of the phase transition. Consequently, a strong baryon density contrast appears.

Although we could calculate the strength of one fundamental parameter J_B, there are two more parameters T_C and σ. Physical consequences of the baryon inhomogeneity are of course dependent upon these remainig QCD parameters as those to be discussed in the following.

3.3 QCD Condition for Baryon Inhomogeneity

There are three macroscopic quantities[14] for describing the inhomogeneous baryon-number density distribution: They are the desnity contrast, $R = n_B^q/n_B^h$, which is the ratio of the baryon-number density of high-density zones to the baryon-number density of low-density zones, the volume fraction of high density zones, f_V, and mean separation distance between the fluctuations, l_F, at the epoch of decoupling quark-gluon plasma from the universal expansion. According to our calculations[21] of these quantities as functions of T_C and σ we discuss the condition on which the inhomogeneous nucleosynthesis could follow or which the primordial strange quark matter could form.

3.3-a Inhomogeneous Baryon-Gas Distribution

The inhomogeneous baryon-gas distribution produced at the QCD phase transition has an important consequence for nucleosynthesis. The spatial distribution of baryons in comoving coordinates does not change substantially until the freeze out of the weak interactions at $T \approx 1$ MeV. After this, the neutrons begin to diffuse out of the high-density zones, but the protons, because of their electromagnetic interactions with the plasma, do not. The result is that by the time nucleosynthesis starts at $T \approx 100$ keV, the neutrons have a nearly uniform distribution, but the protons are largely confined into narrow spaces.[12] The dramatic consequence for the resulting primordial abundances will be discussed in the next section.

These results, however, arise only from specific distributions of protons and neutrons at the time of nucleosynthesis. First, in order to get the uniform neutron distribution at the time of nucleosynthesis, the separation length, l_F, of the high density zones must be comparable to the neutron diffusion length, $10\text{m} < l_n^{\text{diff}} < 100\text{m}$ [ref. 31]. The second condition is $Rf_V \geq 20\Omega_B$ [refs. 5-7, 9, 10]. The light element abundance constraints are satisfied only when the baryon density fluctuations satisfy this condition.

Figure 4 displays these criteria on the two QCD parameter plane.[21] The dashed line corresponds to the marginal value of $Rf_V = 20\Omega_B$ in the $\Omega_B = 1$ universe. Below this line Rf_V is larger than 20 and the fluctuation is large enough to lead to inhomogeneous

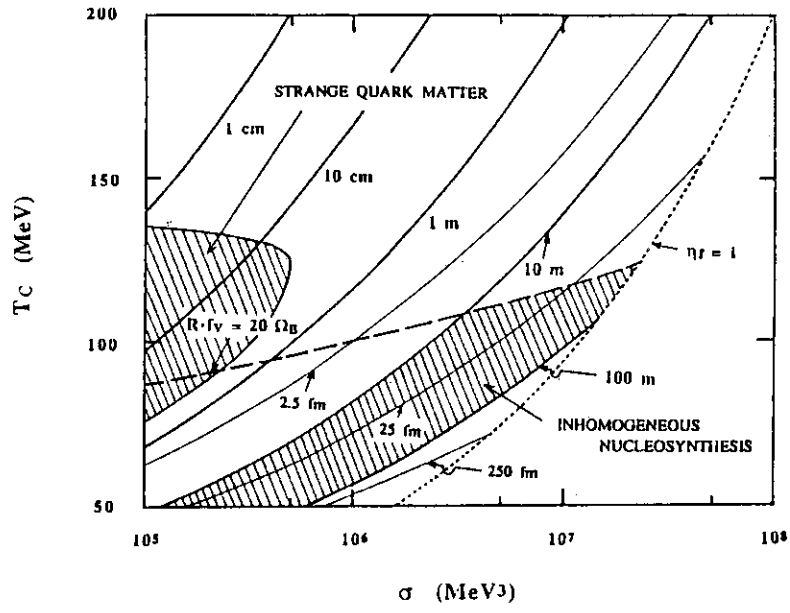

Fig. 4 QCD parameter plane T_C-σ. Two shaded regions lead to the formation of primordial strange quark matter or the interesting inhomogeneous primordial nucleosynthesis. Thick solid curves (1cm - 100m) and thin solid curves (2.5fm - 250fm) denote the mean separation distances between the nucleated hadron bubbles at the epoch of weak supercooling in big-bang and relativistic heavy-ion collisions, respectively[24,37].

nucleosynthesis. The thick solid curves display l_F = 1cm - 100m. The baryon-number density fluctuation for the parameter region between l_F = 10m and 100m curves gives typical inhomogeneous nucleosynthesis, whereas in the other region baryon number density fluctuations lead to ordinary standard big-bang nucleosynthesis.

3.3-b Strange Quark Matter Formation

An example shown in Fig. 3 indicates that $n_B{}^q$ reaches ≈ 0.01 fm^{-3} in the case of T_C =100 MeV and σ =10^6 MeV^3. The nuclear matter density or the higher is attained for the T_C-σ values in the shaded region shown in figure 4.[24] Since the early universe at this epoch is in weak equilibrium at the temperature T = T_C ≈ 100 MeV, almost equal numbers of up, down and strange quarks are degenerate in these high density zones. The hot strange quark matter could be formed on this condition.

Recent extensive study[32] has indicated that these primordial hot quark matter lumps can survive until the present universe, being therefore viable dark matter candidate.

3.3-c Constraints from Lattice Gauge QCD

A recent lattice gauge simulation[33] including the effect of dynamical quarks suggests 100 MeV ≤ T_C ≤ 150 MeV. If the QCD phase transition is first order, it is expected to be a weak one, though controversial,[34] suggesting small intrinsic surface tension. Only the pure gauge simulations[35,36] give a weak constraint on the upper bound $\sigma \leq 10^7$ MeV^3.

These theoretical constraints suggest that both the inhomogeneous baryon-gas distribution and the strange quark matter formation could happen at the epoch of cosmological QCD phase transition in the early universe.[37] (See Fig. 4.)

4. PRIMORDIAL NUCLEOSYNTHESIS

A phenomenological QCD study in the last section clearly indicates that the inhomogeneous primordial nucleosynthesis could happen in the early universe.

It has been widely dicussed[12,15,23] that the intermediate-mass nuclei as well as the light elements are created in the inhomogeneous big-bang models because of the unique history of neutron-rich or proton-rich environments. Since several key reactions in these models are those of radioactive nuclei, the inhomogeneous nucleosynthesis opens a new field of nuclear astrophysics where the precise reaction data of radioactive beams provide definitive information to decide which cosmological theory of primordial nucleosynthesis is a better approximation, homogeneous or inhomogeneous.

In the neutron-rich zones the following reaction chains[15,23]

$$^4\mathrm{He}(^3\mathrm{H},\gamma)^7\mathrm{Li}(\mathrm{n},\gamma)^8\mathrm{Li}(\alpha,\mathrm{n})^{11}\mathrm{B}(\mathrm{n},\gamma)^{12}\mathrm{B}(\mathrm{e}^-\nu)^{12}\mathrm{C}(\mathrm{n},\gamma)^{13}\mathrm{C}\ \ldots \quad (7a)$$

$$(^3\mathrm{H},\mathrm{n})^9\mathrm{Be}(^3\mathrm{H},\mathrm{n}) \quad (7b)$$

$$(\mathrm{n},\gamma)^9\mathrm{Li}(\mathrm{e}^-\nu)^9\mathrm{Be}(\mathrm{n},\gamma)^{10}\mathrm{Be}(\mathrm{e}^-\nu)^{10}\mathrm{B} \quad (7c)$$

produce A ≥ 9 nucleides which could not be formed at all in the homogeneous standard big-bang. The most important key reaction[15] of radioactive nuclei is $^8\mathrm{Li}(^4\mathrm{He},\mathrm{n})^{11}\mathrm{B}$ in the chain (7a) above. A recent measurement of this reaction cross section at E ≥ 1 MeV has provided at least four times larger value than that adopted previously, suggesting that this reaction flow path plays more important role in the production of heavy elements.

In the proton-rich zones take place even helium burning and beta limited CNO cycle;[23]

$$^{4}He(2\alpha,\gamma)^{12}C(\alpha,\gamma)^{16}O(\alpha,\gamma)^{20}Ne(\alpha,\gamma)^{24}Mg \ldots \quad (8a)$$

$$(p,\gamma)^{13}N(e^{+}\nu)^{13}C(p,\gamma)^{14}N(p,\gamma)^{15}O(e^{+}\nu)^{15}N(p,\alpha)^{12}C \quad (8b)$$

$$(p,\gamma)^{14}O(e^{+}\nu) \quad (8c)$$

$$(^{3}He,\gamma)^{7}Be(\alpha,\gamma)^{11}C(e^{+}\nu)^{11}B \quad (8d)$$

In addition to these processes similar to the stellar reactions, a side branch shown in (8d) may play an role in producing ^{11}B even in the proton-rich zones.

Let us remind you the important effect of late-time homogenization[17] resolving high-density zones. This mixes neutrons, protons and all other matter produced during the nucleosynthesis as shown in Fig. 5 schematically. Abundant ^{11}C in the proton-rich zones are destroyed by the $^{11}C(n,2\alpha)\alpha$ reaction where neutrons are back from the neutron-rich zones to the proton-rich zones. Therefore, the proton-rich zones do not contribute very much to the production of ^{11}B [ref. 18].

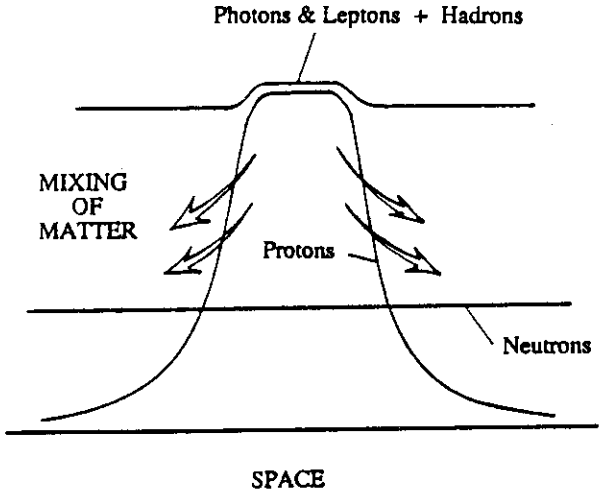

Fig. 5 A schematic illustration of energy densities vs space. High and low baryon-number density zones are mostly occupied by protons and neutrons, respectively, plus helium and others produced by primordial nucleosynthesis. Photon and lepton energy density comes down to the same level as that of the high baryon-number density zones at around $t = 5\times10^{3}$ sec during the nucleosynthesis epoch. This hydrodynamic homogenization causes a mixing of matter.

Another remarkable fact which is caused by the mixing is that the fragile ^{7}Li, ^{9}Be and ^{10,11}B are destroyed by the (p,α) reaction in the neutron-rich zones where protons come into the neutron-rich zones from the proton-rich zones by homogeneization.[17] Does this make the main reaction flow (7a) weaker?

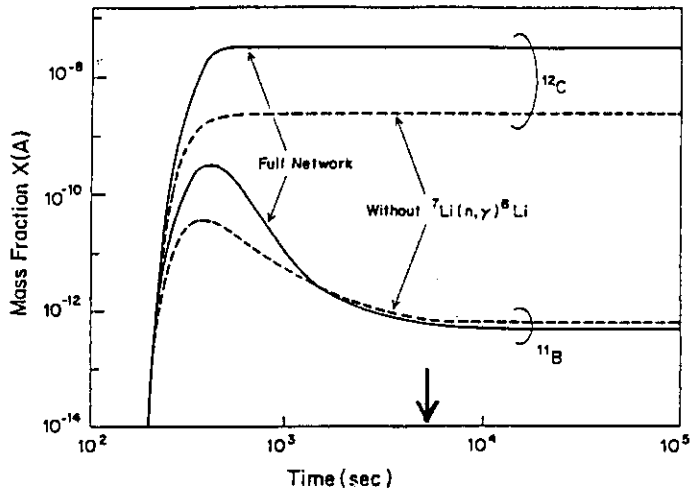

Fig. 6 Time evolution of the ^{11}B and ^{12}C mass fractions in neutron-rich zones in the inhomogeneous models for primordial nucleosynthesis[5]. Arrow shows a typical time scale 5×10^{3} sec at which the homogenization is turned on.

Figure 6 displays time variation of the produced ^{11}B and ^{12}C abundances in the neutron-rich zones without homogenization. A typical time scale 5×10^{3} sec, at which the homogeneization is turned on, corresponding to the homogenixation temperature of 20 keV, is shown in this figure by arrow.[17] Solid and dashed curves are the results with and without the ^{7}Li(n,γ)^{8}Li reaction.[6] It is clear from this figure that the main reaction path (7a) which includes ^{7}Li(n,γ)^{8}Li dominates the production of ^{12}C at the earlier times t $\leq 10^{3}$ sec before the onset of homogenization.

Figure 7 displays the variation of the ^{7,8}Li and ^{12}C abundances in time with the homogenization effect taken into consideration.[18] The adopted inhomogeneity parameters are R = 10^{6} and f_V = 0.016, which are reasonable values from the QCD studies discussed in the previous section, in a Ω_B = 1 universe in two phase separation scenario.[9,14] ^{7}Li is depleted dramatically down to the observed abundance level in Population II stars, as was found for the first time by Alcock et al.[17] However, once ^{12}C is produced via the production of unstable ^{8}Li nucleus in the main reaction chain (7a) before the onset of homogenization, this stable nucleus is not easily destroyed any more by the reactions triggered by protons which are admixed from the proton-rich zones.[18] Since the neutron-capture flow is known to produce heavier elements from ^{12}C like ^{12}C(

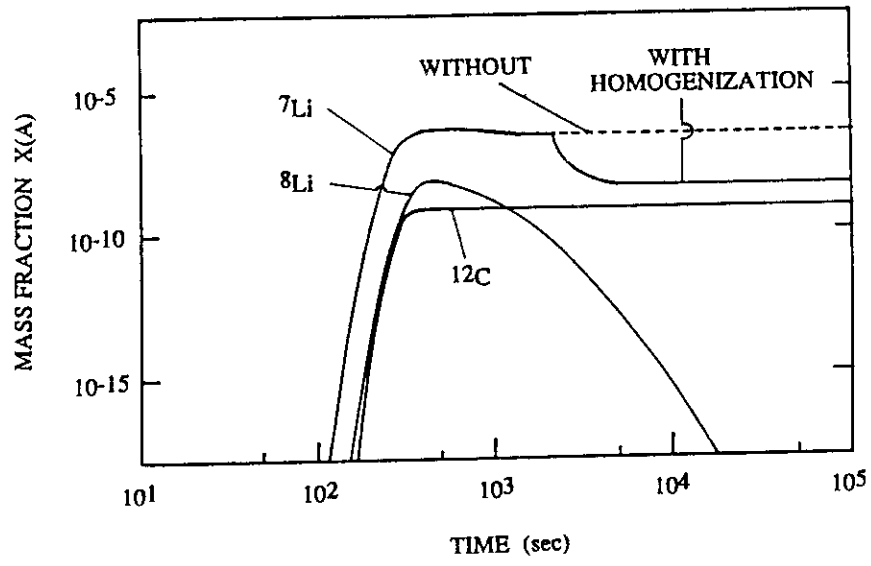

Fig. 7 Time evolution of the ^{7}Li and ^{12}C mass fractions with the homogenization effect taken into consideration[18].

$n,\gamma)^{13}C(n,\gamma)^{14}C(n,\gamma)^{15}C(e^{-}\nu)^{15}N(n,\gamma)$, and so on, the heavy element abundances also do not change very much by the effect of homogenization.

The inhomogeneous big-bang models[23] predict the number abundance of heavy nuclei as large as $N(12\leq A)/N(H) \leq 10^{-8}$ and 10^{-10} in the $\Omega_B = 1$ and 0.1 universe models, respectively. The homogeneous standard model,[23] on the other hand, predicts $N(12\leq A)/N(H) \leq 10^{-13}$ and 10^{-15} in the $\Omega_B = 1$ and 0.1 universe models, respectively. The present astronomical observations in old halo Population II giants[38] constrain the the upper limit of the primordial heavy element abundances to be $\approx 10^{7}$, suggesting that the inhomogeneous model prediction ($\leq 10^{-8}$) is approaching the observational limit. An actual detection of the absorption lines for CNO and heavier atomic nuclei will provide a critical test to the cosmological theories of inhomogeneous nucleosynthesis.

5. SUMMARY

It was first discussed a formation mechanism of the baryon inhomogeneity at the epoch of cosmological QCD phase transition. The chromoelectric flux tube model, which is an effective model of quark confinement, gives smaller baryon penetrability than that estimated in the classical arguments. This causes baryon transfer in non-equilibrium condition between the quark-gluon plasma and the hadron gas and forms largely inhomogeneous baryon density distribution. If the QCD phase transition is weakly first

order and satisfies 80 MeV < T_C < 130 MeV and $\sigma < 10^6$ MeV^3, then the primordial strange quark matter as one of the viable dark matter candidates can be created at this epoch. If the two QCD parameters have values T_C < 150 MeV and 10^6 $MeV^3 < \sigma < 10^7$ MeV^3, several conditions leading to the inhomogeneous nucleosynthesis in the circumstances of almost flat neutron distribution but largely fluctuating proton distribution are satisfied.

It was second discussed that the primordial CNO and heavier element abundances can provide a critical test to the inhomogeneous nucleosynthesis. If the homogenization takes place at relatively later time 10^3 sec < t when almost all ^{12}C and others heavier have already been created by the main reaction chain $^7Li(n,\gamma)^8Li(\alpha,n)^{11}B(n,\gamma)^{12}B(e^-\nu)^{12}C$, homogenization cannot any more destroy these elements. Since the onset temperature and time of homogenization is rather uncertain theoretically, the dependence of the calculated abundances of intermediate-mass elements on this parameter will more clearly show the degrees of mixing of matter due to homogenization. Astronomical search for these elements in old halo dwarfs is highly desirable.

The author acknowledges C. R. Alcock, R. N. Boyd, G. M. Fuller, G. J. Mathews and K. Sumiyoshi for their invaluable discussions and comments through their collaboration. This work is supported by Grant-in-Aid (No. 01540253 and No. 03740152) of the Ministry of Education.

REFERENCES

1. R.V. Wagoner, W.A. Fowler and F. Hoyle, Ap. J. 148 (1967) 3.
2. G.M. Fuller, R.N. Boyd and J.D: Kalen, Ap. J. 372 (1991) L11.
3. G. Gilmore, B. Edvardsson and P.E. Nissen, Ap. J. 378 (1991) 17.
4. S. Ryan, R. Norris, M. Bessell and C. Deliyannis, Ap. J. (1992), in press.
5. R.N. Boyd and T. Kajino, Ap. J. 336 (1989) L55.
6. T. Kajino, and R.N. Boyd, Ap. J. 359 (1990) 267.
7. R.A. Malaney and W.A. Fowler, Ap. J. 345 (1989) L5.
8. For example, see, M. Fukugita, in Dark Matter in the Universe, ed. by H. Sato and H. Kodama (Springer-Verlag 1990) p.32.
9. G.J. Mathews, B. Meyer, C.R. Alcock and G.M. Fuller, Ap. J. 358 (1990) 36.
10. H. Kurki-Suonio, R.A. Matzner, K.A. Olive and D.N. Schramm, Ap. J. 353 (1990) 406.

11. ALEPH collaboration, Phys. Lett. 235B (1990) 399.
12. J.H. Applegate and C.J. Hogan, Phys. Rev. D31 (1985) 3037.
13. S.A. Bonometto, P.A. Marchetti and S. Matarrese, Phys. Lett. 157B (1985) 216.
14. C.R. Alcock, G.M. Fuller and G.J. Mathews, Ap. J. 320 (1987) 439.
15. R.A. Malaney and W.A. Fowler, Ap. J. 333 (1988) 14.
16. N. Terasawa and K. Sato, Ap. J. 362 (1990) L47.
17. C.R. Alcock, D.S.P. Dearborn, G.M. Fuller, G.J. Mathews and B.S. Meyer, Phys. Rev. Lett. 64 (1990) 2607.
18. T. Kajino and R.N. Boyd, in preparation.
19. E. Witten, Phys. Rev. D30 (1984) 272.
20. G.M. Fuller, G.J. Mathews and C.R. Alcock, Phys. Rev. D37, 1380 (1988).
21. K. Sumiyoshi, T. Kajino, C.R. Alcock and G.J. Mathews, Phys. Rev. D42 (1990) 3963.
22. K. Sumiyoshi, K. Kusaka, T. Kamio and T. Kajino, Phys. Lett. 225B (1989) 10.
23. T. Kajino, G.J. Mathews, and G.M. Fuller, Ap. J. 364 (1990) 7,
24. T. Kajino, Phys. Lett. B (1991), in press.
25. C.R. Alcock and E. Farhi, Phys. Rev. D32 (1985) 1273.
26. J. Madsen, H. Heiselberg and K. Riisager, Phys. Rev. D34 (1986) 2947.
27. A. Casher, H. Neuberger and S. Nussinov, Phys. Rev. D20 (1979) 179.
28. B. Banerjee, N.K. Glendenning and T. Matsui, Phys. Lett. 127B (1983) 453.
29. B. Andersson, G. Gustafson and T. Sjostrand, Nucl. Phys. B197 (1982) 45.
30. K. Kajantie and H. Kurki-Suonio, Phys. Rev. D34 (1986) 1719.
31. G.J. Mathews, G.M. Fuller, C.R. Alcock and T. Kajino, in Dark Matter, ed. J. Audouze and J. Tran Thanh Van (Gif sur Yvette: Editions Frontieres, 1989), p.319.
32. K. Sumiyoshi, T. Kajino, C.R. Alcock and G.J. Mathews, Phys. Rev. (1990), submitted.
33. M. Fukugita, H. Mino, M. Okawa and A. Ukawa, Phys. Rev. Lett. 65 (1990) 816.
34. F.R. Brown, F.P. Butler, H.C. Chen, N.H. Christ, Z. Dong, W. Schaffer, L.I. Unger and A. Vaccarino, Phys. Rev. Lett. 65 (1990) 2491.
35. Z. Frei and A. Patkos, Phys. Lett. 222B (1989) 469.
36. K. Kajantie, L. Karkkainen and K. Rummukainen, Nucl. Phys. B333 (1990) 100.
37. T. Kajino, Phys. Rev. Lett. 66 (1991) 125.
38. M.S. Bessell and J. Norris, Ap. J. 285 (1984) 622.

2.7 ADVANCED METHODS FOR NUCLEAR DATA EVALUATION

2.7.1 ADVANCED TECHNIQUES OF INFORMATION PROCESSING

Masaharu Kitamura
Department of Nuclear Engineering, Tohoku University
Aramaki-Aza-Aoba, Aoba-Ku, Sendai, 980 JAPAN

Recent developments in applications of knowledge engineering, fuzzy logic and neural network are reviewed, and applicability of these techniques to assistance of nuclear data evaluation is discussed in this paper. The main obstacle to the development of practical knowledge-based systems for assisting execution of tasks in nuclear data evaluation is the lack of dependable techniques for extracting and documenting expertise of specialists of the task. The potentiality and importance of fuzzy logic and neural network in mitigating this difficulty of knowledge acquisition are demonstrated by simple examples. Combined usage of these new techniques together with the conventional numerical algorithms is recommended to meet the technical needs.

INTRODUCTION

The nuclear industry has always been a front-runner in the use of ever-evolving computation technology. A wide spectrum of challenging technical problems related to design, construction, operation and maintenance of nuclear facilities has been solved with the aid of computers. In brief, the existence of nuclear power can be largely attributed to the computer, or information processing, technology.

The major tasks conducted in conjunction with the above-mentioned problems are mostly categorized as numerical analysis and simulation. Although the

numerical analysis is, and possibly will be, the largest component in the technical applications of computer technology, the importance of recent developments based on other computational paradigms such as knowledge engineering, fuzzy logic and neural network should not be underestimated. Being in their early stages of evolution, these new paradigms have already been proved to be highly powerful in nuclear and other diverse industrial sectors. Application of them to the tasks in nuclear data evaluation is regarded to be at least worthwhile if not promising. The purpose of this paper is to review the state-of-the-art of these technologies to help the reader to judge the applicability of them to his/her own problems.

A comprehensive and exhaustive review of the aforementioned new techniques is by no means possible. This paper focuses on a limited yet essential usages of them, namely, knowledge acquisition and refinement. The computer power of numerical data processing based on algorithms is helpful only when the analyst can specify the problem within a mathematical framework. This is not always the case in most situations of technical problem solving. Most problems are defined in vague and unclear manner at their first phase. Only after laborious iterations of top-down decomposition and bottom-up aggregation, the problem can be transformed into a tractable form suitable to numerical study.

It should be realized that the significant portion of the problem solving, the iteration phase, had not been assisted by the conventional computer technology. The labor-intensive phase had been conducted solely depending on the expertise, or know-how, of the analyst. The author believes that this is the case in nuclear data evaluation also. The value of the new techniques is in that they can contribute to reduction of the mental workload and to assurance of work quality at this earlier phase of problem solving.

OUTLINE OF THE KNOWLEDGE ENGINEERING TECHNIQUES

The expertise of specialists in any discipline is assumed to be represented in a form of declarative statements, mostly in the form of rules. The rules

are typically represented in the IF...THEN...form as below:

[EXAMPLE-1; rule representations]

R1: IF (condition-A holds) THEN (conclusion-P is supported).
R2: IF (condition-B holds) THEN (conclusion-Q is supported).
R3: IF (conditions-B and -P hold) THEN (conclusion-R is supported).
R4: IF (conditions-A and -R hold) THEN (conclusion-S is supported).
.....
RN: .....

The statements and rules are obtained from the specialists by means of interview and then stored in a database called knowledgebase. Also, the problem at hand is characterized by the data representing the current situation. The latter data set is stored in the other database usually called working memory as;

[EXAMPLE-2: data in the working memory]

D1: condition-A is satisfied.
D2: condition-B is satisfied.
.....
DM: .....

Assume that the problem is to determine whether the conclusion-S is supported or not. One can find out that the conclusion-S is supported via careful look at the statements in the sample knowledgebase and in the current memory. He/she may start from D1 and D2, then search the related rules out of the knowledgebase to reach R4. Alternately, he/she may adopt the reverse procedure, starting from R4 and trace back the conditions supporting the related rules and data to reach the D1 and D2. The first search policy is called forward chaining while the latter backward chaining.

Mechanisms for conducting the similar activity, i. e. navigating in the knowledgebase to find a chain of rules needed to solve the given problem, have been developed and made commercially available. By applying the mechanism

(named as inference engine) to the data one can expect to obtain the solutions equivalent to those given by the specialist. The schematic diagram of a typical expert system designed for plant diagnosis is illustrated in Fig. 1.

Although the framework is still crude to substitute the human expertise, a number of software of this type, often called expert system or knowledge-based system, have been developed and reported to be helpful in many areas. The well-known examples of application such as medical diagnosis, process and machine diagnosis, underground resource search, mass-spectroscopy assistance and plant design guidance cover only a limited portion of the real-world applications. Even within the nuclear engineering domain, the applications are diverse enough to include almost all phases of lifetime of nuclear facilities; i. e. design, construction, operation, diagnosis and maintenance[1]. This situation is a clear evidence of usefulness, or at least potentiality, of the knowledge engineering technology.

Simultaneously, however, the knowledge engineering technology has been exposed to various strong critiques[2]. Typical samples of the criticisms are listed below:

1. The human expert employs higher-level reasoning techniques such as analogy, metaphor, abduction, etc. Though attempts have been made to computerize these reasoning techniques, the current status is still in their infancy.
2. The volume and diversity of data referred by the human expert in problem solving are extremely large. Current knowledgebase technology is too poor to handle such volume and diversity.
3. Human expert often utilizes pattern information in problem-solving. The rule-type knowledge representation can deal with the pattern information only in a crude fashion.

These critiques are basically correct if the knowledgebase system is expected to behave like a human expert. The author believes that the system should be designed as an intelligent assistant, rather than substi-

tute, of the user. Also, it should be stressed that the knowledge engineering framework is based on the key hypothesis: knowledge is represented symbolically in some expressions or data structures and can be manipulated to produce useful results. Unless the problem is defined to satisfy the hypothesis, the development of knowledgebase system should not be attempted. Prior to start developing the knowledgebase system, the system designer must pay considerable efforts to redefine the problem to satisfy the hypothesis. In this regard, the above critiques are overemphasizing the weakness of the knowledge engineering paradigm.

Even when the hypothesis is satisfied, however, success of the system critically depends on the quality and quantity of the stored knowledge. Therefore the acquisition of expertise is the central issue in the knowledge engineering technology. It should be noted that the task of knowledge acquisition from domain specialists is quite time-consuming and tedious. Furthermore, the acquired knowledge statements are generally insufficient in many aspects. Their coverage of problem domain is often incomplete, logical and semantic consistency tend to be violated, and organized structure of human expert is hardly reproduced. Though attempts have been made to design assistant systems to support the task of knowledge acquisition from specialist[3)-5)], further studies have to be carried out before the technology becomes practical. The new paradigms of fuzzy logic and neural network are reviewed in this context, since they have potential to contribute significantly to mitigate the difficulty of knowledge acquisition.

IMPLICATION OF NEW TECHNIQUES

Fuzzy Logic

One of the important features of human thinking is the capability of handling problems without clear and precise notions and definitions. The problem of uncertainty handling has been left untouched in the early days of computing technology. However, incorporation of a function for uncertainty handling

became indispensable issue for development of practical expert systems. The fuzzy logic provides us with an appropriate tool to meet this need. It should be also stressed that the number of required rules is often reduced drastically by adopting the fuzzy logic for knowledge description. This is because the coverage of each rule is wider, and thus the need for completeness of the rules is far smaller, in fuzzy framework.

To demonstrate the advantage of the fuzzy framework in knowledge acquisition, consider a simple problem of developing rule-based system for reactor control[6]. The rules for control rod manipulation can be stated as follows:

[EXAMPLE-3; fuzzy rules for control rod manipulation]

FR1: IF(PD is NS.AND.PC is NM) THEN (RC is PS).
FR2: IF(PD is NB.AND.PC is NS) THEN (RC is PL).
.....
FRK: .....

PD: power deviation, PC: power change rate, RC: reactivity change,
NS, NM, NB: negative small, medium, large,
PS, PM, PB: positive small, medium, large.

The fuzzy rule-1 (FR1) is read as "if the power deviation is negative-small, and the power change rate is negative-medium, then reactivity change should be positive-small". Similarly, the FR2 is read as "if the power deviation is negative-big, and the power change rate is negative-small, then reactivity change should be positive-large".

Actual values of PD and PC are obtained from plant instrumentation as non-fuzzy variables. The degree of fitness (DOF) of current situation to each rule is evaluated in terms of membership functions illustrated in Fig. 2 as ST1 and ST12, where the measured PD and PC are given as X1' and X2' respectively. The procedure of determining reactivity change is summarized as follows.

STEP-1: Evaluate the DOF of PD and PC to the FR1.

The matching of measured PD to the statement "PD is NS" is evaluated by the intersection of the X=X1' and the membership function ST11, while the matching of the PC to "PC is NM" is measured by the intersection of X=X2' and the ST12. Since the two statements are combined by AND, overall DOF of current situation to the FR1 is given by the minimum of the two DOFs corresponding to the first and second statements. The membership function of the conclusion part is cut, or chopped, at the level corresponding to the overall DOF to provide the hatched region denoted as AC1'. This conclusion is combined with the outcome of other rules after evaluating all the applicable rules.

STEP-2: Evaluate the DOF of PD and PC to the FR2.

The same procedure is applied to the FR2 to provide the conclusion region AC'.

STEP-3: Repeat the same procedure for all the fuzzy rules.

In this example, assume that none of the other rules resulted to the conclusion region with a measurable size.

STEP-4: Combine the conclusion regions to obtain region AC'.

The widely-utilized procedure is to take the maximum value among the truncated triangular boundaries of AC1', AC2'... for each X-value of the conclusion region. This implies that the goodness of choosing the RC corresponding to the X-value is evaluated in terms of the rule with the highest DOF to the situation.

STEP-5: Determine the amount of reactivity modification based on AC'.

The common practice is to choose X-value corresponding to the center-of-gravity of the region AC'. The overall conclusion is to choose RC corresponding to the U*.

The advantage of the fuzzy rule framework over the conventional rulebase system is well exemplified in this simple example. The two fuzzy rules can

cover fairly wide plant conditions as far as the power deviation and the power change rate are negative. Only a small number of rules are required to cover other regions of the state-space defined by (PD, PC), since the control strategy needs to be defined in a qualitative manner. In order to obtain the similar performance by the conventional rules, the state space needs to be segmented into a number of small subregions and the rules must be defined for each of the subregions. The burden of the knowledge acquisition is thus reduced significantly.

The performance of the fuzzy rule-based system is certainly dependent on the segmentation of the state space, or problem space, and tuning of the membership functions. Several techniques for automated tuning of rules has been proposed and confirmed to be useful in some applications[7]. Though the empirical and heuristic knowledge of specialist is utilized in this phase also, the workload is expected to be reduced owing to the decrease in the number of rules to be tailored.

Neural Network

A neural network consists of a number of signal processing elements connected mutually with weighting coefficients to form a network. Typical architectures of the neural network are given in Fig. 3. Among them, the multilayer network is probably the most widely used in the area of nuclear engineering.

The neural network is generally operated in two modes, learning and recall. The learning means adjustment of the weights assigned to each of the links to provide a desirable input/output relationship for given set of training data. Various algorithms for efficient tuning of the weights have been developed. Through this training, the neural network is tuned to simulate decision-making of a human specialist. The recall is a process to apply the tuned network to data never employed for training. If the training is appropriate, the neural network can provide outputs equivalent to the specialist. Therefore, the

neural network can be regarded as a black-box used for pattern recognition. The neural network is known to be more robust against distortion and/or partial loss of the input data than the conventional techniques of pattern recognition.

The neural network technique can also be applied to acquisition of knowledge related to pattern information, which is difficult to handle by the rule-based methods. The importance of neural network should be recognized in this context as well. A promising method of neural-based knowledge acquisition is to use a modified algorithm of weight tuning called learning algorithm with forgetting[8]. At each step of weight tuning, each weight is forced to be reduced by a small amount irrespective of the incremental adjustment for better learning. Because of the reduction, the weights less influential on the final result of pattern recognition are gradually reduced and become negligible.

The implication of the modified algorithm is demonstrated by the example shown in Fig. 4. The functional requirement to the two multi-layer networks is to determine if the signal waveform given as the input to the network is normal or faulty. By comparing the network structures obtained by the conventional procedure of weight tuning and by the learning algorithm with forgetting, it would be clear that the latter is far simpler. The semantic contents of specialist knowledge can be extracted and documented through careful examination of the simplified network. Note that the pattern recognition performance was not at all deteriorated by the simplification. This procedure can be highly practical in developing knowledgebase systems to support the tasks categorized as the pattern recognition or classification, which are often encountered in the nuclear data evaluation also.

CONCLUDING REMARKS

Significance of the new techniques of information processing has been reviewed from a perspective of knowledge handling. A certain portion of labori-

ous tasks needed during nuclear data evaluation might be supported by these emerging technologies if properly utilized. It is not the author's intention to overemphasize the value of the new techniques. However, it should be understood that the human capability of technical problem solving can be highly enhanced by the best-mix usage of the conventional numerical analysis together with the new techniques. To this end, extensive studies should be conducted to examine and evaluate the applicability of the rapidly evolving new techniques such as fuzzy logic and neural network.

ACKNOWLEDGMENTS

The author would like to express his deep thanks to Mr. S. Iwasaki and Professor K. Sugiyama of Tohoku University for valuable comments and discussions during preparation of this manuscript.

REFERENCES

1) J.A.Bernard and T.Washio: Expert Systems Applications Within the Nuclear Industry, American Nuclear Society, (1989).
2) H.L.Dreyfus and S.E.Dreyfus: MIND OVER MACHINE, The Power of Human Intuition and Expertise in the Era of the Computer, The Free Press, A Division of Macmillan, Inc., (1986).
3) G.Kahn, S.Nolan and J.McDermott: Proc. IJCAI-85, (1985), pp.581-.
4) L.Eshelman and J.McDermott: Proc. AAAI-86, (1986), pp.950-.
5) H.Taki and Y.Fujii: Proc. 3-rd European Workshop on Knowledge Acquisition for Knowledge-Based Systems, (1989), pp.34-.
6) J.A.Bernard: IEEE Control Systems Magazine, 8, (1988), pp.3-.
7) T.Yamazaki and M.Sugeno: Trans. SICE, 20, (1984), pp.50- (in Japanese).
8) M.Ishikawa: Journal of J. Soc. for AI, 5, (1990), pp.595- (in Japanese).

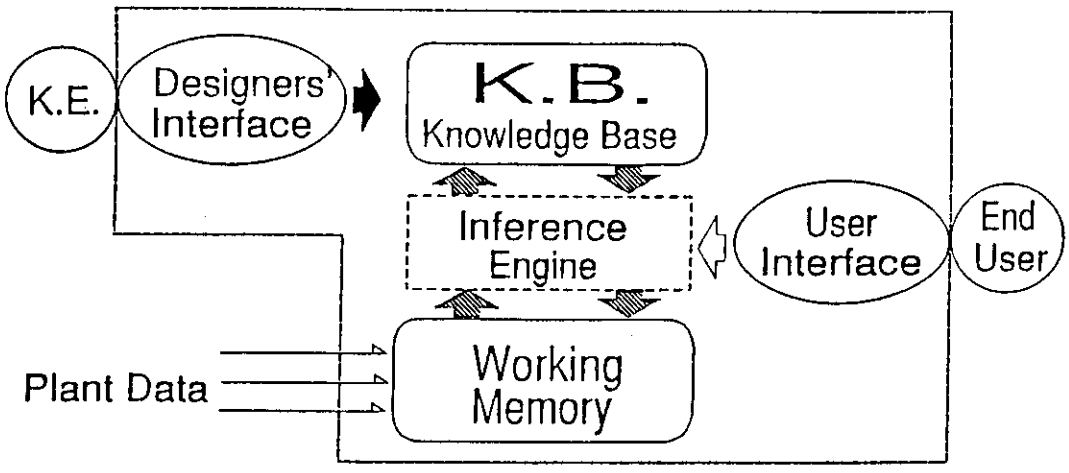

Fig. 1 Schematic diagram of expert system for plant diagnosis.

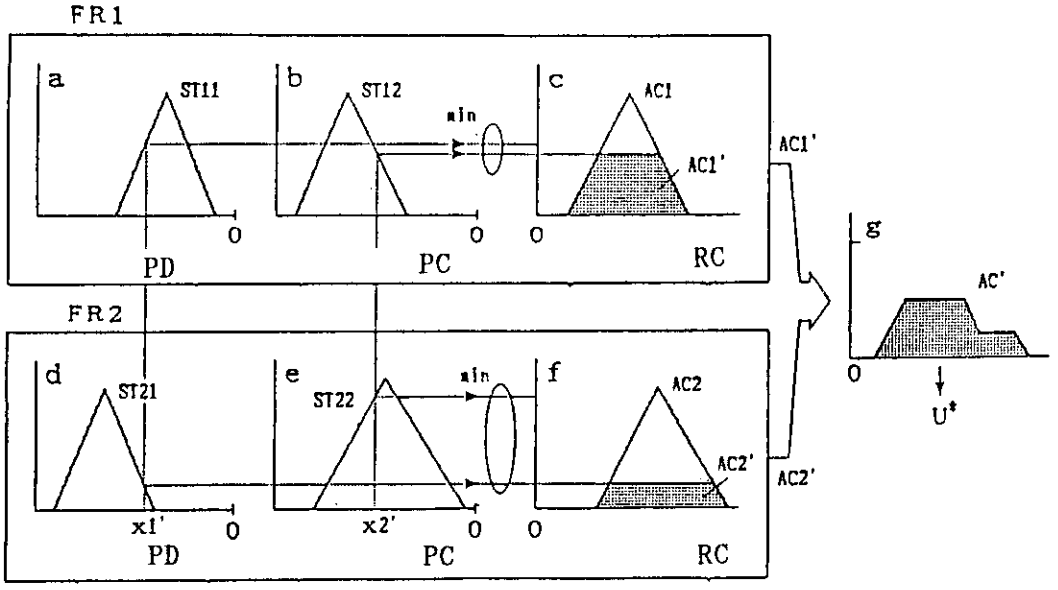

PD: power deviation. PC: power change rate.

RC: reactivity change.

Fig. 2 Example of rules and inference procedure for fuzzy control.

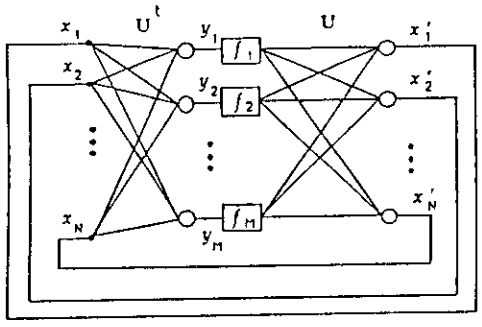

A recurrent network

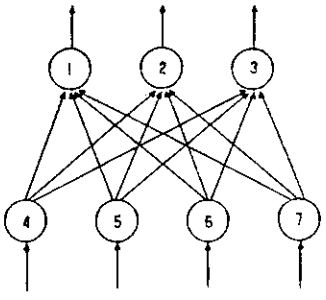

A multi-layer network

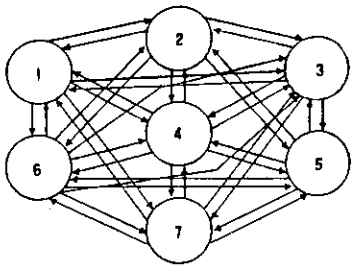

A correlation assosiative network

Fig. 3 Typical architectures of neural network.

(a)

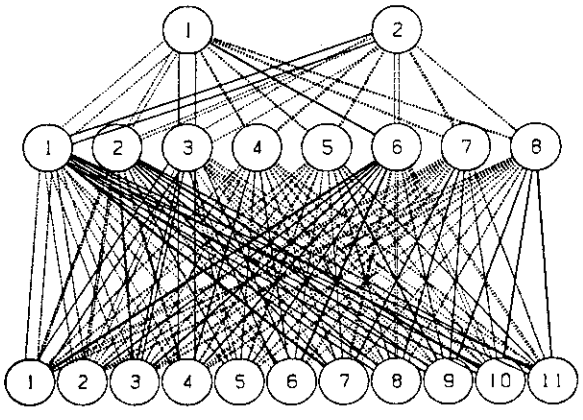

(b)

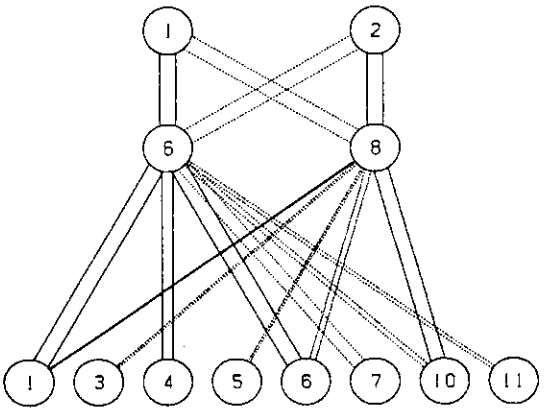

Fig. 4 Neural networks obtained by a conventional algorithm (a), and by the learning algorithm with forgetting (b).

2.7.2 A GUIDANCE SYSTEM OF NUCLEAR DATA EVALUATION IN OBJECT ORIENTED ENVIRONMENT

− ADJUSTMENT PROCEDURE OF NUCLEAR MODEL PARAMETERS −

S. Iwasaki

Department of Nuclear Engineering, Tohoku University
Aramaki-Aza-Aoba, Aoba-Ku, Sendai 980
Japan

ABSTRACT

The object model for the guidance system of the neutron nuclear data evaluation are briefly described. As the example of the system, we take a model for procedure of the nuclear model parameters in the framework of the general least squares method which have become one of the main processes in the contemporary evaluation. In this model, almost all things appearing in the processes were modeled by objects which are connected with each other and with the external processes and data bases. Actually description of the fitting procedures have been made for the case of cobalt-59 as the target nuclide. In this model, a object for the strategic options are important when the expected fitting fails.

1. Introduction

We have proposed a framework of guidance system for the nuclear data evaluation in an object-oriented modeling (OOM) /1/. The OOM has high capability of description of domain complexity, and the model world is rather transparent to developer and even to user.

Additionally, the characteristics of the model are high modularity and extendibility, and kernel of the system is easy to be connected with the conventional nuclear codes, utility programs and data bases as the external processes.

In this model, the various things and tasks appearing in the evaluation process (or imaged by the evaluator) are described as objects: a collection of data and procedures as attributes of the objects. A set of rules which is suitable to describe a shallow knowledge of the domain can also be attached to the objects. The objects communicates with other objects and/or evaluator by

massage sending, and the evaluation proceeds.

Process of the nuclear data evaluation can be categorized into two main part. The first one is consisted of manipulation of the experimental data; collection of data from the raw data base and literature; selection, rejection, and renormalization of these data by closely looking the reports in the literature; and finally application of a statistical procedure including the least-squares method on the selected data base.

Another one is based on the theoretical model calculation, which becomes a main tool of the contemporary nuclear data evaluation because of appreciable progress of the model in recent year, availability of advanced codes, and high capability of the model in the reproduction or prediction of various kind of cross sections for a given nuclide.

These two methods have been being in the relation of mutually complement for the conventional (contemporary) evaluation in the region of nuclides and incident energies below 20 MeV. The methodology on the basis of the theoretical model, however, become to be more highlighted because the frontier of the nuclear data evaluations shifts more and more to uncommon or unstable nuclides, and to higher energy regions where experimental data are generally sparse and required accuracy is not so high. In this paper, we focus our discussion on the theoretical model fitting, particularly by the code GNASH/2/ predominantly used in the evaluation for JENDL-3/3/.

2. MODEL PARAMETER FITTING BY GENERAL LEAST-SQUARES METHOD.

In the theoretical model calculation of the evaluation, the selection and adjustment of the nuclear model parameters are one of the key issues. Very often the semi-automatic parameter search technique has been employed in the optical model or resonance analysis. In the statistical nuclear model calculation, an evaluator, conventionally, chooses and adjusts the parameters to reproduce the experimental data mainly based on his/her heuristics and physical consideration. The general least squares methods (GLSM) based on the Bayes' theorem could be a new rational method to assist the evaluator to obtain an optimum parameter set, and is suitable to be implemented in the system.

This method is in fact powerful, and has been successfully used in the optical and statistical model calculations/4//5//6/. Very recently D.L.Smith/7/ emphasizes that it is the most promising method in contemporary evaluation methodologies, but this area is still growing and there exist unresolved issues.

According to Froener/8/, lets observables y_i, i=1,2,.. I, model parameter x_m, m=1,2,....M, and a theoretical model y=y(x), where $x=(x_1,,..x_m)$, $y=(y_1,...,y_I)$ are vectors in the data and parameter spaces, respectively, and I>M. Suppose (a) that before the data become available one had prior knowledge about the parameter vector, namely an estimated vector ξ and a covariance matrix $C_x=<dxdx^+>$(with $dx=x-\xi$), describing the uncertainties and correlations of the estimated parameters, and (b) that measurements yielded a data vectors η, affected by experimental errors whose uncertainties and correlations are given by the covariance matrix $C_\eta=<d\eta d\eta^+>$ (with $d\eta=\eta-y$).

We can get the posterior distribution of the parameters by the product of the prior distribution and likelihood function using the maximum entropy principle,

$$P(x|C_x,\xi,C_\xi,\eta,y)dM_x \\ \exp[-(x-\xi)^+C_x^{-1}(x-\xi)/2-(\eta-y)^+C_\eta^{-1}(\eta-y)/2]dM_x. \quad .....(1)$$

The minimum of the exponent is required by the maximization of the posterior,

$$(x-\xi)^+C_x^{-1}(x-\xi)+(\eta-y(x))^+C_\eta^{-1}(\eta-y(x))=\min. \quad .....(2)$$

After some approximations, one get the following solution x and its new covariance C_x,

$$x=\xi+[C_x^{-1}+S(x)^+C_\eta^{-1}S(x)]^{-1}S(x)^+C_\eta^{-1}[\eta-y(x)-S(x)(\xi-x)] \quad ..(3)$$

$$C_x'=C_x-C_xS(x)+[C_\eta+S(x)C_xS(x)^+]^{-1}S(x)C_x \quad .....(4)$$

The Eq. (3) is suitable for iteration: we insert the a priori most probable value, $x_0=\xi$, on the right-hand side, find an improved value x_1 reinsert this, and so on, until stationarity is achieved. The minus sign of the Eq. (4) indicates that new data reduce the uncertainties.

3. OBJECT MODEL FOR THE PARAMETER FITTING PROCEDURE

The six quantities $(\xi,C_\xi,\eta,C_\eta,y,S(x))$ appearing in the above equations are represented by the objects in the system. Diagram of the relation of the main objects, external data bases, codes and programs in the system for the parameter fitting is shown in Fig. 1, and a flow diagram of the procedures is also presented in Fig. 2.

Target Level of Fitting

First step of the evaluation in the system, the users is asked to set a target level of the fitting mainly from the application point of views. The set can be done by consulting with the application data base which lists elements and reactions with default target levels according to the requirement of accuracy of respective cross sections and/or model calculations. The system proceed so that the calculated result satisfy the fitting level.

The fitting cross sections η and C_η of selected reactions are created at a suitable energy mesh from the experimental data by a suitable function fitting.

Parameters and Their Error Vectors

The model parameters used in GNASH code can be classified into two groups; the first one is rather fixed type: level structure data (excitation energies and gamma branching ratio), E2 transition probabilities for the first 2^+ excited levels, giant dipole resonance parameters, etc. In the present case, the level density parameters (LDP's) and the Karlbach's constant are considered to be the second group, i.e., semi-adjustable parameters. The LDP is usually determined from the statistics of level spacing from the neutron resonance data of low angular momentum states near the excitation energy just above the neutron separation energy of a given nuclide. The level spacing data are usually accompanied by large uncertainties/9/ and the level density parameters derived from them might have large errors. The Karlbach constant divided by 100, i.e., F2 in the precompound model and normalization factor for pick-up process F3 are also in a similar situation.

The initial values of the parameters ξ are chosen from the parameter data base based on the JENDL-3 evaluations /10/ and by Yamamuro /11/. The diagonal components of C_x define a sort of variable range of the respective parameters, and off-diagonal elements provide a constraint on the parameter variation through the correlation between them. Note that there possibly exists a correlation between the prior parameters and posterior function because the prior ones might be obtained by the fitting with almost the same experimental data base. In such a case, we ought to use more general expression/7/ which include the covariance matrix between them other than Eq.(2). However, in this study we use the Eq.(2) because first the correlation cannot easily be estimated.

From the sensitivity calculation discussed below, we chose

the actual adjustable parameters which have dominant effect on the fitted cross sections.

Calculated Cross Section Sectors and Sensitivity Matrix

The calculated cross section vector can easily been obtained by the model calculation using the GNASH code at the neutron energy mesh points with the initial model parameter set given above or revised values by Eq.(3).

The sensitivity matrix is calculated for each adjustable parameter by increasing respective values by 1% from the initial value of the LDP's and by 5% for F2 parameters. The matrix is also recalculated when the initial parameter set is replaced, or updated according to the Eq. (4) because the theoretical model is nonlinear.

Fitting by GLSM

When the degree of fitting by the initial parameter set is over the target level and all status values of these six objects become "ready"(=yes), an object PARA_ADJ executes the external program 'GLSQ'. CHI2_MON object monitors the χ^2-values of the total and respective reaction data in CS_COMP object given by comparison of the experimental and calculated cross sections. PARA_MON object alerts when a parameter becomes over its preset limit value during the fitting.

Although the capability of the fitting algorithm of the GLSM is so high, often the fitting fails because primarily the theoretical model is not perfect at present and just a model; secondarily the initially selected parameter is not always good ones for a given cross sections; and the last the selected cross section data might have unknown wrong value. STRAT_OB object is invoked when no good fitting is attained. It suggests to user one of the following strategic options : 1) changing the variance/covariance of a particular parameter, 2) replacement of the initial parameter set, 3) exchange the experimental data set if available, 4)test the possibility of the good fitting (discussed in the example) or 5) changing the target level of the evaluation for the given cross sections, etc. INTERP_OB object shows the possible reasons why the fitting did not succeed in the GLSM method.

4. EXAMPLE OF PARAMETER FITTING

We take cobalt as an example of the target element of the parameter fitting, because the cobalt is a mono-isotopic (^{59}Co)

element and thus, the model calculation is simple and easy to understand.

Cross sections for the (n,p), (n,α), (n,2n), particle emission spectra at 14 MeV for neutrons, protons and alpha particles are available from the EXFOR file. The cobalt element is not considered as the prime candidate of the structural material for the controlled fusion reactor/13/. Most important issue of the cobalt is the production of ^{60}Co and ^{58}Co; the former which is a long life activity in reactors from (n,γ) reaction, the latter one is produced by (n,2n) reaction which is important in the neutron dosimetry. Such cross section ought to be fitted at least within 5% in the entire energy range and hopefully few % around 14 MeV. Other reactions, such as (n,p) and (n,α), and particle emission cross sections are therefore not so important for the applications, and their default fitting levels are set as 20%. Among them, neutron emission spectrum at 14 MeV is rather important for the determine the parameter fitting of the LDP and F2. The target level of the first stage of the present evaluation is set slightly higher than the default ones given in the data base.

Fig. 3 show the experimental data for (n,p),(n,α) and (n,2n) reactions and the experimental data vectors at an incident neutron energies in equally interval of 2MeV from 2 to 20 Mev.

Neutron optical potentials for the ^{59}Co was selected by applying a criterion called SPRT /12/. Three candidates of the optical model parameters were tested by this test, and finally a potential set by Watanabe/3/ derived in the evaluation for JENDL-3 was chosen. In this example, we do not search the optimal potential set further.

We adopted the initial parameter values for the LDP's and F2 from those of Yamamuro who had determined those by fitting the cross sections using SINCROS-II/11/. Finally, six LDP's for ^{58,59,60}Co, ^{58,59}Fe, and ^{56}Mn, and F2 were considered as the adjustable parameters from the sensitivity study of the parameters prior to the least squares fitting procedures.

As for the covariance data of the initial parameter, we considered only diagonal elements of the matrix, i.e., variances of the parameters of 1% (with the alert level of 5%) for all LDP's and 10% (50%) for F2.

Example of the 1% sensitivity coefficients of the selected parameters to the (n,p) cross section are calculated as shown in Fig. 4. With a few exceptions, the LDP's represent rather similar

shape with each others as a function of the incident neutron energy neglecting the sign. This means that the existence of the strong correlation between these parameters which have not been discussed.

As seen in Fig. 3, the fitting level of the calculated results with the initial parameter are over the target level for all cross section especially for (n,p) and (n,α) cross sections. The system proceed the fitting process and expected calculation result are also shown in the same figure.

These expected cross sections can be confirmed by the actual model calculation using the updated model parameters. In the same figure, the calculated value is also compared the former one showing a small difference due to the nonlinearity of the theoretical model to the parameters.

The second iteration of the fitting was performed with the updated parameter values, their new covariance, and new sensitivity matrix. We found slight improvement of the cross section because the new variance of the parameters were reduced appreciably from the initial one, and their exist a rather strong correlations between some parameters as shown in Table 2. The stationary of the iteration achieved usually at the second calculation.

The fitting level of all cross sections have been improved appreciably, however, is not still satisfactory, because the cross section for (n,p) and (n,α) reaction, and charge particle spectra are discrepant and over the fitting target level, and the χ^2-values are quite large.

There is no other candidate for cross sections and parameter set, the STRAT_OB first recommends to enlarge the variance of all the parameters i.e., parameters are changeable more freely, but this makes no appreciable improvement in the fitting. Therefore it suggests the user to test the possibility of the good fitting: reduction of the values of variances of only one cross sections, among the (n,p),(n,α) or (n,2n) reactions, artificially down to about 1%, and enlarging the variances of other cross sections and all model parameters to 20% or more. This means that the fitting will be concentrated only one chosen cross section with the almost free model parameters.

Figure 5 shows relative variation of each parameter values from the initial ones (1.0) for the respective best fitting of the above three reactions within a few % in the almost entire energy range. This figure indicates that there is no optimum set of parameters by which these cross sections could be fitted well simultaneously because some parameters apparently varied in the

opposite direction; e.g., the LDP for ^{60}Co being one of the key parameter for (n,p) and (n,α) cross section appreciably decreases for (n,p) and increases for (n,α) reaction fit, respectively. Consequently, we ought to cease further improvement in the fitting by the present adopted theoretical model and parameters, and make a compromise with the present fitting level.

5. Summary

The object model for the guidance system of the neutron nuclear data evaluation have been briefly described. As the example of the system, a model for procedure of the nuclear model parameter fitting in the framework of the general least squares method which have been main process of the contemporary and future evaluation. In this model, almost all things appearing in the process were modeled by objects which are connected with each other, and with the external processes and data bases. Actually description of the fitting procedures have been made for the case of cobalt-59 as the target nuclide. Objects for monitoring and strategic options are important in the failure situation of the fitting.

References

1) S. Iwasaki, and K. Sugiyama: JAERI-M 91-032, p366, Japan Atomic Energy Research Institute (1991).
2) P.G. Young and E.D. Arthur: LA-6947, LANL (1977).
3) K. Shibata, et al.: JAERI 1319, p179, JAERI (1990).
4) F.H. Froener, et al.: Proc. Meeting on Fast Neutron Capture Cross Sections, p116, Argonne, ANL-83-4, ANL (1982).
5) T. Kawano, et al.: Proc. 1990 Symposium on Nuclear Data, p. 355, JAERI-M 91-032, JAERI (1991).
6) Y. Kanda and Y.Uenohara: Proc. IAEA Sp. Meet. Cov. Meth. Practices in Nucl. Data, Report INDC(NDS)-192/L, p98, IAEA(1988).
7) D.L. Smith: "Probability, Statistics, and Data Uncertainties in Nuclear Science and Technology", OECD/NEA/NDC Series vol.4, ANS, (1991).
8) F.H. Froener: "Principles and Methods of Data Evaluation", Data Uncertainty, Sensitivities, Consistency and Adjustment", unpublished manuscript, KfK, FRG (1987).
9) J.L. Cook, et al.: Aust. J. Phys., vol. 20, p.477 (1967).
10) T. Nakagawa: private communication (1990).

11) N. Yamamuro: JAERI-M 90-006, JAERI (1990).
12) J.P. Delaroche, et. al.: Proc. Consult. Meet Use of Nucl. Theory Nucl. Data Eval., IAEA-NDS and ICTP, Trieste, p251, IAEA-190 (1976).
13) K. Maki: Proc. of the Second Specialists' meeting on Nuclear Data for Fusion Reactors, JAERI-M 91-062, p 183, JAERI (1991).

Table 1 The initial and final values of parameter set in the calculation of neutron induced reactions on ^{59}Co+n.

parameter		initial value	final value
LDP	^{60}Co (a1)	9.7	9.37
	^{59}Co (a2)	8.4	8.52
	^{58}Co (a3)	8.6	8.74
	^{59}Fe (a4)	9.8	9.96
	^{58}Fe (a5)	8.7	8.74
	^{56}Mn (a6)	9.8	9.58
F2		0.5	0.58
F3		0.55	0.546

Table 2 A correlation matrix of the parameters obtained by the Eq. (4) after the first iteration for the fitting of the ^{59}Co+n cross sections.

parameter*)	a1	a2	a3	a4	a5	a6	F2	F3
a1	1.00							
a2	-0.20	1.00						
a3	-0.22	-0.05	1.00					
a4	0.26	0.63	0.22	1.00				
a5	0.00	-0.01	0.02	0.00	1.00			
a6	0.07	0.71	-0.09	0.41	0.00	1.00		
F2	-0.37	0.08	-0.04	-0.02	0.00	-0.56	1.00	
F3	-0.36	-0.08	0.04	-0.02	0.00	-0.06	1.00	1.00

*) the same symbol used for the parameters as the Table 1.

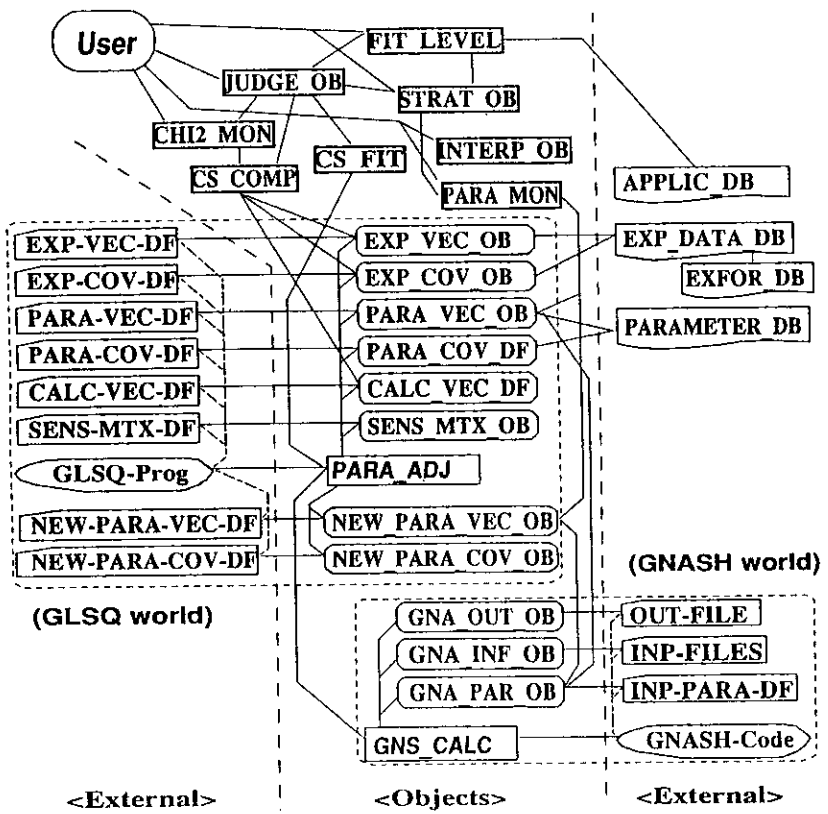

Fig. 1 Object model of the procedures of the nuclear model parameter fitting.

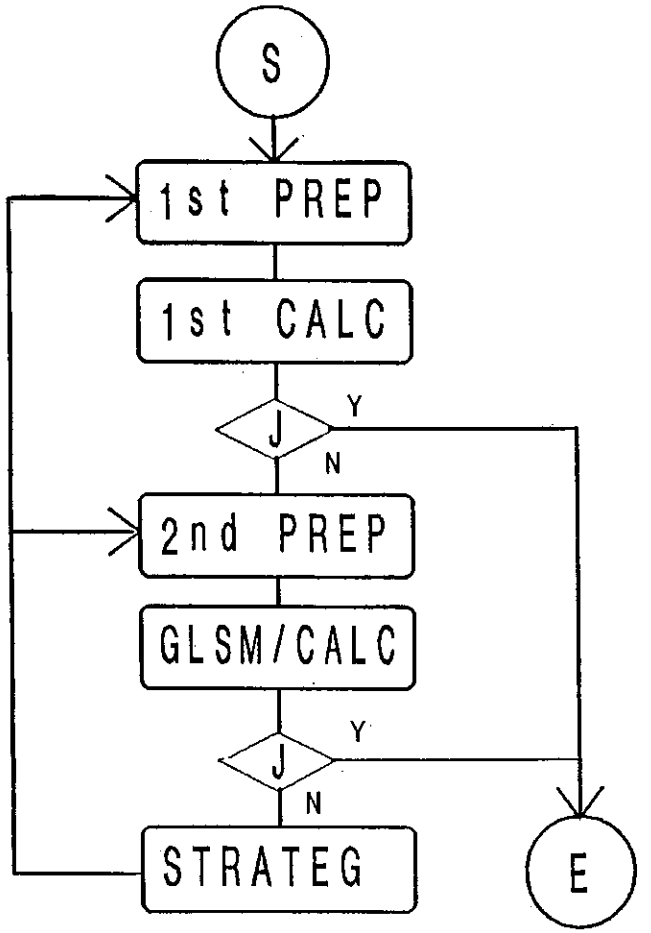

Fig. 2 Flow diagram of the procedure of the fitting. 1st prep.: fit level, exp. data vec. & cov., etc.; 1st. calc.: calc. by initial para, calc. vec.; 2nd. prep.: para vec. & cov., sens. matrix, etc. (see text).

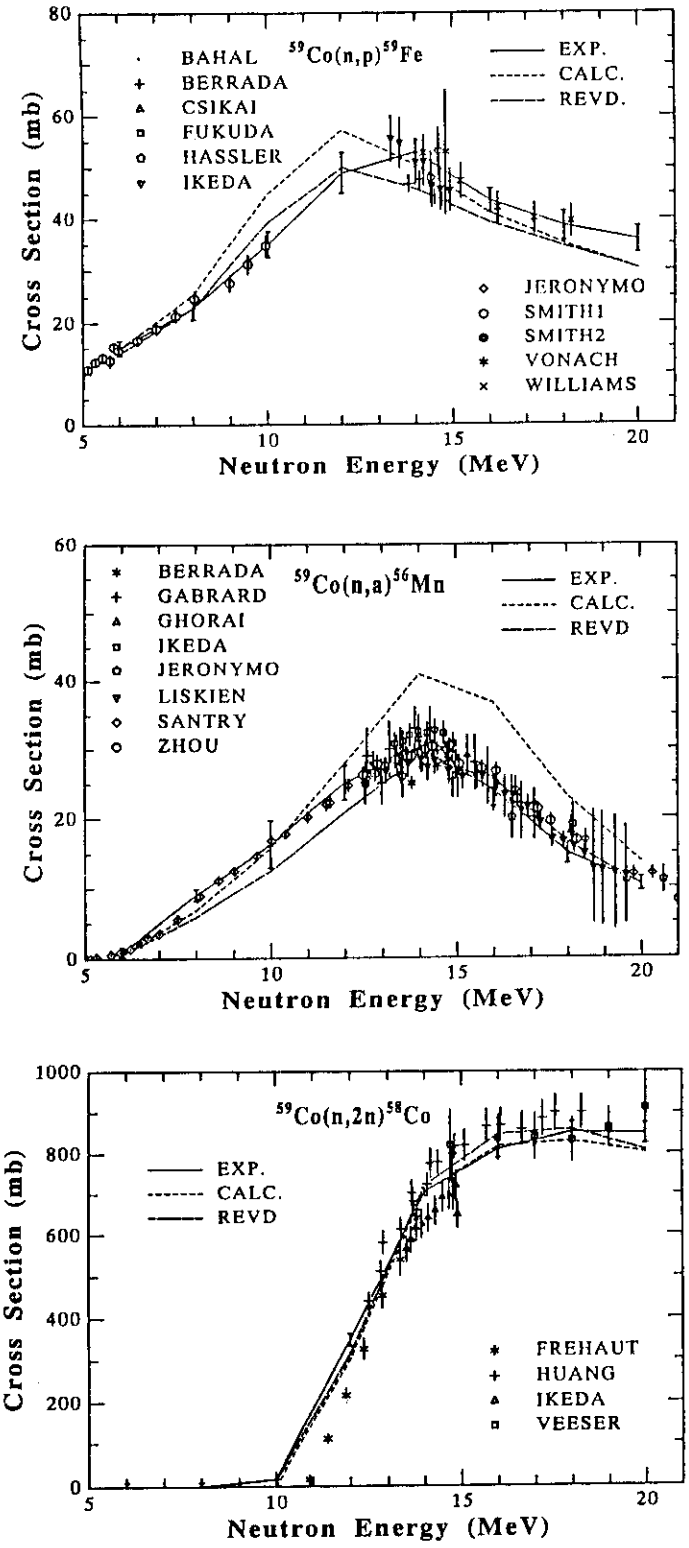

Fig. 3 Raw data of the cross sections taken from the data base and cross section vector for ^{59}Co(n,p) (upper), (n,α) (middle) and (n,2n) reactions (lower), respectively. The model calculations with the initial parameter set (CALC.) and with the predicted one (REVD) are also compared.

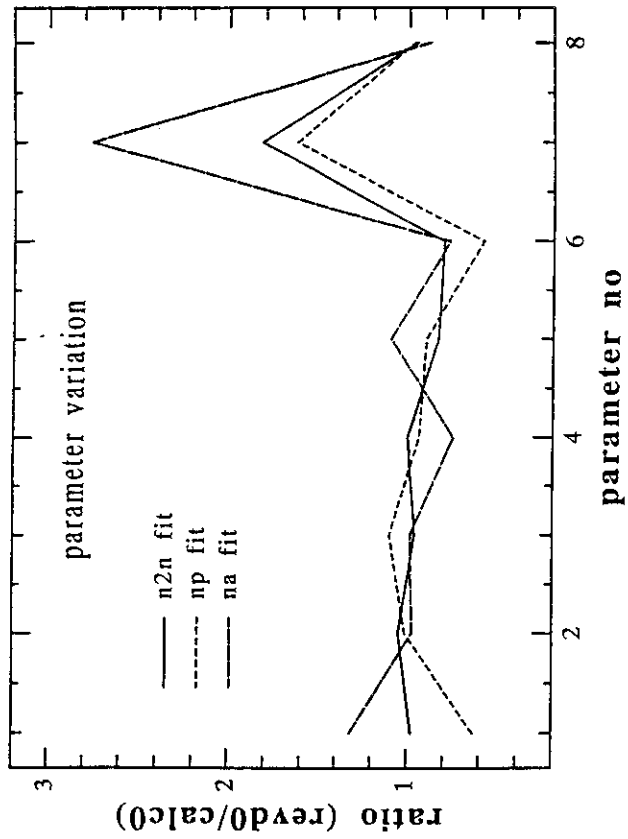

Fig. 5 Parameter variations from the initial values for the individual best fitting of the three cross sections, (n,p), (n,α) and (n,2n) on Co. The abscissa means 1: LDP for ^{60}Co, 2: ^{59}Co, 3: ^{58}Co, 4: ^{58}Fe, 5: ^{57}Fe, 6: ^{56}Mn, 7: F2 and 8: F3.

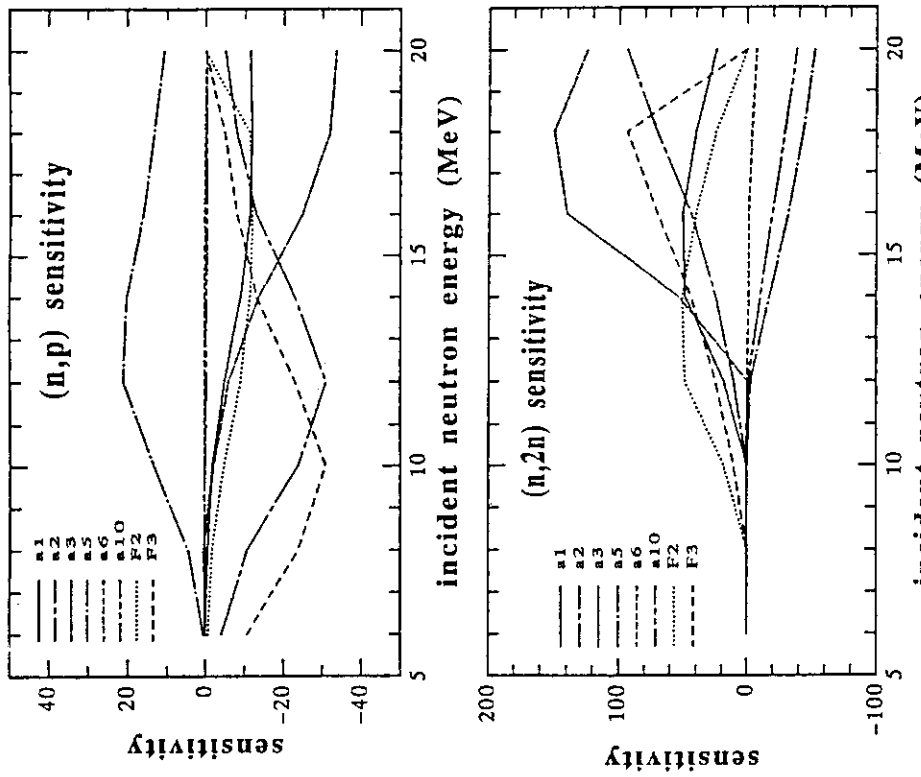

Fig. 4 Sensitivity coefficients of main parameters to the cross sections for the ^{59}Co(n,p) and (n,2n) reactions.

2.8 TOPICS IN REACTOR PHYSICS

2.8.1 THERMAL REACTOR BENCHMARK CALCULATIONS FOR JENDL-3

H. Takano and LWR Integral Data Testing WG*

Advanced LWR Program Team, JAERI
Tokai-mura, Naka-gun, Ibaraki-ken, 319-11

Benchmark calculations for thermal reactor critical assemblies have been performed to assess the applicability of JENDL-3 nuclear data to thermal reactors. Reactor lattice cell calculation codes SRAC, CASMO, TGBLA, WIMS-E, MGCL-ANISN, MGCL-KENO-IV, VMONT and VIM were used in the present calculations.MGCL-KENO-IV and VMONT are Monte Carlo codes using multigroup model, and VIM is a continuous energy Monte Carlo code.

The experiments selected were water-moderated lattices of slightly enriched 1.3% uranium metal rods, TRX-1 and -2. The values of k_∞ calculated with VIM and other codes were in very good agreement each other. However, k_{eff} calculated with VIM was smaller than those for other codes and experimental data.

The TRX cores were analyzed by SRAC using JENDL-2 and -3 data, and these results were compared with those obtained by using JEF-1 data.

Furthermore, water-moderated critical lattice of MOX-fuel (3.0 wt.% Pu) rods at TCA were calculated with these codes and the results were compared. The k_{eff} obtained with VIM was in good agreement with experiment. However, the results obtained with SRAC, CASMO and TGBLA depended on the volume ratios of moderator to fuel.

The discrepancies among the results obtained with the present codes were discussed by comparing neutron spectra and three averaged group cross sections.

* Member of LWR Integral Data Testing WG:
E. Saji (Toden S.W), M. Yamamoto (Toshiba), M. Nakano (MAPI), M. Takami(CRC),
A. Zukeiran, K. Kobayashi (Hitachi), K. Kaneko (Nippon Souken),
H. Akie, F. Masukawa, K. Nakajima, Y. Kikuchi, Y. Ishiguro, H. Takano(JAERI)

1. Introduction

Light water reactors(LWRs) will be the mainstream component of nuclear power generation in a long term view point. For this purpose, the studies of advanced LWRs concepts with high burnup and high conversion ratio are progressed in order to improve safety, economy and uranium resource utilization. The advanced LWRs have a considerably different neutron spectra and fuel compositions with plutonium from the conventional LWRs. The utilization of the existing data and code system for the advanced LWR design will require rigorous validation for prediction quality. To obtain adequate prediction accuracy for design calculation of the advanced LWRs,a great deal of effort are required for the validation of data and method in neutronic calculations. These will be required for critical safety calculations in fuel cycle processing with high plutonium content and burnup composition.

The main objective of the present study is to achieve a benchmarking of data and codes by analyzing well-known LWR critical experiments. We selected the newest nuclear data of JENDL-3 and the experiments with a simple geometric configuration.

The experiments selected were water-moderated lattices of slightly enriched 1.3% uranium metal rods, TRX-1 and -2, recommended by the Cross Section Evaluation Working Group[1]. As for the plutonium fuel lattice experiments, TCA cores with MOX assemblies were selected.

Reactor lattice cell calculation codes SRAC[2], CASMO[3], TGBLA[4], WIMS-E[5], MGCL-ANISN[6], MGCL-KENO-IV[6], VMONT[7] and VIM[8] were used in the present calculations.MGCL-KENO-IV and VMONT are Monte Carlo codes using multigroup model, and VIM is a continuous energy Monte Carlo code.

The discrepancies among the results obtained with these codes were discussed by comparing neutron spectra and averaged group cross sections.

2. Neutronic Calculation Codes and Their Characteristics

Table 1 summarizes neutronic calculation codes and their characteristics used in the present benchmark testing. The CASMO code calculates cell spectrum on the basis of the WIMS-D[5] method which intermediate resonance approximation for absorption rate is employed, leakage can be treated by either the B1 method or the diffusion theory method, and heterogeneity effect is calculated by collision probability method. In the WIMS-E code, leakage is calculated by the diffusion method based on Benoist's theory. The group cross section libraries used for the WIMS-E and CASMO codes were produced by using the data processing code system, NJOY87[9].

In the TGBLA and SRAC codes, leakage is calculated by the B1 method and heterogeneity effect is treated by the collision probability method. In the resonance absorption rate calculation, the TGBLA uses the table lookup method and the SRAC employs the ultra-fine group method. The group cross section library used for these codes was generated by the TIMS-PGG[10] processing system.

The MGCL-ANISN code calculates neutron spectrum by the Sn transport theory, and the 137 group cross section library is used. The Monte carlo code KENO-IV uses this MGCL-library.

The Monte Carlo code VMONT employs the 190 group cross section library generated with the NJOY87 and RESENDD[11] codes. The RESENDD code was used for resonance cross section calculation of Pu-239 based on the Reich-Moore formula. This VMONT code can be used for the cell spectrum calculation only.

The continuous energy Monte carlo code VIM is used either the cell spectrum and full core assembly. The VIM cross section library was produced by using the processing system VIM-J[12]. The VIM gives the most rigorous result as comparing with other code methods, and the calculated result can be considered as a reference value.

3. Benchmark Calculation Models

It would be desirable to select reliable benchmark experiments. We selected the TRX cores with uranium fuel and the TCA cores with plutonium fuel.

3.1 Uranium Fuel Core

The TRX-1 and -2 are recommended by the Cross Section Evaluation Working Group. The experiments are water-moderated lattices of slightly enriched 1.3% uranium metal rods.

In these cores, effective multiplication factor, critical buckling and lattice parameters are measured as shown in Table 2.

3.2 Plutonium Fuel Core

There are scarce water−moderated lattice experiments with plutonium fuels. The valuable experiments with 3.0 w% PuO2−natural UO2 fuel rods of TCA cores[13] were selected. The water−to−fuel volume ratios cover from 2.42 to 5.55 as shown in Table 2.

3.3 Integral Data for Intercomparison

The integral data calculated for intercomparison in each code are k_{eff}, k_{∞}, lattice parameters(reaction rate ratios), neutron spectrum, three group cross sections for capture, fission, total and transport reactions in Table 3. The k_{eff} and lattice parameters can be compared with the measured values. The k_{∞}, spectrum and cross sections are compared among the calculated results. However, the comparison for spectra is not easy, because group energy structure differs in each code. The results of VIM with continuous energy structure were collapsed so as to equal the group one in each code.

4. Comparison of the Calculated Results

4.1 TRX Critical Core

As MGCL−KENO can not calculate k_{∞}, the transport code MGCL−ANISN was used. CASMO, SRAC, WIMS−E and TGBLA calculate k_{eff} by using buckling data. Monte Carlo codes MULTI−KENO and VIM calculate k_{eff} with considering the full geometry assembly model as shown in Figs. 1 and 2.

4.1.1 Effective Multiplication factor

The k_{∞} and k_{eff} calculated for TRX−1 and −2 are shown in Tables 4 and 5. The k_{∞} calculated with VIM and other codes are in very good agreement with each other. However, a significant difference between k_{eff} calculated with CASMO, SRAC and VIM is found by observing the ratio of k_{∞} to k_{eff} in Table 5. The CASMO and WIMS−E show a similar tendency as seen in Table 4. The k_{eff} calculated with VIM was smaller than those for other codes and experimental data. Thus, k_{eff} obtained with the JENDL−3 data is underestimated

4.1.2 Lattice Parameter

The ratios of calculation to experiment for lattice parameters are comparedin Figs. 3 and 4. From these figures, it is observed that δ−28 are overestimated and δ−25 underestimated in each code, and furthermore, ρ−28 is overestimated for TRX−1. Hence, from these results, we can consider that U−235 fission cross section is smaller and U−238 capture cross section is larger in epithermal energy region.

4.1.3 Neutron Spectrum

The neutron spectrum calculated by TGBLA, SRAC, CASMO and MGCL−ANISN is compared with that by VIM, respectively, in Figs. 5 − 8. The results for TGBLA , SRAC and CASMO are in very good agreement with the VIM result excepting for slight discrepancy near 0.1 eV as seen in Fig. 7. However, the MGCL−ANISN result differs significantly from the VIM spectrum in comparison with other code as observed in Figs. 6 and 8.

4.1.4 Averaged Cross Section

Group cross sections averaged over fast, resonance, thermal and whole energy range are

compared for U-235, U-238 and Hydrogen in Tables 6 – 8. One-group capture and fission cross sections for all the codes are in good agreement with each other. However, these fast and thermal cross sections for MGCL-ANISN show slightly larger values than those for the other codes. This tendency was observed also in comparison of neutron spectrum. The most largest discrepancy in resonance total cross section of U-238 is seen between the CASMO and other codes. This cause was investigated and confirmed that the WIMS series including CASMO do not consider self-shielding effect of resonance scattering cross section. This underestimates neutron leakage effect and gives larger k_{eff} value. Furthermore, this answers that the discrepancy in the ratio of k_∞ to k_{eff} between CASMO and SRAC was observed as shown in Table 5.

4.2 Comparison Between Nuclear Data Libraries

The TRX-1 and -2 were analyzed by SRAC using the JENDL-2 data, and these results were compared with those obtained by Pelloni et al.[14] using JEF-1 data as shown in Table 9. The discrepancy between the k_{eff} calculated with JENDL-2 and -3 is very small, but that between JENDL-3 and JEF-1 is 0.5 % as seen from comparing between the CASMO and WIMS-D results. Because, in the CASMO, neutronic calculation method is the same as the WIMS-D method.

4.3 TCA Critical Cores

The water-moderated critical lattice of MOX-fuel (3.0 wt.% Pu) rods at TCA were calculated with the codes CASMO, SRAC, TGBLA, VMONT, MGCL-KENO-IV and VIM, and the calculated results were compared. The Monte Carlo codes VIM and MGCL KENO-IV calculated k_{eff} with full geometrical model as seen in Fig. 9.

4.3.1 Effective Multiplication Factor

The k_∞ and k_{eff} calculated are compared in Table 10, Figs. 10 and 11. As for k_∞, the results calculated with CASMO and TGBLA are about 1 % lower than those with SRAC and VMONT. On the other hand, the VIM results show intermediate values. A good agreement between k_∞ for the TRX uranium cores is not seen for this TCA plutonium cores.

Figure 11 shows the k_{eff} as a function of cell pitch, including the results calculated with MGCL-KENO-IV. The KENO-IV results show the values calculated for three cell pattern with the same cell pitch. However, the k_{eff} for three pattern are not same. It may be large variance of about 0.4 %. The results calculated with VIM and KENO-IV underestimate k_{eff} slightly. However, the results for SRAC, CASMO and TGBLA depended considerably on the volume ratios of moderator to fuel, and underestimate the experimental value more than 1 % for the cell pitch of 1.82 cm.

The k_∞-values calculated with CASMO were smaller than ones of SRAC and similar to TGBLA results. However, the k_{eff} values of CASMO are larger than those for SRAC and TGBLA. This cause is due to different resonance calculation methods among the three codes as described in Section 5.

4.3.2 Neutron Spectrum

Figure 12 shows, as a typical example, the comparison of neutron spectra calculated with VIM and VMONT. The spectra obtained by the other codes were in a very good agreement with the VIM result.

4.3.3 Averaged Cross Section

The cross sections averaged over fast, resonance, thermal and whole energy range are

compared in Table 11 − 13. The fission and capture resonance cross sections of Pu−239 calculated by TGBLA are smaller than those of other codes. Furthermore, the thermal capture cross sections of Pu−240 for CASMO and TGBLA are larger than the VIM and SRAC results. As for CASMO, there is the same difference of U−238 resonance scattering cross sections as described in Section 4.1.4.

5. The Effect of Resonance Calculation Method on k_{eff}

In the CASMO and WIMS−E codes, the self−shielding effect for resonance scattering cross section is not considered. Though TGBLA uses the same group cross section library as SRAC, the table−lookup−method is used in resonance absorption calculation. On the other hand, SRAC uses the ultra−fine group method. Here, the effect of these different resonance calculation methods on effective multiplication factor is studied to make clear the discrepancies between k_{eff}−values obtained with the present used codes.

The SRAC code can calculate the resonance absorption rate by employing several different methods which are the table−lookup , IR−treatment and ultra−fine group methods. Furthermore, the option which does not consider only the self−shielding effect for resonance scattering cross section was added. The calculations were performed for the TCA cores. The results are shown in Figs. 13 and 14. In these figures, PEACO shows the ultra−fine group method. The k_{eff} value calculated without self−shielding effect of resonance scattering cross section becomes larger by 0.4 − 0.8 %, as seen by comparing the results for F−table and F−table (fe=1.0). The table−lookup method produces smaller k_{eff} of 0.2 − 0.4 % than the ultra−fine group method.

6. Conclusion and Discussions

Using the JENDL−3 nuclear data, the results calculated with the most accurate neutronic calculation method of continuous energy Monte Carlo code VIM underpredicted k_{eff} by 0.8% for the uranium fuel TRX cores and 0.2 − 0.5% for the MOX fuel TCA cores. The underprediction for uranium cores had been presented in fast reactor benchmark calculations[15] such as the FCA−IX assemblies with very soft neutron spectrum. Furthermore, in the TRX core calculations, lattice parameter δ−25(the ratio of epithermal to thermal U−235 fission rate) was underestimated. We propose from these facts the reevaluation of U−235 fission cross sections in resonance energy region. Figure 15 shows the comparison of U−235 fission cross sections between the JENDL−3 and ENDF/B−VI data. It is observed that the JENDL−3 data are smaller than the ENDF/B−VI data in the unresolved resonance region.

In the present code comparison, it was found that the most large discrepancy between the calculated k_{eff} was caused by different resonance calculation methods. The calculation without self−shielding effect of resonance elastic scattering cross section of U−238 employed in the WIMS code gave larger k_{eff} of 0.8% for the plutonium fuel TCA cores.

References

1) "Benchmark Specification", ENDF-202, BNL-10302, 1974.
2) K. Tuchihashi et al.: JAERI-1285 (1983) and -1302 (1986).
3) A. Ahlin and M. Edenius:"CASMO-A Fast Transport Theory Assembly Depletion Code for LWR Analysis", Trams. Am. Nucl. Soc., 26, 604(1977).
4) M. Yamamoto et al.:"Development and Validation of TGBLA BWR Lattice Physics Methods", Proc. ANS Topical Meeting on Reactor Physics and Shielding, Chicago, Sept. 17-19 (1984),
5) J. R. Askew et al.: "A General Description of the Lattice Code WIMS", J. Br. Nucl. Energy Soc.,5.564(1966).
6) J. Katakura et al.: Trams. Am. Nucl. Soc., 41, 329 (1982).
7) Y. Morimoto et al.: Nucl. Sci. Eng.,103, 351 (1989).
8) R.E. Prael and L. J. Milton:"A User's Mannual for the Monte Carlo Code VIM", FRA-TM-84, Angonne National Laboratory (1976).
9) R. E. MacFarlane et al.: LA-9303-M(ENDF-324), 1982.
10) H. Takano et al.: JAERI-M 82-072 (1982).
11) T. Nakagawa.: JAERI-M 84-192 (1984).
12) T. Mori.: private communication
13) H. Turuta et al.: JAERI 1254, 1978.
14) S. Pelloni et al.: Nuclear Technol. Vol. 94, p15, 1991.
15) H. Takano et al.:"Benchmark Test of JENDL-3 for Thermal and Fast Reactors", Proc. Int. Conf. Physics of Reactors, Marseilles, France, April 23-27, 1990, Vol. 3, p.I-21.

Table 1 Codes and their characteristics

	Cross Section		Spectrum Calc.
WIMS-E	69Groups	NJOY87	Collision Probability
CASMO	70		
PHOENIX-P	42		
TGBLA	107Groups, TIMS-PGG		Collision Probability
SRAC			
MGCL-ANISN	137Groups		Sn
VMONT	190Groups, NJOY87+RESENDD		Monte Carlo
VIM	Point		Continuous Energy Monte Carlo

Table 2 Benchmark testing cores

・U Cores : TRX-1, -2, Hexagonal Cell
Fuel Metal U, 1.3wt.% U-235
Cladding Al, Diameter 1.082cm

	TRX-1	TRX-2
Cell Pitch(cm)	1.806	2.174
Water/Fuel Volume Ratio	2.35	4.02
$B^2(10^{-3}/cm^2)$	5.7	5.469

・Pu Cores : TCA 2.42PU～5.55PU, Square Cell
Fuel MOX, 3.0wt.% Pu
Cladding Zry-2, Diameter 1.223cm

	2.42PU	2.98PU	4.24PU	5.55PU
Cell Pitch(cm)	1.825	1.956	2.225	2.474
Water/Fuel Volume Ratio	2.42	2.98	4.24	5.55
$B^2(10^{-3}/cm^2)$	8.08	8.28	7.79	6.51

Table 3 Integral data for inter-comparison and three group boundary

- k_{eff}(Experimental)
- k_∞(for Infinite Lattice)
- Reaction Rate Ratios(for TRX, Exp.)
- Neutron Spectrum (with the Energy Structure of the Code)
- Effective Cross Sections(1, 3 Groups)
  Capture, Fission, Total, Transport

3 Group Structure			
Fast	10 MeV	～	9.118 keV
Resonance	9.118 keV	～	4 eV
Thermal	4 eV	～	0 eV

Table 4 Multiplication factors calculated for TRX cores

	TRX-1		TRX-2	
	k_∞	k_{eff}	k_∞	k_{eff}
WIMS-E	1.1817	1.0019	1.1669	1.0021
CASMO	1.1783	0.9994	1.1646	0.9988
SRAC	1.1828	0.9956	1.1699	0.9979
TGBLA	1.1782	0.9936	1.1662	0.9965
MGCL-KENO	1.183	0.9993		
VMONT	1.1799		1.1675	
VIM	1.1826 (0.19%)	0.9924 (0.16%)	1.1679 (0.13%)	0.9917 (0.07%)

Table 5 Comparison of k_∞, k_{eff} and k_∞/k_{eff} for TRX cores

	$\overline{k_\infty}$	S.D. (%)	$\overline{k_{eff}}$	S.D. (%)
TRX-1	1.181	± 0.19	0.9973	± 0.32
	(1.181)	(0.19)	(0.9982)	(0.26)
TRX-2	1.167	± 0.17	0.9979	± 0.34
	(1.167)	(0.17)	(0.9994)	(0.16)

( ):without VIM Code

	k_∞/k_{eff}			
	TRX-1		TRX-2	
CASMO	1.179	0.8%	1.166	0.5%
SRAC	1.188		1.172	
VIM	1.192		1.178	

Table 6 Cross sections in the fuel region of TRX-1 infinite lattice (barns)

<< U-235 Fission >>

Energy Group	Fast	Resonance	Thermal	One Group
CASMO	1.379	20.02	303.7	78.15
MGCL-ANISN	1.381	20.26	310.9	78.12
SRAC	1.379	20.36	303.7	78.09
TGBLA	1.379	20.10	300.9	78.80
VMONT	1.380	20.43	306.8	78.40
VIM	1.379	20.52	302.4	78.45
	(0.0375 %)	(0.318 %)	(0.148 %)	(0.329 %)

<< U-235 Capture >>

Energy Group	Fast	Resonance	Thermal	One Group
CASMO	0.2301	13.76	53.46	15.89
MGCL-ANISN	0.2328	13.87	54.58	15.89
SRAC	0.2355	13.42	53.46	15.79
TGBLA	0.2359	13.59	53.01	15.99
VMONT	0.2364	13.68	53.95	15.92
VIM	0.2359	13.53	53.25	15.88
	(0.188 %)	(0.399 %)	(0.135 %)	(0.297 %)

<< U-235 Total >>

Energy Group	Fast	Resonance	Thermal	One Group
CASMO	9.151	46.26	370.9	104.1
MGCL-ANISN	9.121	46.60	379.4	104.1
SRAC	9.141	46.23	371.8	104.1
TGBLA	9.144	46.12	368.6	105.1
VMONT	9.148	46.54	374.6	104.4
VIM	9.145	46.48	369.4	104.4
	(0.0471 %)	(0.235 %)	(0.141 %)	(0.295 %)

Table 7 Cross sections in the fuel region of TRX-1 infinite lattice (barns)

<< U-238 Fission >>

Energy Group	Fast	Resonance	Thermal	One Group
CASMO	0.1746	1.566E-04	6.268E-06	0.09605
MGCL-ANISN	0.1875	1.465E-04	6.412E-06	0.1038
SRAC	0.1760	1.522E-04	6.275E-06	0.09701
TGBLA	0.1758	1.444E-04	6.227E-06	0.09587
VMONT	0.1747	1.417E-04	6.347E-06	0.09595
VIM	0.1751	1.567E-04	6.263E-06	0.09614
	(0.326 %)	(6.61 %)	(0.124 %)	(0.364 %)

<< U-238 Capture >>

Energy Group	Fast	Resonance	Thermal	One Group
CASMO	0.1337	1.723	1.559	0.8093
MGCL-ANISN	0.1375	1.724	1.593	0.8155
SRAC	0.1360	1.717	1.560	0.8080
TGBLA	0.1358	1.733	1.548	0.8172
VMONT	0.1363	1.722	1.576	0.8164
VIM	0.1370	1.724	1.555	0.8123
	(0.169 %)	(0.401 %)	(0.117 %)	(0.257 %)

<< U-238 Total >>

Energy Group	Fast	Resonance	Thermal	One Group
CASMO	9.163	34.56	10.64	14.83
MGCL-ANISN	9.124	13.92	10.69	10.51
SRAC	9.059	14.07	10.94	10.56
TGBLA	9.052	14.00	10.45	10.43
VMONT	9.077	13.80	10.66	10.46
VIM	9.082	14.12	10.64	10.51
	(0.0483 %)	(0.135 %)	(0.0188 %)	(0.0506 %)

Table 8 Cross sections in the moderator region of TRX-1 infinite lattice (barns)

<< H Total >>

Energy Group	Fast	Resonance	Thermal	One Group
CASMO	7.234	20.31	38.15	18.82
MGCL-ANISN	7.129	20.31	37.24	18.28
SRAC	7.251	20.33	38.03	18.83
TGBLA	7.241	20.33	37.92	18.88
VMONT	7.265	20.31	38.08	18.75
VIM	7.261	20.33	38.09	18.90
	(0.117 %)	(1.48E-3%)	(0.0542 %)	(0.102 %)

<< H Transport >>

Energy Group	Fast	Resonance	Thermal	One Group
CASMO	2.915	6.833	27.61	10.73
SRAC	2.417	6.781	27.71	10.49
TGBLA	2.413	6.780	27.50	10.54

<< H Capture >>

Energy Group	Fast	Resonance	Thermal	One Group
CASMO	8.295E-05	6.121E-03	0.2054	0.05919
MGCL-ANISN	8.216E-05	6.127E-03	0.2093	0.05866
SRAC	8.309E-05	6.143E-03	0.2046	0.05912
TGBLA	8.305E-05	6.127E-03	0.2036	0.05952
VMONT	8.330E-05	6.132E-03	0.2061	0.05878
VIM	8.195E-05	6.137E-03	0.2046	0.05941
	(0.130 %)	(0.134 %)	(0.0976 %)	(0.213 %)

Table 9 Inter-comparison between evaluated data files

		k_{eff}	
		TRX-1	TRX-2
JENDL-2	SRAC	0.9939	0.9963
JENDL-3	SRAC	0.9956	0.9979
	CASMO	0.9994	0.9988
	WIMS-E	1.0019	1.0021
JEF-1*	WIMS-D	0.995	0.995
	MICROX-2	0.992	0.995

*S. Pelloni, et al.: Nucl. Technol., 94, 15(1991).

Table 10 Multiplication factors calculated for TCA cores

	k_∞			
	2.42PU	2.98PU	4.24PU	5.55PU
CASMO	1.3406	1.3373	1.2997	1.2426
SRAC	1.3522	1.3468	1.3067	1.2480
TGBLA	1.3395	1.3360	1.2982	1.2422
VMONT	1.3520	1.3474	1.3074	1.2495
VIM	1.3471 (0.10%)	1.3433 (0.10%)	1.3037 (0.10%)	1.2431 (0.10%)
	k_{eff}			
	2.42PU	2.98PU	4.24PU	5.55PU
CASMO	0.9891	0.9937	0.9974	0.9997
SRAC	0.9887	0.9926	0.9965	0.9993
TGBLA	0.9853	0.9902	0.9948	0.9984
VIM	0.9946 (0.10%)	0.9954 (0.10%)	0.9964 (0.10%)	0.9977 (0.10%)

Table 11 Cross sections in the fuel region of TCA2.42PU infinite lattice (barns)

<< Pu-239 Fission >>

Energy Group	Fast	Resonance	Thermal	One Group
CASMO	1.730	22.93	555.0	129.3
SRAC	1.732	23.11	553.9	129.2
TGBLA	1.732	21.65	550.4	125.5
VIM	1.731	23.39	551.0	129.8
	(0.0141 %)	(0.360 %)	(0.0821 %)	(0.143 %)

<< Pu-239 Capture >>

Energy Group	Fast	Resonance	Thermal	One Group
CASMO	0.1480	17.24	255.4	60.56
SRAC	0.1500	17.51	254.1	60.36
TGBLA	0.1503	15.97	253.8	58.81
VIM	0.1504	17.59	254.0	60.90
	(0.134 %)	(0.451 %)	(0.104 %)	(0.143 %)

<< Pu-239 Total >>

Energy Group	Fast	Resonance	Thermal	One Group
CASMO	8.942	53.92	819.9	198.9
SRAC	8.930	54.19	817.4	198.5
TGBLA	8.932	51.01	813.6	193.3
VIM	8.933	54.54	814.4	199.6
	(0.0246 %)	(0.287 %)	(0.0862 %)	(0.136 %)

Table 12 Cross sections in the fuel region of TCA2.42PU infinite lattice (barns)

<< Pu-240 Fission >>

Energy Group	Fast	Resonance	Thermal	One Group
CASMO	0.9784	0.1079	0.08537	0.5966
SRAC	0.9856	0.1041	0.08424	0.6007
TGBLA	0.9849	0.1043	0.08695	0.6023
VIM	0.9824	0.1029	0.08334	0.5970
	(0.0827 %)	(1.20 %)	(0.373 %)	(0.119 %)

<< Pu-240 Capture >>

Energy Group	Fast	Resonance	Thermal	One Group
CASMO	0.2157	16.65	444.3	102.5
SRAC	0.2169	15.78	438.1	101.0
TGBLA	0.2172	15.85	453.0	102.2
VIM	0.2174	15.75	433.5	100.9
	(0.123 %)	(0.942 %)	(0.387 %)	(0.369 %)

<< Pu-240 Total >>

Energy Group	Fast	Resonance	Thermal	One Group
CASMO	9.136	41.10	466.2	117.6
SRAC	9.123	38.07	463.8	116.5
TGBLA	9.126	38.13	480.9	118.1
VIM	9.128	38.06	454.6	115.4
	(0.0314 %)	(0.666 %)	(0.396 %)	(0.347 %)

Table 13 Cross sections in the fuel region of TCA2.42PU infinite lattice (barns)

<< U-238 Capture >>

Energy Group	Fast	Resonance	Thermal	One Group
CASMO	0.1212	3.099	1.630	1.083
SRAC	0.1281	3.002	1.641	1.065
TGBLA	0.1278	2.992	1.619	1.061
VIM	0.1285	3.000	1.624	1.063
	(0.115 %)	(0.452 %)	(0.0756 %)	(0.267 %)

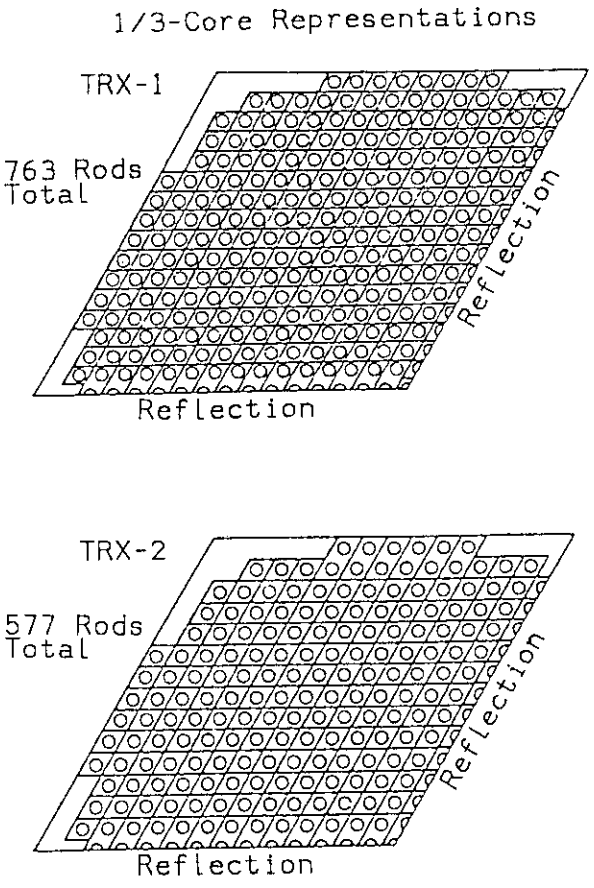

Fig. 1 Configuration model for TRX lattice cores.

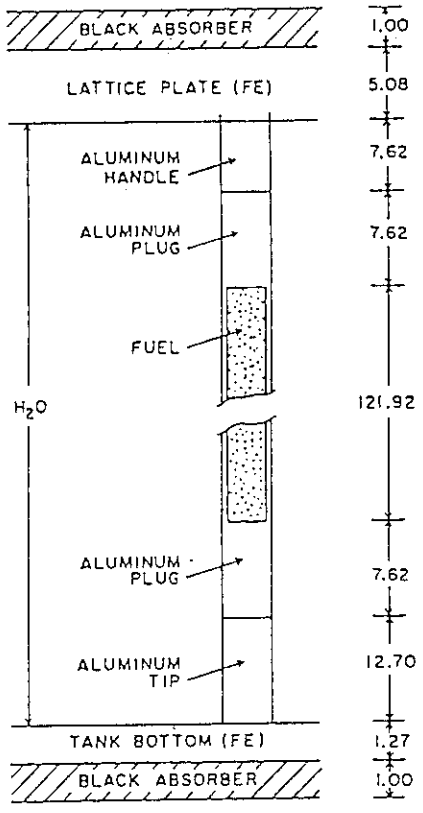

Fig. 2 Axial model of TRX lattice (cm).

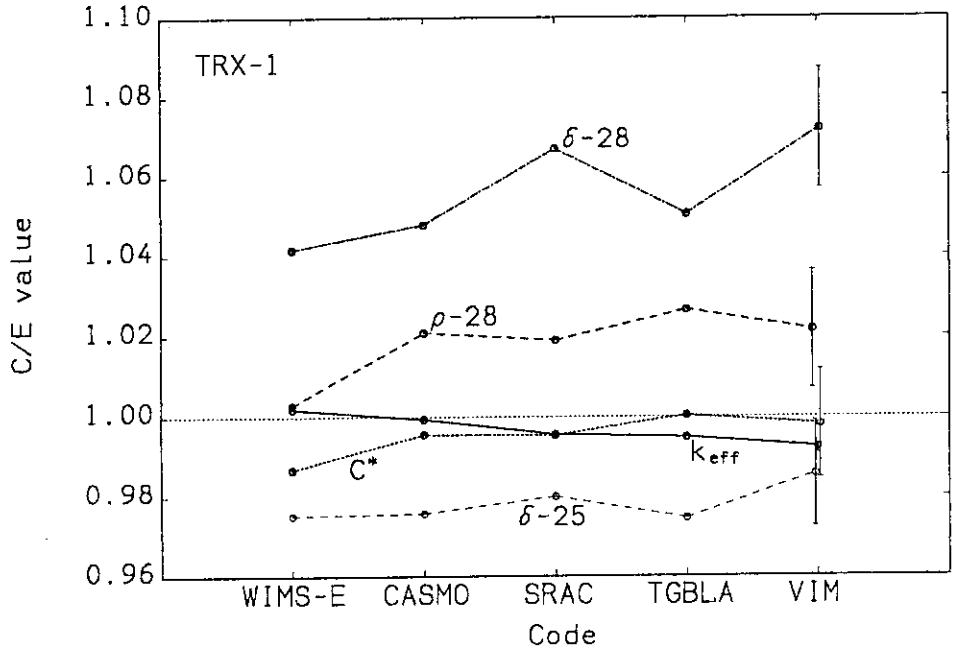

Fig. 3 Lattice parameters in TRX-1. (Calculation/experiment value)

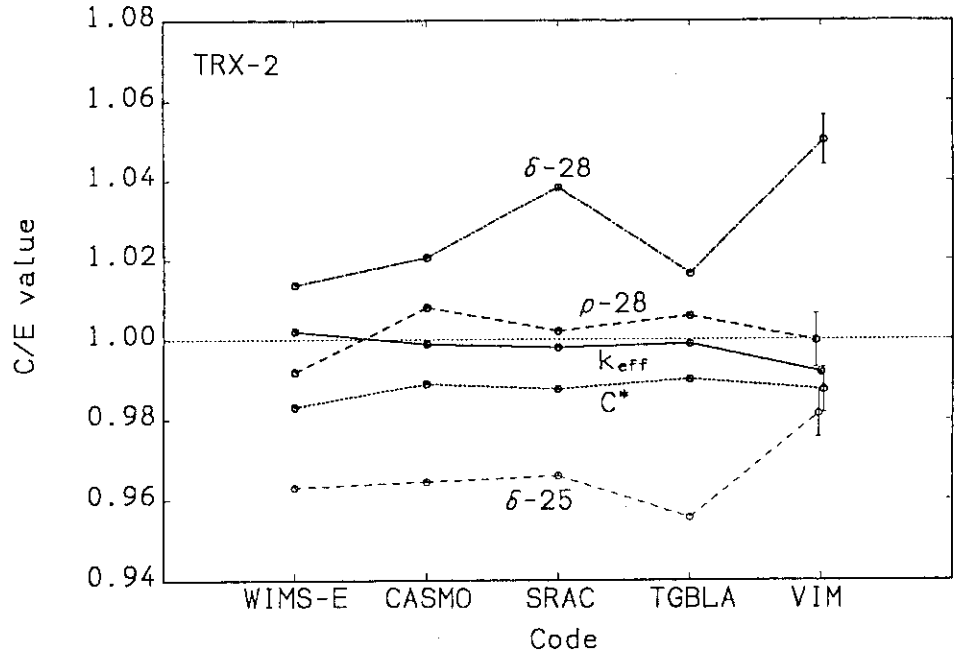

Fig. 4 Lattice parameters in TRX-2 (Calculation/experiment value).

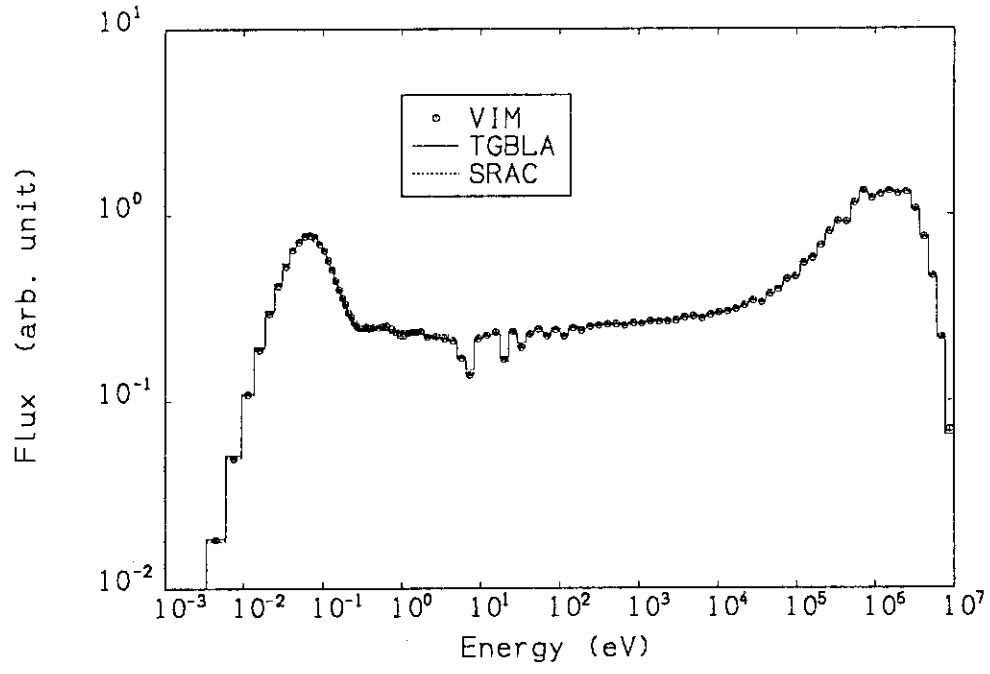

Fig. 5 Neutron spectra in the fuel region of TRX-1 cell (GAM structure).

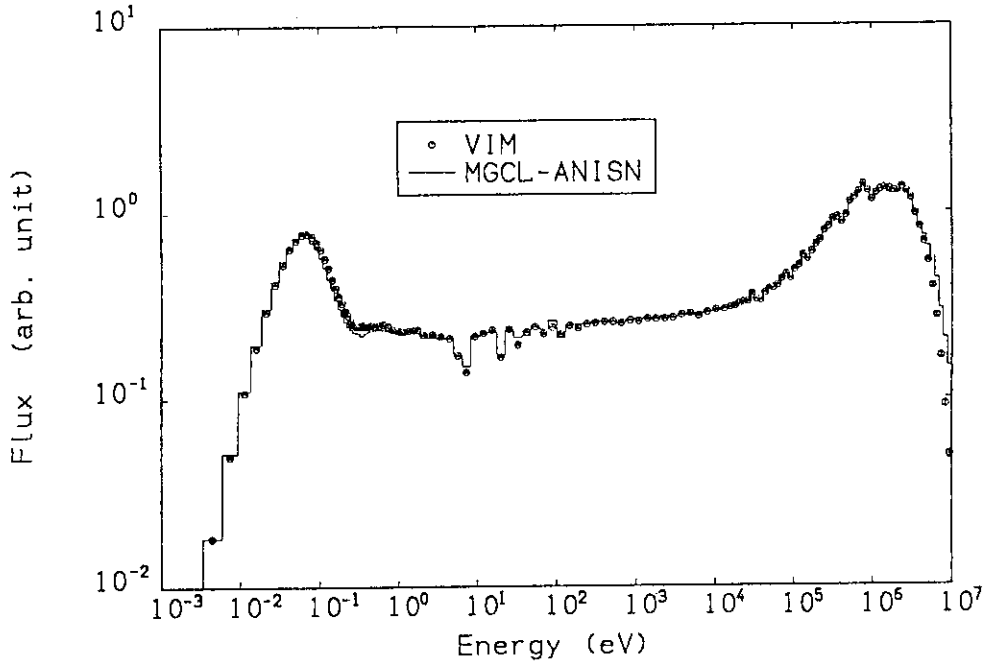

Fig. 6 Neutron spectra in the fuel region of TRX-1 cell (MGCL structure).

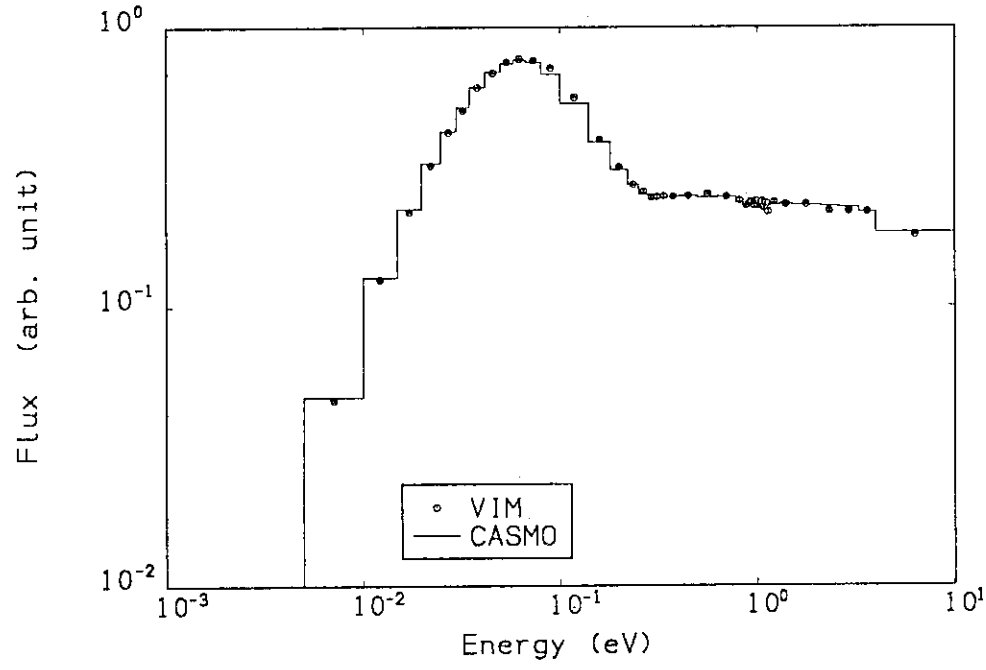

Fig. 7 Neutron spectra in the fuel region of TRX-1 cell (WIMS structure).

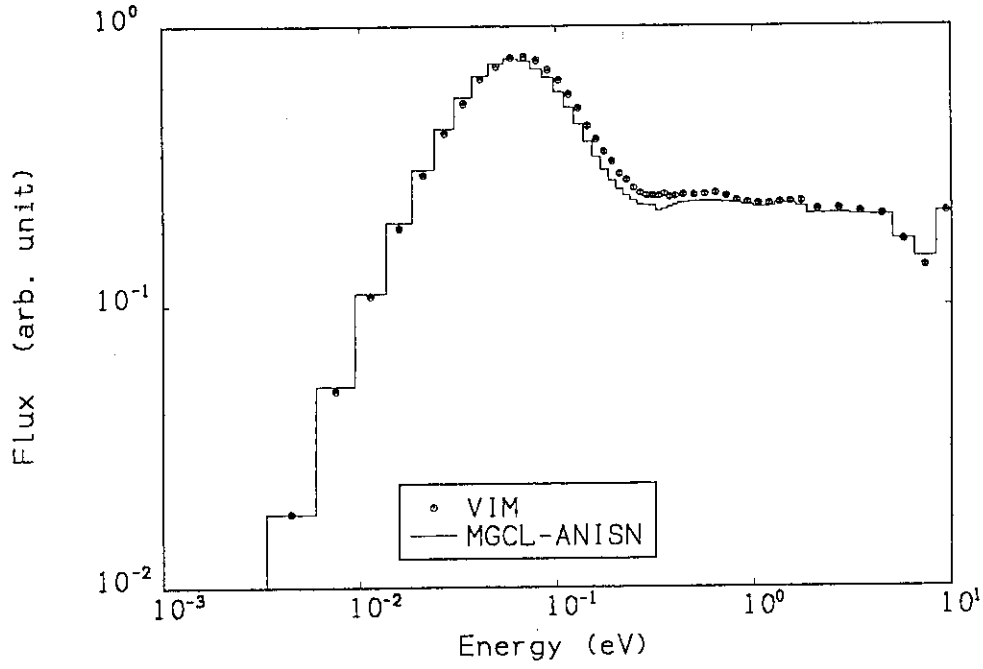

Fig. 8 Neutron spectra in the fuel region of TRX-1 cell (MGCL structure).

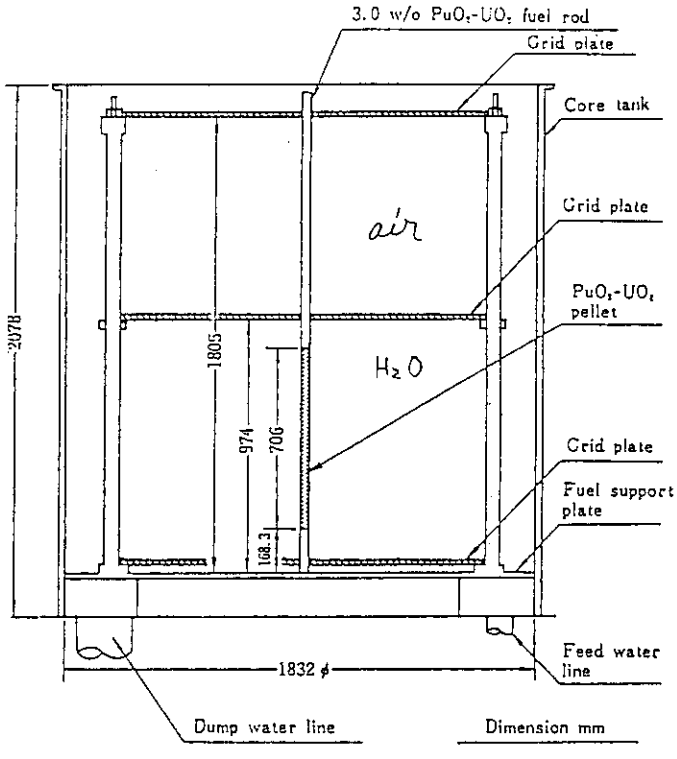

Fig. 9 Vertical cross-sectional view of TCA core tank.

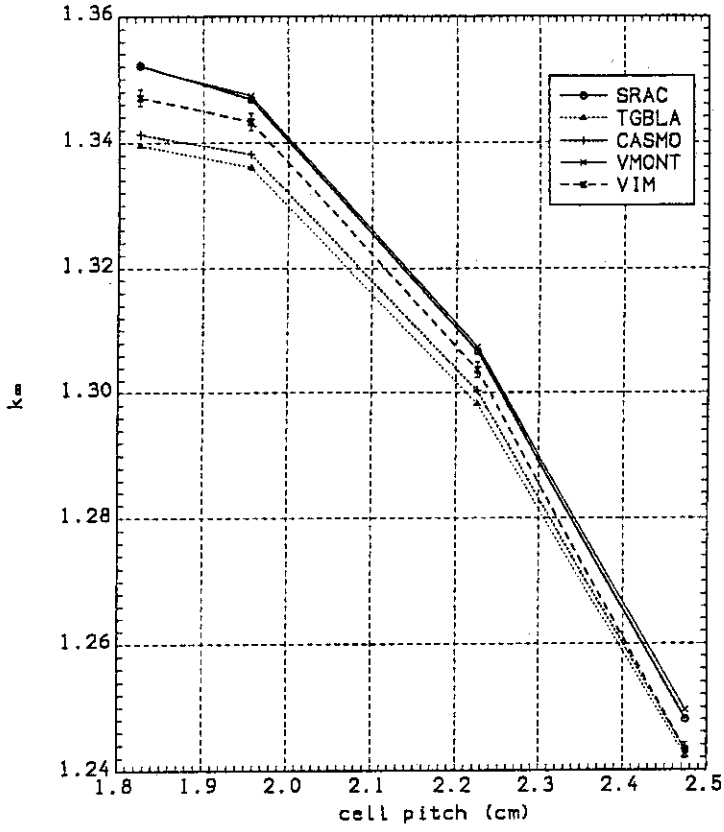

Fig. 10 Comparison of k_∞ for TCA MOX critical experiments.

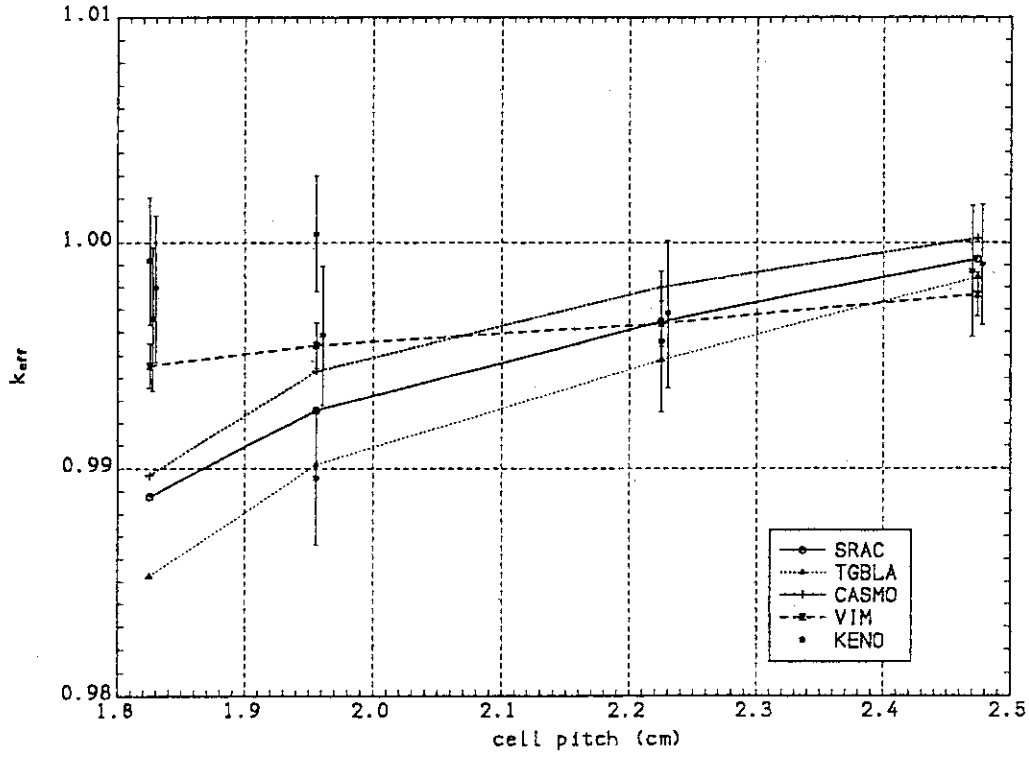

Fig. 11 Comparison of k_{eff} for TCA MOX critical experiments.

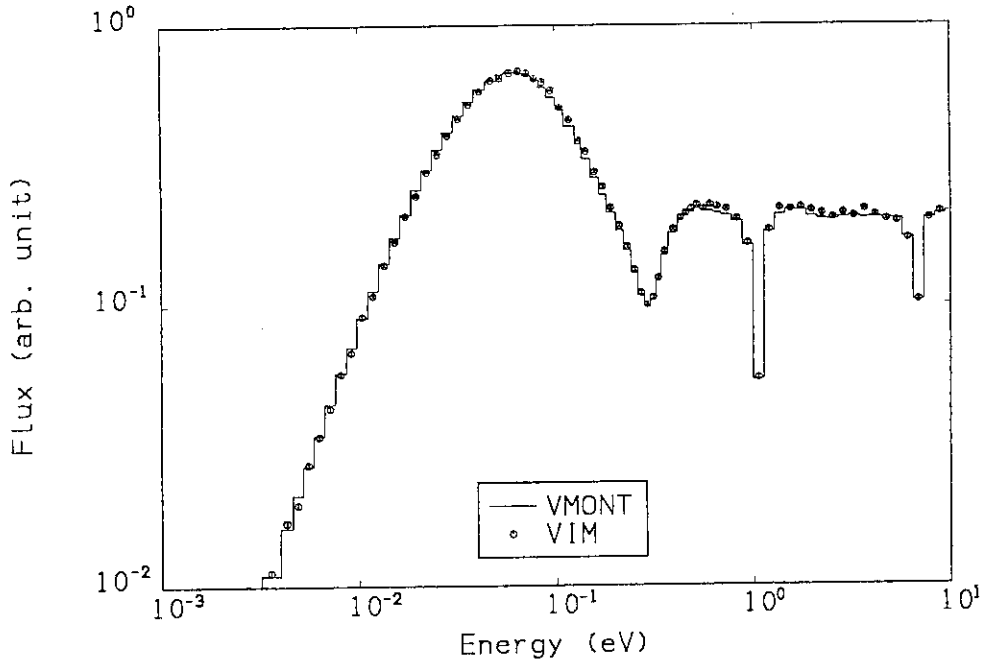

Fig. 12 Neutron spectra in the fuel region of TCA 2.42PU.

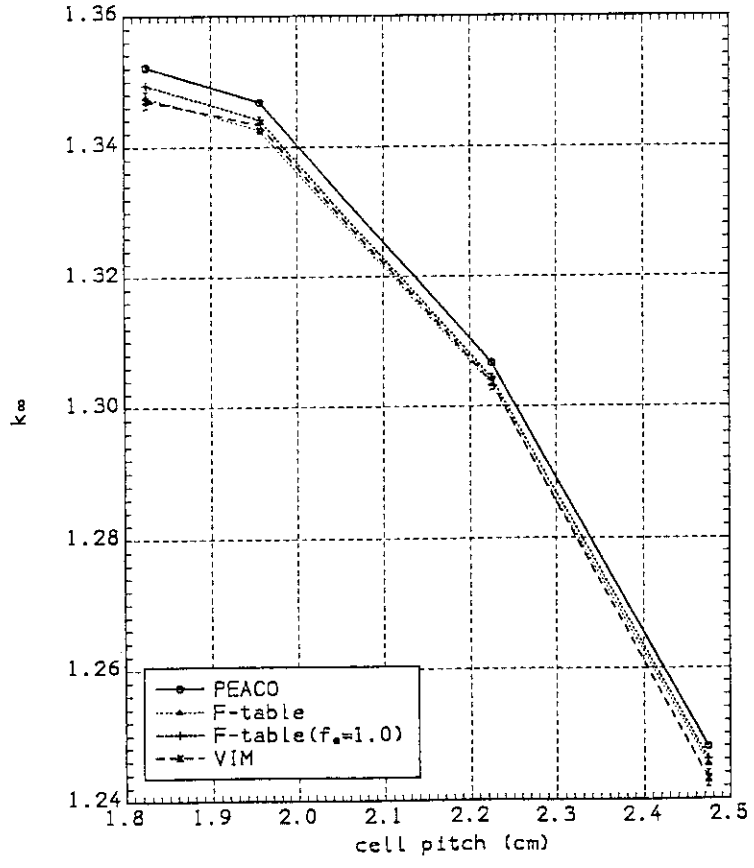

Fig. 13 Comparison of k_∞ obtained with different resonance calculation methods.

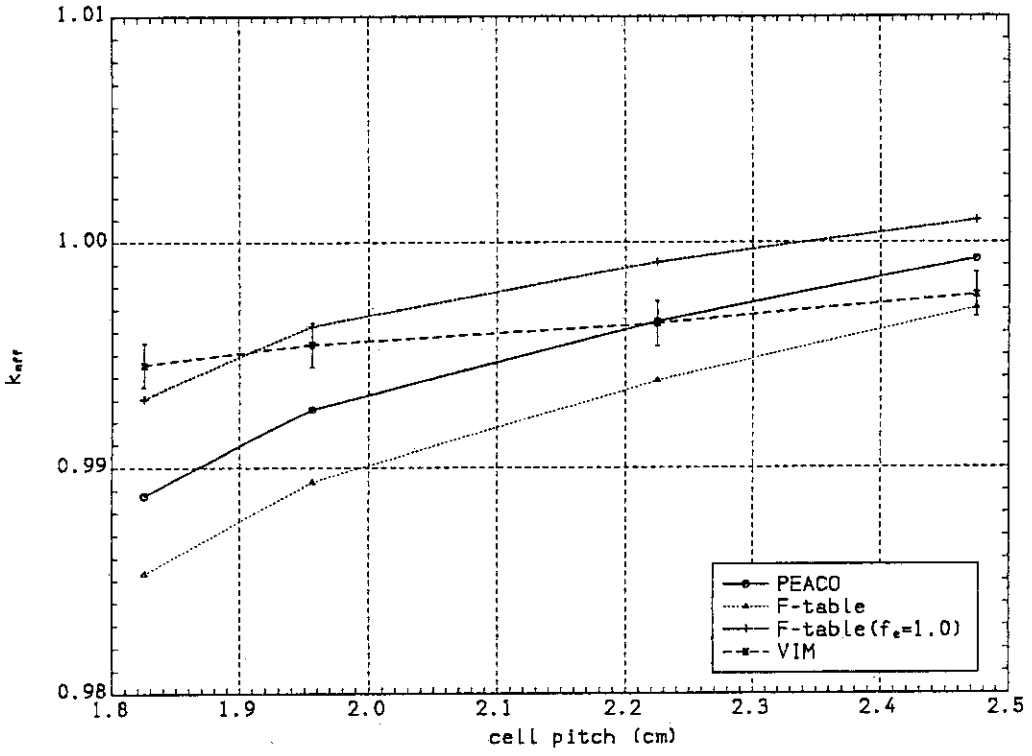

Fig. 14 Comparison of k_{eff} obtained with different resonance calculation methods.

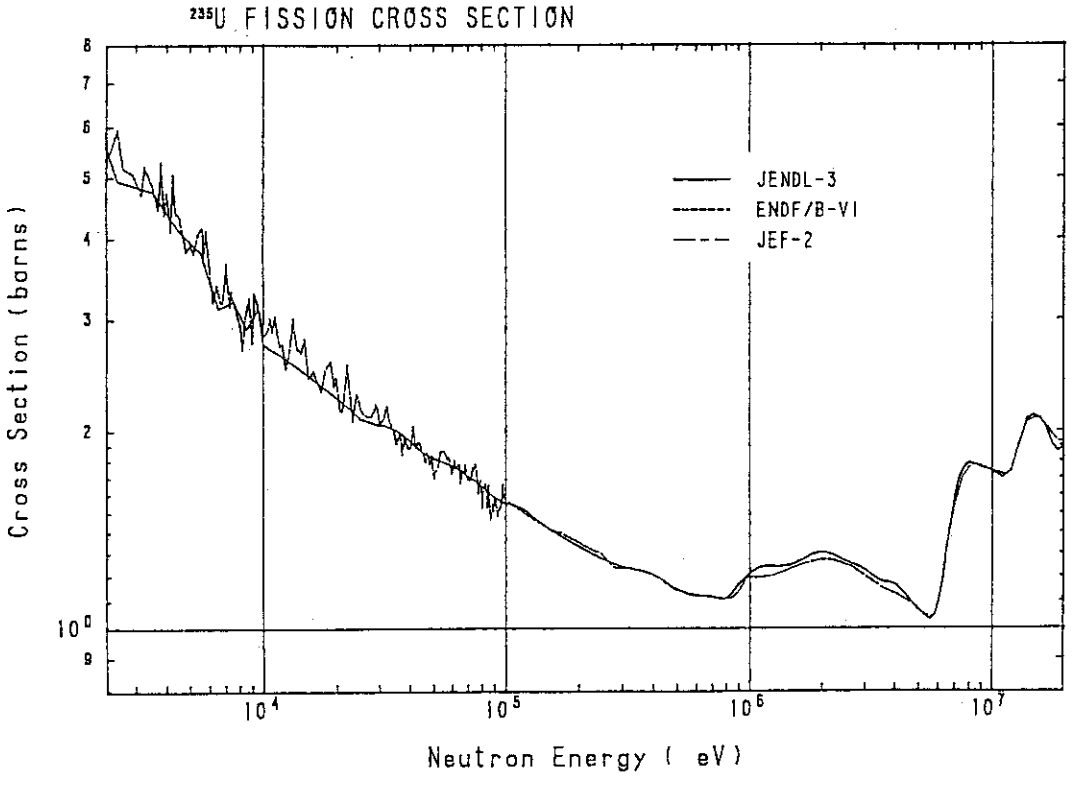

Fig. 15 Comparison of U-235 fission cross sections in the JENDL-3 and ENDF/B-VI data.

2.8.2 REACTIVITY SCALE FOR REACTOR PHYSICS ANALYSIS

— Present Status —

Masafumi NAKANO

Japan Atomic Energy Research Institute
Tokai-mura, Naka-gun, Ibaraki-ken 319-11, JAPAN

The effective delayed neutron fraction, βeff, which allows the comparison between the calculated and measured reactivity values, plays an important role in the theoretical interpretation of reactivity measurement.

Uncertainties of the calculated reactivity scale are discussed through the analysis of a βeff experiment recently made at the fast critical facility FCA. The outline is also presented of the proposed NEACRP βeff benchmark experiment which is planned to be carried out at the MASURCA facility in 1992 to 1993.

1. Introduction

Reactivity parameters such as Doppler reactivity coefficient, void reactivity worth and control rod worth are important in the core characteristics study of fast reactors. Measured reactivity worths are usually obtained in dollor unit, while calculated values are given in Δk/k unit. Therefore, the delayed neutron fraction βeff playes an

important role in the theoretical interpletation of reactivity measurement.

The reactivity scale βeff is generally calculated from the delayed neutron data (absolute delayed neutron yield νd and delayed neutron spectrum χd). A recent study(1) shows the current delayed neutron data contribute significantly to the large uncertainties in reactivity scale for fast reactors. Precise measurement of βeff in zero power critical assemblies would allow appreciable refinement of the absolute scale of reactivity. In this context, a delayed neutron data benchmark test including eff benchmark experiments was proposed as one of the task forces on the international evaluation cooperation of nuclear data by OECD/NEACRP/NEANDC.

In the present paper, uncertainties of the reactivity scale in the reactivity worth experiment are discussed through the analysis of a eff experiment recently made at the FCA XVI-1 core(2). The outline is also presented of the NEACRP βeff benchmark experiment(3) which is planned to be carried out at the MASURCA facility in 1992 to 1993.

2. Calibration of Reactivity Scale

In the critical experiment, the reactivity worths are usually measured relative to movement of the control rods, which have been calibrated by kinetic methods: The positive period techniqe is often used for the calibration of reactivity scale.

The reactivity corresponding to an observed asymptotic period T is given by

$$\rho = \frac{\Lambda_{eff}}{T} + \sum_{m,i} \frac{\beta^{m}_{effi}}{1+\lambda^{m}_{i} T} \qquad (1)$$

where,

m : fissioning isotope, i : delayed neutron group

Λ_{eff} : effective neutron generation time

λ^{m}_{i} : dacay constant of group i for isotope m

β^{m}_{effi} : effective delayed neutron fraction of group i for isotope m

For most periods, the term Λeff/T makes a neglisible contribution to the reactivity in fast and water-moderated thermal reactors.

It is usual in reactor physics calculations to represent delayed

neutron emission by six groups, each having an associated time constant λ_i. Table 1 shows Keepin's evaluation of the temporal group parameters[4] and the relative contribution of each group to the reactivity for a typical period of T=100sec. It is clear that Group 2 (half-life ~20 seconds) is the most significant in calculating the reactivity for both Pu-239 and U-238. The sum of the six group contributions is nearly twice as high for Pu-239 as for U-238.

3. Calculation of Delayed Neutron Parameters

The contribution of the delayed neutron fraction from group i of the delayed neutrons from isotope m are calculated by

$$\beta_{eff} = \sum_{m,i} \beta^{m}_{effi} \tag{2}$$

$$\beta^{m}_{effi} = \frac{\int < \chi^{m}_{di} \phi^{*} > < \nu^{m}_{d} \alpha^{m}_{i} \Sigma^{m}_{f} \phi > dv}{\Sigma_{m} \int [< \chi^{m}_{p} \phi^{*} > < \nu^{m}_{p} \Sigma^{m}_{f} \phi > + \Sigma_{i} < \chi^{m}_{di} \phi^{*} > < \nu^{m}_{d} \alpha^{m}_{i} \Sigma^{m}_{f} \phi >] dv} \tag{3}$$

where, m : isotope, i : delayed neutron group

χ^{m}_{di} : delayed neutron spectrum
ν^{m}_{d} : number of delayed neutrons per fission
α^{m}_{i} : relative abundance
χ^{m}_{p} : prompt fission neutron spectrum
ν^{m}_{p} : number of prompt neutrons per fission,

and the blackets < > indicate energy integral. It should be noted from the above equation that errors associated with real flux ϕ, adjoint flux ϕ^{*} and fission rate ratios contribute to the uncertainties in the calculated values for eff.

Table 2 compares various evaluatins of total delayed neutron yields from fast fissions. The Brady's evaluation[8] are based on the summation results from individual precursor data. The Keepin's data are generally low. A low yield for U-235 and a high yield for U-238 are adopted in the JENDL-3[9]. The most significant variation is seen for U-238 which is one of the main isotopes in the calculation of βeff for fast reactors.

The isotopic contribution for typical LMFBR mockup cores are given

in Table 3. Similar contribution would be found in fresh fuel power reactors. It can be seen that the contribuion from U-238 is very large for fast reactors although the fission rate ratio of U-238 to Pu-239 in the core is in the range of 0.03 to 0.04.

Figure 1 shows the spectra of delayed neutrons and of prompt neutrons from fission together with the adjoint flux spectrum at the center of FCA XVI-1 core[2]. The mean energy is several hundred KeV for delayed neutrons and about 2 MeV for prompt fission neutrons. The adjoint flux spectrum is fairly flat in the energy range of 100 KeV ∼ 1 MeV, while it increases sharply above 1 MeV. Then, the average delayed neutron importance relative to the average prompt neutrons is, in general, less than 0.9. As shown in Table 4, there are little differences in the delayed neutron importances between temporal groups.

Delayed neutron spectra evaluated by Fieg [10] and by Sapphier et al.[11] are widely used in βeff calculations. The uncertainties of calculated βeff due to the delayed neutron spectra were estimated to be about 3∼4% for LMFBR core.[12],[13]

4. Comparison between Measured and Calculated βeff

Integral measurements of βeff were extensively carried out on ZPR[14] and SNEAK[15] fast critical facilities in 1970s to interpret the discrepancies of central reactivity worth observed in fast critical assemblies. A recent re-analysis of these measurements[1] showed a spread of C/E values between 0.93 and 1.05 without observing specific trend on fuel type and composition or U-238 content. Therefore, it would be not possible to perform the βeff calculation within an uncertainty of 5%(1σ).

A βeff measurement was recently made on the FCA XVI-1 core which was a physics benchmark core simulating metallic fuel fast reactor. Table 5 shows the comparison between the measured and calculated βeff of FCA XVI-1. Since mixed fuel of Pu and enriched uranium is used in the core, large contribution from U-235 to the total βeff is seen compared with that of Pu fuel fast reactors(see Table 3).

The calculation was made using the 70 energy group constants JFS-3/J2 based on the JENDL-2. The real and adjoint fluxes were obtained in two-dimentional R-Z geometry and diffusion approximation. The Saphier's delayed neutron spectra and the Keepin's group parameters

(λi, αi) were used for the βeff calculation.

The calculations with the Keepin's, Tomlinson's and Tuttle's evaluations for delayed neutron yield agree fairly well with the experiment, although a trend of slight overestimation is seen for the latter two. The results with the JENDL-3 and the Brady's yield data overpredict the βeff value, the contribution from U-235 and U-238 being completely different between the two.

5. Experimental Program of the NEACRP eff Benchmarks

In order to improve the prediction accuracy of the reactivity scale, an international(OECD/NEANDC/NEACRP) cooperation is now in progress in two domains: Evaluation of delayed neutron data[16] and βeff experimental benchmarking.

In the framework of the NEACRP activities, an international βeff benchmark experiment was proposed to be performed in the MASURCA facility at Cadarache. The first preparatory meeting was held at Cadarache in December 1990 with the perticipation of experts from France, Germany, Great Britain, Italy, Japan and Soviet Union. The main conclusions of the meeting are:

- βeff measurements will be performed in the MASURCA facility on 3 configurations; an uranium core and 2 plutonium cores.
- 2 different methods will be applied to the βeff measurements; Cf-neutron source and reactor noise methods.
- The effort must be forcussed towards reducing the uncertainties of the delayed neutron yield for U-235, U-238 and Pu-239 and towards extracting information about the delayed neutron spectra.

The main parameters of the proposed cores are given in Table 6. The proposed Pu configurations(Zona 2 and Compact cells) were chosen in such a way that the differences in the ratio between U-238 and Pu-239 contributions to β eff were as large as possible. A further U-235 configuration(R2 cell) was added to this program to calibrate and to optimize experimental techniques. The delayed neutron imortance was calculated to be 1.0, 0.9 and 0.8 for the R2, Zona 2 and Compact cells, respectively. This systematic change would allow extracting informations about the delayed neutron spectra.

Four teams from CEA/Cadarache, FEI/Obninsk, JAERI and ANL are expected to praticipate in the experiment. The involvement of several

teams with different experimental technique will provide increased insureance against systematic errors in the measurement. Target accuracies are ±3% for the Cf-source method and ±2% for the reactor noise method. The experiment will be started in the late 1992.

6. Summary

The present status of delayed neutron parameters and the uncertainties of the reactivity scale are briefly discussed. An uncertainty of ±5% is currently estimated on the calculated βeff of LMFBR core. To improve the prediction accuracy of the reactivity scale, the international(OECD/NEANDC/NEACRP) cooperation are now in progress both on the evaluation of delayed neutron data and on the βeff experiment using the critical facility MASURCA.

References

1) D'Angelo, A. : "A Total Delayed Neutron Yields Adjustment using "ZPR" and "SNEAK" effective-Beta Integral Measurements, Proc. PHYSO'90, April, 1990, Marseile(1990).
2) Nakano, M, et al. : "Measurement of Effective Delayed Neutron Fraction in a Fast Critical Assembly", Preprint 1991 Fall Meeting AES Japan, A66, Fukuoka(1991).
3) Martini, M. et al. : "NEACRP βeff Benchmark Measurement at MASURCA - Proposal for the Experimental program -" NEACRP-A-1064(1990).
4) Keepin, G.R. : "Physics of Nuclear Kinetics", Addison-Wesley Publ.Co.(1965).
5) Tomlinson, L. : "Delayed Neutron from Fission", AERE-6993(1972).
6) Tuttle, R.J. : Nucl.Sci.Eng., 56, 37(1975).
7) Tuttle, R.J. : "Delayed Neutron Yields in Nuclear fission", Proc. Consultants' Meeting on Delayed Neutron Properties, IAEA, Vienna, 26-30(1979).
8) Brady, M.C. and England, T.R. : Nucl.Sci.Eng., 103, 129(1989).
9) Shibata, K. et al. : Japanese Evaluated Nuclear Data Library, Version-3 - JENDL-3 -, JAERI 1319(1990).
10) Fieg, G. :J.Nucl.Energy, 26, 585(1972).

11) Saphier, D. et al. : Nucl.Sci.Eng., 62, 660(1977).

12) Nakano, M and Nakamura, H. : "Effective Delayed Neutron Fraction βeff and Reactivity Scale for LMFBR Cross", Proc. 1981 Seminor on Nuclear Data, p.56, JAERI-M 9999(1982).

13) Stevenson, J.M. : "Delayed Neutron Parameter Requirements for Reactor Physics Purpose", Delayed Neutron Properties, Proc. Specialists'' Meeting, Sept. 15-19, 1986, Univ. Birmingham, England(1987).

14) Fisher, E.A. : "Nucl.Sci.Eng., 62, 105(1977).

15) Bennett, E.F.and Schaefer, R.W. : "Effective Beta Measurement on Uranium and Plutonium Fast Reactor Mockups, NEACRP-A-721(1985).

16) Blachot, J. et al :"Status of Delayed Neutron Data-1990", NEACRP-L-323, December 1990.

Table 1 Temporal group parameters and $\alpha_i/(1+\lambda_i T)$ for Pu-239 and U-238.

(Keepin's Evaluation)

Pu-239 T=100sec

Group i	Decay const. λ i(sec^{-1})	Relative α i abundance	α i/(1+α iT)
1	0.0129	0.038	0.0166(15%)
2	0.0311	0.280	0.0681(62%)
3	0.134	0.216	0.0150(14%)
4	0.331	0.328	0.0096(8.7%)
5	1.26	0.103	0.0008(0.7%)
6	3.21	0.035	0.0001(0.1%)
sum		1.000	0.1102

U-238 T=100sec

Group i	Decay const. λ i(sec^{-1})	Relative α i abundance	α i/(1+α iT)
1	0.0132	0.013	0.0056(9.1%)
2	0.0321	0.137	0.0325(53%)
3	0.139	0.162	0.0109(18%)
4	0.358	0.388	0.0105(17%)
5	1.41	0.225	0.0016(2.6%)
6	4.02	0.075	0.0002(0.3%)
sum		1.000	0.0613

Table 2 Comparison of different evaluations of total delayed neutron yields from fast fission

(n/100 fissions)

Isotope	Keepin[4] (1965)	Tomlinson[5] (1972)	Tuttle[6] (1975)	Tuttle[7] (1979)	Brady[8] (1989)	JENDL-3[9]
U235	1.65±0.05	1.65±0.06	1.714±0.022	1.67 ±0.04	2.06±0.20	~1.62
U238	4.12±0.17	4.4 ±0.21	4.510±0.061	4.39 ±0.10	4.05±0.29	4.81
Pu239	0.63±0.05	0.64±0.03	0.664±0.013	0.630±0.016	0.68±0.08	~0.625
Pu240	0.88±0.09	0.88±0.09	0.96 ±0.11	0.95 ±0.08	0.81±0.09	~0.625
Pu241	−	1.59±0.16	1.63 ±0.16	1.52 ±0.11	1.41±0.14	1.60

Table 3 Isotopic contributions to β_{eff} for typical LMFBR mock up cores*

Isotope	β^{m}_{eff} ($\times 10^{-3}$)	
	Pu/(Pu+U)=25%	Pu/(Pu+U)=11%
U-235	0.079 (2.4%)	0.208 (5.1%)
U-238	1.569 (47%)	2.479 (61%)
Pu-239	1.459 (44%)	1.181 (29%)
Pu-240	0.129 (3.9%)	0.081 (2.0%)
Pu-241	0.107 (3.2%)	0.097 (2.4%)
Total	3.34	4.046
F28/F49	0.0406	0.0311

* MASURCA Core proposed for NEACRP β_{eff} benchmark experiments.[3]

Table 4 Delayed neutron importance in FCA XVI-1 core

Group	Pu-239		U-238	
	αi	$\frac{\langle \chi_{di} \phi^* \rangle}{\langle \chi \phi^* \rangle}$	αi	$\frac{\langle \chi_{di} \phi^* \rangle}{\langle \chi \phi^* \rangle}$
1	0.038	0.865 (0.986)	0.013	0.865 (0.987)
2	0.280	0.881 (1.004)	0.137	0.880 (1.004)
3	0.216	0.876 (0.999)	0.162	0.876 (0.999)
4	0.328	0.877 (1.000)	0.388	0.877 (1.000)
5	0.103	0.874 (0.996)	0.225	0.875 (0.998)
6	0.035	0.880 (1.003)	0.075	0.878 (1.001)
Average	−	0.877	−	0.877

( ): Relative value to the average

Table 5 Comparison between measured and calculated β_{eff} of FCA XVI-1

	β^{m}_{eff} ($\times 10^{-3}$)				
	Tomlinson	Keepin	Tuttle('79)	JENDL-3	Brady('89)
U-235	2.030 ± 0.073	2.030	2.058	1.981	2.534
U-238	2.246 ± 0.107	2.134	2.240	2.455	2.067
Pu-239	0.883 ± 0.041	0.871	0.871	0.862	0.938
Pu-240	0.029 ± 0.0003	0.029	0.031	0.021	0.027
Pu-241	0.009 ± 0.0009	0.009	0.009	0.009	0.008
sum	5.197 ± 0.0136 (2.6%)	5.073	5.209	5.329	5.574
C/E	1.044	1.013	1.046	1.07	1.12

* Experimental value = 4.98×10^{-3} (±3.8%)

** Calculation Model : JFS-3-J2. 70 Groups RZ Diffusion

Table 6 Core parameters of the NEACRP β_{eff} measurement

Name	Fissile Isotope	Enrichment (%)	F28/F29	β_{eff}(U8)/β_{eff}(Pu9) core	β_{eff} (10^{-3})
R2	U-235	30	0.0427	0.28	7.17
Zona2	Pu	25	0.0423	0.88	3.29
Compact	Pu	11	0.0296	1.98	4.02

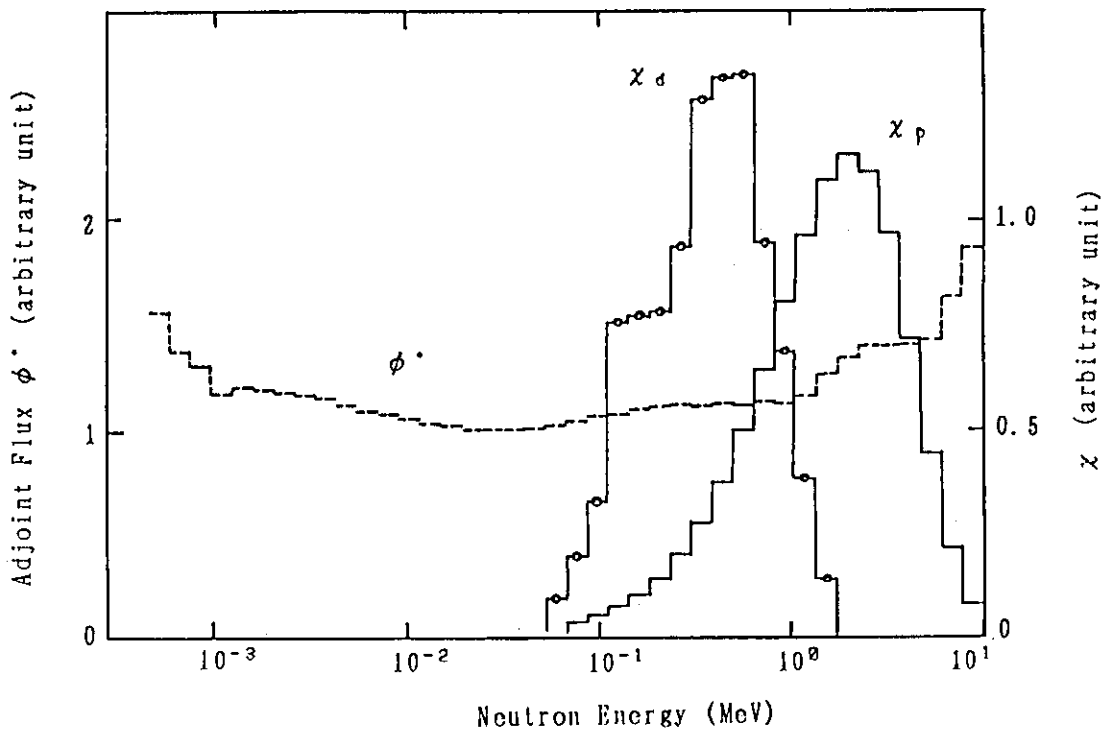

Fig. 1 Delayed and prompt neutron spectra and adjoint flux of FCA XVI-1 core.

3. PAPERS PRESENTED AT POSTER SESSION

3.1 SENSITIVITY ANALYSIS OF JENDL-3 FOR SMALL FAST REACTORS

Toshikazu TAKEDA and Kazuhisa MATSUMOTO

Department of Nuclear Engineering,
Faculty of Engineering, Osaka University

2−1 Yamadaoka, Suita−shi, Osaka, 565, Japan

Abstract

Difference between core performance parameters of small fast reactor cores calculated by JENDL−2 and JENDL−3 has been investigated based on sensitivity analysis. Fast reactor cores with core volume of 12 to 4000*l* were treated. The sensitivity analysis revealed that the difference between ^{235}U fission, ^{238}U transport, ^{239}Pu fission cross sections and fission spectrum of ^{235}U and ^{239}Pu for JENDL−2 and JENDL−3 has remarkably effect on the k_{eff} difference.

1. Introduction

The benchmark test of JENDL−3 was performed for fast, thermal and high−conversion reactors, critical safety, shielding and fusion neutronics, and the results were reported in Ref.(1). Among them the improvement of core parameter over the JENDL−2 results is drastic for large fast reactors.

However, Takano reported[2] that JENDL−3 underestimates k_{eff} of small fast reactors compared to large fast reactors; JENDL−2 produces consistent k_{eff} values for small and large fast reactors.

Therefore, we performed sensitivity analysis to investigate the k_{eff} difference for JENDL−2 and JENDL−3 for small fast reactors. In order to compare the k_{eff} difference for small fast reactors compared to large fast reactors, we treated cores with core volume of 12 to 4000*l*: VERA−11A, VERA−1B, ZPR−3−6F, ZEBRA−3, ZPR−3−12, SNEAK−7A, ZPR−3−11, ZPR−3−54, ZPR−3−53, SNEAK−7B, ZPR−3−50, ZPR−3−48, ZEBRA−2, ZPR−3−49, ZPR−3−56B, ZPPR−2, ZPR−6−7 and ZPR−6−6A.

2. Calculation method

Core performance parameters were calculated using R−Z diffusion calculations. As group constant we used 70 groups constant produced at JAERI by Takano. The correction for transport effect and cell heterogeneous effect calculated in Ref.(3) was adopted to the present results. The spatial mesh effect was taken into account by performing diffusion calculation with about 2cm and 4cm mesh interval, and by extrapolating to zero mesh interval based on Richardson formula.

The anisotropic scattering was treated by using transport cross section instead of total cross section. The transport cross section is defined by

$$\sigma_{tr} = \sigma_t - \mu_{el} f_{el} \sigma_{el\infty}$$

where

$$\sigma_t = f_t \sigma_{t\infty}$$

and f and σ_∞ are the self−shielding factor and the infinite−dilution cross section.

To investigate the difference between core parameters predicted by JENDL−2 and JENDL−3 we performed sensitivity analysis. The 16−group sensitivity coefficients were calculated with the sensitivity calculation code SAGEP[4] based on generalized perturbation theory within the framework of diffusion theory. To check the applicability of diffusion theory we compared the sensitivities calculated by SAGEP with those calculated by transport theory with TWOTRAN−II for ZEBRA−3. Good agreement was seen for the two results, then the sensitivities by SAGEP were used for the sensitivity analysis.

3. Results and Discussion

The C/E values of k_{eff} are shown in Fig.1 together with the results by Takano. Takano used 1−D spherical models and performed S_N calculations. In our calculation, R−Z 2−D models were used. The difference between Takano's results and our results is within 0.8%.

For JENDL−3 the C/E values for small fast reactors are generally smaller than those of large fast reactors: The same trend is seen as Takano's 1−D models.

Nuclide−wise contribution to k_{eff} difference$\{(k_{eff\ \mathrm{JENDL\text{-}2}} - k_{eff\ \mathrm{JENDL\text{-}3}}) / k_{eff\ \mathrm{JENDL\text{-}3}}\}$ is shown in Table 1.

The ^{235}U fission cross section difference{(JENDL−2 − JENDL−3)/ JENDL−3} is shown in Fig.3. The difference is above 5% around 1keV. Therefore the difference has larger contribution for large cores with soft neutron spectrum. Fig.3 also shows the sensitivity and the product of sensitivity and cross section difference, which corresponds to group wise contribution of k_{eff} change. The contribution around 100keV is 0.2%. While Fig.4 shows the results for ZPR−6−6A. The contribution of lower energy groups is much larger. Thus the ^{235}U fission cross section difference has 1.2% effect for VERA−1B and 2.0% effect for ZPR−6−6A.

Next let us consider the effect of the ^{239}Pu fission cross section on k_{eff}. As shown in

Fig.5, the JENDL-2 ^{239}Pu fission cross section is smaller than that of JENDL-3 in the energy range 1 ~ 9keV, and larger in the energy range 10keV ~ 6MeV. The sensitivity and contribution to k_{eff} are shown in Figs.5 and. 6 for VERA-11A and ZPR-6-7, respectively. The sensitivity for ZPR-6-7 is larger in lower energy range compared to VERA-11A. Therefore the contribution of the cross section change in the energy range 1 ~ 9keV is larger for ZPR-6-7. This negative contribution largely compensates the positive contribution in the energy range above 10keV. While for VERA-11A the negative contribution is very small because of small sensitivity in the energy range. Therefore the ^{239}Pu fission cross section effect is larger for small fast reactor cores than for large fast reactor cores.

The k_{eff} change$\{(k_{eff\ JENDL-2} - k_{eff\ JENDL-3})/k_{eff\ JENDL-3}\}$ due to the ^{238}U transport cross section is shown in Fig.7. The neutron leakage is large for small cores. Therefore the effect is large for small cores. The k_{eff} change is shown in Fig.8 and Fig.9 for VERA-11A and ZPR-6-7, respectively. Transport cross section of JENDL-2 is smaller above 1.35MeV than JENDL-3 but larger in the range 0.18 ~ 1.35MeV. For VERA-11A, the contribution in the energy range above 1.35MeV is larger than that in the range 0.18 ~ 1.35MeV. However, for ZPR-6-7 the contribution in the range 0.18 ~ 1.35MeV is almost equal to the contribution above 1.35MeV. Furthermore the sensitivity for VERA-11A is one-order larger than that for ZPR-6-7. Therefore the contribution of ^{238}U transport cross section is large for small cores.

The scattering cross section of JENDL-3 is almost equal to that of JENDL-2. Some of the scattering cross sections treated as inelastic scattering in JENDL-3 was treated as elastic scattering in JENDL-2. Therefore elastic scattering cross section of JENDL-3 is smaller than that of JENDL-2. The contribution of the ^{238}U transport cross section to the k_{eff} difference may be caused by the influence of elastic scattering cross section change through μ_{el} value.

For the fission spectrum, the effect differs for individual cores. The change of the fission spectrum from Maxwell formula of JENDL-2 to the Madland-Nix formula of JENDL-3 increases k_{eff} about 0.5% for large cores. However for VERA-1B the k_{eff} decreases. To investigate the difference we compared sensitivity coefficient of χ for VERA-1B, ZPR-3-6F and ZPR-6-6A in Fig.10. The sensitivity for VERA-1B above 1.35MeV is smaller than that for ZPR-3-6F and ZPR-6-6A, and larger below 1.35MeV. This is because the adjoint spectrum is larger in VERA-1B in lower energy range as shown in Fig.11, though the spectrum is very hard for VERA-1B as shown in Fig.12. The relative change of the ^{235}U fission spectrum between JENDL-2 and JENDL-3 is shown in Fig.13. Fig.14 shows the energy-wise contribution to the k_{eff} change(sensitivity x χ change). From Fig.14 it is seen that for VERA-1B the negative contribution in the energy range 1.35~6.07MeV is small, and the positive contribution is large. Therefore total contribution becomes positive. For other cores the negative contribution surpasses the positive contribution, and total contribution becomes negative.

4. Conclusion

It was found that JENDL-3 underestimates k_{eff} of small fast reactors compared to large fast reactors. The present 2-D results were in good agreement with 1-D results by Takano. For small Pu cores the k_{eff} calculated by JENDL-3 was smaller than that by JENDL-2 by about 0.8%. For large Pu cores JENDL-3 k_{eff} was larger than JENDL-2 k_{eff} by about 0.5%. For U cores the k_{eff} difference was independent of core volumes.

The ^{239}Pu fission cross section, ^{239}Pu fission spectrum, ^{235}U fission cross section and ^{235}U fission spectrum have large effect on the k_{eff} difference for Pu and U cores. Ni transport cross section, Fe transport cross section and Al transport cross section have also large effect for ZPR-3-56B, ZPR-3-54, and ZPR-3-6F, respectively.

From the sensitivity analysis the k_{eff} difference was analyzed group-wise, and the effect of neutron spectrum and leakage was discussed for small and large cores.

References

(1) Asami T. et al.: "Japanese evaluated nuclear data library Version 3(JENDL-3)" , J. At. Energy Soc. Jpn., (in Japanese), **31**[1], 6-33(1989).

(2) Takano H. et al.: "BENCHMARK TESTS OF JENDL-3 FOR THERMAL AND FAST REACTORS", Proc. Int. Conf. on the Physics of Reactors: Operation, Design and Computation, APRIL 1990, **Vol.3**, PI-21.

(3) Hardie et al.: "An Analysis of Selected Fast Critical Assemblies Using ENDF/B-IV Neutron Cross Sections", Nucl. Sci. Eng., **57**, 222(1975)

(4) Hara A., Takeda T. and Kikuchi Y.: "SAGEP: Two-Dimensional Sensitivity Analysis Code Based on Generalized Perturbation Theory", JAERI-M 84-027(1984)

Table 1 Nuclide-wise contribution to k_{eff} difference $\{(k_{eff\ JENDL-2} - k_{eff\ JENDL-3})/k_{eff\ JENDL-3}\}$ (%).

Core	Volume (l)	$^{235}\sigma_f$	$^{235}\nu$	$^{238}\sigma_f$	$^{238}\sigma_c$	$^{238}\sigma_s$	$^{238}\sigma_{tr}$	$^{239}\sigma_f$	$^{239}\nu$
VERA-11A	12	0.05	0.00	0.18	−0.21	0.07	−0.55	1.32	0.14
VERA-1B	30	1.22	0.01	0.15	−0.22	0.11	−0.33	----	----
ZPR-3-6F	50	1.09	−0.07	0.23	−0.31	0.23	−0.32	----	----
ZEBRA-3	60	0.09	0.00	0.42	−0.44	0.04	−0.27	1.58	0.02
ZPR-3-12	100	1.36	0.03	0.31	−0.39	0.24	−0.27	----	----
SNEAK-7A	110	0.13	0.01	0.25	−0.27	0.09	−0.35	0.96	−0.13
ZPR-3-11	140	1.22	−0.02	0.40	−0.56	0.16	−0.13	----	----
ZPR-3-54	190	0.01	0.00	0.08	−0.04	0.04	−0.04	0.61	−0.24
ZPR-3-53	220	0.02	0.00	0.16	−0.17	0.09	−0.25	0.53	−0.24
SNEAK-7B	310	0.22	0.01	0.34	−0.44	0.05	−0.22	1.12	−0.14
ZPR-3-50	340	0.03	0.00	0.24	−0.23	0.08	−0.23	0.64	−0.25
ZPR-3-48	410	0.03	0.00	0.25	−0.31	0.09	−0.21	1.03	−0.18
ZEBRA-2	430	1.78	0.15	0.33	−0.39	0.19	−0.18	----	----
ZPR-3-49	450	0.03	0.00	0.13	−0.34	0.10	−0.23	1.10	−0.15
ZPR-3-56B	610	0.02	0.00	0.19	−0.25	−0.01	−0.08	1.15	−0.20
ZPPR-2	2400	0.03	0.00	0.22	−0.33	0.01	−0.09	1.03	−0.25
ZPR-6-7	3100	0.03	0.00	0.23	−0.38	0.04	−0.09	0.96	−0.29
ZPR-6-6A	4000	2.02	0.18	0.22	−0.44	0.11	−0.06	----	----

$^{239}\sigma_c$	$^{Carbon}\sigma_{tr}$	$^{Carbon}\sigma_s$	$^{Iron}\sigma_s$	$^{Iron}\sigma_{tr}$	χ	$^{Sodium}\sigma_{tr}$	$^{Sodium}\sigma_s$	$^{Oxygen}\sigma_{tr}$	$^{Oxygen}\sigma_s$	sum.[a]	SUM[b]
−0.07	0.10	−0.02	−0.02	−0.07	−0.25*	----	----	----	----	0.59[1]	0.79
----	0.13	−0.18	0.02	−0.06	0.07**	----	----	----	----	0.92	0.67
----	----	----	0.00	−0.06	−0.30**	----	----	----	----	0.93[2]	0.75
−0.07	0.00	0.00	−0.03	−0.03	−0.84*	----	----	----	----	0.73[3]	0.98
----	0.07	0.04	−0.02	−0.04	−0.51**	----	----	----	----	0.82	0.64
−0.11	0.06	0.05	−0.04	−0.04	−0.47*	----	----	0.17	−0.08	0.23	0.35
----	----	----	−0.02	−0.03	−0.79**	----	----	----	----	0.24	0.16
−0.61	0.17	−0.37	−0.01	−0.40	−0.08*	----	----	----	----	−0.89	−0.81
−0.48	0.14	−0.26	−0.01	−0.03	−0.20*	----	----	----	----	−0.71	−0.45
−0.08	0.00	0.01	−0.09	−0.03	−0.70*	----	----	0.20	−0.25	−0.02	0.14
−0.27	0.11	−0.01	−0.05	−0.03	−0.50*	----	----	----	----	−0.46	−0.19
−0.16	0.08	0.07	−0.09	−0.06	−0.55*	0.03	−0.10	----	----	−0.09	0.13
----	0.07	−0.01	−0.02	−0.01	−0.58**	----	----	0.00	0.00	1.32	1.09
−0.10	0.08	0.12	−0.10	−0.07	−0.58*	----	----	----	----	−0.01	0.38
−0.25	0.00	0.00	−0.12	−0.09	−0.42*	0.08	−0.13	0.15	−0.15	−0.47[4]	−0.57
−0.20	0.00	0.00	−0.18	−0.06	−0.53*	0.07	−0.22	0.21	−0.27	−0.57	−0.45
−0.21	----	----	−0.18	−0.04	−0.57*	0.04	−0.22	0.13	−0.27	−0.81	−0.67
----	----	----	−0.06	−0.04	−0.40**	0.05	−0.10	0.12	0.09	1.49	1.18

* fission spectrum of ^{239}Pu, ** fission spectrum of ^{235}U
a):partial sum of this table
b):Direct calculation
1):included $^{Cu}\sigma_s$(−0.09)
2):included $^{Al}\sigma_s$(−0.07) and $^{Al}\sigma_{tr}$(0.51)
3):included $^{Cu}\sigma_s$(0.26)
4):inclured $^{Ni}\sigma_{tr}$(−0.38)

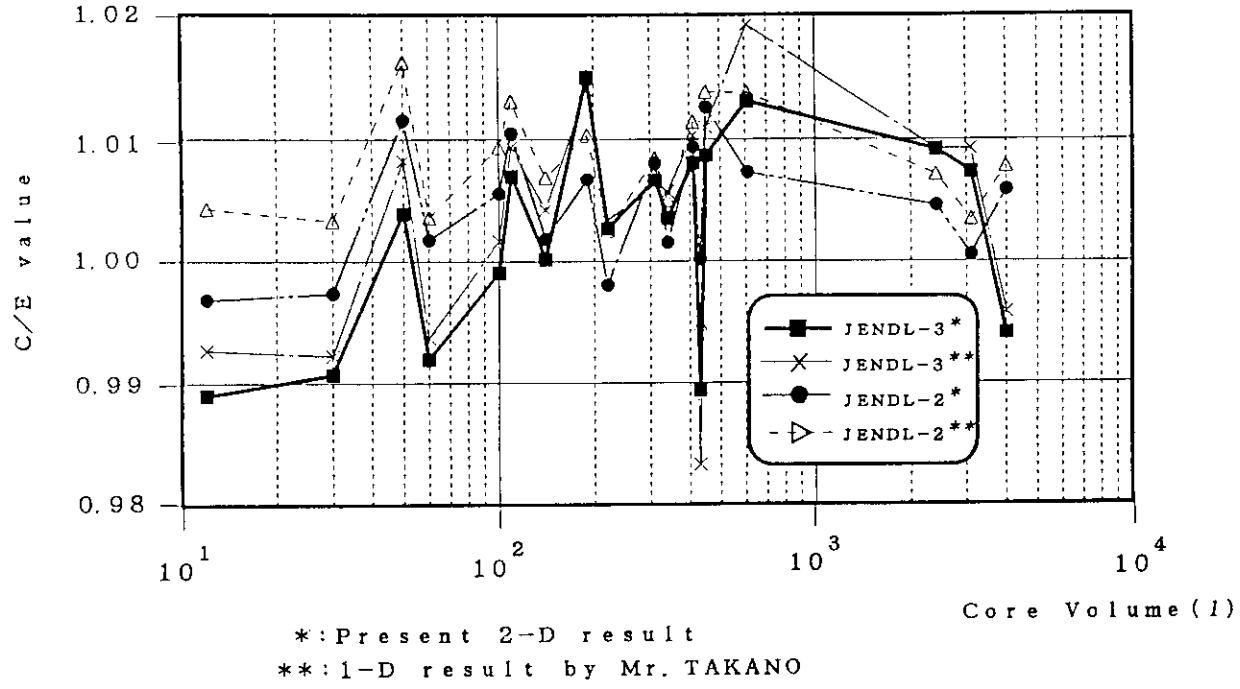

Fig. 1 C/E value of k_{eff} with correction by Hardie et al. (Nucl. Sci. Eng., 57, 222(1975))

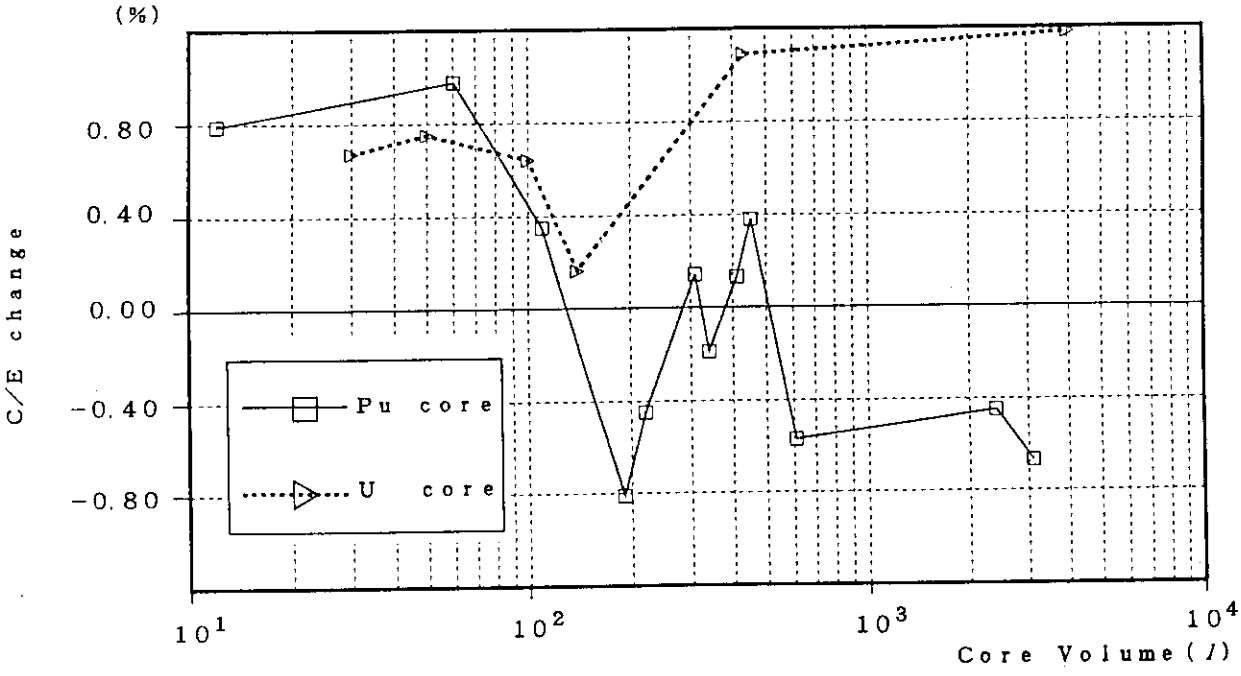

Fig. 2 C/E change of k_{eff} (JENDL-2-JENDL-3)/JENDL-3.

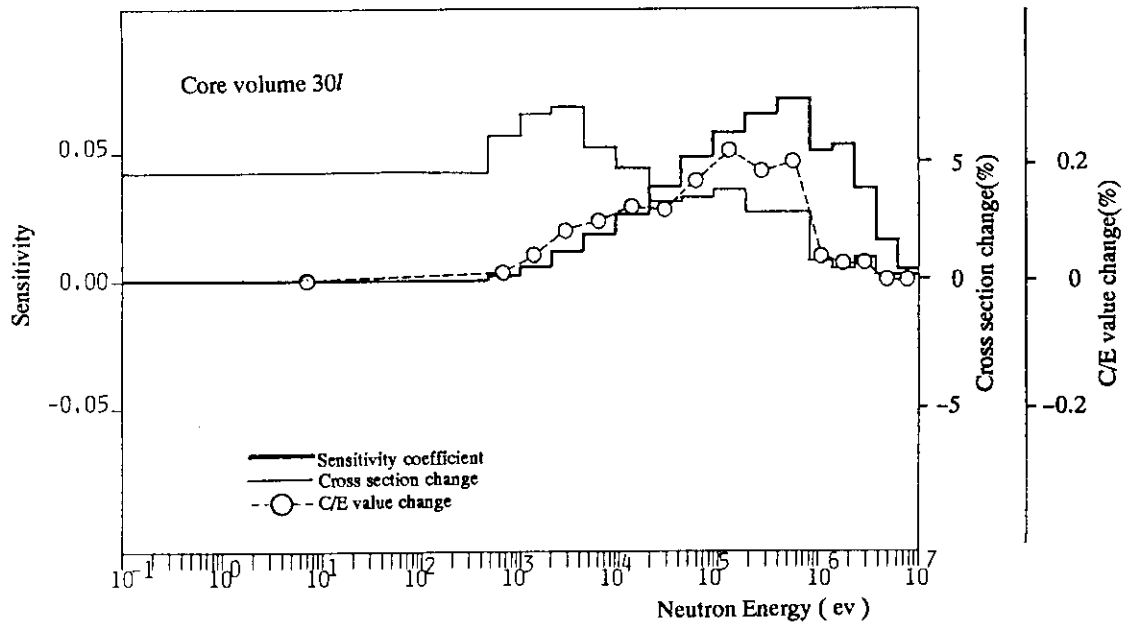

Fig. 3 Energy-group wise contribution of ^{235}U fission cross section to VERA-1B k_{eff} change$\{(k_{eff\ JENDL-2} - k_{eff\ JENDL-3})/k_{eff\ JENDL-3}\}$.

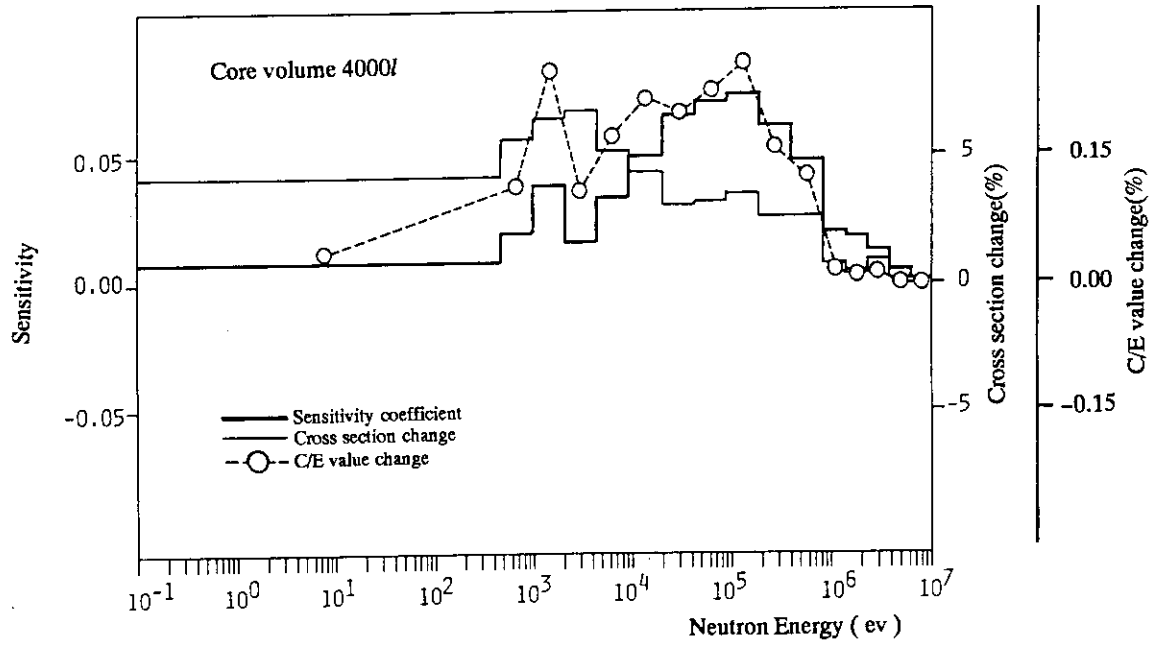

Fig. 4 Energy-group wise contribution of ^{235}U fission cross section to ZPR-6-6A k_{eff} change$\{(k_{eff\ JENDL-2} - k_{eff\ JENDL-3})/k_{eff\ JENDL-3}\}$.

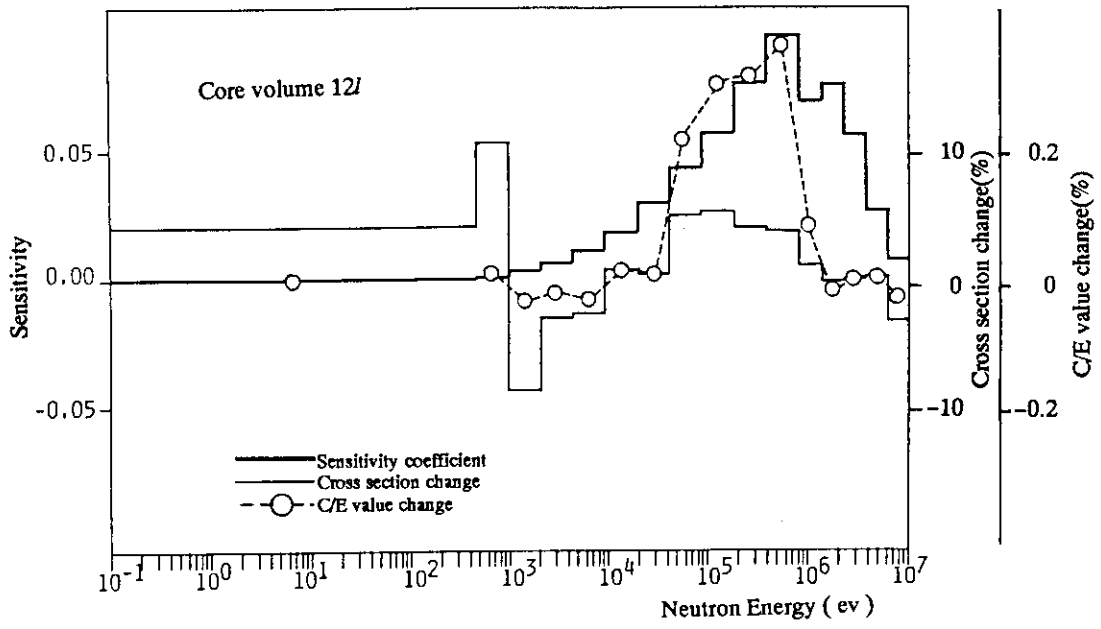

Fig. 5 Energy-group wise contribution of ^{239}Pu fission cross section to VERA-11A k_{eff} change{($k_{eff\ JENDL-2}$ -$k_{eff\ JENDL-3}$)/$k_{eff\ JENDL-3}$ }.

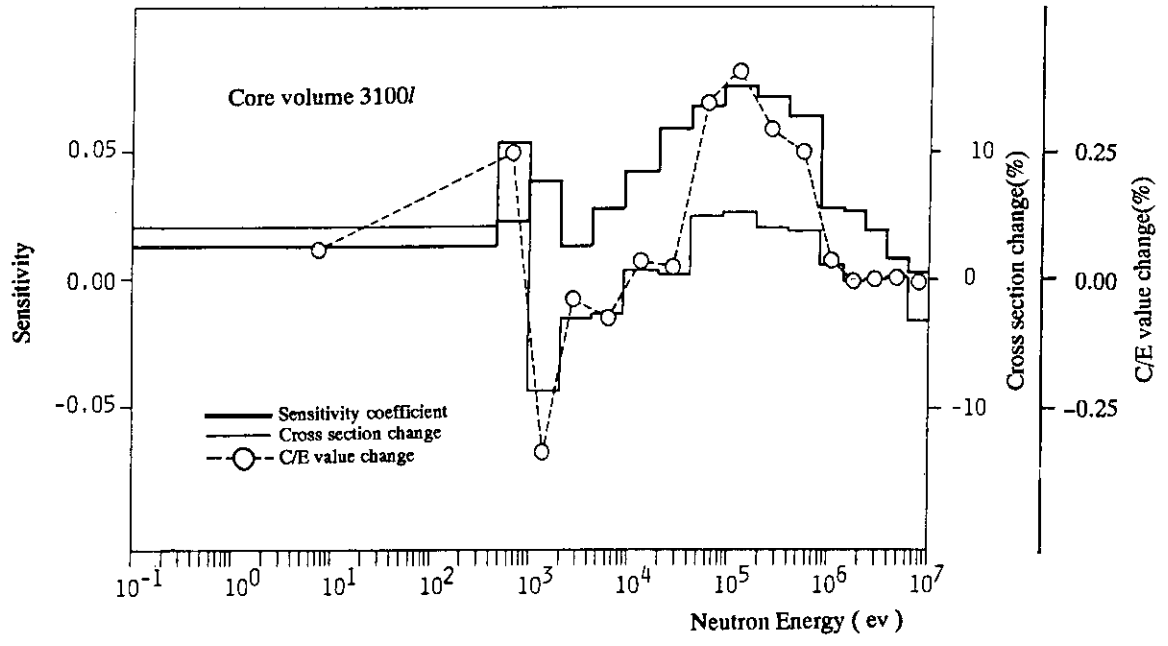

Fig. 6 Energy-group wise contribution of ^{239}Pu fission cross section to ZPR-6-7 k_{eff} change{($k_{eff\ JENDL-2}$ -$k_{eff\ JENDL-3}$)/$k_{eff\ JENDL-3}$ }.

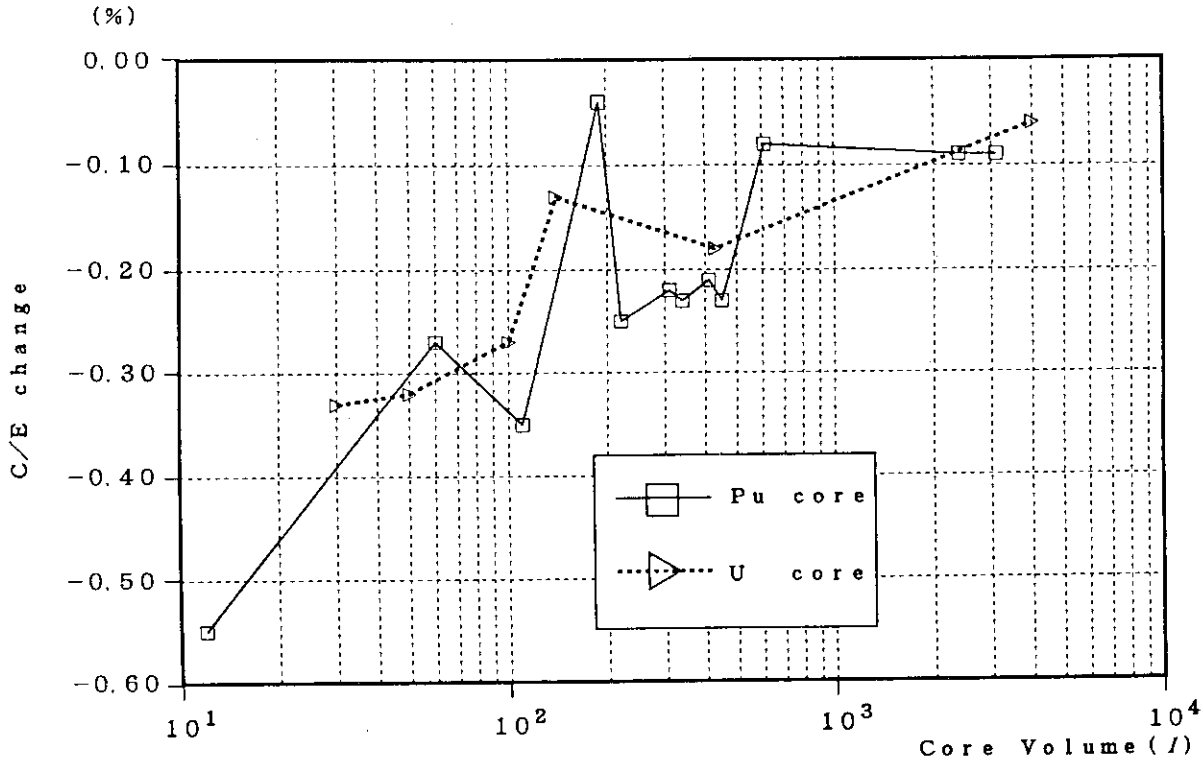

Fig. 7 k_{eff} change (JENDL-2 - JENDL-3)/JENDL-3 due to ^{238}U transport cross section.

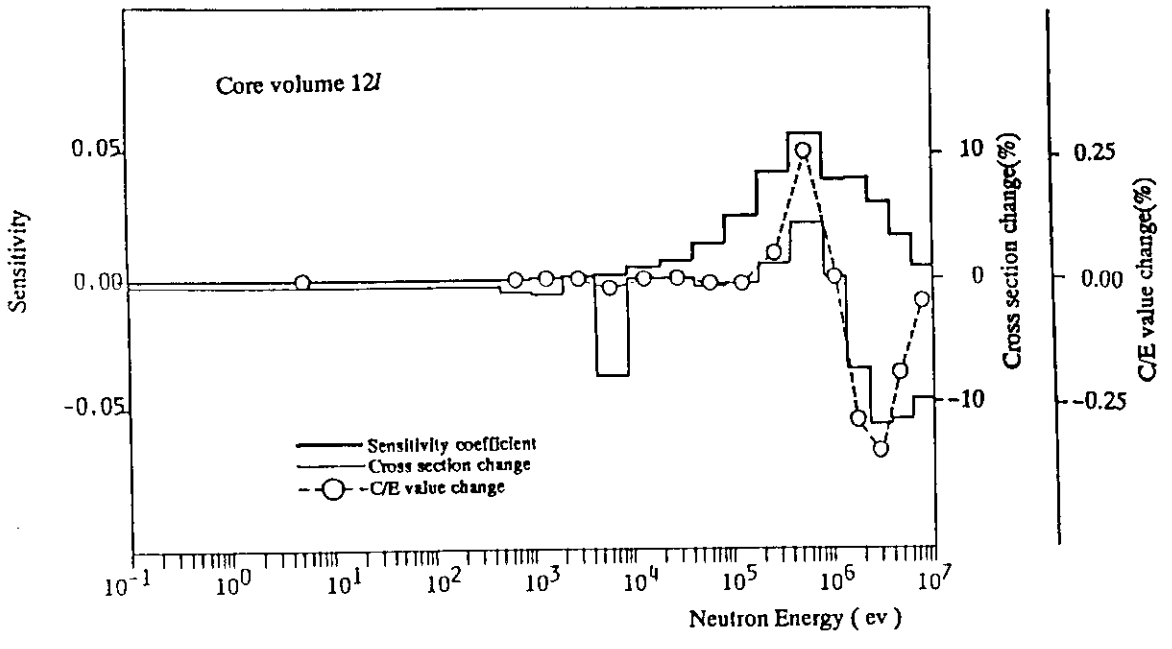

Fig. 8 Energy-group wise contribution of ^{238}U transport cross section to VERA-11A k_{eff} change{($k_{eff\ JENDL-2}$ - $k_{eff\ JENDL-3}$)/$k_{eff\ JENDL-3}$}.

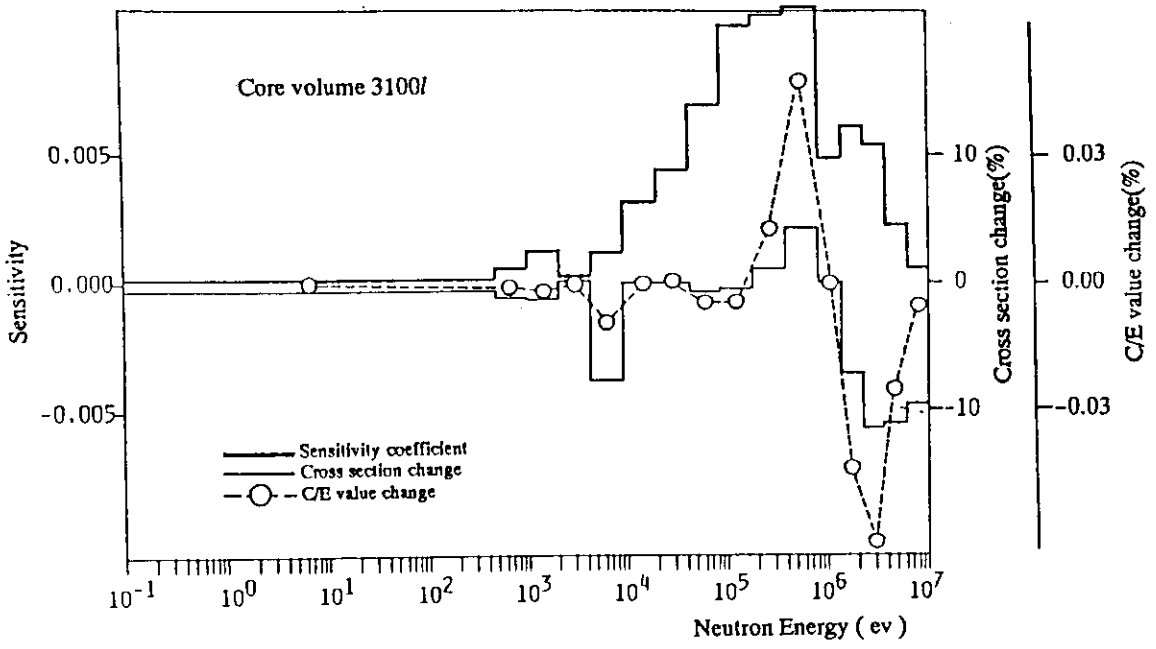

Fig. 9 Energy-group wise contribution of ^{238}U transport cross section to ZPR-6-7 k_{eff} change{$(k_{eff\ JENDL-2} - k_{eff\ JENDL-3})/k_{eff\ JENDL-3}$}.

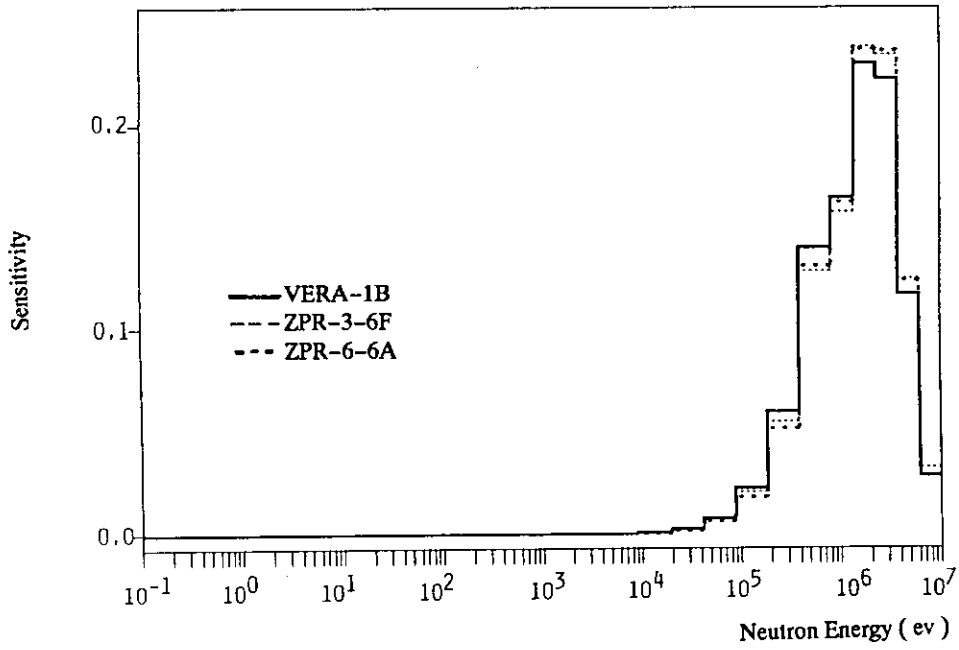

Fig. 10 Comparison of the k_{eff} sensitivity due to ^{235}U fission spectrum for VERA-1B, ZPR-3-6F and ZPR-6-6A.

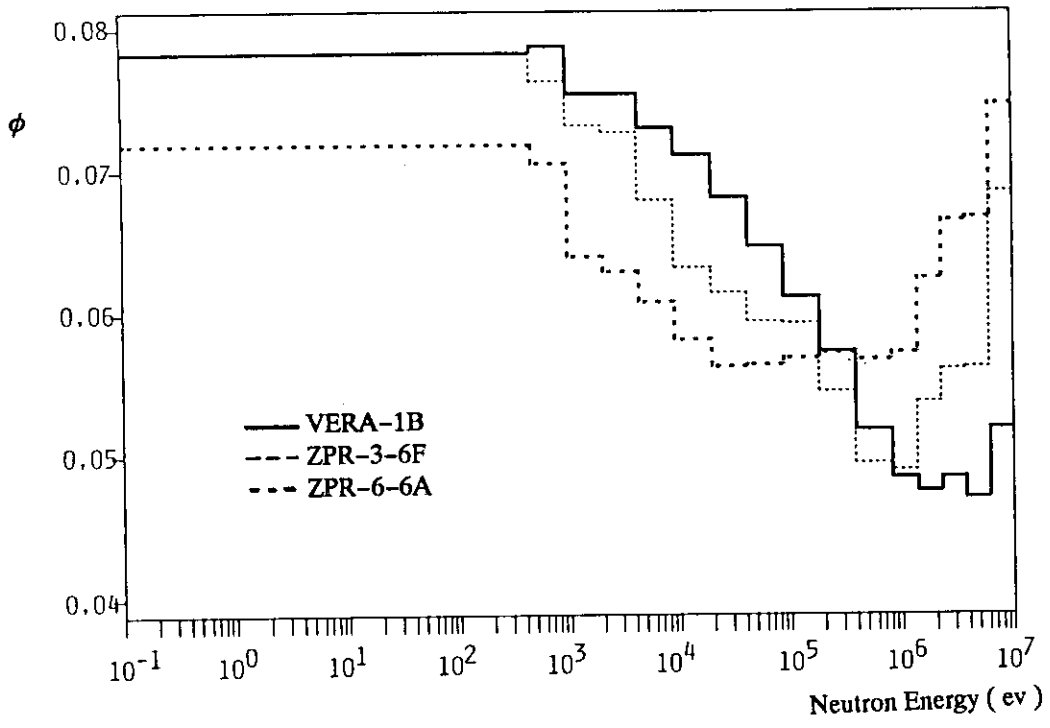

Fig. 11 Adjoint flux spectrum at core center.

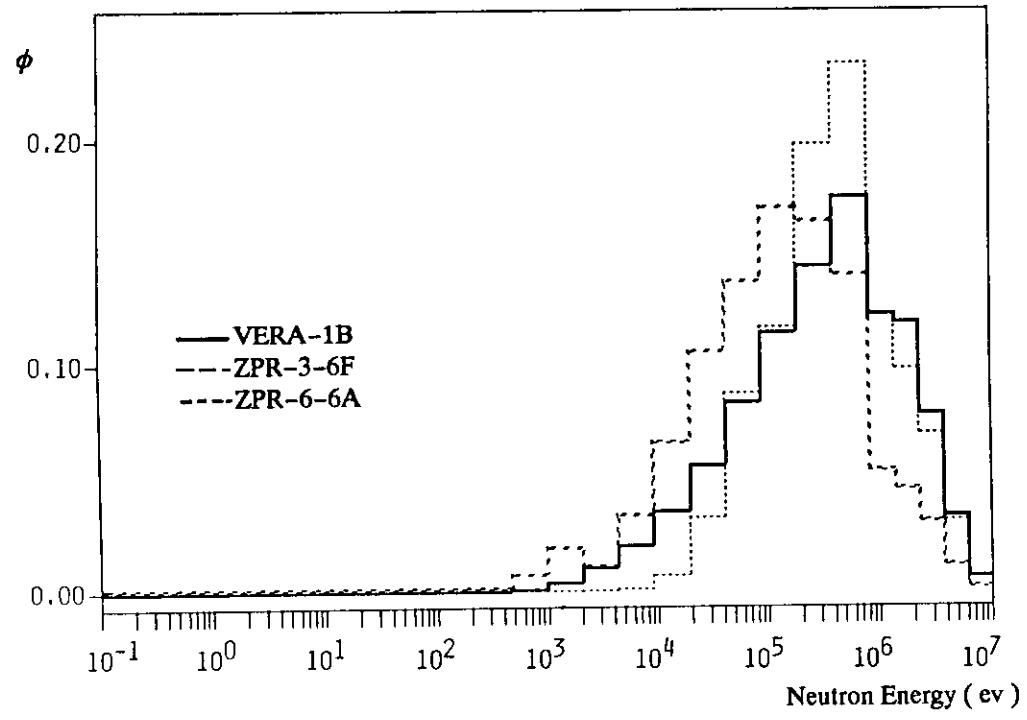

Fig. 12 Flux spectrum at core center.

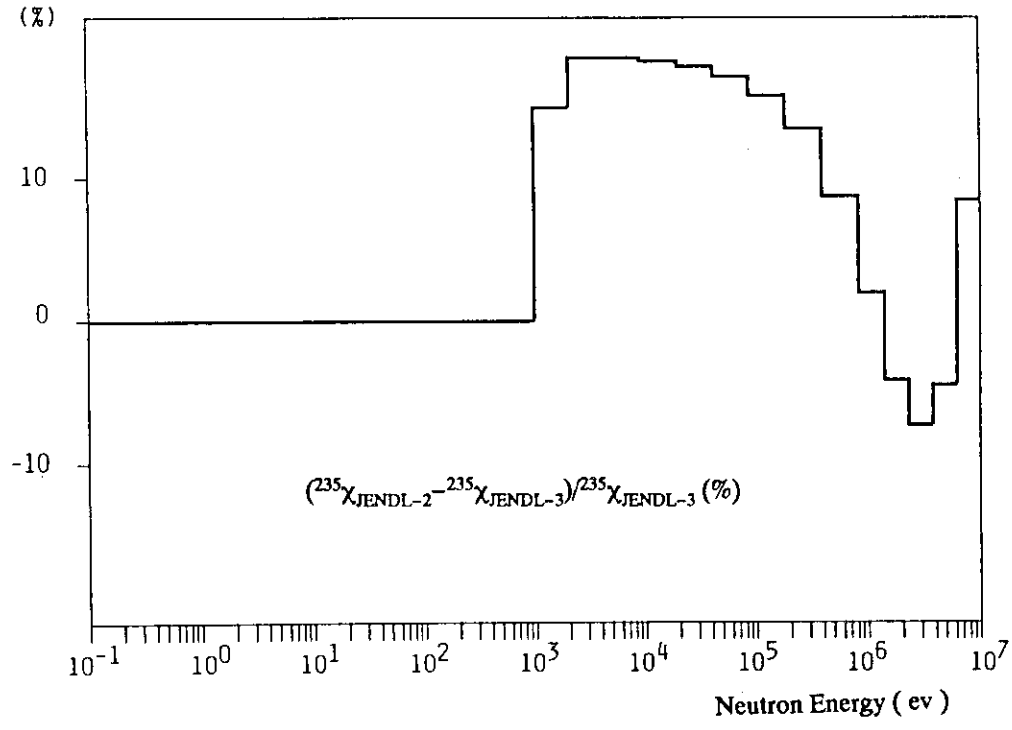

Fig. 13 Difference of ^{235}U fission spectrum.

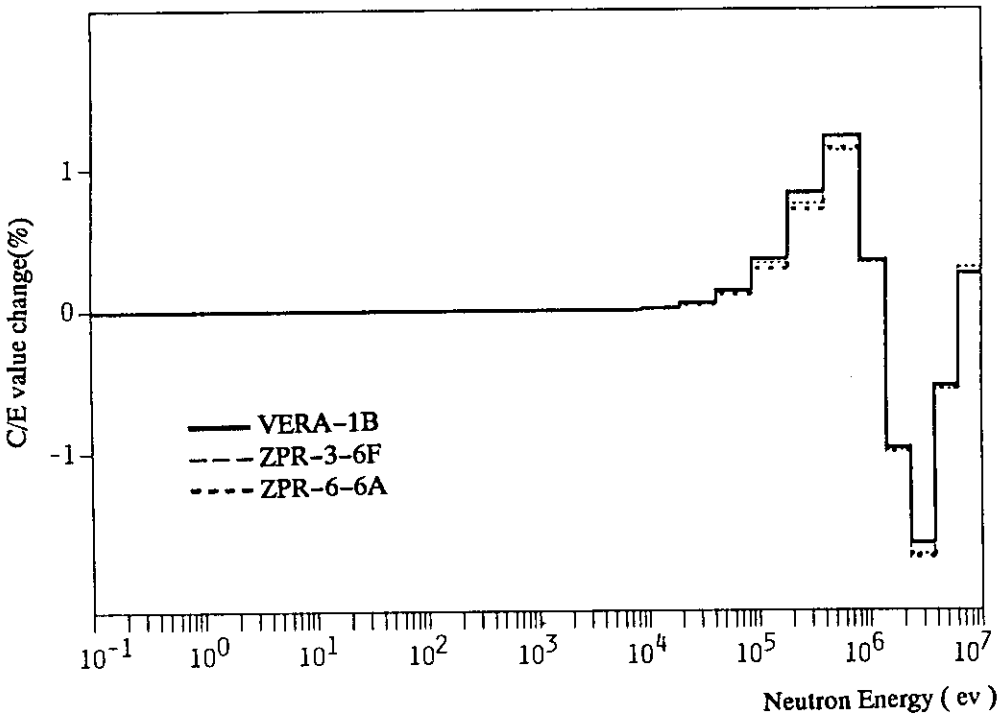

Fig. 14 Energy-group wise contribution of ^{235}U fission spectrum to k_{eff} change{$(k_{eff\ JENDL-2} - k_{eff\ JENDL-3})/k_{eff\ JENDL-3}$}.

3.2 JENDL-3 BENCHMARK TEST FOR HIGH CONVERSION LIGHT WATER REACTOR

Kaoru Kobayashi, Kazuya Ishii and Atsushi Zukeran
Energy Research Laboratory, Hitachi, Ltd.
1168 Moriyama-cho, Hitachi-shi, Japan

[Abstract] Benchmark test of the JENDL-3 was carried out by the 190 group Monte Carlo code VMONT for High Conversion Critical Experiments (Hi-C) of ZPR-7 with slightly enriched UO_2 fuel. The calculated lattice parameters (ρ^{28}, δ^{25}, δ^{28}, ICR) were compared with experimental data and comparison of k_∞s was made for nuclear data files used. Main results of the test are: (1) Differences in nuclear data files, namely JENDL-3, JENDL-2 and ENDF/B-Ⅳ, of k_∞ values are small, i.e., about 0.3%$\Delta k/k$, although large differences in absorption rates are found in the neutron balance based on the above files, e.g. about 1.0%$\Delta k/k$ for ^{238}U. (2) Calculated to experiment data ratio (C/E) of δ^{25} grow with decreasing H/U, and the resonance parameters of ^{235}U should be studied in order to improve these discrepancies. (3) Applicability of JENDL-3 is not so good for the UO_2 fueled HCLWR, as compared with for thermal reactors. Discrepancies between calculations and experiments are enhanced for harder neutron spectra.

1. Introduction

Benchmark tests of LWR and FBR cores have been made for JENDL-3 by JNDC Working Groups,[1),2)] and applicabilities of JENDL-3 were evaluated for typical nuclear properties. In some cores, the calculated values based on JENDL-3 were also compared with JENDL-2 and ENDF/B-Ⅳ. Recently, High Conversion Light Water Reactors (HCLWRs) are expected to be an integral part in advanced fuel management strategies. The typical neutron spectrum of the HCLWR lies between the spectra associated with LWRs and FBRs. The dominant energy region of the reaction rate in the HCLWR is above the electron volt range where large contributions from plutonium and uranium resonances become important, although in LWRs the reaction rates are governed by thermal neutrons. Therefore, JENDL-3 benchmark test of HCLWRs have been

performed for the PROTEUS core with plutonium fuels[1], but not performed for uranium fuels. In the present work, in order to confirm the applicability of the JENDL-3 to uranium fueled HCLWRs, the benchmark test was carried out for the ZPR-7.

2. Benchmark data

Benchmark test of JENDL-3 was carried out for lattice parameters of the ZPR-7 Hi-C with slightly enriched UO_2 fuels. The ZPR-7 cores simulate a wide range of neutron spectra by changing the water to fuel volume ratio (H/U) in a lattice cell as shown in table 1. The table gives the Hi-C core definition and measured data. Core No. 21, with the hardest neutron spectrum, was omitted from the table and our analyses, since its infinite multiplication factor was 0.83, as calculated by VMONT. As shown in Fig. 1, the ZPR-7 neutron spectra obtained by VMONT simulate various neutron spectra from thermal reactors to HCLWRs.

Analyzed ZPR-7 lattice parameters were ρ^{28} (epithermal/thermal ratio of ^{238}U capture), δ^{25} (the epithermal/thermal ratio of ^{235}U fission), δ^{28} (the ratio of ^{238}U fission to ^{235}U fission) and ICR (initial conversion ratio), and in order to compare C/Es for thermal reactors, lattice parameters ρ^{28}, δ^{25}, δ^{28} of TRX cores[5] were calculated.

3. Calculational method

Benchmark analysis was performed by the 190 group vectorized Monte Carlo code VMONT operating on the super computer HITAC S-820, and was based on one million histories. Final statistical errors of the infinite multiplication factor were typically around 0.04%Δk/k or less. Cross section libraries of the VMONT were prepared by NJOY code[6] from JENDL-3, JENDL-2 and ENDF/B-Ⅳ nuclear data files. Then, for some nuclides whose cross sections are described by Reich-Moore formula or Breit-Wigner formula having unknown J-values, point wise cross sections, which were not calculated by the NJOY code, were obtained by the RESENDD code[7].

4. Results and discussion

First, infinite multiplication factors, k_∞s, of the ZPR-7 were investigated by comparing the calculated values based on various nuclear data files, namely JENDL-3, JENDL-2 and ENDF/B-Ⅳ, since no experimental data of k_∞s are suitable for the Hi-C experiment of ZPR-7. Next, a brief comparison was made between the C/E-values for various lattice parameters of ZPR-7 and thermal benchmark cores TRXs.

(1) k_∞

Figure 2 compares k_∞s for various H/U ratios, relation to JENDL-2 values. The H/U dependences are discussed next. Neutron absorptions of each nuclide differ among the nuclear data files used. Figure 3 shows difference of neutron absorptions over 0.1%$\Delta k/k$, which differ from those of JENDL-2. The major differences come from the resonance regions of ^{235}U, ^{238}U and Fe. The ^{238}U and Fe neutron absorptions increase with decreasing H/U, while that of ^{235}U decreases. Consequently, as these effects tend to cancel each other, differences of k_∞s are reduced.

(2) Epithermal/thermal ratio of ^{238}U capture: ρ^{28}

The ρ^{28} is sensitive to ^{238}U thermal capture cross section σ_c^{28} and shielded capture resonance integral I^{28}. The ρ^{28} values calculated by using JENDL-3 for the TRX agree fairly well with experimental data within ±2% ($1.0 \leqq H/U \leqq 4.0$) as shown in Fig. 4, and thus it implies that σ_c^{28} has no special problem for thermal reactors. But for HCLWR, the calculated values are overestimated by about 5% as expected in the H/U range from 0.3 to 1.0.

(3) Epithermal/thermal ratio of ^{235}U fission: δ^{25}

The δ^{25} is sensitive to ^{235}U thermal fission cross section σ_f^{25} and shielded fission resonance integral I^{25}. The C/Es of δ^{25} based on JENDL-3, as shown in Fig. 5, are underestimated by around 5% in ZPR-7 ($0.5 \leqq H/U < 1.5$) and TRX (thermal reactor region: $1.0 \leqq H/U \leqq 8.0$), while they are overestimated in ZPR-7 ($H/U < 0.5$). It is clear that the C/Es of ZPR-7 rapidly decrease as a function of H/U, while these of the TRX have a slight H/U-dependence, the resonance contribution to $^{25}\delta$ seems to be enlarged, and thus the resonance parameters of ^{235}U should be further studied in order to improved these discrepancies.

(4) Ratio of ^{238}U fission to ^{235}U fission: δ^{28}

Calculated δ^{28}s are underestimated about 15% for ZPR-7 as shown in Fig. 6, while calculated δ^{28}s agree well with experimental data for the TRX. Discrepancies of C/Es for the ZPR-7 were investigated as follows.

Calculated δ^{28} is sensitive to ^{238}U fission cross section σ_f^{28} (above 0.5MeV), ^{238}U inelastic scattering cross section σ_{in}^{28}, σ_f^{25} (2200m/s), I^{25} and ^{235}U fission spectrum χ^{25}. The σ_f^{28} and σ_f^{25} of JENDL-3 agree with the cross section data compiled in the experimental data file EXFOR[8] within the experimental errors, and thus, uncertainties of cross sections σ_f^{28} and σ_f^{25} are not primary contributions to the δ^{28} discrepancy.

In order to investigate the sensitivities of δ^{28} due to calculational uncertainties of δ^{25}, defined equation of δ^{28} was transformed into equation (1), and semi-experimental values of δ^{28} were obtained substituting into experimental values δ^{25}.

$$\delta^{28} = \frac{\int_{E_c}^{\infty} \sigma_f^{28} N^{28} \phi \, dE}{\int_0^{E_c} (1+\delta^{25}) \ \sigma_f^{25} N^{25} \phi \, dE} \qquad (1)$$

where

ϕ : neutron flux
E : neutron energy
Ec : cadmium cutoff energy
N^{25} : number density of ^{235}U
N^{28} : number density of ^{238}U

As shown in table 2, this effect is small, being about 5% at most. Therefore, the discrepancy of δ^{25} is not seen to be a key parameter.

The fission neutron spectrum of ^{235}U (χ^{25}) compiled in JENDL-3 is evaluated on the basis of the Madland-Nix formalism which tends to give harder spectrum in comparison with the evaporation model (JENDL-2 and ENDF/B-Ⅳ). Considering the differences of δ^{28} C/Es among the files were about 5%, the hardness of the present χ^{25} cannot explain the significant discrepancy having magnitudes from 10 to 20%.

In order to study the effect of σ_{in}^{28} on δ^{28}, the evaluated data

for σ_{in}^{28} of JENDL-3 were also compared with the EXFOR data, but no reasonable interpretation for the present discrepancy could be derived from the above comparison because of large scatter in measured σ_{in}^{28} data. The σ_{in}^{28} seems to still be a possible source for underestimation of calculated values.

As discussed above, significant underestimation of δ^{28} for the ZPR-7, in spite of good agreement in the TRX, could not be explained from a calculational viewpoint. Further accumulation of HCLWR (U core) benchmark data is needed to the lattice parameters, critical buckling, sample worth, power distribution and so on.

(5) Initial conversion ratio: ICR

ICR is primary sensitive to the I^{28} for HCLWR. Then C/Es of ICR are given Fig. 7, and they show a similar tendency to those of ρ^{28}.

5. Conclusions

JENDL-3 benchmark test for the high conversion light water reactor (HCLWR) was performed for ZPR-7 cores, and the following results were obtained.

(1) Differences in nuclear data files, namely JENDL-3, JENDL-2 and ENDF/B-Ⅳ of k_∞ values were small, i.e. about 0.3%$\Delta k/k$. Such a small difference arose from cancellations among large neutron absorptions by ^{236}U, ^{235}U and Fe. The differences, however, increased with decreasing water to fuel volume ratio (H/U).

(2) Calculated ρ^{28}s agreed well with experimental data for the thermal reactor ($1.0 \leqq H/U \leqq 4.0$), but were overpredicted by 4% for the HCLWR ($H/U < 1.0$).

(3) The calculated to experiment data ratios (C/Es) of δ^{25} grew with decreasing H/U, and the resonance parameters of ^{235}U should be further studied.

(4) Calculated δ^{28}s were underestimated about 15%. Preliminary investigations were made for ^{235}U and ^{238}U cross sections and fission spectra. Consequently, the uncertainties might be related to the ^{238}U inelastic cross section.

(5) The present work showed, applicability of JENDL-3 was not so good

for UO_2 fueled HCLWR as compared with thermal reactors. Discrepancies between calculations and experiments are enhanced for harder neutron spectra.

References

(1) S. Iijima, JAERI-M 90-025 p5 (1990)
(2) Y. Kikuchi, ibid., p29 (1990)
(3) H. Maruyama, et al., Preprint 1987 Fall Mtg. of AESJ (in Japanese), D58(1987)
(4) A. R. Boynton, et al., ANL-7203(1967)
(5) J. Hardy, Jr., et al. Nucl. Sci. Eng. 40 101(1970)
(6) Documentation for PSR-171/NJOY87 Code Package
(7) T. Nakagawa, JAERI-M 84-192(1984)
(8) Y. Nakajima, private communication

Table 1 Core definition and measured data in ZPR-7 experiments

Core No.	H/U	δ^{25}	ρ^{28}	δ^{28}	ICR
4	1.37	0.195	3.05	0.074	0.518
8	0.96	0.286	4.12	0.101	0.500
12	0.76	0.364	5.40	0.116	0.581
14	0.44	0.645	10.0	0.154	0.835
19	0.32	0.870	14.5	0.188	0.913

Table 2 Comparison of calculated and semi-experimental δ^{28} in ZPR-7

Core No.	C[1)]	S[2)]
4	0.855	0.846
8	0.816	0.803
12	0.845	0.835
14	0.929	0.935
19	0.919	0.968

1): Calculation

2): Semi-experiment obtained by equation (1)

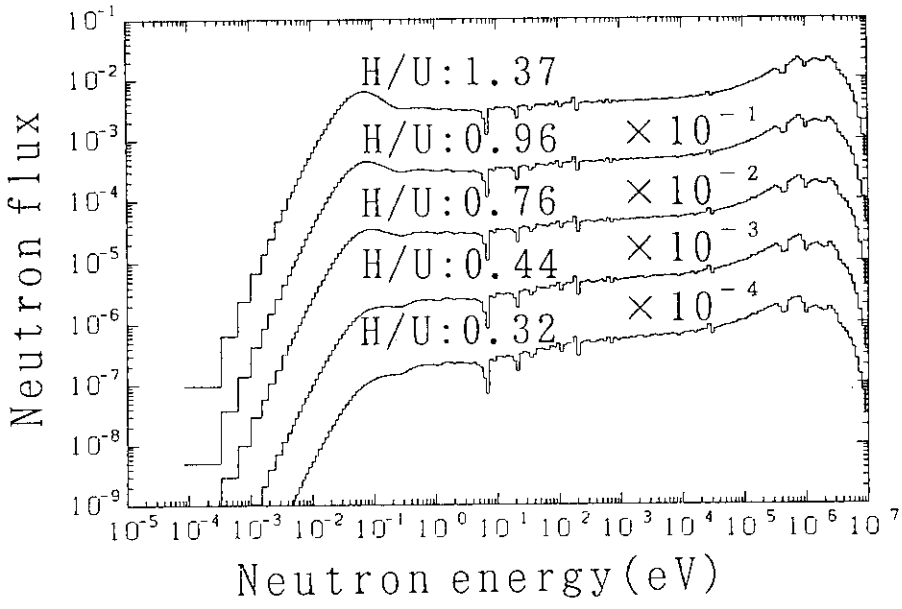

Fig. 1 Comparison of ZRP-7 neutron spectra.

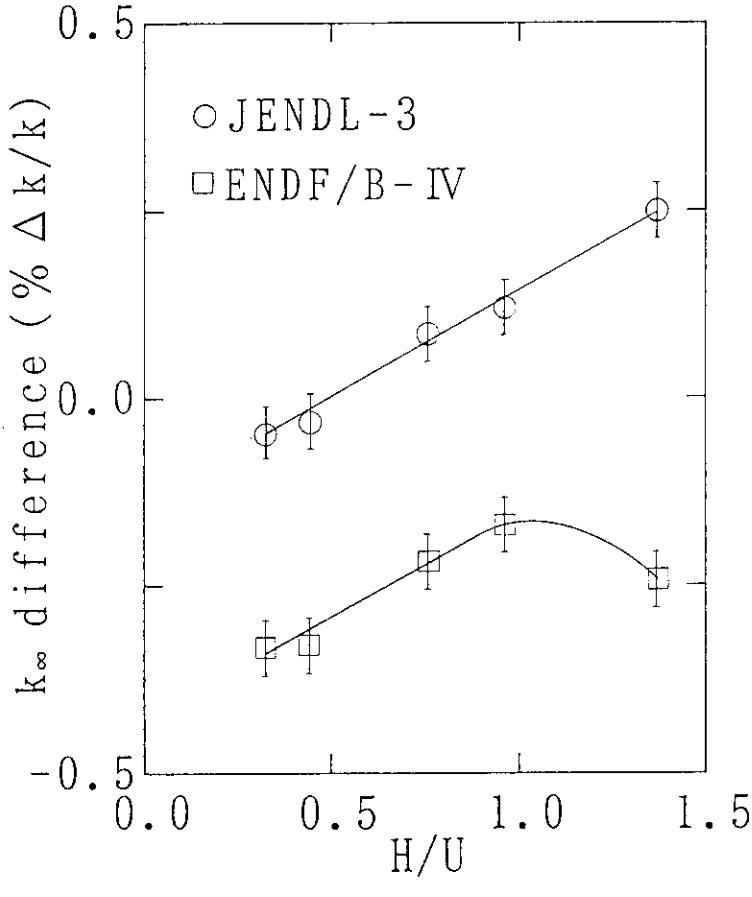

Fig. 2 Comparison of k_∞ in ZPR-7 (relative to JENDL-2).

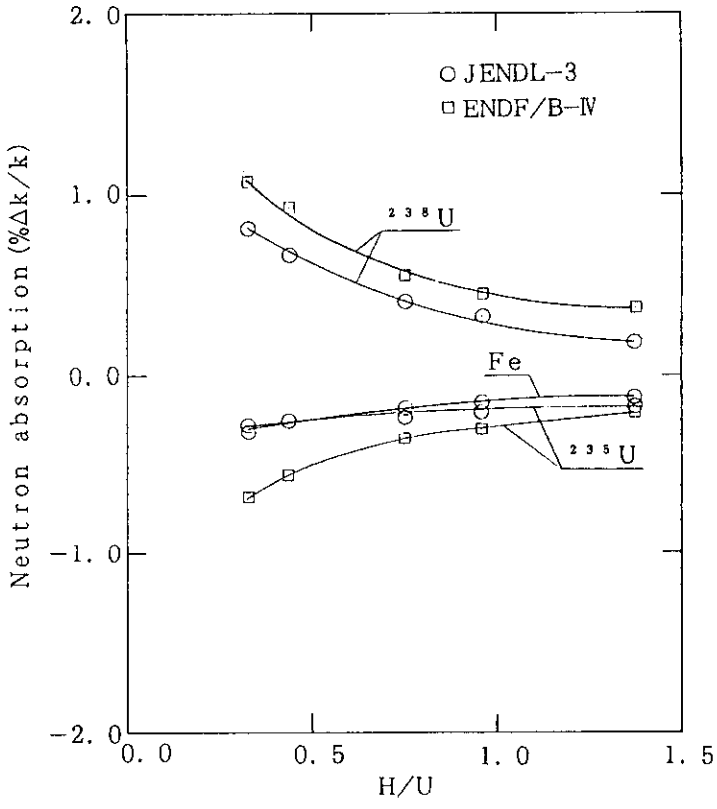

Fig. 3 Comparison of neutron absorption in ZPR-7 (relative to JENDL-2).

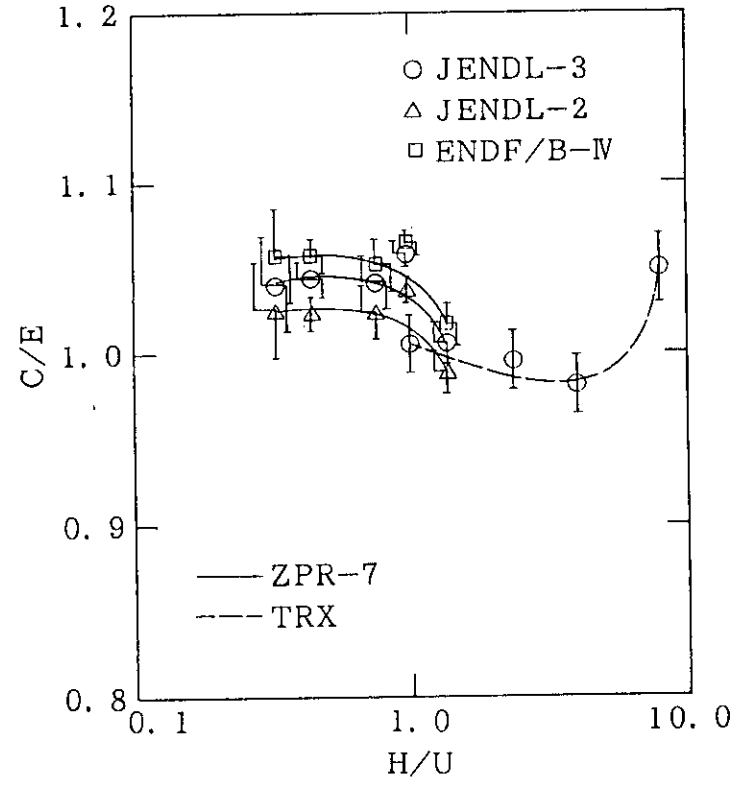

Fig. 4 ρ^{28} C/E vs H/U in ZPR-7 and TRX.

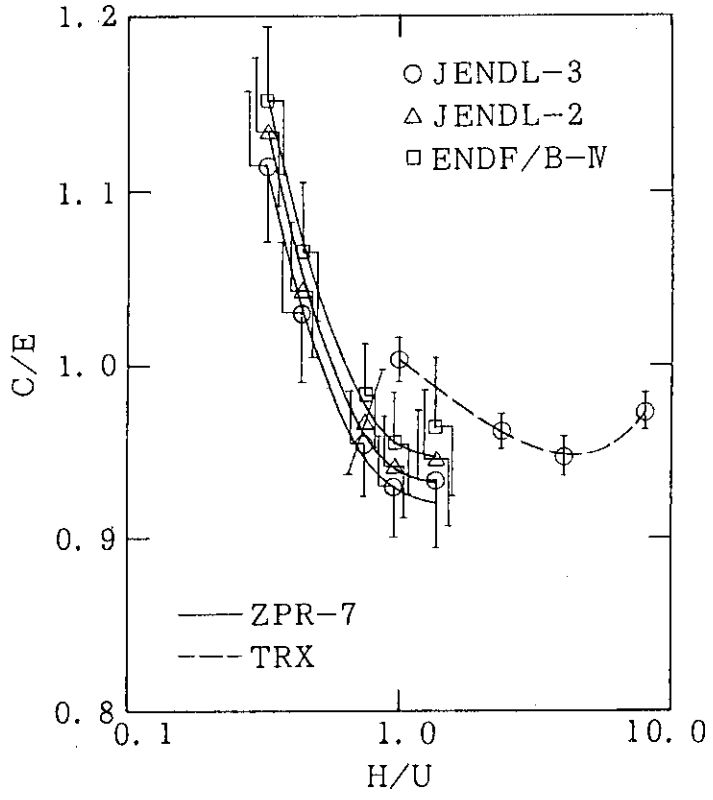

Fig. 5 δ^{25} C/E vs H/U in ZPR-7 and TRX.

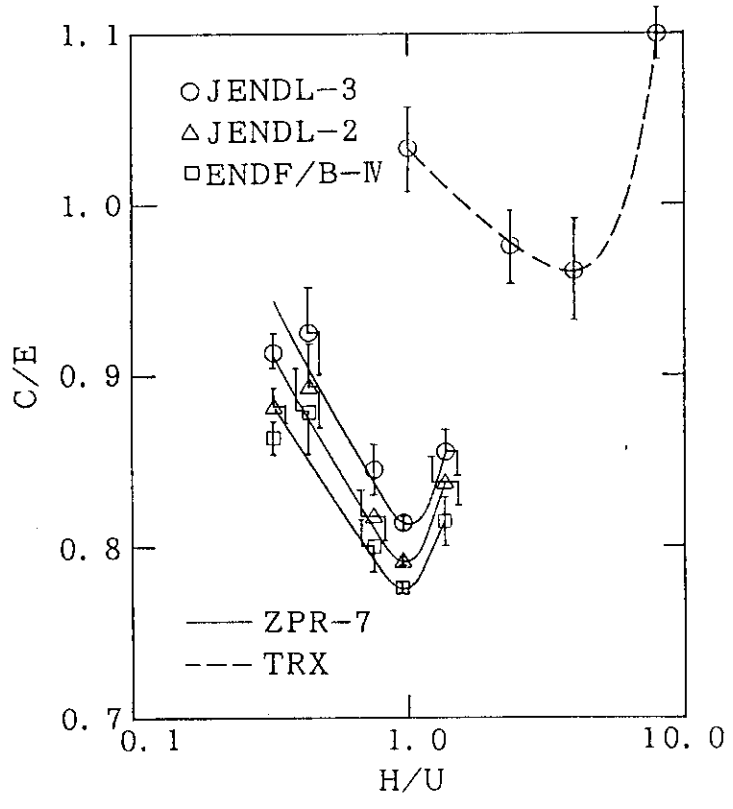

Fig. 6 δ^{28} C/E vs H/U in ZPR-7 and TRX.

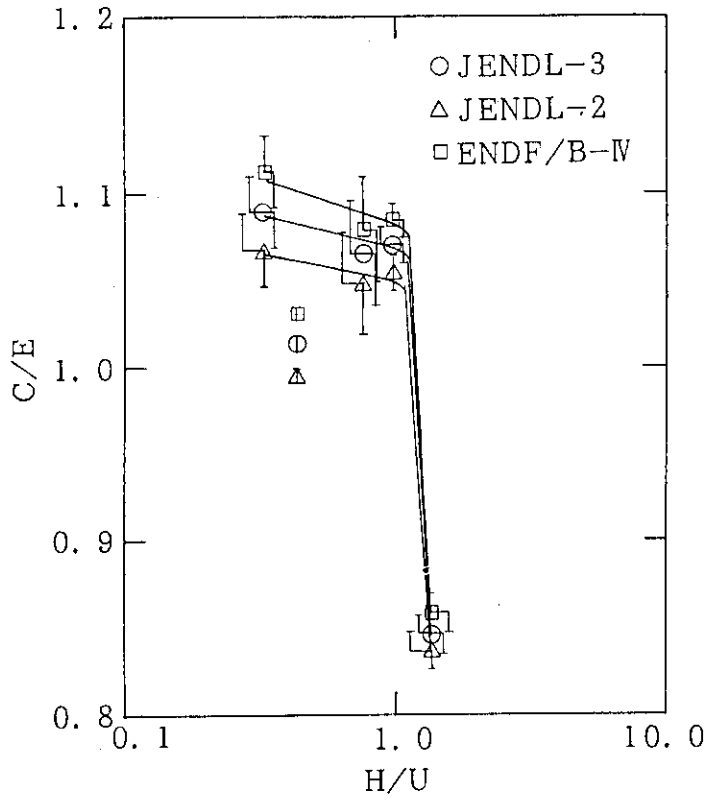

Fig. 7 ICR C/E vs H/U in ZPR-7.

3.3 ANALYSIS OF NEUTRON TRANSMISSION AND REFLECTION EXPERIMENTS WITH JENDL-3

M. Iwaki, T. Sawada and Y. Harima
Tokyo Institute of Technology
2-12-1 Ookayama, Meguro-ku, Tokyo

Abstract

The ANISN-JR and DIAC codes of one-dimensional discrete ordinates transport were used to analyze the results of two benchmark test experiments irradiated by D-T neutrons. One was to measure angular neutron flux spectra of transmission through important materials as fusion blankets, i.e., graphite, beryllium and lithium, of which thickness was 0.6 to 5 mean free path and the leaking angles were 12.2°, 24.9°, 41.8° and 66.8° for 14.8 MeV neutrons. The other was to measure neutron flux of reflection by shielding materials such as iron and aluminum. The measurement was performed at 120° for 15 MeV neutrons generated by an accelerator. The multi-group cross section data of 110 groups up to 16 MeV were generated from JENDL-3 nuclear data by using RADHEAT-V4 code system. The results of both transmission and reflection calculations agreed well with the measurements as well as the calculated results by the Monte Carlo codes, i.e., MORSE-DD and MCNP, in the energy region up to 10 MeV. On the other side, there were some discrepancies between calculations and measurements above 10 MeV and leaking angle of 66.8°.

1. Introduction

For the blanket and shielding materials of fusion reactors, it is crucial to calculate the neutron transmission and reflection of around 14 MeV neutron sources. Although it is desirable to apply multi-dimensional or Monte Carlo codes, sometimes we encounter the problem of massive CPU time. On the other hand, not so much effort has been done to validate the nuclear data library JENDL-3 for high energy neutron sources such as 14 MeV. The purposes of this study are: (1) to examine the applicability and limitation of one-dimensional Sn codes for calculation of high energy neutron transmission and reflection and (2) to validate the JENDL-3.

For this study, we selected two experiments; the one is for the neutron transmission performed by Oyama et al., JAERI /1/ and the other is for the reflection by Shin et al., Kyoto Univ. /2/ /3/.

The transmission experiment was performed by using slabs of candidate blanket materials: C, Be and Li_2O, while the reflection experiment for Al, Fe and Pb. JENDL-3 was used as the nuclear data library for the calculation. The neutron multi-group cross section data for the specified energy group structure were generated by using RADHEAT-V4 code system /4/. Two one-dimensional Sn computer codes, i.e., ANISN-JR /5/ and DIAC /4/, were used for the calculation. The calculated results were compared with experimental measurements as well as already existing calculational results by using Monte Carlo codes such as MORSE-DD and MCNP.

2. Review of Experiments

2.1 Transmission Experiment

The transmission experiment measured the angular-dependent neutron fluxes through slabs where a point-wise neutron source was used. Figure 1 depicts the schematics of the experiment set-up. The materials were graphite, beryllium and lithium oxide. The slabs had pseudo-columnar geometries with cross section radius of 31.5cm and varied thicknesses as listed in Table 1. The neutron source was generated by D-T reactions with the FNS facility in JAERI. The distance between the source and targets was 20 cm. The measured energy range and measured points are: 0.48-20.00 MeV, 150 points for C; 0.03-20.00 Mev, 130 for Be; and 0.03-20.00 Mev, 129 for Li_2O. The measure angles were: 0.0°, 12.2°, 24.9°, 41.8°, and 66.8°.

2.2 Reflection Experiment

Figure 2 depicts the schematics of the set-up for the reflection experiment. The slabs were rectangular and the materials of the slabs were aluminium, iron and lead with width and height of 120 cm x 67 cm, 60 cm x 80 cm, and 50 cm x 50 cm, respectively. The thicknesses were as listed in Table 1. The neutron source was generated by D-T reactions with the 200KeV Cockcroft-type accelerator in Kyoto Univ. The distance between the source and targets was 200 cm. The measured energy range of the reflected neutrons was 1.5-15 MeV. The measured angle was 120°.

3. Cross Section Data

The 110-energy group cross section data were generated by using RADHEAT-V4 code system based on the newest version of JENDL-3. The nuclides to be processed were $^{6}_{3}Li$, $^{7}_{3}Li$, $^{9}_{4}Be$, $^{12}_{6}C$, $^{14}_{7}N$, $^{16}_{8}O$, $^{27}_{13}Al$, $^{nat}_{24}Cr$, $^{55}_{25}Mn$, $^{nat}_{26}Fe$,

and $^{nat}_{28}Ni$. The energy range divided into 110 segments was 0.0669 - 16.375 MeV. The assumed material temperature was 300.0 K. Seven background cross sections were used: 10^{8},0, 1,10,10^{2},10^{3},10^{4} barn. The used weighting function is 1/E.

4. Calculation and Discussion

The transmission experiment was calculated by using DIAC and/or ANISN-JR, while the reflection experiment by DIAC only.

4.1 Transmission Calculation

For the transmission calculations, the input data were made by assuming the slabs to be infinite plainer geometries. The modelled zone and spatial mesh were shown in Fig. 3.

In order to model the shell source, the neutron source was placed on the boundary of the second spatial node and the shell source data were calculated as follows:

$$\text{Shell-Source}(n,g)=\int_{\eta_n}^{\eta_{n+1}} d\mu F(\mu) \int_{u_g}^{u_{g+1}} duh(u)$$

$$\approx\{F(\eta_{n+1})+F(\eta_n)\}(\eta_{n+1}-\eta_n)/2 \times \{h(u_{g+1})+h(u_g)\}(u_{g+1}-u_g)/2$$

where, $u=\ln(E_1/E)$

μ: $\cos(\theta)$, θ: transmission angle

u: lethargy,

F: distribution function of μ,

h: distribution function of u,

n: leaking angle index,

g: energy group index.

The calculations were done to obtain the angular fluxes for all the 17 direction points and for all the 110 energy groups. Fig. 4 - Fig. 7 show the angular fluxes calculated by ANISN-JR and DIAC for graphite compared with measurements and calculation by MCNP. The calculations by MCNP were performed by Ueki and Kawai /6/. It is clear that there is no difference between ANISN-JR and DIAC. The angular fluxes for 12.2°, 24.9° and 41.8° (Fig. 4, Fig. 5 and Fig. 6), the shapes and peaks up to 10 MeV are rather well calculated by ANISN/DIAC, while MCNP shows much better agreement with the

measurements. Here, the data points of MCNP are added only up to 10 MeV. For the energy region above 10 MeV, the flux peaks are not well calculated by ANISN/DIAC. As the angle increases, the values by ANISN/DIAC become greater and the deviation is unacceptable for the angle 66.8° (Fig. 7). In each angle, the discrepancy between the measurements and the ANISN/DIAC calculation is large in the energy region above 10 MeV. It may be desirable to perform further calculation with finer energy widths when generating group cross sections. The overshoot by ANISN/DIAC in the calculation for 66.8° can be ascribed to the fact that ANISN and DIAC are one-dimensional codes which cannot model the two-dimensional geometry of the slabs.

Fig. 8 - Fig. 10 show the angular fluxes for beryllium slab. The ANISN/DIAC values are compared with experiment as well as calculated values by MORSE-DD. The calculations by MORSE-DD were performed by Oyama and Maekawa /7/. The ANISN/DIAC calculations show good agreement with the experiment up to 10 MeV. Sometimes the calculated values are much closer to the measurements than the MORSE results. In the energy region above 10 MeV, the deviation between ANISN/DIAC and the measurement becomes unacceptably large for the angle 66.8°. This is the same tendency as that found for graphite.

Fig. 11 - Fig. 14 show the angular fluxes for lithium oxide. They show good agreement between calculations and measurements for lower energy regions. The same tendency like in graphite and beryllium is found for the deviation around the flux peak at 14.8 MeV.

4.2 Reflection Calculation

The input data were made in the same manner as the transmission calculation. The DIAC calculations were performed for aluminum and iron slabs. Fig. 15 shows the calculated values by DIAC compared with the measurements by Shin et al. It shows that DIAC has enough capability to calculate the high energy, i.e., 15 MeV, neutron reflection by aluminum slab. The calculation for iron slab has shown also good agreement with the measurements.

5. Conclusion

It was shown that one-dimensional discrete ordinates transport codes like ANISN-JR and DIAC have enough capability to calculate the transmission of neutrons around 14 MeV. There was not found any significant difference between the Monte Carlo codes and ANISN/DIAC in the energy region lower than 10 MeV. Also the applicability was confirmed concerning the transmission angle. Namely, for the large angle such as 66.8°, the calculated values showed unacceptable

deviations from the experimental measurements. On the other hand, the reflection of neutrons around 15 MeV was well calculated by DIAC.

Through this study, it was clarified that the one-dimensional codes with JENDL-3 can have the sufficient capability to calculate transmission and reflection of high energy incident neutrons. It is required, however, further calculation and analysis should be carried out for the transmission in the high energy region greater than 10 MeV.

References

/1/ Oyama, Y., et al.: Measurements and Analyses of Angular Neutron Spectra on Graphite and Lithium-Oxide Slabs Irradiated with 14.8 MeV Neutrons, J. Nucl. Sci. Technol., 25[5], pp.419-428 (May 1988)

/2/ Shin, K., et al.: Backscattering of Neutrons and Secondary Gamma-Rays from Aluminum and Lead Slabs for 15-MeV Neutrons, J. Nucl. Sci. Technol., 17[9], pp. 668-676 (September 1980)

/3/ Ban, S., et al.: Backscattering of Neutrons and Emergence of Secondary Gamma-Rays from Iron Slabs for 15-MeV Neutrons, Mem. Fac. Eng., Kyoto Univ., 41, 137 (1979)

/4/ Yamano, N., et al.: RADHEAT-V4: A Code System to Generate Multigroup Constants and Analyze Radiation Transport for Shielding Safety Evaluation, JAERI-1316 (March 1989)

/5/ Koyama, K., et al.: ANISN-JR, A ONE-DIMENSIONAL DISCRETE ORDINATES CODE FOR NEUTRON AND GAMMA-RAY TRANSPORT CALCULATIONS, JAERI-M 6954 (March 1977)

/6/ Ueki, K., and Kawai, M.: Evaluation of Beryllium, Carbon and Iron Neutron Cross Sections in the JENDL-3 by Monte Carlo Analysis of Benchmark Experiments, JAERI-M 91-062, pp.203-217 (March 1991)

/7/ Oyama, Y., and Maekawa, H. : Nuclear Data Test of JENDL-3 Using TOF Experiments at FNS, JAERI-M 91-062, pp. 228-245 (March 1991)

Table 1 The thicknesses of slabs

Material	Thickness (cm)
Graphite	5.06, 20.24, 40.48
Beryllium	5.08, 15.24
Lithium Oxide	4.8, 20.0, 40.0
Aluminum	10.0, 26.0
Iron	5.0, 10.0, 15.0
Lead	5.0

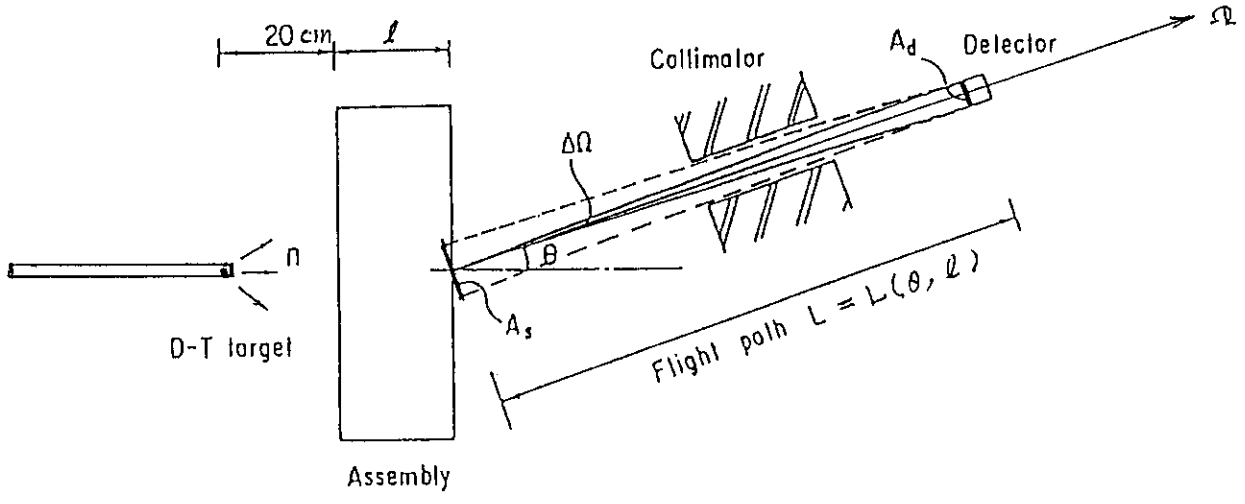

Fig. 1 Schematic set-up of transmission experiment.

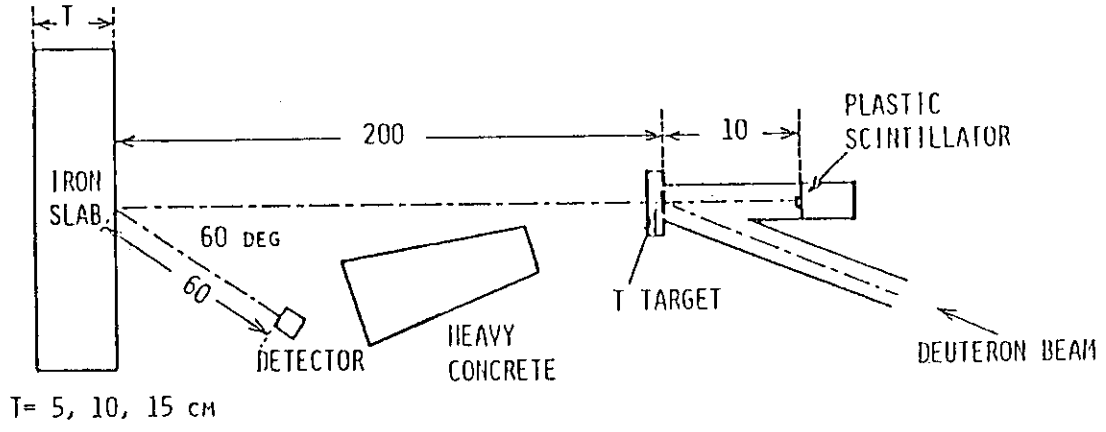

Fig. 2 Schematic set-up of reflection experiment.

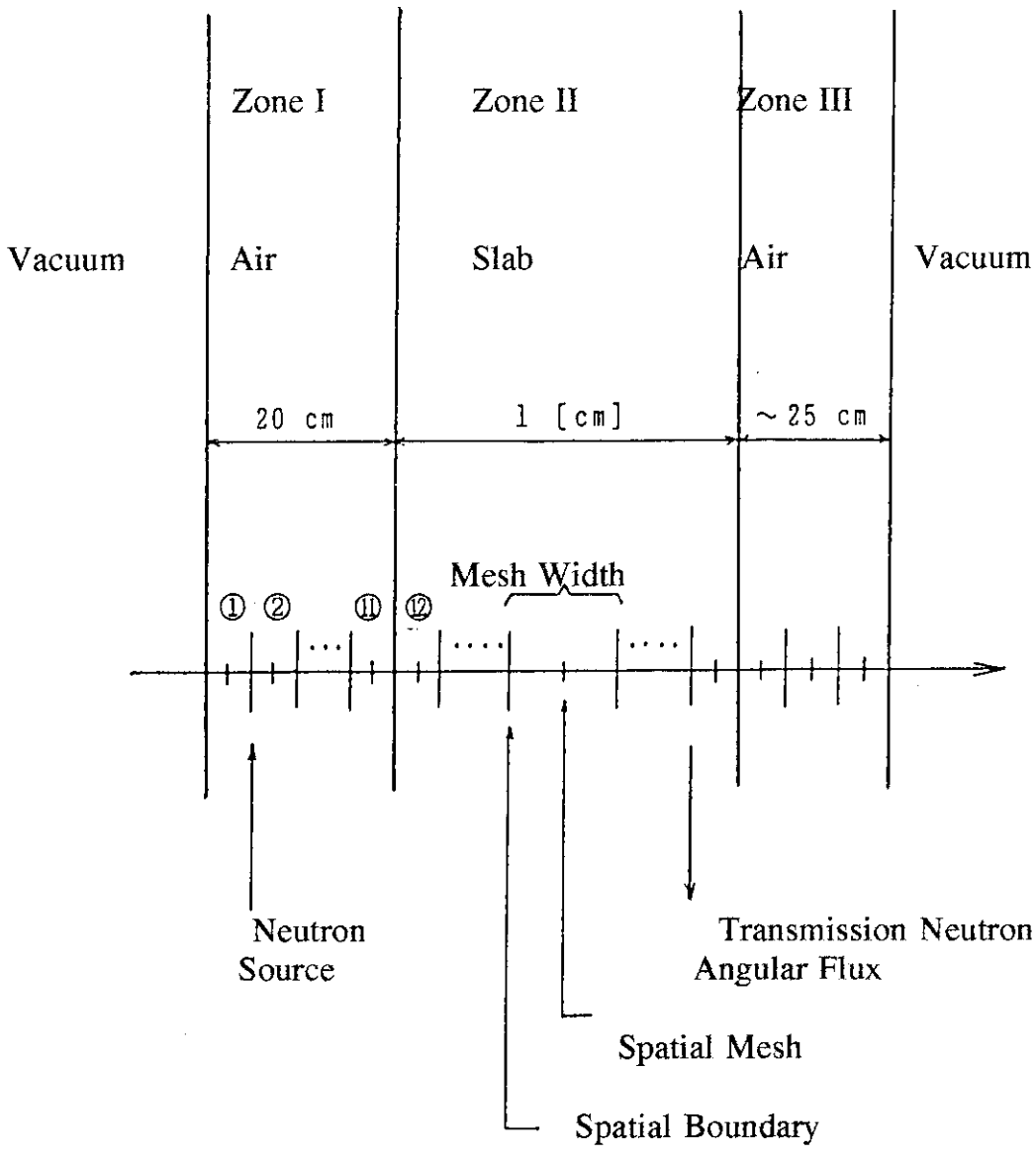

Fig. 3 Spatial mesh modelling for transmission calculation.

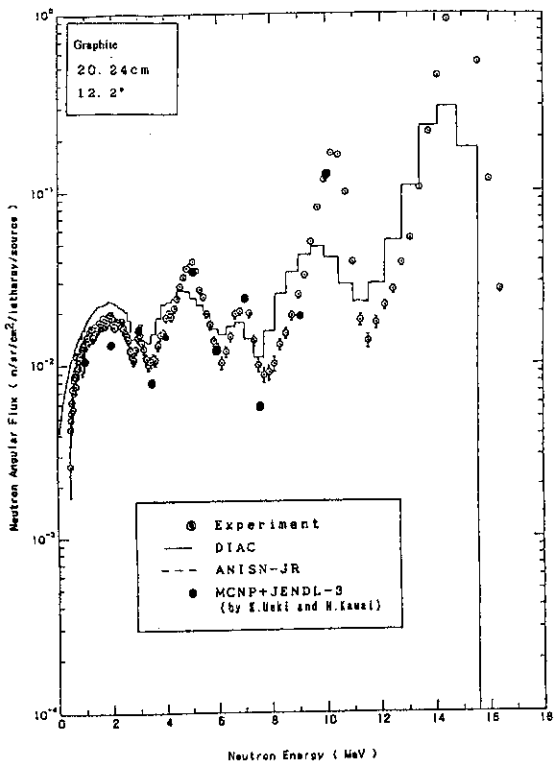

Fig. 4 Comparison among ANISN/DIAC, MCNP and experiment: Graphite 20.24 cm, 12.2°.

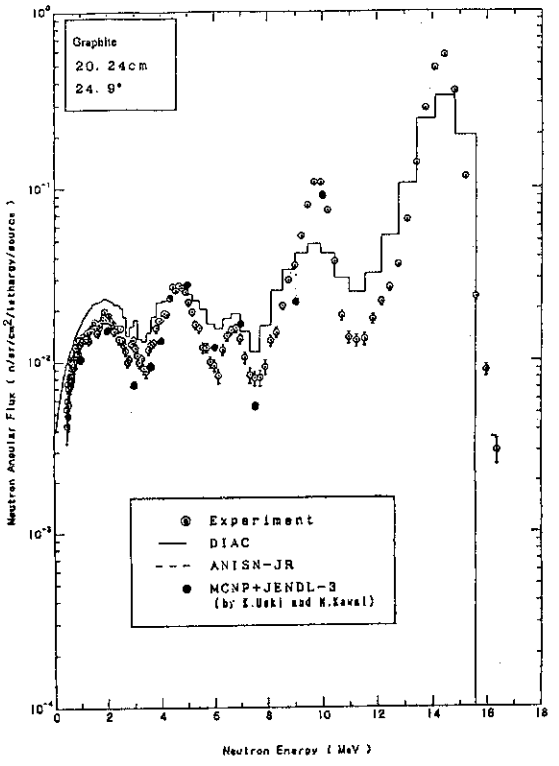

Fig. 5 Comparison among ANISN/DIAC, MCNP and experiment: Graphite 20.24 cm, 24.9°.

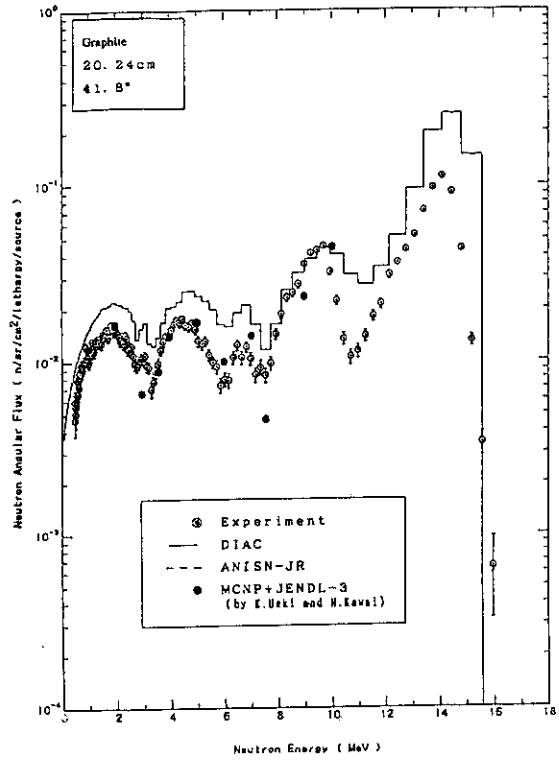

Fig. 6 Comparison among ANISN/DIAC, MCNP and experiment: Graphite 20.24 cm, 41.8°.

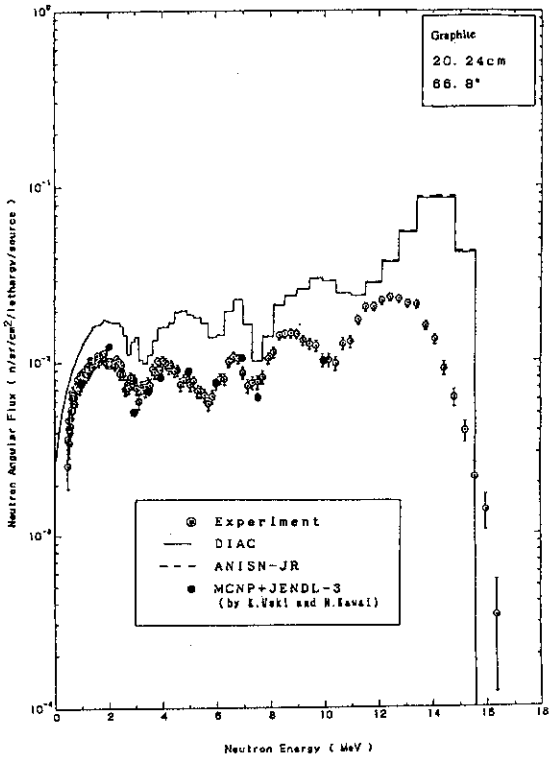

Fig. 7 Comparison among ANISN/DIAC, MCNP and experiment: Graphite 20.24 cm, 66.8°.

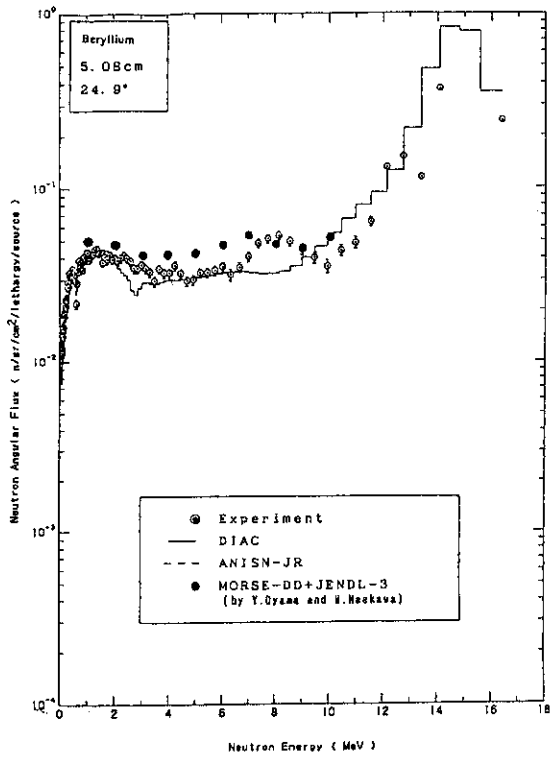

Fig. 8 Comparison among ANISN/DIAC, MORSE-DD and experiment: Beryllium 5.08 cm, 24.9°.

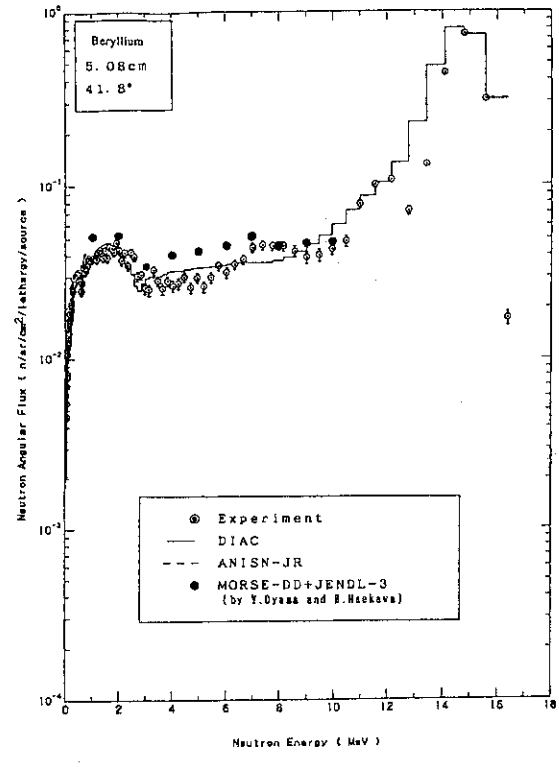

Fig. 9 Comparison among ANISN/DIAC, MORSE-DD and experiment: Beryllium 5.08 cm, 41.8°.

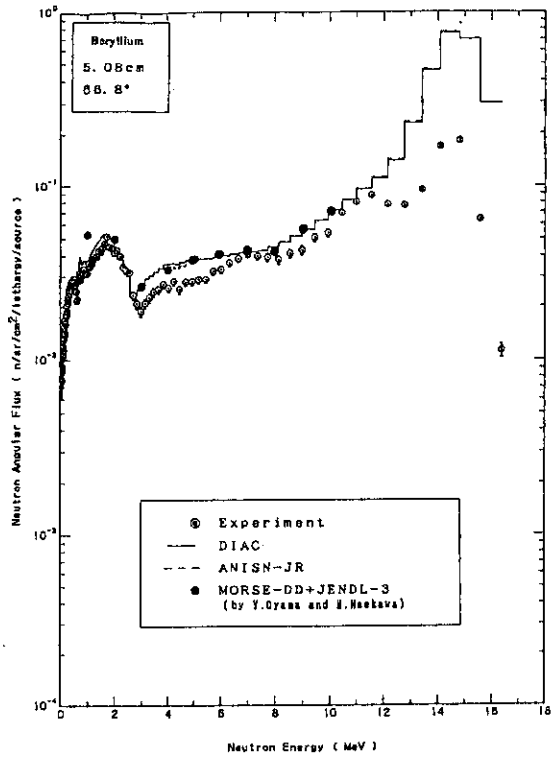

Fig. 10 Comparison among ANISN/DIAC, MORSE-DD and experiment: Beryllium 5.08 cm, 66.8°.

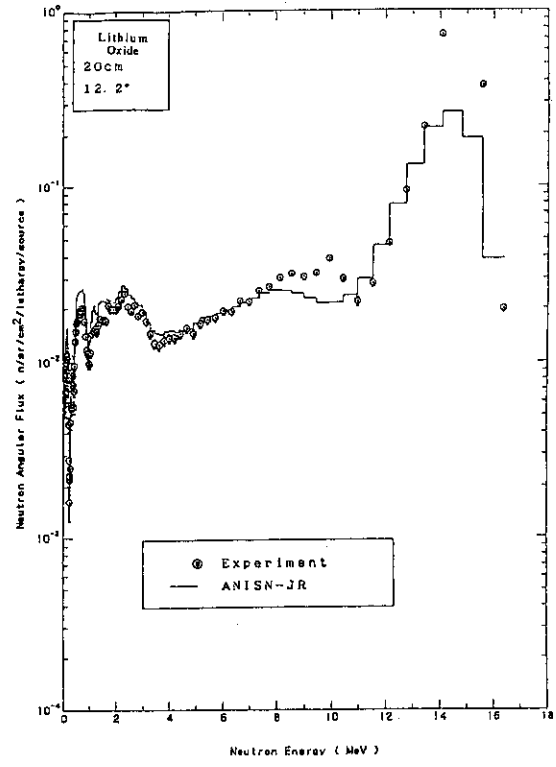

Fig. 11 Comparison between ANISN/DIAC and experiment: Lithium Oxide 20.0 cm, 12.2°.

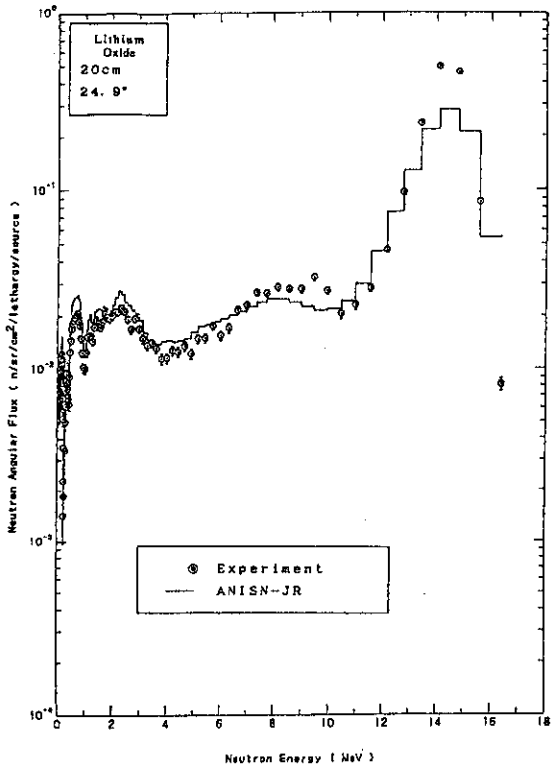

Fig. 12 Comparison between ANISN/DIAC and experiment: Lithium Oxide 20.0 cm, 24.9°.

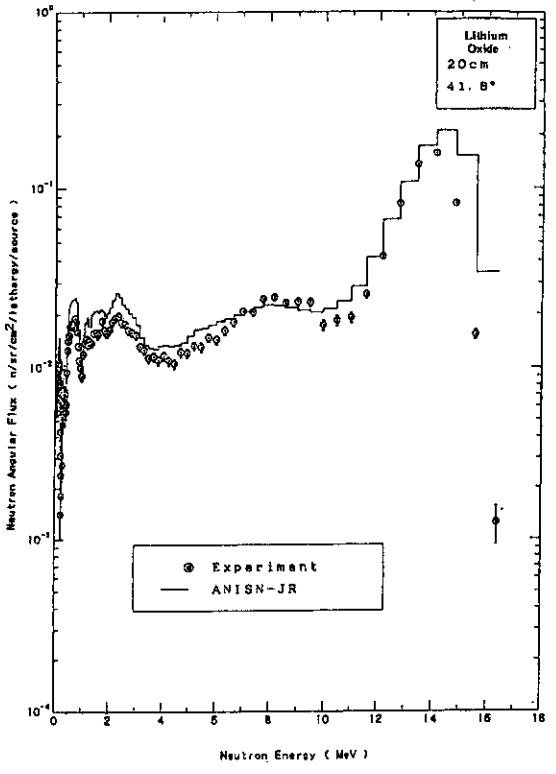

Fig. 13 Comparison between ANISN/DIAC and experiment: Lithium Oxide 20.0 cm, 41.8°.

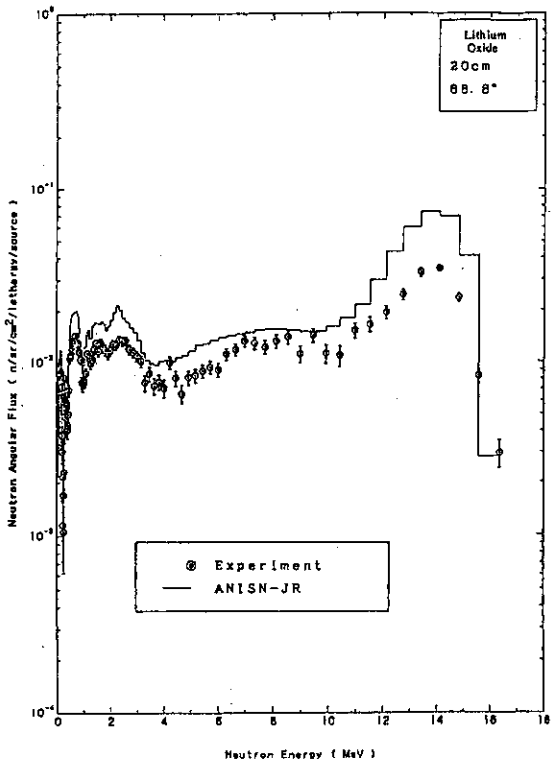

Fig. 14 Comparison between ANISN/DIAC and experiment: Lithium Oxide 20.0 cm, 66.8°.

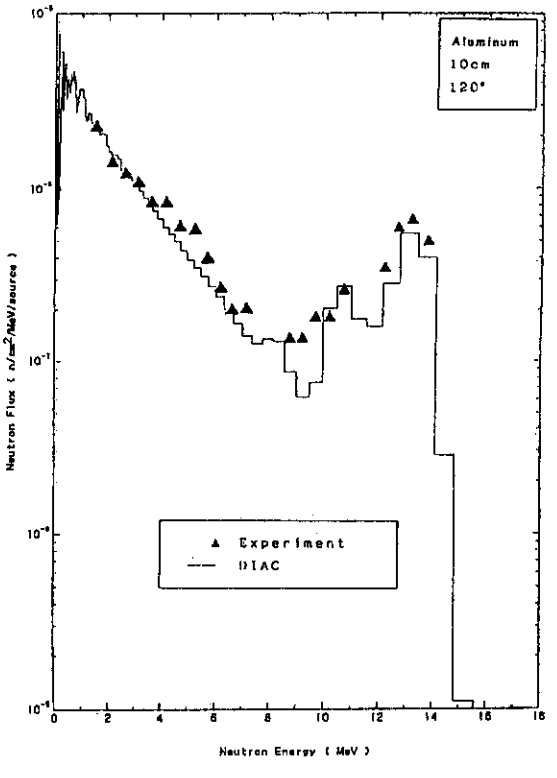

Fig. 15 Comparison between ANISN/DIAC and experiment: Aluminum 10.0 cm, 120°.

3.4 PROTOTYPE OF EVALUATION GUIDANCE SYSTEM IN INTEGRATED NUCLEAR DATA EVALUATION SYSTEM

T. Fukahori and T. Nakagawa
Nuclear Data Center, Japan Atomic Energy Research Institute
Tokai-mura, Naka-gun, Ibaraki, 319-11 Japan

Integrated Nuclear Data Evaluation System (INDES) is being developed to keep experiences of nuclear data evaluation for JENDL-3 and to support new evaluations. One of the INDES functions is to set up input data of theoretical calculation codes automatically. In order to use INDES effectively, a prototype of nuclear data evaluation guidance system (E.T.; Evaluation Tutor) was made to help users in selecting a set of suitable theoretical calculation codes by applying knowledge engineering technology. E.T. consists of an inference engine, frames, a rule-base, two example-bases and calculating modules of certainty factors. The inference engine and the calculating modules are written in FORTRAN77.

1. Introduction

Nuclear data evaluation is a complex work and needs a lot of time. Japanese Evaluated Nuclear Data Library, version 3 (JENDL-3)[1] released in 1989 was supported by great efforts of many evaluators. Integrated Nuclear Data Evaluation System (INDES)[2] is being developed to keep their experiences of nuclear data evaluation for JENDL-3 and to support new evaluations. One of the INDES functions is to set up input data of theoretical calculation codes automatically.

In order to use INDES effectively, a prototype of nuclear data evaluation guidance system (E.T.; Evaluation Tutor) was produced by applying knowledge engineering technology. E.T. supports users in selecting a set of suitable theoretical calculation codes. The theoretical calculation codes considered in E.T. are DWUCKY[3], ECIS[4], JUPITOR[5] and CASECIS[6] for the direct process, EGNASH[3], TNG[7], PEGASUS[8] and ALICE-F[9] for the preequilibrium process, CASTHY[10] and ELIESE-3[11] for the compound process, and RESCAL[12] and HIKARI[13] for other processes. The results of code selection

will be used in INDES.

E.T. consists of an inference engine, frames, a rule-base, two example-bases and calculating modules for certainty factors. The example-bases are used to obtain basic certainty factors from frequencies of use of the theoretical calculation codes. The inference engine and calculating modules of E.T. are written in FORTRAN77, since E.T. will be combined with INDES which is written in FORTRAN77 and FORTRAN77 is the most familiar language to evaluators. This report describes the databases and functions of E.T., and an example run of ^{56}Fe in 1-20 MeV neutron energy region.

2. Description of data required in E.T.

2.1 Example-bases

Two example-bases are used to obtain basic certainty factors of theoretical calculation codes from their frequencies of use. One example-base is created from experiences of JENDL-3 evaluation work, and another one is a supplementary example-base which stores results of code selection performed by E.T. A part of the example-base of JENDL-3 is shown in Fig.1. A unit in the example-bases consists of target isotope identification (TARGET), an incident particle (INCIDENT), and theoretical calculation codes used in the JENDL-3 evaluation (CODE). For instance, in the evaluation of neutron-induced reaction data of ^{56}Fe, four codes, CASTHY, ELIESE-3, EGNASH and ECIS, were used in the energy region from 0.01 meV to 20 MeV. EGNASH on the right hand side of the ELIESE3 line means that ELIESE-3 was used to make some input data of EGNASH.

2.2 Frames

Frames store functions of the theoretical calculation codes. Examples of the frames for DWUCKY and EGNASH are shown in Fig.2. A set of the frame consists of slots of frame name (FRAME), code type (TYPE), theories used in the code (THEORY), incident and outgoing particles treated in the code (INCIDENT and OUTGOING), an energy range (ENERGY), quantities calculated with the code in the MF and MT number expression of the ENDF format (QUANTITY), required input data (INPUT DATA), related codes (IN- and OUT-CODE), codes converting the output into the ENDF format (COMPILE) and comments (COMMENT). Values in the slots, except those of TYPE, QUANTITY and COMMENT, have certainty factors. For example, in the case of EGNASH, the certainty factors are 1.0 for incident particles of neutron and proton, and 0.8 in the energy range from 20 to 50 MeV. The certainty factor of

optical model parameters (OMP) is assumed to be 0.5, because EGNASH has default OMP in it, and OMP is not always needed. If the user does not like default OMP, he has to use ELIESE-3 and another set of OMP to calculate transmission coefficients. Therefore, ELIESE-3 is given in the slot of IN-CODE with the certainty factor of 0.5. Only GAMFIL2 can be used for data compilation in the ENDF format.

2.3 Rule-base

Rules are used to select the theoretical calculation codes in the inference engine. The rules are classified into five types; for the direct process, for the preequiliblium process, for the compound process, for the other process and for the codes related to others. Figure 3 shows the rules in the current rule-base. The rule-base consists of a part asking input data to the user (INPUT) and IF-THEN parts. If the INPUT part exists, prompt messages in the INPUT part are written on a screen of a terminal to require an answer from the user. The answer to the messages is 'Yes' or 'No', or number of options, and used in the IF part. The THEN part is performed when the IF part is satisfied. Available tasks in the THEN part are /PRINT/ to give the information to the user, /SET/ to set the values, /NEXT/ to set the next category of the theoretical calculation process such as direct process, /GOTO/ to go to the next rule, and /SEARCH/ to search codes satisfying conditions.

3. Procedure of selection of recommended codes

A schematic diagram of E.T. is shown in Fig.4. E.T. selects codes for four reaction processes; direct, preequiliblium, compound and other processes. After this selection, auxiliary codes related to the selected codes are chosen if necessary.

A flow chart of the E.T. to select a set of the recommended codes is described in Fig.5. Firstly the user inputs the basic data such as a target nucleus, a projectile and the incident energy region. Then, basic certainty factors which are frequencies of use are calculated from the example-bases by subroutine CFMAK1. The basic certainty factors are obtained for all the theoretical calculation codes registered in the example-bases, in 9 regions of target nuclei, and in the whole region. The 9 regions nuclei are separated into the atomic number Z=1-2, 3-6, 7-10, 11-30, 31-65, 66-83, 84-89, 90-94 and more than 94. Frame data are read in the core memory by subroutine RFRAME to save a calculation time.

Rules in the rule-base are executed in subroutine RULTSK to make a

preliminary decision of code selection. If the rule requires some additional information from the user, a prompt message is printed out on CRT and the user has to answer to it. All the codes in the frames are classified into four reaction processes; direct, preequliblium, compound and other processes. If the process is judged not to need to calculation by any rules, corresponding codes are omitted from the selection.

A functional certainty factor of each code is calculated in CFCHKF by averaging certainty factors given in the frame. Three candidates which have larger functional certainty factors are selected for each process, except the 'other' reaction process. After three candidates of each reaction process are selected, their frequency certainty factors are obtained in CFCHKJ by using the basic certainty factors calculated in CFMAK1 as following;

1) The basic certainty factor, $C1$, obtained from the example-base of JENDL-3 for the corresponding target region is multiplied by 0.5.
2) That of whole region, $C2$, is multiplied by 0.3.
3) 1), 2) and bias of 0.2 are summed up to get the frequency certainty factor, CF from the example-base of JENDL-3.

$$CF = C1 \times 0.5 + C2 \times 0.3 + 0.2$$

4) The same calculation is performed for the frequency certainty factor from the supplementary example-base.
5) The frequency certainty factors obtained from the two example-bases are averaged.

The candidate which has the maximum frequency certainty factor is selected for the recommended theoretical calculation code of each reaction process. For the 'other' process, each code is considered whether it is required by the user or not.

For the codes such as EGNASH requiring other auxiliary codes to make some input data, the related codes are added to the set of recommended codes. The result of the code selection is stored in the supplementary example-base and will be used at the next basic certainty factor calculation.

4. Example run

An example run of selecting a code set for ^{56}Fe neutron induced reaction calculation in the energy range from 1 to 20 MeV is described. The input and output data of E.T. are shown in Fig.6, where characters with underline are input data given by the user. A command 'et' initiates E.T., then prompt messages require basic input data. After this input, the rules are executed one by one. The result of this example is shown in Fig.6 which illustrates

that DWUCKY, EGANSH and CASTHY were selected for the direct, preequiliblium and compound processes with the final certainty factors of 0.65, 0.86 and 0.97, respectively. ELIESE-3 was selected to calculate transmission coefficients for EGNASH calculation since the user's answer was 'no' to the question whether default optical model parameters were used or not.

5. Concluding remarks

The prototype of nuclear data evaluation guidance system, E.T., was developed to support users in selecting theoretical calculation codes. This system helps not only beginners of the nuclear data evaluation being unfamiliar with using the theoretical calculation codes but also evaluators to make input data for preliminary calculations. Some mistakes might be hidden in the data in the rule-base, the example-base of JENDL-3 and the frames, and must be corrected. The rule-base should be expanded to more detailed procedures. The number of codes treated by E.T. should be also enlarged.

References

1) Shibata K., Nakagawa T., Asami T., Fukahori T., Narita T., Chiba S., Mizumoto M., Hasegawa A., Kikuchi Y., Nakajima Y. and Igarasi S., JAERI-1319 (1990).
2) Nakagawa T., Integrated Nuclear Data Evaluation System INDES (1991) unpublished.
3) Yamamuro N., JAERI-M 90-006 (1990).
4) Raynal J., IAEA SMR-9/8 (1970).
5) Tamura T., Rev. Mod. Phys., 37, 679 (1965).
6) Computer Program CASECIS for CASTHY-ECIS combined calculations.
7) Fu C.Y., ORNL/TM-7042 (1980).
8) Iijima S., Sugi T., Nakagawa T. and Nishigori T., JAERI-M 87-025, 337 (1987).
9) Fukahori T., Computer Program ALICE-F for medium energy preequiliblium process calculation (1990) unpublished.
10) Igarasi S. and Fukahori T., JAERI-1321 (1991).
11) Igarasi S., JAERI-1224 (1972).
12) Shibata K. and Chiba S., Computer Program RESCAL for R-matrix theory calculations (1987) unpublished.
13) Kitazawa H., Computer Program HIKARI for direct-semidirect capture calculations (1980) unpublished.

```
TARGET      26-FE- 54
INCIDENT   NEUTRON
CODE                4
           CASTHY      1.000E-05 2.000E+07
           ELIESE3     1.000E-05 2.000E+07          EGNASH
           EGNASH      1.000E-05 2.000E+07
           ECIS        1.000E-05 2.000E+07
END
TARGET      26-FE- 56
INCIDENT   NEUTRON
CODE                4
           CASTHY      1.000E-05 2.000E+07
           ELIESE3     1.000E-05 2.000E+07          EGNASH
           EGNASH      1.000E-05 2.000E+07
           ECIS        1.000E-05 2.000E+07
END
TARGET      26-FE- 57
INCIDENT   NEUTRON
CODE                3
           CASTHY      1.000E-05 2.000E+07
           ELIESE3     1.000E-05 2.000E+07          EGNASH
           EGNASH      1.000E-05 2.000E+07
END
TARGET      26-FE- 54
INCIDENT   NEUTRON
CODE                3
           CASTHY      1.000E-05 2.000E+07
           ELIESE3     1.000E-05 2.000E+07          EGNASH
           EGNASH      1.000E-05 2.000E+07
END
TARGET      27-CO- 59
INCIDENT   NEUTRON
CODE                3
           CASTHY      1.000E-05 2.000E+07
           EGNASH      1.000E-05 2.000E+07
           DWUCKY      1.000E-05 2.000E+07
END
TARGET      28-NI- 58
INCIDENT   NEUTRON
CODE                6
           CASTHY      1.000E-05 2.000E+07
           ELIESE3     1.000E-05 2.000E+07          EGNASH
           ELIESE3     1.000E-05 2.000E+07          PEGASUS
           EGNASH      1.000E-05 2.000E+07
           PEGASUS     1.000E-05 2.000E+07
           ECIS        1.000E-05 2.000E+07
END
```

Fig. 1 A part of example-base from JENDL-3.

```
FRAME                DWUCKY
TYPE                 DIRECT
THEORY               1
          DWBA                                                    1.0
INCIDENT             1
          NEUTRON                                                 1.0
OUTGOING             1
          NEUTRON                                                 1.0
ENERGY               4
           1.000E-05 1.000E+06                                    0.3
           1.000E+06 5.000E+06                                    0.5
           5.000E+06 2.000E+07                                    0.8
           2.000E+07 1.500E+09                                    0.6
QUANTITY            82
           3002 3051 3052 3053 3054 3055 3056 3057 3058 3059 3060 3061
           3062 3063 3064 3065 3066 3067 3068 3069 3070 3071 3072 3073
           3074 3075 3076 3077 3078 3079 3080 3081 3082 3083 3084 3085
           3086 3087 3088 3089 3090 4002 4051 4052 4053 4054 4055 4056
           4057 4058 4059 4060 4061 4062 4063 4064 4065 4066 4067 4068
           4069 4070 4071 4072 4073 4074 4075 4076 4077 4078 4079 4080
           4081 4082 4083 4084 4085 4086 4087 4088 4089 4090
INPUT DATA           2
           OMP                                                     1.0
           LEVEL(T)                                                1.0
IN-CODE              0
OUT-CODE             1
           EGNASH                DIRECT CROSS SECTION              1.0
COMPILE              0
COMMENT              2
          OUTPUT IS SET IN ENDF-5 FORMAT AND EGNASH INPUT FORMAT
          AUTOMATICALLY.
END
```

```
FRAME                EGNASH
TYPE                 PRECOMP
THEORY               2
          EXCITON                                                 1.0
          EVAPORATE                                               1.0
INCIDENT             2
          NEUTRON                                                 1.0
          PROTON                                                  1.0
OUTGOING             7
          NEUTRON                                                 1.0
          PROTON                                                  1.0
          DEUTERON                                                1.0
          TRITON                                                  0.8
          HELIUM3                                                 0.8
          ALPHA                                                   1.0
          GAMMA                                                   1.0
ENERGY               4
           1.000E-05 1.000E+06                                    0.5
           1.000E+06 2.000E+07                                    1.0
           2.000E+07 5.000E+07                                    0.8
           5.000E+07 1.500E+09                                    0.5
QUANTITY           146
           3001 3002 3004 3016 3017 3022 3023 3024 3025 3028 3029 3030
           3032 3033 3035 3036 3037 3041 3042 3051 3052 3053 3054 3055
           3056 3057 3058 3059 3060 3061 3062 3063 3064 3065 3066 3067
           3068 3069 3070 3091 3102 3103 3104 3105 3106 3107 3108 3109
           3111 3112 3113 3114 3115 3116 3201 3202 3203 3204 3205 3206
           3207 4002 4016 4017 4022 4023 4024 4025 4028 4029 4030 4032
           4033 4035 4036 4037 4041 4042 4051 4052 4053 4054 4055 4056
           4057 4058 4059 4060 4061 4062 4063 4064 4065 4066 4067 4068
           4069 4070 4091 5016 5017 5022 5023 5024 5025 5028 5029 5030
           5032 5033 5035 5036 5037 5041 5042 5091 6201 6202 6203 6204
           6205 6206 62071205112052120531205412055120561205712058120591
          2060120611206212063120641206512066120671206812069120701300314
          00315003
INPUT DATA           5
           OMP                                                     0.5
           LDP                                                     0.8
           LEVEL(T)                                                0.5
           LEVEL(C)                                                0.3
           KALBACH                                                 0.5
IN-CODE              2
           ELIESE3               TRANSMISSION COEFFICIENT          0.5
           DWUCKY                DIRECT CROSS SECTION              0.5
OUT-CODE             0
COMPILE              1
           GAMFIL2
COMMENT              0
END
```

Fig. 2 The example of frame.

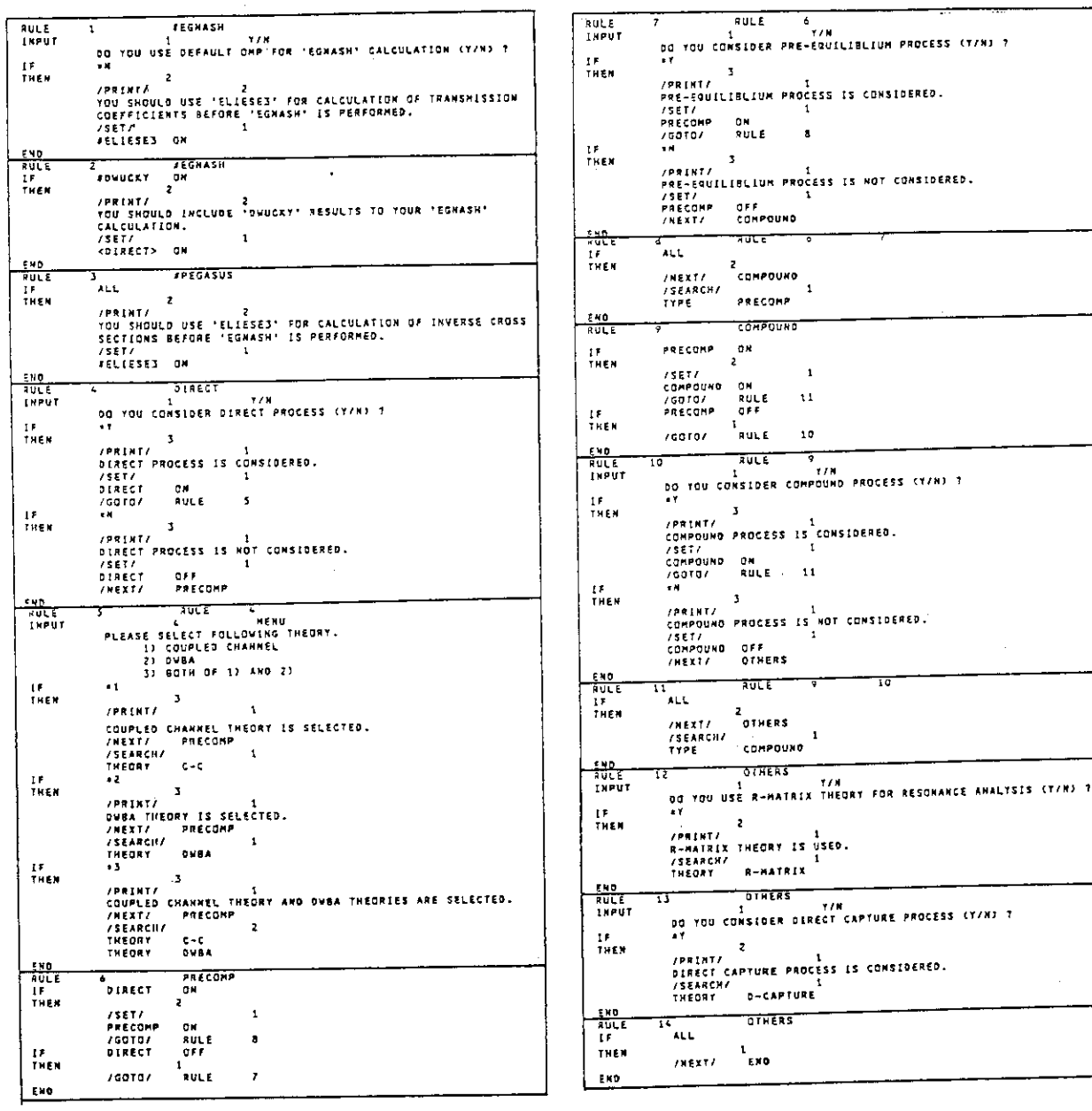

Fig. 3 The rules installed in the E.T.

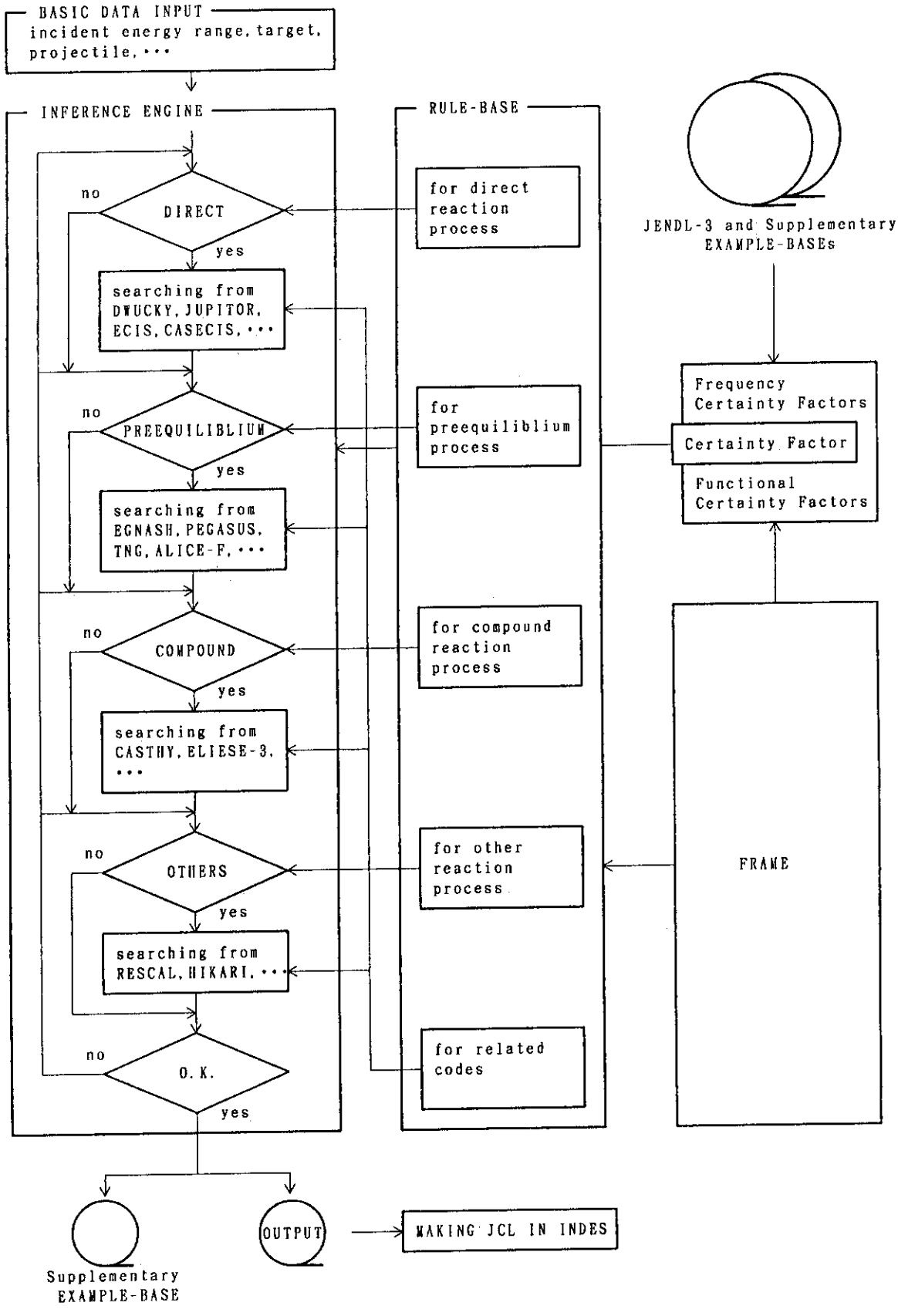

Fig. 4 A schematic diagram of the E.T.

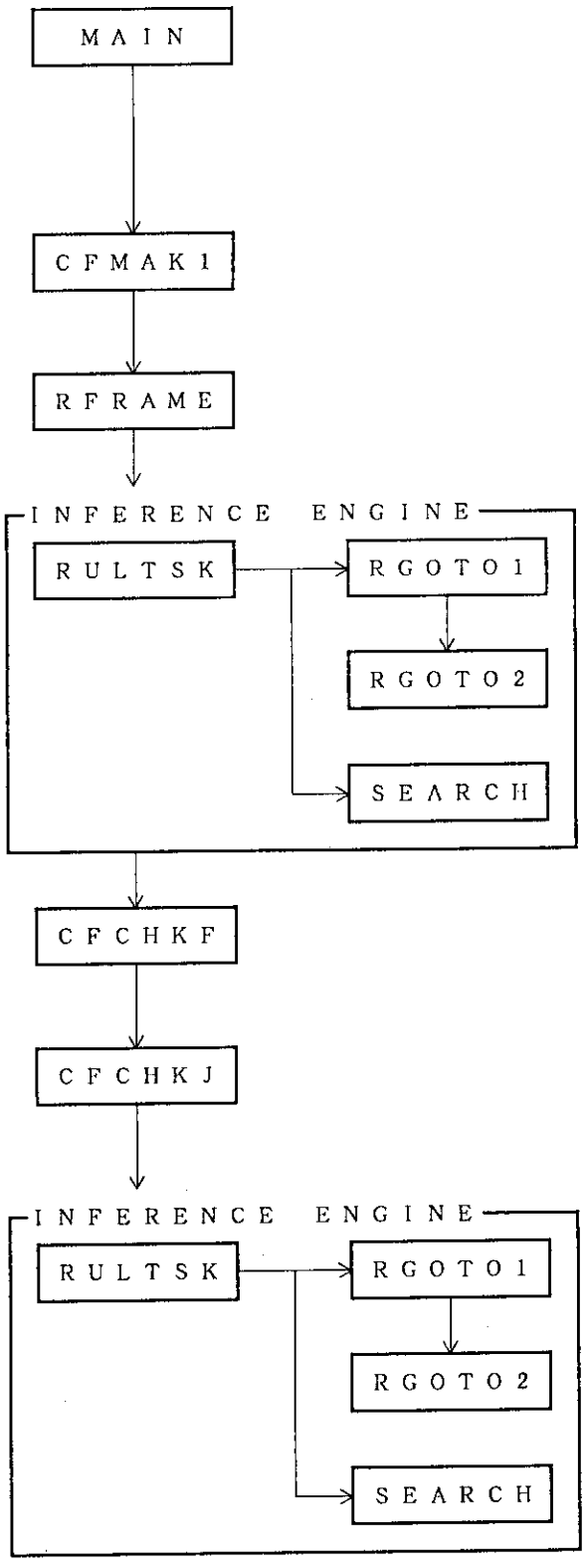

basic data input
task control
selection of a code set
by using rules
by using certainty factors
result output

calculation of
basic certainty foctors
from example-bases

input and strage of
frame data

performing rules
to classify codes

calculation of
functional certainty factors
from frame

calculation of
frequency certainty foctors
from basic certainty foctors

performing rules
for related codes

Fig. 5 Flow chart of the E.T.

```
READY
et
TIME-17:31:49 CPU-00:00:00 SERVICE-8433 SESSION-00:00:09 NOVEMBER 27,1991



E.T.> INPUT IZ, IA, IZAI, EMIN, EMAX
         IZ   : ATOMIC NUMBER OF TARGET
         IA   : MASS NUMBER OF TARGET
         IZAI : ZA OF INCIDENT PARTICLE
         EMIN : MINIMUM INCIDENT ENERGY
         EMAX : MAXIMUM INCIDENT ENERGY
07900 ?
  26, 56,  1,1.000e+06,2.000e+07
E.T.> DO YOU CONSIDER DIRECT PROCESS (Y/N) ?
07600 ?
y
E.T.> DIRECT PROCESS IS CONSIDERED.
E.T.> PLEASE SELECT FOLLOWING THEORY.
E.T.>      1) COUPLED CHANNEL
E.T.>      2) DWBA
E.T.>      3) BOTH OF 1) AND 2)
05700 ?
2
E.T.> DWBA THEORY IS SELECTED.
E.T.> DO YOU USE R-MATRIX THEORY FOR RESONANCE ANALYSIS (Y/N) ?
07600 ?
n
E.T.> DO YOU CONSIDER DIRECT CAPTURE PROCESS (Y/N) ?
07600 ?
n
E.T.> DWUCKY    IS SELECTED.
E.T.> EGNASH    IS SELECTED.
E.T.> DO YOU USE DEFAULT OMP FOR 'EGNASH' CALCULATION (Y/N) ?
07600 ?
n
E.T.> YOU SHOULD USE 'ELIESE3' FOR CALCULATION OF TRANSMISSION
E.T.> COEFFICIENTS BEFORE 'EGNASH' IS PERFORMED.
E.T.> YOU SHOULD INCLUDE 'DWUCKY' RESULTS TO YOUR 'EGNASH'
E.T.> CALCULATION.
E.T.> CASTHY    IS SELECTED.
```

```
********** RESULTS FOR  26-FE- 56  **********


CODE NAME = DWUCKY    FOR DIRECT    PROCESS WITH CF =    0.64664
         COMMENT :
         OUTPUT IS SET IN ENDF-5 FORMAT AND EGNASH INPUT FORMAT
         AUTOMATICALLY.

CODE NAME = EGNASH    FOR PRECOMP   PROCESS WITH CF =    0.86021
         COMPILATION CODE =  GAMFIL2

CODE NAME = CASTHY    FOR COMPOUND  PROCESS WITH CF =    0.97258
         COMPILATION CODE =  CTOB

CODE NAME = ELIESE3   FOR #EGNASH   PROCESS WITH CF =
         COMMENT :
          CALCULATED QUANTITIES DEPEND ON INCIDENT PARTICLE.  SO, MF
          AND MT NUMBERS CANNOT BE DEFINED AT THIS TIME.
         <DIRECT>  ON        #EGNASH

TIME-17:33:27 CPU-00:00:01 SERVICE-20068 SESSION-00:01:47 NOVEMBER 27,1991
READY
```

Fig. 6 Input and output data of the example run.

3.5 PARAMETERS OF REACTION CROSS SECTION CALCULATION FOR MEDIUM NUCLEI

T. Kawano, H. Tanaka, K. Kamitsubo, and Y. Kanda,
Department of Energy Conversion Engineering,
Kyushu University, Kasuga, Fukuoka 816, Japan

Abstract : Cross sections for neutron induced reactions of ^{58,60}Ni, ^{59}Co, and ^{54,56}Fe are calculated employing optical, Hauser-Feshbach, and pre-equilibrium models.

Neutron optical model parameters (OMP's) of target nuclei were estimated previously from experimental total cross sections and differential elastic scattering cross sections. These parameters are adopted for the Hauser-Feshbach calculation, and reaction cross sections are compared with ones when some global OMP's and the other published OMP's are employed. The comparisons of proton OMP's are also performed.

The reaction cross sections are calculated with some combinations of neutron and proton OMP, and the level density parameters are adjusted so as to reproduce available experimental data. Some of these combinations show that it is difficult to reproduce the experimental data by means of adjustment of level density parameters only.

1. Introduction

Cross sections for neutron induced reactions of medium nuclei are calculated employing optical, Hauser-Feshbach, and pre-equilibrium models. In order to use these models, it is essential to examine and determine input parameters that are valid for these models. The important parameters of these models are Optical Model Parameters (OMP) that give transmission coefficients, and level density parameters in Fermi gas model.

The level density parameters in the Fermi gas model are very important quantities in the Hauser-Feshbach calculations. These parameters are, however, regarded as adjustable parameters though the level density is inherent in each nucleus. The reason is that it is impractical to know a level scheme and an average resonance space exactly for every nuclide. Then, for practical calculation of the cross sections, the level density parameters are usually taken from Gilbert and Cameron's study[1] as initial guesses and the parameters are considered to be adjustable, so the parameters are adjusted so as to reproduce the experimental reaction cross section data. At this point, we must take care that changes of the parameters satisfy physical acceptance and that the parameters are able to reproduce many kinds of experimental data consistently. In order to pass these restrictions, we have been used a statistical method[2] for simultaneous estimation

of the nuclear reaction model parameters. However, when we adjust the level density parameters, the changes of the parameters depend on the OMP's employed in the calculation. Under these conditions it is difficult to confirm the level density parameters.

For the neutron OMP, there are many published global and regional OMP's. Almost these parameters, however, have limitations for use. The optical potential parameters sometimes show strong energy dependencies in the low energy region (10≤MeV). And calculated total cross sections with them are sometimes incompatible with the experimental data. Therefore, in order to refine the estimation of the level density parameters, the neutron OMP's should be determined accurately for each target nuclei.

In the previous study[3], the neutron OMP's for ^{58,60}Ni and ^{59}Co were estimated by total cross section and differential elastic scattering cross section data. Recently the OMP for ^{54,56}Fe was also estimated with the same method. In this study, these OMP's are adopted for the Hauser-Feshbach calculation, and reaction cross sections are compared with ones which are deduced when some global OMP's and the other published OMP's are employed. Some combinations of the neutron and proton OMP are employed, and then, the level density parameters are adjusted so as to reproduce available experimental data of ^{60}Ni(n,p), ^{58}Ni(n,p),(n,α),(n,2n), ^{59}Co(n,p),(n,α),(n,2n), ^{56}Fe(n,p),(n,2n), and ^{54}Fe(n,p),(n,α),(n,2n) reactions. The computer program ELIESE-3[4] is used to the optical model calculation, and GNASH[5] is used to the Hauser-Feshbach calculation.

2. Optical Model Parameter

Neutron

The neutron OMP's for ^{60,58}Ni, ^{59}Co, and ^{56,54}Fe was estimated by experimental differential elastic scattering cross section and total cross sections. Hereafter these OMP's are denoted by "estimated OMP's" for convenience' sake. The estimated OMP's have energy dependencies in their potential geometries. Figures 1 and 2 give comparisons of calculated total cross sections of ^{60,58}Ni with the experimental data smoothed with the B-spline function. In these figures, the light solid line and symbols represents the smoothed experimental total cross sections, the heavy solid line is the result of optical model calculation with the estimated OMP in Ref.3, and the other lines are calculated with global OMP's of Walter-Guss[6], modified Walter-Guss[7], Becchetti-Greenlees[8], Wilmore-Hodgson[9], and Rapaport, et al.[10], and OMP for ^{60,58}Ni proposed by Guss, et al.[11], ^{58}Ni proposed by Prince[12], Smith et al.[13]. In general it is difficult for any OMP set to reproduce experimental total cross section data below 4MeV, and the estimated OMP improve the reproduction of experimental data in this energy region.

These neutron OMP set and Gilbert-Cameron's level density parameters are

employed for the Hauser-Feshbach calculations of ^{58}Ni combined with Perey's proton OMP[14] and Lemos' α-particle OMP[15], and calculated results are shown in Fig.3. As seen in Fig.3-(c), (n,2n) reaction is very sensitive to the neutron OMP. In the energy range of E_n= 12~15MeV, excitation energy of residual nucleus of (n,2n) reaction is low(Q=-12.2MeV), then the cross section is almost independent of the level density of the residual nucleus, and it is sensitive to OMP in low energy region in the Hauser-Feshbach calculation. The estimated OMP yields small reaction cross section compared with the other global OMP's below 4MeV. Then the calculated (n,2n) cross section with the estimated OMP is quite small value.

Proton

The OMP of proton is significant for the Hauser-Feshbach calculations because a competition of proton emission process with neutron emission from a compound nucleus is important. Of course it is ideal to determine the proton OMP accurately for each target nuclei if possible. The situation is, however, different from the case of neutron. It is difficult to determine the OMP by experimental data in the low energy region because of existence of Coulomb potential. Therefore we employ some global proton OMP's, and investigate availability and validity of them. The calculated reaction cross sections with some global OMP's[6,8,14,16,17] are shown in Fig.4. In this figure, the neutron OMP is fixed to the estimated value, and the level density parameters are Gilbert-Cameron's. This figure indicates that the change of proton OMP appears in the difference of the absolute value and the excitation functions for each reactions are similar.

As mentioned above, (n,2n) reaction is sensitive to the OMP in the low energy region. It is transmission coefficients that Hauser-Feshbach calculation requires practically. However, it is a convenient way to compare the reaction cross sections instead of transmission coefficients. The reaction cross sections calculated with the global proton OMP are displayed in Fig.5. In these figures, the reaction cross sections are expressed by the ratio to the value calculated with Perey's OMP, and the cross section calculated with Arthur-Young's proton OMP[18] is also displayed. The OMP proposed by Arthur-Young is almost equivalent to the Perey's OMP, then there is no significant difference. The other OMP's show remarkable differences in the low energy region, and order of the reaction cross sections is directly connected with the Hauser-Feshbach calculations, as seen in Fig.4.

Figures 6 and 7 show sensitivities of proton OMP for ^{58}Ni(n,p), (n,2n) reactions when these cross sections are calculated with the estimated neutron OMP and the Perey's proton OMP. The abscissa of these figures is proton energy where the transmission coefficients are calculated, and the ordinate is a relative sensitivity($(\partial\sigma/\partial V_0)\cdot(V_0/\sigma)$, $(\partial\sigma/\partial W_s)\cdot(W_s/\sigma)$) of potential(V, W_s). The real potential V is expressed as $V=53.3(=V_0)-0.55E+27.0\epsilon+0.4ZA^{-1/3}$ [MeV], and the imaginary potential W_s is expressed as W_s=13.5 [MeV]. It is indicated in Fig.6 that

^{58}Ni(n,2n) cross section at E_n=15MeV is sensitive to the proton transmission coefficients in the low energy region, and the sensitivity takes the negative largest value at E_p=3MeV. As shown in Fig.7, the imaginary potential is insensitive to the Hauser-Feshbach calculation.

3. Level Density Parameter

In order to investigate adequacy of the OMP's of both neutron and proton employed for the Hauser-Feshbach calculations, the reaction cross sections of ^{58,60}Ni, ^{59}Co, and ^{54,56}Fe are calculated with some combinations of neutron and proton OMP, and the level density parameters are estimated simultaneously so as to reproduce available experimental data. The combinations are (1)estimated / Perey, (2)modified Walter-Guss[7] / Perey, (3)estimated / Menet, et al., and (4)estimated / Mani, et al. The estimated level density parameters depend on the OMP combinations. The reaction cross sections of ^{58}Ni calculated with the estimated level density parameters are shown in Fig.8. For the case (3), calculated (n,2n) cross sections before adjustment are much lower than the experimental data as seen in Fig.4-(c), then (n,p) and (n,α) reaction cross sections are reduced in order to increase (n,2n) cross section, and consequently, it gives quite different excitation functions from experimental data. It indicates that it is difficult to reproduce the experimental data by means of level density parameters only when incompatible combination of neutron and proton OMP's is used.

For the case (1), (2), and (4), the calculated ^{58}Ni(n,p) and (n,2n) reaction cross sections agree within the uncertainties of the experimental data. The (n,α) reaction cross sections are, however, quite different among them. Numbers of experimental data points of (n,p) and (n,2n) are much larger than that of (n,α), and the (n,α) reaction cross sections also depend on the OMP of α-particle. Therefore the differences of the (n,α) are not essential in this study.

We can regard these cases (1, 2 and 4) as capable of the consistent Hauser-Feshbach calculation with the experimental data by means of level density parameter adjustment. However, the estimated level density parameters are different for each case. Then, it is difficult to conclude which combination of OMP and level density parameters gives reliable calculation of cross section.

4. Conclusion

The estimated OMP's which yield consistent total and differential elastic scattering cross sections are used to the Hauser-Feshbach calculations with some global proton OMP's. The level density parameters are estimated so as to reproduce the available experimental reaction cross section data. When the estimated neutron OMP's are combined with proton OMP of Menet, et al., it is difficult to reproduce the experimental data by means of adjustment of level density parameters only. The

other proton OMP's give consistent reaction cross sections with experimental data, and we can refine the calculated results by means of level density parameter adjustment.

References

[1] A.Gilbert and A.C.W.Cameron : Can. J. Phys., **43**, 1446 (1965).

[2] Y.Uenohara, T.Tsuji, and Y.Kanda : Proc. Int. Conf. on Nuclear Data for Science and Technology, 1988, Mito, p.481.

[3] T.Kawano, et al. : Proc. Int. Conf. on Nuclear Data for Science and Technology, Jülich(1991), to be published.

[4] S.Igarasi : "Program ELIESE-3, Program for Calculation of the Nuclear Cross Sections by Using Local and Non-Local Optical Models and Statistical Model", JAERI-1224, (1972).

[5] P.G.Young and E.D.Arthur : "GNASH, A Pre-equilibrium, Statistical Nuclear-Model Code for Calculation of Cross Sections and Emission Spectra", LA-6947,(1978).

[6] R.L.Walter and P.P.Guss : Proc. Int. Conf. Nucl. Data for Basic and Applied Science, Santa Fe(1985), p.1079.

[7] N.Yamamuro : JAERI-M 88-140(1988).

[8] F.D.Becchetti,Jr. and G.W.Greenlees : Phys. Rev., **182**, 1190(1969).

[9] D.Wilmore and P.E.Hodgson : Nucl. Phys., **55**, 673(1964).

[10] J.Rapaport, V.Kulkarni, and R.W.Finlay : Nucl. Phys., **A330**, 15(1979).

[11] P.P.Guss, et al. : Nucl. Phys., **A438**, 187(1985).

[12] A.Prince : Proc. Int. Conf. on Nuclear Data for Science and Technology, Antwerp(1982), p.574.

[13] A.B.Smith, et al. : "Fast Neutron Total and Scattering Cross Sections of ^{58}Ni and Nuclear Models", ANL/NDM-120(1991).

[14] F.G.Perey : Phys. Rev., **131**, 745(1963).

[15] O.F.Lemos : "Diffusion Elastique de Particules Alpha de 21 a 29.6 MeV sur des Noyaux de la Region Ti-Zn", Orsay report, Series A, No.136(1972).

[16] G.S.Mani, M.A.Melkanoff, and I.Iori : "Proton Penetrabilities using an Optical Model Potential", CEA-2379(1963).

[17] J.J.H.Menet, et al. : Phys. Rev., **C4**, 1114 (1971).

[18] E.D.Arthur and P.G.Young : Proc. of Sym. on Neutron Cross Sections from 10 to 50 MeV, 1980, BNL, p.731.

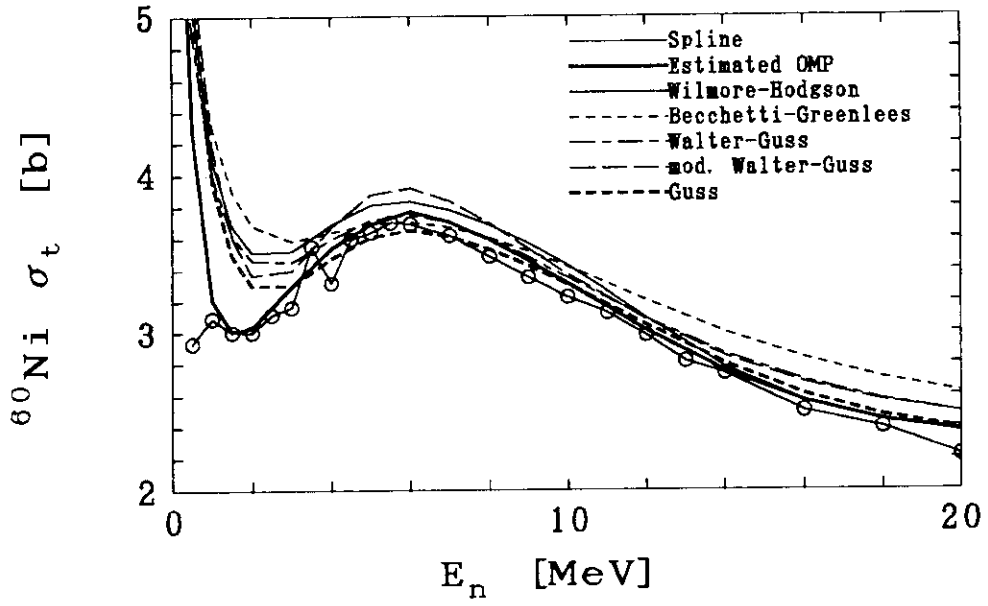

Fig. 1 Comparison of calculated total cross sections of ^{60}Ni with the experimental data smoothed by B-spline function.

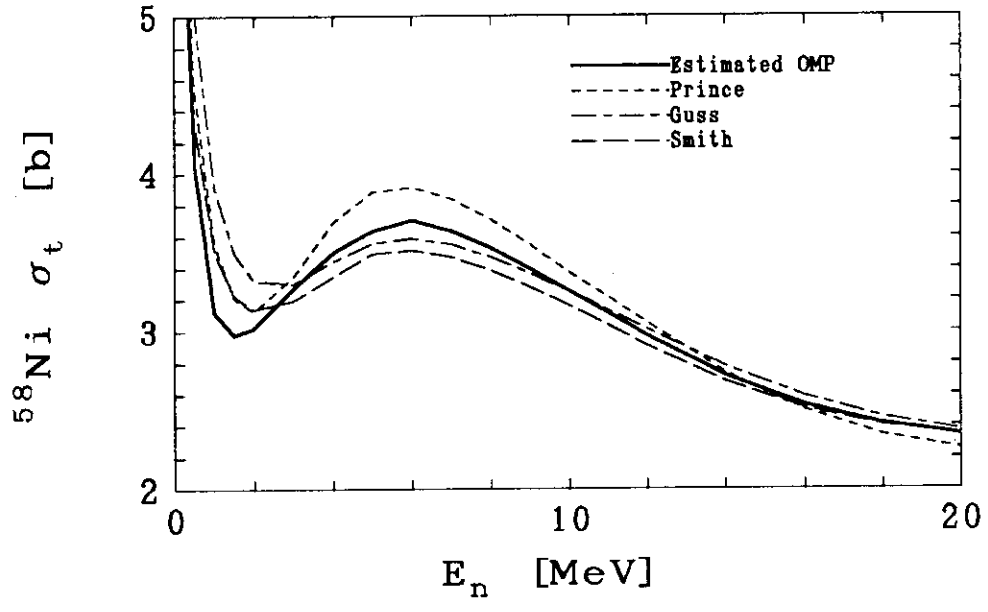

Fig. 2 Comparison of calculated total cross sections of ^{58}Ni.

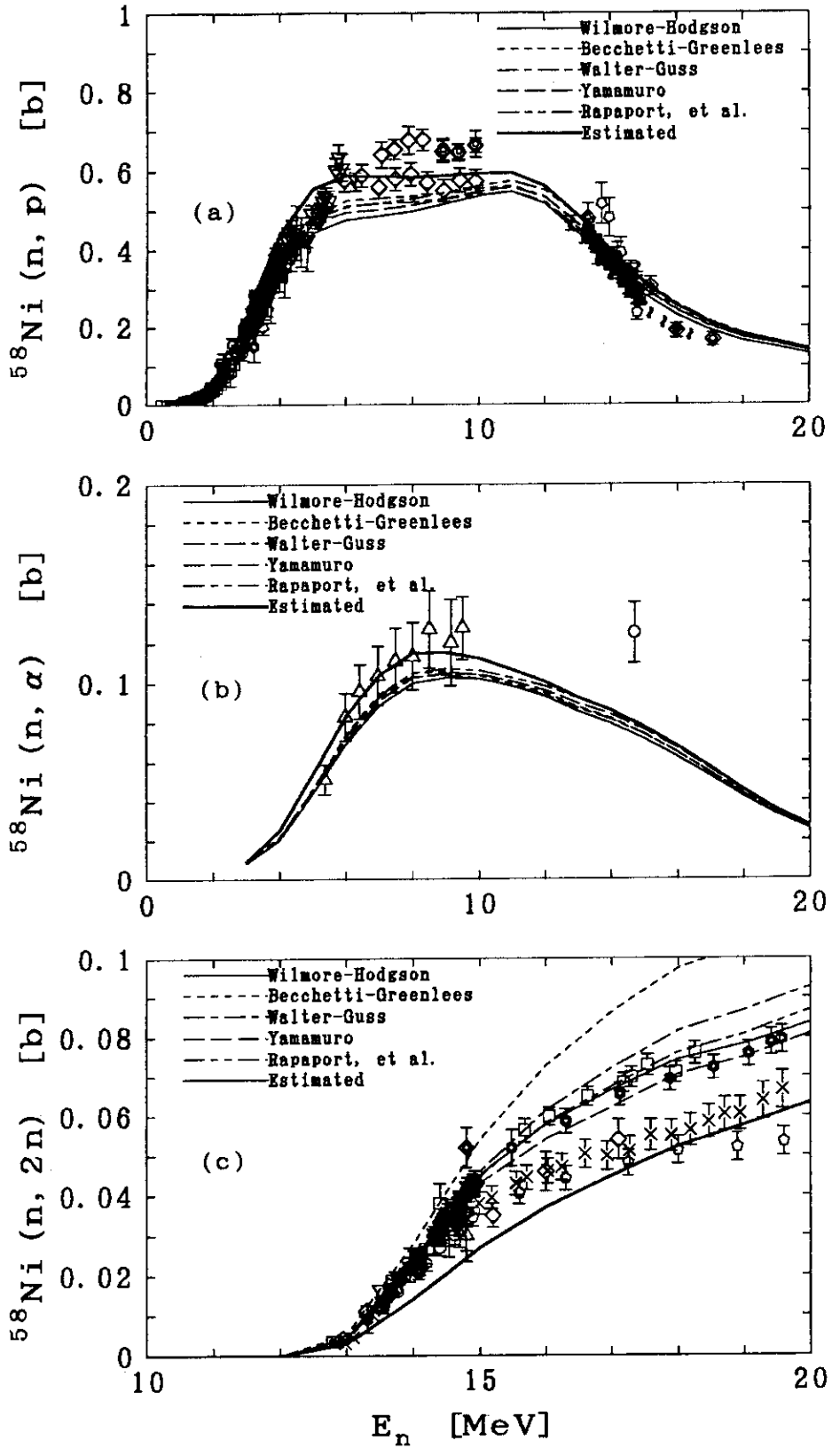

Fig. 3 Comparison of ^{58}Ni(n,p), (n,α), and (n,2n) reaction cross sections calculated with some neutron OMP's.

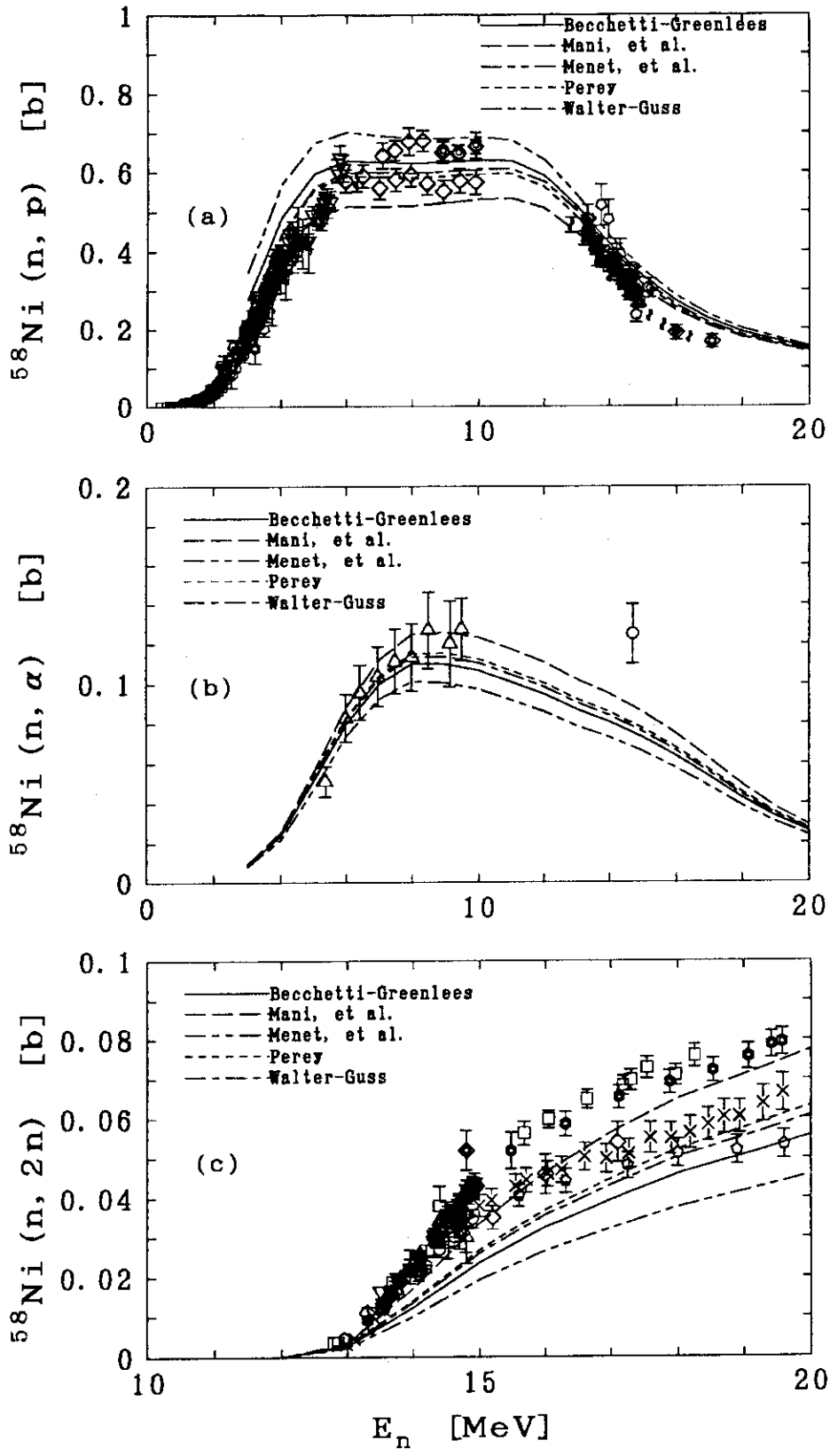

Fig. 4 Comparison of ^{58}Ni(n,p), (n,α), and (n,2n) reaction cross sections calculated with some proton OMP's.

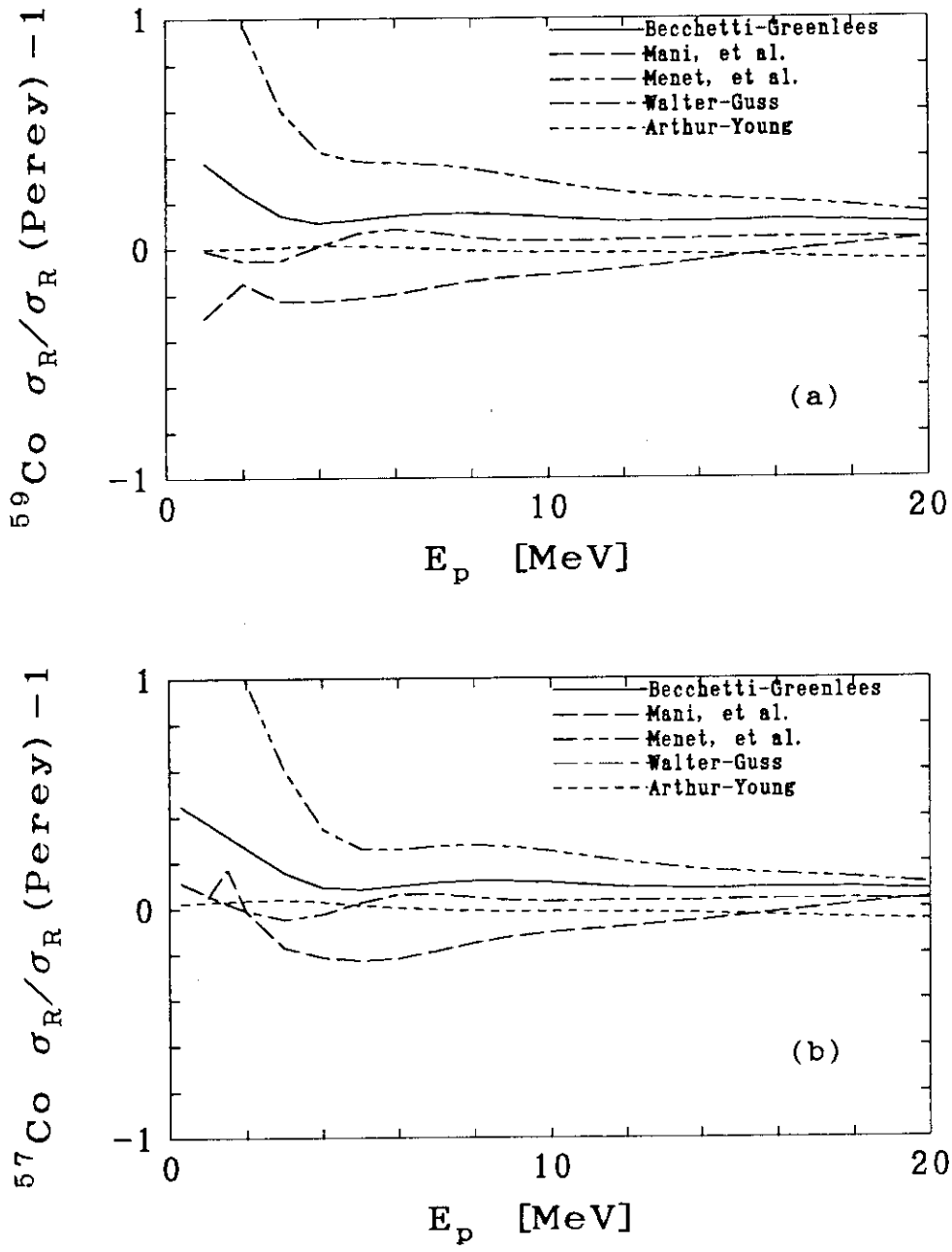

Fig. 5 Reaction cross sections of the global proton OMP's expressed by the ratio to the value calculated with Perey's OMP.
(a): ^{59}Co+p
(b): ^{57}Co+p

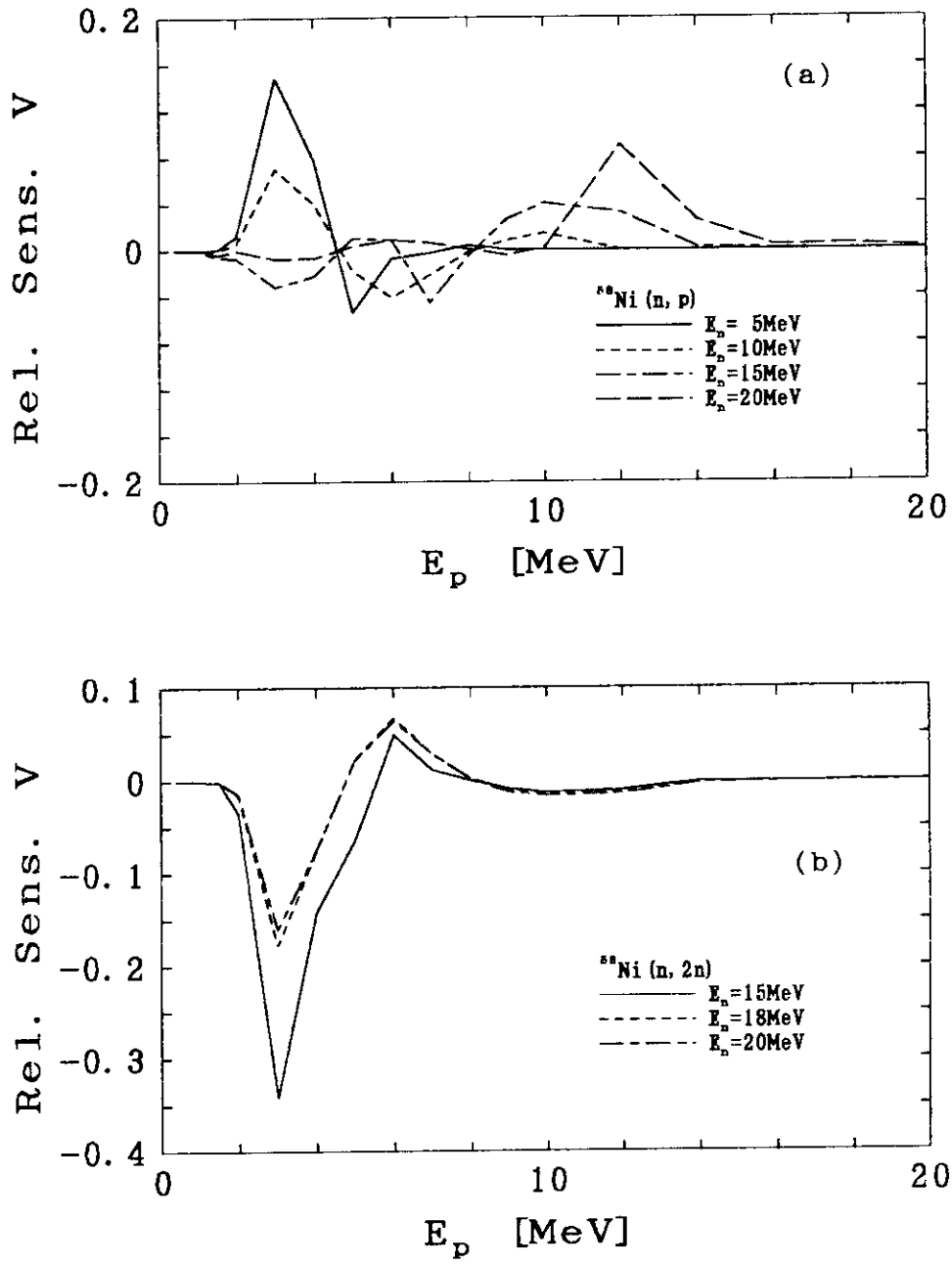

Fig. 6 Relative sensitivities of real potential depth of proton OMP.
(a): ^{58}Ni(n,p) reaction cross section
(b): ^{58}Ni(n,2n) reaction cross section

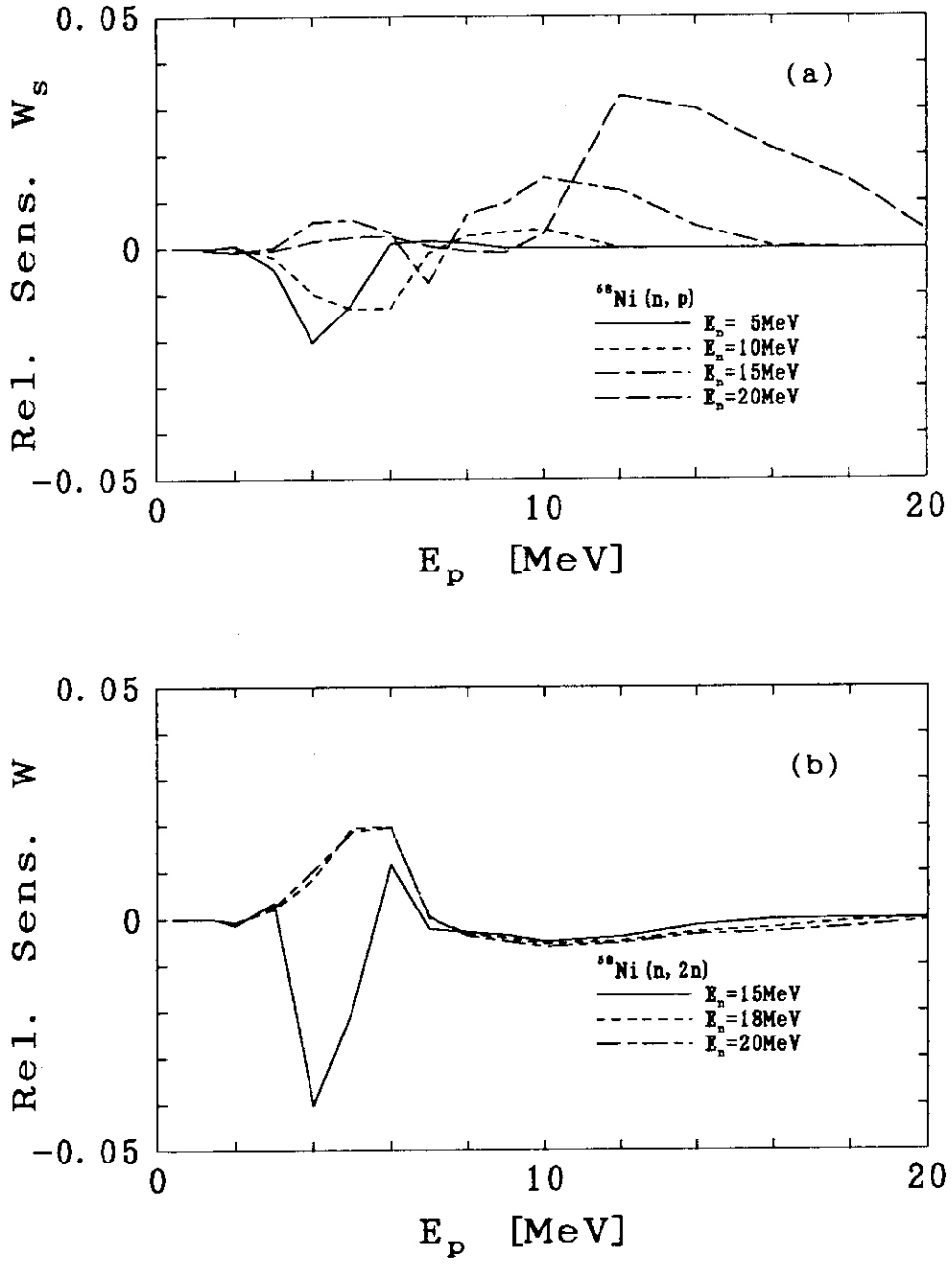

Fig. 7 Relative sensitivities of imaginary potential depth of proton OMP.
(a): ^{58}Ni(n,p) reaction cross section
(b): ^{58}Ni(n,2n) reaction cross section

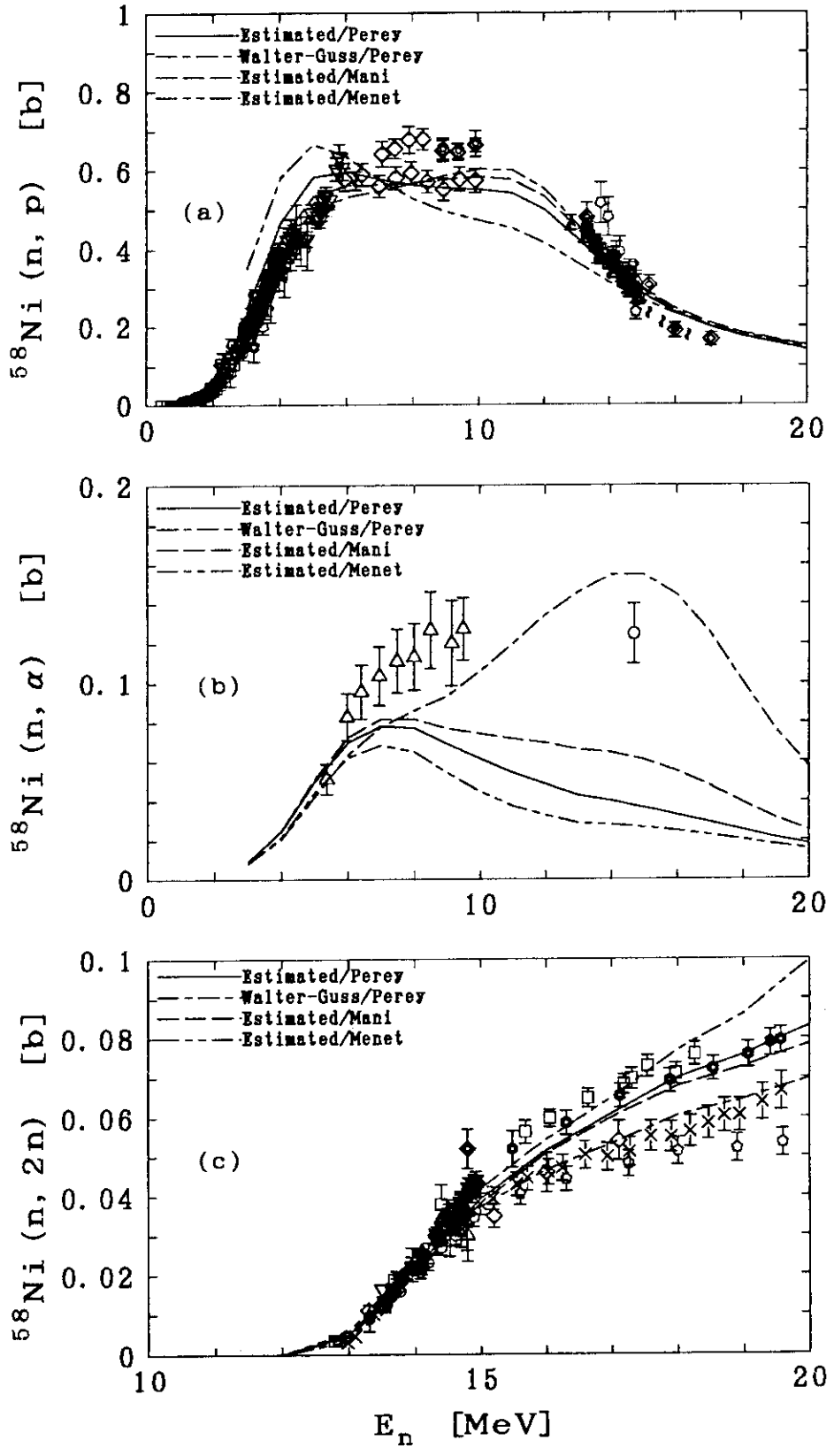

Fig. 8 Comparison of ^{58}Ni(n,p), (n,α), and (n,2n) reaction cross sections calculated with estimated level density parameters.

3.6 SYSTEMATICS OF THE FRAGMENTATION CROSS SECTION FOR 1−3 GeV PROTON INDUCED SPALLATION REACTIONS

Shouitirou SAKAGUCHI, Kenji ISHIBASHI, Tatsushi NAKAMOTO,
Yoshihisa WAKUTA
Department of Nuclear Engineering, Kyushu University
Hakozaki, Fukuoka-shi 812
and
Yasuaki NAKAHARA
Japan Atomic Energy Research Institute
Tokai-mura, Ibaraki-ken 319-11

We investigate the systematics of fragmentation reactions induced by 1-3 GeV protons. A liquid-gas phase-transition model is adopted to represent the fragmentation cross sections for both the mass distributions and the kinetic energy spectra. This model uses the nuclear temperature, which can be estimated by the excitation-energy distribution after the cascade process. The magnitude of the fragmentation cross section is determined by the use of an adjustable parameter. Systematics of heavy-ion-induced fragmentation reactions are also analyzed by the liquid-gas phase-transition model, but the cross sections for these reactions are not completely related to the experimental data of the proton-induced fragmentation reaction. This model is coded as a subroutine set, and incorporated into the high energy transport code HETC.

1. INTRODUCTION

The spallation reaction is caused by bombarding a target with particles having energies above a few hundred MeV. The reaction produces a great number of neutrons. This reaction is applicable to producing the intense spallation-neutron source and transmuting the long-lived radioactive wastes. Up to the proton energies of several hundred MeV, the spallation reaction consists of such processes as cascade, preequilibrium and evaporation. Above these energies, the fragmentation process is induced in addition to these processes. The fragmentation process emits the intermediate-mass fragments such as Na and Mg, which are never released by the cascade, preequilibrium and evaporation processes. Since the accumulation of the spallation data is poor, at present, computer codes such as High Energy Transport Code (HETC) and Nucleon Meson Transport Code (NMTC) are utilized for engineering purposes. The fragmentation process is not included in these codes. We attempt to investigate the systematics of fragmentation reaction, and to incorporate this process into HETC.

2. MODEL OF THE FRAGMENTATION

2.1 Experimental data

For the proton-induced fragmentation reaction, we are interested in cross sections for mass distributions and fragment energy spectra. The data of the mass-distribution were measured for incident protons of 0.48[1], 1.0[2], 4.9[3] and 5.5 GeV[4] on Ag, 1

GeV[2] on Ni, 3.9 GeV[5] on Cu, and 4.9[3] and 5.5 GeV[4] on U. The double differential cross sections were experimentally obtained for incident protons of 0.48 GeV[1] on Ag, and 1.6, 2.3 and 3.1 GeV[6] on Xe. The Xe data were integrated into the total fragmentation cross section taking the forward peak into consideration.

2.2 Liquid-gas phase-transition model

As is well known, the liquid-gas phase-transition takes place in a Van-der-Waals system. We consider this kind of the phase transition in highly-excited nuclei. In this model for the nuclear reaction, a nucleus stays in a liquid phase in an initial state. When an incident proton deposits its energy on the nucleus and makes it in a highly excited state, the nuclear phase is considered to change from the liquid to the gaseous phase. The gaseous-phase region appearing in the nucleus may extend into the liquid region, and this extension leads to break-up of the nucleus. In the treatment of this model, the statistical distribution of probabilities of different states f is assumed to be described by

$$\Delta\Gamma_f = \exp S_f(A_0, Z_0, E_0), \qquad (1)$$

where $\Delta\Gamma_f$ and S_f are the statistical weight and entropy of the state f,respectively, and E_c is the total energy of the system that is related to such quantities of fragments (A,Z) as surface area, nuclear volume, symmetry, Coulomb energy and translational motion. Equation (1) is evaluated for each partition of the nuclear system.

Panagioutou[7] has proposed the probability for the fragment formation by simplifying the liquid-gas phase-transition model:.

$$P(a) \approx A^{-2.0} \cdot \exp\left\{A^{-2/3}\left[-18.4\left(1-\frac{T}{T_c}\right)^2\right]/T\right\} \qquad (2)$$

The nuclear temperature at fragmentation (fragmentation temperature) is the characteristic parameter that expresses the overall shape of the cross section. This model does not determine the magnitude of total fragmentation cross section.

2.3 Evaluation model

The fragmentation process occurs only when the highly excited nucleus is generated after the cascade process. The HETC was used for studying the nuclear temperature after the cascade process: The excitation energy obtained by the HETC was converted into the nuclear temperature through the level density parameter. However, this temperature as calculated does not coincides with the fragmentation temperature deduced by Eq.(2) for reproduction of the experimental data. This means that it is required to consider such effects as a volume expansion and a local development of cascading. Hence, we modify the calculated temperature to be consistent to the fragmentation temperature in the Panagioutou model. Figure 1 shows the results of the calculation based on the modified temperature. The model using the modified nuclear temperature reproduces the experimental fragment mass distribution ranging A=7-50. The same value of the modified nuclear temperature is used for reproducing the emitted-fragment kinetic-energy spectra, as indicated in Fig. 2. The magnitude of the total fragmentation cross section shows a tendency to depend on the energy per nucleon.

Bondorf[8] proposed a crack temperature where the fragmentation takes place. The temperature corresponds to an excitation energy obtained at an incident proton energy of

400 MeV. According to Bondorf, the fragmentation reaction has a threshold energy. However, there is the experimental evidence that the fragmentation occurs to some extent below an incident proton energy of 400 MeV. In addition, the use of his model highly underestimates the fragmentation cross section for 2-3 GeV proton-induced reaction. To improve the total cross section for 2-3 GeV proton reaction, we introduced a function for the fragmentation probability distribution. The probability is given by

$$P = 5.83\times10^{-5}\cdot(E-5.0)^{1.155} \quad , \qquad (3)$$

From this equation, the fragmentation probability distribution is equal to unity at an excitation energy of about 4 GeV. Table 1 shows the values of cross section estimated using the probability distribution and the Bondorf model. Using the present probability distribution function, the fragment mass distribution is well reproduced as shown in Figs. 3-6.

To reproduce the angular distribution of the fragment energy spectra, the moving source model is assumed, where fragments are treated to be emitted isotropically in a moving frame. In addition, in accordance with the expansion of the nuclear volume, the Coulomb barrier height is assumed to decrease to 1/2-1/3 in comparison to the normal density condition. The fragment energy spectra are shown in Figs. 7-10, where the experimental data are well reproduced.

3. INCORPORATION INTO HETC

Using the liquid-gas-phase transition model, we incorporate the fragmentation process into the HETC. The fragmentation process was coded as a subroutine program set like a fission process. Figure 11 shows the flow-chart for insertion of fragmentation process.

4. HEAVY-ION-INDUCED DATA

To investigate systematics of fragmentation phenomena, we analyze heavy-ion-induced fragmentation data. The experimental data on fragment mass distribution are present for the reactions of La+C and La+Al[9], Nb+Be[10] and Al, and C[11]. By use of the liquid-gas phase-transition model, the heavy ion induced data can also be reproduced by a certain fragmentation temperature, as shown in Figs. 12 and 13. The fragmentation temperatures obtained are plotted in Fig. 14 as a function of the total energy in the cm frame. The temperature for heavy-ion-induced reaction is higher than that for the proton-induced, but the shape of temperature is the same as the proton-induced. Hence, we may apply the heavy-ion reaction data to proton-induced reaction by scaling the temperature and energy. In Fig. 18, the total cross section of the heavy-ion-induced data increases with incident energy. Nevertheless, the dependence of the cross section on the target and projectile is not clear.

5. DISCUSSION

The fragmentation process was incorporated into the HETC on the basis of the systematics. The present calculation method is not complete at few points. For instance, the method is unable to treat the multi-fragmentation process where some fragments are emitted from an excited nucleus. The lack of this consideration results in the underestimation of the total fragmentation cross section when incident proton

energies are in the range of 3-5 GeV. For the fragment energy spectra, the Coulomb barrier decreases to 1/2-1/3 corresponding to the volume expansion, but the HETC doesn't have any information about the volume expansion. Volume expansion is importnt for cascade and evaporation calculation, but it is only dealt by the fragmentation process.

6. CONCLUSION

The use of liquid-gas phase-transition model with the modified temperature and the fragmentation probability reproduced the systematic behavior of both the proton induced fragmentation mass distributions and the kinetic energy spectra. Heavy ion induced data didn't show clear dependence of the cross section on the target and projectile. The fragmentation process was successfully introduced into the HETC code.

REFERENCES

(1) GREEN,Ray E.L. et al.:Phys Rev., C29,1806(1984)
(2) ANDRONENKO,L.N. et al.:Phys.Lett.,B174,18(1986)
(3) WESTFALL,G.D. et al.:Phys Rev.,C17,1368(1980)
(4) POSKANZER,A.M. et al.:Phys Rev.,C3,882(1971)
(5) CUMMING,J.B. et al.:Phys Rev.,C10,739(1974)
(6) PORILE,N.T. et al.:Phys.Rev.,C39,1914(1989)
(7) PANAGIOUTOU,A.D. et al:Phys Rev.,C31,55(1982)
(8) BONDORF,J.P. et al:Nucl. Phys.,A443,321(1985)
(9) CHARITY,R.J. et al.:Nucl.Phys.,A511,59(1990)
(10) LUCIANO,G. et al.:Nucl.Phys. A488,377(1988)
(11) WOZNIAK,G.J.:Nucl.Phys. A483,372(1988)

Table 1 Values of cross section used by the probability distribution and the Bondorf model.

	Probability Dist.(mb)	Bondorf Model(mb)	Experiment(mb)
480MeV	12.78	12.24	12.22
1GeV	30.10	50.88	51.92
1.6GeV	74.99	59.14	59.51
2.3GeV	129.82	108.33	125.15
3.1GeV	157.08	135.17	213.52

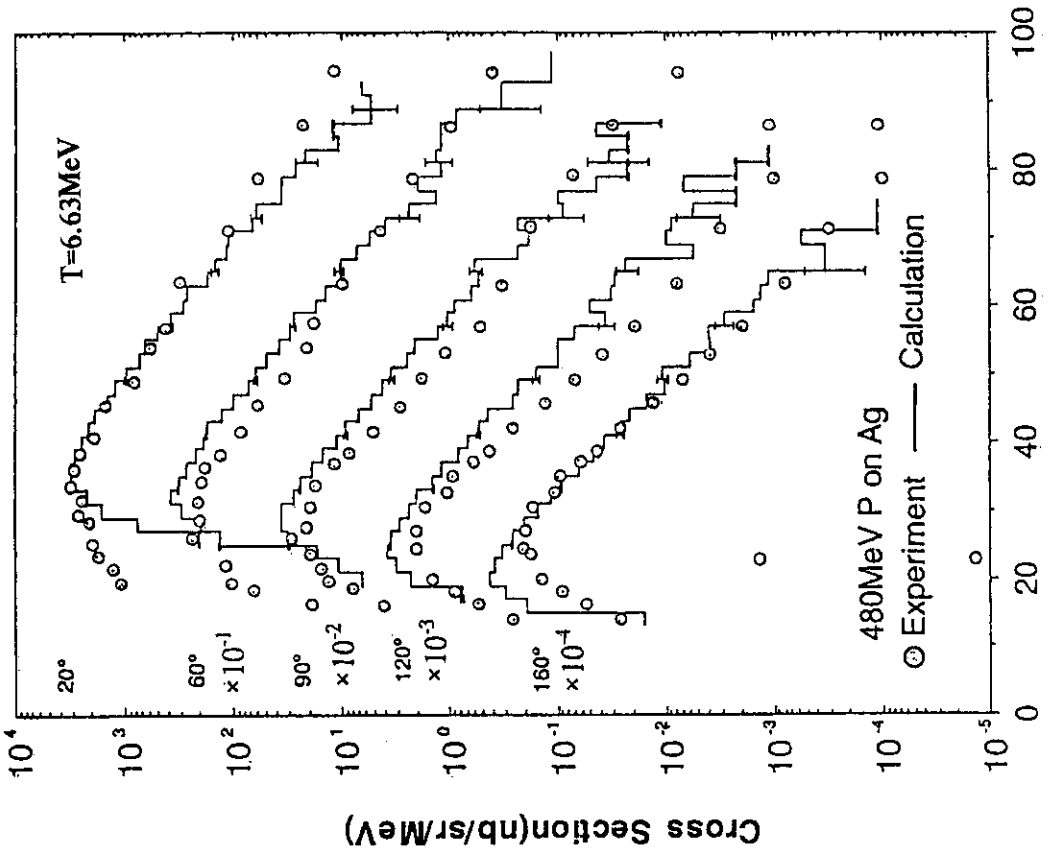

Fig. 2 Experimental ^{12}C kinetic energy spectra and the results of liquid gas phase transition model for Ag target for incident protons of 480 MeV.

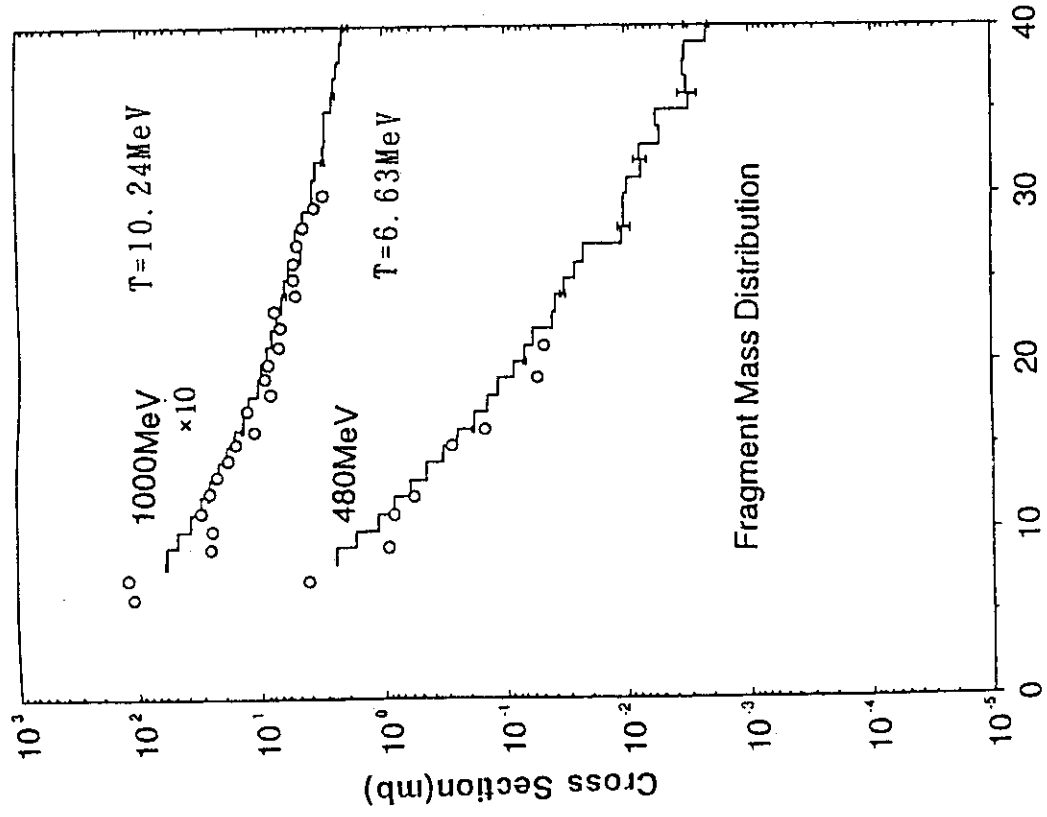

Fig. 1 Experimental fragment mass distribution and the results of liquid gas phase transition model for Ag target for incident protons of 480 and 1000 MeV.

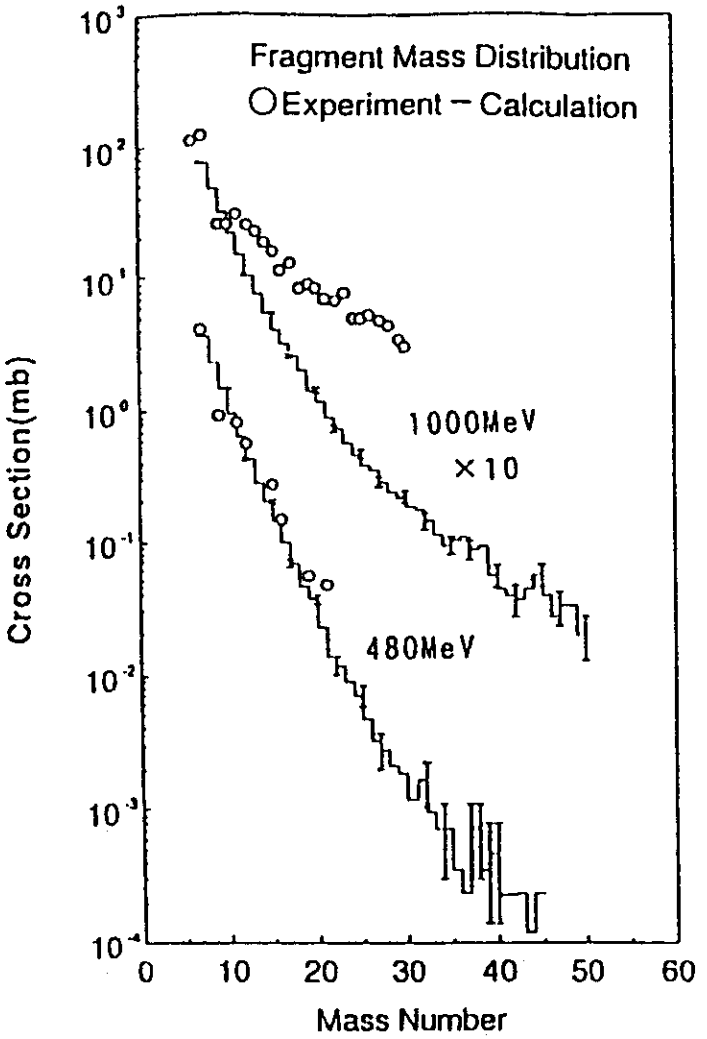

Fig. 3 Experimental data and the results of the liquid gas phase transition model with the fragmentation probability for Ag target for incident protons of 480 and 1000 MeV.

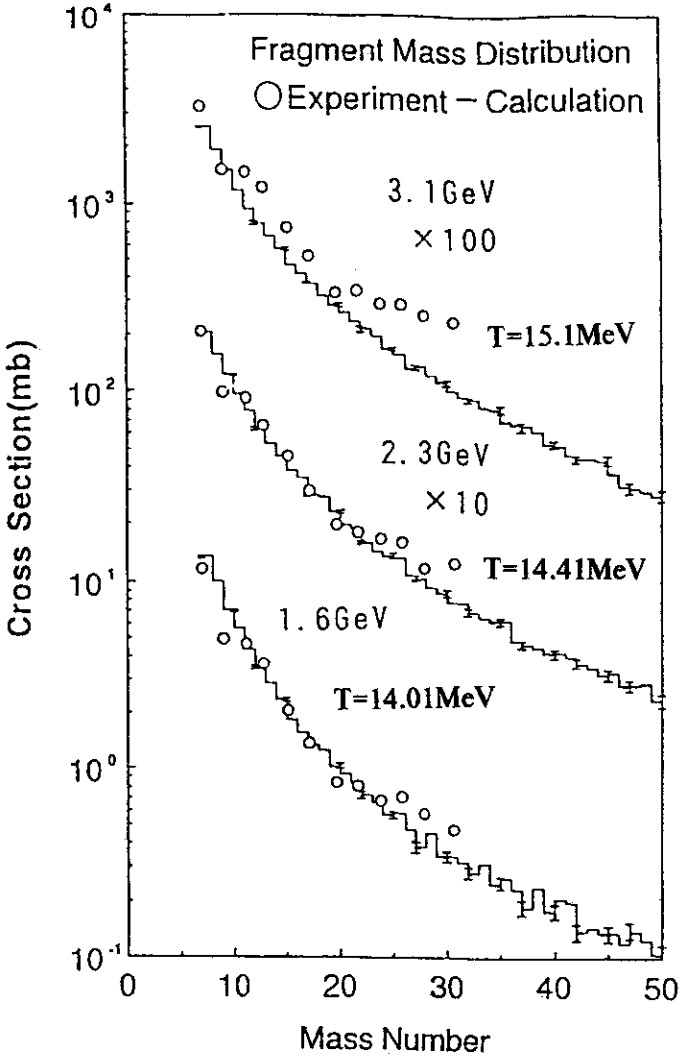

Fig. 4 Experimental data and the results of liquid gas phase transition model with the fragmentation probability for Xe target for incident protons of 1.6, 2.3 and 3.1 GeV.

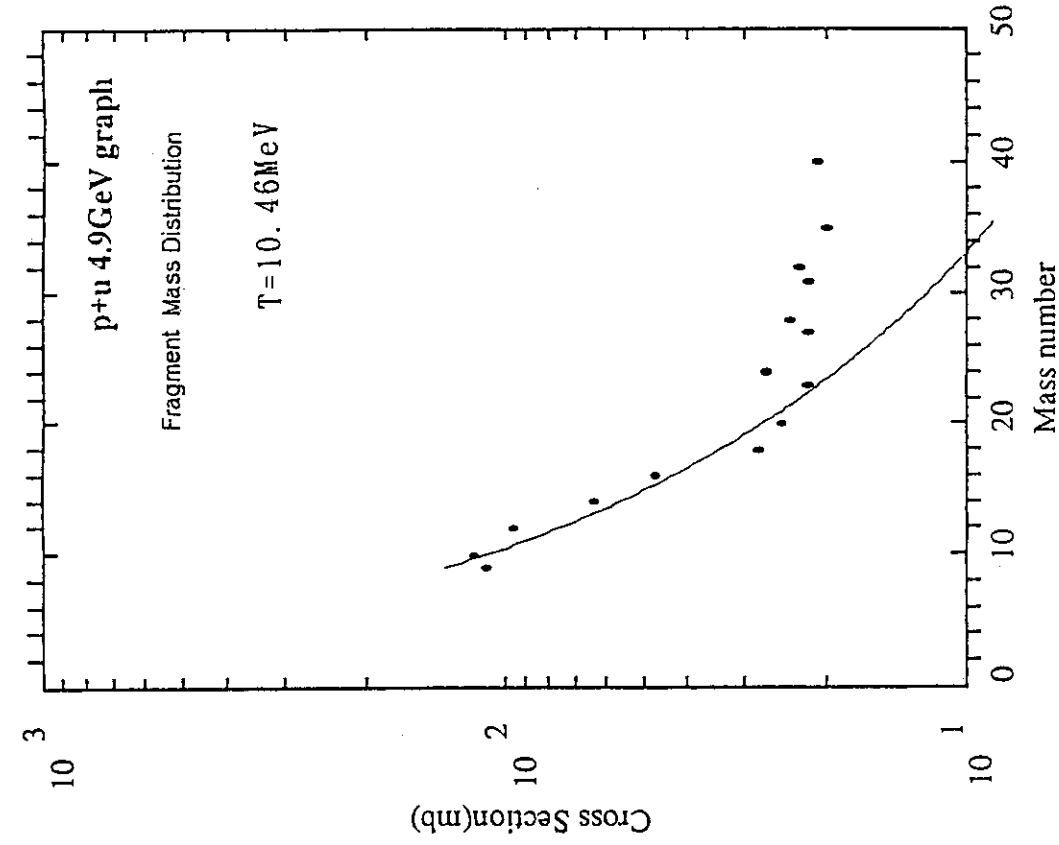

Fig. 6 Experimental data and the results of liquid gas phase transition model with the fragmentation probability for Ag target for incident protons of 4.9 GeV.

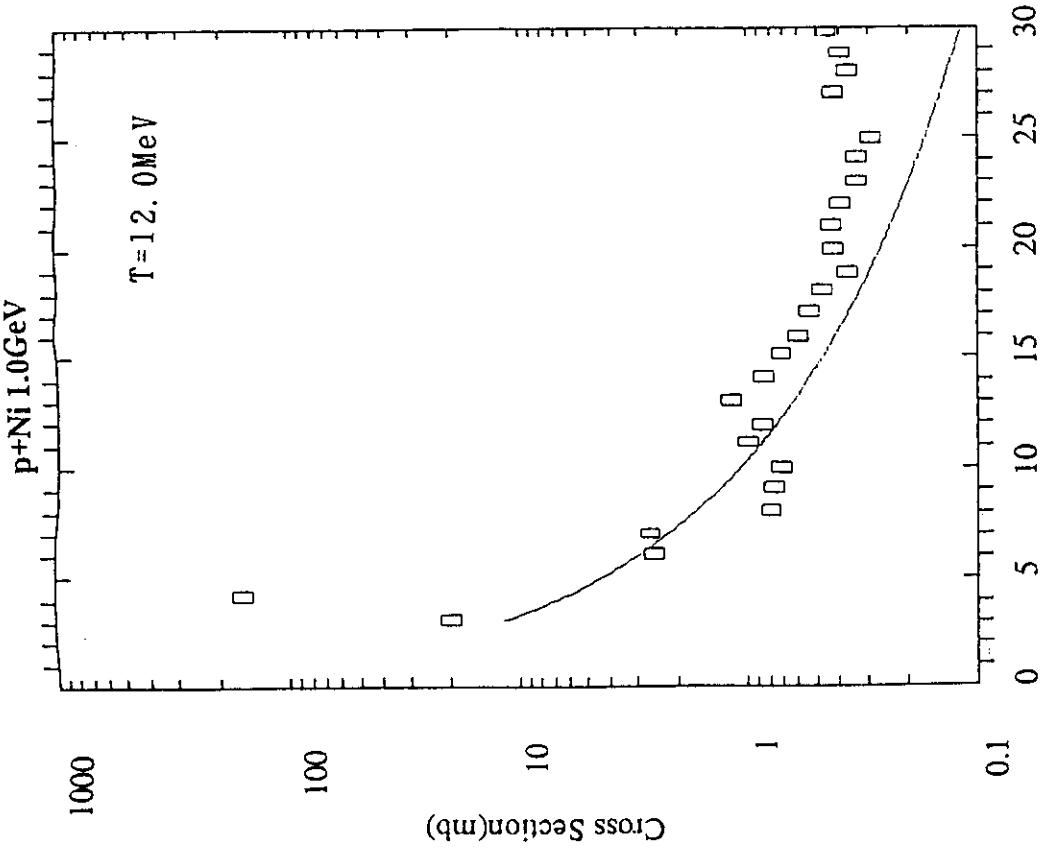

Fig. 5 Experimental data and the results of liquid gas phase transition model with the fragmentation probability for Ni target for incident protons of 1 GeV.

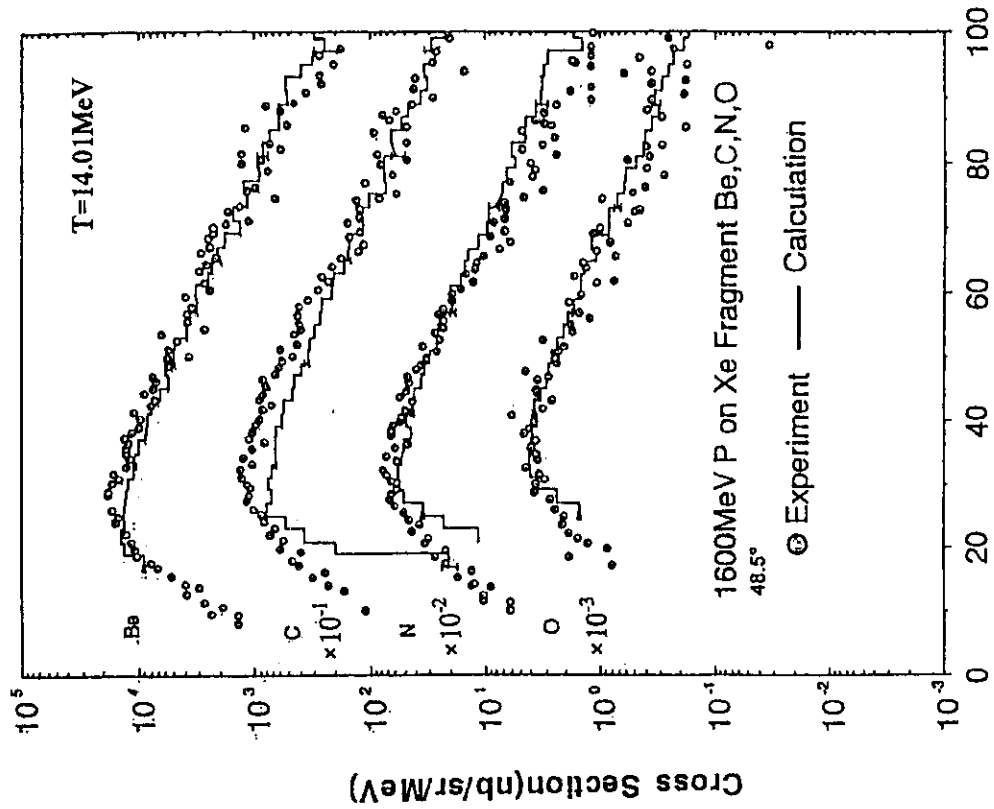

Fig. 8 Experimental Be, C, N, O kinetic energy spectra and the results of liquid-gas phase-transition model with the fragmentation probability for Xe target for incident protons of 1.6 GeV.

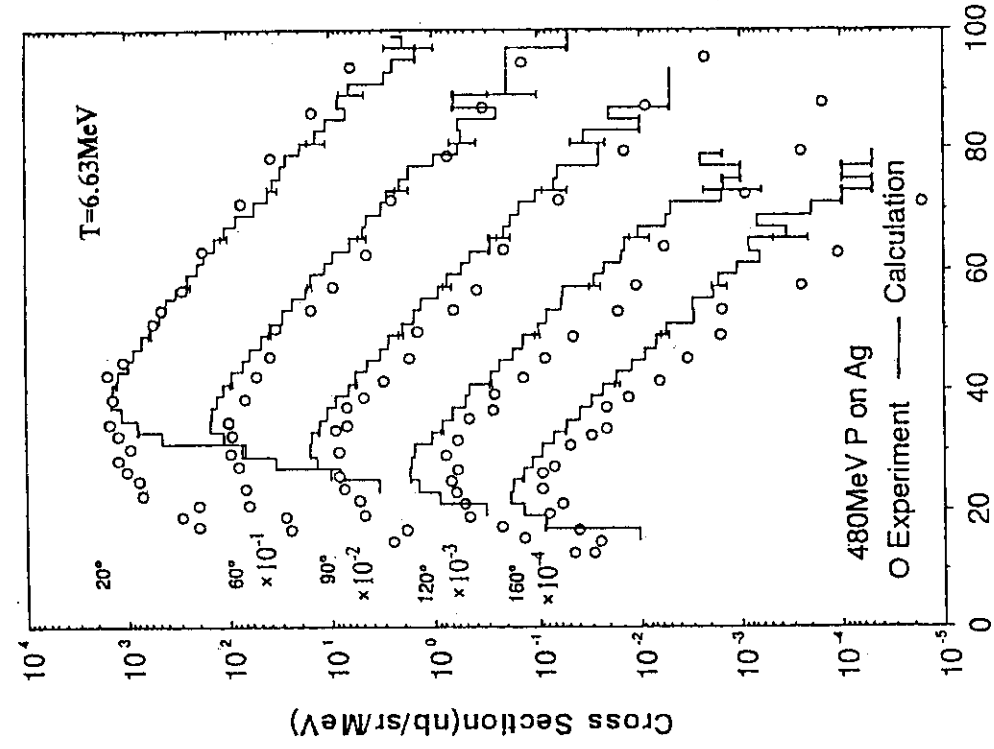

Fig. 7 Experimental ^{15}N kinetic energy spectra and the results of liquid-gas phase-transition model with the fragmentation probability for Ag target for incident protons of 480 MeV.

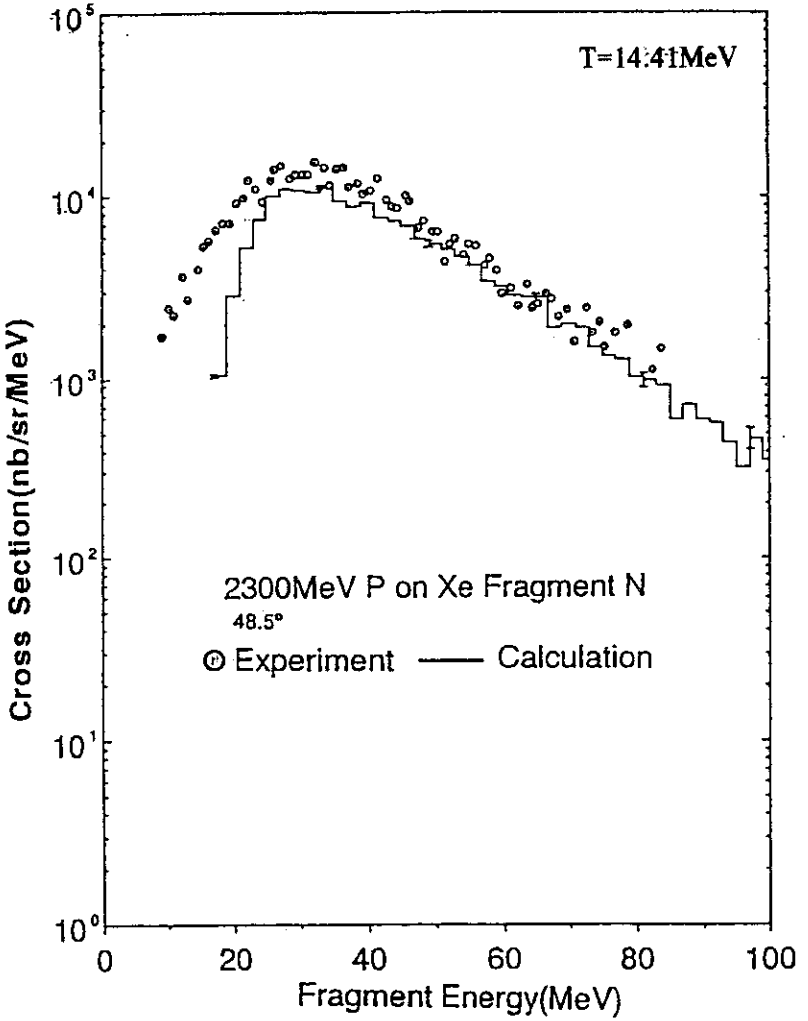

Fig. 9 Experimental N kinetic energy spectra and the results of liquid-gas phase-transition model with the fragmentation probability for Xe target for incident protons of 2.3 GeV.

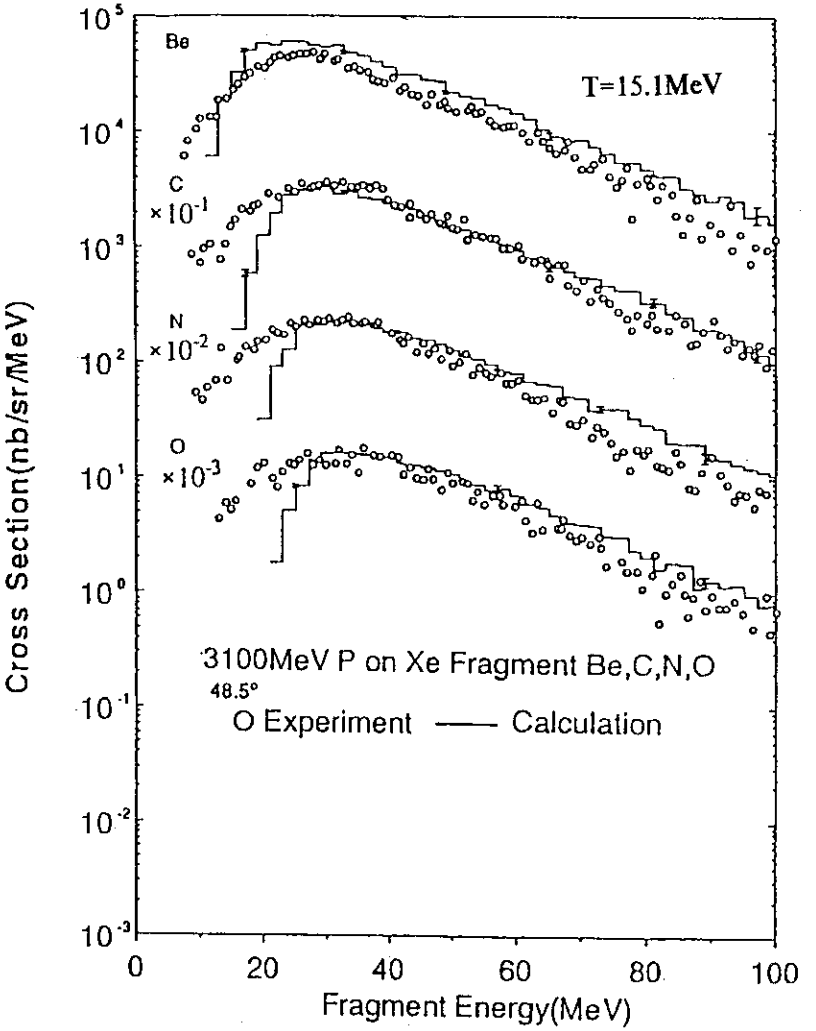

Fig. 10 Experimental Be, C, N, O kinetic energy spectra and the results of liquid-gas phase-transition model with the fragmentation probability for Xe target for incident protons of 3.1 GeV.

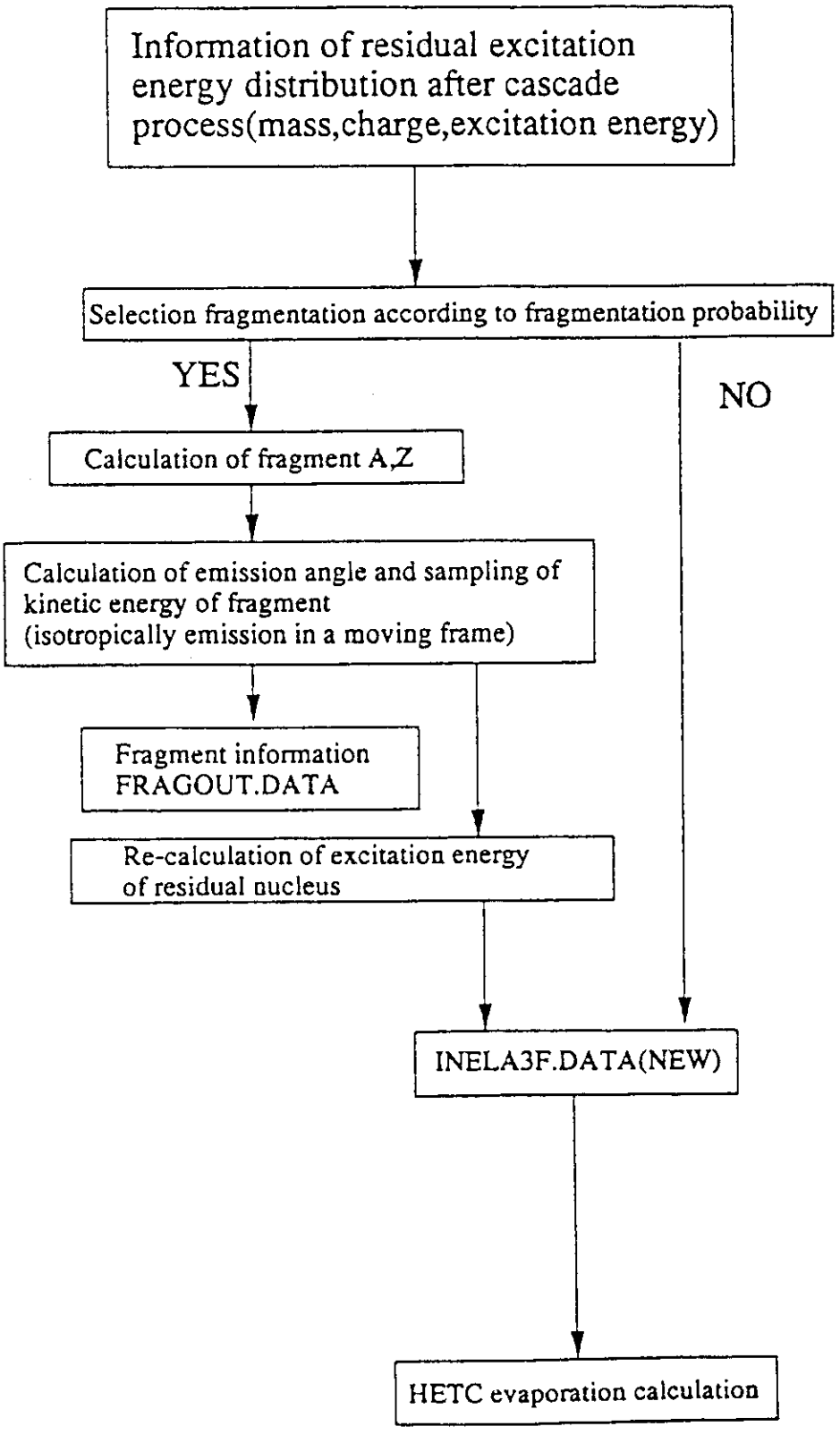

Fig. 11 Flow-chart for insertion of the fragmentation process.

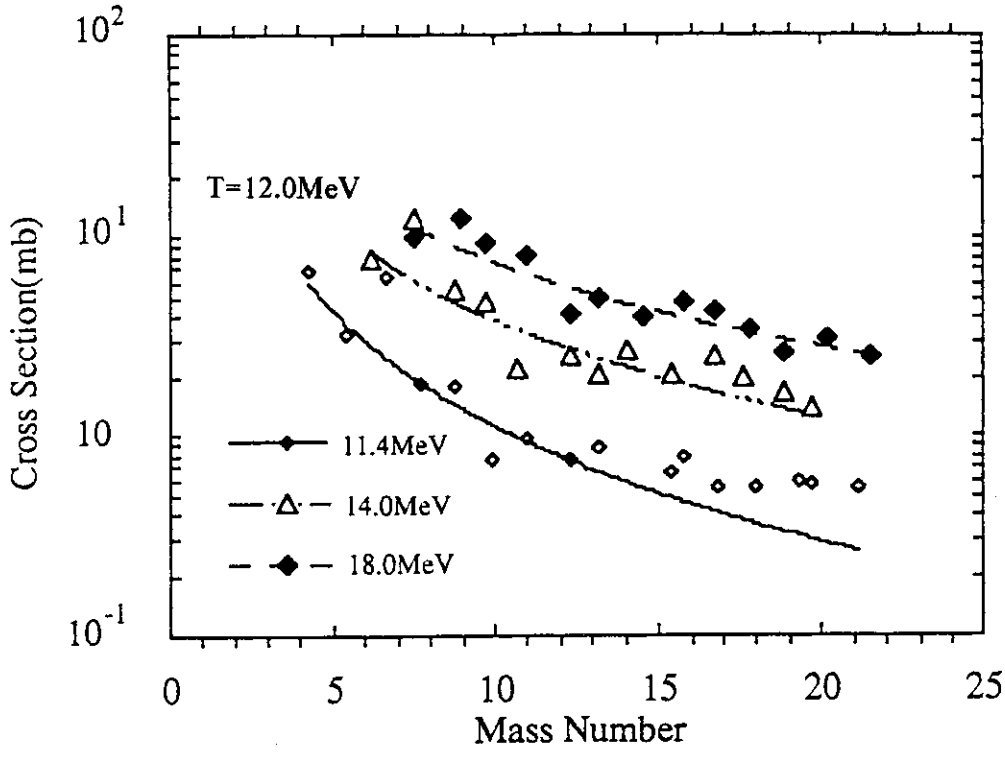

Fig. 12 Experimental data and the results of liquid gas phase transition model for 11.4, 14.0 and 18.0 MeV/n incident Nb on C.

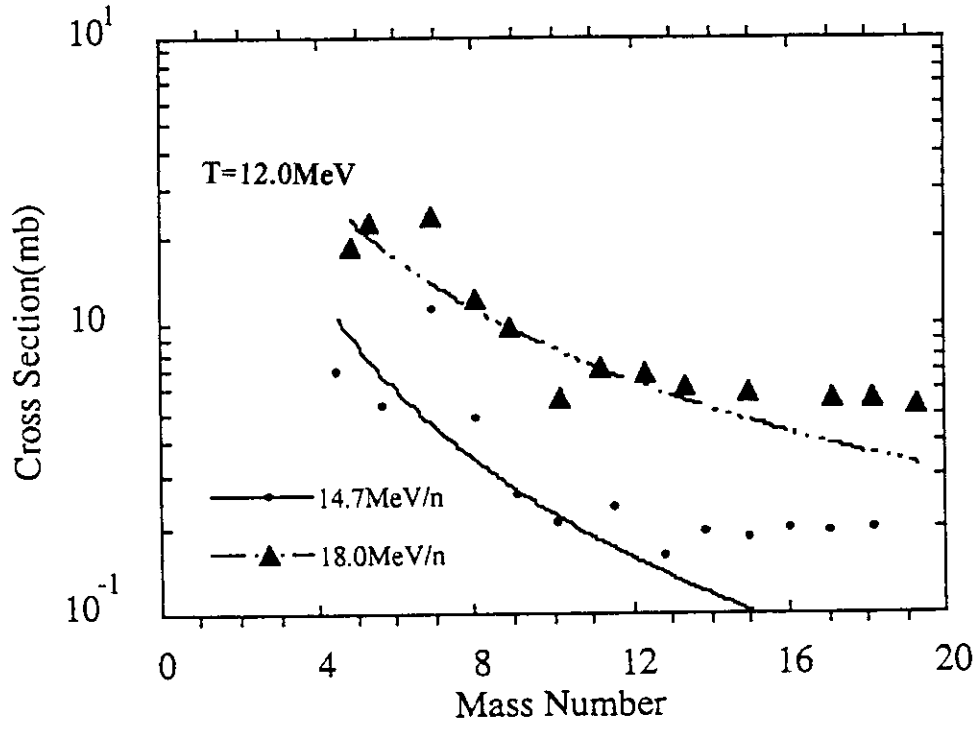

Fig. 13 Experimental data and the results of liquid gas phase transition model for 14.7 and 18.0 MeV/n incident La on C.

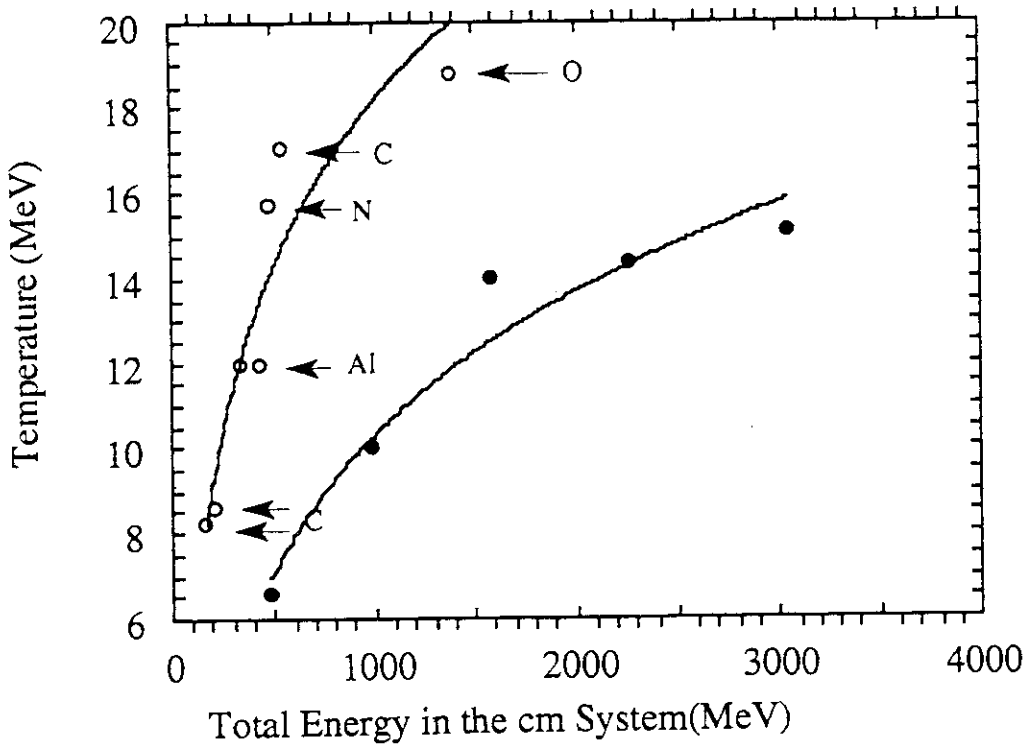

Fig. 14 Nuclear temperature for various targets. Black circles: Proton induced data. Open circles: Ion induced data, where projectiles are indicated by symbols.

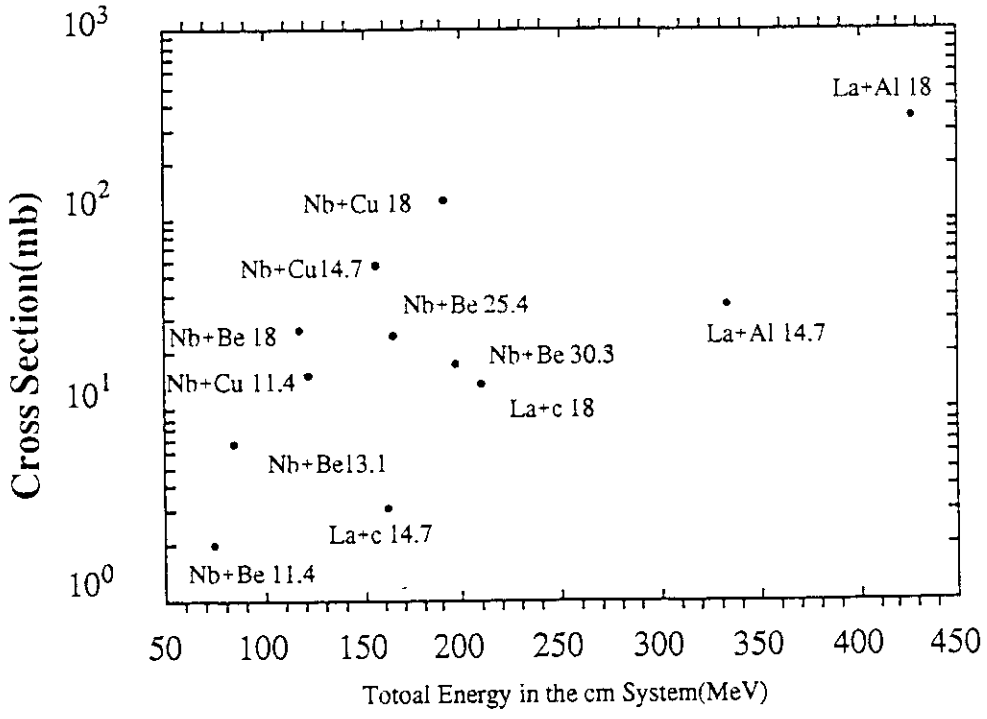

Fig. 15 Fragmentation total cross section as a function of the total energy in the cm frame.

3.7 PRODUCTION AND RADIOLOGICAL IMPACT OF ARGON-39

K. Kitao

National Institute of Radiological Sciences

9-1, Anagawa-4-chome, Chiba-shi 260, Japan

Abstract: The quantity of argon-39 released from the nuclear installation following production of neutrons have been calculated based on cross sections predicted by the theoretical code, EGNASH and ALICE. The population dose given by this nuclide has been estimated. Some remarks are also given on the status of availability for the cross sections for the production of ^{39}Ar.

1. Introduction

Argon-39($T_{1/2}$=269 y) is producing by the (n,2n) or (γ,n) reaction with ^{40}Ar in the air or forming by the decay of ^{39}Cl($T_{1/2}$=55.6min). Chlorine-39 is also formed from ^{40}Ar by the nuclear reaction with neutrons or photons. Then, these nuclides are arising from operation of fusion reactors or high-energy accelerators.

To date, anyone has not concerned with the radiological impact of these nuclides, especially ^{39}Ar. Because the threshold energies of the reactions to produce these nuclides are as high as over 10 MeV, and ^{39}Ar is β-emitter but emitting no gamma-rays. In the view of radiation protection in the nuclear facility, concerned gaseous radionuclides in the air are ^{41}Ar, ^{15}O, ^{14}N, and so on. Although, ^{39}Cl is a contaminant for the atmosphere at the high-energy accelerator facility, but nobody has seen to be an important nuclide.([1]) Because the nuclide has been exclusively considered to product through the $^{40}Ar(\gamma,p)$ reaction in the air and the cross section of the reaction is not so much.

However, one can detect gamma-rays from the decay of ^{39}Cl in a sample collected by an air sampler setting in the target room of the high-energy

accelerator generating neutrons with energy greater than 15 MeV.[2] From the cross sections for production of these nuclides, the fact suggests that ^{39}Ar is also produced in the air at a time.

In fission reactor, to release of ^{85}Kr is usually an issue. The nuclide is a volatile long-lived fission product($T_{1/2}$=10.756 y) and emits beta-rays with energy nearly equal to that from the decay of ^{39}Ar. Argon-39 have a longer half-life to compare with that of ^{85}Kr. Thus ^{39}Ar released accumulates in the environment and continues to give similar radiation effects with ^{85}Kr to populations over a long period.

In present work, we have considered ^{39}Ar produced by neutron only and calculated the activity releasing from the nuclear facility, based on the neutron cross section calculated by the code EGNASH and ALICE. We estimate the amount of ^{39}Ar released in the atmosphere from the fusion facility using D-T reaction, and estimate the possible population exposure given by the nuclide from a large scale utilization of the nuclear fusion.

2. Characteristics and arising of Argon-39

2.1 Properties

Argon-39 and chlorine-39 decays exclusively by the route:

$$^{39}Cl \xrightarrow[\beta-,\ 3438\ keV]{55.6\ min} {}^{39}Ar \xrightarrow[\substack{\beta-,\ 565\ keV\\ no\ \gamma}]{269\ y} {}^{39}K.$$

Argon-39 emits β-rays with maximum energy of 565 keV and not γ-rays with any energy. Its decay properties are shown in Table 1, together with some volatile long-lived radionuclides produced at the nuclear facility. Table 2 shows gamma-rays originating from the radioactive decay of 39Cl produced with neutron induced reaction.

2.2 Reaction of production

Argon-39 is produced from ^{40}Ar by the (n,2n) reaction with neutrons and its threshold energy is 10.12 MeV. Argon-39 is arising from the decay of ^{39}Cl, which is also produced from ^{40}Ar by the (n,np) or (n,d) reaction. To

date, no experimental examination has been made of the cross sections of the $^{40}Ar(n,2n)$ reaction. For the (n,np)+(n,d) reaction, there are three reports to give the experimental cross sections for 14.4 MeV neutrons. Thus we calculated those cross sections by using the code ALICE/Livermore85 and code EGNASH. For the (n,d)+(n,np) reaction, both calculations have the same value, but not for the (n,2n) reaction. Figure 1 shows the results of those calculations, together with experimental values.

3. The amount of argon-39 produced in nuclear facilities

We estimate the activity of ^{39}Ar and ^{39}Cl arising from operation of a fusion reactor and a high-energy accelerator, based on the following path way:

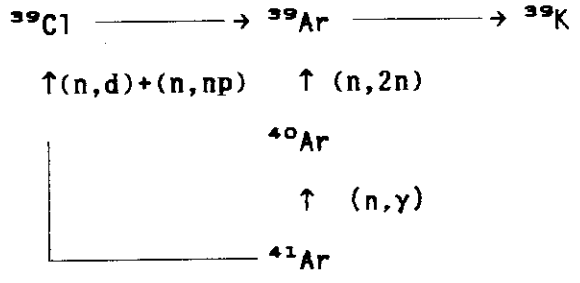

Assume the target room of the accelerator or the reactor hall of the fusion installation to be a sphere with inner-radius of R. And assume thermal neutron flux ($cm^{-1}s^{-1}$) to give by 1.25Q/S, where Q is the strength of fast neutrons generating per second and S is the inner-surface area of the room or hall in cm^2. The activity in an enclosed volume of the air in those space are given by:

$$A_{41}=(0.42)NQ\sigma_{41}R \quad \text{(in Bq)} \quad (1)$$

$$A_{Cl}=NQ\sigma_{Cl}R \quad \text{(in Bq)} \quad (2)$$

$$A_{39}=NQ(\sigma_{39}+\sigma_{Cl})R(1-\exp(-\lambda_{39}T)) \quad \text{(in Bq)} \quad (3)$$

where A is the activity and λ the decay constant. The suffixes 41, cl and 39 correspond to ^{41}Ar, ^{39}Cl and ^{39}Ar, respectively. σ_{41}, σ_{Cl} and σ_{39} are the cross sections of corresponding reactions. N is the number of 40Ar atom per unit volume of the air (in cm^{-3}) and equal to 2.33×10^{17} cm^{-3} for the concentration of 0.93 volume-percent of the air. T the operating time.

Assume R=5 m. Table 3 shows the quantities of these radioactive nuclides generating in the accelerator target room during continuous 120-hours operation.

We also estimate the activity of 39Ar from the operation of a 1GWe D-T fusion power reactor. In this calculation, we assumed the thermal efficiency is of 31.2 %, and the operating period is of 550 days at full-power. The Q-value of T(d,n)^{4}He reaction is 2.82 pJ, and the residual ^{4}He nucleus recoils with the kinetic energy of 0.564 pJ. If the energy of the recoil nucleus converts the thermal energy perfectly, then one neutron is to generate per energy production of 0.564 pJ in the T(d,n) reaction. Then, total neutron generations from the D-T fusion reactor are given as following:

$$Q=(1\times10^{9}\ \mathrm{J})/((0.312)(0.564\times10^{-12}\ \mathrm{J/n})).$$

Using eq.(3) and if T=550 days, R=5 m, one can obtain as the activity of 39Ar:

S_{39}= 5.6×10^{2} TBq (for σ_{39} from code EGNASH),

=20×10^{2} TBq (for σ_{39} from code ALICE).

Table 4 shows the results, together with of 85Kr inventory* in 1GWe light-water reactor with the same operation period and the thermal efficiency.

Next, we calculate the amount of 39Ar released by a worldwide large-scale utilization of fusion power reactors in future. If the total demand of energy in world at 200x year is the 400 MBDOE* and a quarter of the demand is supplied by D-T fusion reactors, and if this condition continues during 50 year. Thus, the total activity of ^{39}Ar released to the atmosphere is to reach that of (2.0 - 6.3) x 10^{20} Bq. It is assumed that the total amount of the air to dilute the activity is the volume of 2.54×10^{24} cm^3, which is the volume of the air in the atmosphere between sea-level to altitude of 5000 m. Then the concentration of ^{39}Ar in the atmosphere is (8 - 25)x 10^{-5} Bq cm^{-3}.

* 1MBDOE (million barrel per day oil equivalent) corresponds to operation of the capacity of 100 GWe electric power plant with the mean load factor is 70 %, the mean thermal efficiency 35 %.([8])

4. POPULATION DOSE FROM ARGON-39 RETAINED IN ATMOSPHERE

We calculate the individual skin dose equivalent for irradiation to whole body from ^{39}Ar in the atmosphere from the above estimate. The conversion factor of 50 uSv Bq-1 cm^3 hr-1 deduced from DAC(derived air concentration) of 5 Bq cm^{-3} is used as that from the concentration of ^{39}Ar to the skin dose equivalent under the condition of submersion.

Individual dose equivalent rate from ^{39}Ar in the atmosphere:

$$H = (50\ uSv\ Bq^{-1}\ cm^3\ hr^{-1})((80 - 250)\ uBq\ cm^{-3})(8760\ hr\ y^{-1}),$$

$$= (35 - 110)\ uSv\ y^{-1}.$$

This value is a same order of that given from cosmic rays.

5. Conclusion

We may conclude that radiological impact from ^{39}Ar is greater than that of ^{85}Kr over a long period of years. (See Fig. 2) If no positive measures to suppress the generation of ^{39}Ar are taken to the air ventilating the fusion reactor hall and if a utilization of fusion power is begun on a large-scale, 39Ar will bring some serious problems on radiation health for population. Our estimate is a speculation, but we recommend fervently to use of the argon-free air at the facility following the production of high energy neutrons.

References

(1) Yoshida, Y., Kitano, K., Serizawa, M., Shiraishi, T.: JAERI-1063 (1964).

(2) Kitao, K.: Private communication (1991).

(3) Gray, P.R., Zander, A.R., Ebrey, T.G.: Nucl. Phys. 62, 172 (1965).

(4) Husain, L., Kuroda, P.K.: J.Inorg.Nucl.Chem. 30, 355 (1968).

(5) Ranakumar, N., Karttunen, K., Fink, R.W.: Nucl. Phys. A128, 333 (1969).

(6) USAEC, Draft report of WASH-1400 (1974).

(7) USAEC, Draft report of WASH-1250 (1973).

(8) "Energy: Global properties 1985-2000", Report of the workshop on Alternative energy strategies held at MIT (1977).

Table 1 Decay properties of the volatile long-lived radionuclides

Nuclide	^{3}H	^{14}C	^{39}Ar	^{85}Kr	^{129}I
Half-life(y)	12.3	5730	269	10.76	1.57×10^{7}
Radiation(MeV)	β− 0.02	β− 0.2	β− 0.57	β− 0.67	β− 0.15
				γ 0.51(1%)	γ G0.04(7.5%)

Table 2 Prominent gamma-rays associated with chlorine-39

Energy (keV)	Abundance per 100 decays
250.16	47.0
985.68	2.17
1090.87	2.55
1267.10	54.3
1517.25	38.6

Table 3 The activity of ^{44}Ar, ^{39}Cl, and ^{39}Ar produced per 1×10^{16} neutrons generating at a target room of an accelerator

^{41}Ar[a]	^{39}Cl[b]	^{39}Ar[c]
3.2×10^{11} Bq/s	9.3×10^{10} Bq/s	1.8×10^{7} Bq/s

[a] from (n,γ), σ_{41}=660 mb (for thermal neutrons)

[b] from (n,d)+(n,np), σ_{cl}=80 mb

[c] from (n,2n)+ β^-decay of 39Cl, $\sigma_{39}+\sigma_{cl}$=350 + 80=430 mb

Table 4 Estimated discharge of argon-39 from a 1GWe D-T fusion reactor

FUSION REACTOR ^{39}Ar	FISSION REACTOR[a] Kr
1.12-4 $\times10^{2}$ TBq	2.6×10^{2} TBq (BWR)[b]
	12 TBq (PWR)[c]

[a] Krypton-85 inventory in a 1 GWe (3.2 GWt) LWR is 220×10^{2} TBq with fuel burn-up of 17.6 MWd/kg and after 550-day full power operation.(6)

[b] Assumes operation with 0.2% clad defects and hold-up time of 1-day delay.(7)

[c] Assumes operation with 0.2% clad defects and hold-up time of 60-day delay.(7)

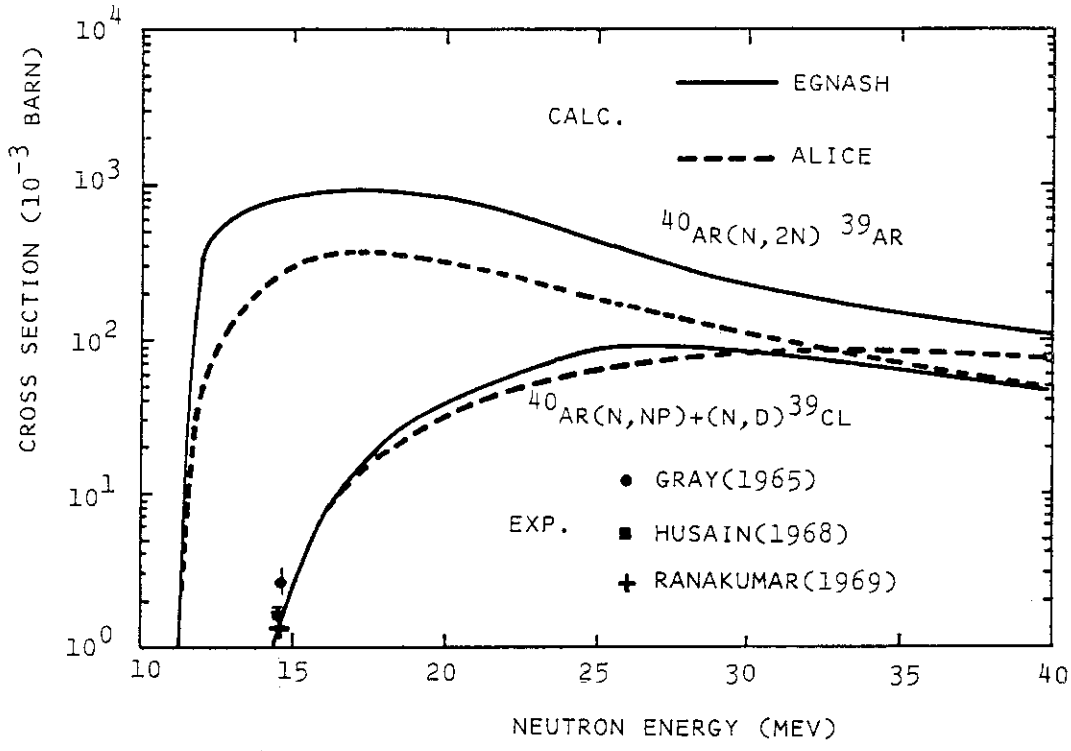

Fig. 1 Cross sections for the $^{40}Ar(n,2n)^{39}Ar$ and $^{40}Ar(n,d)^{39}Cl$+ $^{40}Ar(n,np)^{39}Cl$. Including are those measured by Gray[3], Husain[4] and Ranakumar[5].

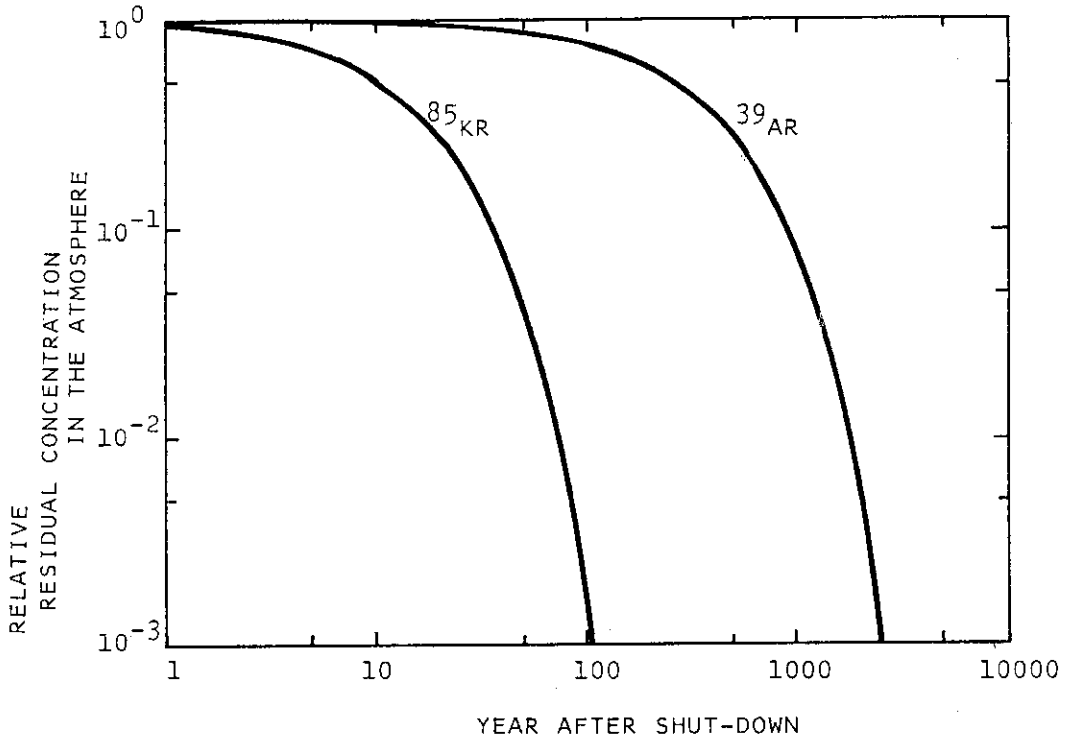

Fig. 2 Residual activities of ^{39}Ar and ^{85}Kr after shut-down of corresponding each reactor.

3.8 MEASUREMENTS OF NEUTRON-INDUCED PROTON AND α-PARTICLE PRODUCTION CROSS SECTIONS USING GRIDDED IONIZATION CHAMBER

N.Ito, M.Baba, F.Huang*, S.Matsuyama, S.Meigo,
M.Yoshioka, I.Matsuyama, and N.Hirakawa

Department of Nuclear Engineering, Tohoku University, Sendai, Japan
*Institute of Heavy Ion Physics, Peking University, Beijing, China

A gridded ionization chamber for measurements of the neutron induced charged-particle production cross sections has been developed and applied to the measurements of (n,p) and (n,α) cross sections for Ni and Cu at incident neutron energies of 4.3 ~ 6.5 MeV and 14.1 MeV. This technique is very effective owing to its large geometrical efficiency. The energy- and angular-differential cross sections and reaction cross sections were deduced and compared with previous experimental and evaluated data.

1. Introduction

Double-differential proton and α-particle production cross sections for fast neutron induced reactions are indispensable for estimation of radiation damage and nuclear heating in structural materials of fission and fusion reactors. The activation method, however, does not provide energy-angular information of emitted particles, and is difficult to apply to the measurements of α-particle production cross sections on structural materials, eg. ^{56}Fe, ^{60}Ni and so on. Therefore, various experimental devices have been developed for the direct measurements of energy- and angular-distributions of emitted particles. However, they have poor geometrical efficiency and require long measuring time due to low count rate and high background.

A gridded ionization chamber is promising for measurements of neutron induced proton and α-particle production cross sections owing to its large geometrical efficiency with capability of energy-angle determination and particle selection. We have developed a gridded ionization chamber suitable for these measurements which has high stopping power and background suppression capability. The performance of the chamber, energy resolution and charge collection under high gas pressure etc., was proved to be proper for these application[1,2].

The gridded ionization chamber was applied to the Ni(n,α), Cu(n,p)

and Cu(n,α) cross section measurements at the incident neutron energies of 4.3 ~ 6.5 MeV and 14.1 MeV. The energy- and angular-differential cross sections and reaction cross sections were deduced and compared with the previous experimental and evaluated data.

2. Experimental Procedure

The gridded ionization chamber applied in this work is shown in Fig.1 schematically. If charged particle emitted from the sample on cathode stops between cathode and Frisch grid, the anode and cathode output signals, P_a and P_c respectively, are represented by the following equations;

$$P_a = E\left(1 - \sigma\frac{\bar{x}}{d}\cos\theta\right) \sim E \qquad (1)$$

$$P_c = E\left(1 - \frac{x}{d}\cos\theta\right) \qquad (2)$$

where

E, θ = energy and emission angle of emitted particle, respectively

σ = grid inefficiency

$\bar{x}$ = distance from the beginning to the center of gravity of the charge distribution of the trace

d = spacing between cathode and grid.

Therefore, we can obtain the emission energy and angle by dealing with two-dimensional spectrum, anode versus cathode, according to these equations.

This chamber can be used to detect α-particles over 20 MeV and protons up to 6.7 MeV with usage of krypton gas. All the electrodes are made by heavy metals, tantalum and tungsten, to reduce background production. A ring electrode is installed around each Frisch grid to suppress background events of long range particles from the sample and those of coming from chamber wall by means of anti-coincidence operation with anode signals. The construction and performance of the chamber are described in detail in Ref.1 and 2.

Kr + 3%CO_2 gas mixture was used because of its high stopping power and low background production. The fraction of CO_2 gas, 3%, was chosen so as to maximize electron drift velocity on our operational electric field, around 0.5 V/cm/Torr. We found electronegative contaminants in counting gas are serious problem, since the chamber is operated under high pressure up to 13 atm.. Thus, the chamber was evacuated for several days before gas filling by a turbo molecular pump. The gain shift of the output signal, anode and cathode, had been monitored during measurements. The gas

pressure (2.8 ~ 12.5 atm.) was optimized for each reaction so as to stop maximum energy particle between cathode and Frisch grid.

Samples of natural nickel, copper foils and polypropylene film, 3, 4 and 10 μm thick respectively, were placed between two cathode plates on a rotatable sample changer which can be operated from outside of the chamber. The polypropylene film was used for neutron flux and energy scale determination. For sample-out measurements, a tungsten foil of 50 μm thick was used.

Figure 2 shows the experimental arrangements; for incident neutron energies of 4.3 ~ 6.5 MeV and 14.1 MeV, monoenergetic neutron beam was obtained by the D(d,n) and the T(d,n) reactions respectively, and collimated within the sample diameter by a copper collimator to reduce backgrounds from the chamber materials. A NE213 detector (2"ϕ×2") monitored source neutrons to normalize neutron fluxes between sample-in and sample-out measurements. For several MeV neutron energy measurements, neutron flux was determined by proton yield from the H(n,p) reaction using the polypropylene sample. For 14 MeV measurements, it is impossible for the gridded ionization chamber to detect 14 MeV proton, so neutron flux was determined by usage of a recoil proton telescope placed instead of the gridded ionization chamber.

Figure 3 illustrates the electronics block diagram; anode and cathode pulse height data were stored by two dimensional data acquisition system. Ring signal was used in anti-coincidence operation as noted above. Energy scale was calibrated using triton peak channel from the $^{6}Li(n_{th},t)$ reaction or proton edge channel from the H(n,p) reaction.

3. Experiment and Data Reduction

Experiments were performed at Tohoku University Dynamitron Facility. Two-dimensional data, anode versus cathode, were acquired for several hours for each reaction.

Figure 4 shows the anode spectrum and two-dimensional spectrum for the Ni(n,α) measurement at 6.0 MeV neutron energy. In anode spectrum which corresponds to energy spectrum, α-particle events from Ni are seen in higher energy region, where there is very little background. A large peaked background due to the $^{16}O(n,\alpha)$ reaction appears in lower energy region, which is not so serious problem because most α-particles from Ni have higher energy. The straight and curved lines in two-dimensional spectrum correspond to 90-deg. and 0-deg. emission angle, respectively. For

emission angle around 90 degree, large energy loss in sample foil disturbs reliable data processing. Thus, we presented the results for emission angle of 0 ~ 60 and 120 ~ 180 degree.

On measurements at 14 MeV neutron energy, background became much larger; main background sources were found to be the $^{12}C(n,\alpha)$ and $^{16}O(n,\alpha)$ reactions in the counting gas.

Two-dimensional spectra were transformed into energy- and angular-differential cross sections (DDXs) according to equations (1) and (2), where $\bar{x}$ data were calculated using stopping power data by Janni[3] instead of ionization density. The reaction cross sections were obtained by integrating DDXs in energy and angle.

4. Results and Discussion

Double-differential α-particle emission cross sections for Ni at 6.5 MeV neutron energy are shown in Fig.5 with those of ENDF/B-VI. No other experimental data are available and only ENDF/B-VI presents DDXs among evaluated data. Energy-integrated angular-distributions at several MeV neutron energy are shown in Fig.6 compared with those by Paulsen et al.[4] and ENDF/B-VI. Present data are in good agreement with those by Paulsen et al., while the ENDF/B-VI evaluation presents isotropic emission. Figure 7 shows angle-integrated energy-distributions for each incident energy; these are overlapping each other in lower α-particle energy region and different only in higher energy region. DDXs at 14.1 MeV neutron energy are shown in Fig.8, while they are still preliminary results, compared with the angle-integrated cross sections at 15 MeV neutron energy by Grimes et al.[5] (divided by 4π) and those of ENDF/B-VI. Although our data have poor statistics, agreement with those by Grimes et al. and ENDF/B-VI is fairly good. Figure 9 shows the α-particle emission cross sections compared with the previous experimental and evaluated data. Present values are in good agreement with those by Paulsen et al.[4] and Wattecamps et al.[7,8] in this neutron energy region and support the evaluation of JENDL-3.

Figure 10 shows the Cu(n,p) cross sections at several MeV neutron energies compared with the evaluations of JENDL-3 and ENDF/B-VI. Present results agree with those of ENDF/B-VI within errors and are smaller than those of JENDL-3. Figure 11 shows the $Cu(n,\alpha)$ cross sections at several MeV neutron energies with earlier experimental and evaluated data. Present results agree with those given in Ref.8; they were obtained by combining activation measurements for ^{63}Cu by Winkler et al. with the small contribu-

tion of ^{65}Cu by Hetrick et al..

5. Conclusion

A gridded ionization chamber with high stopping power suitable for measurements of fast neutron induced charged-particle production cross sections have been developed and applied for Ni(n,α), Cu(n,p) and Cu(n,α) cross section measurements at 4.3 ~ 6.5 MeV and 14.1 MeV neutron energies. The chamber proved very effective because of large geometrical efficiency. Double-differential cross sections and reaction cross sections are deduced by two-dimensional data analysis. The present cross section data are in good agreement with previous experimental data, while no other experimental data are available for DDXs.

Acknowledgment

The authors wish to thank Messrs. T.Takahashi, K.Komatsu, T.Nagaya and C.Akama for their supports in fabrication of the detector system and to Messrs T.Iwasaki, R.Sakamoto and M.Fujisawa for their supports in experiments and accelerator operation.

References

1) N.Ito and M.Baba et al., JAERI-M, 91-032, 302 (1991).
2) M.Baba et al., Proc. Int. Conf. Nuclear Data for Sci. and Tech., Jülich, Germany, (1991) (in press).
3) J.F.Janni., Atomic Data and Nucl. Data Tables, A7 333 (1982).
4) A.Paulsen et al., Nucl. Sci. Eng., 78 377 (1981).
5) S.M.Grimes et al., Phys. Rev., C19 2127 (1979).
6) S.L.Graham et al., Nucl. Sci. Eng., 95 60 (1987).
7) E.Wattecamps et al., Proc. Int. Conf. Nuclear Data for Science and Technology, Antwerp, Belgium, (1982) p.156.
8) E.Wattecamps et al., Proc. Int. Conf. on Fast Neutron Physics, Dubrovnic, Yugoslavia, (1986) p.258.

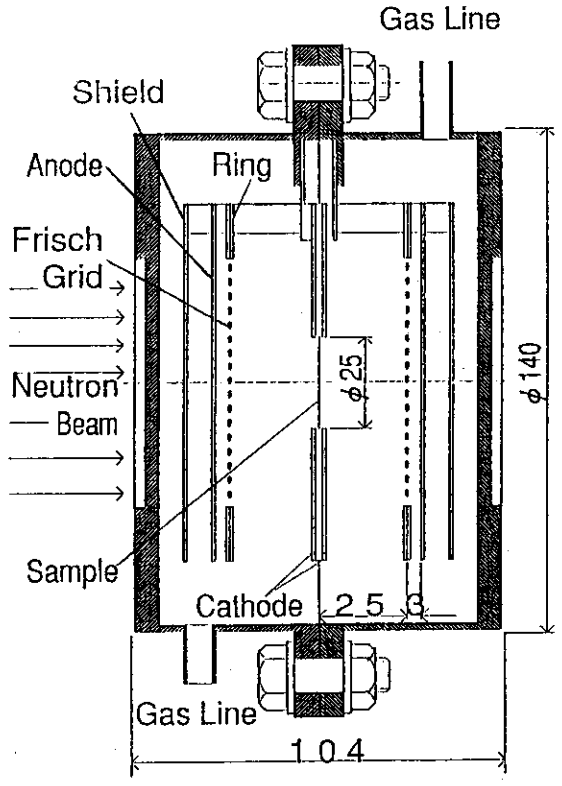

Fig. 1 Schematic view of the gridded ionization chamber applied in this work.

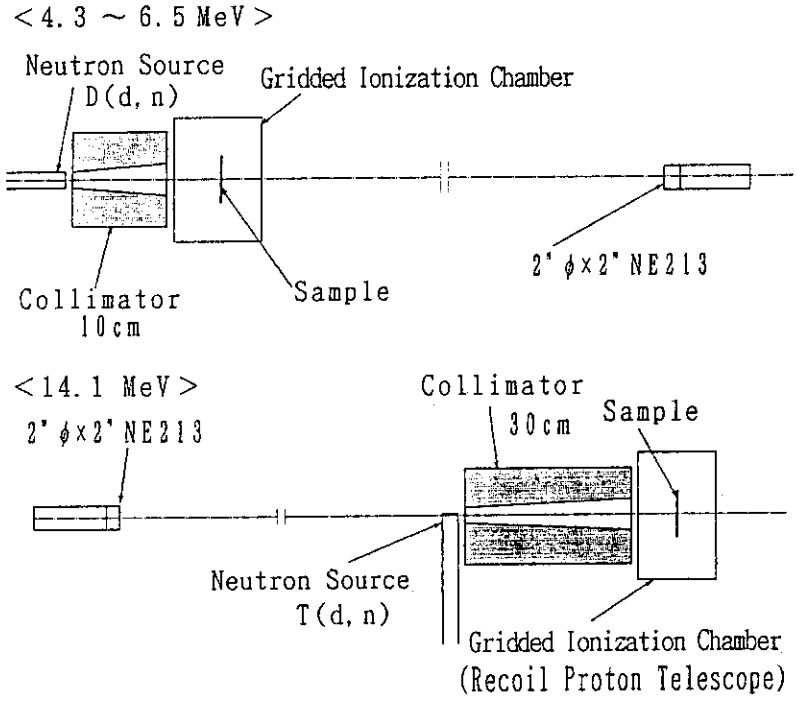

Fig. 2 Experimental arrangements for measurements of several MeV and 14.1 MeV incident neutron energy.

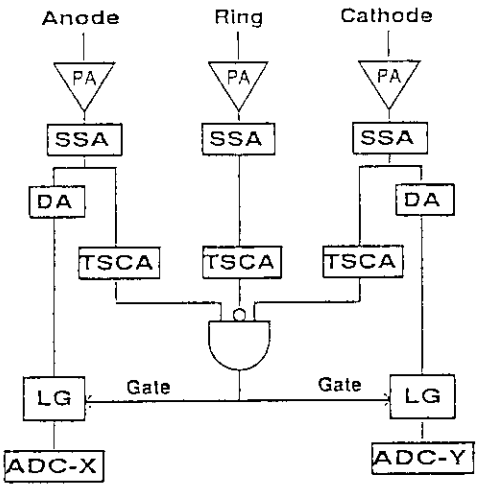

Fig. 3 Electronics block diagram for the measurements.

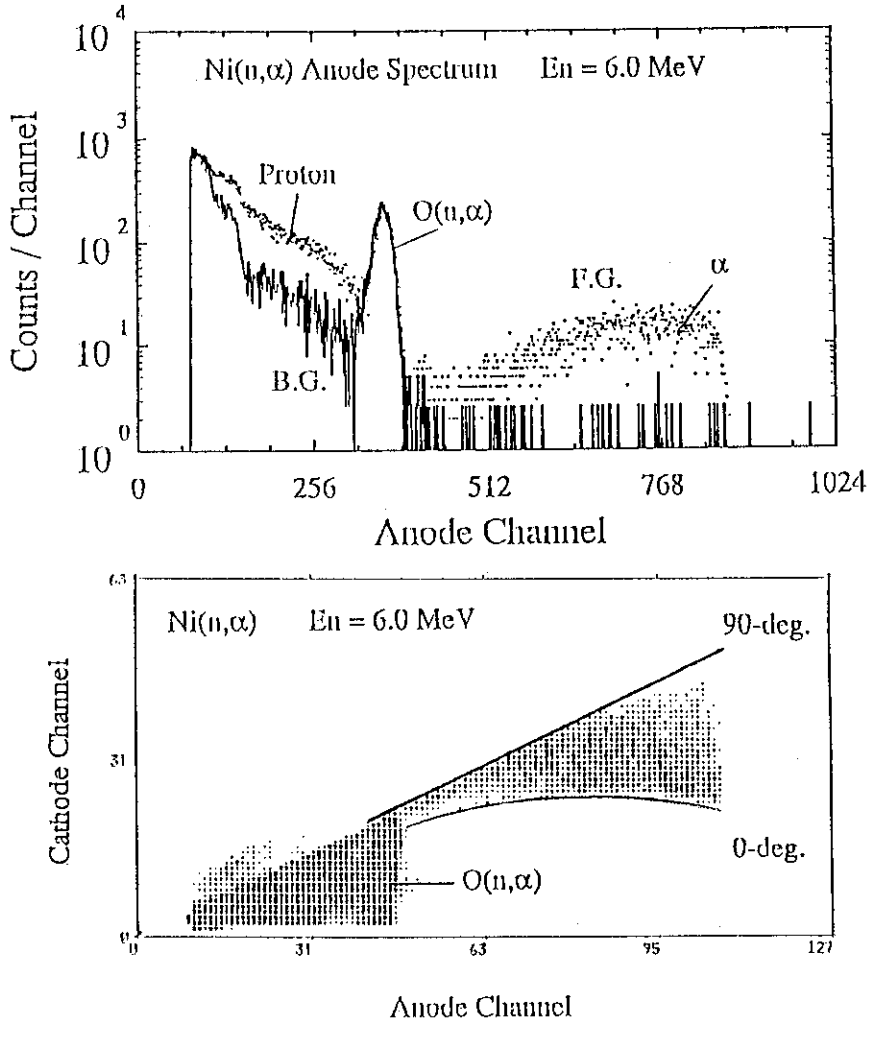

Fig. 4 The anode spectrum and the two dimensional spectrum for the Ni(n,α) measurements at 6.0 MeV neutron energy.

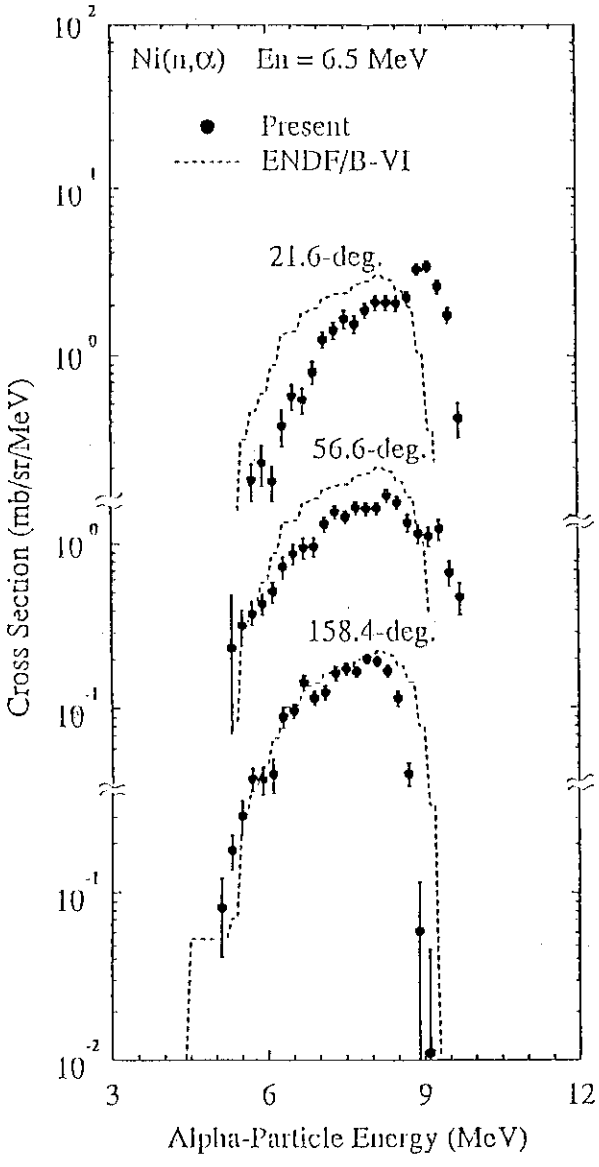

Fig. 5 Double-differential Ni(n,α) cross sections at 6.5 MeV incident energy.

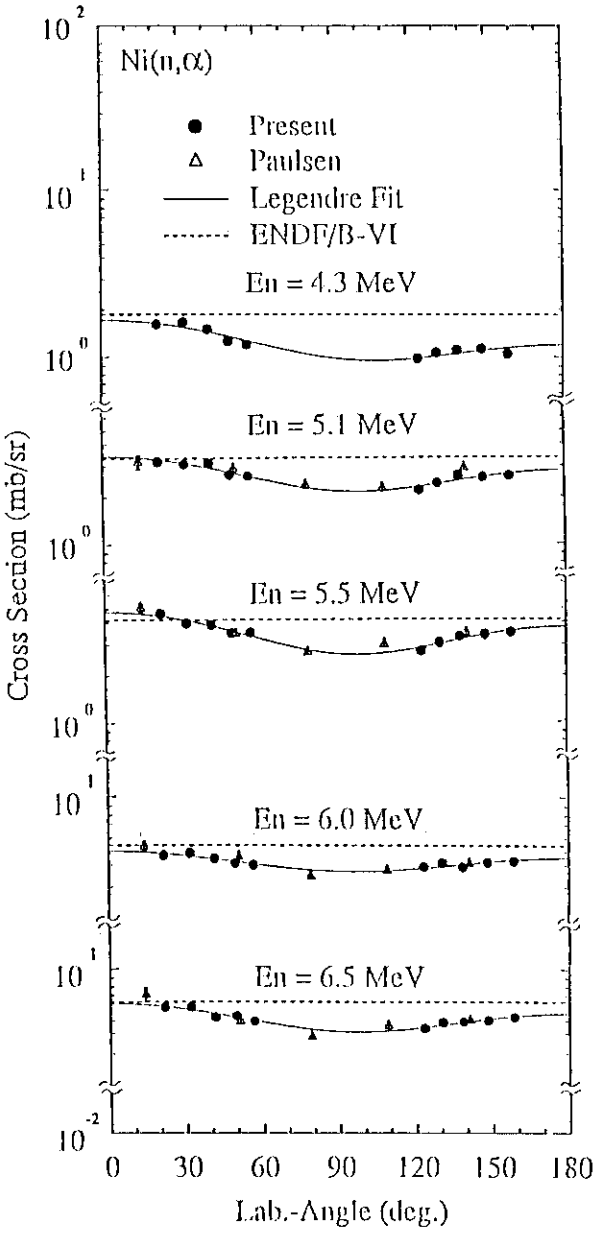

Fig. 6 Energy-integrated angular-distributions for Ni at several MeV neutron energies compared with those by Paulsen et al.[4] and ENDF/B-VI.

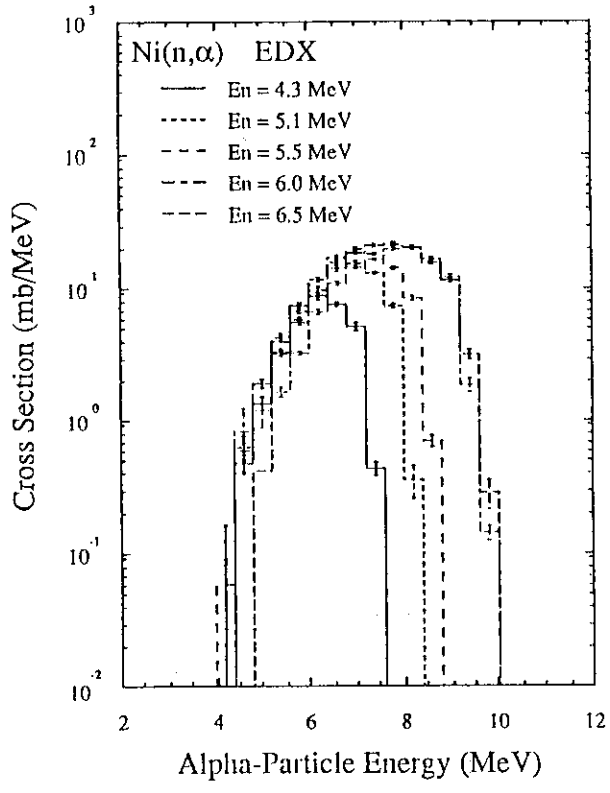

Fig. 7 Angle-integrated energy-distributions for Ni at several MeV incident energies.

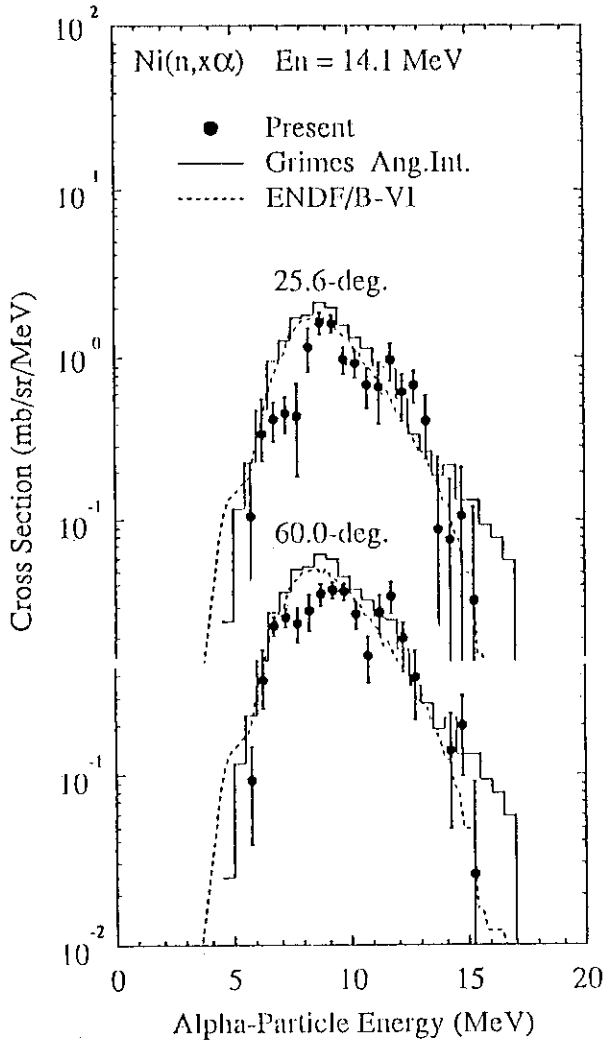

Fig. 8 Double-differential α-particle production cross sections for Ni at 14.1 MeV incident energy compared to those by ENDF/B-VI and angle-integrated cross sections by Grimes et al.[5] (divided by 4π).

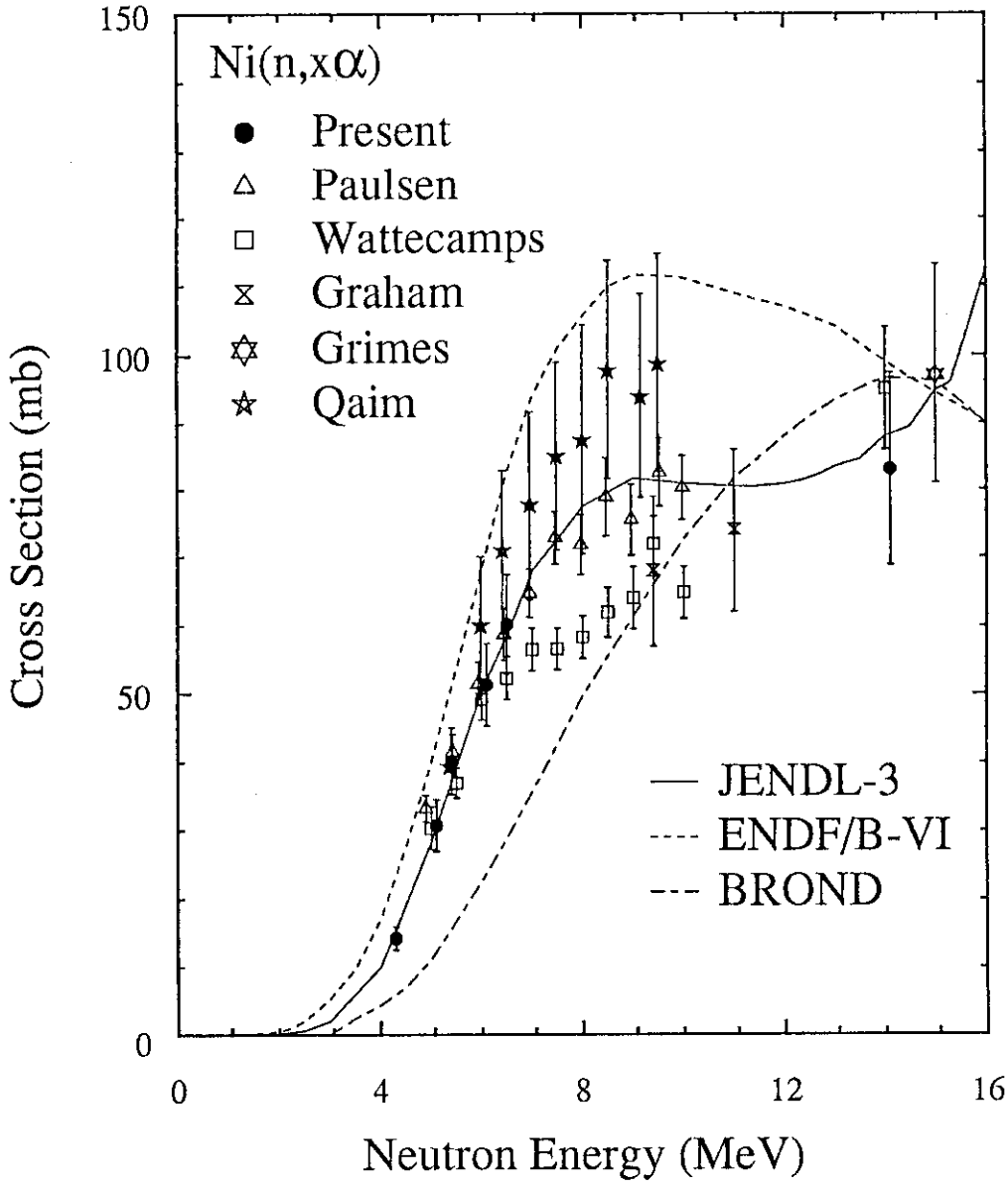

Fig. 9 Neutron induced α-particle production cross sections. Present data are compared with those by Paulsen et al.[4], Grimes et al.[5], Graham et al.[6], Wattecamps et al.[7,8], Qaim et al.[8] and evaluations by JENDL-3, ENDF/B-VI and BROND.

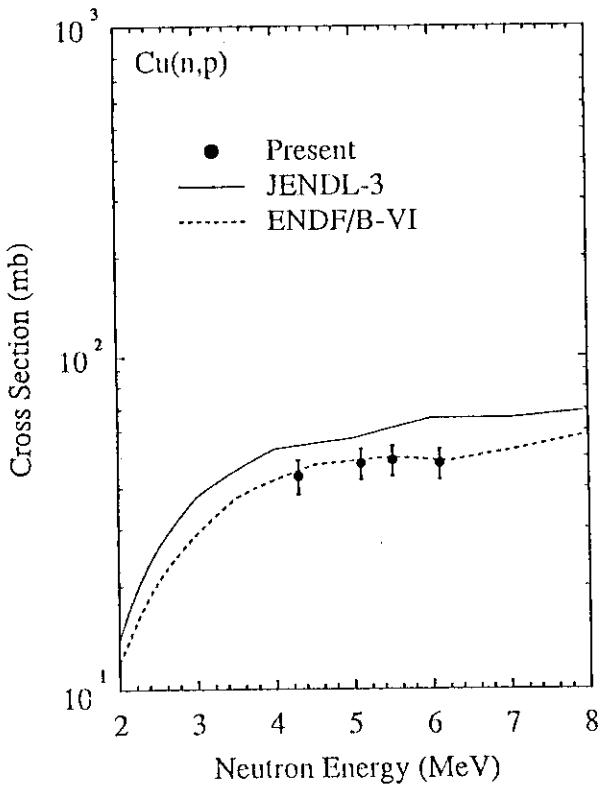

Fig. 10 Cu(n,α) cross sections compared with those by JENDL-3 and ENDF/B-VI.

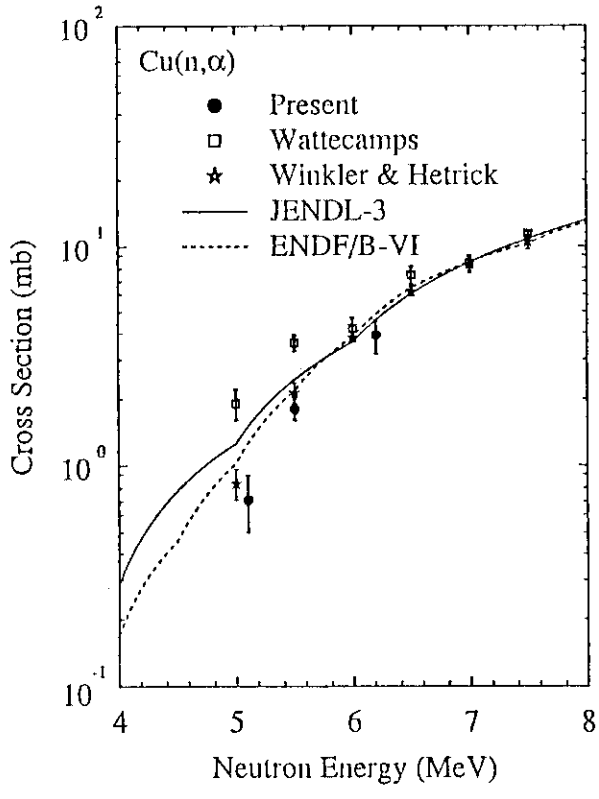

Fig. 11 Cu(n,α) cross sections compared with those by Wattecamps et al.[8], Winkler & Hetrick[8] and evaluations of JENDL-3 and ENDF/B-VI.

3.9 MEASUREMENT OF ACTIVATION CROSS SECTION OF SHORT-LIVED NUCLEI PRODUCED BY 14MeV NEUTRONS — Ru, Pd, Cd, Sn

Y. Kasugai, T. Tokushima, K. Kawade, H. Yamamoto, T. Katoh, *A. Takahashi and *T. Iida

Department of Nuclear Engineering, Nagoya University
*Department of Nuclear Engineering, Osaka University

Neutron activation cross sections of short-lived nuclei with half-lives between 0.5 and 20 min have been systematically measured at neutron energy of 13.4 to 14.9 MeV by activation method. 17 reactions were newly measured. ^{101}Ru(n,p), ^{102}Ru(n,p)^{m}, (n,np), ^{104}Ru(n,p), (n,α), ^{104}Pd(n,p)^{m}, ^{105}Pd(n,p)^{m}, (n,n p)^{m}, ^{106}Pd(n,np)^{m}, ^{108}Pd(n,p)^{g}, (n,2n)^{m}, (n,np), ^{112}Cd(n,α), ^{116}Cd(n,p)^{g}, ^{119}Sn(n,p)$^{m+g}$, ^{120}Sn(n,p)^{m}. The systematics of (n,p), (n,α), (n,2n), (n,np) were investigated, using 73 cross sections which we have measured up to now.

1. Introduction

Neutron activation cross section data around 14MeV have become important from the viewpoint of fusion reactor technology, especially for calculations on radiation damage , nuclear transmutation, induced activity and so on. Cross sections for the reactions leading to short-lived nuclei were measured by activation method.

2. Experiment and Results

Experiments were performed at the Intense 14-MeV-Neutron Source Facility (OKTAVIAN) of Osaka University. For the activation of sample, pneumatic tube were set at 6 directions (between 0°, 50°, 75°, 105°, 125° and 155°) for incident beam direction. The distance between the T-target and irradiation points were 15cm. The induced activities were measured with two Ge detectors(12%, 16%) at an equivalent distance of 5cm. The effective neutron energies were determined by the Zr/Nb method (1). The errors are estimated to be about 50 keV. The neutron flux at the irradiation points was monitored by using two aluminum foils(purity:99.2%, 1cm×1cm×0.2mm^{t}) The reference reaction for the flux measurement was the ^{27}Al(n,p)^{27}Mg (9.46 min)

,which was determined by referring to the standard $^{27}Al(n,a)^{24}Na$ reaction (ENDEF/B-V). Separated isotopes or natural samples were used for irradiation. The samples were between 15 and 70 mg in weight (size:1cm×1cm).

In Table.1, measured reactions and associated data(2) of the half-life ($T_{1/2}$), the γ-ray energy ($E\gamma$), the absolute intensity in photons per disintegration ($I\gamma$) are listed together with the Q-value.

Corrections were made for time fluctuation of neutron flux , thickness of samples, self absorption of γ-ray , sum-peak effect of γ-ray, and contribution of low energy neutrons below 10 MeV. The details of the correction are described in Ref.(3).

The total errors (δt) were described by combining the experimental error(δe) and the error of nuclear data (δr) in quadratic:

$$\delta t^2 = \delta e^2 + \delta r^2$$

Estimated major sources of the errors are listed in Table 2. Accuracy of the obtained cross sections were around 3.5% in case of good statistics. The results are listed in Table 3 and some of them are shown in Fig 1.

3. Discussion

Systematic trends for (n,p), (n, α), (n,2n), (n,np) reactions at 14.9 MeV are shown in Fig.2 as a function of (N-Z)/A, using the data obtained by us and the data in Ref.(4). No definite difference between data of short lived nuclei ($T_{1/2}$=0.5-20 m) and long-lived nuclei (longer than 1 h) is seen. The systematics of (n,p) reactions in Fig.3 clearly shows a mass (A) dependence.

References

(1) V.E.Lewis and K.J.Zieba : Nucl.Instr.and Meth. 174(1980)141.
(2) E.Browne, R.B.Firestone and V.S.Shirley:Table of Radioactive Isotopes "John Wiley & Sons , New York" (1986)
(3) T.Katoh, K.Kawade and H.Yamamoto:JAERI-M 89-083 (1989)
(4) Y.Ikeda, C.Konno, K.Oishi, T.Nakayama, H.Miyade, K.Kawade, H.Yamamoto, and T.Katoh :JAERI 1312 (1988)

Table 1 Reactions and decay parameters

Reaction[a]	$T_{1/2}$	Eγ (keV)	Iγ (%)	Q(MeV)[b]
^{101}Ru(n,p)^{101}Tc	14.2(1)m	363.8	88(4)	-0.84
^{102}Ru(n,p)^{102m}Tc	4.35(7)m	475.1	85.3(20)	-3.74
(n,np)^{101}Tc	14.2(1)m	363.8	88(4)	-10.1
^{104}Ru(n,p)^{104}Tc	18.3(3)m	358.0	79(8)	-4.84
(n,α)^{101}Mo	14.6(1)m	191.9	18.8(10)	-1.06
^{104}Pd(n,p)^{104m}Rh	4.34(5)m	51.4	48.3(5)	-1.79
^{105}Pd(n,np)^{104m}Rh	4.34(5)m	51.4	48.3(5)	-8.89
(n,p)^{105m}Rh	42.4(5)s[c]	129.6	20.0(4)	0.086
^{106}Pd(n,np)^{105m}Rh	42.4(5)s[c]	129.6	20.0(4)	-9.48
^{108}Pd(n,p)^{108g}Rh	6.0(3)m	581.0	59(12)	-3.65
(n,2n)^{107m}Pd	21.3(5)s	214.9	69.0(10)	-9.43
(n,np)^{107}Rh	21.7(4)m	302.8	66(5)	-9.95
^{116}Cd(n,p)^{116g}Ag	2.68(1)m	513.5	76(4)	-1.40
^{112}Cd(n,α)^{109m}Pd	4.69(1)m	188.9	55.8(7)	2.45
^{119}Sn(n,p)^{119g}In	2.4(1)m	763.1	99.08(14)	-1.55
(n,p)^{119m}In	18.0(3)m	311.4	0.99(20)	-1.86
^{120}Sn(n,p)^{120m}In	44.4(10)s	1171.4	97.1(5)	-4.52

[a] (n,np) means [(n,d)+(n,n'p)+(n,pn)].

[b] Q(n,n'p) is given here. Q(n,d)=Q(n,n'p)+2.225 MeV.

[c] measured by us.

Table 2 Principal sources of uncertainty in the measured cross sections

Experimental error (δe)	
Source of error	Uncertainty(%)
Counting statistics	0.5-40
Sample mass including purity	0.1
Neutron flux fluctuation	<0.1
Gamma-peak area evaluation	0.5
Detector efficiency	1.5 ($E\gamma$ >300keV)
	3 (300-80keV)
	5 ($E\gamma$ <80keV)
Efficiency calibration at 0.5 and 5 cm	1.0
Correction for true coincidence sum	<0.3
Correction for random coincidence sum	<0.4
Correction for sample thickness	0.2-0.4
Correction for self-absorption of γ-rays	0-0.3
Correction for low energy neutrons	0-5
Secondary reference cross section for $^{27}Al(n,p)^{27}Mg$	0.5 (only statistics)

Error of nuclear data (δr)	
Source of error	Uncertainty(%)
Reference cross section for $^{27}Al(n,\alpha)^{24}Na$ (ENDF/B-V)	3.0
Absolute γ-ray intensity	0-20
Half-life	0-5

Table 3 Activation cross sections of short-lived nuclei

En(MeV)	^{101}Ru(n,p)^{101}Tc	^{102}Ru(n,p)^{102m}Tc	^{102}Ru(n,np)^{101}Tc
14.87	25.8(15)mb	7.08(38)mb	2.95(20)mb
14.58	25.6(15)	6.99(38)	2.21(16)
14.28	23.1(14)	5.64(33)	1.47(12)
13.88	20.5(12)	5.39(29)	0.94(6)
13.65	19.7(12)	4.75(27)	0.71(7)
13.40	18.8(11)	4.00(23)	0.58(7)

En(MeV)	^{104}Ru(n,p)^{104}Tc	^{104}Ru(n,α)^{101}Mo	^{104}Pd(n,p)^{104m}Rh
14.87	7.81(87)mb	2.53(32)mb	21.5(23)mb
14.58	7.53(85)	2.60(37)	22.3(24)
14.28	6.41(73)	2.01(33)	21.4(22)
13.88	5.26(59)	1.81(25)	19.5(20)
13.65	4.85(72)	1.40(29)	18.6(19)
13.40	4.02(46)	1.52(23)	17.1(18)

En(MeV)	^{105}Pd(n,np)^{104m}Rh	^{105}Pd(n,p)^{105m}Rh	^{106}Pd(n,np)^{105m}Rh
14.87	9.7(12)mb	5.45(35)mb	1.3(4)mb
14.58	7.9(10)	4.16(28)	1.5(5)
14.28	9.1(13)	2.97(21)	1.0(4)
13.88	8.6(11)	2.11(15)	0.5(2)
13.65	8.3(11)	1.73(13)	
13.40	6.8(9)	0.98(9)	

En(MeV)	^{108}Pd(n,np)^{107}Rh	^{108}Pd(n,p)^{108g}Rh	^{108}Pd(n,2n)^{107m}Pd
14.87	1.83(38)mb	3.29(67)mb	387(20)mb
14.58	1.16(25)	2.78(59)	389(20)
14.28	0.88(21)	1.96(44)	373(20)
13.88	0.55(13)	1.83(38)	356(18)
13.65	0.30(8)	1.53(33)	388(22)
13.40	0.33(9)	1.61(34)	353(19)

Table 3 Continued from the previous page

En(MeV)	$^{116}Cd(n,p)^{116g}Ag$	$^{112}Cd(n,\alpha)^{109m}Pd$	$^{120}Sn(n,p)^{119m}In$
14.87	2.28(26)mb	0.63(19)mb	4.39(48)mb
14.58	1.66(18)	0.60(16)	3.72(50)
14.28	1.47(18)	0.54(12)	3.08(46)
13.88	1.27(15)	0.55(11)	2.38(35)
13.65	0.89(12)	0.38(10)	2.57(35)
13.40	0.78(11)	0.39(10)	1.77(27)

En(MeV)	$^{119}Sn(n,p)^{119g}In$	$^{119}Sn(n,p)^{119m}In$
14.87	6.25(45)mb	5.4(13)mb
14.58	5.36(43)	4.6(11)
14.28	5.12(43)	4.4(11)
13.88	4.08(33)	3.5(8)
13.65		
13.40	3.00(26)	2.6(6)

* Error of neutron energy is estimated as about 50 keV.

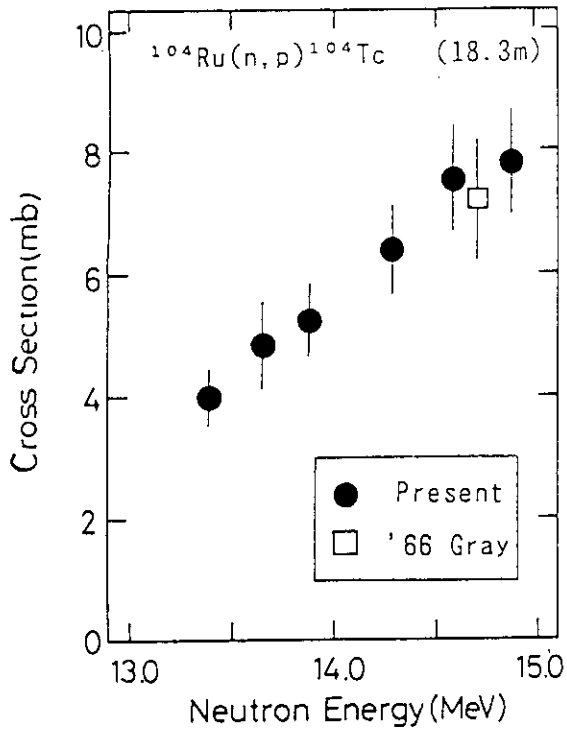

Fig. 1-1 Cross section of ^{104}Ru(n,p)^{104}Tc.

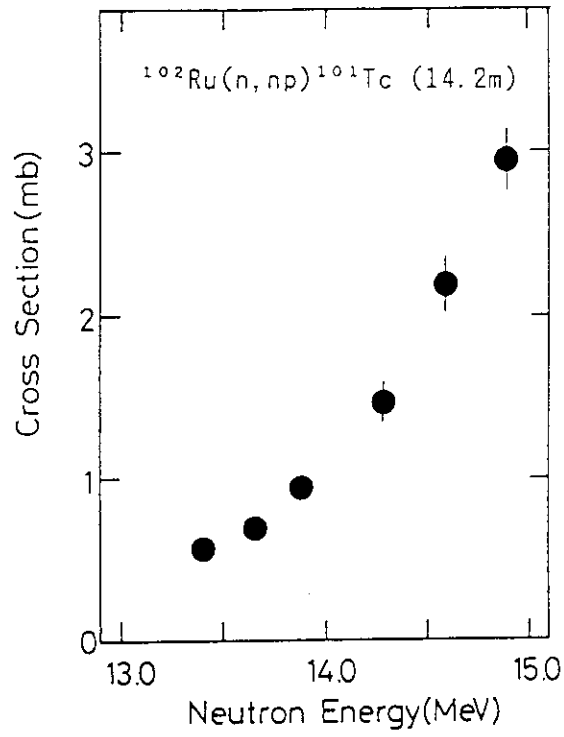

Fig. 1-2 Cross section of ^{102}Ru(n,np)^{101}Tc.

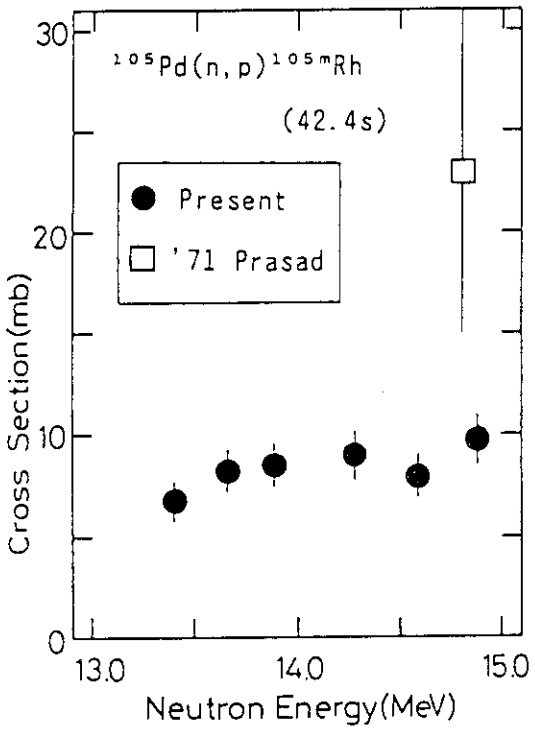

Fig. 1-3 Cross section of ^{105}Pd(n,p)^{105m}Rh.

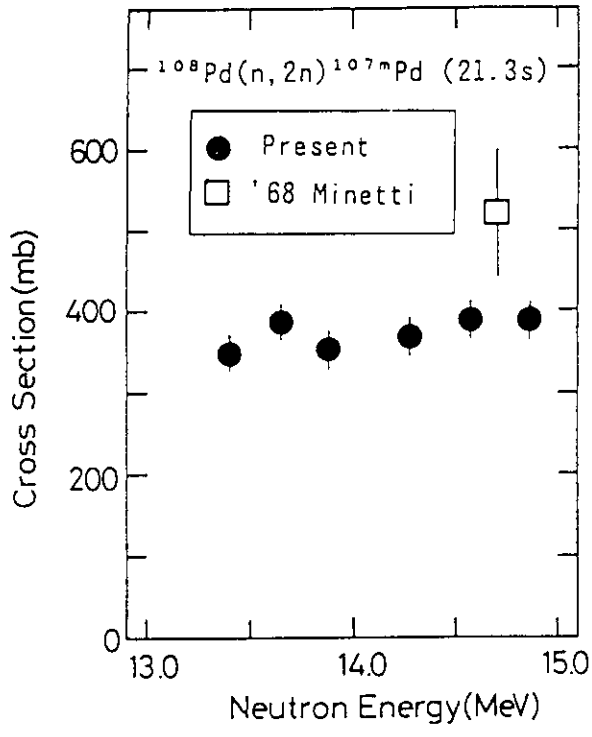

Fig. 1-4 Cross section of ^{108}Pd(n,2n)^{107m}Pd.

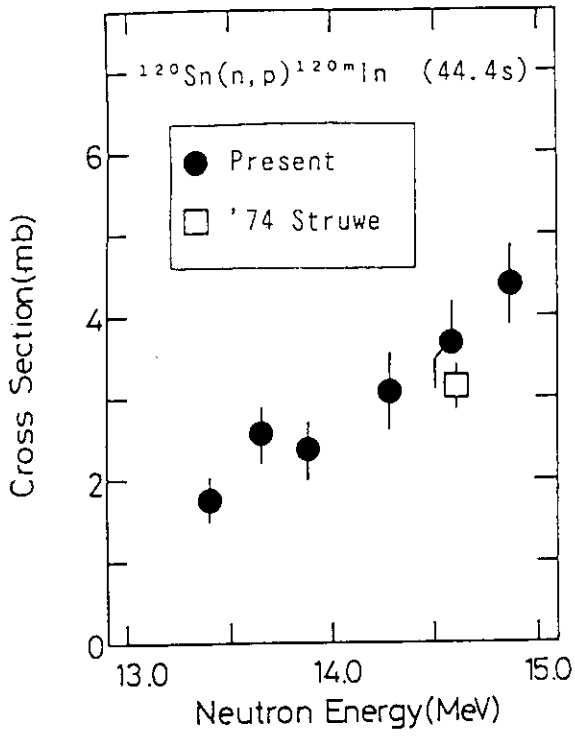

Fig. 1-5 Cross section of $^{120}Sn(n,p)^{120m}In$.

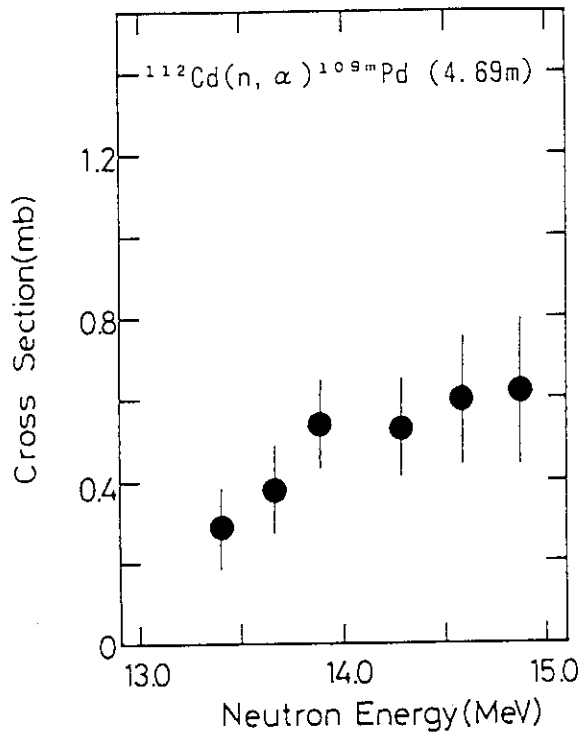

Fig. 1-6 Cross section of $^{112}Cd(n,\alpha)^{109m}Pd$.

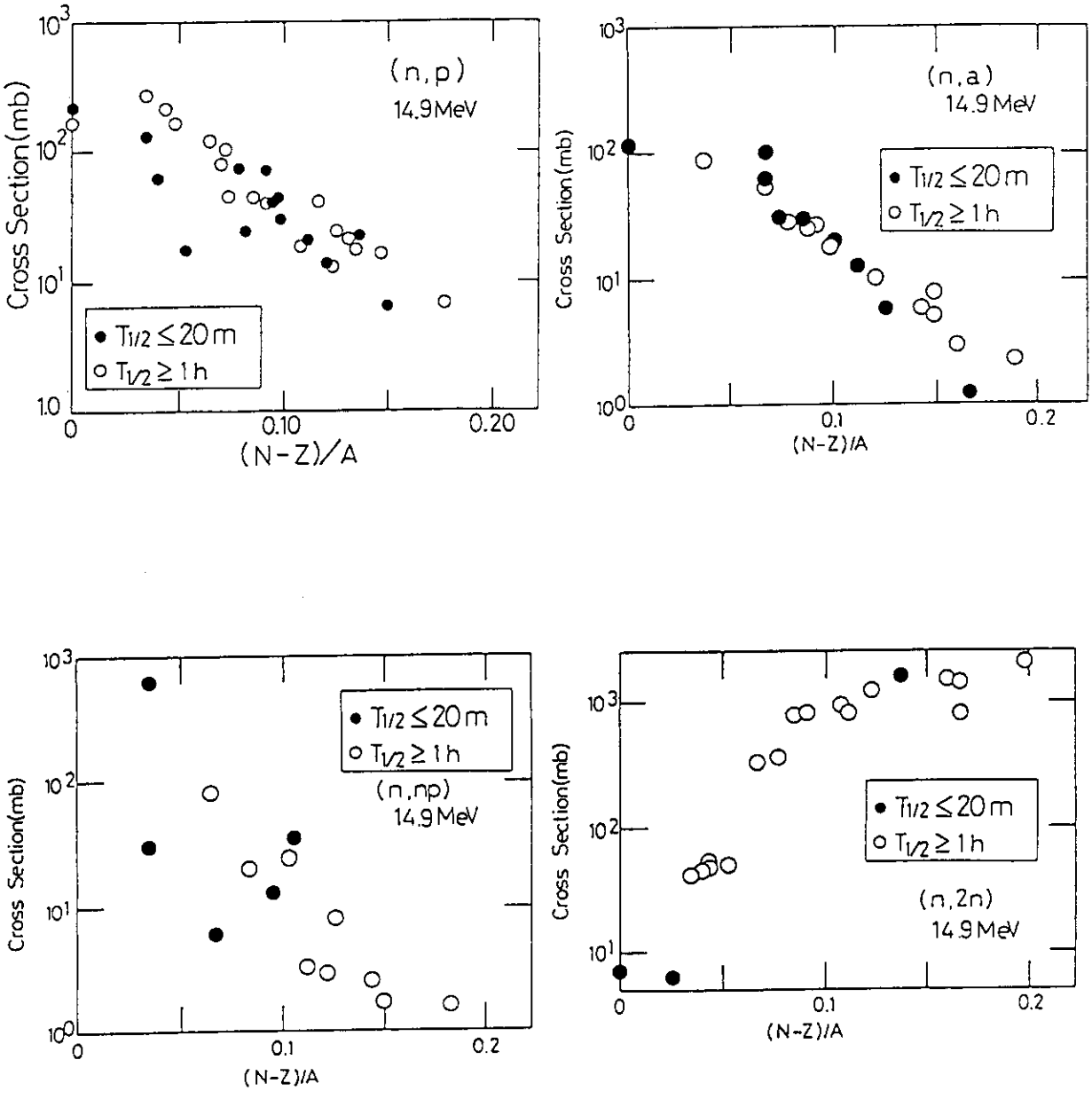

Fig. 2 Systematics of (n,p),(n,α),(n,np),(n,2n) reaction cross sections at 14.9 MeV. Open circles show cross sections with half-lives longer than 1 h. Closed circles show cross sections with half-lives shorter than 20 m. No definite difference between data of short-lived nuclei and long-lived nuclei.

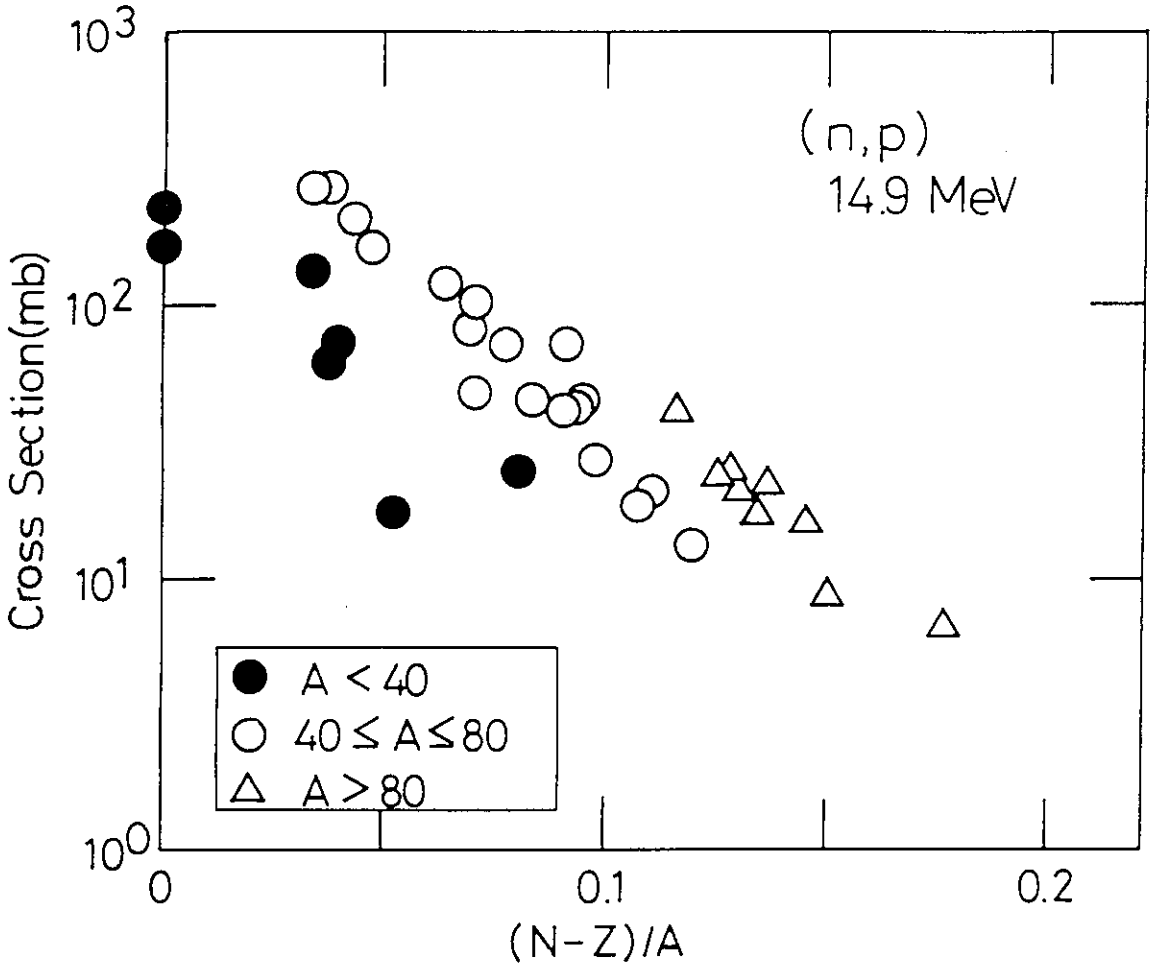

Fig. 3 Systematics of (n,p) reaction cross sections at 14.9 MeV. Mass(A) dependence is clearly seen.

3.10 MEASUREMENT OF (n, 2n) CROSS SECTIONS FOR SEVERAL DOSIMETRY REACTIONS BETWEEN 12 AND 20MeV

M. Sakuma, S. Iwasaki, H. Shimada, N. Odano, K. Suda, J.R. Dumais,
and
K. Sugiyama

Department of Nuclear Engineering, Tohoku University
Aramaki-Aza-Aoba, Aobaku, Sendai 980, Japan

ABSTRACT

Reliability of cross sections for the ^{93}Nb$(n,2n)^{92m}$Nb, ^{197}Au$(n,2n)^{196}$Au reactions of the recently–compiled dosimetry files (JENDL Dosimetry File and IRDF–90) was examined by measuring cross section ratios of these reactions to the standard ^{27}Al$(n,\alpha)^{24}$Na reaction in the neutron energy range from 12 to 20 MeV. In addition, the (n,2n) cross sections of ^{23}Na, ^{55}Mn and ^{58}Ni have been measured in the energy range from 16 MeV to 20 MeV by means of the activation technique relative to the ^{93}Nb$(n,2n)^{92m}$Nb reaction given in IRDF-90.

1. Introduction

For the neutron dosimetry application above 10 MeV, (n,2n) reaction is appropriate because of its high threshold energy and being insensitive to the low energy neutrons. For this purpose, the reliable cross section data are indispensable in the energy range from the threshold energies up to 20 MeV or more. Three dosimetry files[1] ~ [3], which have recently been compiled, include several important (n,2n) reactions. Nevertheless, some of the reactions are apparently discrepant between the files, and show inconsistency with the integral test in the Li+d neutron field[4]. Specifically, remarkable difference of a factor of about two is found in the excitation function of the ^{23}Na$(n,2n)^{22}$Na reaction between JENDL Dosimetry File[1] and ENDF/B–VI[2]. Furthermore, even among very recent measurements, reported data are still inconsistent with each other [5] ~ [7].

In such cross section measurements by the activation method, the cross section for the ^{27}Al$(n,\alpha)^{24}$Na reaction has been employed as the standard one to determine the neutron flux at sample position. However, depending on the experimental conditions,

some features of this reaction become disadvantageous, for example, small cross section, steep excitation function and relatively short half life of the residual activity. In recent literature, some cross sections have been measured relative to those of ^{93}Nb$(n,2n)^{92m}$Nb or ^{197}Au$(n,2n)^{196}$Au reactions. Neither of the reaction is, however, considered to be established as the standard or reference one so far.

In the present study, first as to JENDL Dosimetry File and IRDF−90[3] reliability of above two cross sections was tested by measuring the cross section ratios to the standard ^{27}Al$(n,\alpha)^{24}$Na reaction. Next, the (n,2n) reaction cross sections of ^{23}Na, ^{55}Mn, and ^{58}Ni were measured by the activation method relative to the ^{93}Nb$(n,2n)^{92m}$Nb reaction.

2. Test of ^{93}Nb$(n,2n)^{92m}$Nb and ^{197}Au$(n,2n)^{196}$Au cross sections

2.1. Experimental procedures

Source neutrons for the irradiation experiment were produced by the T$(d,n)^4$He reaction using the Dynamitron accelerator at Fast Neutron Laboratory of Tohoku University. A deuteron beam(10 μA average current) of about 3 MeV bombarded an air-cooled Ti-T target (Ti layer of 11 mm in diameter, 10.1 mg/cm^2 in thickness) on copper backing(0.5mm in thickness) mounted in a thin copper chamber. Two series of the irradiations were conducted. The conditions of the two irradiations are summarized in Table 1. Figure 1 shows the experimental arrangement of the second irradiation, while both irradiations have been arranged in almost the same way. The size of the rectangular foils was 10×10×0.5t mm in the first irradiation and 20×5×0.5t mm in the second, except that the Au foils were 0.2 mm in thickness. One sample set was composed of two Al foils sandwiched between Nb foils with a Au foil opposite to the target. The packages were fixed on an Al holder consisted of two thin ring-shaped plates, at angles from 0 to 140 degree with respect to the incident deuteron beam. The center of the holder ring was adjusted to the neutron target center. It was 57mm from the target to the front surface of the sample set. During the irradiations, neutron intensity was monitored with an 2"ϕ×2"t NE-213 liquid scintillation detector. The neutron pulse counts from the detector were recorded in multi-channel-scaler(MCS) mode.

Characterization of the neutron source has been performed by the neutron time-of-flight method with a pulsed beam from the accelerator before and after the irradiations. The neutron energies were measured at angles from 0 to 150 degree at intervals of 10 or 5 degree with the NE-213 detector in a shielded-goniometer at about 6.5 m from the target.

After the irradiation, gamma-rays from the sample foils were measured using an 80cc high-purity Ge detector. Full energy peak efficiencies of the detector were calibrated with a set of standard γ-ray sources. For fitting of the efficiency curve, conditions were calculated by means of least squares method considering the covariance between the parameters.

2.2. Data analysis

2.2.1. Calculation of cross section ratios

Reaction rate R_j for the reaction j can be obtained from the γ-ray full energy peak counts C by the formula,

$$R_j = \sigma_j \phi = \frac{\lambda C}{\eta \varepsilon N (1 - e^{-\lambda t_i}) e^{-\lambda t_c} (1 - e^{-\lambda t_m})}, \tag{1}$$

where σ_j is the cross section for the reaction and ϕ is the neutron flux at sample position, λ – the decay constant of the product, η – the γ-ray emission probability, ε – the efficiency of the γ-ray , N – atom number of the target nuclide in the sample, t_i ,t_c ,t_m – the irradiation ,cooling time and the time for γ-ray measurement,respectively.

Assuming that the irradiating neutrons are monoenergetic and the flux at Nb foil equals to at Al foil , the cross section ratio r_σ can be simply given by the formula,

$$r_\sigma = \frac{R_{Nb}}{R_{Al}} = \frac{\sigma_{Nb}\phi_{Nb}}{\sigma_{Al}\phi_{Al}} = \frac{\sigma_{Nb}}{\sigma_{Al}}. \tag{2}$$

Corrections required to apply this formula are described in the next section.

2.2.2. Corrections and error analysis

The effects of the following items on the reaction rates were considered.

1. Fluctuation of the neutron flux during the irradiation.

   — The correction factors for respective reactions were calculated using the MCS records.

2. Difference of the neutron flux between the foils.

   — The flux at the Al foils was estimated from the flux at two neibouring Nb foils by interpolation, and the flux at Au foil was calculated by extrapolation.

3. Nonmonochromaticity of the irradiating neutrons.

— It is mainly due to the finite solid angle of the samples,the energy loss of the incident deuteron beam in the Ti-T target, and neutron scattering by the materials surrounding the target and samples. The effects were totally estimated by a Monte-Carlo simulation using MCNP code[8].

4. Contribution of parasitic $D(d,n)^3He$ neutrons to the reaction rate of $^{27}Al(n,\alpha)^{24}Na$.

   — The intensity ratio of the neutron flux by the $D(d,n)^3He$ to by the $T(d,n)^4He$ was estimated from the time-of-flight spectrum. The contribution was calculated with the $^{27}Al(n,\alpha)^{24}Na$ cross section data from IRDF–90.

5. Self-absorption of γ-rays in the foils.

   — The self-absorption factor f_a for sample was evaluated from the formula,

$$f_a = \frac{1 - e^{-\mu t}}{\mu t}, \tag{3}$$

   where μ is the mass absorption coefficient of sample material and t is the thickness of sample.

Table 2. lists the components and magnitudes of estimated uncertainty. Main sources are counting statistics and detection efficiency of γ-ray. The large error (2.6%) in the γ-ray emission probability is due to those of ^{196}Au.

2.3. Results and discussion

The results of cross section ratios of the $^{93}Nb(n,2n)^{92m}Nb$ and $^{197}Au(n,2n)^{196}Au$ to the $^{27}Al(n,\alpha)^{24}Na$ reaction are compared with the calculated ratios based on the dosimetry files, IRDF–90 and JENDL Dosimetry File, in Figure 2 and Figure 3. The cross section for the $^{27}Al(n,\alpha)^{24}Na$ reaction is nearly equal between the files, because the data of IRDF–90 have slightly been changed from ENDF/B–V[9], from which the cross section of JENDL Dosimetry File was actually taken. These figures show that for both reactions the ratios based on IRDF–90 are in good agreement with the present results and appear to be better than the ratios based on JENDL Dosimetry File over the tested energy range, except for the ratio of Nb to Al in the region above 18 MeV. The reason of these results could be interpreted as the difference of the evaluation methodologies adopted in both files; in IRDF–90 the statistical method has been employed, while in JENDL Dosimetry File the evaluation was mainly based on fitting of the theoretical model to the experimental data. Consequently, it is concluded that the cross

sections of the dosimetry files for the ^{93}Nb$(n,2n)^{92m}$Nb and the ^{197}Au$(n,2n)^{196}$Au reactions can be used as the reference ones in the energy range from 12 to 20 MeV, although further differential and integral studies are necessary. In the (n,2n) cross sections measurement described in the following section, the cross section for the ^{93}Nb$(n,2n)^{92m}$Nb reaction of IRDF–90 was used to determine the neutron flux at sample position.

3. Measurement of (n,2n) Reaction Cross Sections for ^{23}Na, ^{55}Mn and ^{58}Ni.

3.1. Experimental procedures

The experimental set up was almost the same as described in the preceding section. The conditions of the irradiation are given in Table 3. A set of sample was shown in Figure 4. The size of high-purity metal foils was 25×15×0.2t mm for nickel and 25×15×0.5t mm for niobium. For sodium and manganese, samples were prepared in the form of NaCl compound and metallic Mn powder respectively, which were packed in rectangular boxes made of aluminum. Then they are fixed at angles from 0 to 80 degree to the beam. The standard dimension of the boxes was 25×15×5t mm. Larger boxes were also prepared for NaCl of 25×15×10t mm so as to obtain sufficient yields of the residual activity. Thickness of the side wall of boxes was 1.5mm, Al foils at front and end window were 0.2mm thick. Ni foil was put in front of Mn sample set. All the samples were put between Nb foils to determine the neutron flux in the sample and attached to the holder. The irradiation was conducted for about 80 hours under the beam condition described in Table 3.

3.2. Results and discussion

Reaction rate were calculated from the equation (1) for each sample. The estimated uncertainty of the results is summarized in Table 4. The reference cross section data are the main source of the uncertainty in addition to the γ-ray counting statistics and detection efficiency.

In Figures 5,6 and 7 preliminary results of the (n,2n) cross sections are compared with the data in literature and dosimetry files. For the ^{23}Na$(n,2n)^{22}$Na reaction, the data can be divided into three groups; the larger cross section group represented by ENDF/B–VI, the smaller group by IRDF–85[10] and JENDL Dosimetry File, and the intermediate group. The present result belongs to this intermediate group, together with the recent ones by Strohmaier et al.[5] and Lu Hanlin[6]. It is fairly in good agreement with the result of the integral test in the Li(d,n) neutron field[4]. The

result for the $^{55}Mn(n,2n)^{54}Mn$ reaction is consistent with the recent files. It is close to the measurement by Bormann et al.[11] and Menlove et al[12]. For the $^{58}Ni(n,2n)^{57}Ni$ reaction, the present work gives relatively lower values than the recent files. Further study is necessary for this reaction.

4. Summary

The cross sections for the $^{93}Nb(n,2n)^{92m}Nb$ and the $^{197}Au(n,2n)^{196}Au$ reactions of JENDL Dosimetry File and IRDF-90 were examined by measuring the cross section ratio to the $^{27}Al(n,\alpha)^{24}Na$. The results indicate that the data of IRDF-90 are more reliable as the 'reference' cross sections in the neutron energy range from 12 to 20 MeV.

The cross sections for the $^{23}Na(n,2n)^{22}Na$, $^{55}Mn(n,2n)^{54}Mn$ and $^{58}Ni(n,2n)^{57}Ni$ reactions were measured in the energy range from 16 to 20MeV.

These are preliminary and not final results yet. More accurate estimation of corrections and error analysis are needed.

The authors wish to express their thanks to the staffs of Fast Neutron Laboratory for their technical assistance.

References

(1) M. Nakazawa, K. Kobayashi, S. Iwasaki, T. Iguchi, Y. Ikeda, K. Sakurai, and T. Nakagawa, to be published in JAERI-REPORT, (1991) JENDL Dosimetry File.

(2) BNL/National Nuclear Data Center, ENDF/B-VI, (1990).

(3) N.P. Kocherov and H. Vonach, Proc. of the 7th ASTM-EURATOM Symposium on Reactor Dosimetry, Strasbourg, France,27-31 August, 1990 (to be published), IRDF-90.

(4) J.R.Dumais, S.Iwasaki, N.Odano, M.Sakuma and K.Sugiyama, Proc. of the Int. Conf. on Nucl. data for Science and Technology, Jülich, Federal Republic of Germany, 13–17 May, 1991 (to be published).

(5) B. Strohmaier, M. Wagner and H. Vonach, Proc. of the Int. Conf. on Nucl. data for Science and Technology, Jülich, Federal Republic of Germany, 13–17 May, 1991 (to be published).

(6) Lu Hanlin, quoted in ref.(5).

(7) Xu Zhi-zheng, Pan Li-Min, Wu Zhi-hua, Proc. of the Int. Conf. on Nucl. data for Science and Technology, Jülich, Federal Republic of Germany, 13–17 May, 1991 (to be published).

(8) Los Alamos Monte Carlo Group, LA-7396-M(1981), MCNP-A General Monte Carlo Code for Neutron and Photon Transport .

(9) BNL/National Nuclear Data Center, ENDF/B-V, (1979).

(10) D.E. Cullen, N. Kocherov, and P.M. Mclaulin,IAEA-NDS-41/R, rev.0 (1982). IRDF-85 is a modified version with additional cross section data.

(11) M. Bormann and B.Lammers Nucl.Phys.section A,**130**,195 (1969)

(12) H.O. Menlove, K.L.Coop, H.A.Grench and R.Sher, Phys.Rev.,**163**,1308(1967)

Table 1 Conditions of neutron irradiations for the test of two cross sections, $^{93}Nb(n,2n)^{92m}Nb$, $^{197}Au(n,2n)^{196}Au$.

	Exp.-(1)		Exp.-(2)	
Neutron energy	19.9–12.8	MeV	19.4–12.7	MeV
Angle for irradiation	0–140	deg.	0–140	deg.
d^+ energy	3.26	MeV	2.85	MeV
Beam current	10	μA	10	μA
Irradiation time	50	hour	36	hour

Table 2 Sources of uncertainty for the test of the two cross sections, $^{93}Nb(n,2n)^{92m}Nb$ and $^{197}Au(n,2n)^{196}Au$.

Component	Magnitude(%)
Counting statistics of γ-ray	0.7–2.0
Detection efficiency of γ-ray	2.1–4.5
Sample mass	< 0.1
Sample purity	< 0.1
Decay half life of nuclide	0.1–0.2
Emission probability of γ-ray	0.002–2.6
Total uncertainty	2.5–7.0

Table 3 Conditions of neutron irradiation for the measurement of (n,2n) cross sections of ^{23}Na, ^{55}Mn and ^{58}Ni.

Neutron energy	19.4–15.9	MeV
Angle for irradiation	0–80	deg.
d^+ energy	2.83	MeV
Beam current	10	μA
Irradiation time	84	hour

Table 4 Sources of uncertainty for the measurement of (n,2n) cross sections of ^{23}Na, ^{55}Mn and ^{58}Ni.

Component	Magnitude(%)
Counting statistics of γ-ray	0.5–2.0
Detection efficiency of γ-ray	2.5–4.0
Sample mass	$\leq$ 0.1
Sample purity	$\leq$ 0.1
Decay half life of nuclide	0.03–0.6
Emission probability of γ-ray	0.02–0.5
Uncertainty of reference cross section data (IRDF-90)	2.2–3.0
Total uncertainty	3.5–5.5

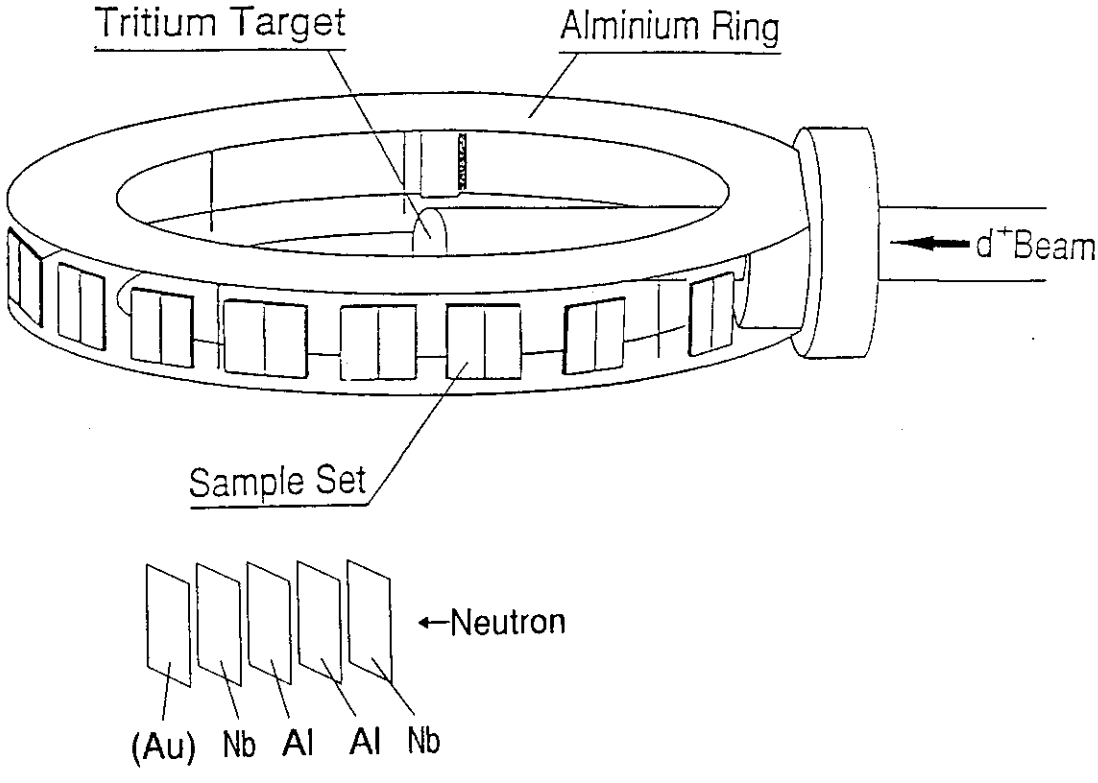

Fig. 1 Experimental arrangement for sample irradiation and a sample set (test of two cross sections, $^{93}Nb(n,2n)^{92m}Nb$ and $^{197}Au(n,2n)^{196}Au$).

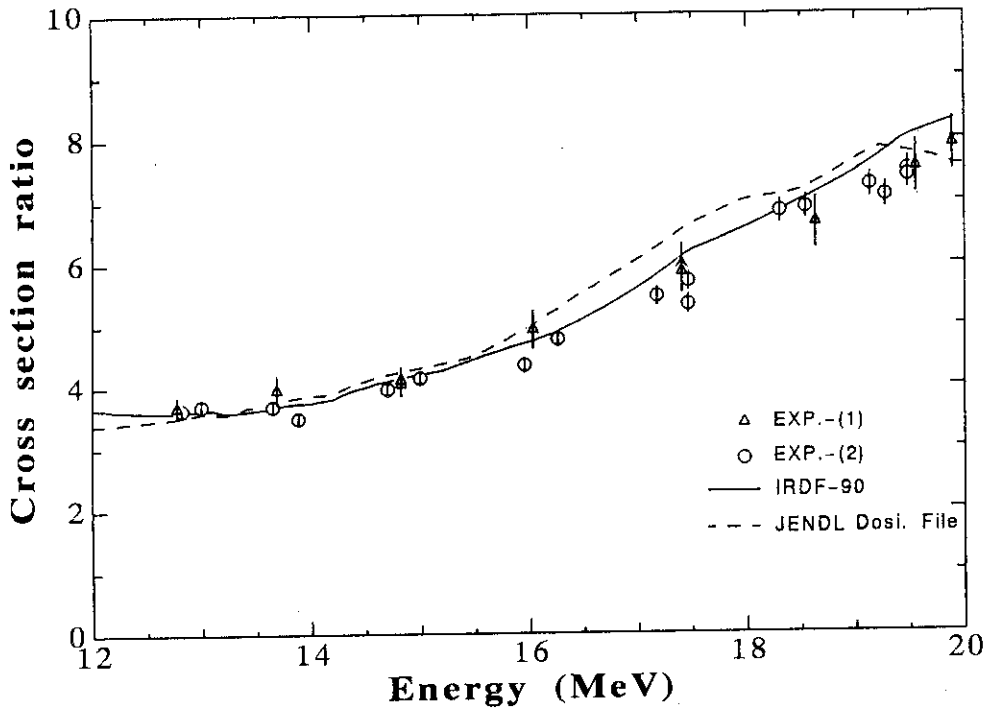

Fig. 2 The cross section ratio of the $^{93}Nb(n,2n)^{92m}Nb$ to $^{27}Al(n,\alpha)^{24}Na$ with the data calculated from the dosimetry files (JENDL Dosimetry File and IRDF-90).

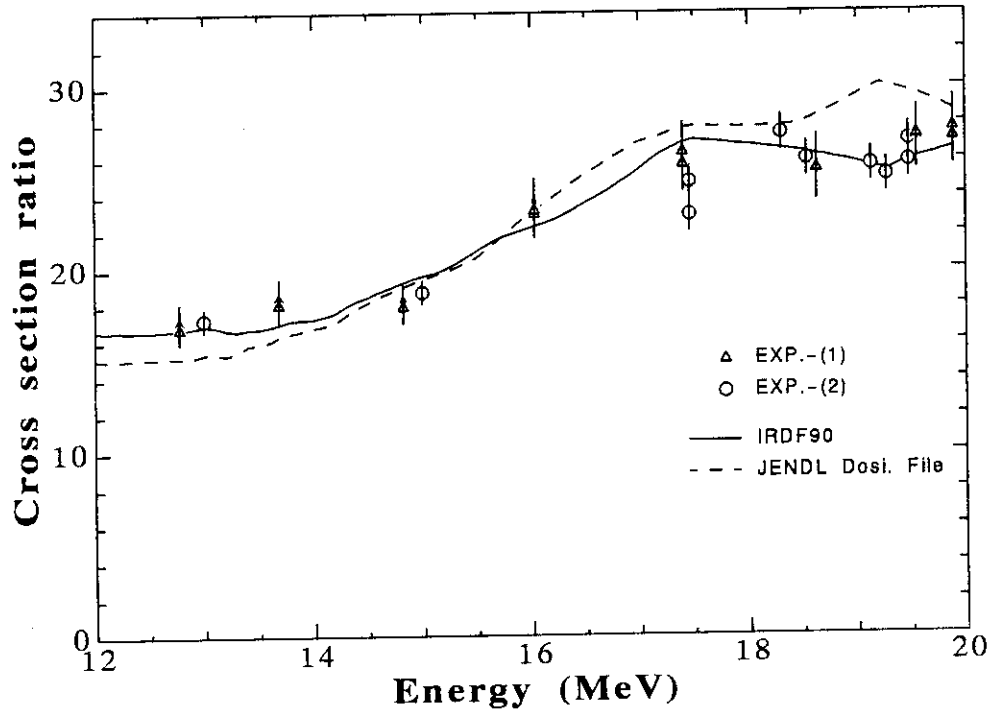

Fig. 3 The cross section ratio of the $^{197}Au(n,2n)^{196}Au$ to $^{27}Al(n,\alpha)^{24}Na$ with the data calculated from the dosimetry files (JENDL Dosimetry File and IRDF-90).

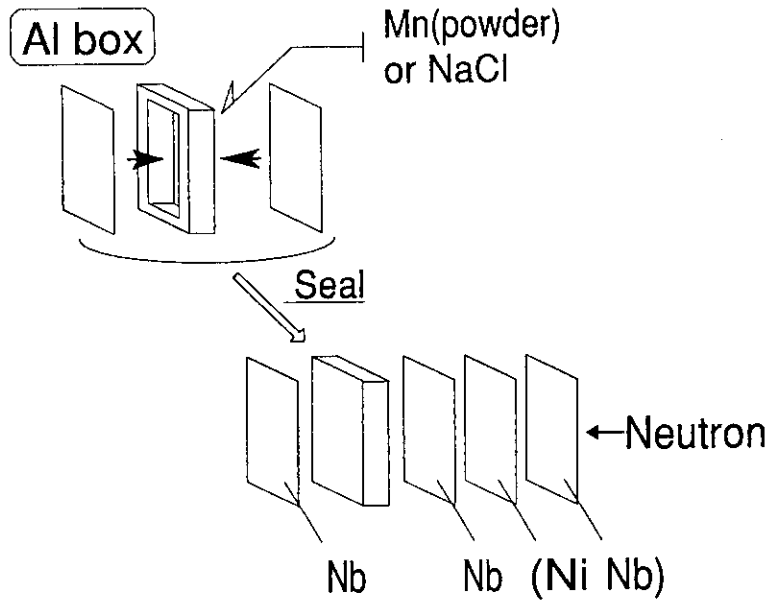

Fig. 4 A sample set for the measurement of (n,2n) cross sections of ^{23}Na, ^{55}Mn and ^{58}Ni.

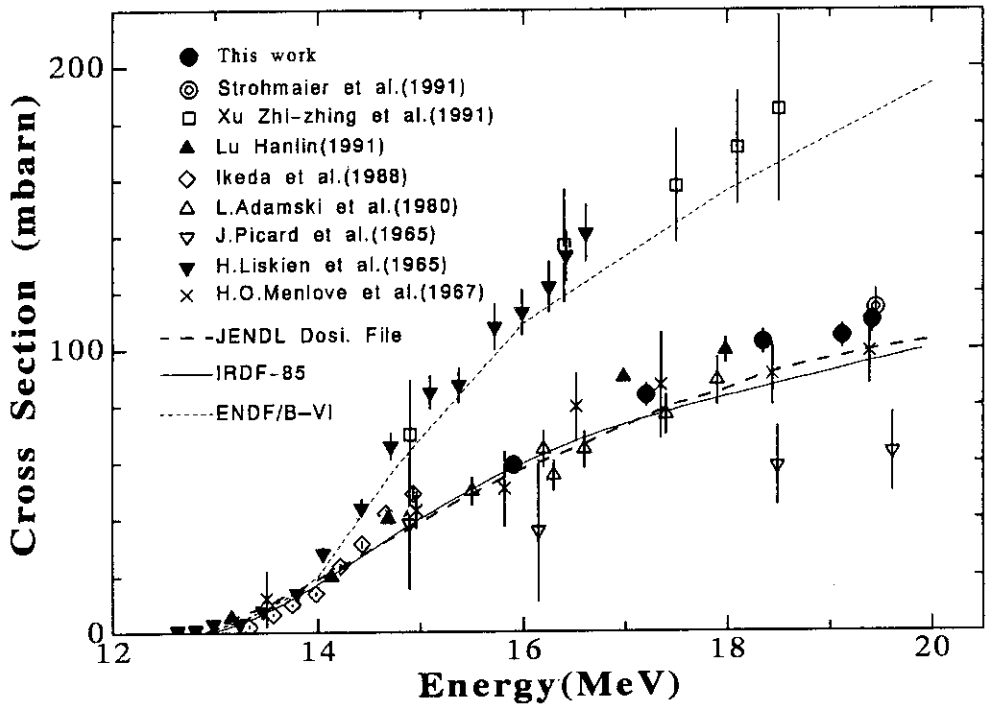

Fig. 5 Cross section for $^{23}Na(n,2n)^{22}Na$ reaction.

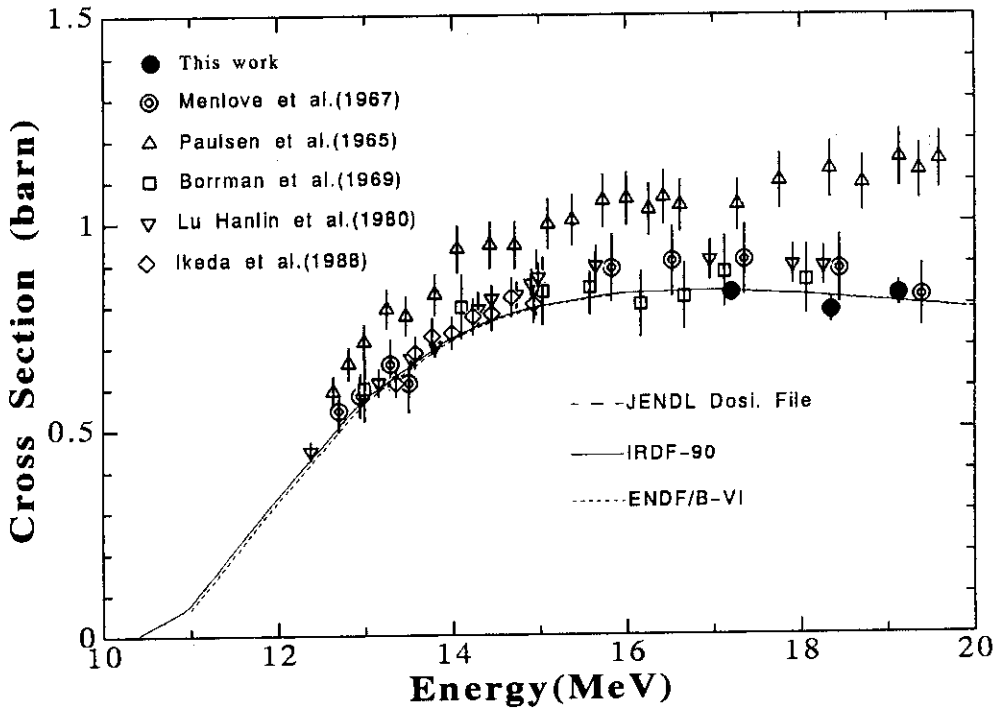

Fig. 6 Cross section for $^{55}Mn(n,2n)^{54}Mn$ reaction.

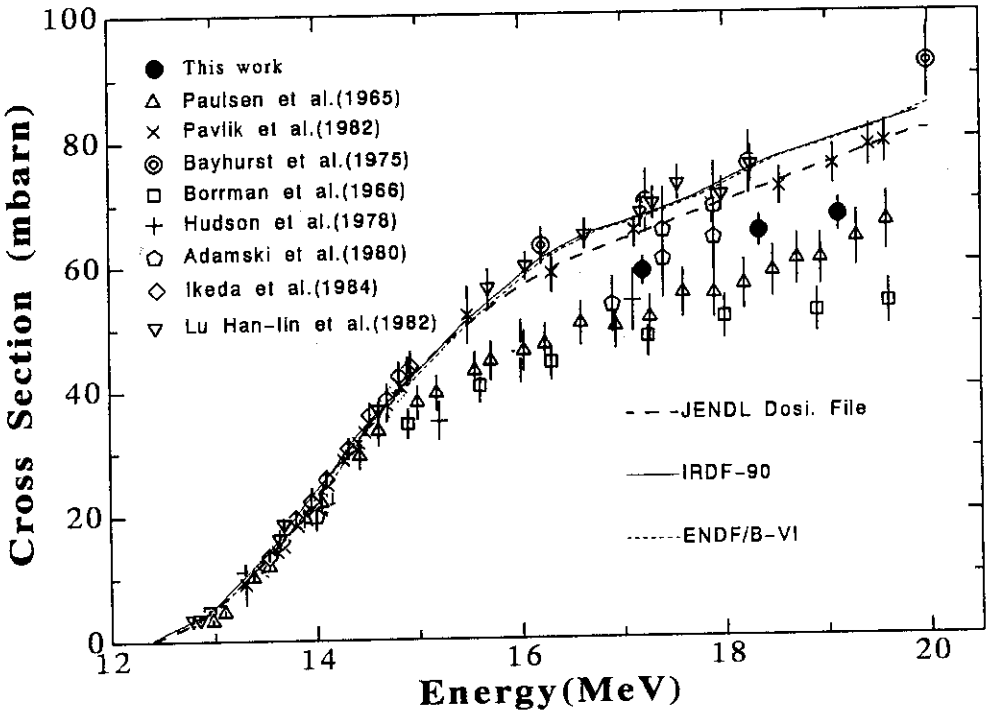

Fig. 7 Cross section for $^{58}Ni(n,2n)^{57}Ni$ reaction.

3.11 FUSION REACTOR SHIELDING EXPERIMENT I

C.Konno, F.Maekawa, Y.Ikeda, Y.Oyama, K.Kosako and H.Maekawa

Department of Reactor Engineering, Japan Atomic Energy Research Institute
Tokai-mura, Naka-gun, Ibaraki-ken, 319-11, Japan

Abstract

Various fusion reactor shielding experiments have been planned for next fusion devices such as ITER. At the first step the bulk shielding experiments using SS316 materials were performed. Two experimental assemblies were adopted. One was a cylindrical assembly of SS316 (1.2 m in diameter and 1.12 m in thickness) and was set at 0.3 m from the tritium-titanium target (Experimental assembly 1). The other surrounded the tritium-titanium target by 0.2 m thick SS316 adding to the experimental assembly 1 (Experimental assembly 2). In-situ neutron and gamma-ray spectra were measured. As neutron spectrum indices, fission and activation reaction rates were also measured by fission counters of ^{235}U and ^{238}U, and foils of Al, Ti, Fe, Co, Ni, Zr, Nb, In and Au, respectively. Experimental analysis was performed by the DOT3.5 code with the cross section set FUSION-J3 based on the JENDL-3 nuclear data file. The calculation by DOT3.5 underestimated gamma-ray and low energy neutron spectra, fission-rates of ^{235}U and reaction rates of $^{197}Au(n,\gamma)^{198}Au$ by more than factor 2 in the rear positions of the both assemblies.

1. Introduction

In the design of next fusion devices such as ITER and FER, the deep penetration of neutron in shielding materials is an important problem for the nuclear heating of superconducting magnet and biological safety. Various shielding experiments have been performed using iron and stainless steel assemblies[1)-8)]. There is, however, little or no experimental data for low energy neutron and gamma-ray in a large assembly. And the effects of cooling water and voids in shielding materials have not been examined experimentally, either. Therefore we planned a series of fusion reactor shielding experiments (bulk shielding, coolant channel effect, void effect, additional shielding material effect) to contribute to the ITER/EDA program. At the first step the bulk shielding experiments using type 316 stainless steel (SS316) materials were performed. This paper reviews a progress of the experiments.

2. Experiments

The experiments were performed in the first target room of the Fusion Neutronics Source (FNS) facility of Japan Atomic Energy Research Institute. Deuterium-tritium reaction neutrons were generated by bombarding a water-cooled 3.7 x 10^{11} Bq tritium-titanium target with a 350 keV deuteron beam. Two experimental assemblies were adopted. The experimental assembly 1 was a cylindrical assembly (1.2 m in diameter and 1.118 m in thickness) made of SS316 and was set at 0.3 m from the target shown in Fig. 1. In the experimental assembly 2, a source can of 0.2 m-thick SS316 surrounded the target, adding to the experimental assembly 1, shown in Fig. 2. It was expected that the source can increased low energy neutrons into the test region and decreased room-returned neutrons. The chemical compositions of SS316 were 67.3 % iron, 16.9 % chromium, 11.9 % nickel, 2.1 % molybdenum and 1.1 % manganese. These experimental assemblies had 6 experimental holes (36 mm ϕ x 727 mm or 50 mm ϕ x 727 mm). The positions of the experimental holes were 0.10, 0.23, 0.36, 0.53, 0.71 and 0.91 m from the front surface of test region. Detectors were inserted into the experimental hole from the side vertically in the beam direction with adjustable detector holders. Unused experimental holes were filled by SS316 rods.

A 14 mm-diam NE213 spectrometer[10] and small size proton-recoil gas proportional counters (PRC)[9] were adopted to measure neutron spectra above 2 MeV and from a few keV to 1 MeV, respectively. Neutron spectra were measured at the 6 experimental holes and the front surface of test region.

Gamma-ray spectra were measured by a 40 mm-diam NE213 spectrometer[11] at 0.10, 0.36, 0.71 and 0.91 mm from the front surface of test region. Gamma-ray heating rates were measured using thermoluminescent dosimeters (TLD)[12] (Mg_2SiO_4, Sr_2SiO_4 and Ba_2SiO_4). The gamma-ray heating rate for SS316 was interpolated from those TLD responses using their effective atomic number.

As neutron spectrum indices, the fission-rates of ^{235}U and ^{238}U were measured using micro fission counters. And the reaction-rates of $^{27}Al(n,\alpha)^{24}Na$, $Ti(n,x)^{47}Sc$, $Ti(n,x)^{48}Sc$, $Fe(n,x)^{56}Mn$, $^{59}Co(n,\alpha)^{56}Mn$, $^{58}Ni(n,2n)^{57}Ni$, $^{58}Ni(n,p)^{58}Co$, $^{64}Zn(n,p)^{64}Cu$, $^{90}Zr(n,2n)^{89}Zr$, $^{93}Nb(n,2n)^{92m}Nb$, $^{115}In(n,n')^{115m}In$ and $^{197}Au(n,\gamma)^{198}Au$ were also measured using Al, Ti, Fe, Co, Ni, Zr, Nb, In and Au foils.

3. Calculation

The experimental analysis was performed by the two-dimensional transport code DOT3.5[13] with P_5-S_{16} approximation. The calculation model was R-Z cylindrical one. The first collision source was calculated using the modified GRTUNCL code[14] that considered the angle dependency of source neutron spectrum. The cross section set used was FUSION-J3[15] (infinite dilution model) with neutron 125 groups and gamma 40 groups based on the JENDL-

3[16] nuclear data file.

4. Results and discussion

The neutron spectra measured at 0.40 and 1.21 m from the tritium-titanium target in the experimental assembly 2 are shown in Figs. 3 and 4 with the calculated ones. The fine structure due to iron resonances around 10, 30, 100, 150, 200, 400 and 800 keV is clearly appeared in these spectra. The calculation overestimates neutron spectra from 10 keV to 1 MeV at the front region and underestimates below 1 MeV at the rear region.

Figures 5 and 6 show measured and calculated gamma-ray spectra at the same positions in the experimental assembly 2. The calculated spectra are not smeared by the energy resolution of the detector. Inelastic and capture gamma-rays by SS316 are observed around 860 keV, 1.3 MeV and 8 MeV. The gamma-ray spectra calculated by DOT3.5 agree well with the measured ones in the front region, but the calculation underestimates the measured ones in the rear positions. Although the measured spectra overestimate by a few tens of percent in the whole energy regions due to perturbation of the detector itself and by a factor of 2 at a peak around 0.5 MeV due to $^{10}B(n,\alpha)$ reactions of the detector glass container[17], the underestimation of DOT3.5 are not canceled.

Figure 7 shows the measured and calculated reaction-rate distributions of $^{197}Au(n,\gamma)^{198}Au$ in both experimental assemblies. The reaction-rates in the experimental assembly 2 are a few times larger than those in the experimental assembly 1 at the front region due to the scattered neutron on the source can. The calculation underestimates the measured reaction-rates by more than factor 2 in the rear region. The same tendency is observed in the fission rate of ^{235}U.

Since the experimental data are under data processing, the discussion about the gamma-ray heating will be done elsewhere.

5. Concluding remarks

Various experimental data for neutron and gamma-ray in two large cylindrical SS316 assemblies were obtained. The calculation by DOT3.5 using the cross section set FUSION-J3 underestimated gamma-ray and low energy neutron by more than factor 2 at the rear region in the assemblies. The analysis using the continuous-energy Monte Carlo code MCNP[18] is under way.

Next step we are planning the following shielding experiments,

i) Coolant water effect,

ii) Void effect,

iii) Additional shielding material (W, B_4C/Pb) effect,

iv) Simulated super conducting magnet.

The experimental assemblies are shown in Fig. 8. It is expected that the nuclear design accuracy in complicated fusion devices will be improved based on these data and the reduction of the nuclear design margin will lead to the lower construction cost of future fusion devices.

References

[1] L.F. Hansen, et al.: Nucl. Sci. Eng., 60(1976), p.27.
[2] F. Kappler, et al.: Proc. Int. Symp. on Physics of Fast Reactor, Tokyo (1973), p.883.
[3] G.L. Morgan, et al.: ORNL-TM-4193(1973).
[4] R.H. Johnson, et al.: Trans. Am. Nucl. Sci., 22(1975), p.799.
[5] N.E. Hertel, et al.: Fusion Technology, 9(1986), p.345.
[6] K. Oishi, et al.: Proc. 7th Int. Conf. on Radiation Shielding, Bournemouth (1988), p.331.
[7] H. Nakashima, et al.: Proc. 1st Int. Sym. on Fusion Nucl. Tec., Tokyo(1989), part C p.121.
[8] Y. Oyama, et al.: Proc. Int. Conf. Nuclear Data for Science and Tech. 13-17. May Jülich (1991), to appear.
[9] C. Konno, et al.: Proc. 2nd Int. Sym. on Fusion Nucl. Tec., Karlsruhe(1991), to apear.
[10] Y. Oyama, et al.: Nucl.Instr. and Meth. A256(1987), p.333.
[11] F. Maekawa, et al.: presented at the Fall Meating of Atomic Energy Society of Japan, Univ. of Kyusyu, October 15-18 (1991).
[12] S. Yamaguchi, et al.: Proc. 1st Int. Sym. on Fusion Nucl. Tec., Tokyo(1989), part C p.163.
[13] W.A. Rhodes and F.R. Mynatt, ORNL-TM-4280 (1973).
[14] K. Kosako: private communication.
[15] K. Maki, et al.: JAERI-M 91-072 (1991).
[16] K. Shibata, et al.: JENDL-3: JAERI 1319 (1990).
[17] F. Maekawa: private communication.
[18] J.F. Briesmeister (edited), LA-7396-M (1986).

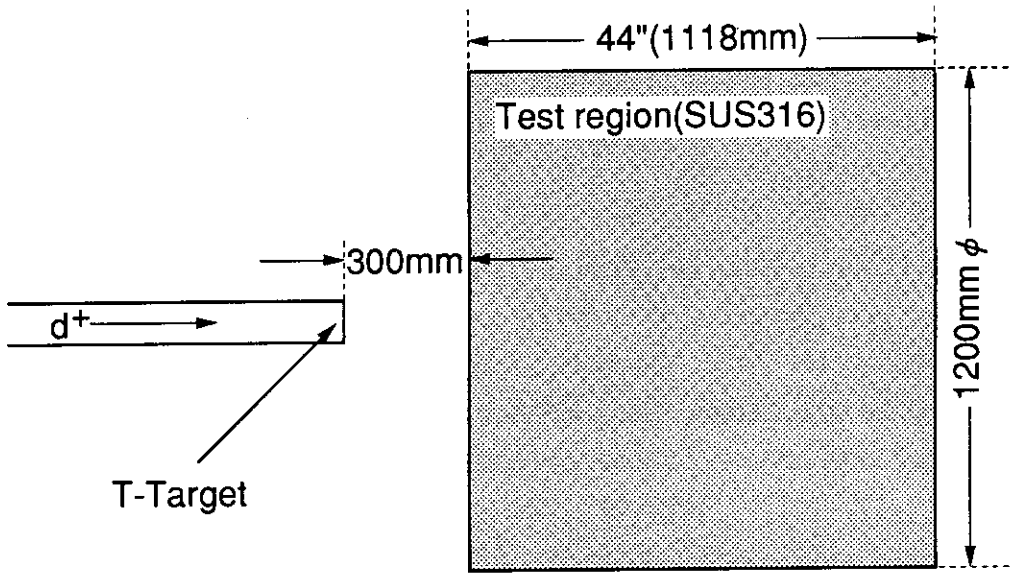

Fig. 1 Experimental assembly 1.

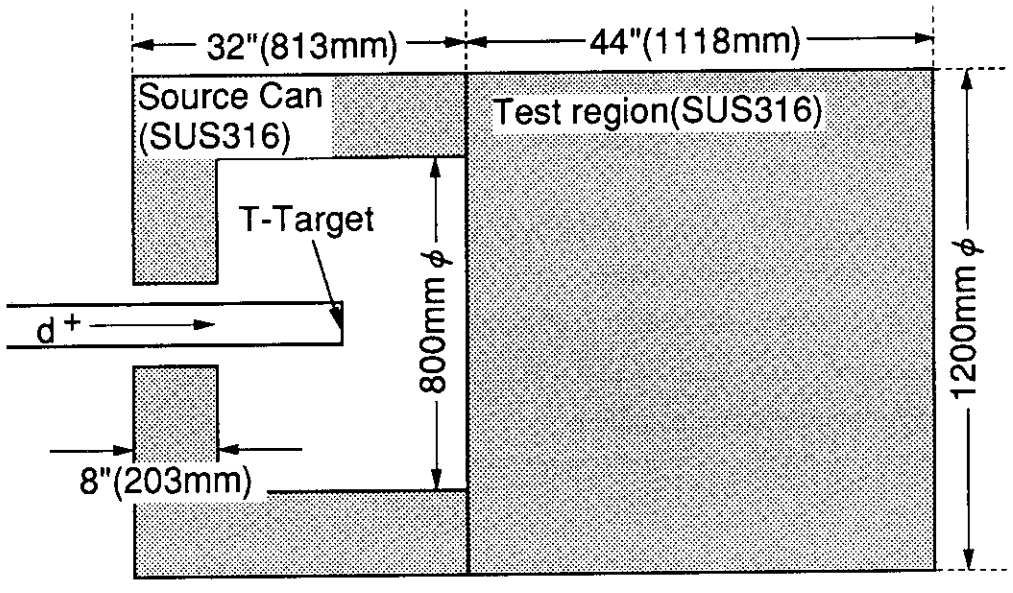

Fig. 2 Experimental assembly 2.

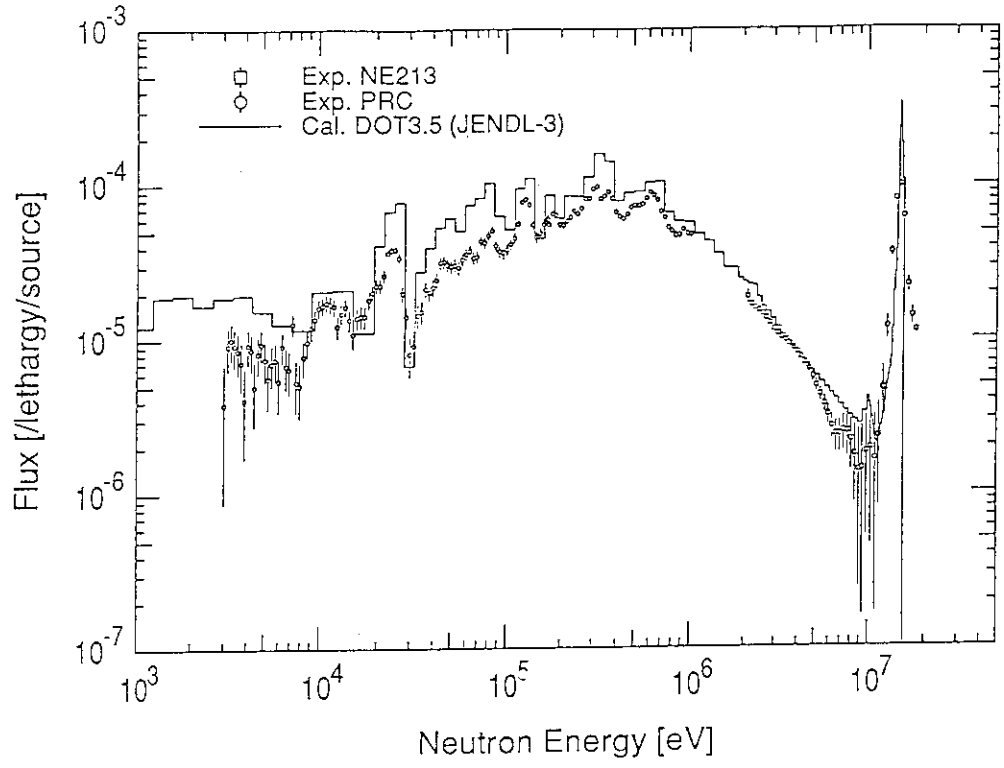

Fig. 3 Measured and calculated neutron spectrum at 0.40 m from D-T neutron source in the experimental assembly 2.

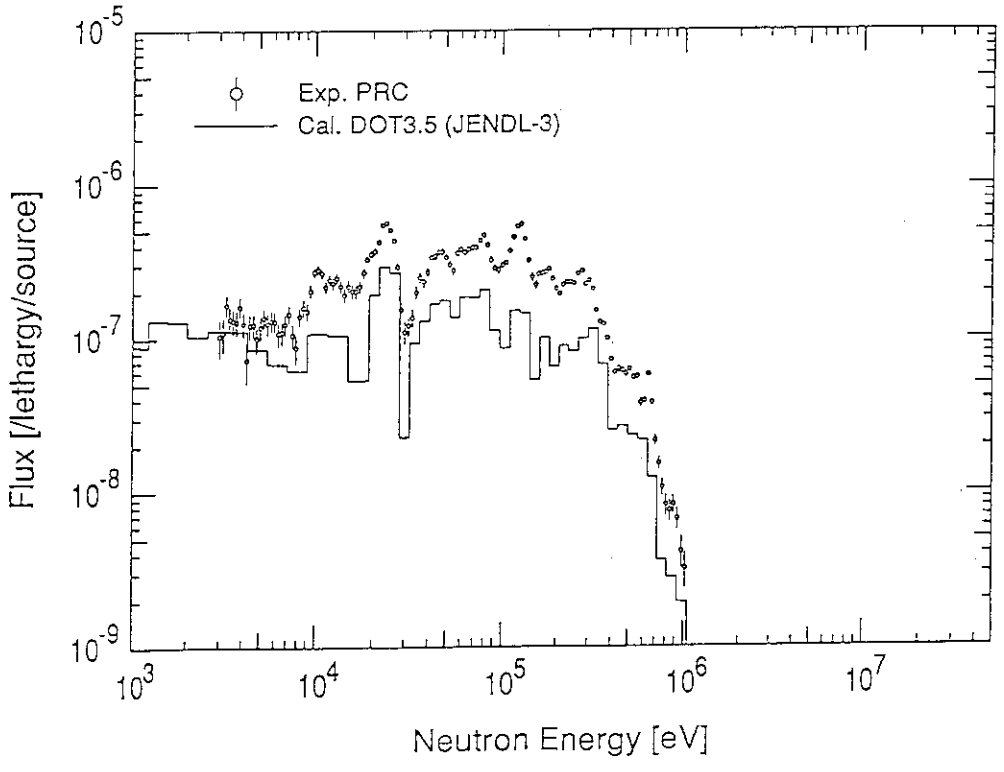

Fig. 4 Measured and calculated neutron spectrum at 1.21 m from D-T neutron source in the experimental assembly 2.

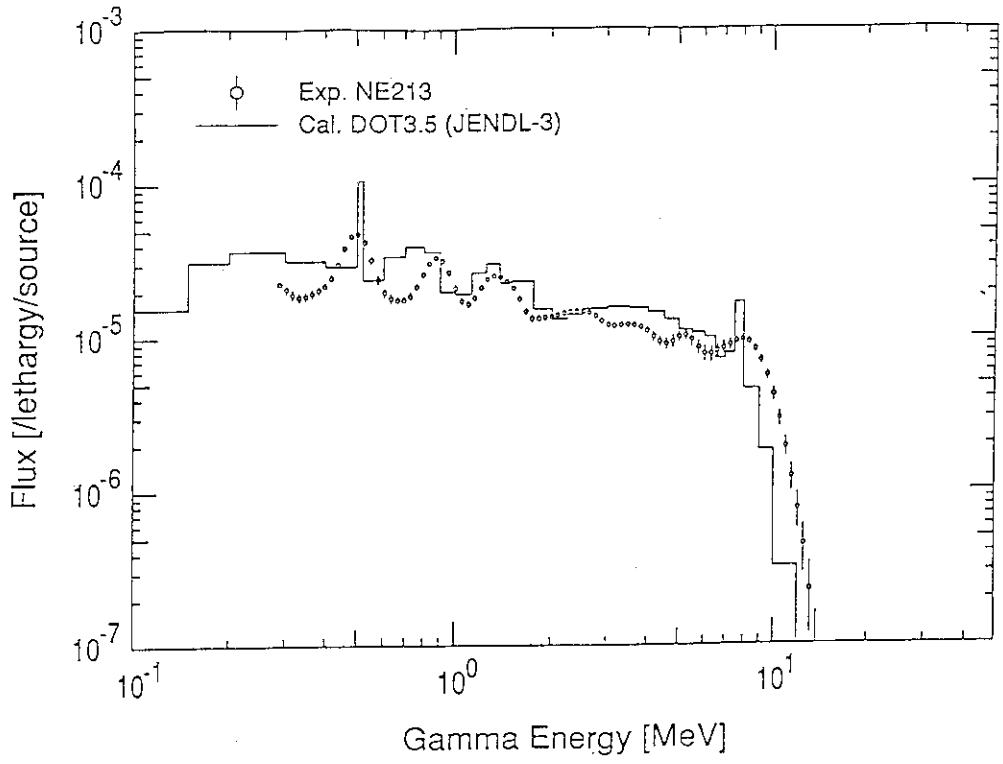

Fig. 5 Measured and calculated gamma-ray spectrum at 0.40 m from D-T neutron source in the experimental assembly 2.

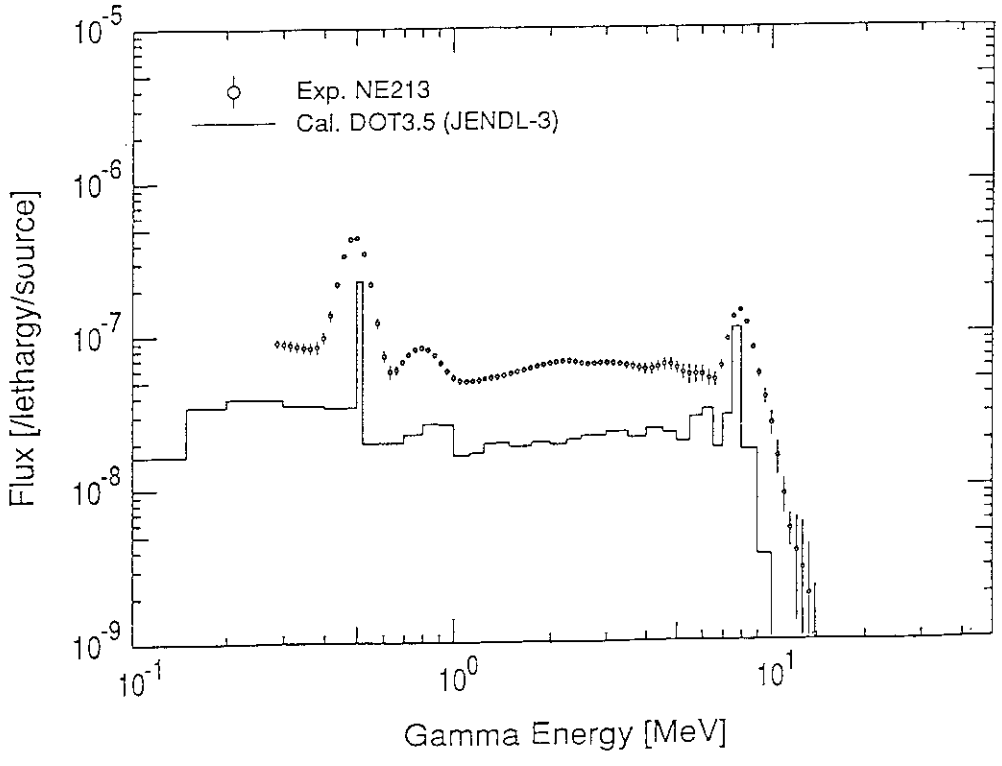

Fig. 6 Measured and calculated gamma-ray spectrum at 1.21 m from D-T neutron source in the experimental assembly 2.

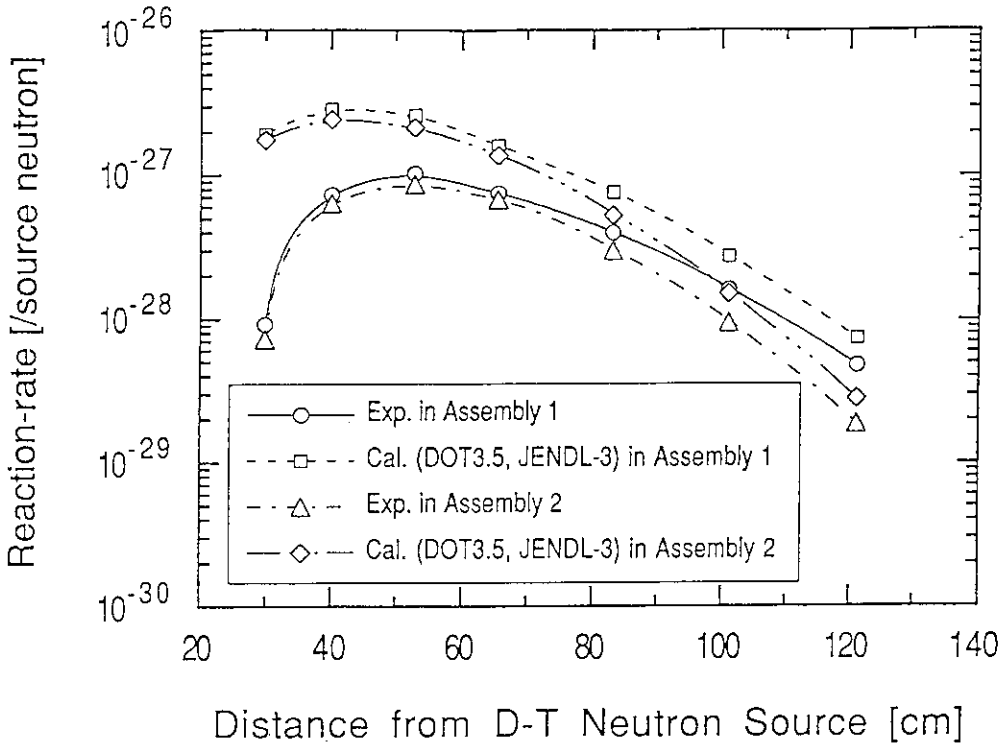

Fig. 7 Measured and calculated reaction-rate distribution of $^{197}Au(n,\gamma)^{198}Au$ in the experimental assembly 1 and 2.

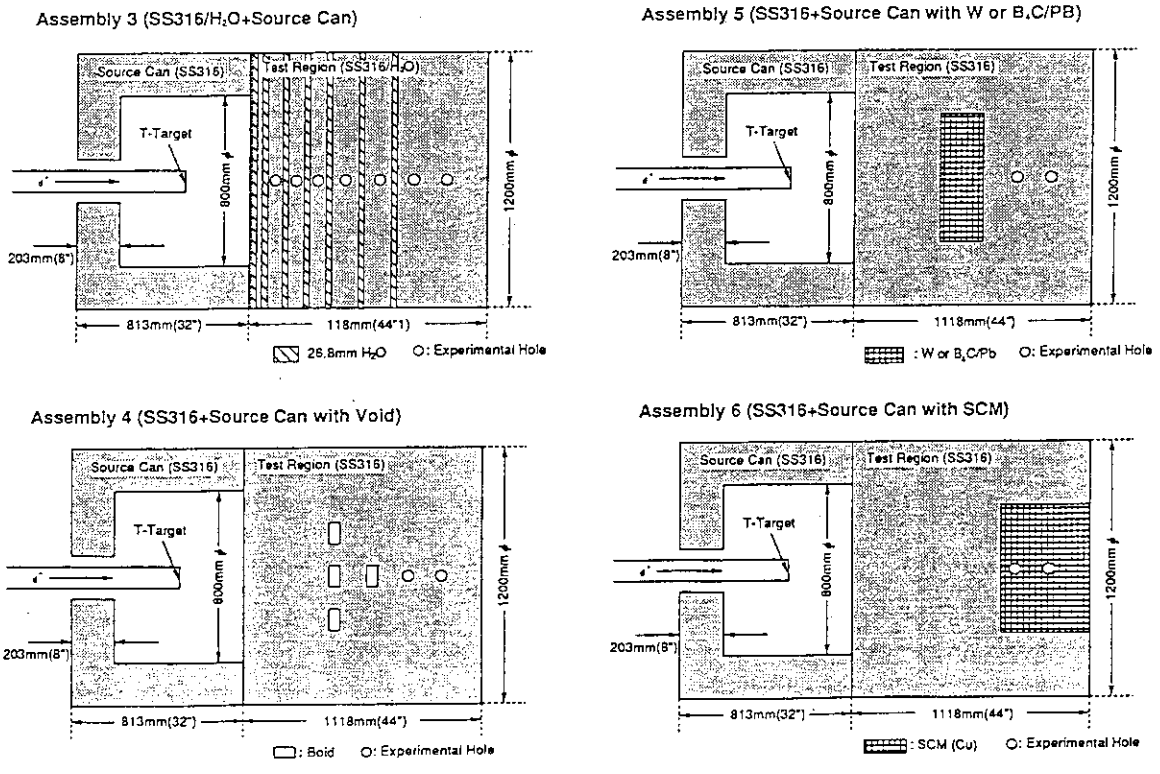

Fig. 8 Experimental assemblies used in the future experiments.

3.12 MEASUREMENT OF THE THERMAL NEUTRON CROSS SECTION OF THE $^{90}Sr(n, \gamma)^{91}Sr$ REACTION

H. Harada,[1] T. Sekine,[2] Y. Hatsukawa,[2] N. Shigeta,[2] K. Kobayashi,[2]
T. Ohtsuki,[2,*] and T. Katoh[3]

[1]Nuclear Fuel Technology Development Division, Power Reactor and Nuclear Fuel Development Corp., Tokai−mura, Naka−gun, Ibaraki−ken 319−11

[2]Department of Radioisotopes, Japan Atomic Energy Research Institute, Tokai−mura, Naka−gun, Ibaraki−ken 319−11

[3]Department of Nuclear Engineering, Nagoya University, Furo−cho, Chikusa−ku, Nagoya 464−01

*Present address: Laboratory of Nuclear Science, Tohoku University, 1−2−1 Mikamine, Taihaku−ku, Sendai 982

Absract

The thermal neutron cross section of the $^{90}Sr(n,\gamma)^{91}Sr$ reaction was measured by a radiochemical method. By using a ^{90}Sr sample containing a γ−ray emitter ^{85}Sr as a target, the radioactivity ratio between ^{90}Sr and ^{91}Sr was determined by γ−ray spectrometry. The resulting cross section value 15.3±1.3 mb is as small as one−sixtieth of the value reported by Zeisel (Acta. Phys. Austr., **23**, 223 (1966)) but in good agreement with the value reported by Mcvey *et al.* (J. Radioanal. Chem., **76**, 131 (1983)).

INTRODUCTION

In an experimental program[1,2] to obtain fundamental data needed for research of the transmutation of nuclear waste, the present work aims at the determination of the thermal neutron cross section of the $^{90}Sr(n,\gamma)^{91}Sr$ reaction. For this reaction cross section, two different values have been reported: 0.8±0.5 b by Zeisel[3] and 14.0±2.4 mb by Mcvey *et al.*[4] In a feasibility study[5] on the transmutation of ^{90}Sr, Zeisel's value is cited preferably.

In our experiment, a neutron−irradiated ^{90}Sr sample was chemically purified and measured

with a highly efficient HPGe detector to enhance the signal-to-noise ratio in a radioactivity measurement. As a target, a $^{90}Sr/^{85}Sr$ mixture was used. The γ-ray emitter ^{85}Sr was added as a tracer of ^{90}Sr, so that the amount of ^{90}Sr in a sample could be determined together with that of ^{91}Sr by γ-ray spectrometry.

EXPERIMENTAL

A $^{90}Sr/^{85}Sr$ target was prepared by evaporating a small amount of $SrCl_2$ solution containing 2.8 MBq of ^{90}Sr and 5.4 kBq of ^{85}Sr in a polyethylene bottle. The polyethylene bottle was sealed by heat and housed in a polyethylene capsule together with neutron-flux monitor wires of Co/Al and Au/Al alloys. The target was irradiated for 10 min in the JRR-4 reactor at JAERI. After irradiation, the strontium was purified by a cation exchange method. Using 2N HNO_3 as an eluent, ^{90}Sr and ^{85}Sr were eluted, ^{90}Y being kept on the resin. Finally the strontium was precipitated as $SrCO_3$. The γ-ray spectrum of the strontium sample was measured with an HPGe detector having a 90% efficiency and a data acquisition system described elsewhere.[1] To absorb β-rays from a growing ^{90}Y isotope, a 5-mm thick lucite is placed between the sample and the detector. In addition, a 4-mm thick lead was inserted between the lucite and the detector to absorb low-energy bremsstrahlung.

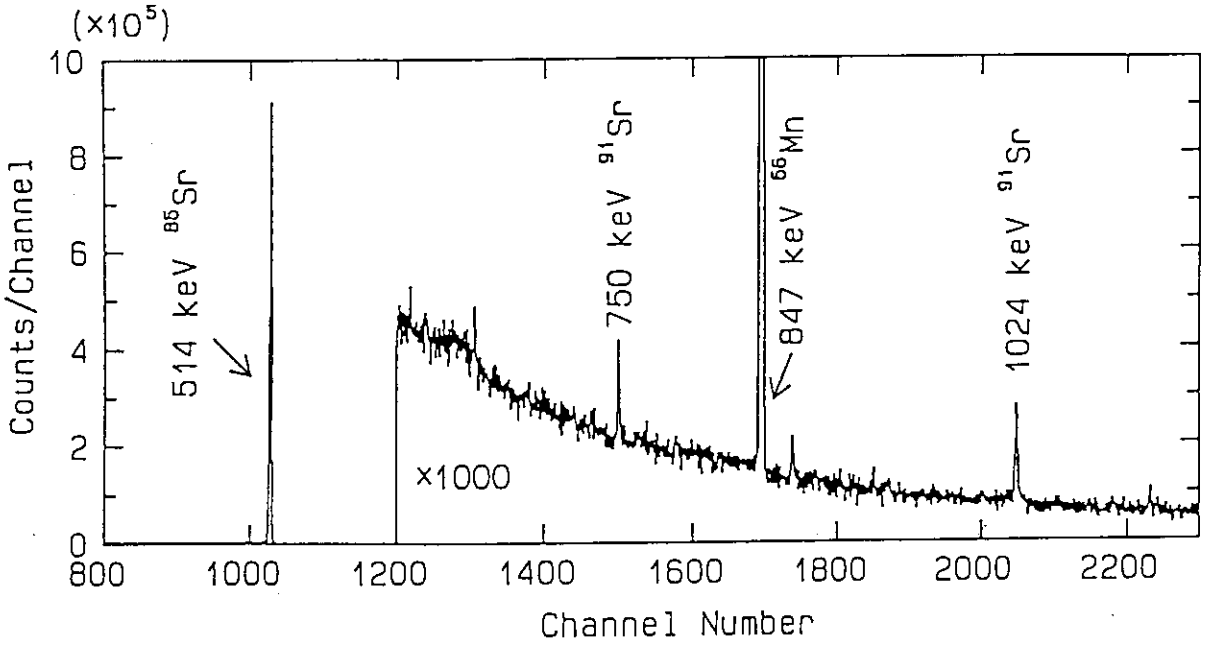

Fig. 1 A γ-ray spectrum of the $^{90}Sr/^{85}Sr$ sample irradiated with reactor neutrons and chemically purified.

RESULTS AND DISCUSSION

The γ-ray spectrum obtained in counting for 10 h is shown in Fig. 1. The γ-rays of 750 and 1024 keV from ^{91}Sr are seen together with the γ-ray of 514 keV from ^{85}Sr. The γ line at 847 keV was assigned to ^{56}Mn; manganese behaved the same as strontium in our chemical process.

The thermal neutron cross section of the ^{90}Sr(n,γ)^{91}Sr reaction was determined from the radioactivity ratios between ^{91}Sr and ^{85}Sr and between ^{85}Sr and ^{90}Sr and the neutron flux data. The resulting value 15.3±1.3 mb is as small as one-sixtieth of the value reported by Zeisel,[3] but in good agreement with the value reported by Mcvey *et al.*[4] The present experimental data should likely be used for studies of the transmutation of ^{90}Sr with thermal neutron reaction.

REFERENCES

1) H. Harada, H. Watanabe, T. Sekine, Y. Hatsukawa, K. Kobayashi and T. Katoh, J. Nucl. Sci. Tech., **27**, 577 (1990).

2) T. Sekine, Y. Hatsukawa, K. Kobayashi, H. Harada, H. Watanabe and T. Katoh, Proc. Int. Conf. Nucl. Data for Science and Technology, Jülich, FDR, May 13-17, 1991.

3) G. Zeisel, Acta. Phys. Austr., **23**, 223 (1966).

4) L.A. Mcvey, R.L. Brodzinski, T.M. Tanner, J. Radioanal. Chem., **76**, 131 (1983).

5) C.D. Bowman, P.W. Lisowski and E.D. Arthur, Proc. of 2nd Int. Symp. Advanced Nuclear Energy Research - Evolution by Acceleratos -, Japan Atomic Energy Research Institute, Jan. 24, 1990, Mito, Japan, p.149.

3.13 MEASUREMENT OF DOUBLE DIFFERENTIAL NEUTRON EMISSION CROSS SECTIONS AT E_n=14.1MeV FOR Ge AND As

Masami Gotoh and Akito Takahashi

Department of Nuclear Engineering,

Faculty of Engineering, Osaka University

2−1, Yamada−Oka, Suita, Osaka

Abstract:

Double Differential Neutron Emission Cross Sections for natural germanium and arsenic at incident neutron energy of 14MeV were measured using the time of flight facility (8.3m flight path) at OKTAVIAN. Number of scattering angles are 16 for Ge and 15 for As. Measured energy range of secondary neutrons is from 0.8MeV to 15MeV. The spectra consist of components by the equilibrium, preequilibrium and direct processes, and they are compared with calculated spectra by ENDF/B−VI and JENDL−3.

1. Introduction

Recent experimental interests for nuclear data are concentrated in measuring charged particle emission data induced by neutrons, and neutron emission cross sections at En=14MeV are not so much discussed as before. In fact, double differential neutron emission cross sections (DDXs) at 14MeV for most principal elements like Li, Cr, Fe, Ni etc. for fusion reactor are already available; actually DDXs for twenty−six elements have been measured at OKTAVIAN. However, from a viewpoint of radia−

tion damage, accurate estimations of neutron emission cross sections are still needed for some elements not used directly as constituents of fusion reactor, like Ge, As, which consists of semiconductors. In addition, for some elements of fission products in the mass region of A=100 to 200, the experimental neutron emission energy at 14MeV may help the analysis of fission spectrum. These double differential cross sections are not available up to now and first to be measured so far as we know. At the OKTAVIAN facility, the first measurements of DDXs for elements whose atomic number are thirtys have been done in this work to fill the missing zone of the series DDX measurement. These data will be helpful to carry out evaluation work for natural germanium and arsenic−75 in future.

In this report, measured double differential neutron emission cross sections, neutron emission spectra and angular differential cross sections for Ge and As are shown and compared with available evaluated data (ENDF/B−VI and JENDL−3).

2. Experimental Procedure

Pulsed neutrons produced by OKTAVIAN[1] are with less than 2ns pulse width in FWHM and 1/2MHz in repetition frequency. Angular distribution of source neutron yield was known by the Al(n,alpha) foil activation measurement. (The experiment was carried out in 1991.5.) The accuracy of this measurement is within 2.4% errors. Neutron flight path is 8.25m at 90deg in the laboratory system. Shadowbar, collimator and pre−collimator are set up along the neutron flight path to shield room scattering and other backgrounds . Used neutron detector was an NE213 (25.4cm diam. 10cm thick). Scattering samples are cylindrical ones; 3cm diam. 7cm length; in changing scattering angle, they are moved around the tritium target. The present experiments were carried out by changing scattering angles in the laboratory system from 15deg to 160deg for Ge (16 points), and 15deg to 150deg for As (15 points). Differential cross sections of H(n,n) are used for calibration. Detail of the experiment and schematic view of neutron TOF facility are described elsewhere[2,3].

3. Results

As for both elements, Ge and As, correction factors for the multiple scattering occurred in samples and the low−energy tail of source neutron were calculated using the MUSCC3 code[4]. In the calculation, consulted cross section data are from JENDL−3[5] and ENDF/B−VI[6]. However, the factors calculated using ENDF/B−VI distort the spectra so seriously due to very primitive evaluation, that we could not use these for the correction.

Graphs of experimental double differential neutron emission cross sections compared with those of JENDL−3 or ENDF/B−VI are shown in figures. Experimental data are compared with evaluated data used in the MUSCC3 code. But in the comparison with ENDF/B−VI, correction factors are not applied. They are not corrected. And also show correction factors calculated by the MUSCC3 on the same figures. Integrated data (neutron emission spectra in the center of mass system and angular differential data) are described later.

3.1 Error Estimation

In the graphs, only statistical errors are shown. We have to take account of other error sources, there are errors in determining energy dependent efficiency curve of the NE213 detector (especially at the rising part of curve), in estimating multiple scattering correction factors and ambiguity of sample size & positions (contain source neutron yield (angular distribution)). Estimated errors for an "averaged" DDX data are shown in table 1. Here, "averaged" is valid for each of usually measured DDX data. For the multiple scattering corrections, error estimations are given for the cases that used evaluated nuclear data for the calculation are considerably reasonable. Others are usual error estimations.

3.2 Germanium

Figure 1,4,6 are the graphs for germanium ; double differential neutron emission

cross sections, neutron emission spectra and angular differential cross section. At first The particular thing we could say first is that the structural patterns of spectra are the same with those of other medium heavy nuclei; they are understood as the competition of equilibrium, pre−equilibrium and direct processes.

Some peaks can be seen; the largest one corresponds to elastic peak, and the others to discrete inelastic scatterings from direct processes. In the figure 1, it will be hard to distinguish a peak (Q=−0.9MeV) from elastic peak. However, at the backward angle, peak appears to be distinguished we do not show on this paper.

There are five isotopes in natural germanium. In ENDF/B−VI, evaluation is not done for every isotope, and no clear differences are given among isotopes. Angular distributions (File 4) are not given even for the elastic scattering. We cannot compare angular differential cross sections for the elastic scattering. The measured data are not corrected because correction factors using ENDF/B−VI distort the spectra much. The evaluated values for Ge have not been published in JENDL−3 up to now.

3.3 Arsenic

Atomic number of arsenic is 33, compared with 32 of germanium. The spectra resemble much each other on the viewpoints of shape, magnitude and Q−value of discrete inelastic scatterings. Almost the same things with the germanium data can be said as for arsenic. After the Symposium on Nuclear Data in 1991, we could have the evaluation data JENDL−3 for arsenic, so that graphs compared with JENDL−3 are shown in this report. The experimental data are corrected using JENDL−3. As in the case of germanium, the correction factors calculated using ENDF/B−VI can not be applied. The comparison among two evaluation data and experimental data is hard to be shown in the same graph. As you can see in the graph, differences between evaluated data induce large differences in correction factors.

As for the evaluated data; File 4 does not exist in ENDF/B−VI. On the contrary in JENDL−3, angular distributions are considered and many reactions are taken into ac−

count.

4. Conclusion

Double differential neutron emission cross sections with incident energy of 14MeV became available for natural germanium and arsenic. Correction factor are calculated using evaluated data, however, they are still primitive. So calculation of correction factors should be carried out again after new version of evaluation would be published.

References

(1) Sumita,K,et al. : Nucl.Sci.and Eng.,106,249–265 (1990)

(2) Takahashi,A.,et al. : J.Nucl.Sci.and Technol.,16,1–15 (1979)

(3) Takahashi,A,et al.:J.Nucl.Sci.and Technol.,25,215–23 (1988)

(4) Ichimura,E, Takahashi,A. : OKTAVIAN Rep.,A–87–02 (1987)

(5) JENDL Compilation Group (Nuclear Data Center, JAERI)

(6) ENDF/B Summary documentation,BNL–NCS–17451

Table 1 Error estimation

E-bin (lower (MeV)) (2nd neutron)	1	2	3	4	5	6	7	8	9	10	11	12	13	14
efficiency curve	←	～3%	→	←	～ 2%		→	←		～ 1%				→
Multiple scattering corrections *	←	～2%	→	←	～1%		→	←	～ 3%		→←		～1%	→
Sample sizes & positions**	←						～ 4%							→
Summation(%) ***	←	5.4	→	←	4.6		→	5.4 ←	5.0	→	←	4.2		→

* in the case consulted evaluation value are reasonable

** ambiguity of angles : 2～3 deg in LAB. system
dependent on sample size (in this case 3cm diam. 7cm length)
source neutron yield distributions (angular dependence) : ～ 2.4%

*** $\sigma_s=\sqrt{\sum \sigma_i^2}$

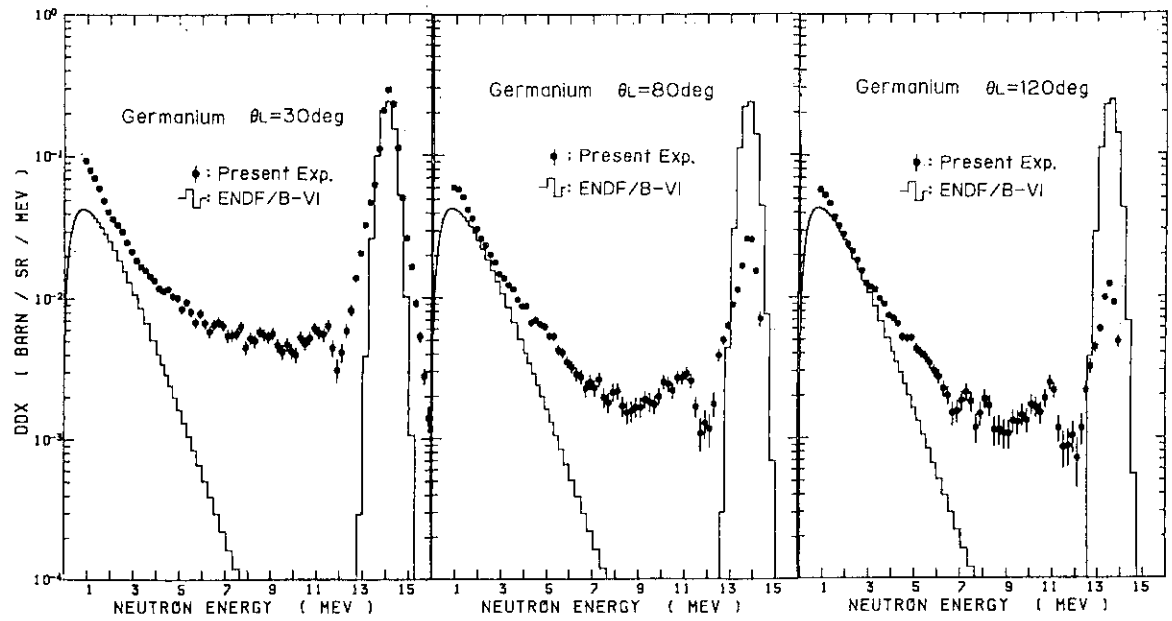

Fig. 1 Double differential neutron emission cross sections for germanium at (a) 30 deg in LAB system (b) 80 deg (c) 120 deg. Not corrected.

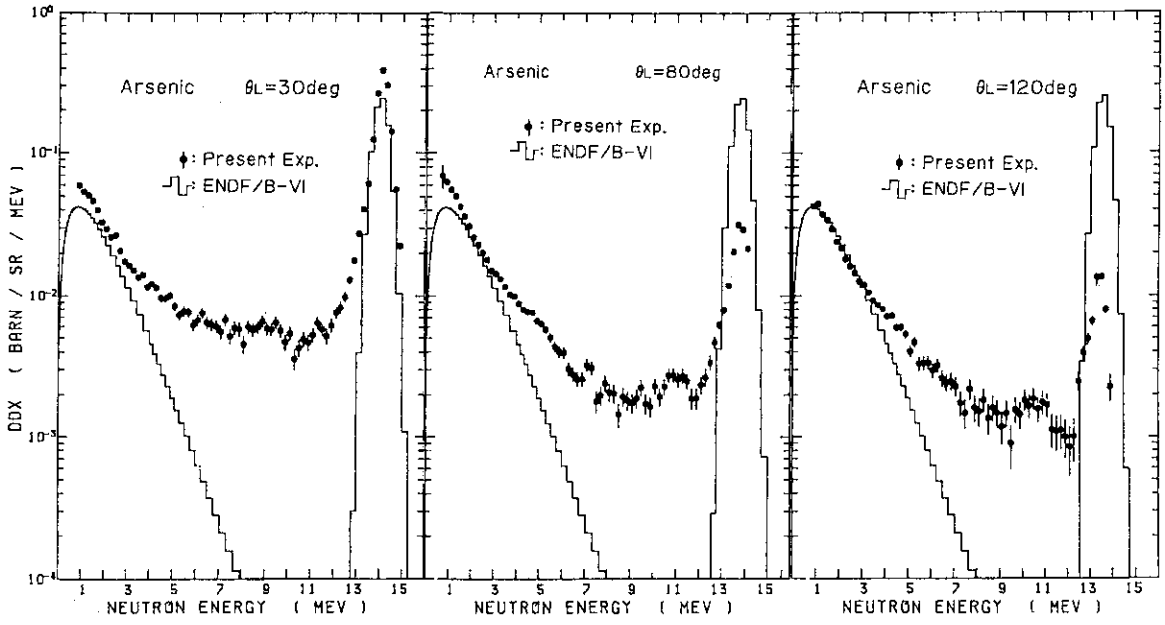

Fig. 2 Double differential neutron emission cross sections for arsenic at (a) 30 deg in LAB system (b) 80 deg (c) 120 deg. Not corrected.

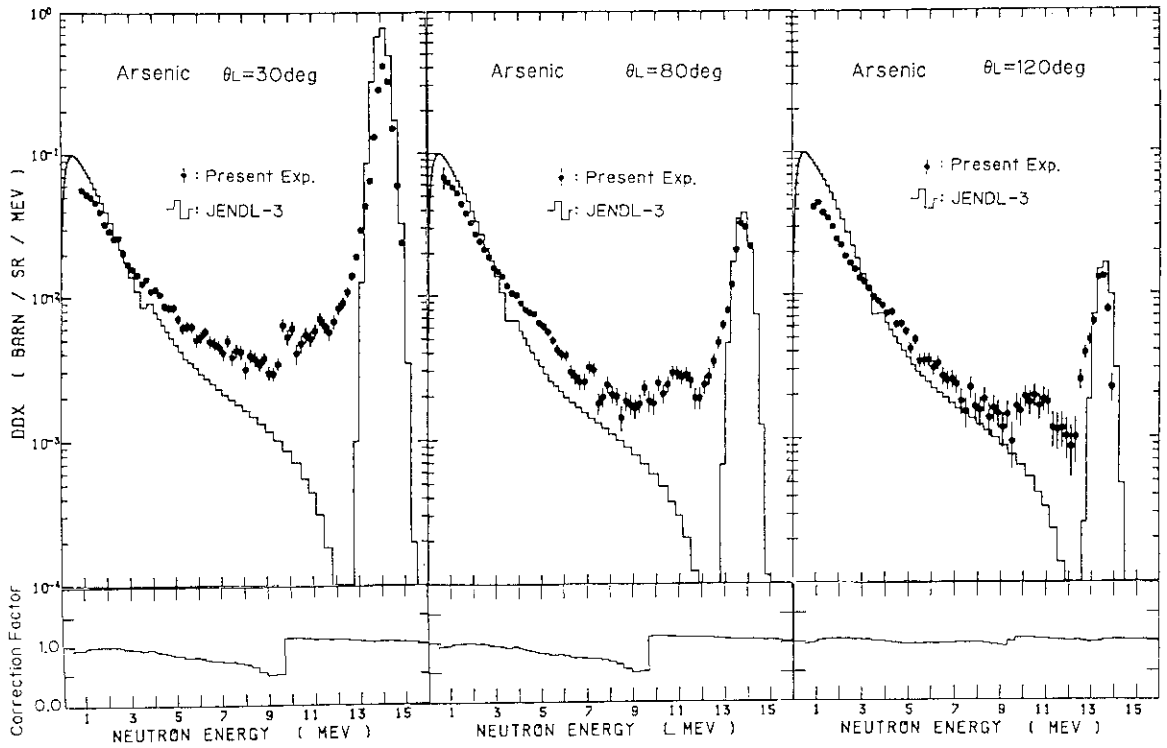

Fig. 3 Double differential neutron emission cross sections for arsenic at (a) 30 deg in LAB system (b) 80 deg (c) 120 deg. Correction factors are calculated using JENDL-3.

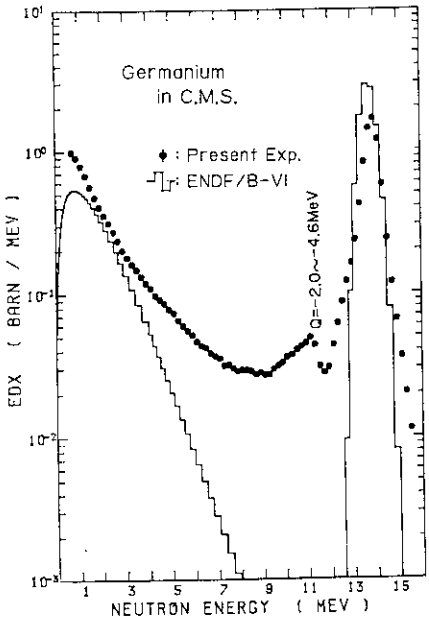

Fig. 4 Neutron emission spectra in CM system for germanium. Not corrected.

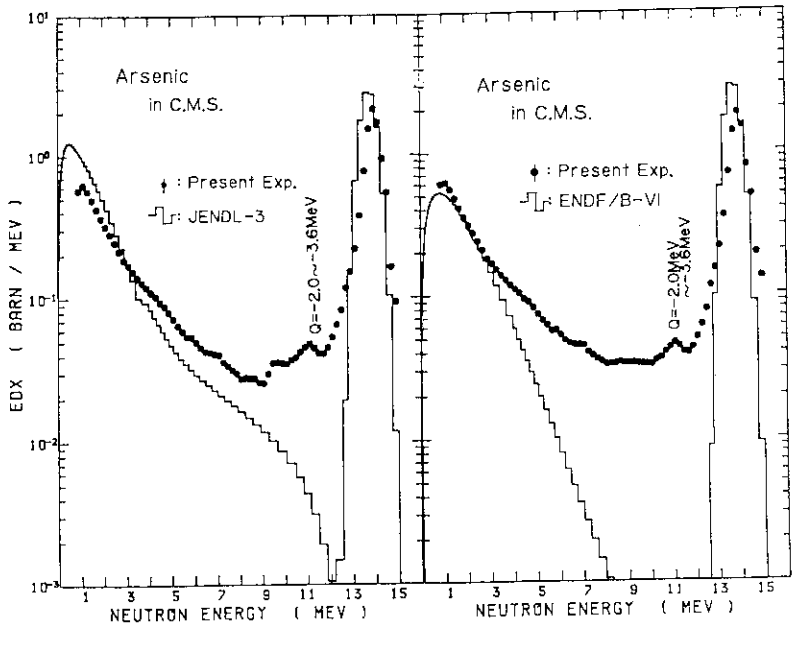

Fig. 5 Neutron emission spectra in CM system for arsenic (a) Corrected using JENDL-3 (b) Not corrected.

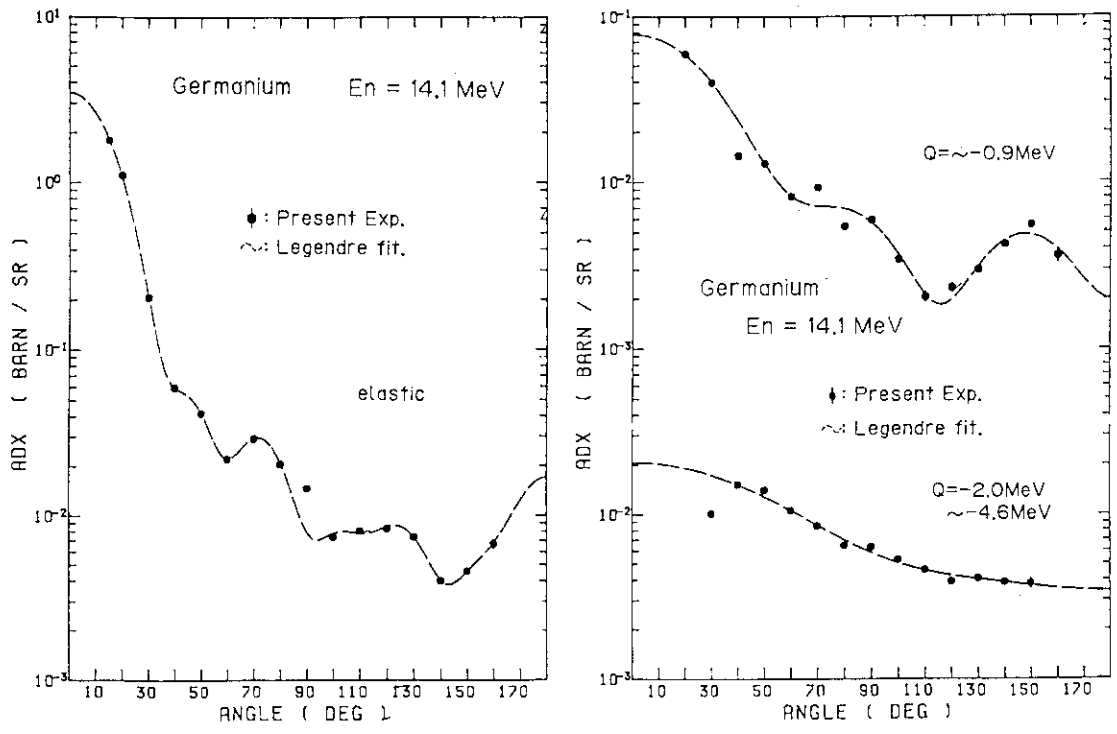

Fig. 6 Angular differential cross section for germanium (a) elastic (b) discrete inelastic scattering. Not corrected.

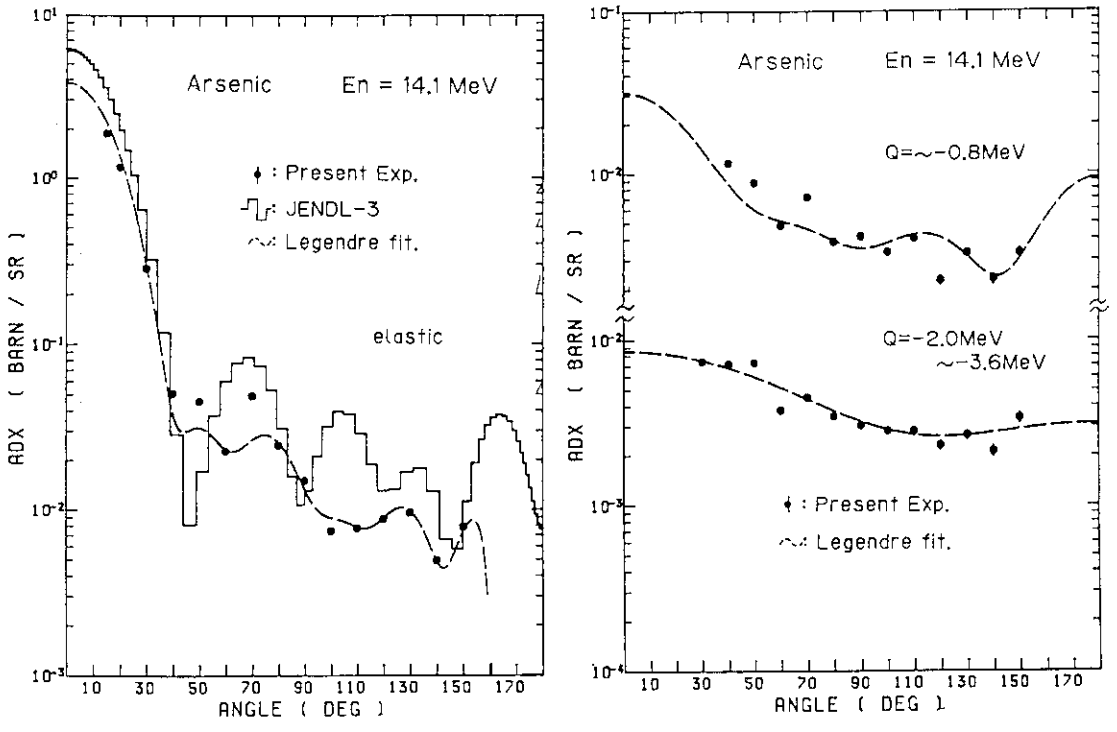

Fig. 7 Angular differential cross section for arsenic (a) elastic (b) discrete inelastic scattering. Corrected using JENDL-3.

3.14 MEASUREMENTS OF DOUBLE-DIFFERENTIAL NEUTRON EMISSION CROSS SECTIONS OF Nb-93 AND Bi-209

S.Matsuyama, T.Ito, M.Baba, N.Ito, H.Ide, T.Okubo and N.Hirakawa
Department of Nuclear Engineering, Tohoku University
Aoba, Aramaki, Aoba-ku, Sendai 980, Japan

Double-differential neutron emission cross sections of Nb and Bi have been measured for 14 MeV and 18 MeV incident neutrons using Tohoku university Dynamitron time-of-flight spectrometer. The angle-integrated spectra of both nuclides for 14 MeV primary neutrons are in good agreement with other experimental data. On the other hand, the data derived from evaluated nuclear data of JENDL-3 and ENDF/B-VI do not reproduce our data. The angular distributions of continuum neutrons are compared with the well known systematics proposed by Kalbach-Mann and Kalbach.

1. Introduction

Fast neutron induced cross sections are important for many applications: e.g. fusion technology, radiobiology and accelerator technology. Particularly, double-differential neutron emission cross sections are needed for the estimation of radiation damage, nuclear heating, PKA spectra and of kerma factors. Many experimental data for fusion reactor structural materials have been accumulated for 14 MeV neutrons. But the data for other nuclides and for other incident energy are still lacking. Hence nuclear reaction model and systematics are used in evaluation.

In this work, we have measured the double-differential neutron emission cross sections of Nb-93 and Bi-209 for 14.1 MeV and 18 MeV neutrons. The neutron emission spectra of those nuclides are expected for the reference data for the theoretical calculations.

2. Experiments

The experiments were carried out using Tohoku university 4.5 MV Dynamitron time-of-flight spectrometer. The experimental method was almost same as those in previous studies /1,2/.

The 14.1 MeV and 18 MeV neutrons were obtained via the T(d,n) reaction at emission angles of 97.5-degree and 0-degree, respectively. A Ti-T metallic target was bombarded by pulsed deuteron beam about 1.5 nsec duration.

The scattering samples were metallic cylinders of elemental Nb-93 and Bi-

209, 3 cm-diam and 5 cm long, and placed 12 cm from the target.

Scattered neutrons were detected by a NE213 liquid scintillator, 14 cm-diam and 10 cm thick, placed in a massive shield on a rotating table. This shield can be positioned at angles from 0 to 160-degree and provide flight paths of 4 to 7 m. The flight path length was 6.5 m for 14.1 MeV measurements and 4 m for 18 MeV measurements. For the 14.1 MeV measurements, an additional preshield was placed to suppress room-returned neutrons. In order to distinguish neutrons and gamma-rays, standard pulse shape discrimination(PSD) technique was used. Two separate PSD systems, having different bias setting, were employed to get adequate neutron-gamma separation for wide neutron energy range. Neutron energy was determined by using time-of-flight method. Fast timing signals from the detector are converted to fast logic signals via a wide dynamic-range constant-fraction timing discriminator. The time differences between the detector pulses and delayed beam pick-off signals are measured by time-to-amplitude converter.

Relative detector efficiency was determined by measuring time-of-flight spectrum of fission neutrons from Cf-252 for energy region lower than 4 MeV and the calculation results of O5S code for higher energy region. Absolute cross section was determined referring elastic scattering cross section of hydrogen.

Another small NE213 scintillator, 2"-diam and 2" thick, was used to provide the normalizations between sample-in and sample-out runs and to monitor time-correlated parasitic neutrons.

The neutron emission spectra were measured at several angles between 30 and 150-degree. For each measurement, sample-in and sample-out runs were carried out without stopping the beam using remotely-controlled sample-changer.

3. Data Analysis

The raw time-of-flight spectra were transformed into energy spectra considering detector efficiency after subtracting sample-out spectra. Then, these energy spectra were corrected for the effects of finite sample size and of backgrounds caused by parasitic and target-scattered neutrons. The effects of finite sample size were estimated by Monte-Calro calculations using a program "SYNTHIA" /3/. In this program, "Real" and "Ideal" spectra are calculated, respectively, with and without the distortions due to flux attenuation and multiple scattering. The data used in the calculations were mostly derived from JENDL-3. However the neutron emission spectra derived from JENDL-3 do not reproduce the experimental data, then we combined JENDL-3 with experimental data and Kalbach-Mann systematics. In the corrections, "Real" and "Ideal" spectra were

calculated separately for primary neutrons and for background neutrons. "Real" spectra for background neutrons were added to "Real" ones for primary neutrons. Ratio of the "Ideal" spectra for primary neutrons to summed "Real" spectra served correction factors. The spectra of the background neutrons were measured before and after the scattering experiments. The intensities of them were determined by calculation for 14 MeV and by measurements for 18 MeV. In order to consider time dependence of parasitic neutrons due to accumulation of contaminant elements, "Real" spectra were evaluated by interpolation between two "Real" spectra which correspond to each background spectrum /1/. Figure 1 shows the typical results of simulated spectra in comparison with the raw experimental data and the correction factors.

4. Results and Discussions

Angle-integrated neutron emission spectra of Nb-93 and Bi-209 for 14.1 MeV incident neutrons are shown in Fig. 2, respectively, compared with the data by A.Pavlik and H.Vonach /4/. Our data are generally in good agreement with other ones.

Nb-93

Typical results of Nb-93 for 14.1 MeV and 18 MeV incident neutrons are shown in Figs. 3 and 4, compared with the data derived from JENDL-3 and ENDF/B-VI. The experimental spectra consist of peak due to elastic scattering, broad peak probably due to collective excitation, and of continuum neutrons. Strong angle-dependence can be seen in the energy region above a few MeV because of pre-equilibrium mechanism.

In comparison with the evaluated nuclear data, the present data are not consistent with both evaluations for all energy region. Particularly angle-dependence is not considered in ENDF/B-VI, then there exist larger discrepancies in higher energy region at backward angles.

The angular distributions of continuum neutrons are compared with the systematics proposed by Kalbach-Mann (KM) and Kalbach. In the calculations of these systematics, it need to divide the cross section into two components: statistical multistep compound (MSC) and statistical multistep direct (MSD) /5,6/. We assumed Blann-Lanzafame's exciton spectrum /7/ for MSD component and Weisskopf-Ewing's evaporation /8/ and Lecouteur-Lang's cascade neutron emission /9/ spectra for MSC. Relative cross section and nuclear temperature were determined by fitting the angle-integrated spectra. Figure 5 shows the angular distributions of secondary neutrons. Kalbach systematics reproduced better the experimental data.

Bi-209

Typical neutron emission spectra are given in Figs. 6 and 7, compared with evaluated data. Both evaluated data do not reproduce the experimental data.

The angular distributions of secondary neutrons are illustrated in Fig. 8, compared with the KM and Kalbach systematics. The experimental data are closer to the KM systematics, while Nb data are represented better by Kalbach's ones. It has been pointed out that the KM systematics overemphasize the forward rise of the angular distributions for medium-heavy nuclides /2/. It is likely that there is mass dependence in angular distributions of pre-equilibrium neutrons.

In order to make this point clear, we compared reduced legendre coefficients $B_1(=a_1/a_0)$ derived by fitting the experimental angular distributions with ones expected from KM systematics. Figures 9 and 10 show the values of B_1 against the mass number for 14.1 MeV and 18 MeV incident neutron energies, respectively. The values of B_1 derived from experimental data increase with the mass number, while B_1s expected from KM systematics are almost constant. In KM systematics, the magnitudes of B_1 depend on the MSD/MSC ratios. This result suggests that there is stronger mass dependence in angular distributions of pre-equilibrium neutrons than that expected by KM systematics, while further consideration is necessary for division of MSD/MSC ratios and for contributions of direct process.

5. Summary

We have measured double-differential neutron emission cross sections of Nb-93 and Bi-209 for 14.1 MeV and 18 MeV incident neutrons and derived 1) the double-differential neutron emission cross sections, 2) angle-integrated neutron emission cross sections and 3) angular distributions of continuum neutrons. Angle integrated neutron emission spectra are in good agreement with other experimental data. Evaluated nuclear data of JENDL-3 and ENDF/B-VI do not reproduce the experimental data.

References

1. S.Matsuyama et. al. ;JAERI-M, 91-032, p.219(1991).
2. M.Baba et. al. ;J. Nucl. Sci. Technol., 27(7) p.601(1990).
3. T.Sakase ;Private communication.
4. A.Pavlik & H.Vonach ;ISSN 0344-8401, No.13-4(1988).
5. C.Kalbach and F.M.Mann ;Phys. Rev., C23(1) p112(1981).
6. C.Kalbach ;Phys. Rev., C37(6) p.2350(1988).
7. M.Blann & F.M.Lanzafame ;Nucl. Phys., A142 p.559(1970).
8. D.Hermsdorf et.al. ;J. Nucl. Eng.,27 p.747(1973).
9. M.Lecouteur & D.W.Lang ;Nucl.Phys., 13 p32(1959).

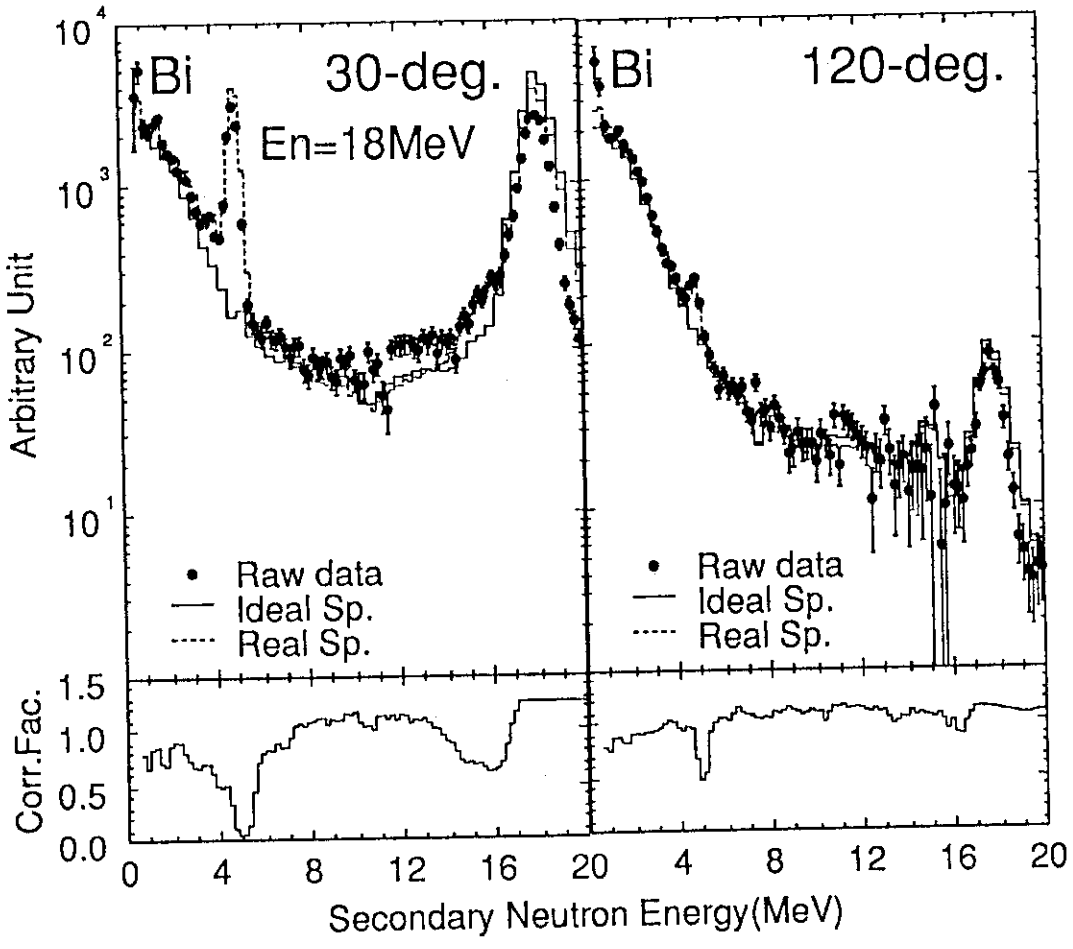

Fig. 1 Calculated and observed neutron emission spectra and correction factors of Bi-209 for correction.

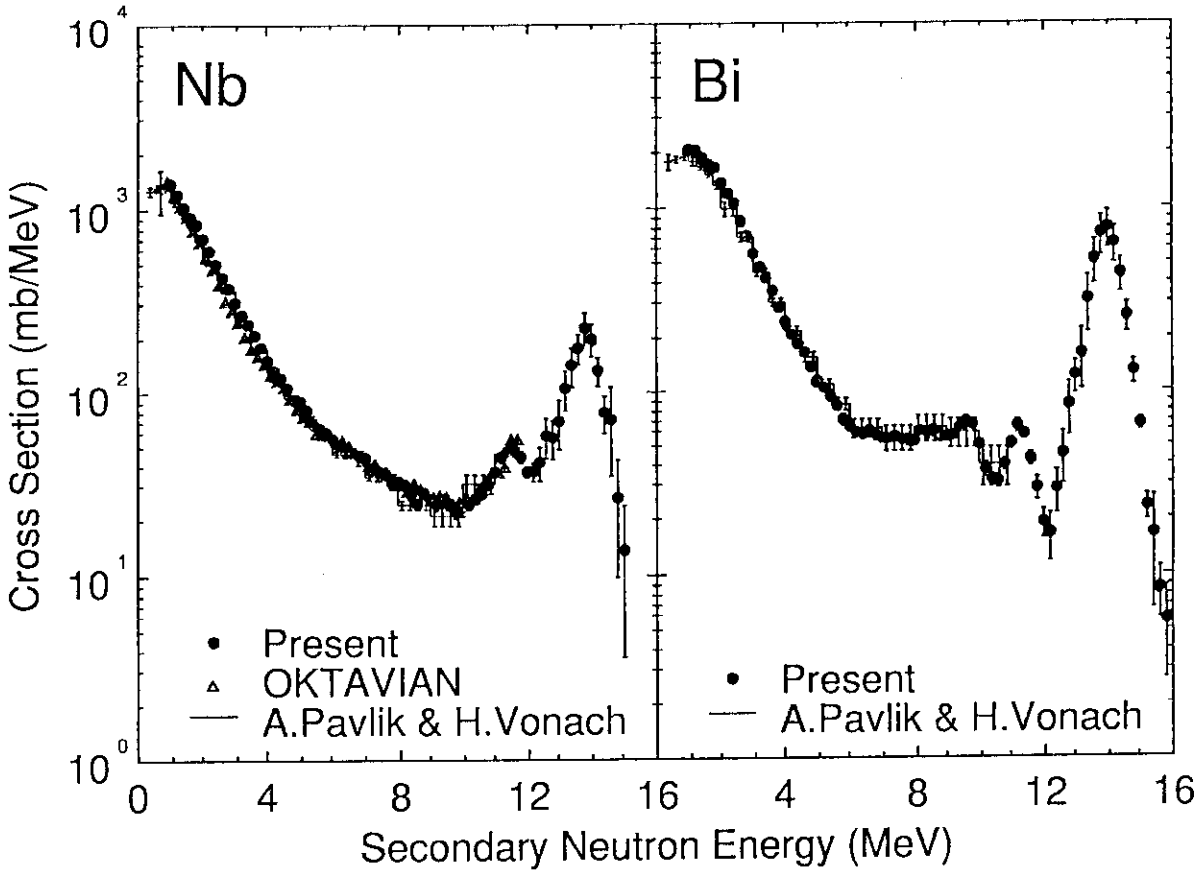

Fig. 2 Angle integrated neutron emission spectrum of Nb-93 and Bi-209 for 14.1 MeV neutrons, compared with other experimental data.

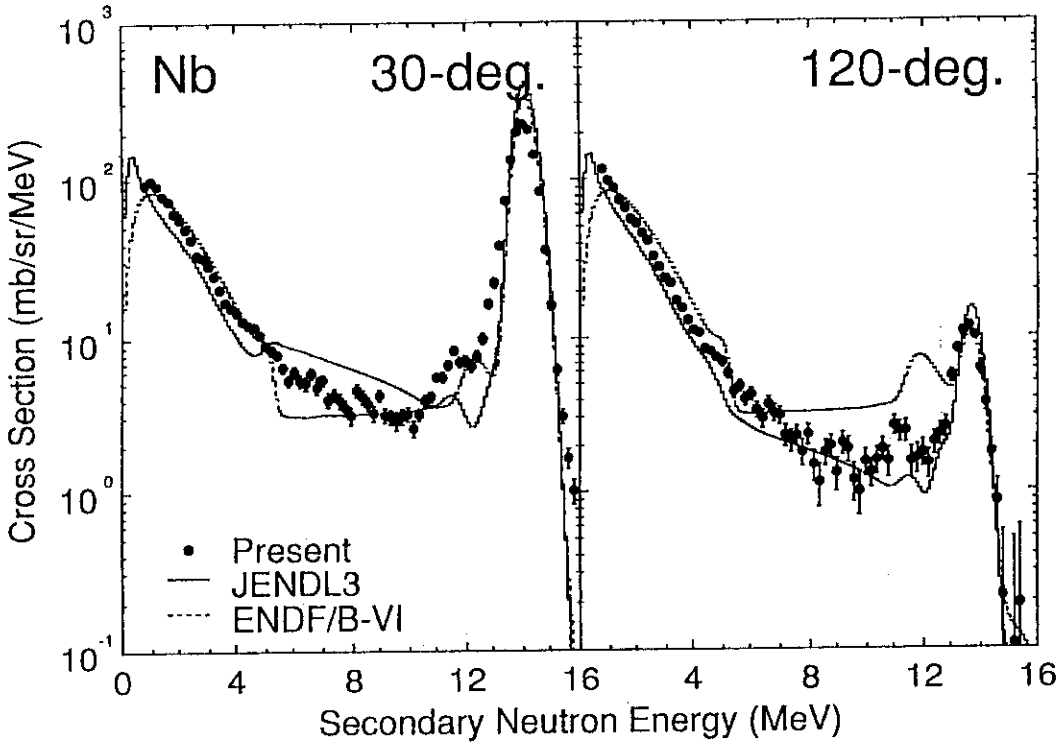

Fig. 3 Double-differential neutron emission cross sections of Nb-93 for 14.1 MeV incident neutrons.

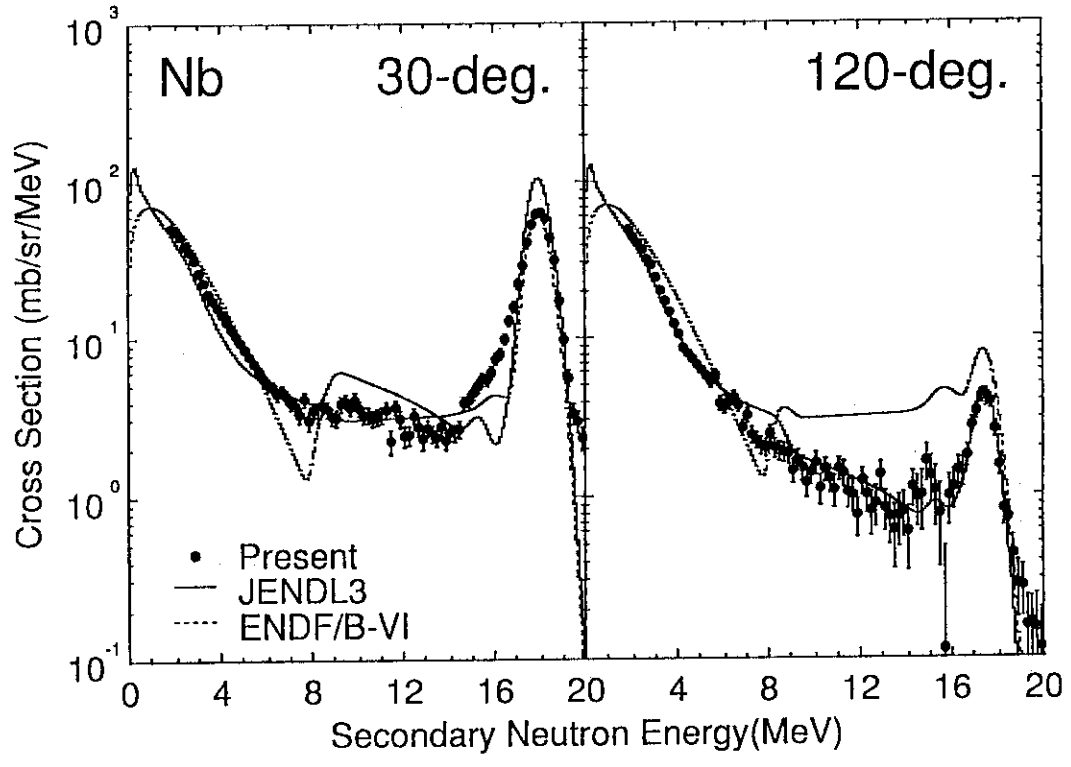

Fig. 4 Double-differential neutron emission cross sections of Nb-93 for 18 MeV incident neutrons.

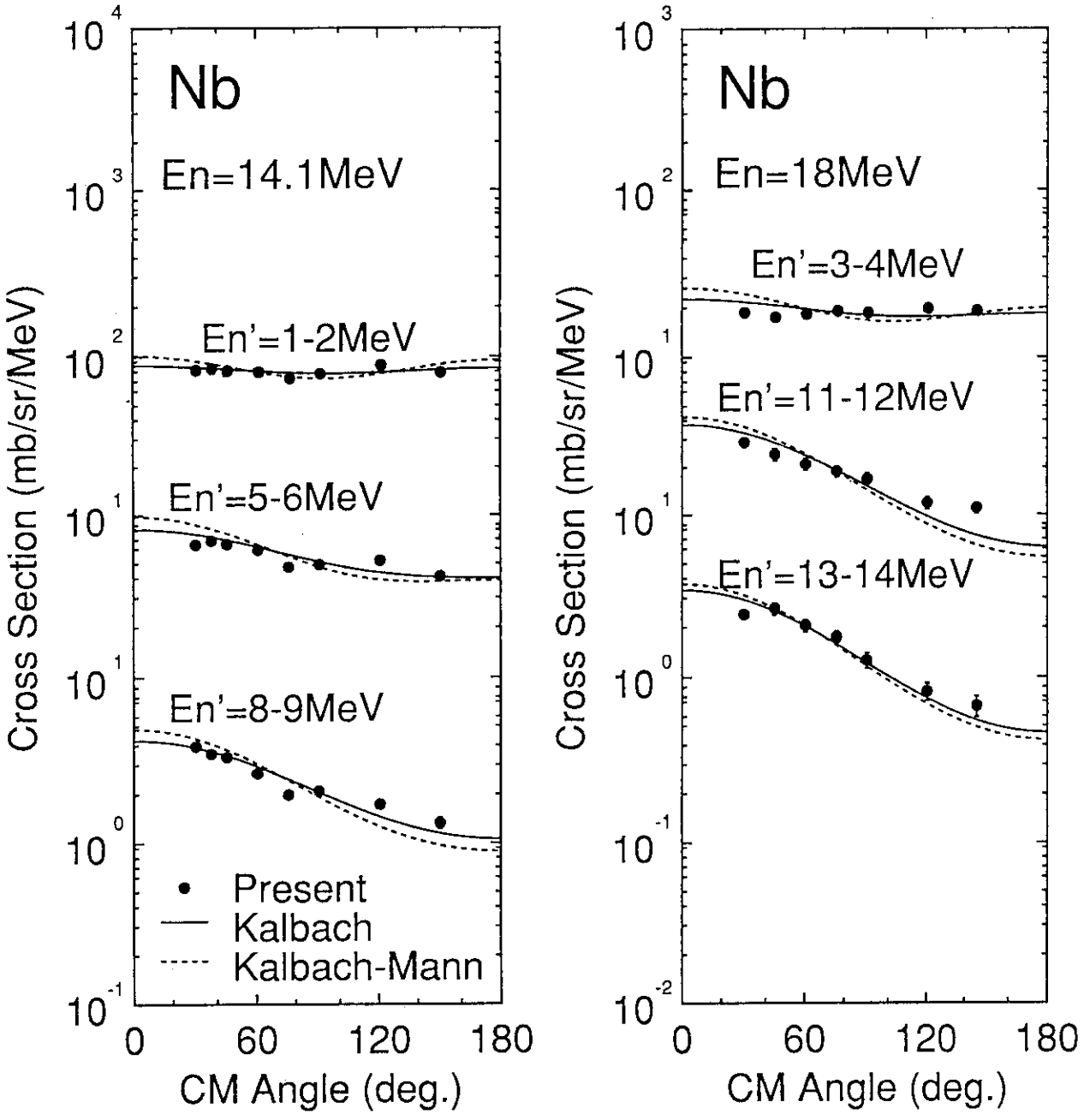

Fig. 5 Angular distributions of continuum neutrons for Nb-93.

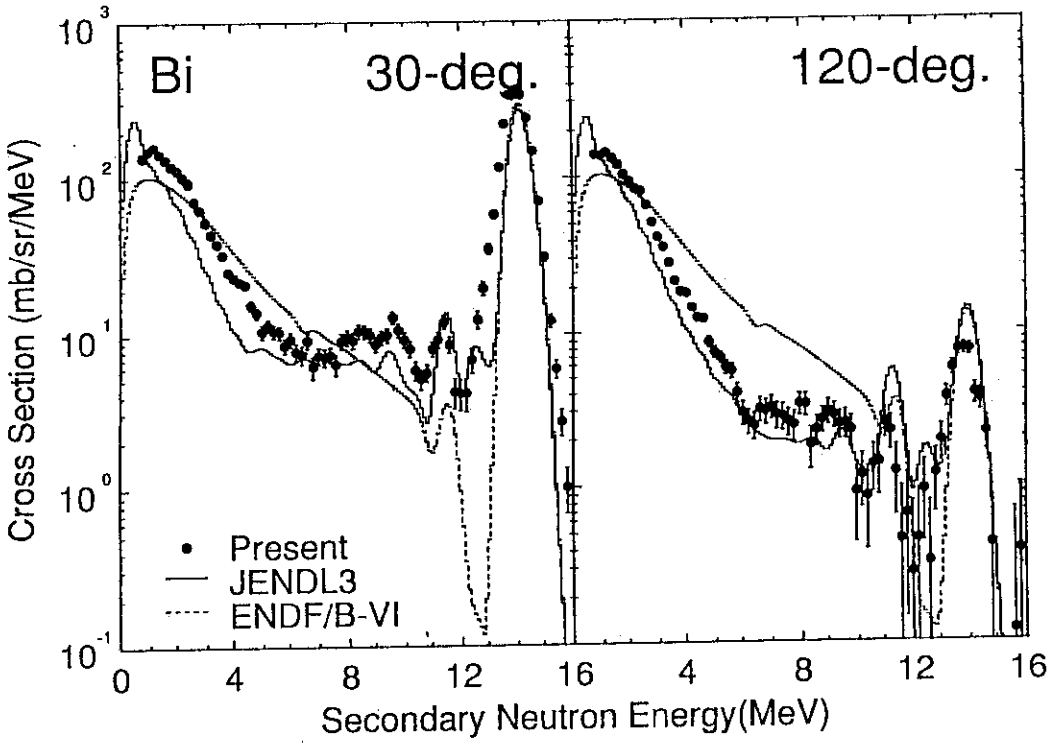

Fig. 6 Double-differential neutron emission cross sections of Bi-209 for 14.1 MeV incident neutrons.

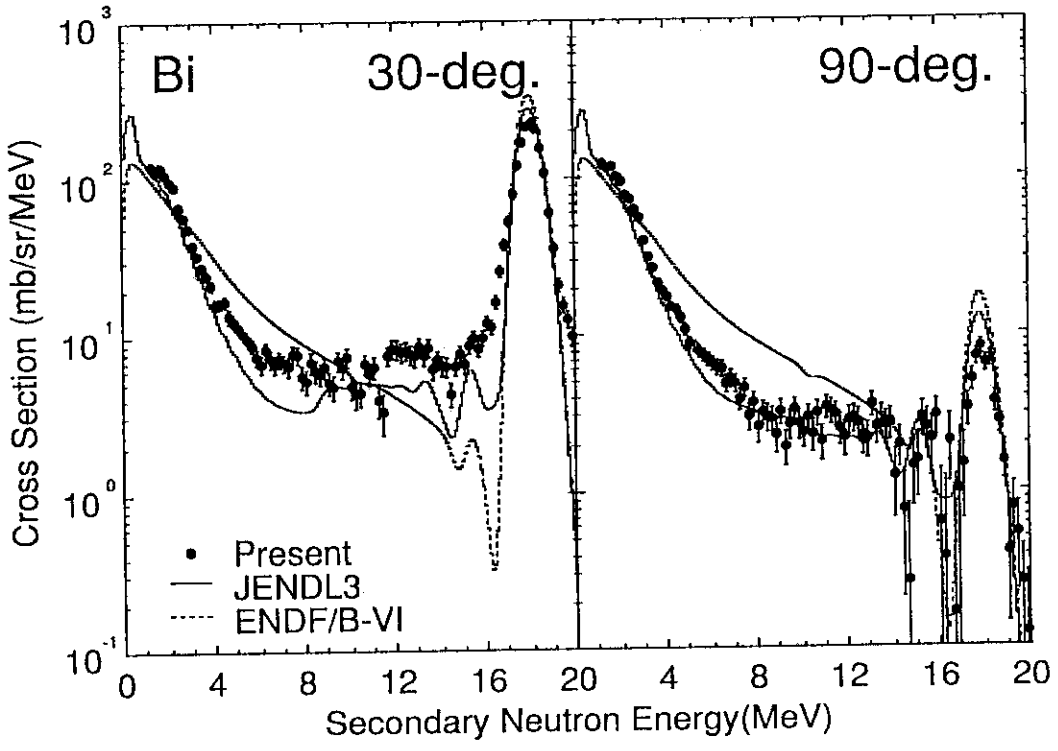

Fig. 7 Double-differential neutron emission cross sections of Bi-209 for 18 MeV incident neutrons.

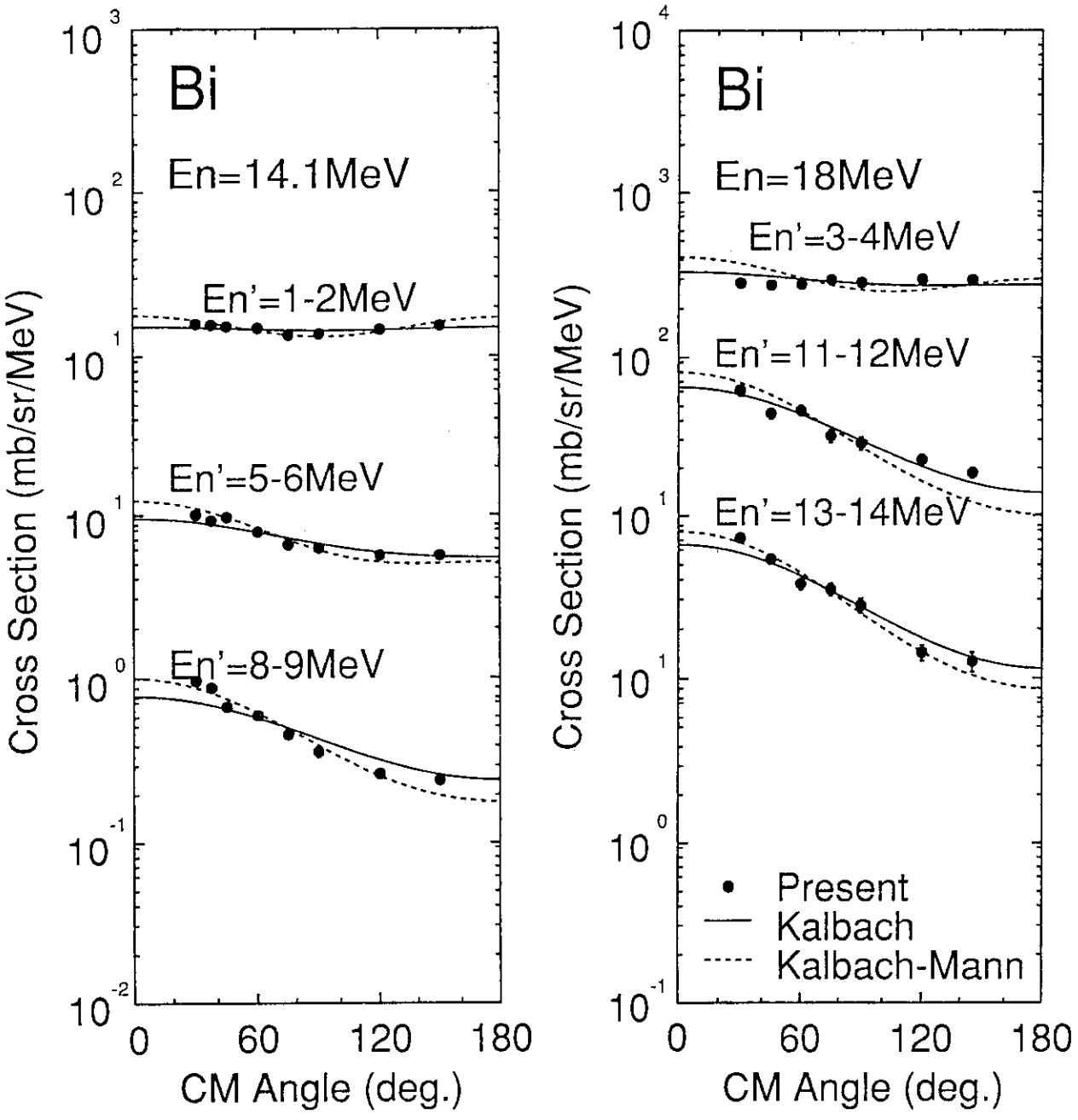

Fig. 8 Angular distributions of continuum neutrons for Bi-209.

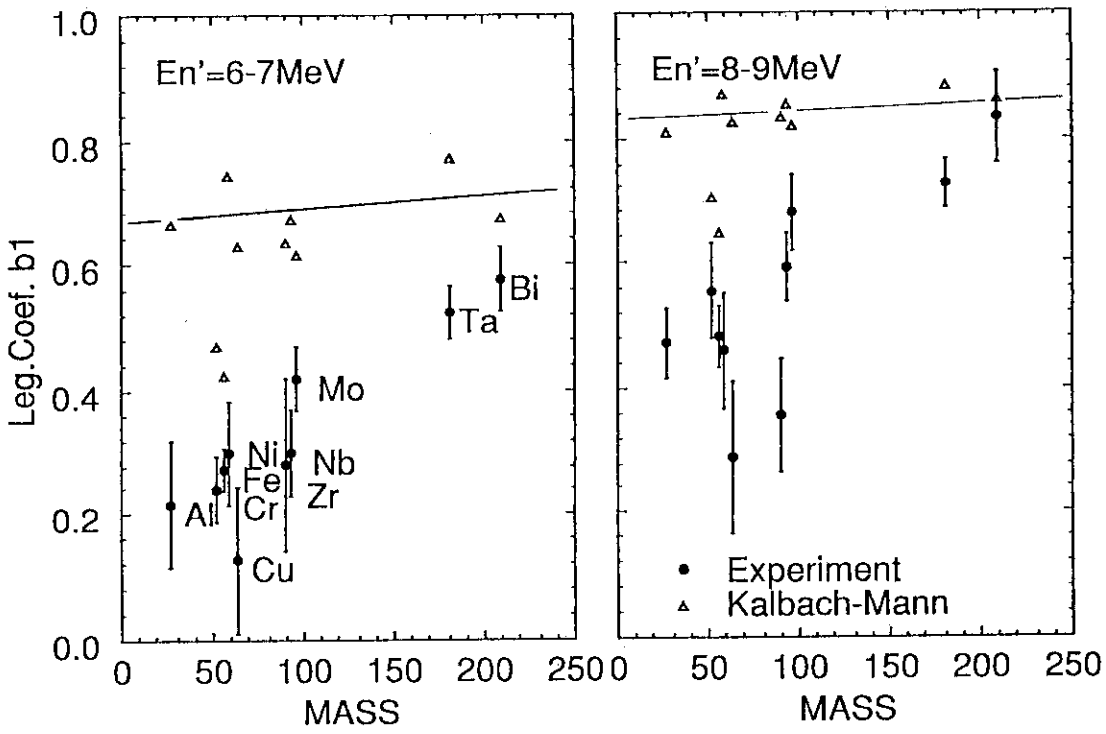

Fig. 9 Reduced Legendre coefficients B1 against mass number for 14 MeV incident neutrons.

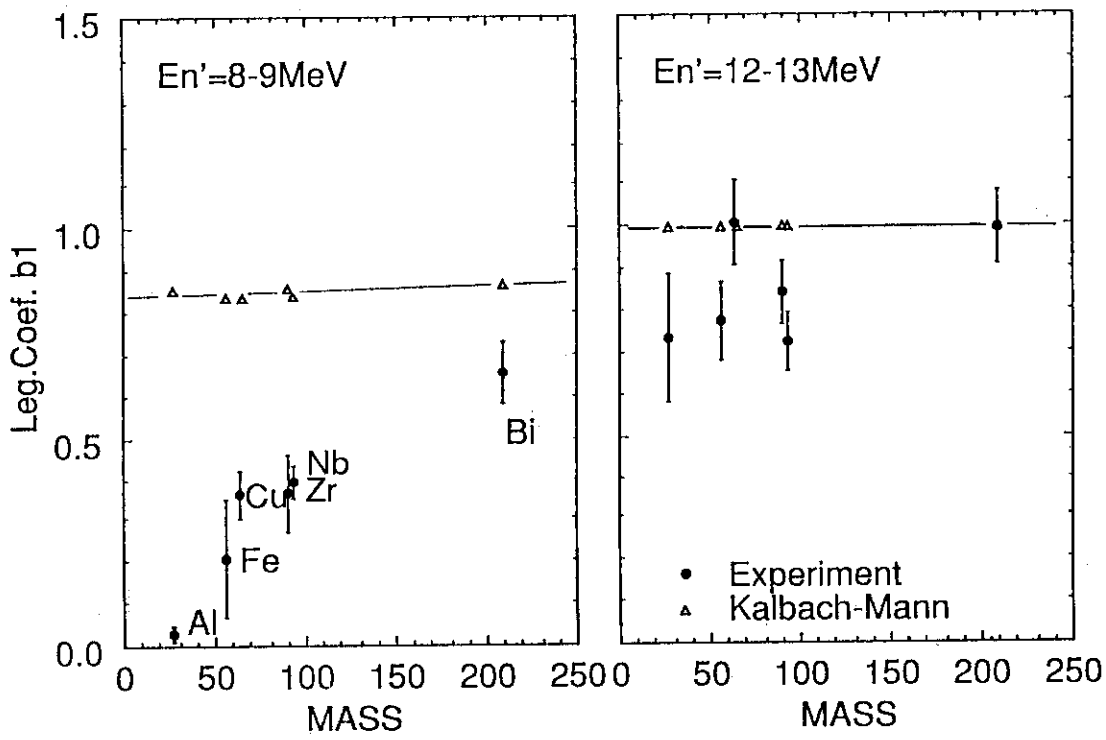

Fig. 10 Reduced Legendre coefficients B1 against mass number for 18 MeV incident neutrons.

3.15 DIFFERENTIAL CROSS SECTIONS FOR ELASTIC AND INELASTIC NEUTRON SCATTERING FROM ^{12}C AT 14.1MeV

S. Shirato, K. Hata* and Y. Ando

Department of Physics, Rikkyo University, Nishi-Ikebukuro 3,

Toshima-ku, Tokyo 171, Japan

Double differential cross sections and energy-integrated differential ones for elastic and inelastic neutron scattering from ^{12}C have been measured at forward angles from 10^{o} to 50^{o} in 10^{o} steps using the neutron time-of-flight (TOF) facility of the 300 kV Cockcroft-Walton accelerator of Rikkyo University.

The experimental data have been compared with the experimental ones published by other authors and with the predictions of optical model and DWBA calculations as well as those of JENDL-3. New optical model parameters are proposed as the result of the analyses using a reasonable value (β_2 = 0.65) of the quadrupole deformation parameter for the reaction $^{12}C(n,n')^{12}C^{*}$(1st).

1. Introduction

Double differential cross sections (DDX) for elastic and inelastic neutron scattering from ^{nat}C and ^{nat}Fe at 14.1 MeV, which were measured at forward angles from 10^{o} to 50^{o} in 10^{o} increments using the neutron time-of-flight (TOF) facility of the 300 kV Cockcroft-Walton accelerator of Rikkyo University, have been preliminarily analyzed[1]. However, for ^{12}C especially, some discrepancies between the theoretical predictions of optical model and DWBA calculations and the evaluations based on JENDL-3T

---

* Present address: Hitachi Seisakusho Co.

are found[1], as well as among presently available experimental data. For the reaction $^{12}C(n,n')^{12}C^*$(1st, 2^+, 4.4391 MeV), the derived value (β_2 = 0.90)[1] of the quadrupole deformation parameter in this exited state seems to be unreasonable, using the potential parameters of the entrance channel for the parameters of the exit one in the DWBA calculation. This situation is quit different from those for the case of the reaction $^{56}Fe(n,n')^{56}Fe^*$(1st, 2^+, 0.8468 MeV).

In this paper, the results of our preliminary data and reanalyses are presented only for ^{12}C and CH_2, since our experiment is still continued to obtain more precise data with improved statistical errors at the present time.

2. Experiment

Neutron TOF spectra were obtained from the signals of scattered neutrons and the associated α-particles produced in the $^3H(d,n)^4He$ reaction at 165 keV, using an NE213 liquid scintillator of 2 in ϕ x 2 in ("small neutron detector") for the neutron detector and a thin (50 μm) NE 102A plastic scintillator for the α-particle detector[2]. The cylindrical scattering samples of 3 cm ϕ x 3 cm were made of natural graphite and iron of 99.9 % purity. We are still performing the measurement of neutron TOF spectra with a large NE213 scintillator of 10 cm ϕ x 30 cm ("large neutron detector"), by using the same and alternative ^{nat}C and ^{nat}Fe targets as well as a CH_2 target of the same size, in order to improve the statistical errors and to obtain cross sections relative to the absolute ones measured with the small neutron detector[1,3].

The neutron TOF spectra were converted to the energy spectra through a relation between time T (ns) and energy E_n (MeV) of the neutron passing flight distance L (cm):

$$T = 0.723\ L\ /\ E_n^{1/2}. \qquad (1)$$

The overall time resolution of our TOF system was measured to be 0.70 ns in FWHM at L = 180 cm and E_n = 14.1 MeV. The FWHM of the incident neutron energy distribution was estimated to be 320 keV. The detailed descriptions of the experiment using the large neutron detector and the data analysis should be reported in the near future[4], together with the measured energy spectra of scattered neutrons for ^{nat}C, CH_2 and ^{nat}Fe in comparison with the theoretical curves[5] based on JENDL-3.

3. Results and discussion

Measured and calculated[5] DDXs for 14.1 MeV neutron scattering from ^{12}C at 40° are shown as an example of the data measured with the small neutron detector in fig. 1. Our CH_2 DDX data measured with the large neutron detector is shown also as an example in fig. 2. The 40° value of the n-p differential cross section at 14.1 MeV, which was obtained from the CH_2 DDX data, was in good agreement with our previously published value of the n-p cross section ($\sigma(40^\circ)$ = 167.7 ± 3.3 mb/sr) [6].

Our measured angular distribution for elastic scattering from ^{12}C is in good agreement with the optical model calculation as seen in fig. 3 where the recent 14.7 MeV forward data of Wan et al.[7] are drawn together with the data of other authors[8-13]. The optical model parameters[8] adopted in this calculation using the code DWUCK4[14] are given in table 1.

The result of the reanalysis of measured differential cross section for inelastic neutron scattering from the first excited state of ^{12}C using the code DWUCK4 of DWBA is shown in fig. 4. The differential cross section for collective excitations in momentum transfer L is given[14] by

$$d\sigma/d\Omega = \beta_L^2\ (d\sigma/d\Omega)_{DWUCK4}, \qquad (2)$$

where β_L is the deformation parameter of multipolarity L. The quadrupole

(L = 2) deformation parameter in the liquid drop model is given by

$$\beta_2 = (4\pi / 3R^2Ze)\, B(E2)^{1/2}, \qquad (3)$$

where $R = 1.2\ A^{1/3}$ is the nuclear radius in fm and B(E2) is the electric quadrupole (E2) transition probability in e^2fm^4. Eq. (3) predicts β_2 = 0.60 using $B(E2)\uparrow = 41.0\ e^2fm^4$ of Raman et al.[15] A value[16] of β_2 = 0.4 predicts too small cross sections compared to our data. In our analysis, we adopted $\beta_2 = -0.65$ and $\beta_4 = 0.05$, which were obtained by Olsson et al.[17] This value of β_2 is in good agreement with the value (-0.67 ± 0.04) of Woye et al.[18] Then, the optical potential parameters for the exit channel (E_n = 9.29 MeV) were searched in a region of deeper real potentials and shallow imaginary ones to fit the experimental data. The result obtained is also given in table 1. Detailed comparison of this result with the potentials of Woye et al.[18], who measured the analyzing power in the energy range from 8.9 to 14.9 MeV in 1 MeV steps, will be given elsewhere[4].

The result of the DWBA calculation for the reaction $^{12}C(n,n')^{12}C^*$(1st) is in agreement with experimental data[1,8,11-13]. Consequently, fig. 5 of ref. 1 should be replaced by this figure. It is noted that our optical potential parameters of the exit channel in this reaction for ^{12}C, as given in table 1, are somewhat different from those[8] in the entrance channel. The DWBA calculation is satisfactory in our case of 14.1 MeV, in spite of the claim of Olsson et al.[17] who analyzed their data of higher incident neutron energies (> 16 MeV) and performed coupled-channels calculations.

It is also mentioned that our DWBA calculation for the reaction $^{56}Fe(n,n')^{56}Fe^*$(1st) confirmed the value of the deformation parameter (β_2 = 0.23) of Hyakutake et al.[19] by using their potential parameters[1] without changing those of the exit channel.

4. Conclusion

The DDXs and energy-integrated differential cross sections for elastic and inelastic neutron scattering from ^{nat}C and CH_2 as well as ^{56}Fe at 14.1 MeV were absolutely measured at forward angles from 10^{o} to 50^{o} in 10^{o} steps. The present data will be improved in statistics soon.

The optical model prediction of elastic scattering for ^{12}C using the optical potential parameters of Gul et al.[8] reproduced fairly well the present data as well as the published data of other authors[7-13] within experimental errors. The small discrepancies between these data should be resolved in a comparison at larger angles. The DWBA prediction for the reaction $^{12}C(n,n')^{12}C^{*}(1st)$ is also in good agreement with the present data, using the deformation parameter $\beta_2 = 0.65$ and the different exit-channel parameters from the entrance-channel ones of the optical model potential.

This report is a part of the works performed under the Research-in-Trust in 1990 -1991 fiscal years from the Japan Atomic Energy Research Institute (JAERI).

References

1) K. Hata, S. Shirato and Y. Ando: JAERI-M 91-032, 328 (1991).

2) S. Shirato, S. Shibuya, Y. Ando, T. Kokubu and K. Hata: Nucl. Instr. Methods A278, 477 (1989).

3) K. Hata, S. Shirato and Y. Ando: private communication (1990).

4) S. Shirato, K. Hata and Y. Ando: JAERI-M, to be published.

5) T. Fukahori and I. Tazaki: private communication for DDXs (1988). T. Fukahori and S. Chiba: private communication for their code PLDDX (1991) and the evaluated data file JENDL-3.

6) S. Shirato and K. Saitoh: J. Phys. Soc. Japan 36, 331 (1974).

7) D. Wan, J. Cao, Y. Dai and X. Liang: High Energy Phys. Nucl. Phys. 15, 165 (1991).

8) K. Gul, M. Anwar, M. Ahmad, S. M. Saleem and N. A. Khan: Phys. Rev. C24, 2458 (1981).

9) J. H. Coon, R. W. Davis, H. E. Felthauser and D. B. Nicodemus: Phys. Rev. 111, 250 (1958).

10) H. H. Hogue: Nucl. Sci. Eng. 68, 38 (1978).

11) R. Bouchez, J. Duclos and P. Perrin: Nucl. Phys. 43, 628 (1963).

12) D. W. Glasgow, F. Purser, R. Hogue, J. Clement, K. Stelzer, G. Mack, J. Boyce, D. Epperson, S. Buccino, P. Lisowski, S. Glendinning, E. Bilpuch, H. Newson and C. Gould: Nucl. Sci. Eng. 61, 521 (1978).

13) G. Haouat, J. Lachar, J. Siguad, Y. Patin and F. Cocu: Nucl. Sci. Eng. 65, 331 (1978).

14) P. D. Kunz: University of Colorado Report, unpublished.

15) S. Raman, C. H. Malarkey, W. T. Milner, C. W. Nestor Jr. and P. H. Stelson: At. Data Nucl. Data Tables 38, 1 (1987).

16) L. Jarczyk, B. kamys, A. Magiera, R. Siudak, A. Strzalkowski, and G. R. Satchler: Nucl. Phys. A518, 583 (1990).

17) N. Olsson, B. Trostell and E. Ramstrom: Nucl. Phys. A496, 505 (1989).

18) E. Woye, W. Tornow, G. Mack, C. E. Floyd, P. P. Guss, K. Murphy, R. C. Byrd, S. A. Wender, R. L. Walter, T. B. Clegg and W. Wylie: Nucl. Phys. A394, 139 (1983).

19) M. Hyakutake, M. Matoba, T. Tonai, J. Niidome and S. Nakamura: J. Phys. Soc. Japan 38, 606 (1975).

Table 1 Optical potential parameters for the reaction $^{12}C(n,n')^{12}C^*(1st)$. $[U_C(r) = 0]$

V (MeV)	W_s (MeV)	V_{so} (MeV)	r_0 (fm)	r_0' (fm)	a (fm)	b (fm)	Ref.
Entrance channel:							
46.5	8.88*	4.39+	1.28	0.86	0.39	0.39	8)
Exit channel:							
55.0	2.60*	4.39+	1.20	0.86	0.39	0.39	

V: Real volume Woods-Saxon potentials with range parameters r_0 and a.

W_s: Imaginary surface Woods-Saxon potential with range parameters r_0' and b.

* Note $W_s = V_I/4$ using the DWUCK4 notation.

+ Note $V_{so} = V_{LS}/4$ in the $\underline{l}\text{-}\underline{\sigma}$ form using the DWUCK4 notation.

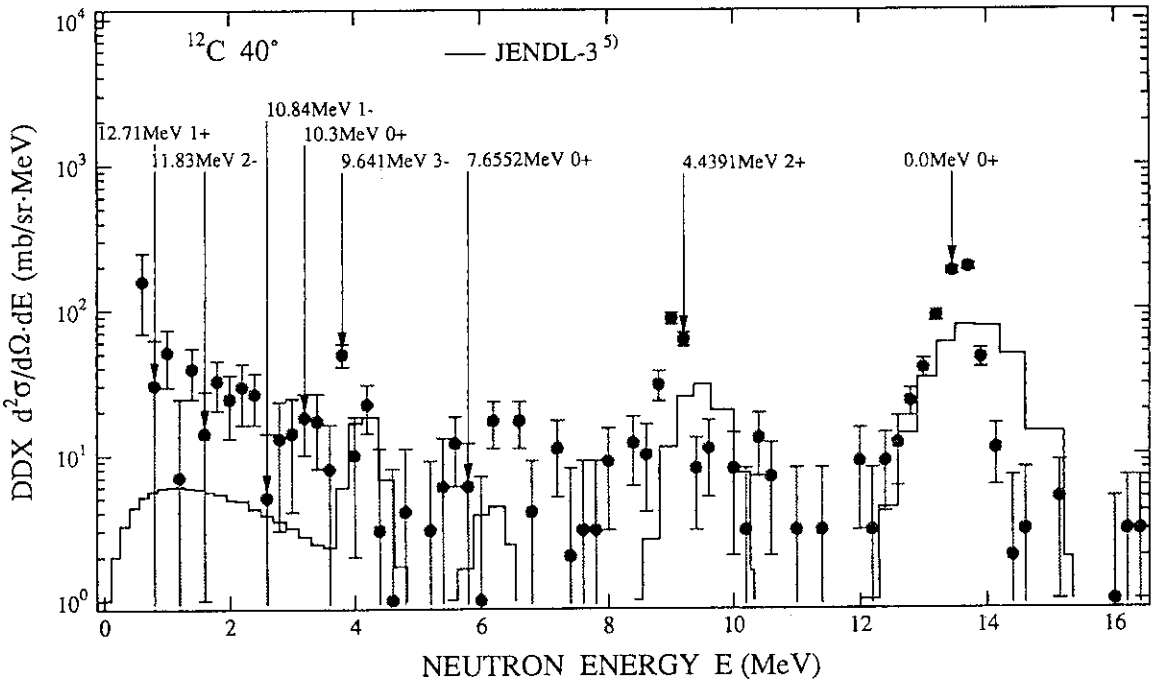

Fig. 1 Measured and calculated[5)] double differential cross sections for 14.1 MeV neutron scattering from ^{nat}C at 40°.

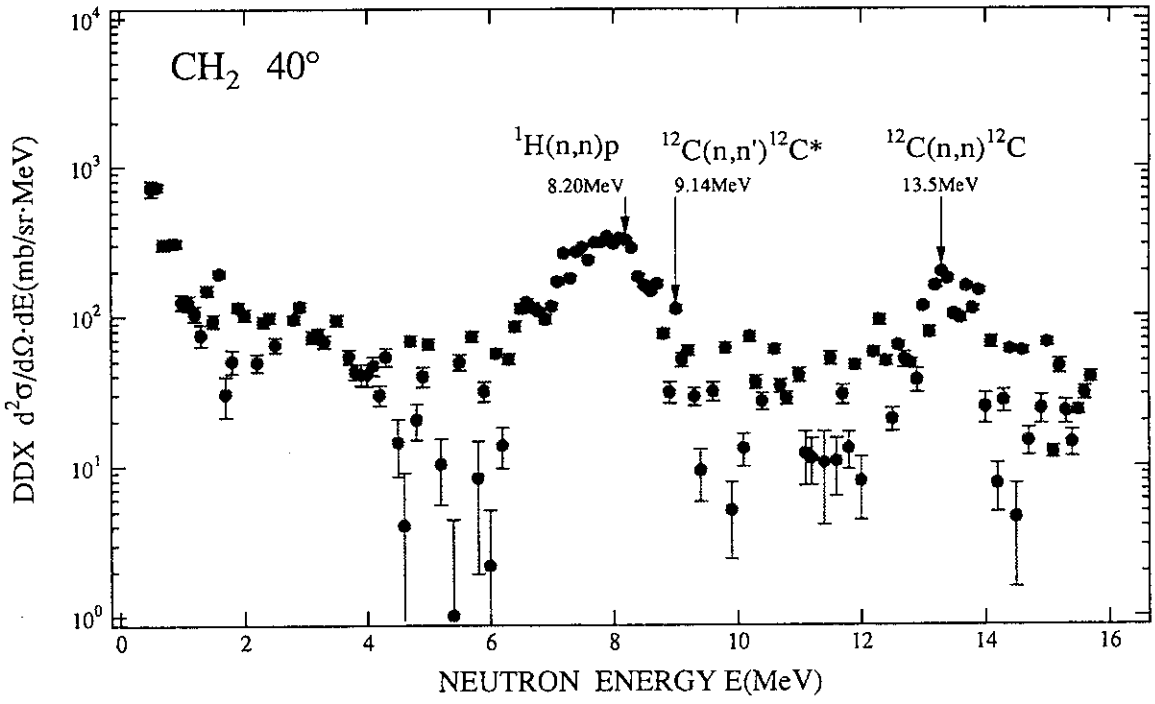

Fig. 2 Measured double differential cross section for 14.1 MeV neutron scattering from CH_2 at 40°.

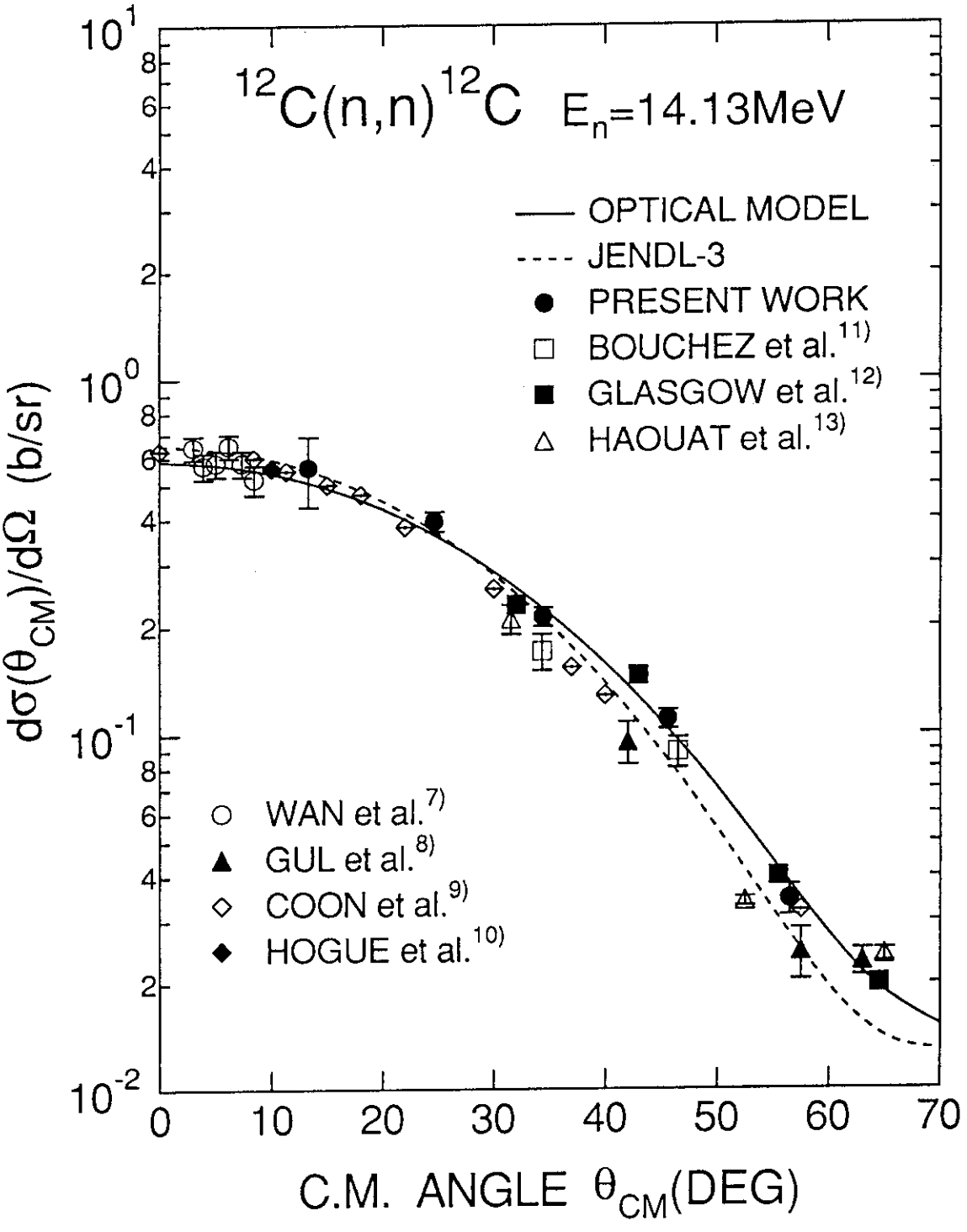

Fig. 3 Measured and calculated angular distributions for elastic neutron scattering from ^{12}C.

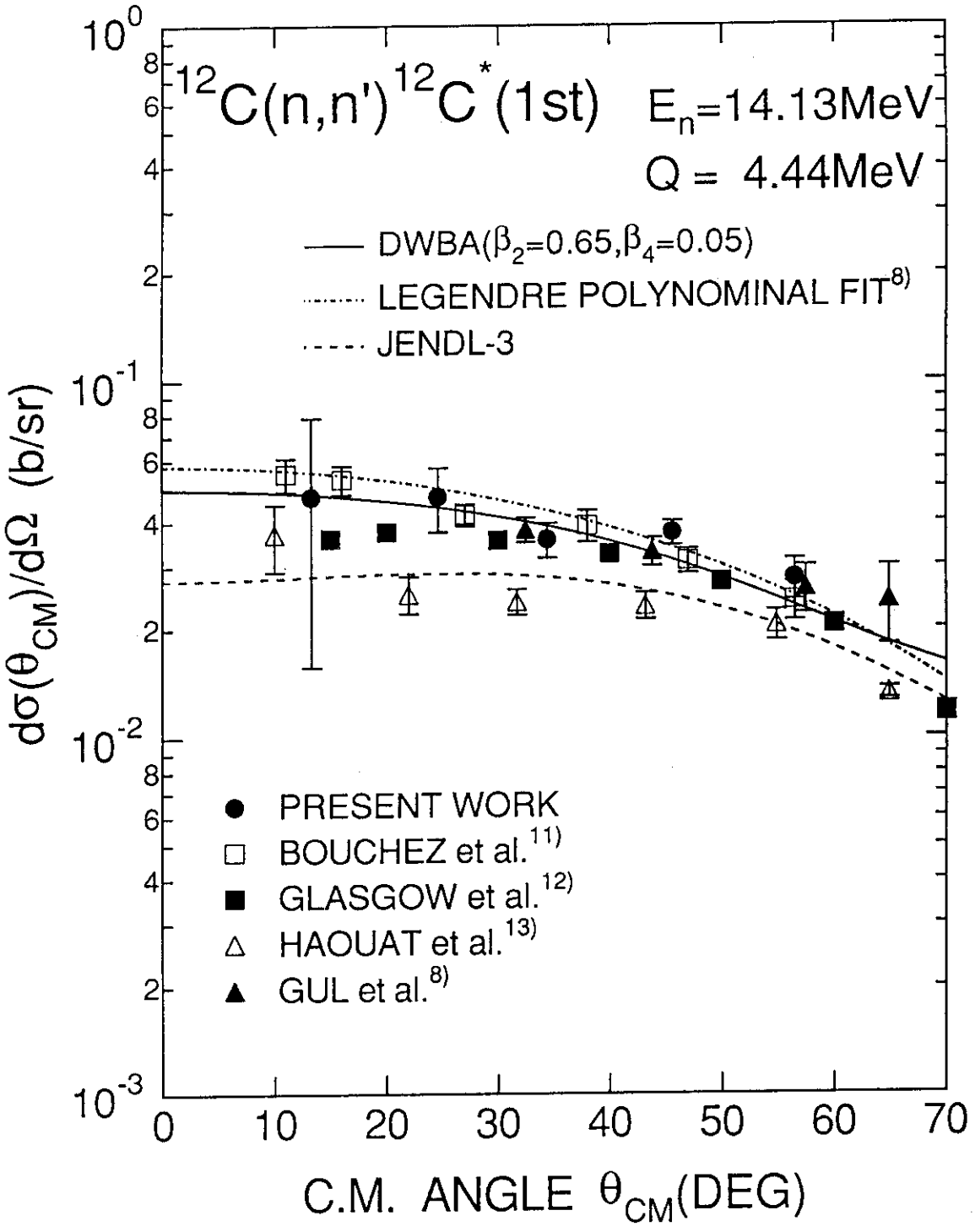

Fig. 4 Measured and calculated angular distributions for inelastic neutron scattering from $^{12}C^*$(1st).

3.16 MEASUREMENT OF DOUBLE DIFFERENTIAL CHARGED-PARTICLE EMISSION CROSS SECTIONS FOR REACTIONS INDUCED BY 20 — 40MeV PROTONS

A. Aoto, Y. Watanabe, H. Hane, H. Kashimoto, Y. Koyama, H. Sakaki, Y. Yamanouchi*, M. Sugimoto*, S. Chiba*, and N. Koori**

Department of Energy Conversion Engineering, Kyushu University, Kasuga, Fukuoka 816, Japan

** Japan Atomic Energy Research Institute, Tokai-mura, Ibaraki, 319-11 Japan*

*** College of General Education, The University of Tokushima, Tokushima 770, Japan*

Double differential cross sections of 25.6 MeV (p,xp) and (p,xd) reactions for ^{98}Mo have been measured for investigation of preequilibrium processes in nucleon-induced reactions. The exciton model calculation using the same parameters as those obtained from the previous analysis in 10-20 MeV region shows good agreement with the measured proton spectra. Preliminary calculations based on the two-component exciton model and the SMD-SMC model are also compared with the experimental (p,xp) and (p,xn) spectra.

1. Introduction

In nuclear reactions induced by several tens of MeV nucleon, substantial contribution from preequilibrium process is observed in continuous spectra of particles emitted with forward-peaked angular distributions. Systematic measurements of double differential charged-particle emission cross sections have so far been performed for proton-induced reactions in 10 to 20 MeV region at Kyushu University[1,2]. Through these experiments, the preequilibrium reaction mechanism in nucleon-induced reactions has been investigated and some of the derived results have been applied to the evaluation of neutron nuclear data based on nuclear model calculations.

In the present work, the incident proton energy range is extended to 20-40 MeV using the JAERI tandem accelerator, and similar measurements of charged-particle spectra from proton-induced reactions are planned for further studies of the preequilibrium process as follows: (i) incident energy dependence of the preequilibrium component (ii) simultaneous analysis of both energy spectra of (p,p') and (p,n) reactions that are main reaction channels in the proton-induced reaction (iii) test of the validity of several preequilibrium models through the above analyses. Furthermore, the present measurements may serve recent needs of intermediate nuclear data in the energy range of 20 MeV - 1GeV[3].

As the first stage, we have carried out measurements of double differential cross sections for protons and deuterons emitted from the proton-induced reaction on ^{98}Mo at 25.6

MeV, because the (p,xn) spectra on Mo-isotopes have already been measured at the same energy by the other group[4], and the (p,p') spectra have also been measured in 12-18 MeV by ones of the authors[5]. The measured (p,p') spectra are analyzed together with the (p,n) spectra on the basis of the exciton model[5] and the SMD-SMC model[6]

2. Experimental Procedure

The experiments have been performed using a 25.6 MeV proton beam from the JAERI tandem accelerator two times: the first measurement (Dec. 1990) is referred to as the measurement I and the second one (Nov. 1991) as the measurement II. In those experiments, the proton beam was transported in a scattering chamber 50 cm ϕ which was newly installed in N1 beam line as shown schematically in Fig.1. It was focused within about 2 mm ϕ on a target and its current was from about 50 nA to 300 nA, depending on the experimental condition. The beam intensity was monitored by means of a current integrator connected to a Faraday cup. A target of ^{98}Mo was a self-supporting metallic foil whose thickness and enrichment were 0.45 mg/cm^2 and 97.1%, respectively.

A charged particle detecting system consists of a ΔE-E counter telescope of two silicon surface barrier detectors having thickness of 200 μm (or 300 μm) and 5000 μm, respectively: hereafter the value in parentheses will indicate that of the measurement II. A defining aperture 2.5 mm (or 3.0 mm) in diameter was placed just in front of the ΔE detector and was located 147 mm from the target.

Standard commercially available NIM modules were used as the electronic equipments. Schematic block diagram of the electronics used in the measurement II is shown in Fig.2. Both signals of ΔE+E (the energy spectrum) and PI (the mass spectrum) from a particle identifier module (MPS-1230) were processed using the Canberra MPA/PC Multiparameter system. A contour plot of (ΔE+E) versus PI is shown in Fig.3 as the typical output. Protons, deuterons and tritons are separated very well. In the measurement I, on the other hand, a different data-acquisition system was used. The system consisted of a simple multichannel analyzer operating in single mode and the signals corresponding to proton and deuteron spectrum were recorded separately in the multichannel analyzer. An example of the measured mass spectrum is shown in Fig.4. Separation of protons and deuterons is found to be so good as in Fig.3.

Energy spectra of emitted protons and deuterons were measured at six angles of 30°, 40°, 60°, 90°, 120°, and 150° in the measurement I, and 30° to 150° in step of 10° in the measurement II. The data processing is similar to that described in more details in Ref.7.

3. Experimental results

Figure 5 shows measured differential cross sections of protons elastically scattered from ^{98}Mo at 25.6 MeV and those calculated using the spherical optical model with the global

parameters of Menet et al.[8] The experimental values (the measurement II) are in good agreement with the calculated ones in the angular region except 120° to 150°.

Measured double differential proton emission cross sections are shown for 40°, 90°, and 150° in Fig.6(a). Closed and open circles indicate the experimental data for the measurement I and II, respectively. Both data show agreement within about 15% except the low outgoing energy region. The discrepancy at low energies is due to the difference of the threshold energy that is determined from the thickness of ΔE detector. Solid lines present the proton spectra calculated in terms of the exciton model. The details of the calculation will be mentioned in the following section. As can be seen in Fig.6(a), the angular distributions are peaked forward in the continuum region between 10 and 20 MeV. This result suggests that the preequilibrium process or the direct process is dominant in this energy region.

Figure 6(b) shows experimental energy spectra of deuterons emitted into 30°, 60°, and 120° for the measurement II. Stronger forward-peaked angular distributions are observed at outgoing energies of 10 to 18 MeV than those for the proton spectra in Fig.6(a). Bump structure are exhibited around 15 MeV at the forward angle.

4. Analyses and discussion

The (p,xp) spectra were analyzed preliminarily on the basis of the one-component exciton model[5] in which isospin conservation was taken into account. The same model parameters as in our previous analysis[5] were employed and a modified version[9] of Kalbach - Mann systematics was applied to calculations of angle-dependent energy spectra. The calculated results are shown by the solid lines in Fig.6(a). The calculated spectra reproduce the experimental ones quite well in 10-20 MeV region for all angles. The exciton model includes an adjustable parameter in the square of average effective matrix element . An empirical relation[10] $M^2=KA^{-3}E^{-1}$ is widely used for the matrix element, where A and E are the mass number and excitation energy of the composite nucleus and K is the adjustable parameter. From the present analysis, it was confirmed that the parameter K-value[5] derived from the previous analysis of 12-18MeV (p,p') spectra on ^{98}Mo is applicable to higher incident energy.

Next we have analyzed simultaneously two dominant preequilibrium decay channels - (p,p') and (p,n) reactions - within the framework of the exciton model. Firstly, the result for the one-component exciton model mentioned above is compared with the experimental data in Fig.7. The experimental (p,n) data are taken from Ref.4. In the calculation, the Q-factor[11] was employed as the correction factor for the distinguishability of proton and neutron degrees of freedom. If the K value is adjusted so as to reproduce the (p,p') energy spectra well as indicated in Fig.7, the calculated (p,n) spectra show large overestimate in the preequilibrium region. The overestimate is somewhat improved as shown by the dotted line if the effective Q value[12] is used. Secondly, the two-component exciton model[13] was applied to the

calculation of (p,p') and (p,n) spectra. The result is shown in Fig.8. The parameters and assumptions used in the calculation is the same as those for proton-induced reactions on Zr and Pd-isotopes at 18MeV[2]. Both the calculated (p,p') and (p,n) spectra show good agreement with the experimental ones. The similar result has been obtained from the analysis of 18 MeV data[2].

As shown in Figs.6-8, the calculated (p,p') spectra underestimate the experimental ones in the outgoing energy region above 17 MeV. The reason may be due to the contribution from direct process which is not involved in the exciton model. Thus, the SMD-SMC model, one of quantum-mechanical models, is applied to take into account the direct process consistently. In the calculation, a EXIFON code[6] based on the SMD-SMC model is used and the default values implemented in the code are employed as the option parameters. Comparisons of the experimental (p,p') and (p,n) spectra and the calculated ones are shown in Fig.9. The bump structure at 23.5 MeV of the proton outgoing energy corresponds to the overlap of inelastic scattering to 2^+ and 3^- low lying states. The underestimate in 17-20 MeV for the exciton model is improved obviously, but the agreement becomes worse in the outgoing energy range below 17 MeV. For the (p,n) spectra, the agreement is not better than that shown in Fig.8. The present analysis is preliminary and it will be necessary to adjust the option parameter, especially the pairing energy so as to reproduce the (p,p') and (p,n) spectra consistently.

5. Conclusion

The detecting system of charged particles emitted from proton-induced reactions has been installed in the N1 beam line in the JAERI tandem accelerator. Using the system, the first experiment has been performed for measurement of the double differential cross sections of (p,xp) and (p,xd) spectra for ^{98}Mo at 25.6 MeV. Forward-peaked angular distributions were observed in the continuum region between 10 and 20 MeV of the outgoing energy, where the preequilibrium process or the direct process is dominant. The experimental (p,xp) data were analyzed preliminarily together with the (p,xn) data by the following three models: the one-component and the two-component exciton models and the SMD-SMC model. As a result, both the experimental (p,xp) and (p,xn) spectra showed better agreement with the model calculation based on the two-component exciton model. Further analysis will be necessary to draw a clear conclusion on the validity of those models.

In future, we intend to perform systematic measurements of double differential cross sections of emitted charged particle from proton-induced reactions over the wide mass range and at higher incident energies in order to enhance understandings of preequilibrium processes for medium-heavy nuclei and multiparticle breakup processes for light nuclei.

Acknowledgements

The authors would like to thank the members of the accelerator division of JAERI for their kind help during the experiment.

References

1) Y. Watanabe et al., *Proceedings of the XX th Int. Symp. on Nuclear Physics, Nuclear Reaction Mechanism*, Germany, Nov. 12-16, 1990, pp.151.
2) Y. Watanabe et al., *Proceedings of the 1989 Seminar on Nuclear Data*, JAERI-M 90-025, p 216 (1990).
3) INTERMEDIATE ENERGY NUCLEAR DATA FOR APPLICATIONS, *Proceedings of the Advisory Group Meeting organized by the IAEA*, Vienna, 9-12, October 1990, Edited by N.P. Kocherov, (1991).
4) E. Mordhorst et al., Phys. Rev. C **34**, 103 (1986).
5) Y. Watanabe et al., Z. Phys. A **336**, 63 (1990).
6) H. Kalka, Phys. Rev. C **40**, 1619 (1989); private communication (1991).
7) Y. Watanabe et al., Phys. Rev. C 36, 1325 (1987); Y. Watanabe, Doctor thesis, Kyushu University (1988).
8) J.J.H. Menet et al., Phys. Rev. C **4**, 1114 (1971).
9) I. Kumabe et al., Nucl. Scie. and Eng. **104**, 280 (1990).
10) C. Kalbach, Nucl. Phys. A **210**, 590 (1973).
11) C. Kalbach, Z.Phys. A **283**, 401 (1977).
12) I. Kumabe and Y. Watanabe, Phys. Rev. C **36**, 543 (1987); *ibid.* **40**, 535 (1989).
13) C. Kalbach, Phys. Rev. C **33**, 816 (1986); S.K. Gupta, Z. Phys. A **303**, 329 (1983); J. Dobes and W. Betak, Z. Phys. A **310**, 329 (1983).

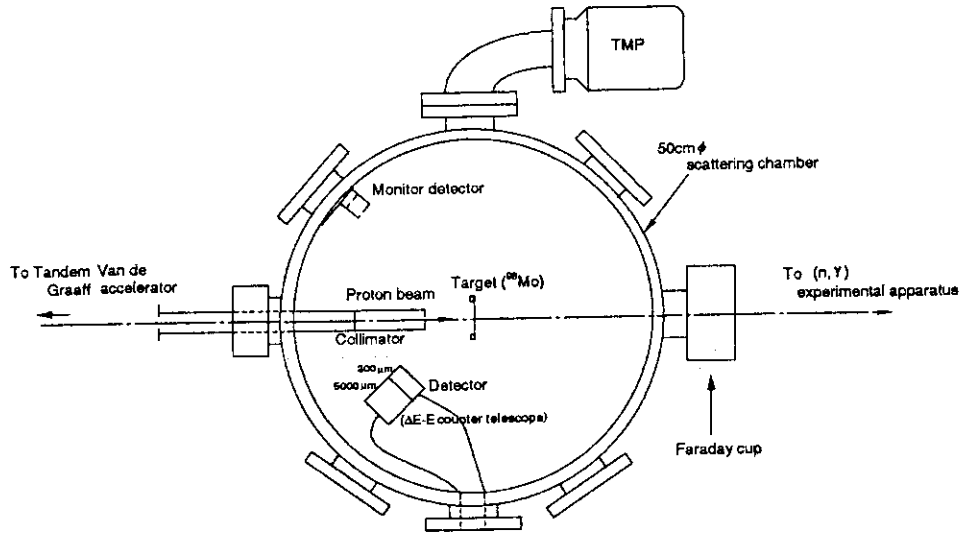

Fig. 1 Schematic diagram of the experimental apparatus including a charged particle spectrometer.

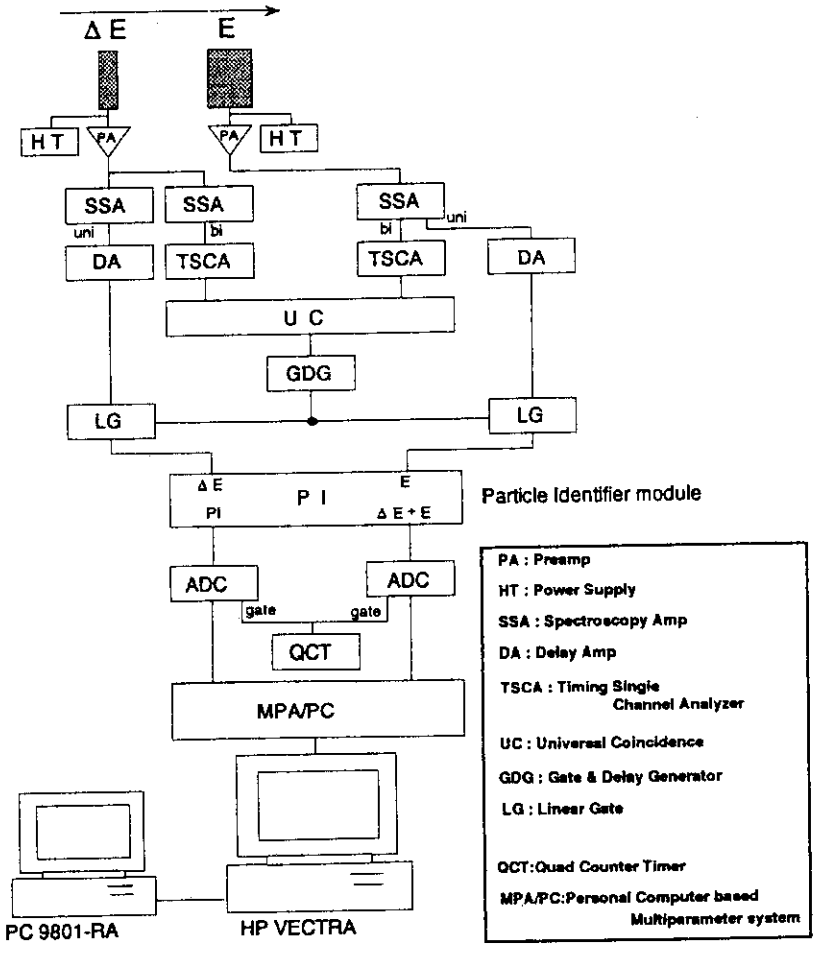

Fig. 2 Block diagram of electronics system used in the JAERI experiment (the measurement II).

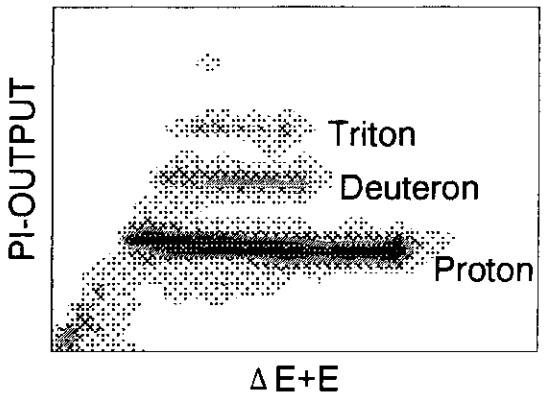

Fig. 3 A typical contour plot of output signals from a particle identifier (MPS-1230) used in the measurement II.

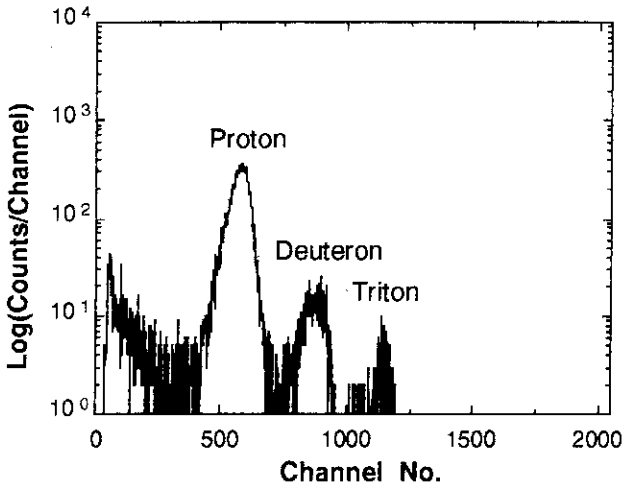

Fig. 4 A typical example of the measured mass spectrum from a particle identifier (MPS-1230) used in the measurement I.

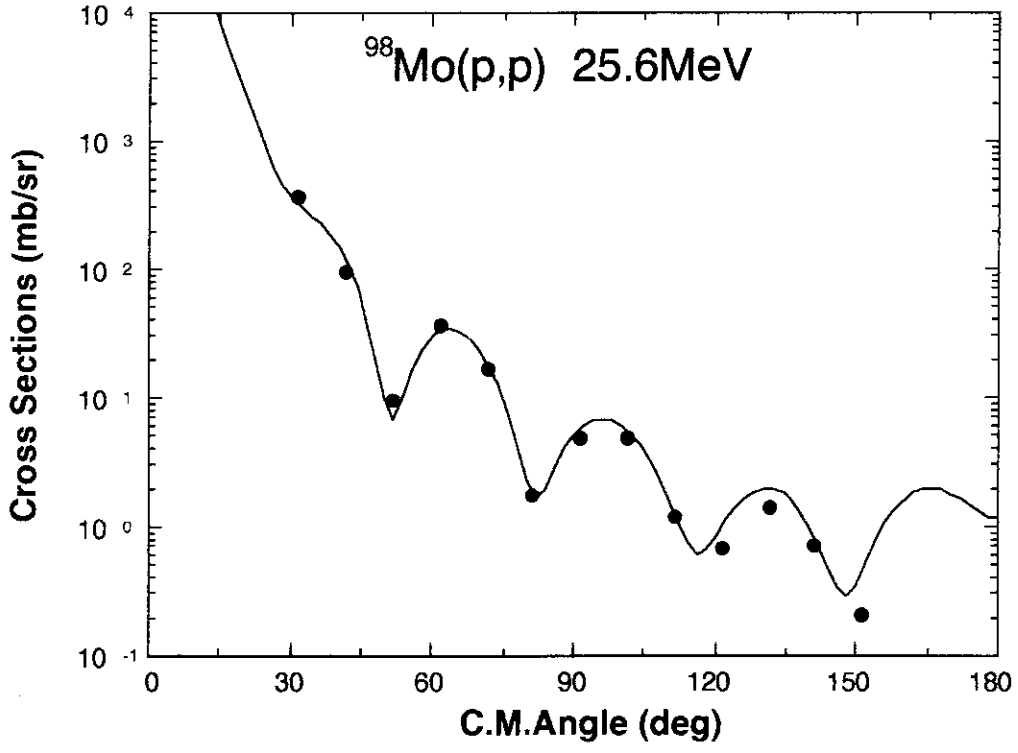

Fig. 5 Experimental differential cross sections of protons elastically scattered from ^{98}Mo at 25.6 MeV (the measurement II) and those calculated on the basis of the spherical optical model.

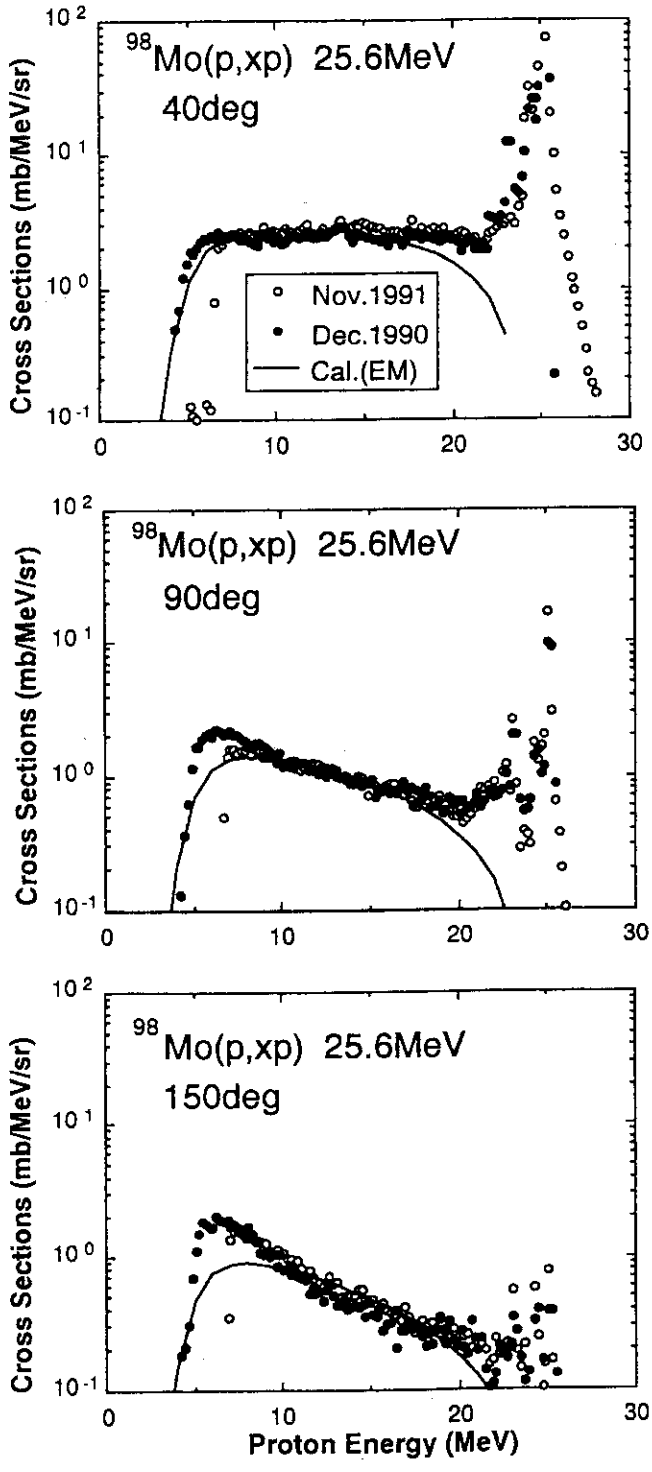

Fig. 6(a) Measured double differential proton emission cross sections for ^{98}Mo and those on the basis of the exciton model. Closed and open circles present the experimental data for the measurement I and II, respectively. The same parameters are used as those in the previous analyses for the incident proton energy of 10-20 MeV[5].

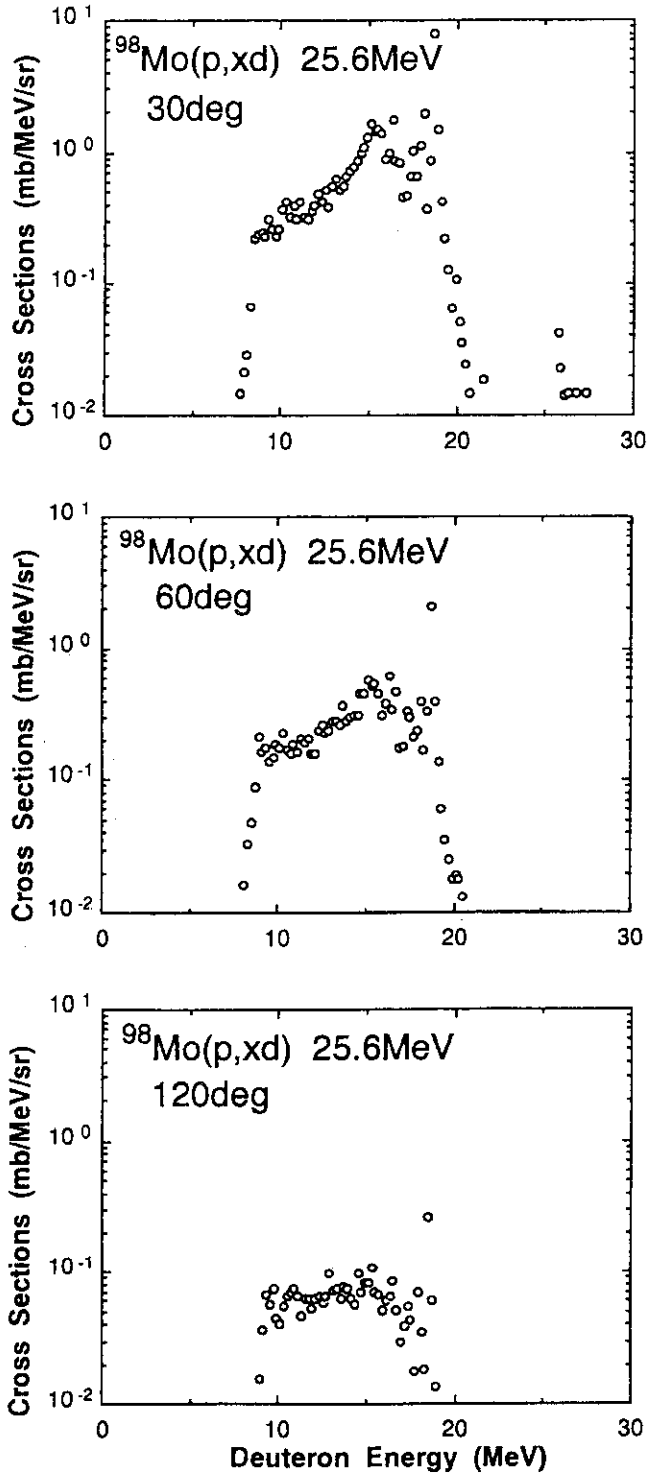

Fig. 6(b) Measured double differential deuteron emission cross sections for ^{98}Mo and those on the basis of the exciton model. Closed and open circles present the experimental data for the measurement I and II, respectively. The same parameters are used as those in the previous analyses for the incident proton energy of 10-20 MeV[5].

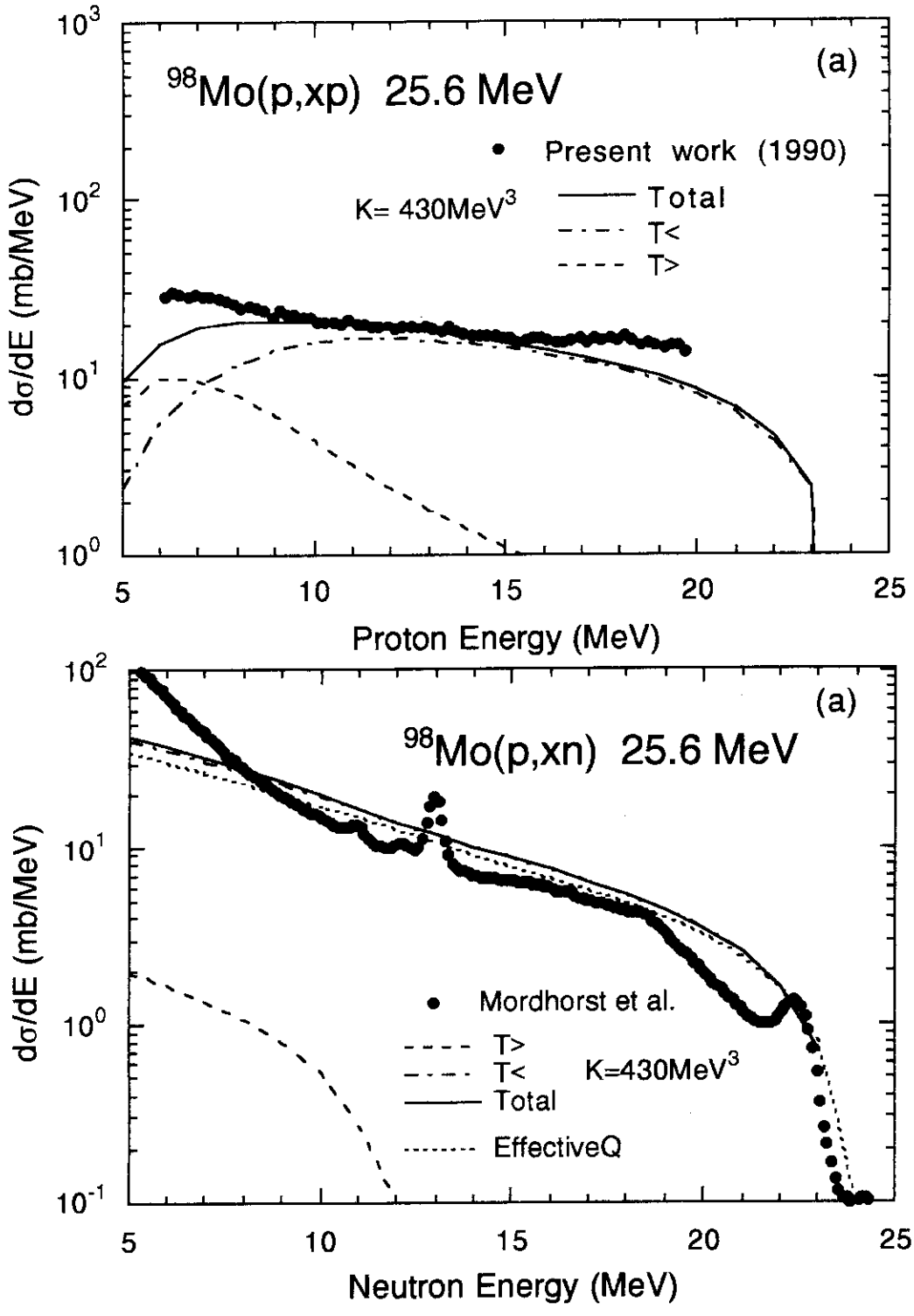

Fig. 7 Comparisons of experimental energy spectra and those calculated by the one-component exciton model for 25.6 MeV (p,xp) and (p,xn) reactions on ^{98}Mo. Dash-dotted lines and dash lines denote $T_<$ components and $T_>$ components, respectively.

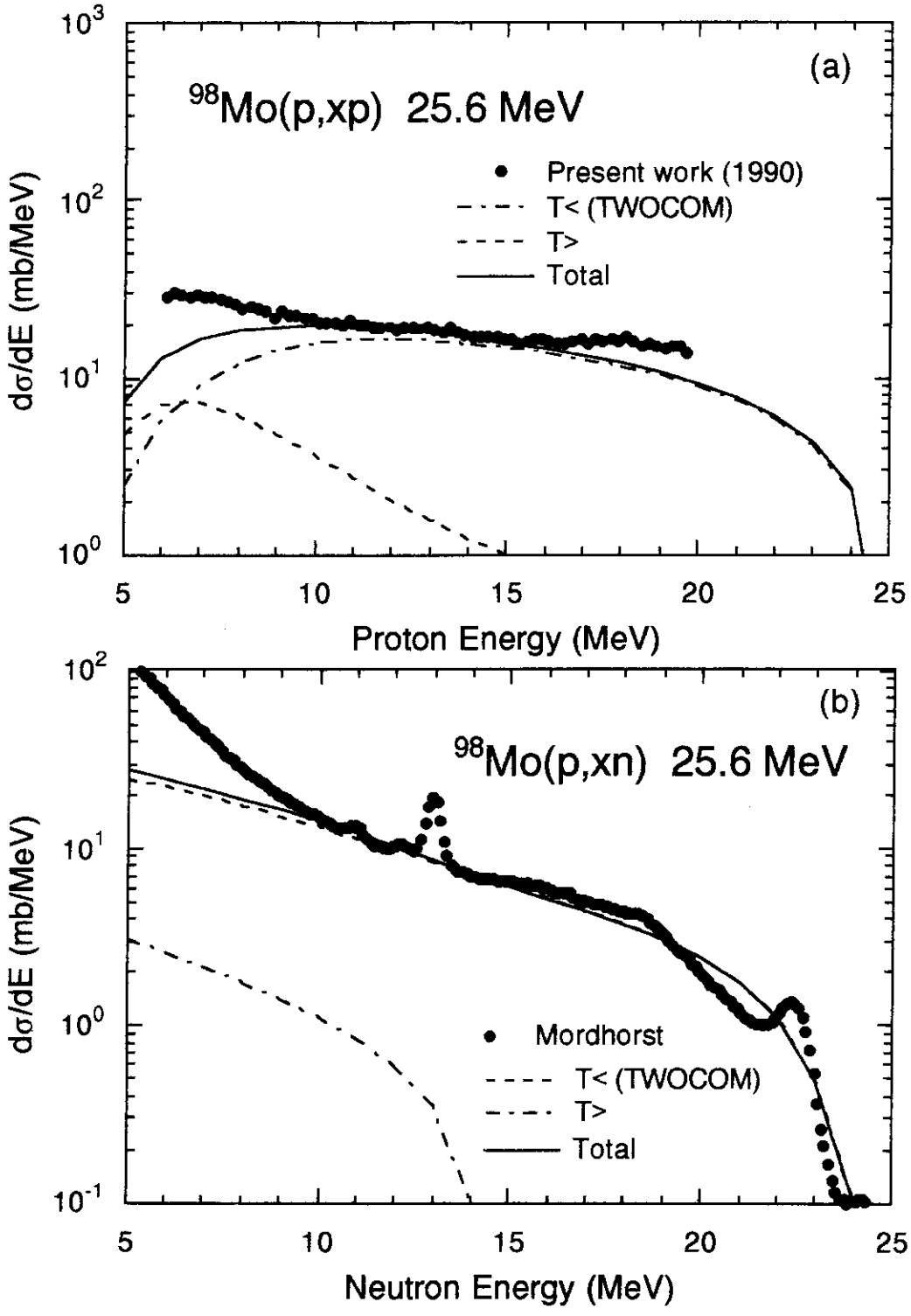

Fig. 8 Comparisons of experimental energy spectra and those calculated by the two-component exciton model for 25.6 MeV (p,xp) and (p,xn) reactions on ^{98}Mo.

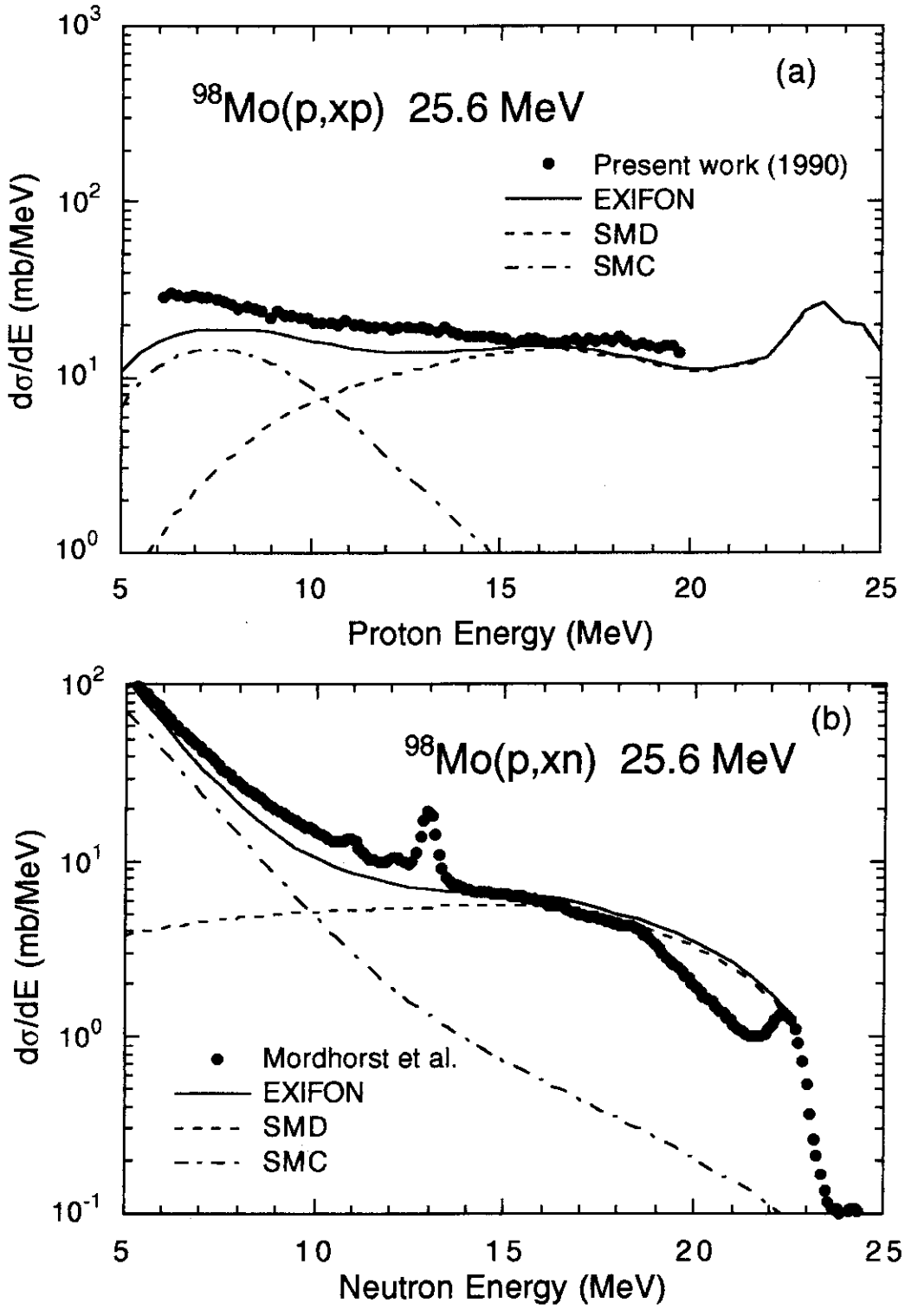

Fig. 9 Comparisons of experimental energy spectra and those calculated by the one-component exciton model for 25.6 MeV (p,xp) and (p,xn) reactions on ^{98}Mo. Dash lines and dash-dotted lines represent statistical multistep direct (SMD) component and statistical multistep compound (SMC) component, respectively.

3.17 ELASTIC AND INELASTIC PROTON SCATTERING FROM LIGHT NUCLEI

－^{6,7}Li, ^{12}C AND ^{16}O－

N. Koori, H. Hane*, Y. Watanabe*, A. Aoto*, H. Kashimoto*, H. Sakaki*,
Y. Koyama*, H. Shinohara*, H. Ijiri*,
K. Sagara+, H. Nakamura+, K. Maeda+, S. Shimizu+, and T. Nakashima+

College of General Education, The University of Tokushima, Tokushima 770, Japan
**Department of Energy Conversion Engineering, Kyushu University, Kasuga, Fukuoka 816, Japan*
+ Department of Physics, Kyushu University, Fukuoka 812, Japan

Differential cross sections and analyzing powers of elastic and discrete inelastic proton scattering have been measured for ^{6,7}Li, ^{12}C and ^{16}O in a program of polarized proton experiments around 14 MeV. These data are analyzed on the basis of the spherical optical model and the coupled channel method.

1. Introduction

We have been studying experimentally and theoretically the mechanism of proton-induced reactions on light and medium-heavy nuclei, paying special attention to the continuum in the energy spectra of emitted particles [1-4]. In our program of polarized proton experiments covering the energy range 12 to 16 MeV, several data on elastic and discrete inelastic proton scattering have also been accumulated for light nuclei. In the present work, these data are analyzed on the basis of the optical model and the coupled channel (CC) method and are compared to available neutron data. Among these results, the analyses of elastic proton scattering from ^{12}C and ^{16}O with the spherical optical model (SOM) are described mainly in this report.

2. Experimental procedures

The experiments have been carried out using a polarized proton beam from the Tandem Van de Graaff accelerator in Kyushu University. Differential cross sections and analyzing powers of elastic and discrete inelastic proton scattering from ^{6,7}Li, ^{12}C, and ^{16}O (1p-shell nuclei) have been measured at bombarding energies of 12 to 16 MeV. In these experiments, a counter telescope consisting of three silicon detectors was used to detect protons emitted from

bombarded targets. More details of the experimental procedure have been described elsewhere [1-4], except for the latest measurement for ^{16}O in which a gas target was used.

In the experiment for ^{16}O, natural oxygen gas (the purity 99.5 %) was filled at a pressure of 0.4 atm (at room temperature) in a gas cell made of stainless steel cylinder of 38 mm in diameter and of 34 mm in height. The experimental arrangement is schematically illustrated in Fig.1. The cell windows were 2.2 μm havar foils for the beam entrance and exit and 6 μm mylar for scattered particles. The effect of multiple Coulomb scattering in the gas and the cell windows was estimated and it was found to be negligible for the proton energy of interest. A counter telescope with double slit geometry was used to detect scattered protons : the first slit with opening of 2 mm was located 23.8 mm from the center of the gas cell and the second one was located just in front of ΔE detector and the distance from the first one was 176.4 mm.

3. Experimental results and analyses

3.1 $^{6,7}Li(\vec{p},p)$ and $(\vec{p},p')$ scattering around 14 MeV

We have already reported measurement and analysis of the polarized proton scattering on the $^{6,7}Li$ around 14 MeV [1,2]. The data were analyzed on the basis of the SOM and CC method. Both differential cross sections and analyzing powers of the elastic scattering were fitted very well, but good fits were not obtained for the inelastic scattering, especially for the analyzing powers. This situation is appreciably improved by a parameter search in which the optical potential parameters for the exit channel is also treated as adjustable ones: the derived parameters are largely different from those for the ground state, especially for the spin-orbit term. This may be related to the fact that the excited states of ^{6}Li (2.185 MeV, 3^+) and ^{7}Li (4.63 MeV, $7/2^+$) are unbound and decay into d+α and t+α, respectively.

3.2 $^{12}C(\vec{p},p)$ and $(\vec{p},p')$ scattering at 14 and 16 MeV

Figures 2 and 3 show experimental differential cross sections and analyzing powers of proton elastic and inelastic scattering from ^{12}C at 14 and 16 MeV [4]. The differential cross sections for 14 MeV (full circles) are compared with neutron data [5] (open circle). Both proton and neutron data show fairly good agreement in shape as well as in magnitude, except around the first minimum ($\theta = 80°$) for elastic scattering and at forward angles for the 2^+ transition.

The differential cross sections and analyzing powers of proton elastic scattering from ^{12}C at 14 and 16 MeV are compared with the prediction based on the spherical optical model (SOM) in Fig.4. Solid and dashed curves indicate the results calculated with the potential parameters derived from p + ^{12}C scattering analysis by Nodvik et al.[6] and those derived from

n + ^{12}C scattering analysis by Woye et al.[7], respectively. In the latter case, the fixed Coulomb corrections $\Delta V=0.4Z/A^{1/3}$ was taken into account. Each value of parameters used is given in Table I. The former shows much better agreement with the experimental differential cross sections for both 14 and 16 MeV, but does not reproduce the experimental analyzing powers well. On the other hand, the latter can reproduce the analyzing powers better, especially at medium angles, but can not provide so good agreement with the differential cross sections as the former.

Since the above two sets of parameters were not found to be adequate for consistent description for differential cross sections and analyzing powers, SOM fits were made to our data for ^{12}C in order to obtain improved parameter sets. The results are shown in Fig.5 and Table I. The code ECIS79 [8] was used for the parameter search. From Table I, it is found that the depth of imaginary part becomes much larger than the results by Woye et al.[7] and the diffuseness of spin-orbit term becomes smaller than those. The present results are preliminary and further discussions and comparisons with other results will be necessary. In addition, the effect of resonance structure and coupling of the excited states (2^+_1, 0^+_2, 3^-_1, etc.) should be investigated because such effect is known to be important for ^{12}C [9].

3.3 ^{16}O($\vec{p}$,p) and ($\vec{p}$,p') scattering at 14 and 16 MeV

Figures 6,7 and 8 shows experimental differential cross sections and analyzing powers of proton elastic and inelastic scattering from ^{16}O at 14 and 16 MeV. In Fig.6, the results of SOM fits are also shown by solid curves. The derived parameters are given in Table II. The experimental results for ^{16}O show more remarkable variations with incident energy than those for ^{12}C, especially for the analyzing powers. This may be due to strong resonance in the compound nucleus ^{17}F; it has been reported that there are a broad $f_{7/2}$ single particle level in ^{17}F around 17.5 MeV [10] and appreciably sharp resonance at 14.7 MeV in the elastic scattering excitation functions [11]. As seen in Fig.6, agreement of the SOM prediction and experimental data is not so good with respect to the analyzing powers. Further analyses will be necessary in order to investigate the effect in details.

References

[1] N. Koori et al., JAERI-M 89-167 (1989).

[2] N. Koori et al., JAERI-M 91-009 (1991).

[3] Y. Watanabe et al., to be published in *Proc. Int. Conf. on Nuclear Data for Science and Technology, May 13-17, 1991, Julich, Germany*

[4] Y. Watanabe et al., *Proceedings of the XX th Int. Symp. on Nuclear Physics, Nuclear Reaction Mechanism, Germany, Nov. 12-16, 1990, pp.151*

[5] S. Matsuyama et al., Fast Neutron Laboratory Progress Report NETU-52, Tohoku University (1990), p.5

[6] J.S. Nodvik et al., Phys. Rev. **125**, 975 (1962)

[7] E.Woye et al., Nucl. Phys. **A394**, 139 (1983)

[8] J. Raynal, code ECIS79, unpublished: J. Raynal, *Workshop on Applied Nuclear Theory and Nuclear Model calculations for Nuclear Technology Applications*, Trieste, Italy (1988), Ed. M.K. Mehta and J.J. Schmidt (World Scientific 1989), p.506

[9] W.W. Daehnick and R. Sherr, Phys. Rev. **133**, B934 (1964); R.M. Craig et al., Nucl. Phys. **79**, 177 (1966).

[10] H.R. Hiddleston, J.A. Aymar and S.E. Darden, Nucl. Phys. **A242**, 323 (1975)

[11] S. Kobayashi, J. Phys. Soc. Japan **15**, 1164 (1960)

Table I Optical potential parameters for ^{12}C at 14 and 16 MeV

Spherical optical model (ECIS79)

	V_0 (MeV)	R_0 (fm)	a_0 (fm)	W_s (MeV)	r_i (fm)	a_i (fm)	V_{so} (MeV)	r_{so} (fm)	a_{so} (fm)
14MeV	64.668	1.000	0.679	26.143	1.476	0.101	6.510	0.962	0.040
16MeV	62.422	1.023	0.667	22.210	1.479	0.095	6.177	0.969	0.059

Spherical optical model parameters by Nodvik et al.[6]

	V_0 (MeV)	R_0 (fm)	a_0 (fm)	W_s (MeV)	r_i (fm)	a_i (fm)	V_{so} (MeV)	r_{so} (fm)	a_{so} (fm)
14MeV	51.8	1.25	0.41	18.4	1.25	0.25	5.7	1.25	0.41
16MeV	52.47	1.25	0.41	17.76	1.25	0.25	5.4	1.25	0.41

*Gaussian surface absorption form factor is used for this analysis.

Spherical optical model parameters by Woye et al.[7]

	V_0 (MeV)	R_0 (fm)	a_0 (fm)	W_s (MeV)	r_i (fm)	a_i (fm)	V_{so} (MeV)	r_{so} (fm)	a_{so} (fm)
14MeV	55.52	1.06	0.54	6.66	1.54	0.28	7.88	0.76	0.36
16MeV	54.92	1.06	0.54	6.34	1.54	0.28	7.12	0.76	0.36

Table II Optical potential parameters for ^{16}O at 14 and 16 MeV

Spherical optical model (ECIS79)

	V_0 (MeV)	R_0 (fm)	a_0 (fm)	W_s (MeV)	r_i (fm)	a_i (fm)	V_{so} (MeV)	r_{so} (fm)	a_{so} (fm)
14MeV	51.067	1.244	0.528	11.673	1.354	0.120	5.406	1.052	0.493
16MeV	53.034	1.216	0.680	19.203	1.455	0.127	3.430	1.289	0.032

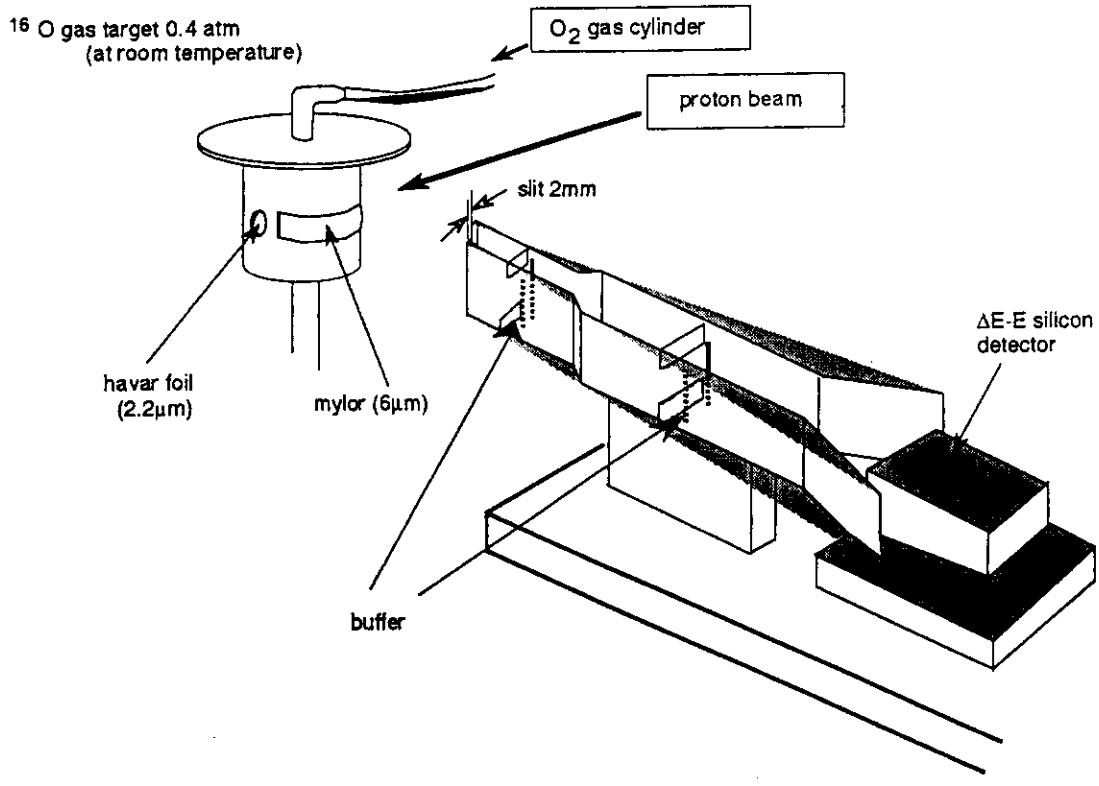

Fig. 1 Schematic view of an apparatus for the proton experiment using O_2 gas target.

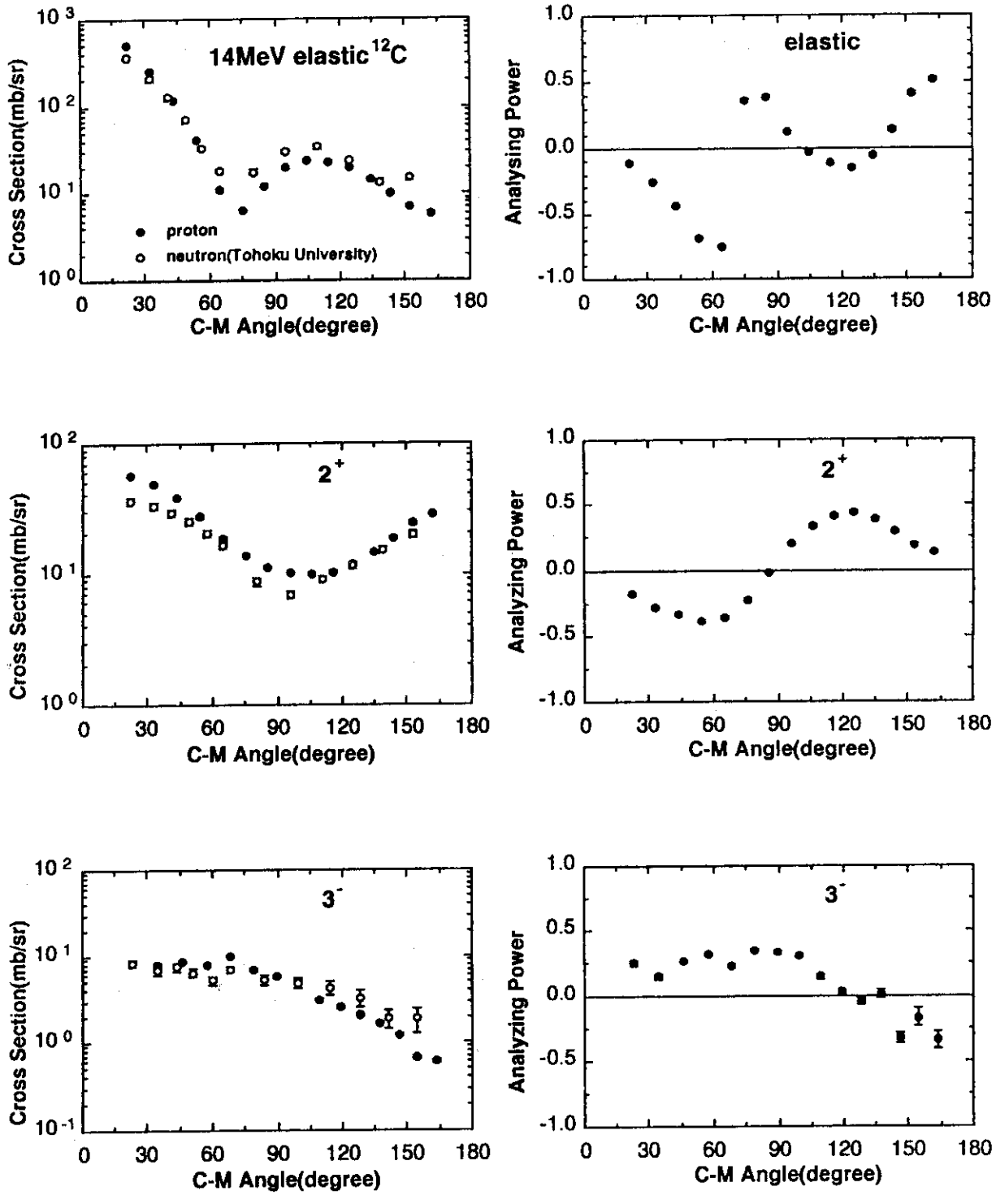

Fig. 2 Experimental differential cross sections and analyzing powers of proton elastic and inelastic scattering from ^{12}C at 14 MeV. Open circles are experimental data for neutron elastic scattering taken from Ref. 5.

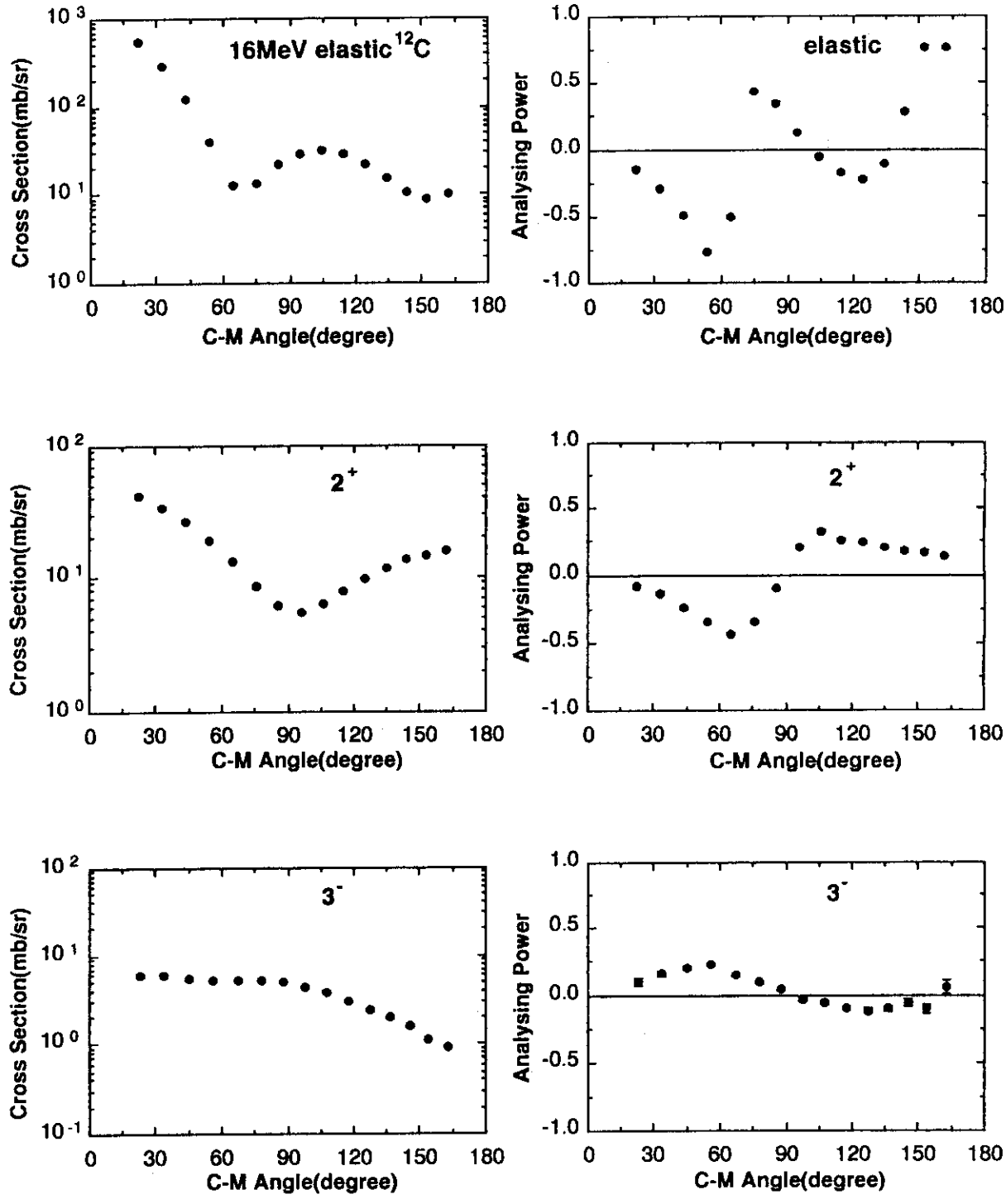

Fig. 3 Experimental differential cross sections and analyzing powers of proton elastic and inelastic scattering from ^{12}C at 16 MeV.

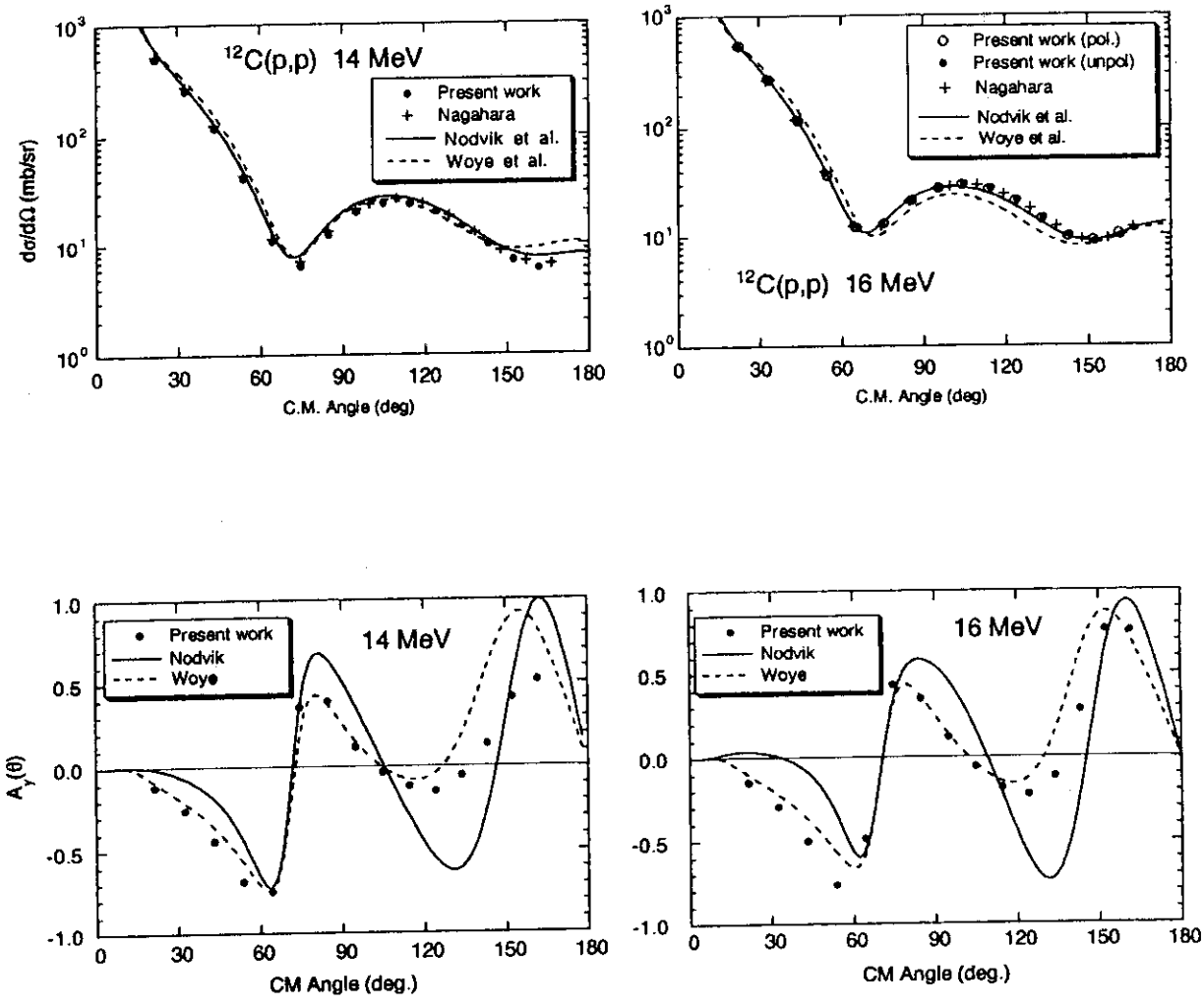

Fig. 4 Differential cross sections and analyzing powers of ^{12}C(p,p) scattering at 14 and 16 MeV. Solid and dashed lines are for calculations with the optical potential parameters by Nodvik et al.[5] and Woye et al.[6], respectively.

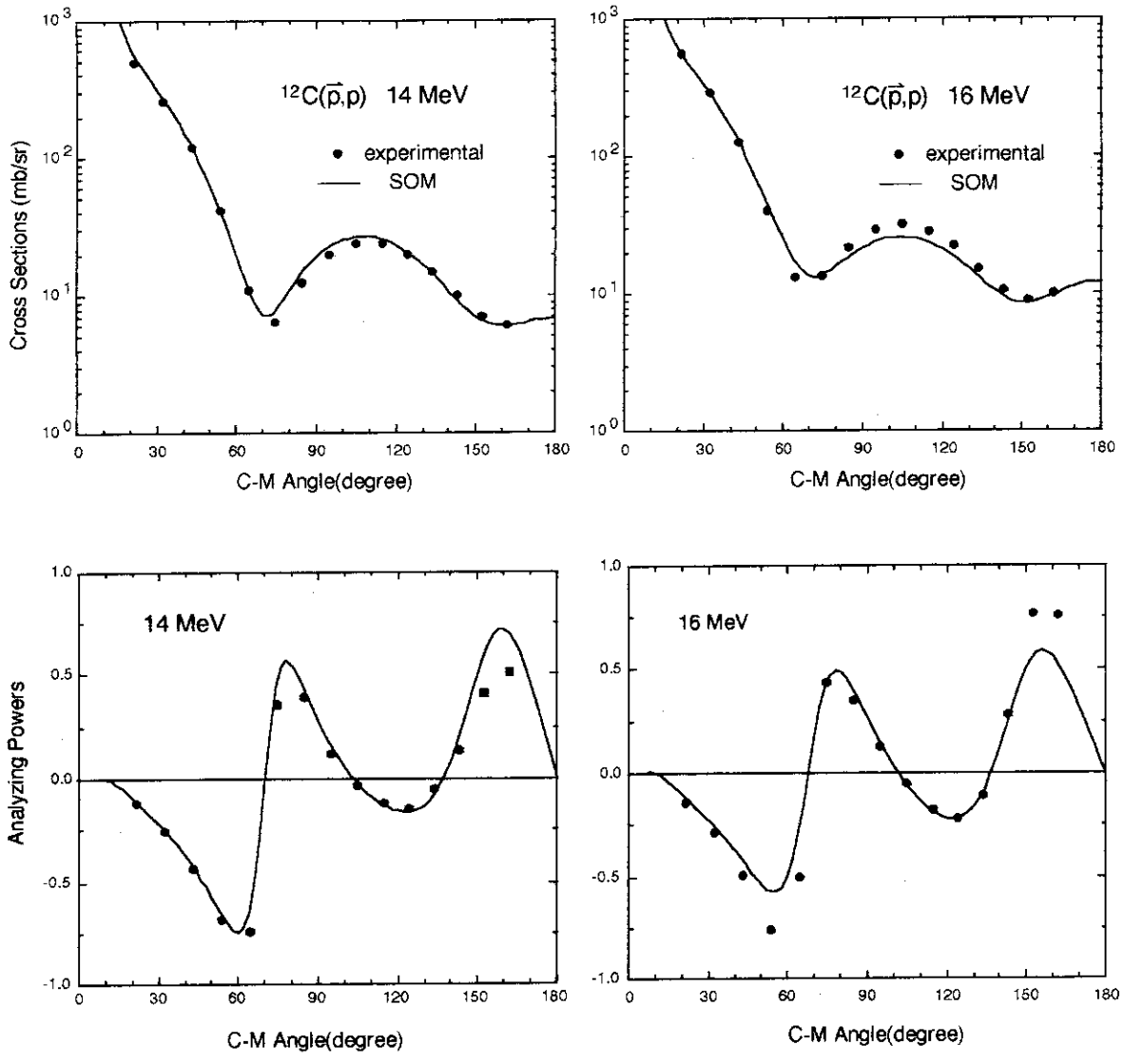

Fig. 5 Comparison of experimental differential cross sections and analyzing powers of $^{12}C(p,p)$ scattering at 14 and 16 MeV and the SOM fits.

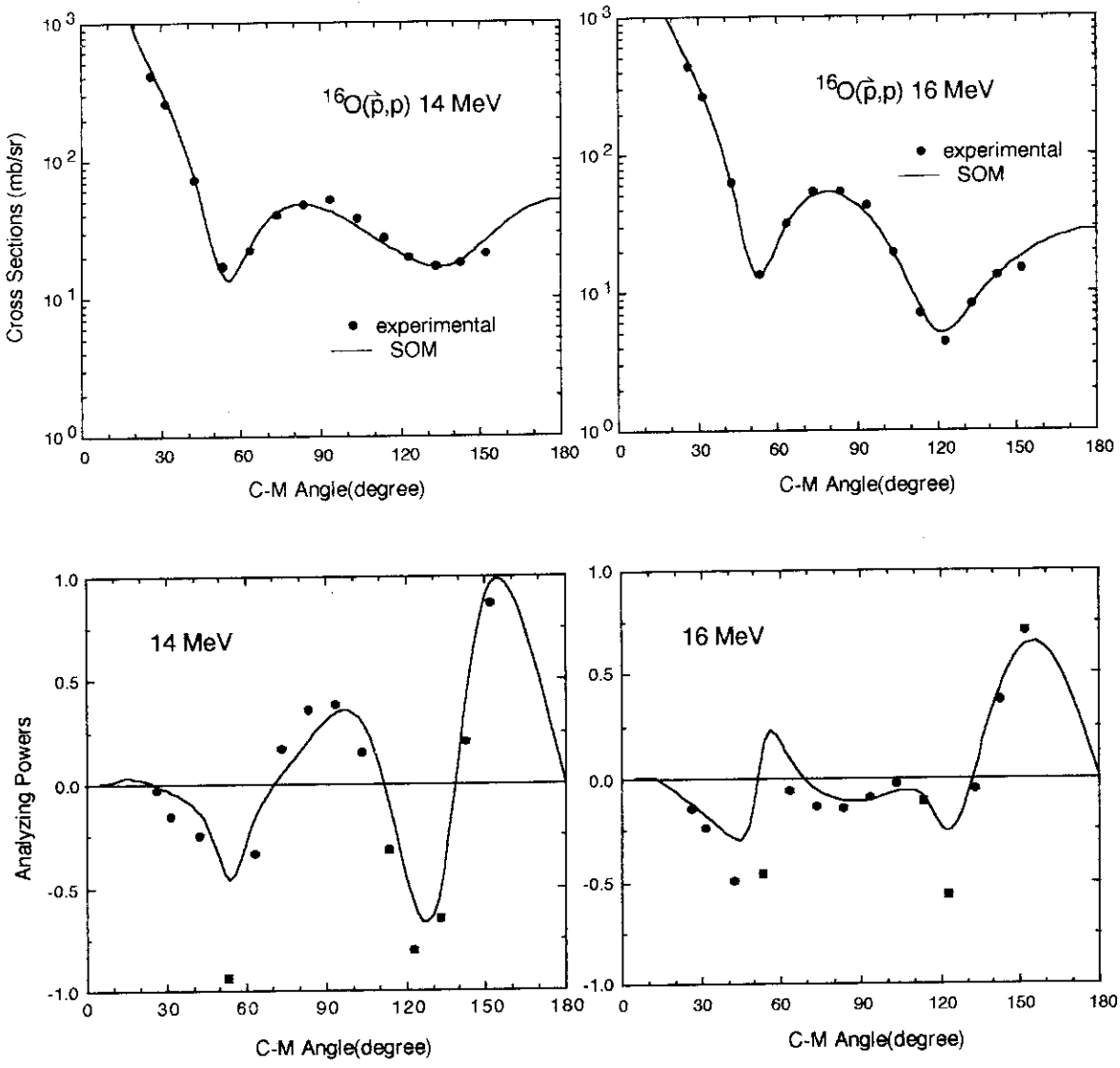

Fig. 6 Comparison of experimental differential cross sections and analyzing powers of ^{16}O(p,p) scattering at 14 and 16 MeV and the SOM fits.

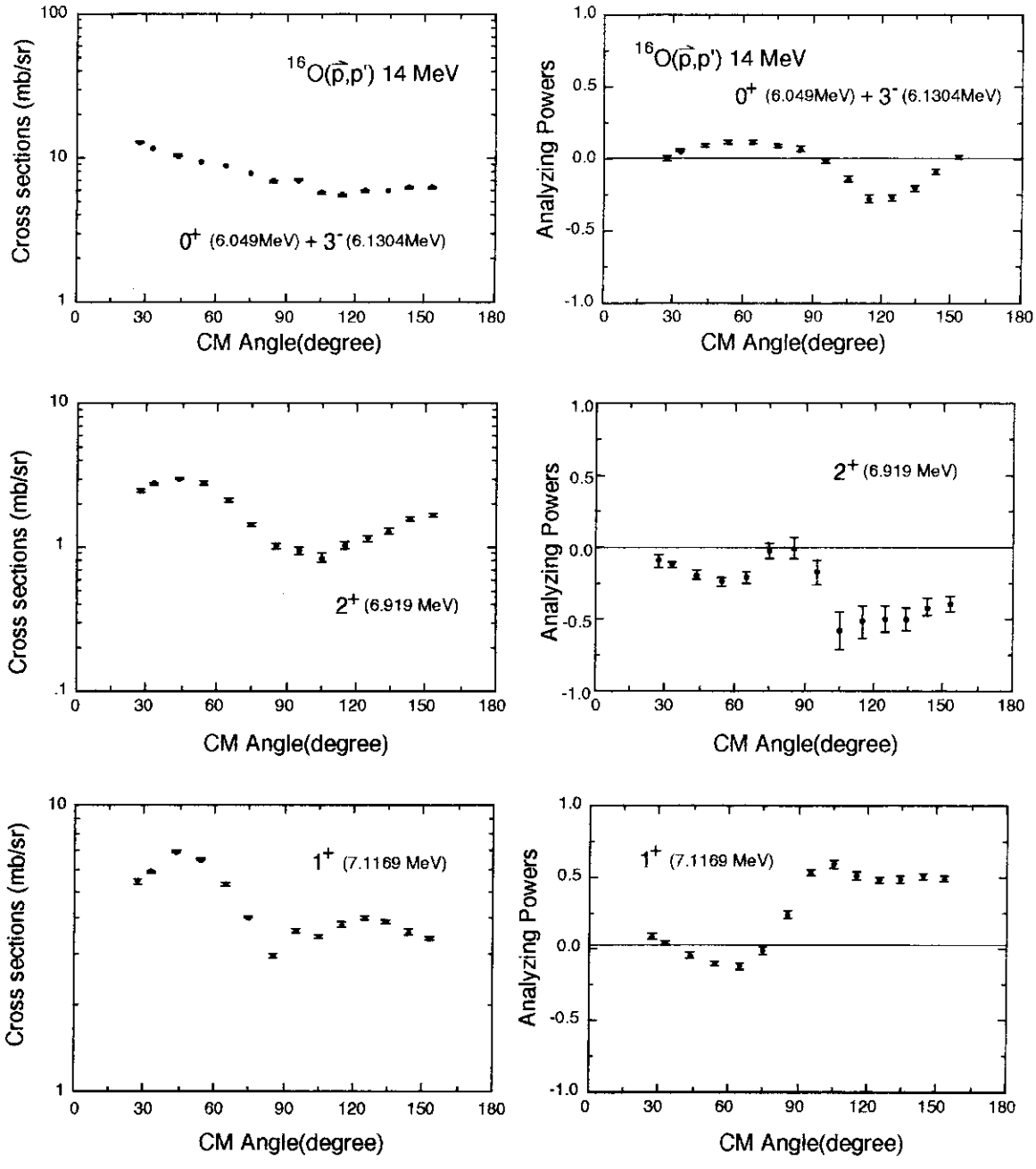

Fig. 7 Experimental differential cross sections and analyzing powers of proton inelastic scattering from ^{16}O at 14 MeV.

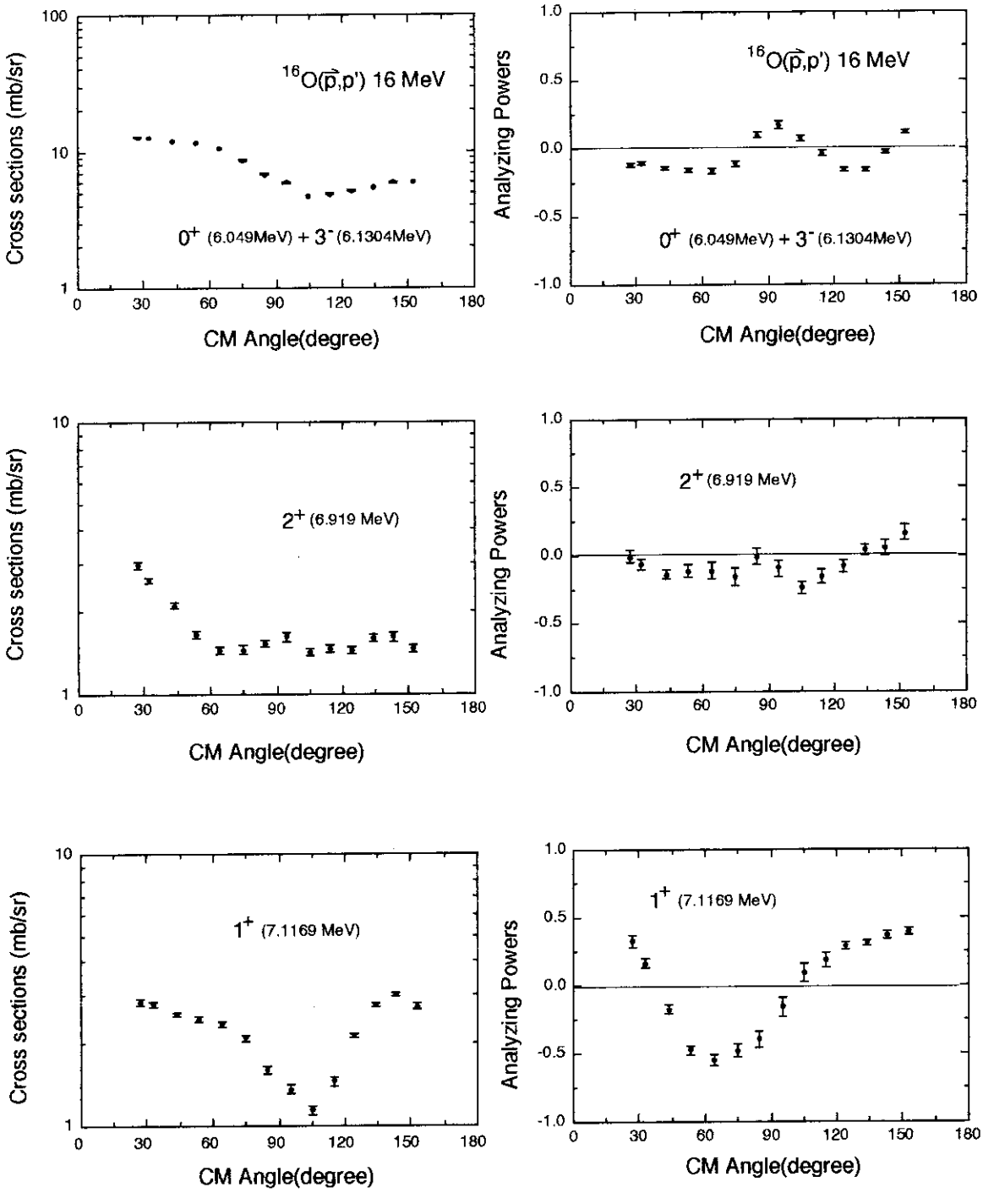

Fig. 8 Experimental differential cross sections and analyzing powers of proton inelastic scattering from ^{16}O at 16 MeV.

3.18 NEUTRON ACTIVATION CROSS SECTION MEASUREMENT FROM ^{7}Li(p,n) IN THE PROTON ENERGY REGION OF 20MeV TO 40MeV

Titik S. Soewarsono, Y. Uwamino* and T. Nakamura
Cyclotron and Radioisotope Center, Tohoku University
Aramaki Aoba, Aoba-ku, Sendai 980, Japan
*Institute for Nuclear Study, University of Tokyo
3-2-1 Midoricho, Tanashi-shi, Tokyo 188, Japan

We have measured the neutron activation cross sections for fifteen samples in the energy region from 15 MeV to 40 MeV by using the five monoenergetic neutrons produced from the ^{7}Li(p.n) reaction. Two types of target were used; one is 2 mm-thick ^{7}Li target backed by 12 mm-thick graphite and the other is only 12 mm-thick graphite target. The true neutron spectrum was obtained from the difference of two spectra produced from these two targets measured with the TOF method and the activation rate was also got from the difference of the repeated irradiations with two targets. The absolute value of the neutron spectrum was accurately estimated to measure the ^{7}Be yield produced by the ^{7}Li(p,n) reaction. As the first analysis, we could estimate the ^{197}Au(n,4n) reaction cross section.

1. Introduction

Activation cross sections for high energy neutrons, especially above 20 MeV, are very scarce and no evaluated data file presently exists. We measured the neutron activation cross sections in the energy region of 15 MeV to 40 MeV for various elements by using semi-monoenergetic neutrons produced from the ^{9}Be(p,n) reaction, coupled with the unfolding technique.[1)]

In order to avoid an inevitable ambiguity coming from the unfolding method, we further tried to use ^{7}Li as a target with its advantage [2)]. The neutrons produced from the ^{7}Li(p,n) reaction give much better monoenergetic neutron spectrum, which will need no unfolding.

A 99.98 % enriched ^{7}Li whose thickness was 2 mm and diameter 22 mm was mounted on the target holder and used as a target for obtaining neutrons by bombarding with protons of energies of 20, 25, 30, 35 and 40 MeV,

respectively. A 12 mm thick graphite was placed at the back of the target to stop protons completely.

Two types of experiments, one used the ^{7}Li target backed by the graphite and the other only the graphite target, were repeated both for the neutron spectral measurements and the sample irradiations. The difference between these two experimental results gave the monoenergetic neutron spectrum from $^{7}Li(p,n)$ and the reaction rate for determining the activation cross section.

2. Experimental

a. Neutron flux

The monoenergetic neutron spectrum from the $^{7}Li(p,n)$ reaction was measured at the TOF facility of the Cyclotron and Radioisotope Center (CYRIC), Tohoku University. A 127 mm diam. by 127 mm long NE-213 scintillation detector was placed at the distance of about 10 m away from the ^{7}Li target. For proton energies of 20, 25, 30, 35 and 40 MeV, two types of irradiations were arranged; one used the ^{7}Li target backed by 12 mm graphite, and the other just the graphite target. The 'true' neutron spectrum $\Phi(E)$ is then given by

$$\Phi(E) = \Phi_a(E) - \Phi_b(E) , \qquad (1)$$

where $\Phi_a(E)$ is the spectrum for ^{7}Li plus graphite target,

$\Phi_b(E)$ is the spectrum for graphite target.

The peak neutrons produced by the $^{7}Li(p,n)^{7}Be$ reactions correspond to the ground state and the first excited state (0.43 MeV) of ^{7}Be. The 2nd (4.57 MeV) and the higher excited states of ^{7}Be decay with the proton and alpha emission, and do not remain as ^{7}Be. From this reason, the absolute value of the neutron spectrum of the peak energy at 0 deg, $\Phi(E_p)$ can be obtained with good accuracy from the ^{7}Be yield produced by $^{7}Li(p,n)$ at 0 deg. By definition, $\Phi(Ep)$ is determined as,

$$\Phi_{(E_p)} = N(^{7}Li).\, Ip.\, (\frac{d\sigma}{d\Omega})\theta=0 , \qquad (2)$$

where $N(^{7}Li)$: number of ^{7}Li in the target,

Ip : number of injected protons,

$(\frac{d\sigma}{d\Omega})\theta=0$: $^{7}Li(p,n)^{7}Be$ cross section in the peak neutron energy region at 0 deg.

The number of ^{7}Be produced from $^{7}Li(p,n)$, $N(^{7}Be)$ is given by,

$$N(^{7}Be) = N(^{7}Li)\ \ Ip\ \ \sigma\ . \qquad (3)$$

The quantity σ is the total cross section of $^{7}Li(p,n)^{7}Be$, i.e.,

$$\sigma = \int_{4\pi} \frac{d\sigma}{d\Omega}\ .\ d\Omega,$$

where $\frac{d\sigma}{d\Omega}$ is the angular distribution of the peak neutrons or the double differential cross section in relative value.

By combining Eqs. (2) and (3), the peak neutron yield at 0 deg, $\Phi(E_p)$ can be obtained as follows,

$$\Phi\ (E_p) = \frac{N(^{7}Be)\ .\ (\frac{d\sigma}{d\Omega})\theta=0}{\int_{4\pi} \frac{d\sigma}{d\Omega}\ .\ d\Omega}\ . \qquad (4)$$

The relative angular distribution of peak neutrons was measured by rotating the angle of the incident beam from 0 to 125 deg at 20, 30 and 40 MeV proton energies with the beam swinger. The value of $N(^{7}Be)$ can easily be measured by gamma-ray spectrometry. Low energy neutrons are also produced by the $^{7}Li(p,n)$ reaction. Then, the absolute value of the full energy spectrum, $\Phi(E)$, can be obtained from the relative value of the full neutron energy spectrum at 0 deg., $\Phi_r(E)$, which were also measured at CYRIC, as follows ,

$$\Phi(E) = \Phi_r(E)\ .\ \frac{\Phi(E_p)}{\int_{peak} \Phi_r(E).\ dE}\ . \qquad (5)$$

b. Activation rate

The enriched samples of ^{24}Mg(99.93%), ^{25}Mg(98.81%), ^{28}Si(99.58%), ^{29}Si(95.65%), ^{54}Fe(97.20%), ^{56}Fe(99.87%), ^{63}Cu(99.89%), ^{65}Cu(99.69%), ^{64}Zn(99.50%) and ^{66}Zn(98.41%), and natural samples of ^{12}C, ^{27}Al, ^{23}Na, ^{55}Mn and ^{197}Au were irradiated by the monoenergetic p-Li neutron beam, settled at the SF Cyclotron of Institute for Nuclear Study (INS), the University of Tokyo. The target system and sample irradiation arrangement at INS is shown in Fig.1. Samples were placed at 10 cm away from the ^{7}Li target. Similarly as the neutron spectrum experiment, two types of sample irradiation measurements, one using the ^{7}Li target backed by the 12 mm graphite, and the other just the graphite target were also employed, by changing the position of ^{7}Li target, as could be seen in Fig. 1. The 'true' activation rate, A is obtained by substracting the latter activation rate, A_b, from the former one, A_a.

The gamma-ray activities of the irradiated samples were counted by using a high purity Ge detector. The peak counts of identified gamma rays were analyzed by the KEI-11EF analysis code[3] and the activation rates were obtained by using the detector peak efficiency measured with several gamma-ray standard sources and corrected by the sum-coincidence effect.

c. Cross section

By using the neutron energy spectrum $\Phi(E)$ given by Eq. (5) and the activation rate, A, the activation cross section $\sigma(E)$ can be estimated in the following way. A is given by

$$A = N \int_{E_{th}}^{E_2} \sigma(E)\, \Phi(E)\, dE \quad , \tag{6}$$

where N : number of target atoms relevant to nuclear reaction,

E_{th} : threshold energy,

E_2 : maximum energy of neutron energy spectrum.

The activation rate, A is divided into two parts; one is induced by the peak energy neutrons and the other by the low energy neutrons, as

$$A = N \int_{E_{th}}^{E_1} \sigma(E)\, \Phi(E)\, dE + N\, \sigma(E_p)\, \Phi(E_p), \qquad (7)$$

where E_1 : lowest energy of the peak neutron energy region,
$\sigma(E_p)$: cross section at peak neutron energy.
We then get $\sigma(E_p)$ as

$$\sigma(E_p) = \frac{A - N \int_{E_{th}}^{E_1} \sigma(E)\, \Phi(E)\, dE}{N\ \Phi(E_p)}, \qquad (8)$$

Since $\Phi(E_p)$ can be obtained from Eq. (4), we have to determine the second integration term in the numerator. If the threshold energy E_{th} is higher than E_1, this term must be zero, then we can easily get

$$\sigma(E_p) = \frac{A}{N\, \Phi(E_p)} \qquad \text{for } E_{th} \geq E_1 .$$

Otherwise, this term can be estimated by successive substraction method using the neutron flux $\Phi(E)$ having lower peak energy. In this method, the $\sigma(E)$ values of energy lower than 15 to 20 MeV were cited from the evaluated data files, ENDF/B-V[4], McLane et al.[5] and so on. Thus we can finally get the point-wise cross section values of $\sigma(E)$ for five neutron energies of 17.2, 22.4, 27.6, 32.7 and 37.7 MeV corresponding to proton energies of 20, 25, 30, 35 and 40 MeV, respectively, without unfolding.

3. Results and discussions

The measured neutron energy spectra at 0 deg of proton energies of 20, 25, 30, 35 and 40 MeV, $\Phi(E)$, are shown in Fig.2 a, b, c, d and e, respectively. Both measurements of the ^{7}Li target backed by graphite and the only graphite target are depicted for each proton energy. Each spectrum shows two peaks of the ^{7}Li(p,n)^{7}Be reaction. The higher peak has a full width of 2 MeV at half maximum and belongs to the ground state and the first excited state (0.43 MeV) of ^{7}Be. The first excited state of 0.43 MeV is less than the energy loss

of proton in the target, 1.2 MeV for 40 MeV proton. The second peak corresponds to the second excited state (4.57 MeV) of ^{7}Be. Due to the Q value of -18.14 MeV of ^{12}C(p,n), the spectrum without the ^{7}Li target has a plateau peak in the low neutron energy region for proton energy higher than 25 MeV. A small amount of neutrons of energy higher than the Q value come from the ^{13}C(p,n) reaction and the room-scattered neutron components.

Fig. 3 shows the measured angular distributions of the peak neutron, $\frac{d\sigma}{d\Omega}$, normalized to unity at 0 deg, compared to other experimental data given by Schery et al.[2] and by Orihara et al.[6] The forwardness of the angular distribution becomes stronger with increasing the proton beam energy.

The differential ^{7}Li(p,n) cross section in the peak energy region were obtained by integrating these angular distribution data and is shown in Fig. 4. Our data for proton energies of 20, 30 and 40 MeV and Schery's data for proton energies of 24.8 and 35 MeV well fit to one smoothly-decreasing curve.

As an example, we first estimated the activation cross section of ^{197}Au(n,4n)^{194}Au according to Eq. (8). The three data estimated for neutron energy of 27.6, 32.7 and 37.7 MeV are shown in Fig. 5. In Fig. 5, our present data are compared with our previous data[1] obtained from ^{9}Be(p,n) neutrons with three unfolding techniques of SANDII, NEUPAC and LSF[7], and also the data for 24.48, 26.06 and 28.08 MeV neutrons by Bayhurst, et al. [8] Our present results give very good agreement with these experimental results. The result calculated by Greenwood [9] is almost two times higher than these experimental data. We are now proceeding to analyze the activation cross sections for other irradiated samples.

References

1. Y. Uwamino, H. Sugita, Y. Kondo and T. Nakamura, Nucl. Sci. Eng., in press
2. S.D. Schery, et al., Nucl. Instr. and Meth. 147 (1977) 399
3. K. Komura, University of Tokyo, Institute for Nuclear Study Report INS-TCH-7 (1972), (in Japanese)
4. Evaluated Nuclear Data File, B-format, version V National Cross Section Center, BNL (1971)
5. V. McLane, C.L. Dunford and P.F. Rose, Neutron Cross Section Vol.2 Neutron Cross Section Curves, Academic Press, INC. (1988), BNL-NCS-17541
6. H. Orihara, et al., Nucl. Instr. and Meth. A257 (1987) 189

7. H. Sugita, Master thesis, CYRIC, Tohoku University, Sendai (1990)
8. Bayhurst, et al., PR/C 12 (1975) 451
9. L.R. Greenwood, Extrapolated Neutron Activation Cross Section for Dosimetry to 44 MeV, ANL/FPP/TM-115, Argonne National Lab. (1978)

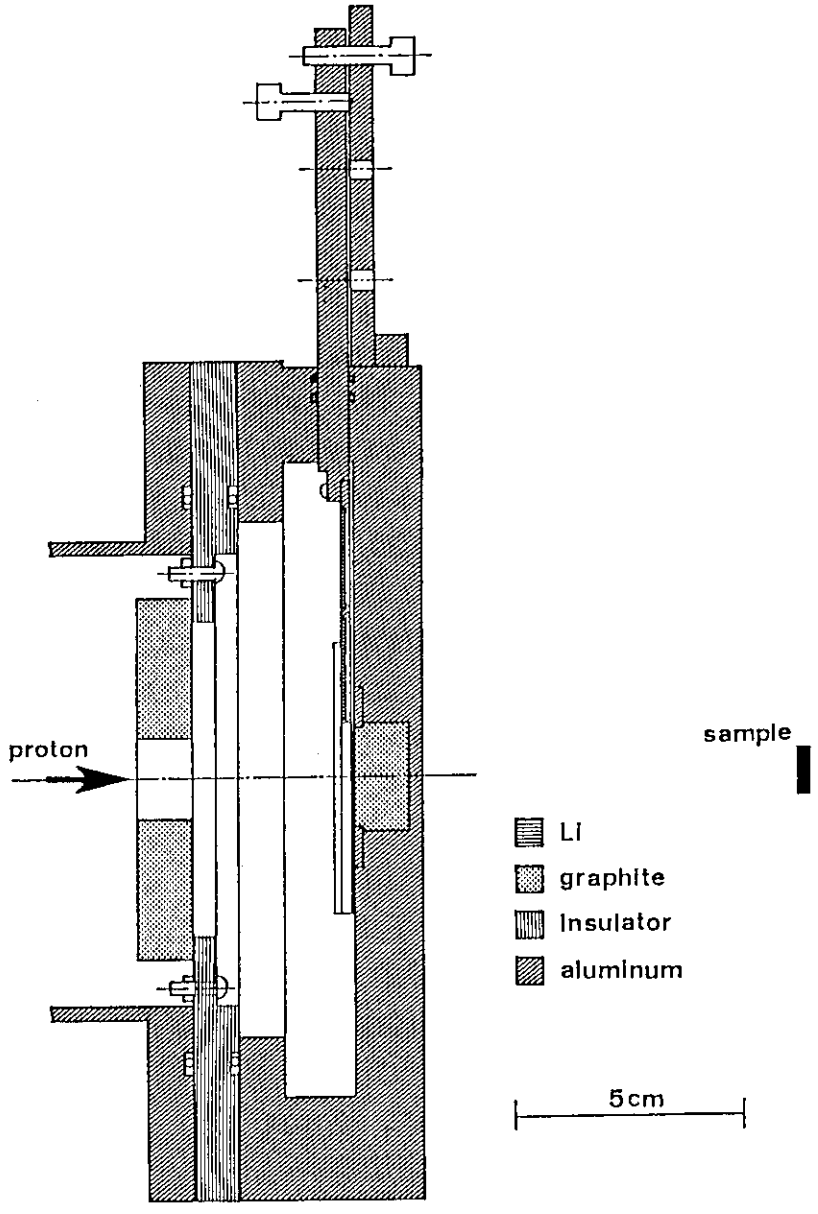

Fig. 1 Target system and sample irradiation arrangement at Institute for Nuclear Study, The University of Tokyo. The ^{7}Li target position can be changed according to the need of bombardment.

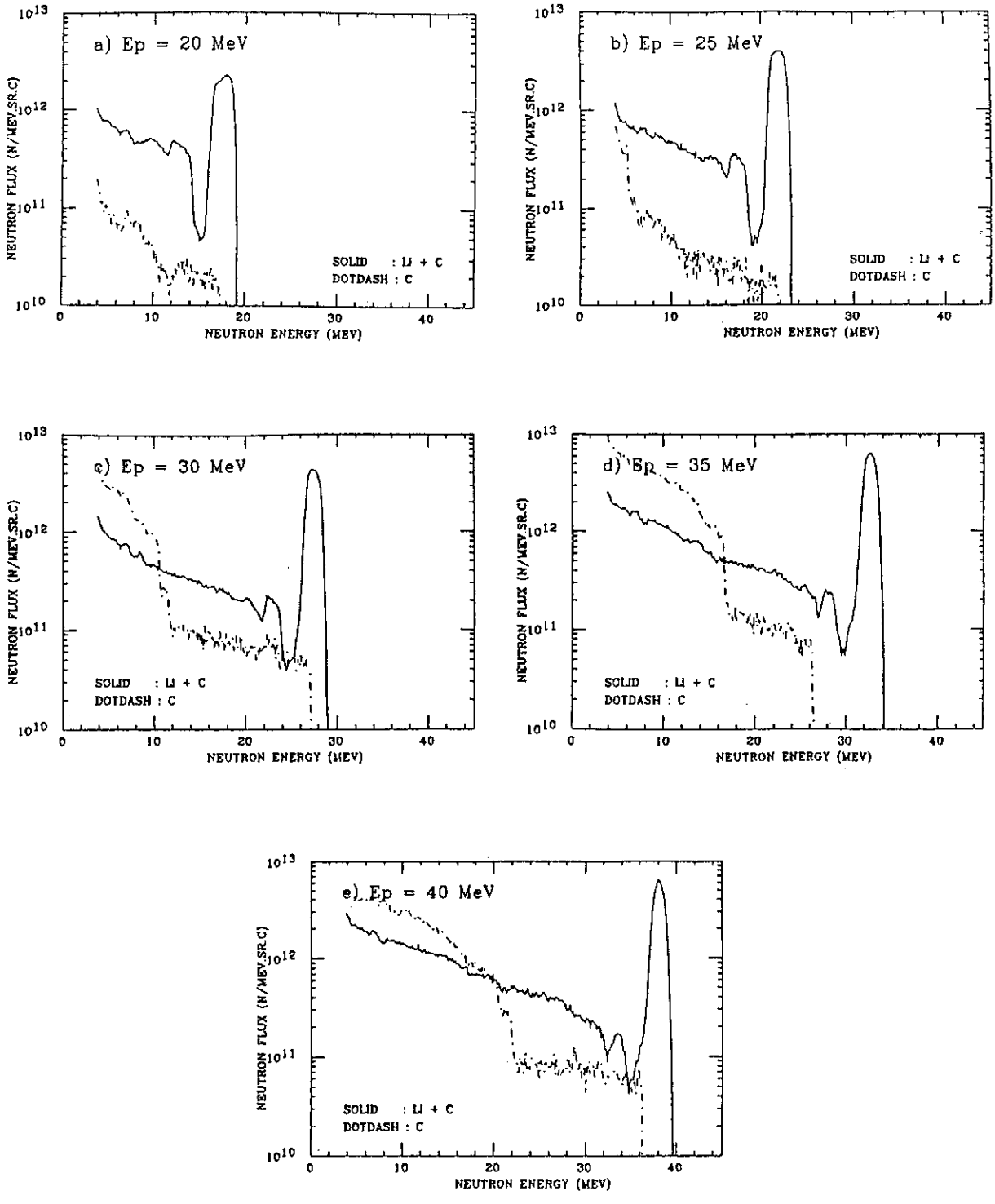

Fig. 2 Neutron energy spectra of $^{7}Li(p,n)^{7}Be$ undertaken at the TOF facility, CYRIC both for 2 mm-thick ^{7}Li target backed by 12 mm thick-graphite and for 12 mm thick graphite.

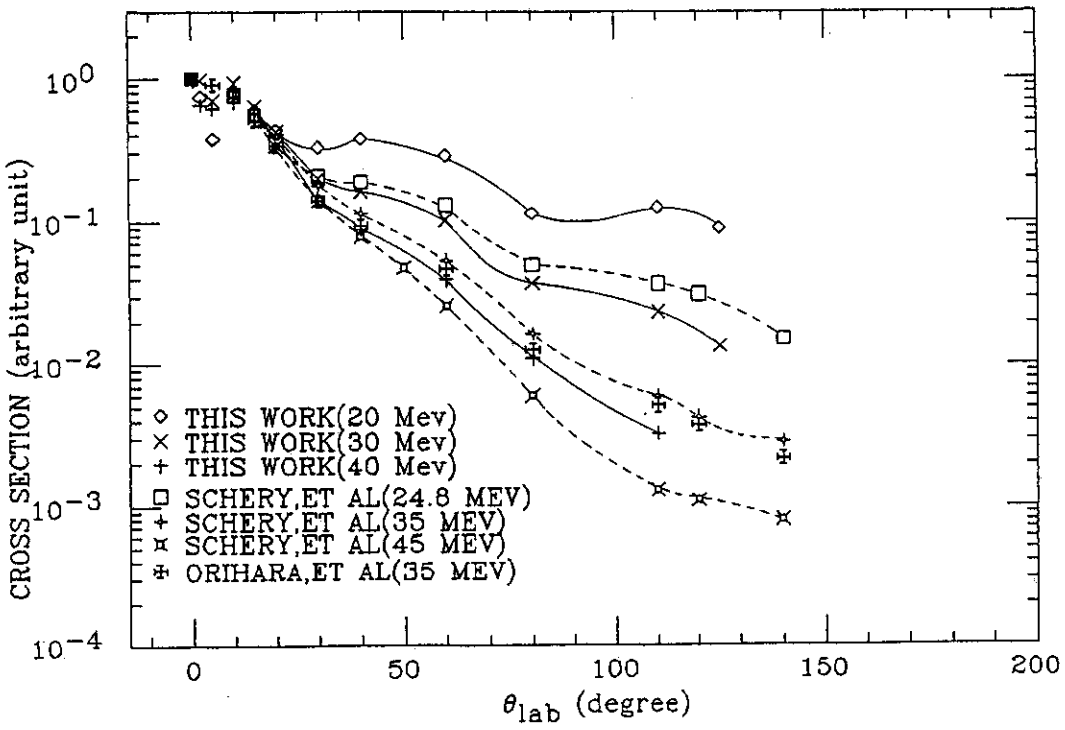

Fig. 3 Angular distribution of the peak neutrons from ^{7}Li(p,n) obtained from the proton energies of 20, 30 and 40 MeV compared to other data of Schery et al. and Orihara et al.

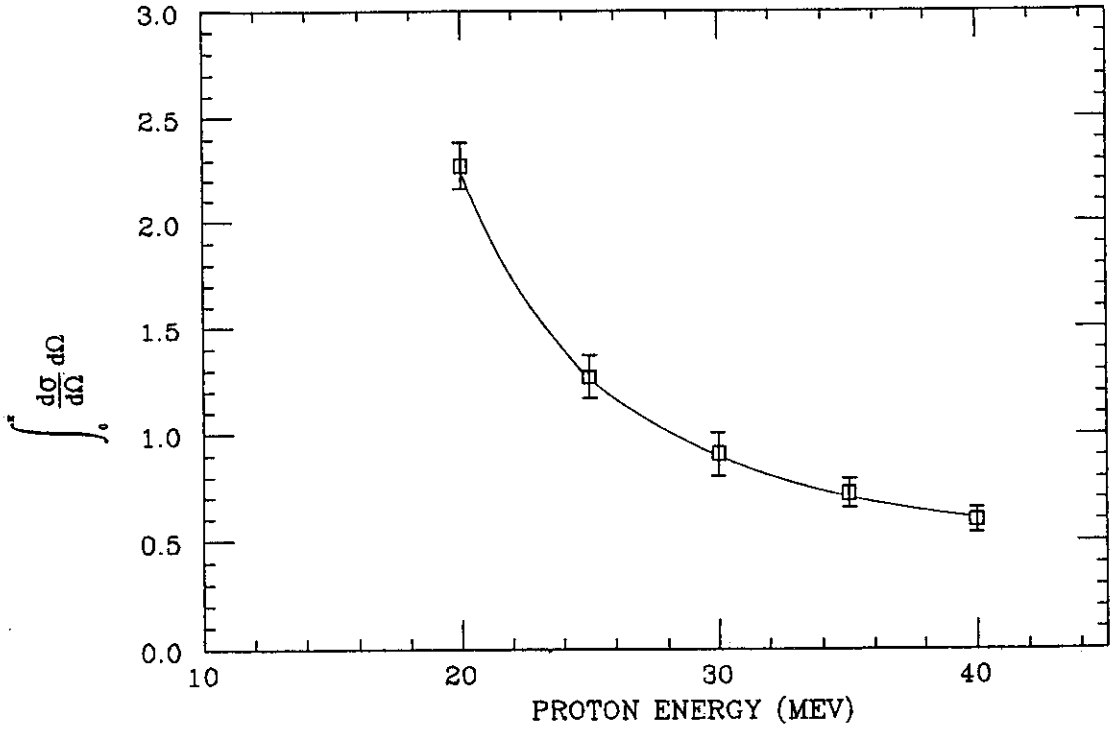

Fig. 4 Normalized ^{7}Li(p,n) cross section producing peak energy neutrons as a function of proton energy.

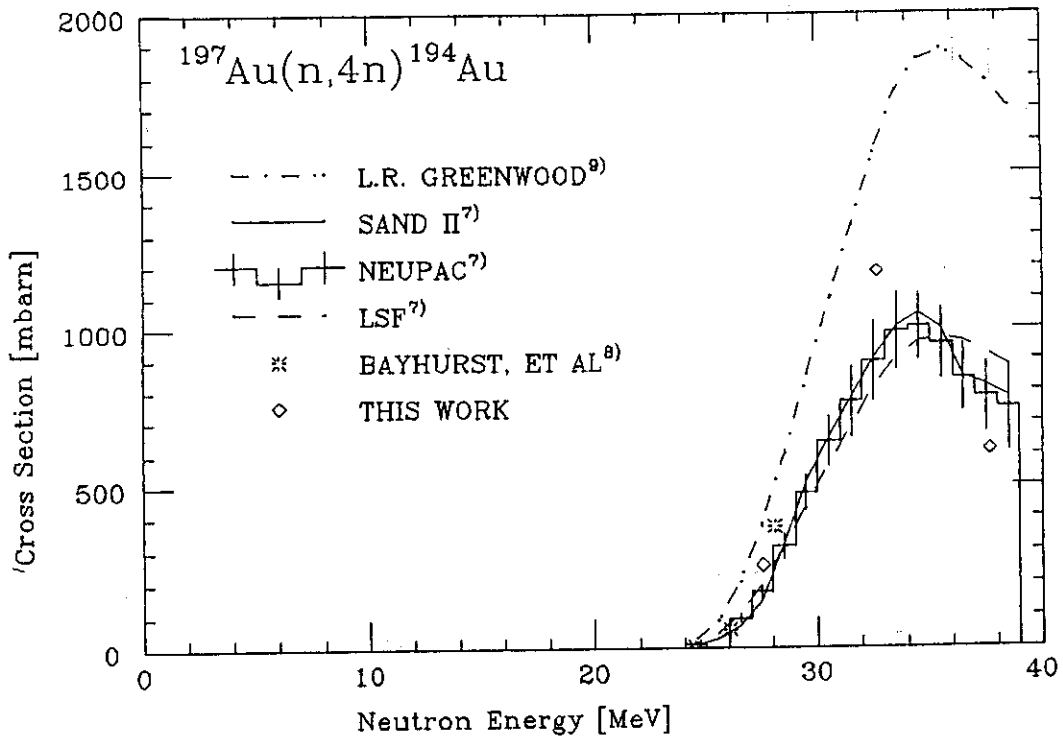

Fig. 5 ^{197}Au(n,4n) cross section as a function of neutron energy, compared to other data.

3.19 MEASUREMENT OF BETA-DECAY HALF-LIVES OF SHORT-LIVED NUCLEI

K. Kawade, H. Yamamoto, A. Tanaka, A. Hosoya
T. Katoh, *T. Iida and *A. Takahashi

Department of Nuclear Engineering, Nagoya University
Furo-cho, Chikusa-ku, Nagoya, 464-01, Japan
*Department of Nuclear Engineering, Osaka University
Yamadaoka, Suita-shi, Osaka, 565, Japan

The half-lives of short-lived nuclei produced by 14 MeV or thermal neutron bombardments were measured with Ge detectors in the spectrum multi-scaling mode. The corrections for the pile-up loss and the dead time were performed by applying both source pulser methods. Eleven half-lives of ^{51}Ti, ^{60m}Co, ^{66}Cu, ^{89m}Zr, ^{91m}Mo, ^{91g}Mo, ^{97m}Nb, ^{104m}Rh, ^{105m}Rh, ^{108}Ag and ^{109m}Pd were determined with accuracies of 0.2 ~ 3%.

1. Introduction

The half-life of β-decay is one of the most fundamental constants on radioactive isotopes. In the activation cross section measurements, the uncertainty brings a strong effect to the results. Most of the values previously published were obtained with GM counters, ionization chambers, proportional counters and scitnllation counters. In order to improve the precision and reliability of the half-lives of short-lived nuclei ($T_{1/2}$ = 40 s ~ 15 min), Ge detectors were used for the present work.

2. Experiment

The γ-rays were measured with the ORTEC 15 % and 20 % Ge detectors in the spectrum multi scaling mode. Decay was followed for about 10 times the half-life at equal intervals of 1/3 to 1/6 of the half-life. A long-lived γ source and a constant-pulser were simultaneously measured together with the short-lived activity for the correction of the pile-up and the dead time losses (source method, constant-pulser method). The initial counting rates were always kept to be less than

9 X 10^3 cps. The detailed procedures are described elsewhere[1].

Sources of ^{51}Ti, ^{60m}Co, ^{89m}Zr, ^{91m}Mo, ^{91g}Mo, ^{97m}Nb and ^{105m}Rh were produced by 14 MeV neutron bombardments at OKTAVIAN. Sources of ^{51}Ti, ^{60m}Co, ^{66}Cu, ^{104m}Rh, ^{108}Ag and ^{109m}Pd were produced by thermal neutron irradiation at the TRIGA-II reactor of Rikkyo University (100 kW).

3. Results

In Fig. 1 a decay curve in the decay of ^{51}Ti is shown. The results are summarized in Table 1 together with production reactions, γ-rays followed and previous works[2]. In Fig. 2 some of the results are compared with previous works. In Fig. 3 relative deviations of previous values from the present ones are shown. It is clearly seen that previous values[3] shorter than about 10 min systematically deviate and those become larger as the half-lives become shorter. The cause might result from insufficient corrections for pile-up and dead time losses. It is likely to start measurements at too high counting rates in order to get good statistics. If the corrections at high counting rates are not enough, the decay curve will show a longer half-life compared with the true value.

4. Summary

The half-lives of short-lived nuclei were determined with accuracies of 0.2 ~ 3%. Previous values shorter than about 10 min systematically deviate and those deviations become larger as the half-lives become shorter.

References

1) M. Miyachi et al.: Nucl. Data for Sci. and Tech. 897(1988, Mito)
2) E. Browne et al.: "Table of Radioactive Isotopes" (1986) John Wiley & Sons, New York
3) C. M. Lederer and V. S. Shirley: "Table of Isotopes" 7th Ed.,(1978), John Wiley & Sons, New York

Table 1 Results of half-life measurement

Nuclide	Production reaction	Eγ (keV)	Reference[a] (Eγ in keV)	Half-life Present	Reference[b]
^{51}Ti	^{51}V(n,p) ^{50}Ti(n,γ)	320.1	^{57}Co (122.1)	5.759(9)m	5.80(3)m
^{60m}Co	^{60}Ni(n,p)^{m} ^{59}Co(n,γ)^{m}	58.6 1332.5	[c] ^{137}Cs(661.7)	10.424(20)m	10.47(2)m
^{66}Cu	^{65}Cu(n,γ)	1039.4	^{137}Cs (661.7)	5.080(12)m	5.10(2)m
^{89m}Zr	^{90}Zr(n,2n)^{m}	587.7	^{137}Cs (661.7)	4.145(9)m	4.18(1)m
^{91g}Mo	^{92}Mo(n,2n)^{g}	511($\gamma^{\pm}$)	^{133}Ba (356.0)	15.473(34)m	15.49(1)m
^{91m}Mo	^{92}Mo(n,2n)^{m}	653.0	^{133}Ba (356.0)	62.2(10)s	65.2(8)m
^{97m}Nb	^{97}Mo(n,p)^{m}	743.3	^{137}Cs (661.7)	58.7(18)s	60(8)s
^{104m}Rh	^{103}Rh(n,γ)^{m}	555.8	^{133}Ba (356.0)	4.256(13)m	4.34(5)m
^{105m}Rh	^{105}Pd(n,p)^{m}	129.6	^{170}Tm (84.3)	42.4(5)s	45s
^{108}Ag	^{107}Ag(n,γ)	633.0	^{133}Ba (356.0)	2.353(9)m	2.37(1)m
^{109m}Pd	^{108}Pd(n,γ)^{m}	188.9	^{57}Co (122.1)	4.663(11)m	4.69(1)m

[a] These sources were used for corrections of dead-time and pile-up losses.

[b] taken from ref. 3.

[c] No source was used. Pulser was only used.

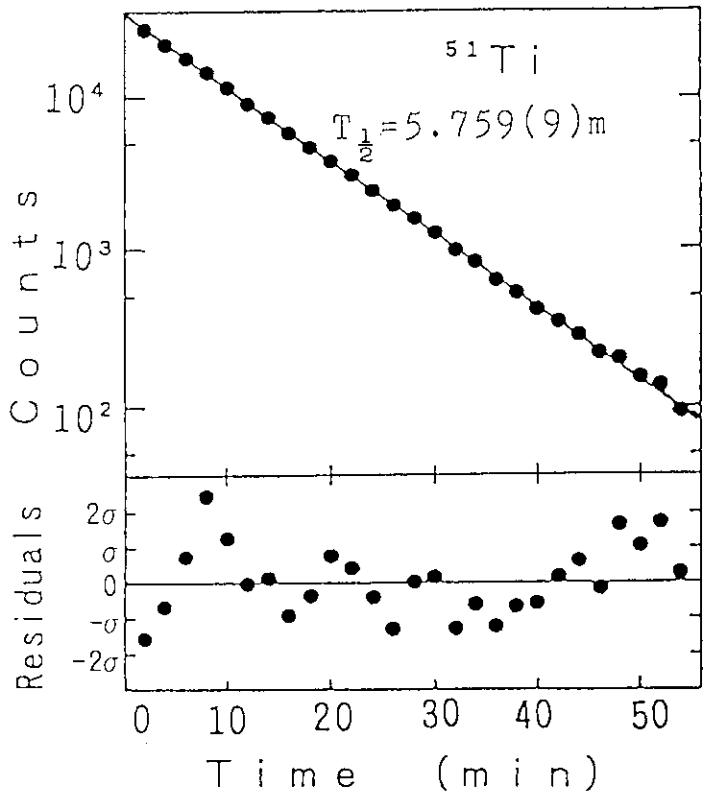

Fig. 1 Decay curve of ^{51}Ti and residuals from a least squares fitting analysis.

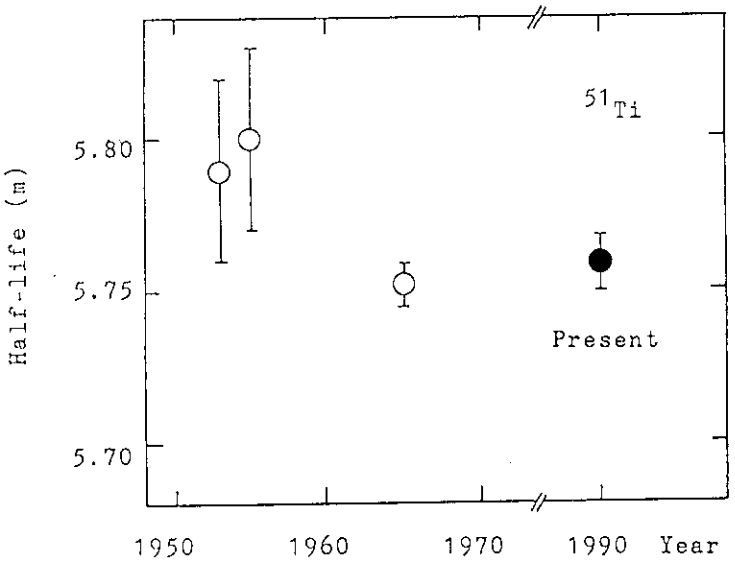

Fig. 2(a) Comparison with previous works taken from ref. 4.

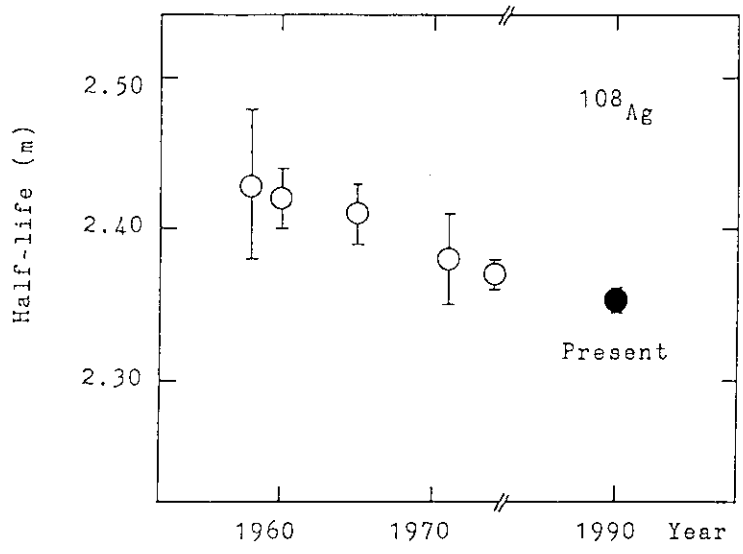

Fig. 2(b) Comparison with previous works taken from ref. 4.

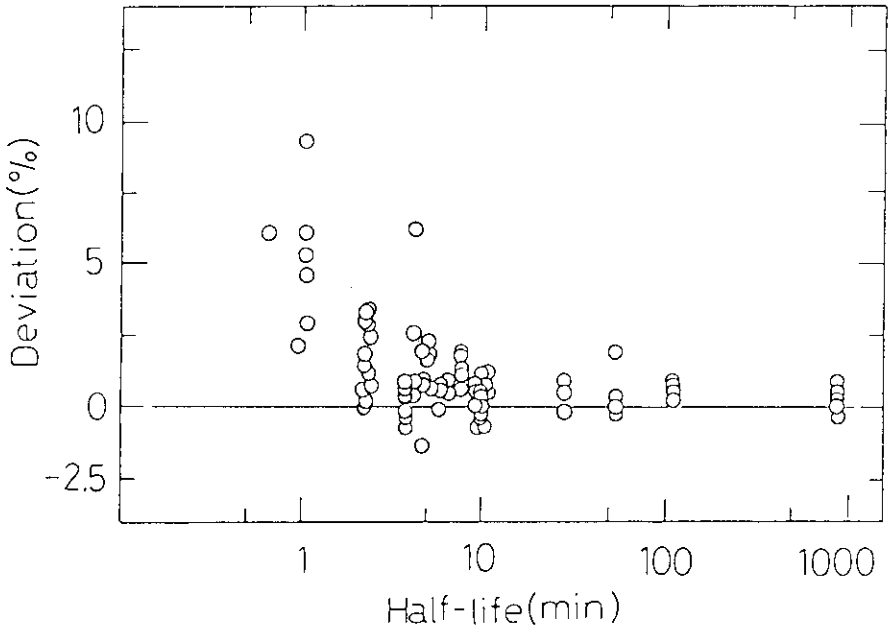

Fig. 3 Deviation of previous half-live values from the present ones in percent (%).

3.20 LEAD SLOWING-DOWN SPECTROMETER COUPLED TO ELECTRON LINAC (I)

－OUTLINE OF THE SPECTROMETER－

Yoshihiro Nakagome, Katsuhei Kobayashi, Shuji Yamamoto,
Yoshiaki Fujita, Akihiro Yamanaka*, Satoshi Kanazawa*
and Itsuro Kimura*

Research Reactor Institute, Kyoto University
Kumatori-cho, Sennan-gun, Osaka 590-04, Japan
*Department of Nuclear Engineering, Kyoto University
Yoshidahonmachi, Sakyo-ku, Kyoto 606, Japan

Abstract: The Research Reactor Institute, Kyoto University (KURRI) set up a lead slowing-down spectrometer recently. The spectrometer (Kyoto University Lead Slowing-down Spectrometer : KULS) is a cube of 1.5 x 1.5 x 1.5 m^3 and about 40 tons, which is assembled with about 1,600 lead blocks (10 x 10 x 20 cm^3 each) of 99.99% purity. The spectrometer is coupled to the 46 MeV electron linear accelerator (linac) at KURRI. We can obtain higher neutron source intensity of the order of 10^{11} photoneutrons per second at the center of the spectrometer than that using previous DT source. KULS can cover the neutron energy range of 0.1 eV to about 50 keV, but the energy resolution is 40 to 50%. Twelve experimental holes are made in the spectrometer and one of them is covered by bismuth layer to shield high energy gamma-rays by the Pb(n,γ) reaction in the spectrometer. By using the KULS system, it is possible to study small neutron cross sections.

1. Introduction

A lead slowing-down spectrometer has much higher neutron flux intensity by 3 to 4 orders of magnitude comparing with the widely applied normal neutron time-of-flight method[1,3,6], although the energy resolution is about 30%. In spite of this disadvantage, by virtue of the intense neutron source, the spectrometer is though to be a valuable tool for cross section measurements for actinide nuclei, fission products and/or limited quantity

of sample materials below about 100 keV[6].

The neutron slowing-down time method is to measure the slowing-down time of pulsed neutrons in some medium and to deduce the neutron energy by using an equation of $E_n=K/t^2$ where En is neutron energy, K constant and t slowing-down time. As the medium, heavy mass element such as lead is used because of small neutron capture cross section and long slowing-down time. In 1955 Bergmann et al.[1] presented a practical lead spectrometer, and in 1970s several lead slowing-down spectrometers were constructed in the world as shown in Table 1. In general, a small pulsed neutron generator or electron linear accelerator is coupled to the spectrometer as a neutron source.

Recently, the Research Reactor Institute, Kyoto University (KURRI) set up a lead slowing-down spectrometer coupled to the KURRI electron linear accelerator. This paper describes the outline of the spectrometer to help understanding the following papers.

2. History of the KULS

The origin of the Kyoto University Lead Slowing-down Spectrometer, KULS, is a lead spectrometer of the University of Tokyo, LESP[3]. The LESP was coupled to a small pulsed neutron generator and had four experimental holes. In order to develop the neutron-induced cross section measurements in the eV to keV energy region for actinide nuclei which has very small cross section, the University of Tokyo transferred LESP to Kyoto University on January, 1991 to be coupled to the 46 MeV electron linear accelerator (linac) at KURRI and to obtain higher neutron flux intensity.

About 1,600 lead blocks (10 x 10 x 20 cm^3 and 10 x 5 x 20 cm^3) were broken up and carried into the target room of KURRI linac facility to pile up again.

3. Specification and Characteristics

The KULS is a lead spectrometer of a cube 1.5 m on a side and the total weight is about 38 tons. The purity of lead is 99.99%, and each lead block has been degreased carefully by using alcohol or acetone before piling up. The spectrometer is set on a movable platform in the target room of KURRI linac facility as shown in Fig. 1. When the normal neutron time-of-flight measurements are made, the KULS is moved from the target room.

The horizontal and vertical cross sections of KULS are shown in Fig. 2. All surfaces of the spectrometer are covered by 0.5 mm thick cadmium plate to keep off intrusion of the room returned neutrons. In order to promote a various experimental research with the spectrometer, eight experimental holes were prepared anew in addition to the original four holes of LESP. One of the new experimental holes is surrounded by bismuth blocks to shield high energy gamma-rays produced by the Pb(n,γ) reaction. The thickness of bismuth layer is 10 to 15cm. Since the neutron-capture gamma-ray energy of Bi is low (approximately 4 MeV), the Bi-hole is available for experiments under the condition of low gamma dose and low gamma energy.

A photoneutron target made of tantalum plates is set in the center of the spectrometer and cooled by compressed air. The target system is separated from the linac vacuum system to prevent troubles with the linac machine.

At the following operation condition of the linac, neutron flux of an order of 10^{11} photoneutrons/sec at the center of the spectrometer is attained: electron energy, 30 MeV; pulse width, 10 to 33 nsec; repetition rate, 100 pps; target power, about 60 Watt (target temperature, 300 °C). Available neutron energy range of the KULS system is 0.1 eV to about 50 keV, and the energy resolution is approximately 45% in eV region, 40% in keV region and 50% in the energy region of more than 20 keV.

4. Summary

The Research Reactor Institute, Kyoto University (KURRI) set up a lead slowing-down spectrometer coupled to the 46 MeV electron linear accelerator. The original of this spectrometer KULS is LESP, University of Tokyo. It was transferred to KURRI and modified. The KULS system is a powerful equipment for studying small neutron cross sections up to about 50 keV.

We have just started the characteristic experiments with the KULS, and some of the recent results are presented in this proceedings. Successively, we will use the KULS system to measure neutron-induced nuclear data for actinides and/or fissile and fertile materials.

5. Acknowledgments

We deeply thank Professors T. Nakazawa and T. Kosako of the University of Tokyo for their cooperation and help for transferring the LESP to KURRI.

The comments concerning architectural design by Dr. K. Kamae of KURRI are also appreciated.

References

1) Bergmann, A. A.,Isakov, A. I., Murin, I. D., Shapiro, F. L., Shtranikh, I. V., Kazarnovsky, M. V.: Proc. 1st Int. Conf. Peaceful Uses Atomic Energy, 4, 135 (1955).
2) Mitzel, F., Plendl, H. S.: Nucleonik, **6**, 371 (1964).
3) Wakabayashi, H., Sekiguchi, A., Nakazawa, M., Nishino, O.: J. Nucl. Energy, **27**, 811 (1973).
4) Fujino, J.: private communication.
5) Sawan, M., Conn, R.: Nucl. Sci. Eng., **54**, 127 (1974).
6) Slovacek, R. E., Cramer, D. S., Bean, E. B., Valentine, J. R., Hockenbury, R. W., Block, R. C.: Nucl. Sci. Eng., **62**, 455 (1977).
7) Yamauchi, T.: private communication.

Table 1 Lead slowing-down spectrometers of several laboratories

Facility	Year	Size of Lead Assembly	Ref.
Bergmann et al.	1955	2 x 2 x 2.3 m^3	1)
Mitzel et al.	1964	1.6-m cube	2)
LESP	1970	1.5-m cube	3)
HITACHI	1972	1.8-m cube	4)
Sawan et al.	1974	1.33-m cube	5)
RINS	1977	1.8-m cube	6)
YAYOI	1982	2.5-m octagon	7)
KULS	(present)	1.5-m cube	

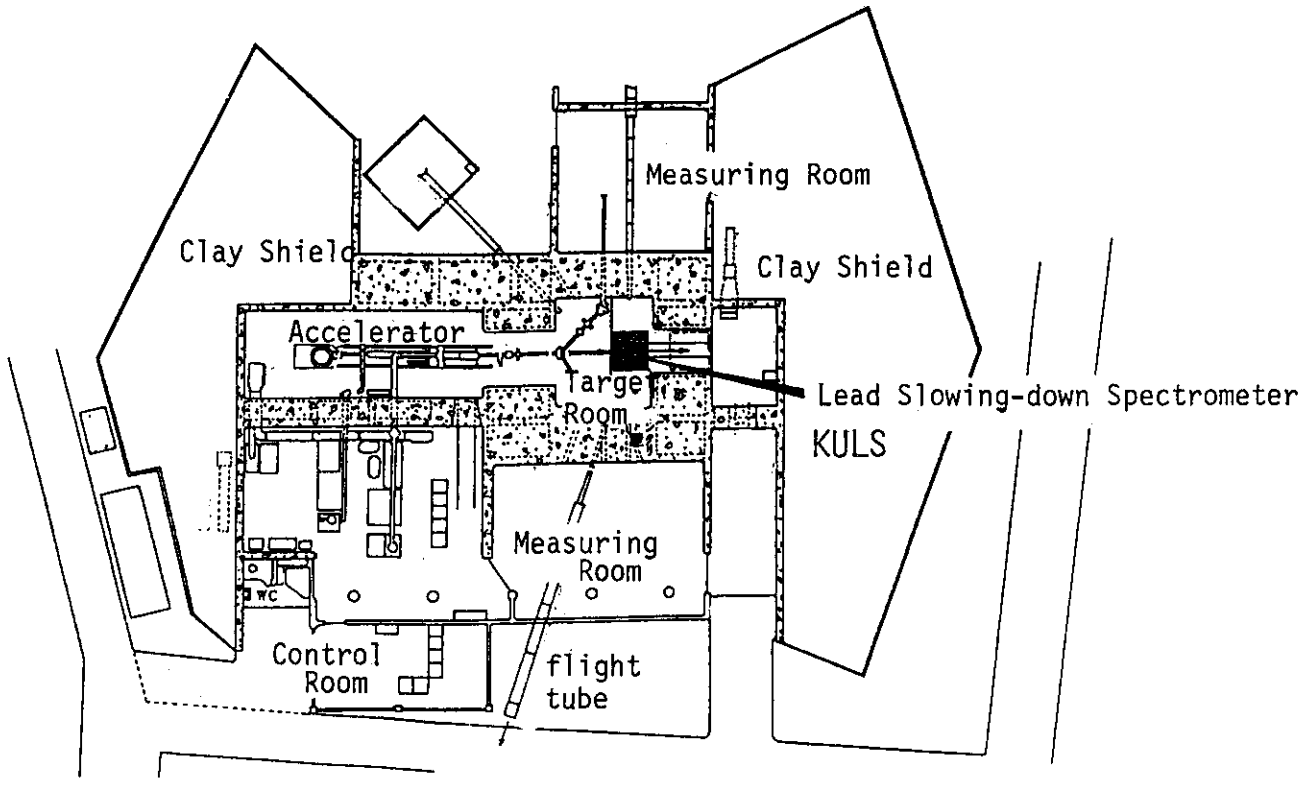

Fig. 1 Setting arrangement of the KULS at the KURRI linac facility.

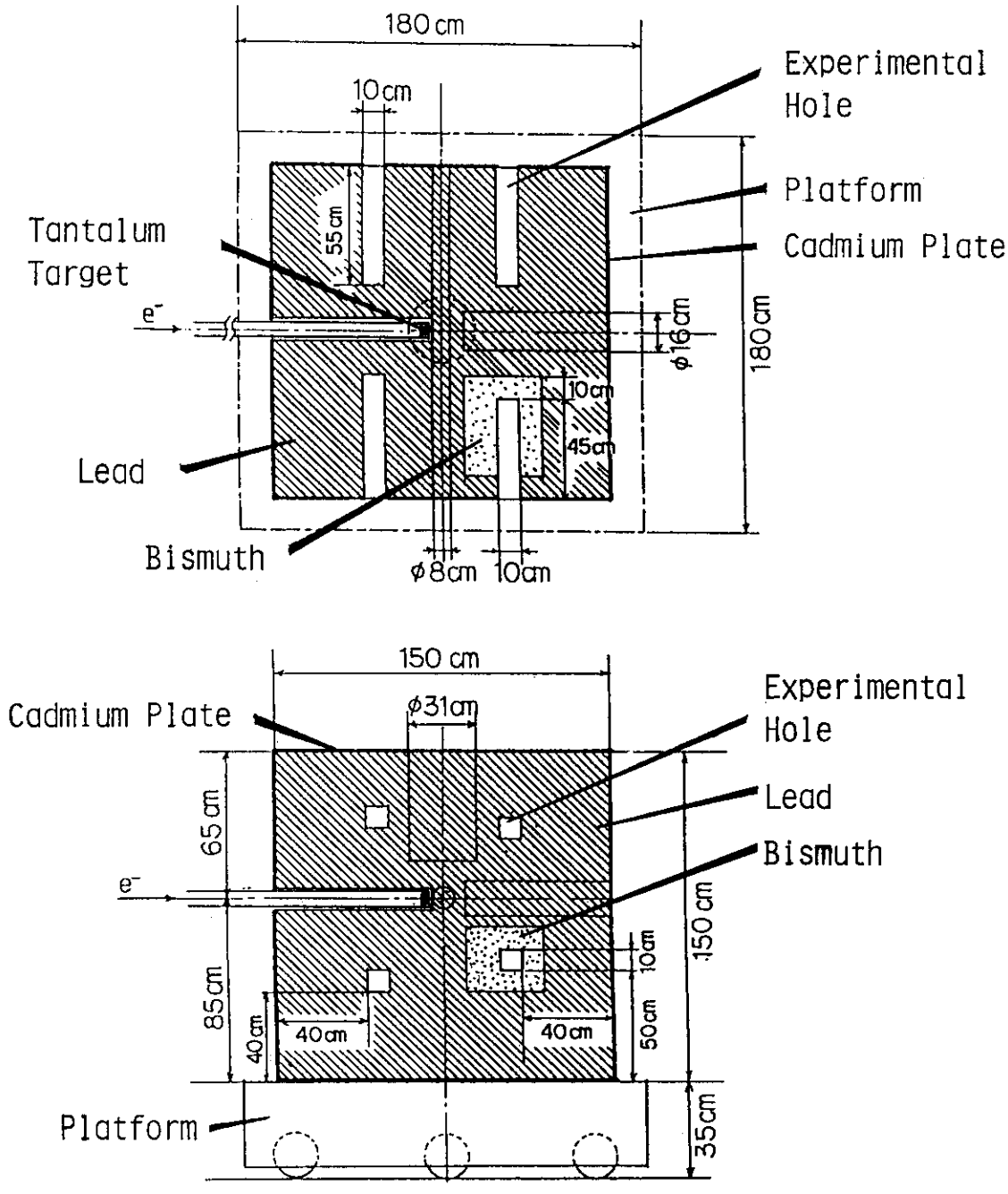

Fig. 2 Horizontal (upper) and vertical (lower) cross sections of the KULS.

3.21 LEAD SLOWING-DOWN SPECTROMETER COUPLED TO ELECTRON LINAC (II)

－NEUTRON TIME BEHAVIOR IN LEAD－

Akihiro Yamanaka*, Satoshi Kanazawa*, Itsuro Kimura*,
Katsuhei Kobayashi, Yoshihiro Nakagome, Shuji Yamamoto and Yoshiaki Fujita.

Research Reactor Institute, Kyoto University, Kumatori-cho, Sennan-gun, Osaka 590-04, Japan.
** Dept. of Nucl. Eng., Fac. of Eng., Kyoto University, Yoshidahonmachi, Sakyo-ku, Kyoto 606-01, Japan*

Abstract

In the Kyoto University Lead Slowing-down Spectrometer, abbreviated KULS, the relation between neutron slowing-down time and energy has been measured with a BF_3 proportional counter covered with 7 kinds of resonance filters. The following relation has been experimentally determined with $K=191\pm3$ [keV μsec^2] and $t_0=0.3$[μsec];

$$E = K / (t + t_0)^2$$

where E is neutron energy in kev, K is constant, t_0 is zero energy time and t is slowing-down time in μsec. The neutron energy resolution has been also derived from the measured slowing-down time spectrum using the resonance filters, and found to be around 40 to 45% at FWHM with Gaussian spectrum at energies between 4 eV to 300 eV. Calculations using the Monte Carlo code MCNP have been also made and compared with the above experimental results. Good agreement between the calculations and the measurements has been found in general.

1. Introduction

In a heavy slowing-down medium whose Σ_a is negligibly small, such as lead, fast neutrons are slowed down by inelastic and elastic scatterings and (n,2n) reaction. Especially, below the inelastic scattering threshold energy(nearly 570 keV), elastic scattering takes most part of the slowing-down process. So, below 100 keV, neutron time-dependent spectrum becomes an asymptotic form, and neutrons are slowed down keeping its form[1]. Hence lead slowing down spectrometer has almost constant energy resolution in wide energy range from 4 eV to several hundreds eV, and neutron

energy can be determined only by the slowing-down time[1].

In the present measurement, we have experimentally investigated the neutron slowing-down time behavior in the Kyoto University Lead Slowing-down Spectrometer, KULS, by using the resonance filters method. Considering their sharp and large resonance peaks, 7 resonance materials of In, Ta, Au, Ag, Mo, Co and Mn were chosen. As neutrons corresponding to the resonance energy can hardly penetrate through the filtering material, we can observe the resonance dip in the time-dependent spectrum measured with BF_3 proportional counter covered with the resonance filters. The relation between the neutron slowing-down time and energy has been experimentally obtained in the KULS. Calculation using the Monte Carlo code MCNP has been also performed and the results have been compared with the above measured ones.

2. Theoretical Aspect

In a heavy mass medium, an energy loss per one collision in slowing-down process is very small. In the case of lead, we can take advantage of its property that most component of total cross section is elastic scattering, then neutrons are hardly captured by the lead. Moreover, provided that slowing-down medium is sufficiently large, neutrons scarcely leak from the assembly. The neutron slowing-down equation is given as,

$$\frac{1}{v}\frac{\partial \phi(E,t)}{\partial t} = \int \sigma(E' \to E)\phi(E',t)dE' - \sigma(E)\phi(E,t) + S(E)\delta(t) , \qquad (1)$$

where ϕ is neutron flux, v is neutron velocity, σ is microscopic cross section, S is neutron source. Applying the time moment method, we can get the following asymptotic solution[2],

$$\phi(E,t) = \frac{1}{E}\frac{1}{\sqrt{2\pi}\sigma} exp\left(-\frac{(t-<t>^2)}{2\sigma_t^2}\right) . \qquad (2)$$

So, in the heavy mass medium, whose Σ_a is negligibly small, it is assumed that the neutron spectrum comes to be a gaussian form. Then the relation between energy and

slowing-down time, and the energy resolution are related to the following formulae as below[3],

$$E = \frac{m}{2}\frac{A^2}{(\Sigma_s t)^2} = \frac{K}{t^2}, \qquad (3)$$

$$\left(\frac{\Delta E}{E}\right)_{FWHM} \simeq 2.35\sqrt{\frac{8}{3A}} \simeq 0.27, \qquad (4)$$

where m is neutron mass, A is mass number, Σ_s is macroscopic scattering cross section, K is slowing-down constant. One can obtain energy resolution of about 27% with A=207 as the theoretical value. The constant K and the neutron energy resolution, however, depend on the conditions of the slowing-down medium. In the practical case, there could be hydrogenous and carbonic compound like grease or water in the pile. Therefore, K is a characteristic constant of the lead slowing-down spectrometer, and the energy resolution may be broadened by the experimental conditions.

3. Spectrum Calculation

After pulsed fast neutrons are generated at the center of the pile, they are slowed down and diffuse in it. We employed the continuous energy Monte Carlo code, MCNP[4] to investigate neutron behavior in the KULS. As an initial spectrum for the calculation, we selected the tantalum photoneutron source spectrum which was obtained in the previous experiment[5]. In the KULS, one of the experimental holes was constructed and covered with bismuth layer of about 10 cm thickness to cut off neutron capture gamma-rays of lead. This geometrical configuration was taken into account in the calculation. The MCNP calculation was performed with 3-dimensional cartesian coordinate, nuclear data based on ENDF/B-IV and 100,000 neutron histories. Figure 1 shows the time-dependent spectrum, at 40 cm from the photoneutron source. Neutron spectrum is to be an asymptotic form in 10μsec in the KULS and after that, its form is kept in the slowing down process.

4. Experiment

The measurement has been made with the Kyoto University Lead Slowing-down Spectrometer coupled to the 46 MeV electron linear accelerator, linac, at the Research Reactor Institute, Kyoto University, KURRI. To generate pulsed fast neutrons, an air-cooled tantalum photoneutron target was placed at the center of the KULS. The target was newly designed for the KULS; it consists of 12 tantalum plates of 8 cm in diam., and gradually thicken from 1 mm to 5 mm to improve neutron generation efficiency. The total effective thickness is 29 mm. Electrons hit the tantalum target and induce intense bremsstrahlung radiations that produce neutrons by the (γ,n) reaction. Copper-constantan thermocouples were attached to the target case made by thin titanium to monitor the temperature during the linac operation.

The KULS has eight experimental holes, 10×10 cm^2, and 55 or 65 cm depth, a through hole 8 cm in diameter and two holes for big lead stringers. As seen in Figure 2, present measurement has been made at the Bi hole which is one of the experimental holes. The experimental hole is made of Bi blocks and the thickness is 10 cm to protect the high energy neutron capture γ-rays from the lead material. We have put a BF_3 proportional counter into the Bi hole at the distance of 40 cm from the photoneutron target. The BF_3 counter is 12 mm in diam., 50 mm in effective length, and contains 1 atm gas mixed with Ar and BF_3. In the present measurement, linac electron beam pulse was utilized as a start pulse for the multi- channel time analyzer, and the BF_3 signal as an event signal. The data were accumulated in the 4096-ch multi-channel time analyzer. Three kinds of channel widths, 0.125μsec, 0.25μsec, and 0.50μsec were selected as the need arises. By covering the BF_3 counter with a resonance filter, a dip structure is observed in the slowing-down time spectrum corresponding to the resonance energy, as seen in Figure 3. Table 1 lists the resonance filters and their resonances used in this measurement. Since the resonance energies for these filters are well-known[6], we can calibrate the relation between slowing-down time and energy by the least squares fitting to these dips. The width in the resonance cross section was narrow enough compared with inherent resolution of the KULS.

5. Result

On the assumption that the resonance dip in the slowing-down time spectrum is a gaussian form, we fitted the measured spectrum to a gauss function, and determined center channel in the dip region, namely slowing-down time against the known resonance energy, and derived the full width at half maximum, FWHM. Figure 4 shows the relation between the resonance energy and the slowing-down time, where good linearity can be seen. It means that the relation $E=K/t^2$ is valid in wide range. Applying the method of least squares fitting to these data, the slowing-down constant can be determined to be $K=191\pm3$[keV. μsec^2]. On the other hand, the MCNP calculation gives K=192, so the agreement between experiment and calculation is good. Slowing-down constants are given in Table 2, comparing with other facilities' values. As realized from this table, the constant is not always depend on the spectrometer size, and is thought to be its own characteristic for the spectrometer.

As shown in Table 3, energy resolution for the KULS is almost energy independent and about 45%, between 4 eV and 300 eV. In the higher and lower energy regions, energy resolution increases a little as seen in Table 3. The dispersion may be due to some impurities in lead, air gap between lead blocks, broadening of the source spectrum and neutron energy fluctuation in the lower energy region in the KULS. The resolving power measured by the present experiment is, in general, in good agreement with that by the MCNP calculation, and a consistent agreement is shown between the measured and calculated energy resolutions.

6. Conclusion

The characteristic experiment for the KULS has been performed, and the slowing-down constant and energy resolution have been experimentally obtained. The constant and the energy resolution are 191 ± 3[keV. μsec^2], and 40 to 45%, respectively, as given in the following relation; $E=191/(t+0.3)^2$, where E is neutron energy in keV and t is neutron slowing-down time in μsec.

The slowing-down constant and the energy resolution were also calculated with the Monte Carlo code MCNP and the results are K=192 and about 40%, respectively. These calculated values are in satisfactory agreement with the measured ones.

References

1. A. A. Bergman, et al., *Proc. 1st Int. Conf. Peaceful Uses At. Energy,* **4**, 135 (1955).

2. M. M. R. Williams, *Nucl. Sci. Eng.,* **19**, 221 (1964).

3. K. H. Beckurts, K. Wirtz, "Neutron Physics", Springer−Verlag (1964).

4. Los Alamos National Laboratory, "MCNP − A General Monte Carlo Code for Neutron and Photon Transport, Version 3A", La−7396−M (1986).

5. K. Kobayashi, et al., *Nucl. Sci. Eng.,* **99**, 157 (1988).

6. S. F. Mughabghab, "Neutron Cross Sections", Vol.1, Vol.2, Academic Press, Inc. (1984).

7. F. Mitzel and H. S. Plendl, *Nukleonik,* **6**, 371 (1964).

8. H. Wakabayashi, et al., *J. Nucl. Sci. Technol.,* **7**, 487 (1970).

9. J. Fujino, private communication.

10. M. Sawan and R. Conn., *Nucl. Sci. Eng.,* **54**, 127 (1974).

11. R. E. Slovacek, et al., *Nucl. Sci. Eng.,* **62**, 455 (1977).

12. T. Yamauchi, private communication.

Table 1 Resonance materials

Material	Energy [eV]	thickness[mm]	
In	1.4	0.2	foil
Ta	4.3	2.0	foil
	10.4		
Au	4.9	0.1	foil
Ag	5.2	0.5	foil
Mo	44.9	7.0	powder
Co	132.0	7.0	powder
Mn	336.0	7.0	powder

Table 2 Constants of slowing-down time

Facility	Lead Assembly	K [keV•μsec^2]
Present	1.5−m cube	Exp. 191±3 Calc. 192
Bergman et al.[1)]	2×2×2.3 m^3	183
Mitzel et al.[7)]	1.6−m cube	179±5
LESP[8)]	1.5−m cube	155
HITACHI[9)]	1.8−m cube	166±1
Sawan et al.[10)]	1.33−m cube	166±4
RINS[11)]	1.8−m cube	165±3
YAYOI[12)]	2.5−m octagon	74.7

Table 3 Energy resolution

Energy [eV]	Resolution [%]	
	Exp.	Calc.
1.4	51±3	56
4.9	40±2	40
10.4	43±1	34
44.9	38±1	36
132.0	41±2	44
336.0	40±3	44
2370.0	53±3	45

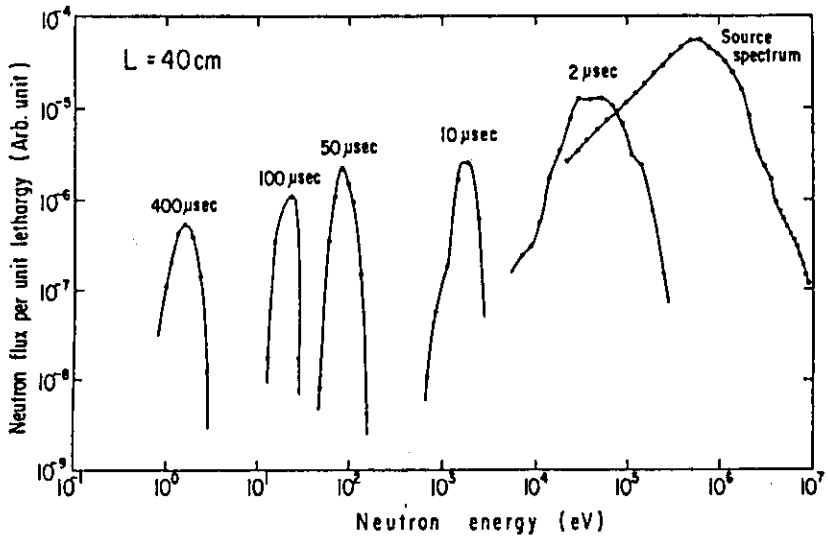

Fig. 1 Time dependent neutron spectrum in KULS.

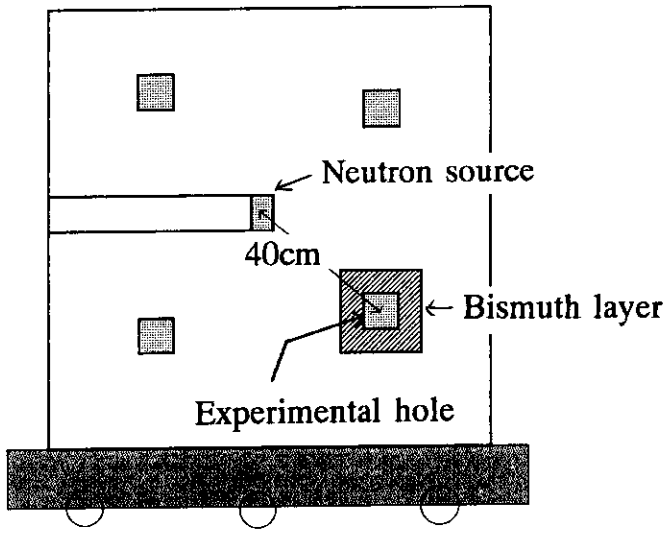

Fig. 2 Experimental configuration.

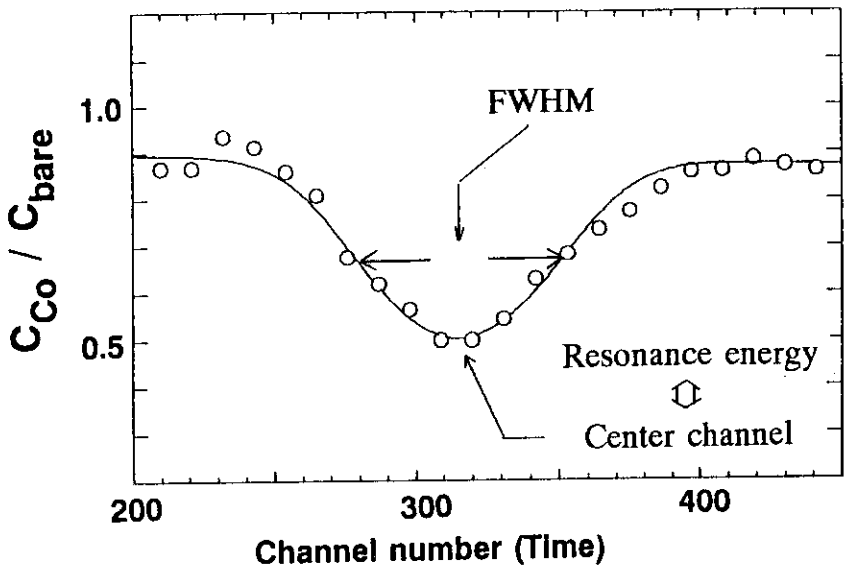

Fig. 3 The count ratio of BF_3 with Co-filter to BF_3 with no-filter.

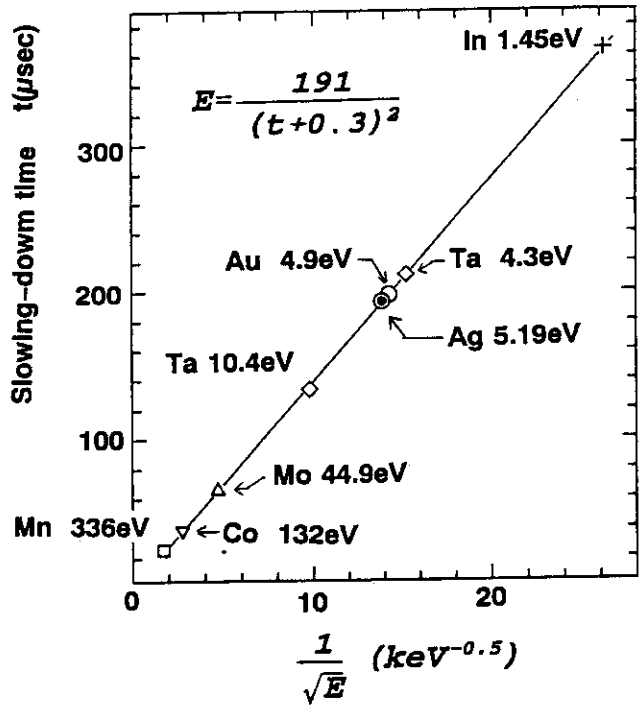

Fig. 4 Relation between mean energy and slowing-down time for KULS.

3.22 LEAD SLOWING-DOWN SPECTROMETER COUPLED TO ELECTRON LINAC (III)

－NEUTRON SPECTRUM－

Katsuhei Kobayashi, Li Zhaohuan*, Yoshiaki Fujita,
Shuji Yamamoto, Yoshihiro Nakagome,
Akihiro Yamanaka+, I. Kimura+ and S. Kanazawa+

(Research Reactor Institute, Kyoto University, Kumatori-cho, Sennan-gun, Osaka 590-04, Japan,
* Visiting scientist from Institute of Atomic Energy, Beijing, China.
+ Dept. of Nucl. Eng., Fac. of Eng., Kyoto University,Yoshidahonmachi, Sakyo-ku, Kyoto 606, Japan)

As a part of the characteristic experiments with the Kyoto University Lead Slowing-down Spectrometer, KULS, neutron spectrum in the KULS has been obtained by adjusting with multi-foil activation data using the NEUPAC code and the SAND-II type code, NEUSPEC, which has a sub-program generating uncertainties in the neutron flux spectrum with the Monte Carlo method. Fourteen kinds of activation reactions, which were measured at the irradiation position distant 15 cm from the photoneutron target at the center of the KULS, were employed to obtain the neutron spectrum. The cross section libraries were taken from the ENDF/B-V Dosimetry File mainly for the NEUPAC code and the JENDL Dosimetry File for the SAND-II type code NEUSPEC, respectively.

The neutron spectra adjusted with the NEUPAC and the NEUSPEC codes show, in general, good agreement with each other considering that the resultant uncertainties are in several percent, and these spectra are close to the calculation using the Monte Carlo code, MCNP. The neutron spectrum in the slowing-down energy region is harder than 1/E neutron spectrum, and it has been found by the Cd ratio measurements using Au and Mn foils that there exist scarcely thermal neutrons in the KULS.

1. Introduction

Lead is one of the heavy mass elements and its neutron total cross section mainly consists of elastic scattering cross section

and the absorption cross section is very small. Therefore, when pulsed fast neutrons are put into the central region of the large lead assembly, the neutrons are slowed-down gradually by the elastic scattering process[1], because the neutron leakage is small. There exists a certain relation between the neutron slowing-down time and its energy, as described in the Reference[2]. In such a large lead assembly, that is called a lead slowing-down spectrometer, it is said that the neutron intensity is much higher than that obtained by the normal neutron time-of-flight method with a 5 m flight path[3], for example.

The multi-foil activation method is one of candidate spectrometries to experimentally characterize the neutron spectrum. For the purpose of these activation data analyses, in recent years, some unfolding or adjusting codes such as SAND-II and NEUPAC codes[4,5], have been developed and applied to obtain neutron spectra in and around research reactors[6,7] and in some neutron spectrum fields[8,9].

The Kyoto University Lead Slowing-down Spectrometer (KULS) was set up at the Research Reactor Institute, Kyoto University (KURRI) and coupled to the 46 MeV KURRI electron linear accelerator, as reported in the literatures[10]. In the present work, as a part of the characteristic experiments, neutron spectrum in the KULS of 1.5 x 1.5 x 1.5 m^3 has been obtained by adjusting with multi-foil activation data using the NEUPAC code[5] and the SAND-II type code NEUSPEC[7,11]. Fourteen kinds of activation reactions were employed to obtain the neutron spectrum which was measured at the irradiation position distant 15 cm from the photoneutron target at the central region of the KULS. The adjusted results were compared with that calculated with the Monte Carlo code MCNP[12].

2. Experimental Methods

2.1 KULS

The Kyoto University Lead Slowing-down Spectrometer (KULS) coupled to the 46 MeV electron linear accelerator (linac) is a cube of 1.5 x 1.5 x 1.5 m^3 and made of about 40 tons of lead with 99.99 % purity. At the central region, an air-cooled photoneutron target of lead, 8 cm in diameter and 5 cm thick, was placed to generate fast neutrons by bombarding high energy electrons. As shown in Fig. 1, the KULS has a through hole and its central region is distant 15 cm from the photoneutron source. Activation foils were irradiated at this experimental position, where the higher neutron flux would be attained in the KULS.

2.2 Activation foils and reactions

Eleven kinds of activation foils were selected in the present measurement. Table 1 shows the diameter, thickness and purity of the activation foils used. Most of these foils are same as those that the authors have often used in the previous activation measurements[6-9]. Fourteen nuclear reactions measured in this experiment are summarized in Table 2, including the half lives, gamma-ray energies and intensities.

2.3 Irradiation and induced activities

Four irradiation runs were performed with the following linac operating conditions: pulse width of 33 ns, repetition rate of 30 Hz, electron peak current of about 2 A and the electron energy of about 32 MeV, respectively, which corresponded to the electron beam power of about 63 W. Four or five foils were selected for four hours irradiation, which was repeated four times, because it was rather difficult to irradiate the whole foils at once from the points of the experimental space and/or

conditions. Finally, the fourteen reactions were measured at the central region in the KULS. The experimental normalization between the runs was made by gold and aluminum foils which were commonly put in each set of the irradiation foils. Gamma-rays from the induced activities were measured with the HPGe detector, whose detection efficiency had been calibrated with standard sources of mixed radioactive nuclei purchased from the Amersham. The reaction rates and the uncertainties obtained are shown in Table 3.

3. Calculation

The energy spectrum of neutrons at the position where activation foils were irradiated in the KULS has been calculated with the continuous energy Monte Carlo code MCNP[12]. In this calculation, the initial photoneutron source spectrum from lead was taken from the experimental data obtained by the neutron time-of-flight method[13]. The geometrical parameters and the size of the KULS were referred to the actual size[10], 1.5 x 1.5 x 1.5 m^3. The MCNP code has its own nuclear data library, which were generated from the evaluated data file ENDF/B-IV and used for the calculations. The code can give us not only steady state neutron spectrum but also time dependent neutron spectrum after the fast neutron burst was produced in the photoneutron target. In the present calculation, we have firstly obtained the neutron time behavior or the slowing-down time spectrum in the KULS. Finally, the time dependent neutron spectrum was integrated over a few tens milli-seconds from the burst trigger to get the steady state scalar neutron spectrum from 0.01 eV to 20 MeV.

4. Spectrum Adjustment

Multi-foul activation data have been successfully applied to adjust and obtain neutron spectra by using the NEUPAC code and the SAND-II type code NEUSPEC. The principle of the NEUPAC code, which was developed by Nakazawa et al.[5], is due to the J-1 type unfolding method[5,14,15] which gives an approximate solution with the Bayes' theorem. The NEUPAC code contains energy dependent group cross section libraries including the error matrices for main important neutron dosimetry reactions in ENDF/B-V. These constants with 135 groups were processed by the N-JOY code[16] in the energy range from 0.01 eV to 16.4 MeV. In the NEUPAC calculation, variance-covariance errors for every input data and initial neutron spectrum are required. The output gives not only neutron spectrum with its covariance errors but also relating integral quantities and their uncertainties. The chi-squares tests in the calculation can be performed to check a physical validity of the resultant spectrum.

The SAND-II code[4] has been widely applied to the spectrum derivation using multi-foil activation techniques in a wide energy range from 0.1 meV to 20 MeV. The code named NEUSPEC was developed by the group at Institute of Atomic Energy who revised the original SAND-II code to deduce the analytical uncertainties using the Monte Carlo method[7,11]. The group cross sections of 642 energy bins for the NEUSPEC code were taken from the JENDL Dosimetry File which has been recently released[17]. In addition, 427 group constants of total and scattering cross sections have been prepared for the self-shielding correction in the foil[18].

The spectral result obtained with the MCNP code was used as an initial spectrum for the adjustment calculations with the NEUPAC and NEUSPEC codes.

5. Results and Discussion

Energy spectrum of scalar neutron fluxes at the central region of the KULS has been calculated from 0.01 eV to 20 MeV with the MCNP code. Figure 2 shows the result at the position where the activation foils were irradiated at the distance of 15 cm from the photoneutron target. The statistics due to the Monte Carlo calculation seem to be poor in the lower energy region although the histories of random number were 100,000. The uncertainties would be thought to be in the band of the spectrum derivation. The calculated results were used as an initial neutron spectrum for the spectrum adjustments using the NEUPAC and NEUSPEC codes.

Neutron spectra in the KULS have been adjusted in the energy region from 0.01 eV to 20 MeV with the multi-foil activation data, using the NEUPAC and NEUSPEC codes. The results are shown in Fig. 2, where the MCNP calculation is also given for the comparison. The spectral uncertainties in these adjusted results are 2 to 3 % at least and 7 to 8 % above 10 MeV and below a few hundreds keV, where the activation responses are poor. The neutron spectra by the NEUPAC, NEUSPEC and MCNP codes are, in general, good agreement with each other. Some deviations observed among the adjusted flux spectra are due to the lack of responses of the activation data to control the adjustments in the spectrum analysis. Spectral shape in these calculated and adjusted results is, in general, close to that of photoneutron source spectrum in the MeV region, and harder than that of 1/E spectrum in the neutron slowing-down energy region. By the Cd ratio measurements using Au and Mn foils, it was found that there exist scarcely thermal neutrons in the KULS, as observed in Fig. 2.

6. Conclusion

By making use of the NEUPAC and the SAND-II type code NEUSPEC, neutron spectra in the KULS have been adjusted with fourteen kinds of activation data in the energy region from 0.01 eV to 20 MeV. The results obtained were also compared with that by the Monte Carlo code MCNP. Good agreement was seen, in general, between the spectra adjusted by the NEUPAC and NEUSPEC code and also between the MCNP and the adjusted spectra. Some discrepancies were observed in the energy region where the responses of the activation data were poor at energies above 10 MeV and below several eV. The problems would be improved and more reliable spectrum would be obtained when more reaction rate data which cover the whole energy range are employed.

References

1) A. A. Bergman, et al., Proc. 1st Int. Conf. on Peaceful Uses At. Energy, 4, 135 (1955).
2) A. Yamanaka, et al., Proc. of the 1991 Symp. on Nuclear Data, published in this JAERI-M report (1992).
3) R. E. Slovacek, et al., Nucl. Sci. Eng., 62, 455 (1979).
4) W. N. McElroy, et al., Nucl. Sci. Eng., 27, 533 (1967).
5) M. Nakazawa and A. Sekiguchi, Proc. of the 2nd ASTM-Euratom Symp. on Reactor Dosimetry, NEUREG/CP-0004, Vol.3, p.1423 (1977).
6) K. Kobayashi, et al., Annu. Rep. Res. Reactor Inst. Kyoto Univ., Vol.20, 1 (1987).
7) K. Kobayashi, et al., Proc. of the 3rd Asian Symp. on Research Reactor, held on 11-14 Nov. 1991, at Hitachi, p.526, JAERI (1991).

8) I. Kimura and K. Kobayashi, Nucl. Sci. Eng., 106, 332 (1990).
9) K. Kobayashi, et al., Proc. of the 7th ASTM-Euratom Symp. on Reactor Dosimetry, held on 27-31 Aug. 1990, at Strasbourg, France, in print.
10) Y. Nakagome, et al., Proc. of the 1991 Symp. on Nuclear Data, published in the JAERI-M report (19992).
11) Z. Li, et a., Proc. of the 7th ASTM-Euratom Symp. on Reactor Dosimetry, held on 27-31 Aug. 1990, at Strasbourg, France, in print.
12) Los Alamos National Laboratory, LA-7396-M, Rev.2 (1986).
13) K. Kobayashi, et al., Nucl. Sci. Eng., 99, 157 (1988).
14) T. Taniguchi, et al., NEUT Res. Rep. 83-10 (1983).
15) M. Nakazawa, et al., J. Fac. Eng., Univ. Tokyo, A-22, 44 (1984).
16) R. E. MacFarlane, et al., LA-9303 M (1982).
17) M. Nakazawa, et al., in print as JAERI report.
18) Argonne National Laboratory, ANL-5800, 2nd Ed., p.667 (1963).

Table 1 Activation foils used for the present measurement

Material (Foil)	Diameter (mm)	Thickness (mm)	Purity (%)
Au	10.0	0.05	99.99
MnCu	12.7	0.2	84.34
Co	12.7	0.177	99.9
W	12.7	0.127	99.95
Mg	12.7	0.127	99.78
Al	12.7	0.5	99.95
Ti	12.7	0.3	99.7
Ni	12.7	0.5	99.8
Fe	12.7	0.5	99.99
Zn	12.7	0.3	99.99
In	10.0	0.15	99.99

Table 2 Nuclear reactions, half lives, gamma-ray energy and its intensity

No.	Reaction	Half life	γ -ray energy (MeV)	γ -ray intensity (%)
1	$^{197}Au(n,\gamma)^{198}Au$	2.696 d	0.412	95.5
2	$^{55}Mn(n,\gamma)^{56}Mn$	2.676 h	0.8468	98.87
3	$^{59}Co(n,\gamma)^{60}Co$	5.271 y	1.173	100.0
4	$^{186}W(n,\gamma)^{187}W$	23.85 h	0.6858	29.3
5	$^{24}Mg(n,p)^{24}Na$	15.02 h	1.369	100.0
6	$^{27}Al(n,p)^{27}Mg$	9.46 m	0.8438	73.0
7	$^{27}Al(n,\alpha)^{24}Na$	15.02 h	1.369	100.0
8	$^{46}Ti(n,p)^{46}Sc$	83.80 d	0.8893	100.0
9	$^{47}Ti(n,p)^{47}Sc$	3.422 d	0.1594	68.5
10	$^{48}Ti(n,p)^{48}Sc$	43.67 h	0.9833	100.0
11	$^{58}Ni(n,p)^{58}Co$	70.79 d	0.8108	99.44
12	$^{54}Fe(n,p)^{54}Mn$	312.2 d	0.8348	100.0
13	$^{64}Zn(n,p)^{64}Cu$	12.70 h	0.511	35.8
14	$^{115}In(n,n')^{115m}In$	4.486 h	0.3362	45.9

Table 3 Reaction rates and uncertainties for the present measurement

No.	Reaction	Reaction rates x 10^{-20}	Uncertainties (%)
1	$^{197}Au(n,\gamma)^{198}Au$	45882.2	3.11
2	$^{55}Mn(n,\gamma)^{56}Mn$	2299.75	3.06
3	$^{59}Co(n,\gamma)^{60}Co$	6302.87	3.30
4	$^{186}W(n,\gamma)^{187}W$	20299.1	3.30
5	$^{24}Mg(n,p)^{24}Na$	10.9195	4.91
6	$^{27}Al(n,p)^{27}Mg$	26.9827	5.98
7	$^{27}Al(n,\alpha)^{24}Na$	5.3125	3.63
8	$^{46}Ti(n,p)^{46}Sc$	75.6741	9.86
9	$^{47}Ti(n,p)^{47}Sc$	243.426	4.57
10	$^{48}Ti(n,p)^{48}Sc$	2.8025	7.50
11	$^{58}Ni(n,p)^{58}Co$	721.384	3.26
12	$^{54}Fe(n,p)^{54}Mn$	534.498	8.56
13	$^{64}Zn(n,p)^{64}Cu$	417.486	3.45
14	$^{115}In(n,n')^{115m}In$	2429.76	5.61

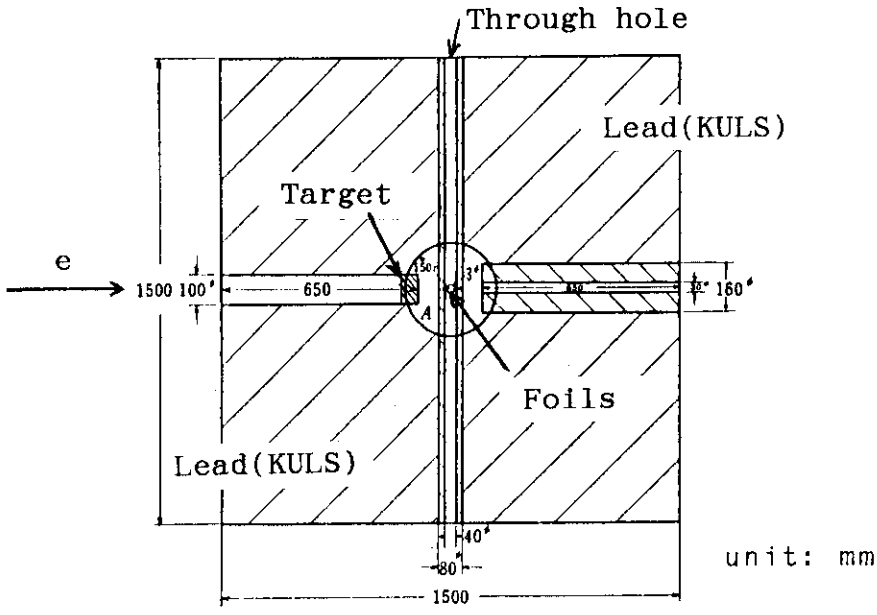

Fig. 1 Plane view of the KULS. Activation foils were put at the center of the through hole distant 15 cm from the photoneutron target.

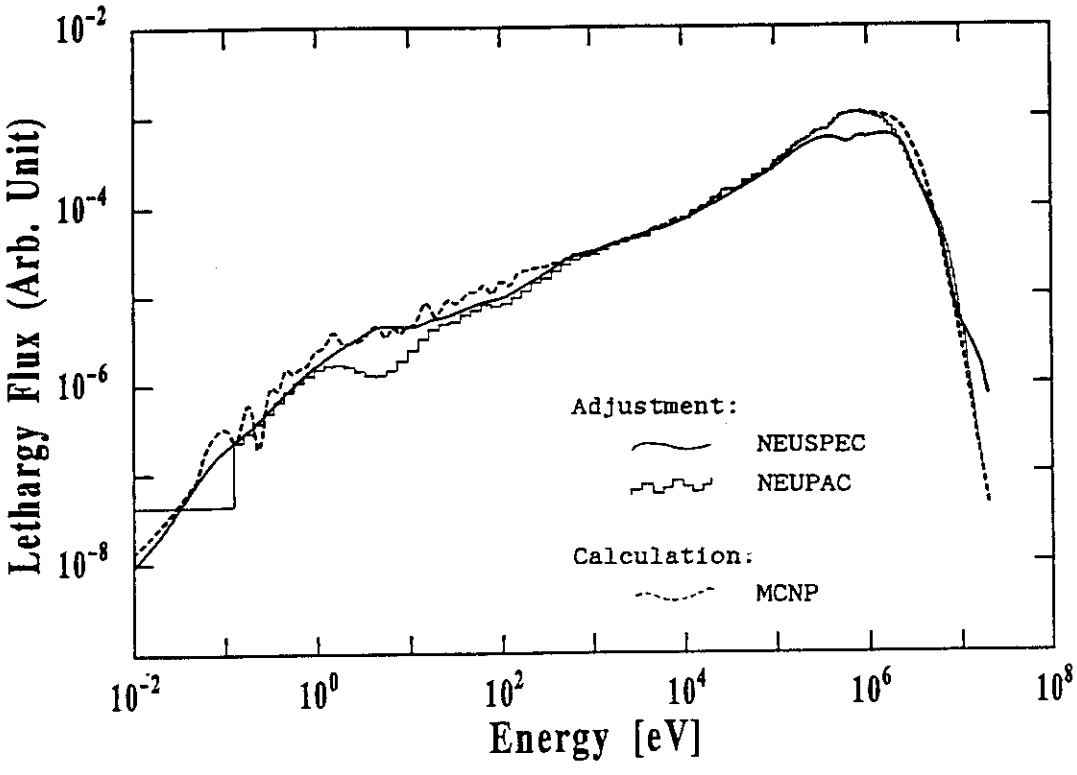

Fig. 2 Neutron spectra adjusted with the multi-foil activation data by the NEUSPEC and NEUPAC codes and calculated by the MCNP code.

3.23 THERMAL REACTOR BENCHMARK CALCULATIONS USING ENDF/B-VI BASED WIMS CROSS SECTION LIBRARY

Jung-do Kim and Choong-Sup Gil
Korea Atomic Energy Research Institute
P.O.Box 7, Daeduk-danji, Daejon, Korea

Abstract

The latest version of the U.S. evaluated data library, ENDF/B-VI, was released in recent year by the U.S. NNDC at BNL. In order to test an applicability of the newly released data to thermal reactor problems, an ENDF/B-VI based 69-group cross section library was generated with the NJOY 89.31 processing system. And then a number of thermal critical experiments were analyzed with the WIMS-KAERI code. This report presents the thermal reactor benchmark results. The lattices analyzed are TRX, BAPL-UO_2, ZEEP and three Savannah River Laboratory lattices.

1. Introduction

In nuclear design analysis for reactor, nuclear data are of the primary importance. Uncertainties in cross section data can result in excessive reactor design and operating margins, which are manifested as economic penalties to utilities. In recent year, the latest version of the U.S. evaluated nuclear data library, ENDF/B-VI[1], was released by the U.S. NNDC at Brookhaven National Laboratory on behalf of the U.S. CSEWG. In order to test an applicability of the newly released data to thermal reactor problems, an ENDF/B-VI based 69-group cross section library was generated with the NJOY 89.31 processing system. And then a number of thermal critical experiments were analyzed with the cell code WIMS-KAERI. In Sec. 2 the scope of benchmark testing are described. The procedures for data processing are explained in Sec. 3. Lattice cell calculations are stated in Sec. 4. Calculated criticalities and lattice parameters are compared with measured data and/or ENDF/B-V data, and the results are discussed in Sec. 5.

2. Scope of Testing

The U.S. CSEWG[2] has recommended a variety of integral experiments for checking the data of interest for thermal reactor calculations. The study reported here considered a number of these benchmark lattices, and in addition, one series of lattice that has been suggested as benchmark, and one series that was not accepted as benchmark.

The benchmark lattices include the following series : TRX, BAPL-UO_2, ZEEP and Savannah River Laboratory natural uranium/D_2O single rod lattices.

The Westinghouse experiments known as the TRX lattices are frequently quoted as standards for benchmark calculations. The lattices were H_2O-moderated, fully reflected, simple assemblies operated at room temperature. The fuel rods were of uranium metal clad in aluminum. Those of BAPL-UO_2 series were of high-density uranium oxide. ZEEP series[3] consists of a D_2O-moderated lattices of natural uranium metal. Savannah River Laboratory[4] had provided precise measurements of the material bucklings of D_2O-moderated lattices of natural uranium metal rods. Three lattices of them (lattice number 1-7-I, 1-8-I and 1-9-II) were selected in this calculation. Brief characteristics of the lattices are summarized in the following.

Lattice	Fuel	Cladding	Moderator	Fuel Radius(cm)	Mod.-to-Fuel Volume Ratio	
TRX-1~2	1.3% enriched U-metal	Al	H_2O	0.4915	2.35,	4.02
BAPL-1~3	1.3% enriched UO_2	Al	H_2O	0.4864	1.43, 2.40	1.78,
ZEEP-1~3	natural U-metal	Al	D_2O	1.6285	40.43, 13.97	10.13,
SRL-1~3	natural U-metal	Al	D_2O	1.26746	53.05, 95.18	71.09,

The following integral parameters were measured at the center of each lattices : the epithermal to thermal ratio of U-238 capture (ρ^{28}) and of U-235 fission (δ^{25}), the ratio of U-238 capture to U-235 fission (C*), and the ratio of U-238 fission to U-235 fission (δ^{28}). Also measured were axial and radial bucklings in the full lattices.

3. Data Processing

The data processing to convert ENDF-6 formatted source data to 69-group data requires a number of routines such as pointwise, Doppler-broadening, thermal scattering kernel, self-shielding, group weighting etc. For these, the NJOY 89.31[5] data processing system and an auxilliary routine, WIMSKR, were used. The RECONR reconstructs ENDF/B resonance representations and interpolation laws so as to obtain a pointwise ENDF tape. In the BROADR the cross sections are Doppler broadened and thinned. The UNRESR is used when self-shielded average cross sections for the unresolved energy region are required, and the THERMR is used to compute energy-to-energy thermal scattering kernels and the thermal elastic scattering cross sections. The GROUPR is used to obtain multigroup averages. The final WIMSKR routine is used to prepare data for the WIMS-KAERI library. In the group averaging, a combined Maxwellian + 1/E + fission spectrum was used for weighting. The thermal portion is Maxwellian with a temperature of 0.0253 eV which joins 1/E at 0.1 eV. The fission spectrum joins 1/E at 674.0 keV and has a characteristic temperature of 1.27 MeV. In this processing, a weighting flux of uranium nuclides was produced by a pointwise solution of the slowing down equations for the heavy absorber mixed with a light moderator in order to take accurately account of broad and intermediate resonance effects in the epithermal region. Fission spectra of U-235 were generated from Madland-Nix type data. Processed materials in ENDF/B-VI are the followings :

Nuclide	MAT.	Nuclide	MAT.
1-H-1	125	13-Al-27	1325
1-H-2	128	92-U-235	9228
8-O-16	825	92-U-238	9237

* Scattering Law Data (H in H_2O, D in D_2O) : ENDF/B-III

4. Calculations

The cell calculations were made using the WIMS-KAERI code, which is a KAERI version of WIMS/D4[9] code. The WIMS code is a general code for reactor lattice cell calculations on a wide range of reactor systems. The basic library has been compiled with 14 fast groups, 13 resonance groups and 42 thermal groups. The treatment of resonances is based on the use of equivalence theorems with a library of accurately evaluated resonance integrals for equivalent homogeneous systems at a variety of temperatures. In the present calculations, the cylindrical cell approximations were used to simplify the geometry of the cell. Solution of the transport equation was performed by use of the discrete ordinates method with eight discrete angular distributions and leakage was treated by the Benoist and B1 method. Calculated results were compared with the measurements and ENDF/B-V benchmark results reported by Craig.

5. Results and Discussion

A number of critical experiments were analyzed using measured bucklings as input to fundamental mode calculation. These calculations give only approximate eigenvalues due to the uncertainties in the experimental bucklings, but still serve as an indicator of the reliability of multigroup cross section library.

Benchmark data testing of the TRX and BAPL-UO_2 series using ENDF/B-V cross sections has been done by a number of organizations in the U.S.[7] and AECL in Canada[3]. The calculated results are compared in Table 1 and 2 with measurements and results reported by Craig. Table 1 gives the calculated eigenvalues for the H_2O- and D_2O-moderated criticals, respectively. The result gives an average K-effective value of 0.9966 for H_2O-moderated and 0.9997 for D_2O-moderated lattices. And the average K-effective for these 11 lattices is 0.9983. There is a tendency for the ENDF/B-VI using WIMS-KAERI code to underestimate eigenvalues of the H_2O-moderated lattices. Table 2 gives the ratios of calculation-to-experiment (C/E) values for the integral lattice parameters. The values of ρ^{28} for all lattices compared are high, and the values of δ^{25} are low. ENDF/B-VI results of δ^{25} are lower than ENDF/B-V results. Figures 1 to 4 show the differences between the ENDF/B-V and VI results. Comparison of calculated reaction rates in TRX-1 and TRX-2 is given in Table 3. The differences of δ^{25} are from epithermal reaction rate values. Figures 5 to 8 show the comparisons for the 69-group absorption cross sections of U-235 and U-238, and fission spectrum of U-235 in ENDF/B-V and VI. Figure 6 shows well low fission cross sections of ENDF/B-VI in the resolved resonance region.

Reference

1. H.D.Lemmel, IAEA-NDS-100 Rev.3 (1990)
2. P.F.Rose et al., BNL-19302(1981)
3. D.S.Craig, AECL-7690 Rev.1(1984)
4. T.J.Hurley et al., Nucl. Sci. Eng., 12, 341(1962)
5. R.E.MacFarlane, LA-UR89-2057(1989)
6. J.R.Askew et al., J.Br.Nucl. Energy Soc. 5,564(1966)
7. J.Hardy, Jr., BNL-NCS-31531(1981)

Table 1 Calculated infinite and effective multiplication factors

Lattice	K-inf.		K-eff.	
	ENDF/B-V	ENDF/B-VI	ENDF/B-V	ENDF/B-VI
TRX -1	1.18310	1.17467	0.99583	0.99424
TRX -2	1.16857	1.16063	0.99775	0.99348
BAPL-UO2 -1	1.14953	1.13730	1.00398	0.99885
-2	1.15346	1.14183	1.00401	0.99830
-3	1.13885	1.12866	1.00433	0.99796
ZEEP -1	1.23893	1.22938	1.00360	0.99932
-2	1.17968	1.16787	1.00161	1.00017
-3	1.13339	1.12293	1.00089	1.00006
SRL -1		1.22916		0.99936
-2		1.23201		0.99942
-3		1.22510		1.00000

ENDF/B-V values are from reference 3.

Table 2 Ratios of calculation-to-experiment values of lattice parameters

Parameter	TRX-1		TRX-2	
	ENDF/B-V	ENDF/B-VI	ENDF/B-V	ENDF/B-VI
ρ^{28}	1.034	1.049	1.012	1.039
δ^{25}	1.020	0.966	1.005	0.953
δ^{28}	1.045	1.061	1.012	1.026
C*	1.003	1.015	0.991	1.005

Parameter	BAPL-UO2 -1		BAPL-UO2 -2		BAPL-UO2 -3	
	ENDF/B-V	ENDF/B-VI	ENDF/B-V	ENDF/B-VI	ENDF/B-V	ENDF/B-VI
ρ^{28}	1.005	1.036	1.035	1.071	1.001	1.035
δ^{25}	1.007	0.964	1.013	0.971	1.017	0.981
δ^{28}	0.976	1.000	0.933	0.957	0.940	0.965

ENDF/B-V values are from reference 3.

Table 3 Comparison of calculated reaction rates in TRX-1 and TRX-2 lattices

. TRX -1

Nuclide	Reaction	Energy Range	ENDF/B-V	ENDF/B-VI	Ratio (VI/V)
U-235	Capture	Epithermal	0.01511	0.01365	0.90
		Thermal	0.05751	0.05715	0.99
	Fission	Epithermal	0.03355	0.03190	0.95
		Thermal	0.33316	0.33460	1.00
U-238	Capture	Epithermal	0.16904	0.17207	1.02
		Thermal	0.12390	0.12428	1.00
	Fission	Epithermal	0.03628	0.03678	1.01

. TRX -2

Nuclide	Reaction	Energy Range	ENDF/B-V	ENDF/B-VI	Ratio (VI/V)
U-235	Capture	Epithermal	0.00985	0.00891	0.90
		Thermal	0.06121	0.06076	0.99
	Fission	Epithermal	0.02203	0.02088	0.95
		Thermal	0.35670	0.35673	1.00
U-238	Capture	Epithermal	0.11140	0.11398	1.02
		Thermal	0.13146	0.13147	1.00
	Fission	Epithermal	0.02655	0.02684	1.01

ENDF/B-V values are from reference 3.

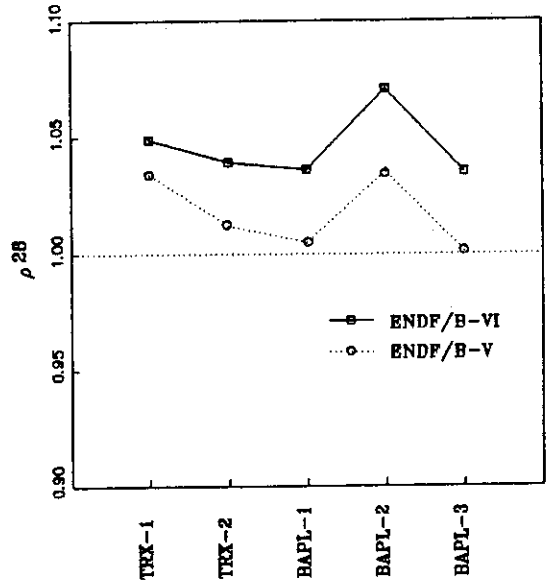

Fig. 1 C/E values of epithermal to thermal ratio of U-238 capture for TRX and BAPL-UO_2 lattices.

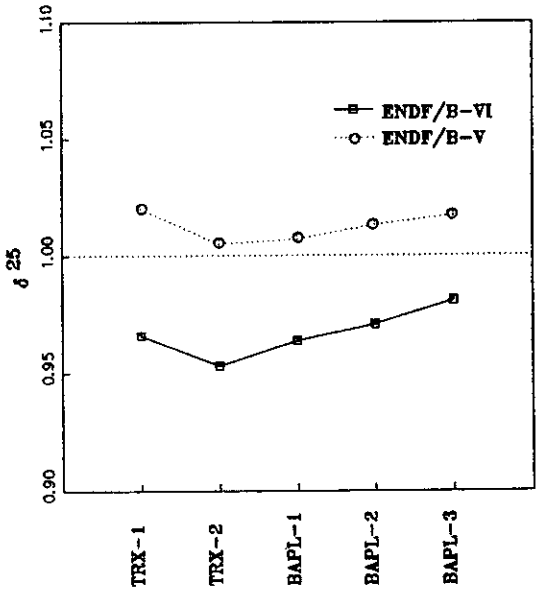

Fig. 2 C/E values of epithermal to thermal ratio of U-235 fission for TRX and BAPL-UO_2 lattices.

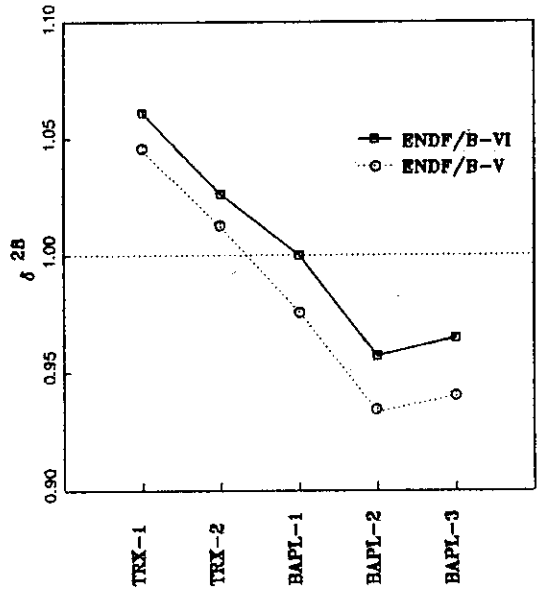

Fig. 3 C/E values of ratio of U-238 fission to U-235 fission for TRX and BAPL-UO_2 lattices.

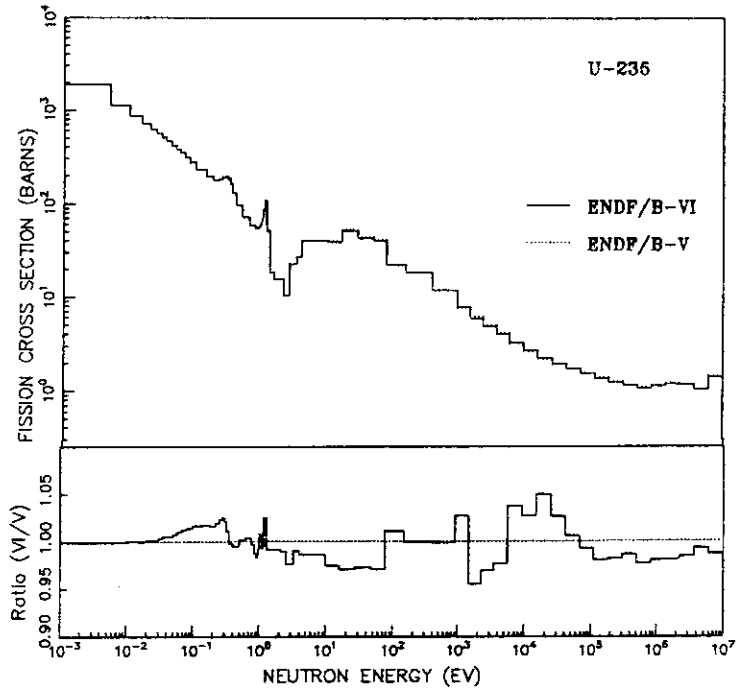

Fig. 4 Fission cross section of U-235.

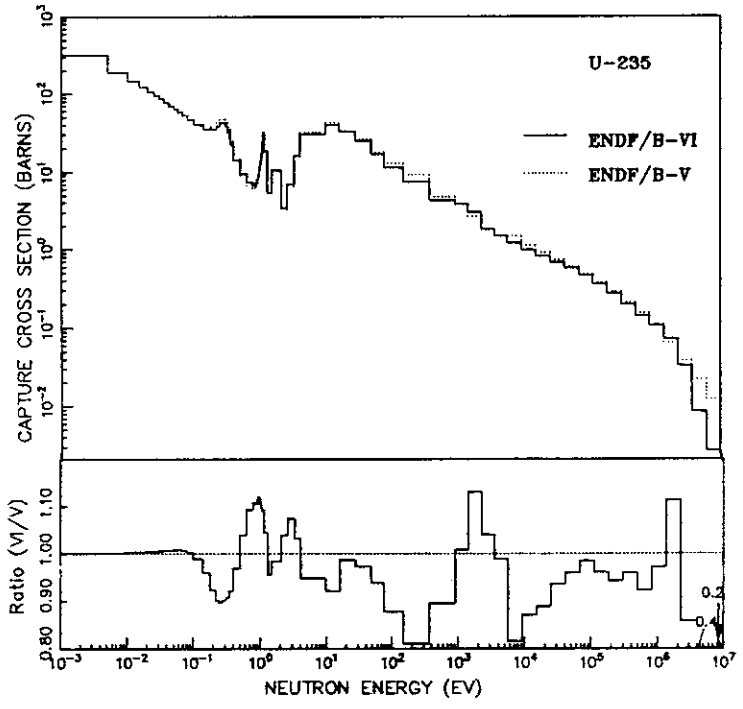

Fig. 5 Capture cross section of U-235.

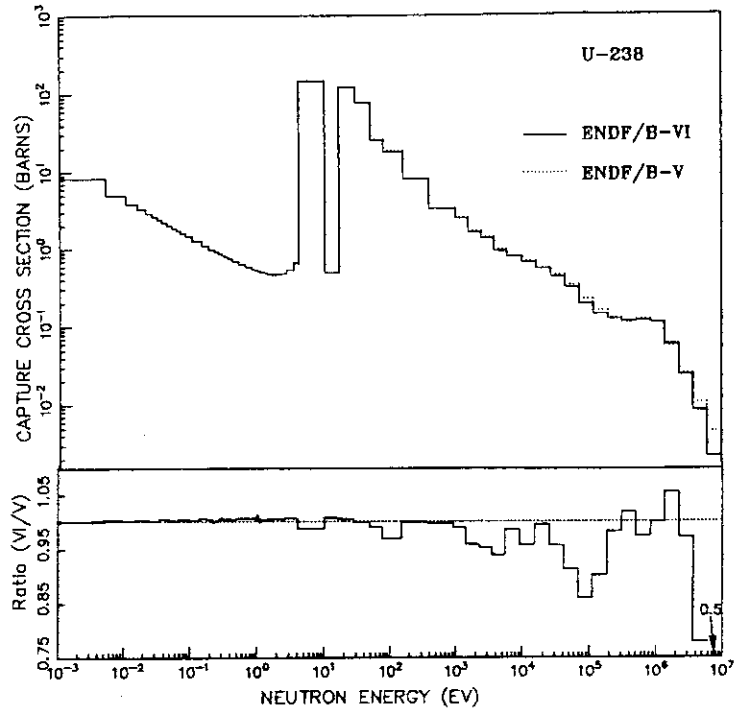

Fig. 6 Capture cross section of U-238.

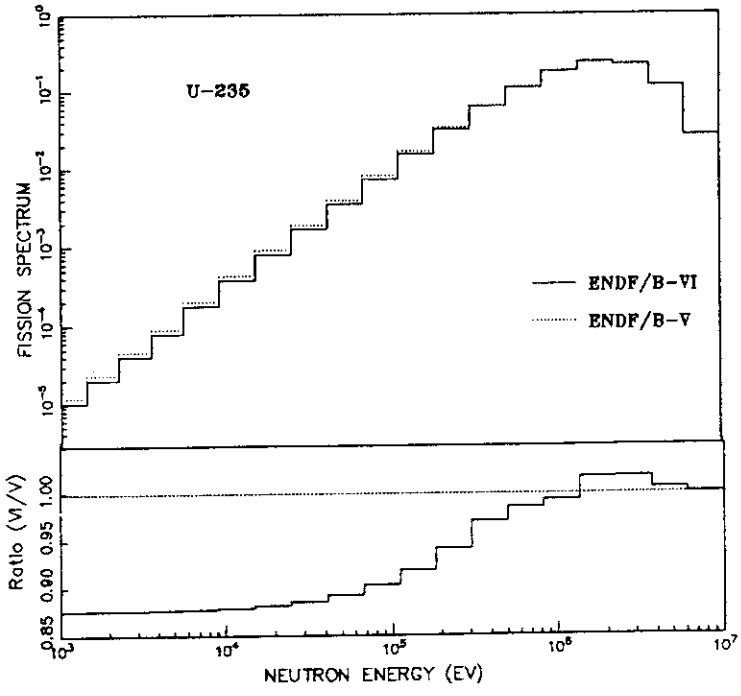

Fig. 7 Fission spectrum of U-235.